Petrology and mineral chemistry of shallow intrusive carbonatites: examples from the Kola Peninsula and Cape Verde

Barbara Smith
Principal Supervisor: Prof Hilary Downes

Submitted in fulfillment of the requirements for a PhD,
Birkbeck University of London

I Barbara Smith hereby declare that this thesis and the work presented in it is entirely my own. Where I have consulted the work of others, this is always clearly stated.

Signed: Barbara Smith Date: 19/06/2022

DEPARTMENT OF EARTH AND PLANETARY SCIENCES

ABSTRACT

Analysis of hypabyssal carbonatite and associated silicate rocks from three locations was undertaken to establish the processes leading to their textural and chemical diversity. Carbonatite dykes from Vuorijarvi (Kola Peninsula) show good evidence of magmatic processes and were least affected by fenitization. Globular calcite and apatite inclusions in silicate phases indicate precipitation from a silicate melt; subsolidus recrystallisation of olivine to monticellite implies an early stage of carbonatite formation; complex substitution in perovskite formed Zr-garnet. Occurrences of xenocrysts suggest extensive wall-rock interaction. Primary tabular calcite was replaced by secondary mosaic calcite, and amphibole was formed by early fenitisation. Calcite and apatite host LREE; Zr-garnet and perovskite show strong compatibility for Zr, Nb and all REE.

Hypabyssal carbonatites of Fogo, Cape Verde, contain glimmerite sheets which formed hydrothermal pathways in which accessory minerals crystallised. Shearing also formed pathways for oxidised low-temperature REE-rich hydrothermal fluids which caused veined and pervasive K- and Na-fenitization that modified the texture and chemistry of primary phases. Hf-bearing phlogopite is associated with Hf-poor titanite, zirconolite, zircon and pyrochlore; Nb-Th-U-rich pyrochlore formed via hydrothermal dissolution of Zr-rich precursors; post-magmatic changes progressively altered magnetite to titanomagnetite, ilmenite, garnet and titanite. Calcite and apatite are the main trace-element-bearing phases; post-magmatic garnet and titanite are enriched in REEs and U, Th and Nb.

Carbonatites and syenites from Brava, Cape Verde, show extensive fenitisation. Sövites contain primary (Sr-calcite, Ca-strontianite, carbocernaite), metasomatic (parisite) and hydrothermal (burbankite, barite) phases. Apatite and calcite show several orders of REE enrichment. Clinopyroxene evolved from diopside towards aegirine enriched in Zr, Th, U and LREEs; amphibole is both primary and secondary; phlogopite mica evolved towards late-stage phengite and pennantite; magnetite progressively formed titanomagnetite, ilmenite, titanite, rutile and henrymeyerite. Lower temperature Mn-, Sr- and Zr-rich hydrothermal fluids exploited fractures, forming LREE-, Zr-rich hilairite, REE-törnebohmite; rhabdophane, lanthanite and LREE-rich ilmenite.

CHAPTER 1

INTRODUCTION TO CARBONATITES

1.1 Definition of carbonatites

Carbonatites are very unusual and rare igneous rocks that are volumetrically minor with respect to silicate rocks. Carbonatites are mainly composed of carbonate minerals (>50% as defined in the IUGS system), some silicates, phosphate minerals such as apatite, and minerals from the humite group. Carbonatites are often associated with alkaline silicate rocks. An idealised section through a carbonatite complex is shown in Fig. 1.1.

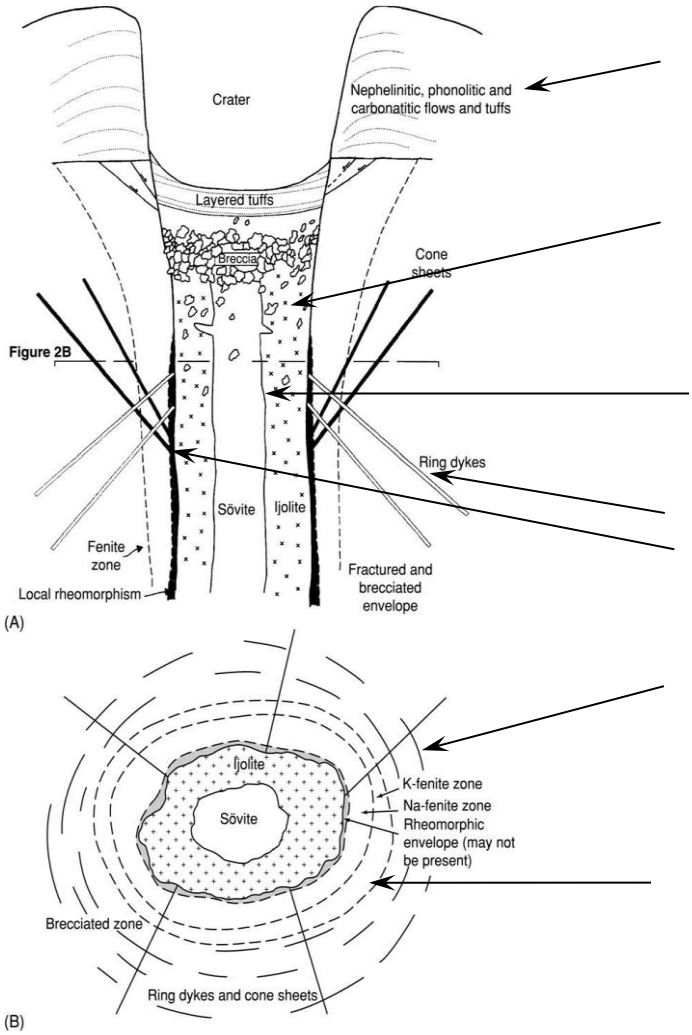

Extrusive carbonatites (lava, spatter, lapilli)

Early silicate rocks cut by carbonatite

Intrusive sövite, coarse carbonatite rock

Hypabyssal carbonatites are often the last events to occur:
ring dykes
cone sheets
and dykes

Plan view showing the concentricity of the intrusion (carbonatites and rocks associated with carbonatites)

Fenite aureoles (loss of alkalis from carbonatites to surrounding rocks)

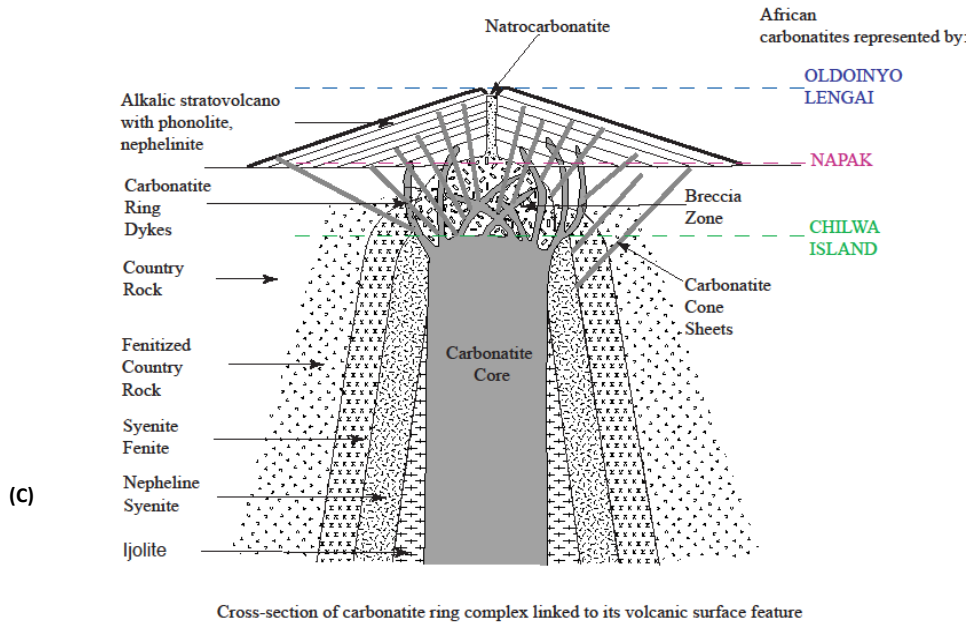

Fig. 1.1 Idealised section through a carbonatite complex: A) cross section, B) bird's eye view. A) and B) modified after Sage and Watkinson (1991). C) a representative cross-section of a carbonatite-bearing alkaline ring complex with an indication of the nature of the volcanic and subvolcanic products shown on different (erosional) levels as can be observed in East Africa. Different extrusive styles are included such as lava, pyroclastic deposits and intrusive carbonatite core which could be interpreted as sövites C) modified after Bowden (1985).

A glossary of terms for carbonatites and associated rocks is given in Table 1.1. Different kinds of carbonatites vary in their chemical and mineralogical composition (Table 1.1). The classification follows the IUGS sub-commission on the systematic of igneous rocks (Le Maitre, 1989). This study mainly will focus on silico-carbonatites as many samples from Fogo and Brava contain > 20 wt% SiO_2 and calcio-carbonatites that contain < 10 wt% SiO_2 (minority of Brava and Fogo samples). Analysed silica-rich carbonatites from Vuoriyarvi are uncommon (forming only 10-20% of samples), reflecting an unusual assemblage and a xenogenic origin of some minerals.

Figure 1.2 shows a map of the locations of carbonatites worldwide (Woolley and Kjarsgaard, 2008) with emphasis on the locations of the carbonatites analysed in this study. The locations are the Vuoriyarvi complex in the Devonian Kola Alkaline Province (NW Russia), and two oceanic islands in the Cape Verdes (eastern Atlantic Ocean) in which the carbonatites form part of the uplifted seamount series. Carbonatites from the Kola Alkaline Province and Cape Verde fundamentally differ in tectonic setting, being continental and oceanic respectively (Bell, 2001), but both are associated with plume activity (Gwalani et al., 2010). Marty et al. (1998) linked generation of Kola carbonatites with a mantle plume source by analysing the noble-gas data; Dunworth and Bell (2001)

ROCK TYPES	BRIEF ROCK DESCRIPTION	ROCK-FORMING MINERALS	ACCESSORIES	REFERENCE
Sövite (calcite carbonatite)	A coarse-grained carbonatite consisting of calcite (more than 50%)	Primary calcite, apatite, subordinate phlogopite, monticellite, pyroxene, alkali amphibole	Zr-Ti garnets, perovskite, Fe-Ti-oxides, baddeleyite, pyrochlore,	Woolley and Kempe, 1989
Älvikite	A medium to fine-grained variety of calcite carbonatite	Mainly calcite	Apatite, phlogopite, titanite, pyrochlore	Le Bas, 1999
Beforsite and rauhaugite	Magnesiocarbonatite, coarser and finer grained variety respectively	Dolomite is the dominant carbonate mineral	Apatite, phlogopite, zircon, pyrochlore	Woolley and Kempe, 1989 Seifert et al., 2000
Ferrocarbonatites. subdivided to: siderite cbt, ankerite cbt, hematite-calcite cbt (cbt=carbonatite)	A variety of carbonatite in which the main minerals is iron-rich: ankerite, siderite, hematite-calcite respectively	Dominant ankerite/siderite/hematite-calcite and minor calcite	Rutile, magnetite, pyrochlore	Drüppel et al., 2005 Gittins and Harmer, 1997
Natrocarbonatite	Alkali-rich porphyritic carbonatite (known only as an effusive product)	Composed of rare sodium and potassium carbonate minerals, nyeryite etc.	Fluorite and sylvite	Gittins and Jago, 1998
Fenite	Metasomatised country rock (aureoles) associated with alkaline/carbonatite complexes	Na- and K-rich minerals: K-feldspar, plagioclase, nepheline, aegirine	Na-amphiboles, apatite, silicates	Smith, 2007
Phoscorite	A medium to coarse-grained igneous ore-rock associated with carbonatites	Magnetite, forsterite (or diopside), apatite	Tetraferri-/phlogopite, baddelyite, pyrochlore, zirconolite	Lee et al., 2006
Olivinite	Originally: ore-bearing olivine rocks. Later: olivine plutonic rock. Additionally: olivine-rich rocks with accessory magnetite to distinguish from dunite with accessory chromite	Mainly olivine, pyroxene, amphibole	Magnetite	Le Maitre, 2002

Aillikite	Carbonate-rich ultramafic lamprophyres	Macrocrysts or phenocrysts of olivine, phlogopite, clinopyroxene in a carbonatite matrix	Ti-garnets, rutile, apatite, perovskite	Tappe et al., 2006 Tappe et al., 2009
Glimmerite	An ultrabasic rock consisting almost wholly of dark mica	Phlogopite or biotite and could be present substantial amounts of apatite	Clinopyroxene, illmenite	Becker et al., 1999
Ijolite	A coarse-grained rock consisting of 1/3 pyroxene and 2/3 feldspathoid	Augite and nepheline	Apatite, cancrinite, calcite, titanite, iivaarite (garnet)	Wittke and Holm, 1996
Syenite	A coarse-grained rock consisting essentially of feldspars and small amounts of quartz	Orthoclase and plagioclase (such as albite)	Quartz and ferromagnesian minerals	Le Maitre et al., 2002
Nepheline syenite	Variety of syenite containing nepheline	Nepheline, clinopyroxene, K-feldspar	Apatite, biotite, titanite	Le Maitre et al., 2002
Nephelinite	Variety of volcanic rock consisting of nepheline and clinopyroxene	Nepheline, diopside, Fe-Ti-oxides	Olivine	Simonetti et al., 1995
Pyroxenite	Plutonic rock with dominant pyroxene	Clinopyroxene and /or orthopyroxene	Phlogopite/biotite, amphibole, olivine	Streckeisen, 1973
Silico-carbonatite	Carbonatite with SiO_2 content > 20 wt%	Primary carbonate mineral and apatite with subordinate phlogopite, monticellite, pyroxene, alkali amphibole, feldspar, feldspathoids etc	Pyrochlore, Ti-Zr-Nb-rich phases, zeolites etc.	Le Maitre et al., 2002

Table 1.1 Glossary of names of carbonatites and associated rocks used in this study. Classification follows the IUGS sub-commission on the systematics of igneous rocks (Le Maitre, 1989). Additional references are given.

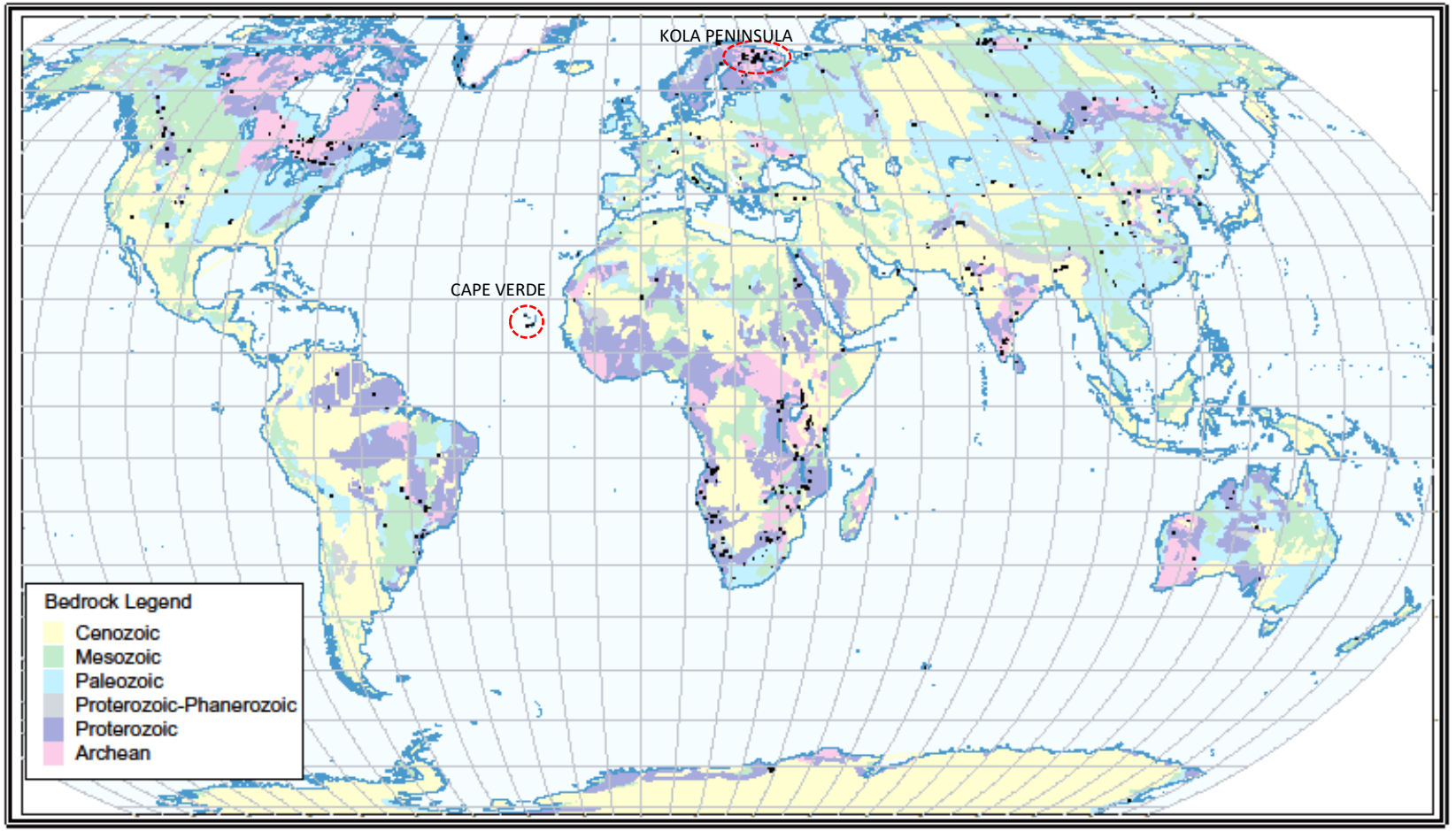

Fig. 1.2 Worldwide distribution of carbonatites showing the age of the bedrock and locations of study areas (Modified after Woolley and Kjarsgaard, 2008 "World Carbonatite Map").

went further by favouring a model involving a lower-mantle plume influence.

Intrusive carbonatites are the most commonly found because extrusive ones are easily weathered and eroded. The petrology of shallow intrusive carbonatites is the subject of this thesis. Intrusive carbonatites can be emplaced in a range of depths. Shallow hypabyssal bodies can form small plugs, dykes or pipe-like carbonatitic complexes usually consisting of annular or cylindrical bodies, many less than 5 km across. The process of fenitization (alteration) is often associated with such intrusions, as alkali-rich fluids are expelled during crystallisation of carbonatites via a network of fractures forming aureoles in surrounding country rock (Elliott et al., 2018). Na-fenitization is found frequently at deeper levels and formed earlier at higher temperatures (>600ºC). Thus, Na would remain close to a carbonatite intrusion (deeper levels) but K shows higher mobility and can move to higher (shallower) levels in the crust.

1.2 Literature review – origin of carbonatites

Carbonatites can originate in several different ways, e.g., as mantle-derived primary liquids (Dawson, 1966; Wallace and Green, 1988; Gittins, 1989), by liquid immiscibility (Le Bas, 1977; Kjarsgaard and Hamilton, 1989; Mitchell 2005; Jones et al. 2013), or by fractional crystallisation (Watkinson and Wyllie, 1971; Lee and Wyllie 1994; Veksler et al. 1998). For example, Yang et al. (2011) recognised three types of carbonatite (dolomite-carbonatite, calcite-carbonatite and calcite-dolomite carbonatite) in the Bayan Obo complex (China). They showed that incompatible trace element (Sr and LREE) contents increased due to crystal fractionation from dolomite carbonatite, through calcite-dolomite to calcite carbonatite. In contrast, Weidendorfer et al. (2015) suggested that the carbonatites on Brava (Cape Verdes) were primarily formed by fractional crystallisation of alkaline silicate magmas leading to strong enrichment in alkalis and CO_2, which progressed to immiscibility between carbonatites and Si-undersaturated alkaline melts. Formation of carbonatites frequently involves a combination of two or three processes.

The genetic association of silicate-carbonate liquids was established by Le Bas et al. (1984) and Demeny et al. (1998). Ackerman et al. (2021) investigated the evolution of two carbonatite suites from East Africa and two from the western USA. These suites contain abundant silica-rich carbonatites in close proximity to “pure” carbonatite end-members. Ackerman et al. (2021) directly related both rock-types and showed that silica-rich carbonatites may represent a link between silicate and carbonate melts (Fig. 1.2). “Hydrous” Mg-rich carbonatites such as Sukulu (E Africa) and Lemitar (USA) have <10

wt.% SiO_2 and contain phlogopite ± olivine. "Dry" carbonatites such as Tororo (E Africa) and Iron Hill (USA) have higher SiO_2 (6–14 wt.%) and high alkali content with aegirine-augite present. The authors concluded that formation of carbonatitic magmas was intimately connected by progressive fractionation of parental silicate melts and carbonate melt segregation through liquid immiscibility (Fig. 1.2).

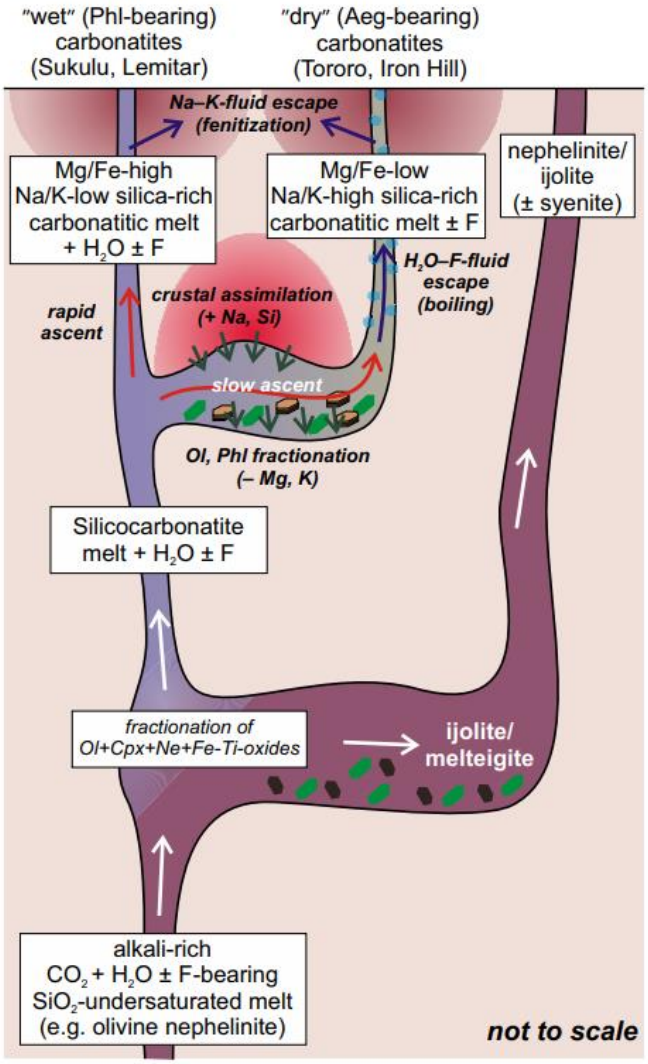

Fig. 1.**2**. Model of petrogenesis of silicocarbonatite–silica-rich carbonatite–carbonatite association, leading to silicate–carbonate melt separation, after Ackerman et al. (2021). Aeg = aegirine, Cpx = clinopyroxene, Ne = nepheline, Ol = olivine, Phl = phlogopite. Fractionation of parental carbonated (and H_2O–F-bearing) silicate melts would cause separation of silicate and carbonate melts. Next step would depend on Si–Na–K–Mg contents, water activity, and melt ascent rate. This model explains contrasting petrogenetic signatures of spatially-related carbonatites by different ascent rates. Rapidly ascending magmas would preserve the original mantle signature, but slower ascending melts may be more strongly affected by fractionation and assimilation processes and may gain a more crustal-like signature during its ascent.

An additional complication about the origin of carbonatites arises from the natrocarbonatite magma composition erupted at Oldoinyo Lengai volcano in Tanzania (Dawson, 1962; Cooper et al., 1975; Gittins and McKie, 1980). Some workers, e.g., Veksler et al. (1988) consider that all carbonatites were natrocarbonatites prior to losing

their alkali elements. In contrast, Weidendorfer et al. (2017) considered that natrocarbonatites are the final product of fractional crystallisation of Ca-carbonatites. Their experiments on natrocarbonatite from Oldoinyo Lengai showed that removal of CaO (fractional crystallisation of calcite and apatite) can move a carbonatite melt towards a natrocarbonatite. This proves that Na- and Ca-carbonatites have similar parental melts and that Ca-carbonatite magma was originally more alkaline than the composition of intrusive carbonatites might suggest. Le Bas (1987) emphasised the presence of fenites in many intrusive complexes and explained them as a result of the transfer of alkalis from a crystallising natrocarbonatite to the country rock.

Eggenkamp et al. (2020) investigated the behaviour of halogens in magmatic systems and showed that solubility of halogens in silicate magmas can be significant. Solubility of F is higher than that of Cl, though it increases with decreasing SiO_2 content. Eggenkamp et al. (2020) stated that peralkaline igneous rocks ((Na+K)/Al>1) show strong enrichment in halogens. These rocks also display high concentration in HFSE (Zr, Hf, Nb, Ta and U) and the REEs, leading to crystallisation of halogen-rich minerals. According to Kamenetsky et al. (2015), Cl reduces the mantle solidus temperature permitting carbonatite/carbonate-silicate melts to occur at lower temperature. Mangler et al. (2014) investigated halogens at Oldoinyo Lengai and their influence on silicate–natrocarbonatite melt separation. They showed that halogen abundances in natrocarbonatites and their alteration products can be similar to associated silicate rocks. Unaltered natrocarbonatite contains up to 3.6 wt% F and up to 5.9 wt% Cl. Although meteoritic alteration can leach out Cl from chlorine-rich minerals (e.g., gregoryite and sylvite) which are easily dissolved, F-rich minerals remain unchanged. Aiuppa et al. (2019) showed that silicate melt inclusions and matrix glass in alkali-rich tephrites and phonolites contain up to 1 wt% F. The carbonatites in this study contain apatite with up to 4 wt% F, so there is a strong possibility of the presence of F in the parental magmas.

The key influence of F and Cl is to lower the liquidus temperature in the virtually water-free natrocarbonatite melt (Mangler et al., 2014). Bell and Tilton (2002) stated that, because carbonatite melt has very low viscosity and density, it can rise swiftly through the crust, thus interaction with the crust is reduced to a minimum. Experimental work of Mattsson and Caricchi (2009) confirmed that carbonatitic magma has very low viscosity (as low as that of water) and a low temperature of crystallisation (around 630 ºC at 1atm pressure). This has a strong effect on the textures of intrusive carbonatites, as discussed in the next section.

1.3 Literature review – textures in intrusive carbonatites

Gittins (1979) and Andersen (1989) first recognised difficulties in the preservation of primary calcite features, as late- or post-magmatic recrystallisation often obliterates early magmatic features. Chakhmouradian et al. (2016) investigated textures and compositions of calcite in carbonatites. Strong emphasis was placed on the formation of carbonate minerals during magmatic processes but also alteration of the texture (and composition) of carbonate during post-magmatic processes such as fluid-rock interaction, deformation, etc. Old carbonatites and those emplaced at depths more than 3 km rarely preserve their original igneous textures (Chakhmouradian et al., 2016) but become recrystallised. Frequently "hybrid" carbonatite-silicate magmas develop either by immiscibility or fractional crystallisation where precipitation of silicate phases will proceed before reaching carbonate liquidus (Lee and Willie 1998a). Vuoriyarvi carbonatites investigated in this study contain high temperature early-crystallised silicate minerals like olivine and monticellite. In contrast, Cape Verde calciocarbonatites are considered to be associated with immiscibility (Mourão et al. 2012; Weidendorfer at al. 2016). Chakhmouradian et al. (2016) examined the textural variations of carbonate minerals formed during sub-solidus recrystallisation as well as textures formed by fragmentation and dissolution. Some globular textures have been interpreted as resulting from immiscibility between silicate and carbonatite melts (Kjarsgaard and Peterson 1991).

Comin-Chiaramonti et al. (2014) studying carbonatites and related rocks in Paraguay identified the presence of ocelli-like texture in a silicate rock (glimmerite) (Fig. 1.4). The restriction of differentiation of the CO_2-bearing melts, such as basanite to phonotephrite, assuming exsolution of small amounts of carbonatitic melt, can lead to in situ crystallisation of ocelli in the host alkaline rock. Nédli and Tóth (2003) analysed ocelli in alkali basalts from Hungary, which are mostly of globular shape, although they can be ellipsoidal or spherical, rarely irregular, often with core of one composition (e.g., carbonate) surrounded by a complex rim (e.g., clinopyroxene and rhönite) (Fig. 1.4b). Lee and Wyllie (1998a) indicated that formation of ocelli could be unrelated to immiscibility if crystallisation of globules from associated silicate rocks lack early precipitated silicate phases (Lee et al., 1994).

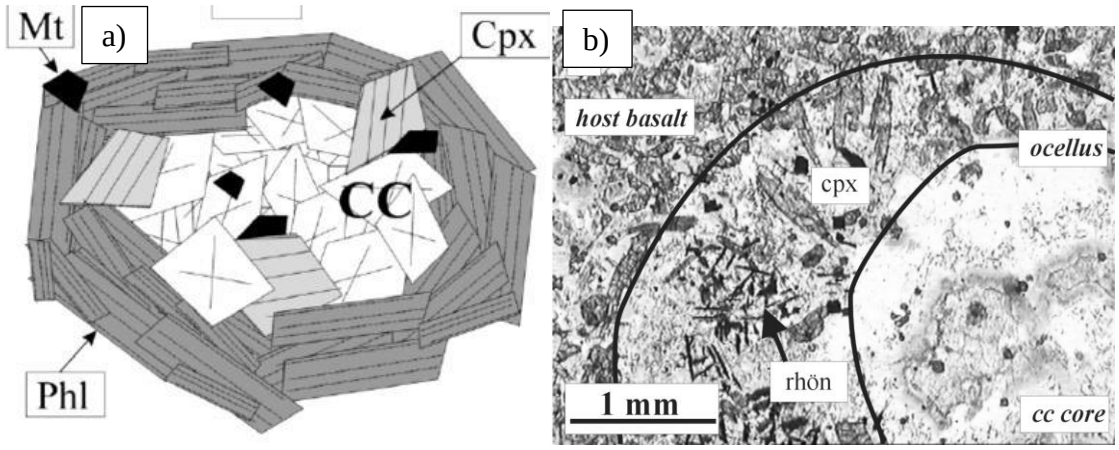

Fig. 1.4. a) Ocelli-like texture in glimmerites from Cerro Sarambí complex (Mt magnetite; Cpx clinopyroxene; Phl phlogopite; CC carbonate (FOV 2cm) (Comin-Chiaramonti et al., 2014). b) Typical ocellus with carbonate core surrounded by a complex rim with clinopyroxene and rhönite microphenocrysts (Nédli and Tóth (2003).

Moore et al. (2008) analysed silicocarbonatites in the Chagatai Complex (Uzbekistan) which contain globular textures consisting of microscopic magmatic enclaves of silicate composition and corroded microphenocrysts with crystal overgrowths. These textures were interpreted to represent magma mingling during rapid and turbulent rise of the carbonatite magma invading a silicate magma. This process is rarely recorded in nature. Figure 1.5 illustrates ocelli in investigated Cape Verde carbonatites.

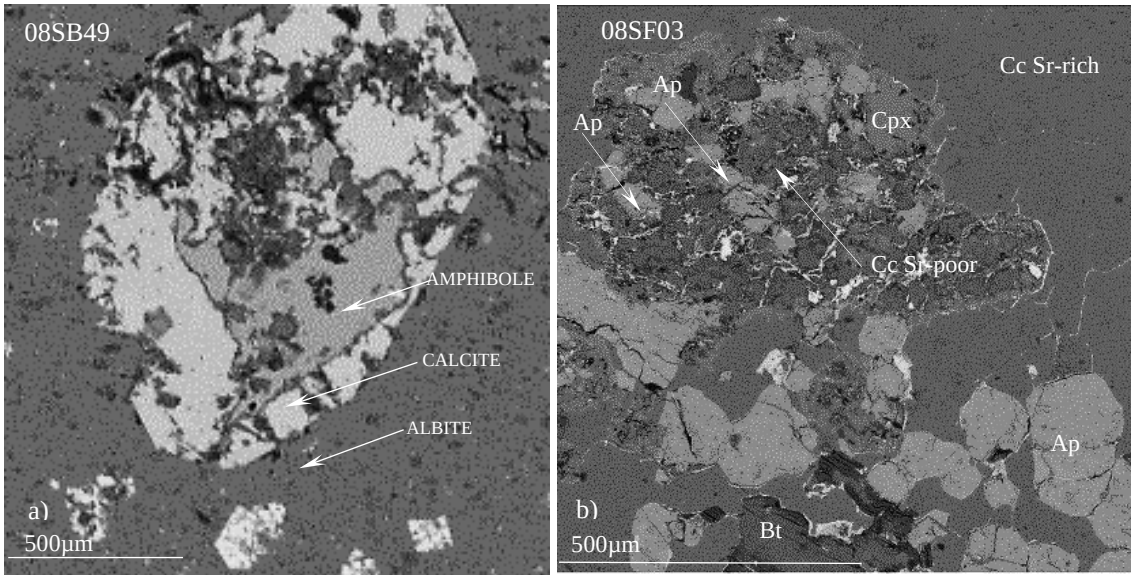

Fig. 1.5a Back-scatter electron (BSE) images of a) silicate ocelli in Brava feldspar/feldspathoid pegmatite (08SB49) and b) Fogo carbonatites 08SF03, analysed in this study.

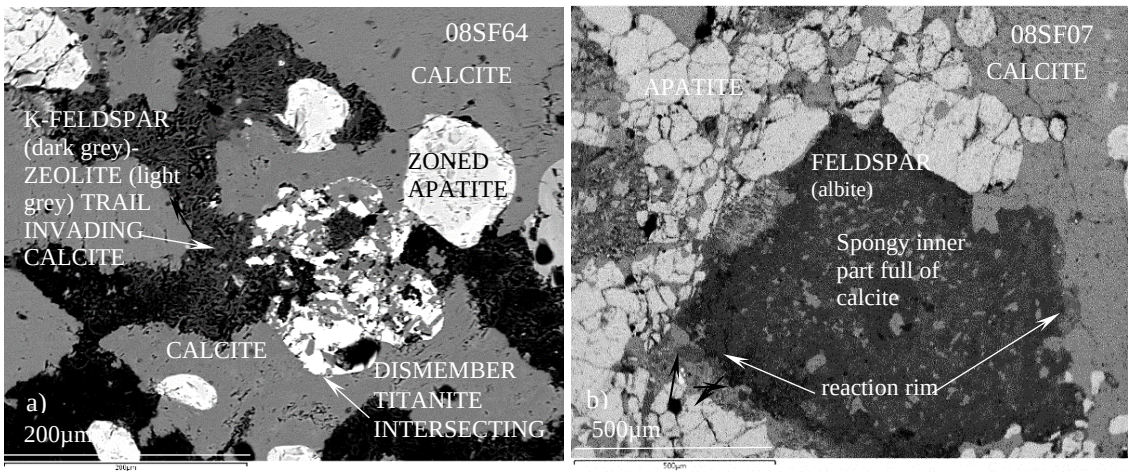

Fig. 1.5b Back-scatter electron (BSE) images of a) silicate trail invading calcite in carbonatite 08SF64 and b) ocellar texture with a single crystal core of albite mantled by apatite in carbonatite 08SF07. Both samples are from Fogo and are analysed in this study

Calcite is a dominant phase in the silico-carbonatites analysed in this study. The complexity of calcite texture depends on both primary and secondary processes that occur during the formation of carbonatites (Chakhmouradian et al., 2015). Understanding the textual variations of carbonates and other constituent phases is crucial to an appropriate assessment and interpretation of carbonatites, particularly whether they formed by magmatic or post-magmatic processes. Processes that can be deduced from textural analysis include exsolution, subsolidus re-equilibration, hydrothermal crystallisation and tectonic mobilisation. Chakhmouradian et al. (2016) established that well-preserved primary igneous textures of calcite in shallow intrusive carbonatite dykes can display spinifex-like texture near the chilled margins, progressively changing into tabular randomly orientated crystals near the centre, and finally reaching an equigranular texture at the centre of the body. Also, assimilation of the wall-rock is common in carbonatites, which can result in the presence of xenoliths. Such as xenoliths/xenocrysts are present in Vuoriyarvi carbonatite containing minerals incorporated from the associated pyroxenite (Fig. 1.6). Furthermore, Le Bas et al. (2004) and Tichomirova et al. (2013) investigated the occurrence of hybrid carbonatites composed of two or more different magmas, which naturally causes an increase in the petrographic complexity of carbonatites.

Post-magmatic deformation events can overprint the primary texture of carbonatites. Chakhmouradian et al. (2016) investigated the post-magmatic evolution recorded in carbonate textures such as diffusion of elements leading to zonation in primary calcite due to decreasing Sr and Ba content towards the crystal rim and in fractures. Elements released by deformation can form secondary minerals such as strontianite, barytocalcite and other Ba-Ca-Sr carbonates. Late-stage hydrothermal calcite can be redeposited in fractures in the form of drusy rhombohedral calcite. The late-stage

hydrothermal carbonates can crystallise over wide temperature range and can affect distribution of the Rare Earth Elements (REE). Inclusions of other phases in calcite would weaken it even more. Generally primary calcite is free from inclusions in samples from Cape Verdes analysed in this study, although secondary carbonates show alteration by invasion by hydrothermal fluids (Fig. 1.7).

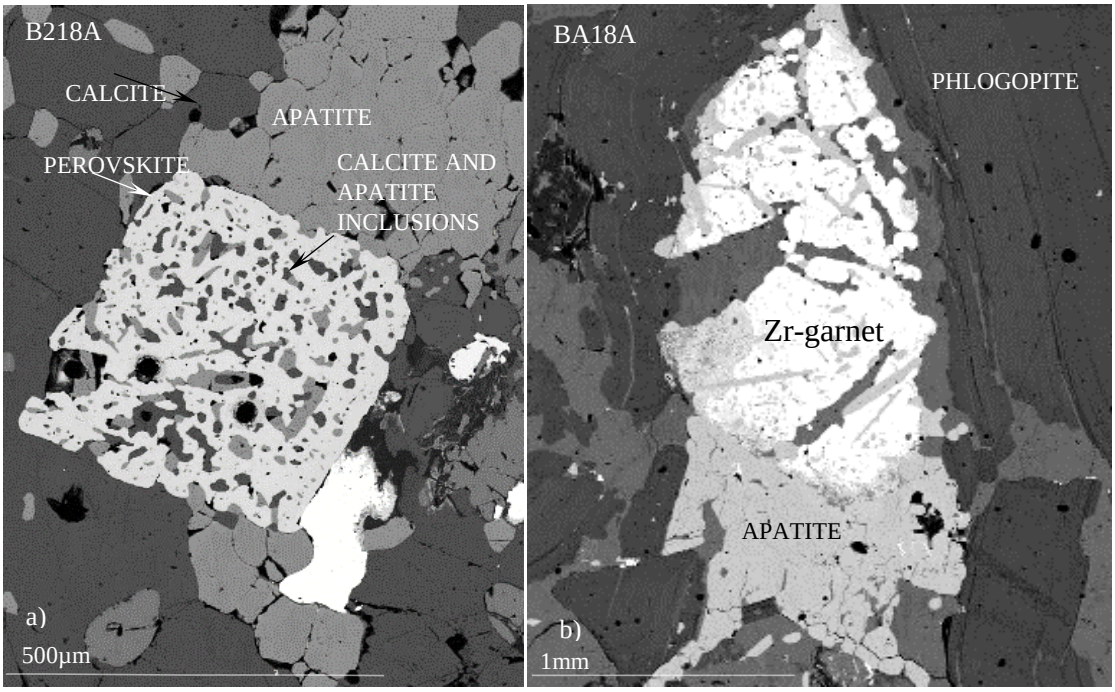

Fig. 1.6 BSE image showing xenocrysts/xenoliths in Vuoriyarvi carbonatites analysed in this study a) perovskite with inclusions of apatite and calcite. b) Zr-garnet converting to apatite.

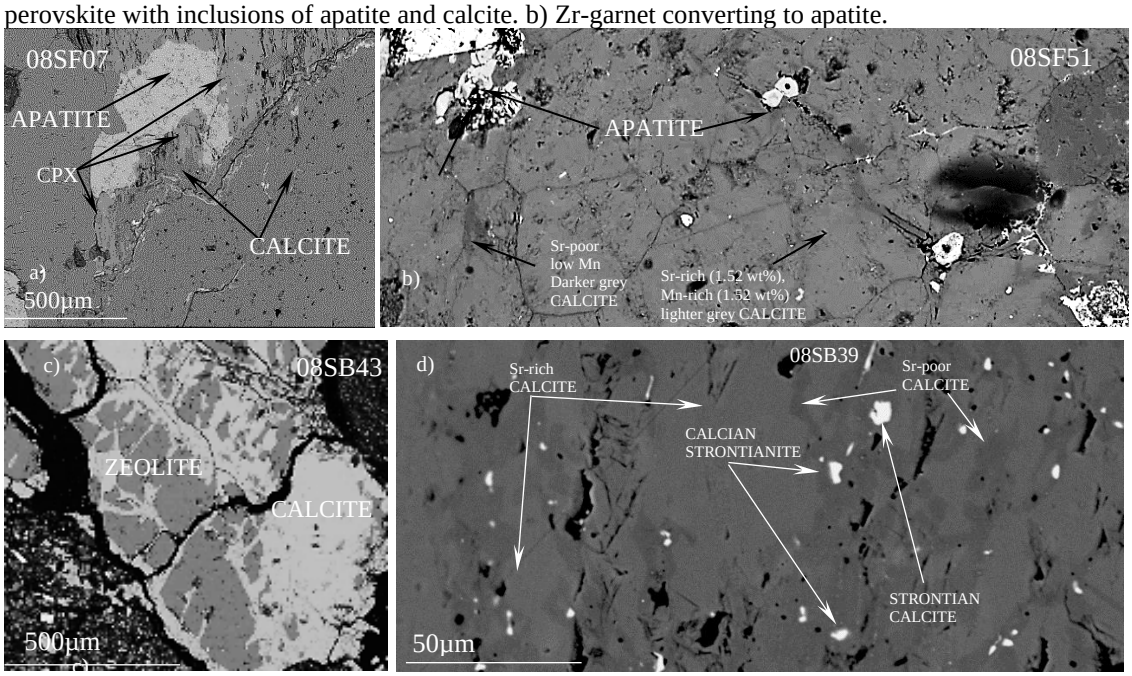

Fig. 1.7 a) BSE image of calcite containing inclusions of apatite and clinopyroxene in Fogo sample 08SF07. b) BSE image of calcite showing its association with apatite and varied Sr-Mn content in Fogo sample 08SF51. c) BSE image of calcite showing alteration to zeolite. d) BSE image of Brava sövite 08SB39 containing inclusion of calcian strontianite and strontian calcite.

Treiman and Schedl (1983) assessed processes in carbonatite magma chambers using extrapolations from scale model studies which emphasised the low viscosity of carbonatite magmas. They calculated that, if carbonatite magma would undergo only processes of convection (turbulent flow) and rapid settling of crystals >0.1 cm in diameter, leaving behind in suspension grains >0.01 cm, it would crystallise only fine-grained primary carbonates. Gravitational accumulation was evaluated by Treiman (1989) who showed settling of grains 0.5 mm in size, as larger crystals will not grow while suspended in the magma, giving rise to fine-grained cumulates. Consequently, coarse-grained textures are most probably associated with calcite crystallisation onto the walls of the carbonatite magma chamber (Treiman and Schedl, 1983), driven by conductive heat loss and aided by the rapid transport of ions giving rise to crystallisation *in situ*. Progressive metamorphic recrystallisation changes the structure of calcite from tabular to granular (Fig.1.8). Le Bas (1987) investigated Kerimasi carbonatites and distinguished high-Sr primary igneous (phenocrystic) calcite from low-Sr pseudomorphic calcite which contains detectable levels of Mg and Na. This is a convenient way to distinguish primary and secondary calcite in carbonatites.

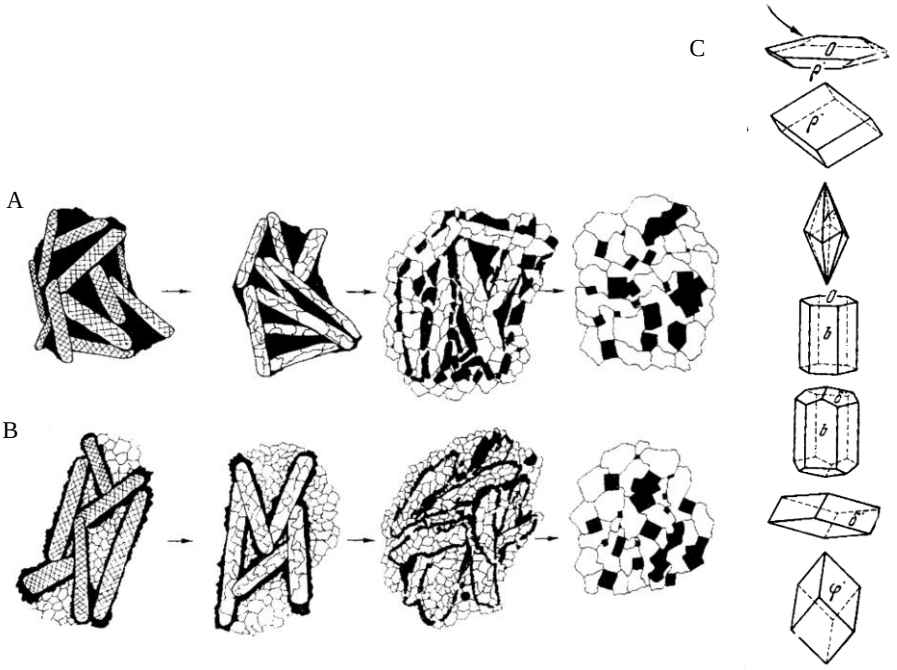

Fig. 1.8 A) and B) Schematic illustration showing metamorphic evolution (progressive recrystallisation from left to right) of primary calcite (cross-hatched) in carbonatites. Black areas consist of minerals like magnetite, olivine, apatite and clinopyroxene. The white represents granular calcite. A) Interstitial arrangement of mafics, opaques and apatite between tabular calcite. B) Coarse, bladed flow aligned calcite overgrown by equant mafics, opaques, olivine, pyroxene and apatite (dendritic texture similar to spinifex in komatiites) set in fine grained granular calcic groundmass. C) Evolution of calcite structure from the early, tabular expected to find in high temperature (flattened perpendicular to the c-axis) progressively changing with the falling temperature. From the top down common calcite forms: *0*(0001) – ρ*(10$\bar{1}$1) – κ(21$\bar{3}$1) – b(1010) – δ*(01$\bar{1}$2) – φ(02$\bar{2}$1). Modified after Aliev (1966) and Zhabin (1971).

As calcite is mechanically weak, plastic deformation can happen even with application of a small amount of any kind of pressure (e.g., flow of magma close to the wall, weight of crystallised magma, exsolution of vapour, penetrative deformation, slumping, etc) (Schmidt et al., 1981; Knapp and Norton, 1981; Treiman and Schedel, 1983). Treiman and Schedel (1983) concluded that the maximum flow velocity within the magma chamber is unable to keep crystals suspended and will not allow them to grow over 1 mm in size with a growth rate of cm/year on the chamber walls. Consequently, they concluded that the gneissic textures commonly found in carbonatites could be produced at sub-liquidus conditions through subsolidus plastic deformation. This texture is present in Cape Verde carbonatites analysed in this study (Fig. 1.9).

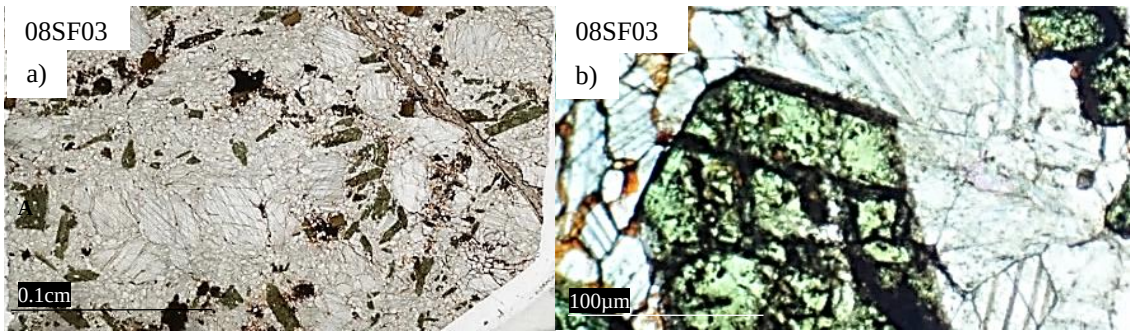

Fig. 1.9 a) Gneissic texture in pyroxene-rich sövite, Fogo 08SF03. b) Protruding prismatic clinopyroxene induced development of curved calcite lamellae (Fogo 08SF03).

Carbonatite magma has the property of an ionic liquid where silica forms mainly orthosilicate anions SiO_4^{4-} (Treiman 1989). Also, oxyanions of aluminium bear great importance in carbonatite genesis since most carbonatites contain aluminosilicate minerals (such as biotite). With a higher concentration of aluminosilicate anions, polymerised silica would form sheets/chains and would increase the viscosity of the melt. Furthermore, extensively polymerised anions would give rise to two separate immiscible melts (carbonatite and aluminosilicate).

Treiman (1989) also concluded that the low viscosity of $5x10^{-2}$ Pas enhances rapid crystal settling from carbonatite magma with settling velocity reaching 60 cm/sec for cm-size grains of common carbonatite minerals. In an intrusive system, the flow is turbulent. In plug-shaped intrusions rapid flow is also recognised. As fast ionic transport in carbonatites is responsible for rapid crystal growth, porphyritic and dendritic crystals can

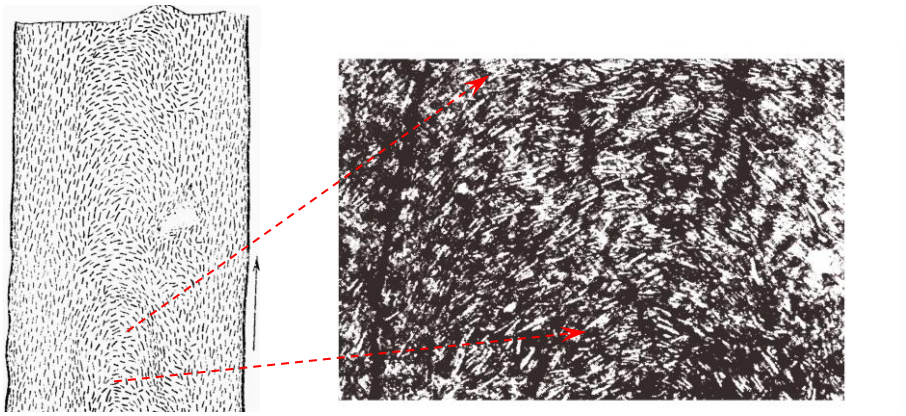

Fig. 1.10 Sketch of the outcrop (to the left) drawn in scale 2-3x smaller (typically carbonatite dykes are 15-20cm wide) showing flow alignment of the phenocrystic calcite in carbonatite dykes of Maimecha-Kotui province, Guli volcano-plutonic complex of the northern Siberian platform, Russia (after Zhabin, 1971). The appropriate photomicrograph in plane polarised light (to the right) showing higher magnification of the porphyritic texture (60-80% of the phenocrysts) of the tabular calcite with characteristic flow alignment.

be found with calcite showing a tabular form being large, monocrystalline and parallel to (0001) (Cooper and Reid, 1991). Fig.1.10 shows the texture of a carbonatite dyke, giving a snapshot of turbulent flow frozen in time, with the primary tabular calcite being aligned in a semi-circular manner. Treiman (1989) discussed the formation of this texture (Fig. 1.8), as in a fast turbulently flowing ionic liquid, the rapid settling of crystals would favour rather fine-grained igneous bodies. His explanation involves a process of emplacing carbonatite dykes in the form of crystalline mushes.

Moore et al. (2009) analysed globular magmatic enclaves of silicate composition in the Chagatai carbonatite-silicate Complex in Uzbekistan. They rejected the interpretation of the unusual texture by assimilation of the country rock and instead concluded that and other were caused by trachyte magma being entrained by carbonatite magma during rapid and turbulent ascent. Similar textures can be observed in hand specimens and thin sections from Cape Verdes carbonatites and associated silicate rocks analysed in this study (Fig 1.11).

Simandl and Paradis (2018) reviewed the association of carbonatite with alkali-silicate rocks and emphasised the significance of fenitization. Fenitizing fluids are critical regarding mobility of elements within carbonatite-alkaline complexes (Arzamastsev et al., 2011, Dowman et al., 2017, Elliot et al., 2018). Carbonatites from Vuoriyarvi and Cape Verdes analysed in this study were also affected by movement of Na and K from alkaline fluids (Fig. 1.12).

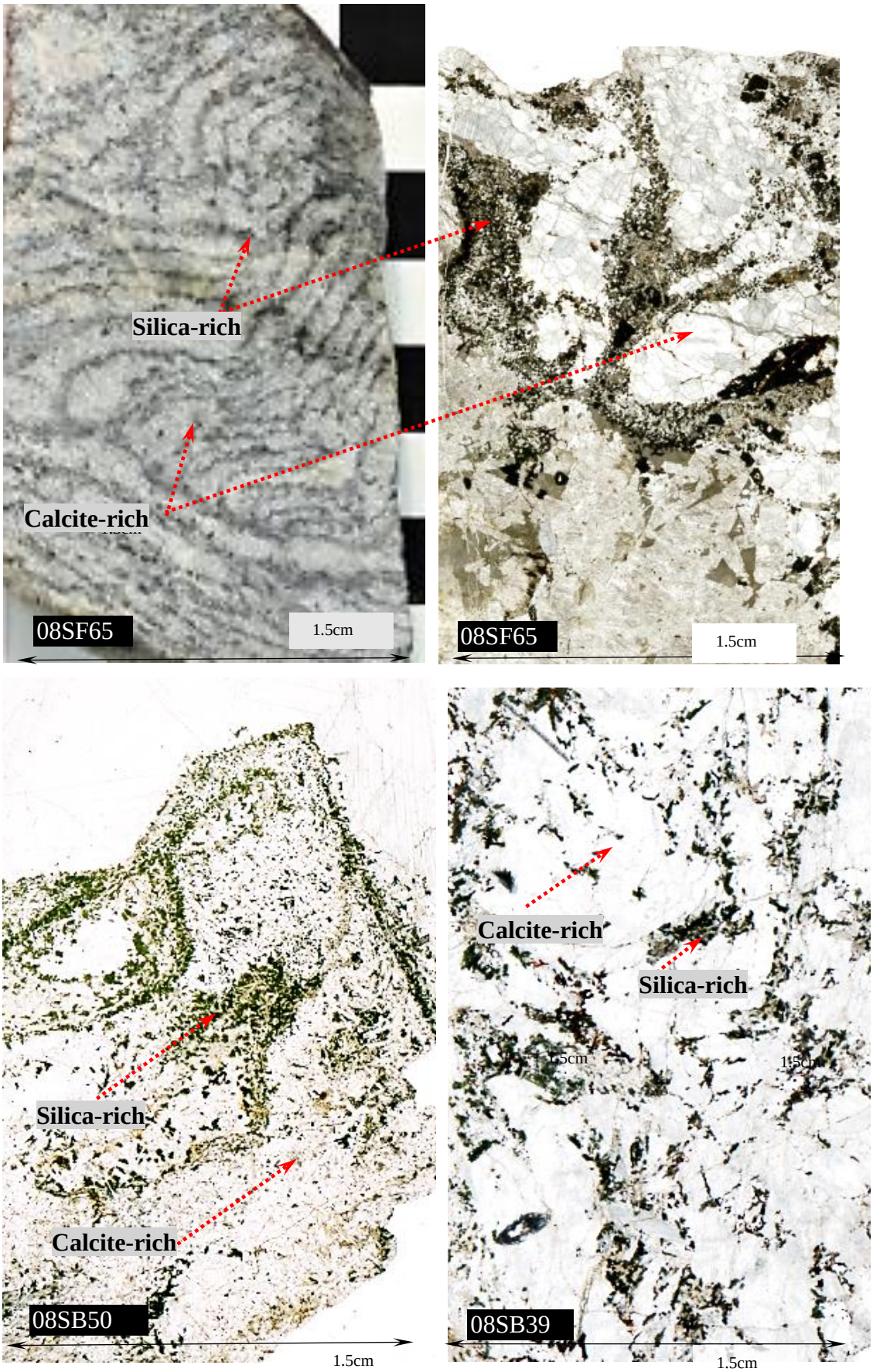

Fig. 1.11 Photograph of hand specimen of carbonatite from Fogo, displaying turbulent flow of carbonatite rimed by silica-rich fluid. Also scanned images of thin-sections of Fogo carbonatite (08SF65) and Brava syenite-calcite rock (08SB50) and silica-rich sövite (08SB39), showing textural association between carbonate-silicate rich regions in greater detail.

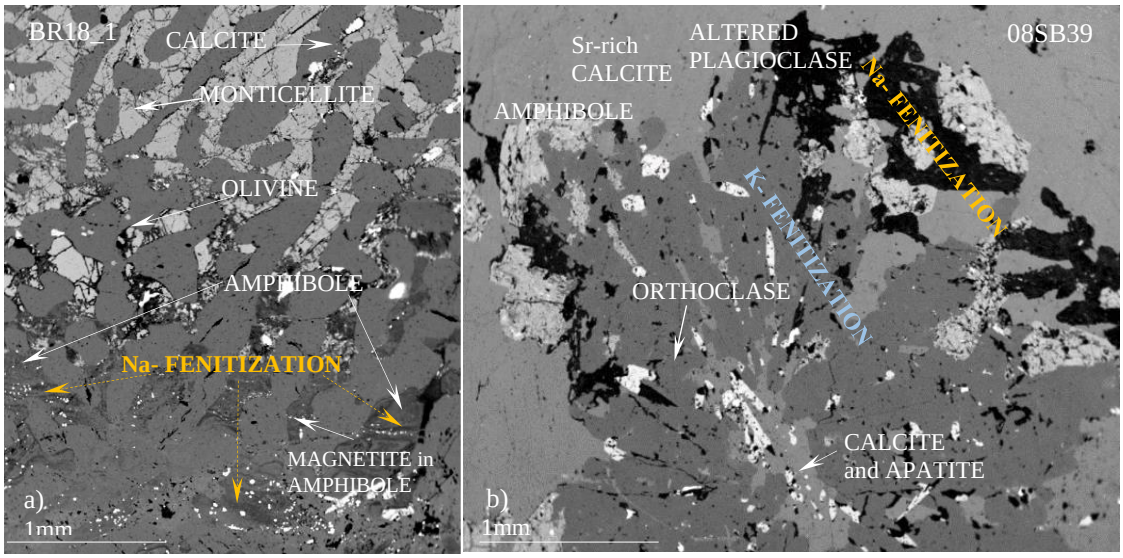

Fig 1.12 a) Backscatter electron image (BSE) of silico-carbonatite BR18_1 from Vuoriyarvi showing Na-fenitization. b) Brava carbonatite 08SB39 exhibits progressive evolution from K- to Na-fenitization with possible remnants of fenitizing fluid interacting with calcite thus forming Na-K carbonate.

1.4 Literature review – trace element geochemistry of bulk rock carbonatites

According to Wang et al. (2020), carbonatites contain the highest quantity of REEs amongst all igneous rocks, which makes them economically important. Chondrite–normalised patterns for incompatible elements in whole rock carbonatites. phoscorite and associated silicate rocks in the study areas of this thesis are presented in Fig. 1.13a. Doroshkevich et al. (2017) analysed the Belaya Zima carbonatite complex (Russia), showing that REE and HFSE mineralisation resulted from extensive fractionation of parental nephelinite magma. Rass et al. (2020) presented a study on the Kovdor carbonatite-phoscorite complex (Kola Peninsula). They established that separation from a silicate parental magma occurred during extensive fractional crystallisation, forming an Fe-rich phosphate-carbonatite liquid. Such liquids could subsequently split via immiscibility into separate carbonatite and phoscorite melts (Fig. 1.13a). According to the authors, they contain key trace elements such as Ti, Nb, and Zr which form multi-cation oxide minerals such as the perovskite, pyrochlore and ilmenite groups (Chakhmouradian, 2006; Chakhmouradian and Williams, 2004), which are more abundant in phoscorites than carbonatites. This separation can be seen in the trace element plots of bulk rock phoscorite (Zaitsev et al., 2015) and carbonatite compositions from Vuoriyarvi (Fig. 1.13a) which show a positive Hf-Zr and Nb-Th anomaly and lower MREE and HREE enrichment in phoscorite, while there are negative anomalies and higher REE enrichment in the carbonatite. Vuoriyarvi, Brava and Fogo carbonatites show negative Hf-Zr and Ta anomalies which is characteristic for carbonatites (Carnevale et

al., 2021). Lack of uniformity between the whole rock trace element composition in all Brava carbonatites is most likely due to processes affecting the ascending carbonatitic melts (Carnevale et al., 2021).

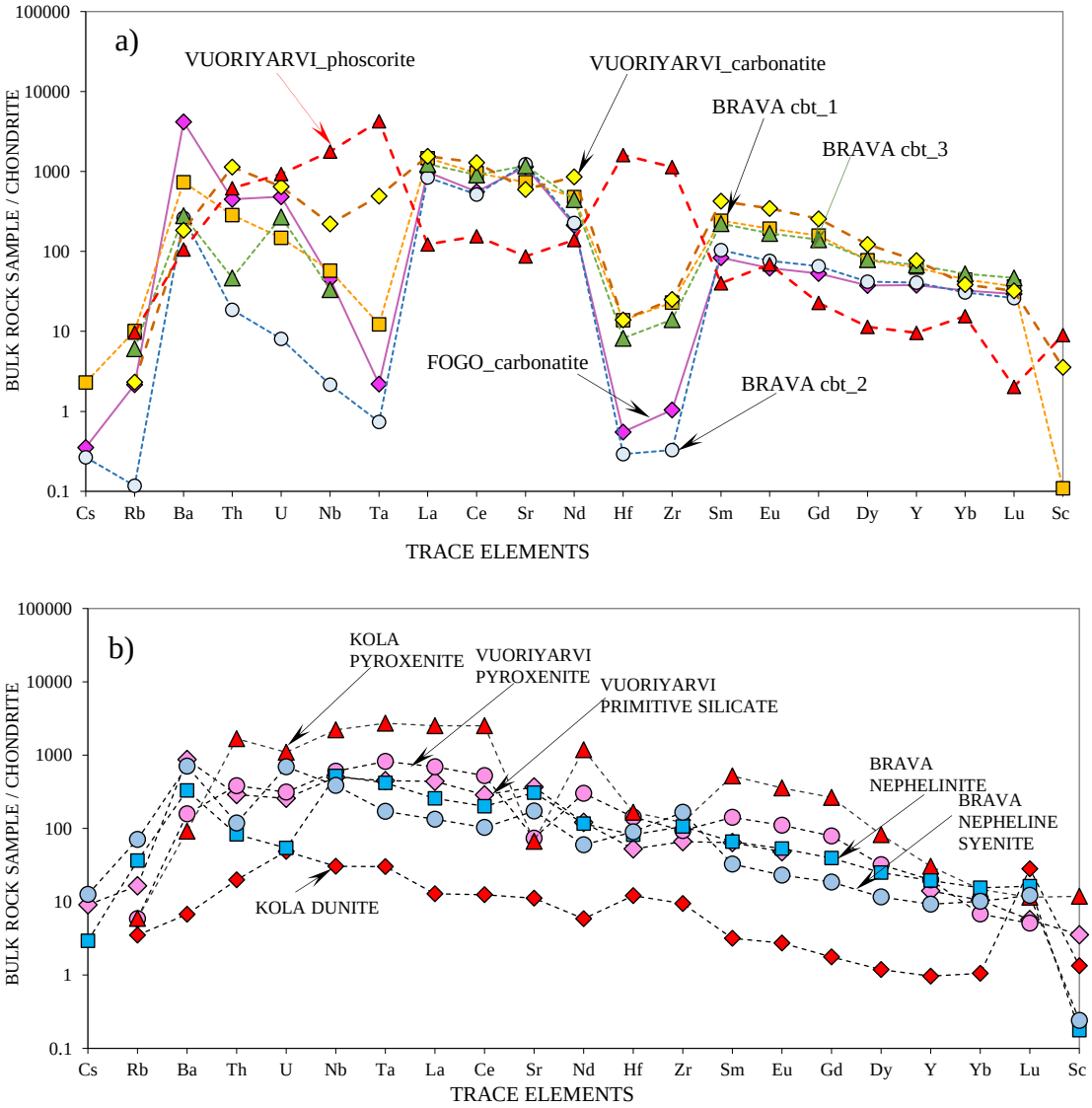

Fig. 1.13 a) Chondrite-normalised trace element spiderdiagrams for bulk rock carbonatites from Fogo, Brava and Vuoriyarvi: Hoernle et al. 2002 (cbt_1), Weidendorfer et al. 2016 (cbt_2), Doucelance et al. 2010 (cbt_3). Carbonatite stage 1 (Brassinnes 2006), phoscorite stage 1 CFM 125/39.8 125/42 125/51 (calcite-phoscorite-magnetite) (Zaitsev et al., 2015. b) Chondrite-normalised trace element spiderdiagrams for bulk rock types associated with carbonatites from Kola Alkaline Province and Cape Verdes such as pyroxenite, dunite, Vuoriyarvi primitive silicate (Arzamastsev et al., 2002) and Vuoriyarvi pyroxenite (Brassinnes 2006), nephelinite and nepheline syenite from Brava (Weidendorfer et al. 2016). Normalisation after Sun and McDonough (1994)

Early carbonatite melt enriched in REEs, Nb and Zr, led to crystallisation of Nb- and Zr-rich minerals. Extensive fractional crystallisation consequently reduced Nb and Zr concentrations in the residual liquid, although enrichment in REE continued during further fractional crystallisation. In contrast, Schleicher (2019) investigated the distribution of trace elements in the pyroxenite-carbonatite-syenite complex of Sevattur

(India), concluding that crystallisation and fractionation of apatite during progressive evolution did not cause enrichment in REE composition of carbonatite but instead depleted the residual melts in REE.

Fractionation of some HFSE-bearing phases such as zircon, pyrochlore and titanite in carbonatite can have an impact on final chemistry as they show different degrees of enrichment in Hf-Zr and Nb-Ta. Variable amounts of F and Sr in apatite and calcite also affects the final chemistry of Brava carbonatites taking into account processes influencing the final chemistry such as fractionation, accumulation or dissolution**.** Differences in LREE abundances depend on the abundance of apatite in carbonatite rocks only if they are accumulative. Higher Sr again depends on the magma composition that controls the minerals, forming primary calcite and Sr-bearing apatite. Consequently, Brava carbonatites differ in REE enrichment (Fig. 1.13a).

For the associated silicate rocks, Kola pyroxenite (Fig. 1.13b) demonstrates similar trend to Vuoriyarvi pyroxenite although it is one order higher with the exception of MREE and HREE showing similar enrichment to Kola peridotite. Kola dunite shows the lowest enrichment and has a positive Hf-Zr anomaly while the other rock types have negative anomalies. Final crystallisation of REE-rich carbonatites resulted from multi-stage fractional crystallisation of silicate-carbonate melts (Chakhmouradian and Zaitsev, 2012).

1.5 Literature review – trace element geochemistry in minerals in carbonatites

Constituent minerals such as calcite and apatite have widely been investigated for trace elements in carbonatites (Hornig-Kjaarsgaard, 1998). It is well established that REEs preferentially enter some minerals like perovskite or apatite in carbonatites than others. Hornig-Kjaarsgaard (1998) concluded that high REE concentrations in carbonates and apatite and REE-enrichment in accessory phases such as perovskite and pyrochlore can increase the overall REE concentration in carbonatites (assuming they are xenocrystic). Also, fractionation of Ca-silicate minerals like melilite, monticellite and diopside can cause higher abundance as their LREE/HREE ratios and ΣREEs are high. Silicate phases including olivine, phlogopite, amphibole and others do not display high enrichment in LREEs and show much lower ΣREEs, so fractionation of these phases does not change the concentrations of the REE in the magma.

The composition of calcite from several carbonatite complexes was analysed for REEs and other trace elements by Chakhmouradian et al. (2016). They showed that $(La/Yb)_{cu}$ values in primary carbonates can significantly differ and concluded that REE concentration in magmatic carbonates is controlled by fractional crystallisation of fluorapatite, monazite and other minor phases. Removal of HREEs from carbonatite magma by crystallisation of calcic garnet could account for the steep negative REE pattern. The authors established that post-magmatic processes, such as interaction of primary calcite with hydrothermal fluids, can cause unpredictable changes in LREEs and Large Ion Lithophile (LIL) elements, causing either enrichment or depletion.

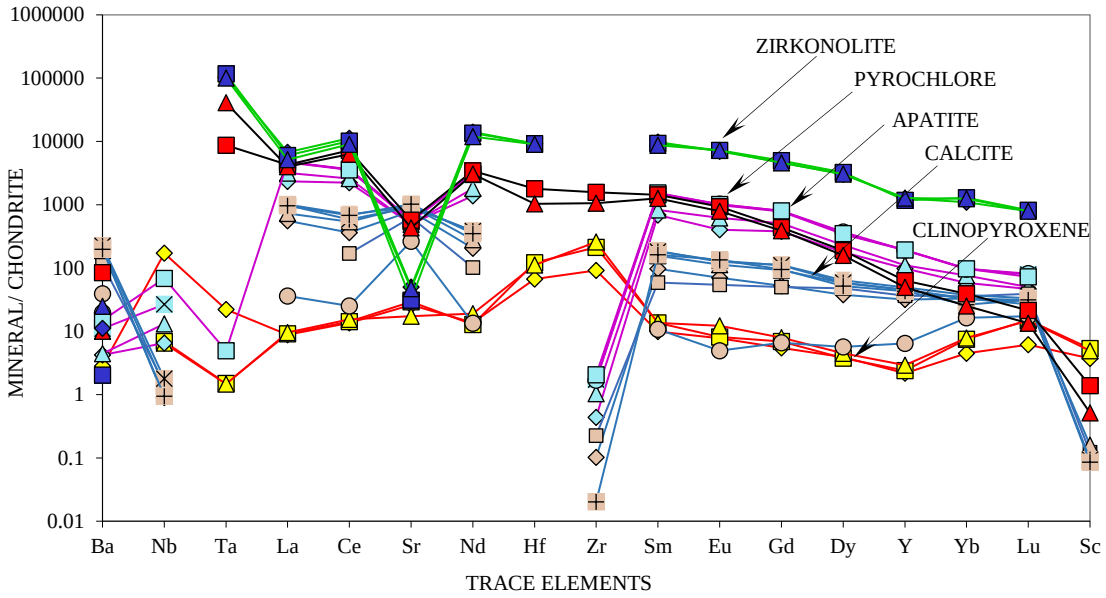

Fig. 1.14 Chondrite-normalised trace element spiderdiagrams for constituent and accessory minerals from intrusive silica-bearing calcio-carbonatite in Belaya Zima complex, petrogenetically link to ijolite series and nepheline syenite (Doroshkevich et al., 2017); data are missing for some elements, e.g Hf, Ta.

Analysed constituent and accessory minerals from intrusive silica-bearing calcio-carbonatite in Beleya Zima complex, Russia (Doroshkevich et al., 2017) plotted on chondrite-normalised trace element spiderdiagrams show different levels of enrichment (Fig. 1.14). Accessory zirconolite and pyrochlore have the highest enrichment in trace elements with exception of Sr which forms a trough. Primary phases such as apatite and calcite are highly enriched in REEs, although apatite shows one order higher enrichment equal to that of pyrochlore. Pyroxene contain considerable amounts of HFSE such as Hf, Zr and Nb. Doroshkevich et al. (2017) came to conclusion that enrichment in Zr, Nb and REEs progressed from the silicate to carbonatite magmas via extensive fractional crystallisation generating the highest levels of Nb and Zr in the calcitic carbonatite. The higher REE enrichment is found in the associated dolomite and ankerite carbonatites.

Wall and Zaitsev (2004) examined REE-rich carbonatites in the Kola peninsula, and divided REE minerals into two groups such as primary (magmatic) and secondary (e.g., hydrothermal replacement of originally formed phases). However, very little trace element data has been obtained on silicate phases in sövites such as phlogopite, garnet and perovskite but these are included in this study. Brassiness et al. (2005) investigated REE in apatite in Vuoriyarvi alkaline rocks and carbonatites and showed that they define a single continuous chemical trend that suggests that all the rocks are related by fractional crystallisation. Zaitsev et al. (2015) established the threshold for rare earth-rich Kola carbonatites, such as Khibina, Kovdor, Vuoriyarvi and Turiy Mys. Originally it was defined as having a bulk rock concentration of REE oxides ≥1 wt.%, an updated value for this threshold is 2000-3000 ppm. Above this, REE-minerals are likely to be present (either primary magmatic or/and secondary hydrothermal-metasomatic). REE are concentrated mostly in apatite and calcite and to a lesser degree in pyrochlore and zirconolite.

1.6 Literature review - The Kola carbonatites: origin, tectonic setting and association with alkaline rocks

The Vuoriyarvi ultramafic carbonatite complex (Figs. 1.15, 1.16a and 1.16b) belongs to the Palaeozoic Kola Alkaline Province (Kuharenko et al., 1965; Kogarko 1989; Bulakh et al., 2004; Downes et al., 2005; Lee et al., 2006).

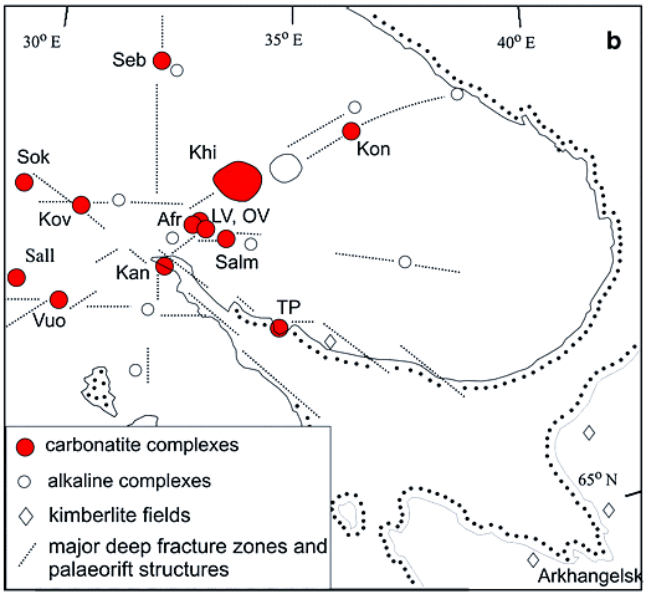

Fig. 1.15 Map of the Kola Peninsula, NW Russia, showing the main carbonatites complexes (solid circles) and alkaline complexes (open circles) of the Palaeozoic Kola Alkaline Province (after Bell and Rukhlov 2004; Woolley and Kjarsgaard 2008). Vuoriyarvi is the carbonatite complex labelled "Vuo" in the SW of the province.

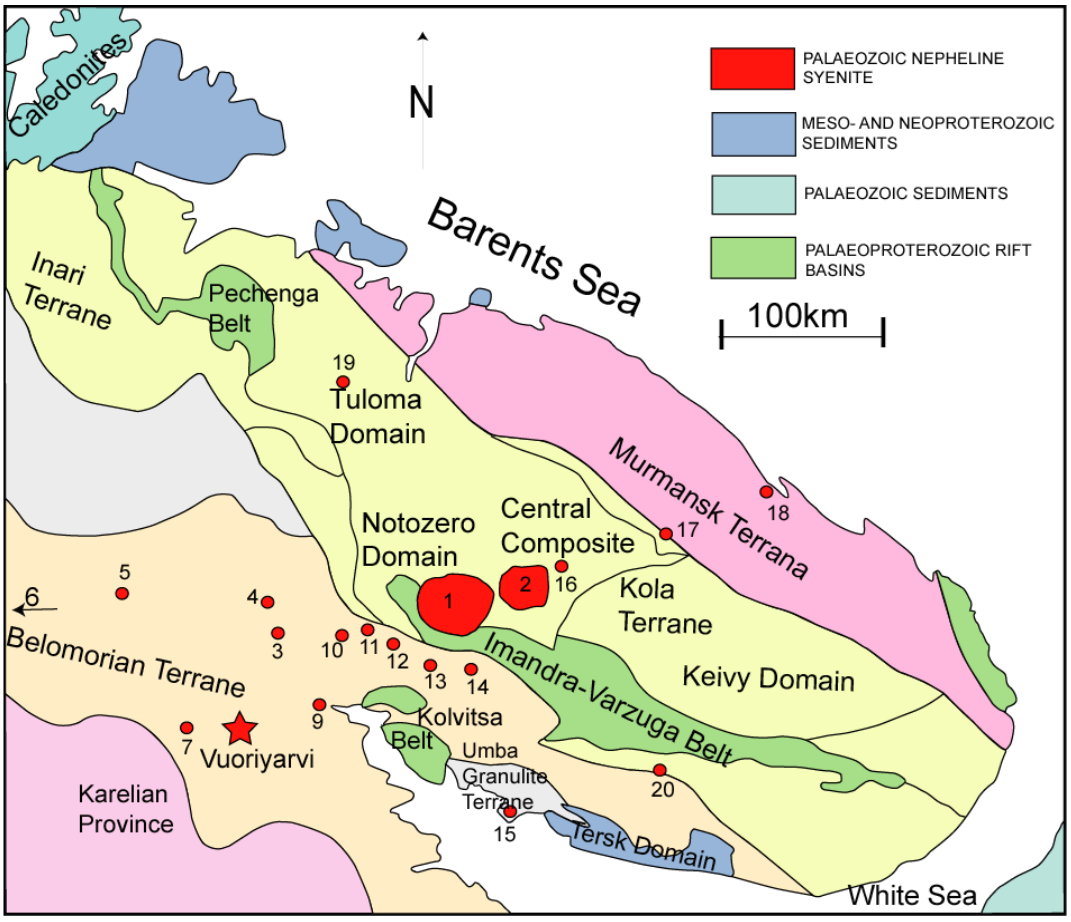

Fig. 1.16a The Palaeozoic complexes (alkaline intrusions): 1-Khibina, 2-Lovozero, 3-Niva, 4-Mavraguba, 5-Kovdor, 6-Sokli, 7-Sallanlatva, 8-Vuoriyarvi, 9-Kandaguba, 10-Afrikanda, 11-Ozernaya Varka, 12-Lesnaya Varka, 13-Salmagora, 14-Ingozero, 15-Turiy Mys, 16-Kurga, 17-Kontozero, 18-Ivanovka, 19-Seblyavr, 20-Pesochny (modified after Balagansky in Daly et al., 2001).

According to Pell (1996), carbonatites frequently occur in alkaline, ultramafic or cumulate complexes, which is the case here. The complex itself comprises mainly ultramafic and alkaline rocks and volumetrically subordinate carbonatites that form stockworks and dyke systems (Subbotin et al., 1998; Kapustin, 1976). Two stockworks (north one called Neske-Vara, south one Tukhta-Vara) and dyke systems at Vuoriyarvi follow a particular pattern of evolution and emplacement, generating four stages of successive carbonatites, each one exhibiting a specific assemblage of minerals. The studied carbonatite samples were derived from drill core from the poorly exposed Tukhta-Vara stockwork (Fig. 1. 16b). They show a close spatial relation to phoscorites and cross-cut the pyroxenite deposit (Karchevsky and Moutte, 2004).

The multi-stage formation of carbonatites from the Kola Alkaline Province and their association with alkaline rocks (Fig. 1.16) started with development of now-eroded alkaline volcanism followed by emplacement of plutonic pyroxenite/melilitolite and intrusion of syenite forming the rim (Arzamastev et al., 2002). During development of

the ring complex, emplacement of ijolite was followed by nepheline syenite in the core and ending with injection of carbonatites and phoscorites. Brassiness et al. (2003) linked the Vuoriyarvi ultramafic (clinopyroxenite) and carbonatite-phoscorite rocks together by showing that they have similar initial Nd-Sr isotopic compositions.

Vuoriyarvi carbonatites are also strongly associated with pyroxenite (Brassinnes, 2006) and phoscorite (Krasnova et al., 2004), forming a multiphase phoscorite-carbonatite series (Zaitsev and Bell, 1995). A very low degree of partial melting of the mantle is often considered to be responsible for the high trace element enrichment in carbonatites. Martins et al. (2009) analysed silicate lavas from the Cape Verde Islands and concluded that carbonatite-like metasomatism in the lithospheric mantle led to the high enrichment in incompatible elements in the lavas. This complex was investigated by Brassinnes et al. (2003) and (2005) who provided bulk rock compositions of Vuoriyarvi carbonatites (Table 1.3). The higher SiO_2+MgO content reflects the higher percentage of the Mg-Fe-Si minerals such as olivine, pyroxene and phlogopite. Thus, BR18 contains olivine, magnetite, phlogopite, diopside, apatite and calcite, while BR64 contains tetraferriphlogopite, apatite, magnetite and calcite (Brassinnes et al., 2005).

Sample	BR 18	BR 30	BR 35	BR 64
SiO_2	7.01	2.23	2.49	1.25
TiO_2	0.29	0.08	0.12	0.08
Al_2O_3	0.81	0.03	0.40	0.31
Fe_2O_3	2.35	0.54	1.01	2.57
FeO	1.62	1.37	0.86	2.05
MnO	0.17	0.25	0.10	0.12
MgO	4.17	2.43	2.57	1.84
CaO	45.38	49.39	52.09	52.19
Na_2O	0.30	0.32	0.09	0.11
K_2O	0.57	0.25	0.23	0.26
P_2O_5	4.36	5.79	1.74	3.41
LOI	33.34	37.03	38.71	36.65
Total	100.37	99.71	100.41	100.84

Table 1.3 Whole rock analysis of major elements of carbonatites from Vuoriyarvi. Brassinnes et al. (2005).

Investigation of the Kola Alkaline Province (Rimskaya-Korsakova and Krasnova (2002) revealed the existence of unique rock types (Fig, 1.16b) which are associated spatially and temporally with carbonatites, including phoscorites (plutonic ultramafic rocks essentially composed of apatite, magnetite and forsterite). Krasnova et al. (2004) explained the generation of phoscorites as a product of separation from carbonatites by crystal fractionation or liquid immiscibility (or both processes operating at the same time). Rass et al. (2020) established the formation of the Kovdor phoscorite-carbonatite association by liquid immiscibility

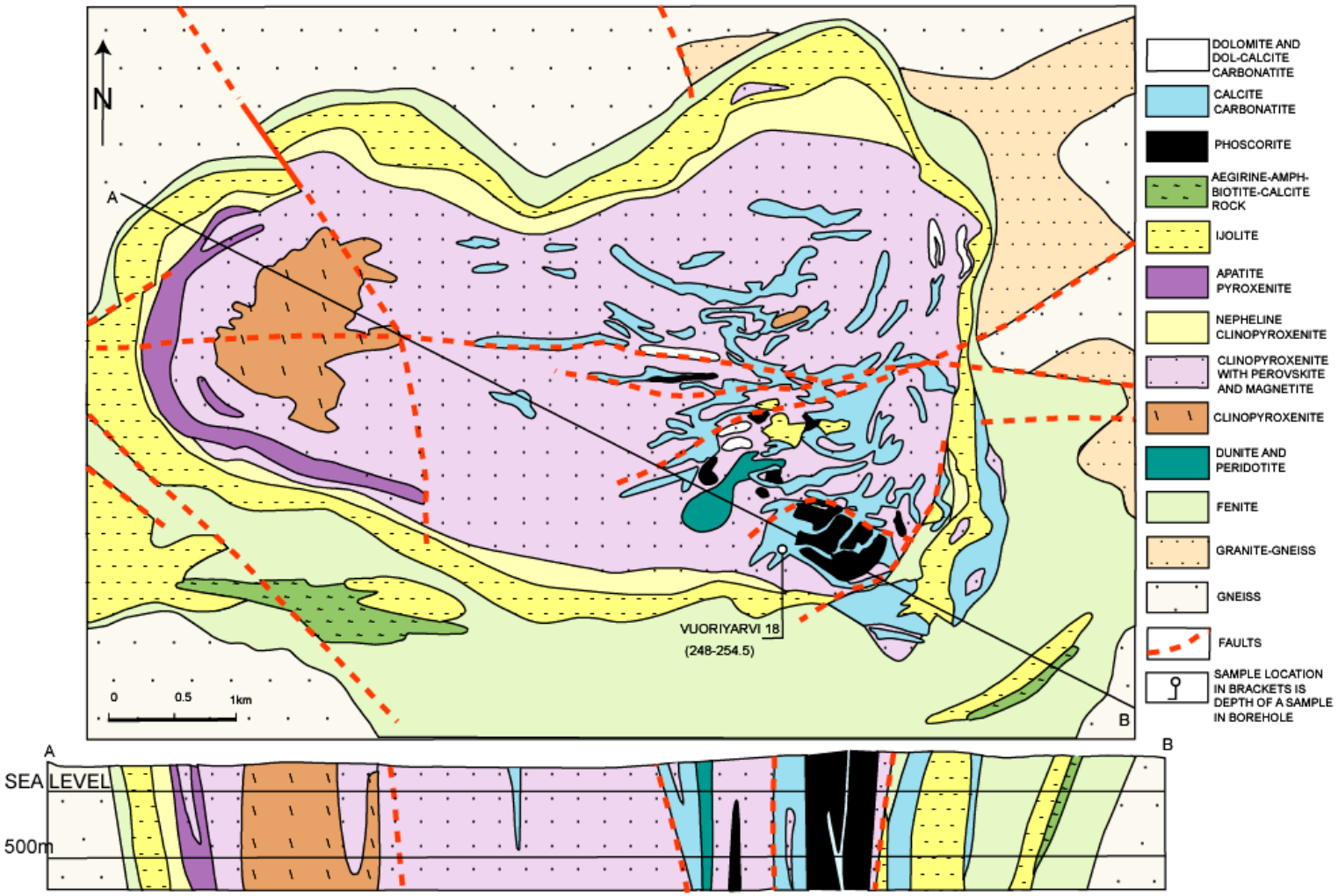

Fig. 1.16b Schematic geological map of the Vuoriyarvi complex (adapted after Subbotin, 1986), showing location of boreholes where samples were obtained.

Zaitsev et al. (2015) reviewed ultrabasic and alkaline rocks from the Kola Alkaline Province. According to their order of formation they are: olivinites, clinopyroxenites, melilititic rocks (turjaites, uncompahgrites, okaites) and foidolites (melteigites, ijolites, urtites). The two largest complexes Khibina and Lovozero, also contain nepheline syenites (foyaites, khibinites, luyavrites). Diverse carbonatites, being the youngest rocks, formed during the multi-stage complex intrusions, reflect the composition of the major rock-forming constituent phases such as calcite, dolomite, ankerite, followed by other typical minerals such as forsterite, diopside, phlogopite, tetraferriphlogopite, magnesioarfvedsonite, richterite, apatite and magnetite. Most Kola carbonatites contain various late-stage accessory minerals such as pyrochlore, uranpyrochlore and bariopyrochlore. Also, numerous primary and subsolidus REE minerals were formed, such as burbankite and carbocernaite in Khibina and Vuoriyarvi. All carbonatites are more enriched in LREE compared to HREE with $(La/Lu)_{CN}$ ratios between 9.3 and 1230.

The Vuoriyarvi complex comprises mainly ultramafic and alkaline rocks and volumetrically subordinate carbonatites. The core of the Vuoriyarvi massif consists largely of clinopyroxenites cut by carbonatite stockworks and dykes (Kapustin, 1975; Subbotin et al., 1998; Karchevsky and Moutte, 2004). These minor intrusions follow a particular pattern of evolution and emplacement, which generated four stages of successive carbonatites, each one exhibiting a specific assemblage of minerals (Kapustin, 1980). Our studied sövite samples are from the Tukhta-Vara stockwork and are part of the earliest stage of carbonatite formation. Brassinnes et al. (2003, 2005) studied some of the same samples for bulk rock compositions and he concluded that they contain less than 10 wt% of SiO_2 as the analysed BR18 rock sample contain 7.01 wt% of SiO_2 and belong to group of calcio-carbonatite.

Arzamastev et al. (2002) analysed rocks and minerals from the Kola Alkaline Province for their REE content, and distinguished three separate patterns (Fig. 1.17). The first consists of the Kovdor, Afrikanda and Salmagora massifs, and is the one followed by the Vuoriyarvi complex. It shows progressive REE depletion from earlier to later melt derivatives. The second is the Kovdor-type where intense REE depletion is controlled by crystallisation of perovskite and apatite. The third, associated with alkaline ultramafic massifs such as Kihibiny, involves mixing of phonolitic and olivine melanephelinitic melts, enriching the later batches in incompatible elements.

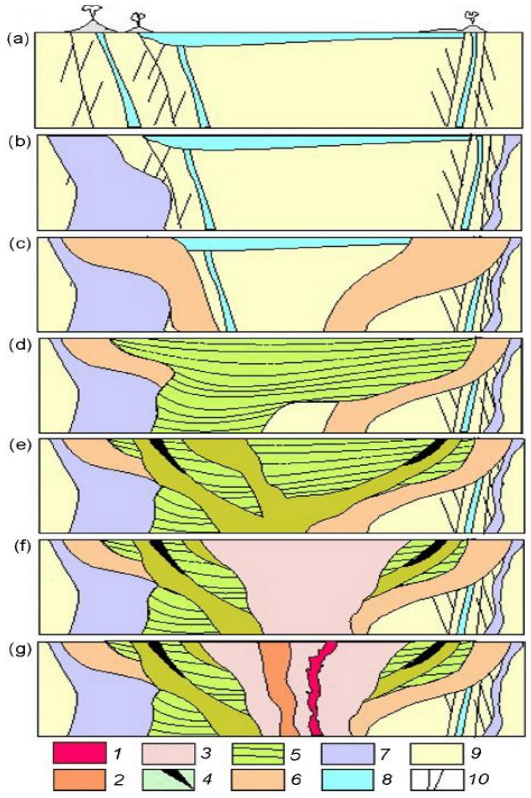

Multiphase emplacement of the plutonic alkaline intrusions of the Kola Alkaline Province:

1. Peridotites, pyroxenites, and melilitolites are emplaced first, being injected prior to the syenites.

2. Further development of the ring complex by emplacement of (marginal) nepheline syenites followed intrusion of ijolite-melteigites.

1=CARBONATITE, 2=PULASKITE, 3=NEPH SYENITE=core, 4=KALSILITE+OTHER, 5=IJOLITE and MELTEIGITE, 6= NEPH SYENITE=rim, 7=OL PYROXENITE+MELILITOLITE, 8=ALKALINE VOLCANITES, 9= PRECAMBRIAN BASEMENT, 10=FAULT.

Fig. 1.17 (a) – (g) phases of emplacement of the Kihibiny complex after Arzamastsev et al. (2002) representing general concept of multiphase emplacement of the plutonic alkaline intrusion that also produced carbonatites and associated exotic rock types.

Kapustin (1976) undertook structural studies of the Vuoriyarvi complex, concluding that there are differences between the clinopyroxenite-ijolite and phoscorite-carbonatite structural associations. Clinopyroxenites-ijolites were emplaced following differentiation and crystallisation of the alkaline silicate series while phoscorites-carbonatites are more complex and formed in three stages: C1-P1, C2-P2 and C3-P3 (C=carbonatites and P=Phoscorites). Each stage was characterised by a phoscorite intrusion being emplaced around carbonatites with a zone of intermediate composition between them but occasionally carbonatites cut phoscorites (Karchevsky and Moutte, 2004). The analysed Vuoriyarvi samples were collected from C1, which is regarded as the very early stage of carbonatite formation.

Karchevsky (2010, unpublished notes, St Petersburg University) concluded that the Vuoriyarvi carbonatites in every case postdate the phoscorites and, in most cases, generation of carbonatites was accompanied by incorporation of phoscorite followed by its partial replacement, resulting in the presence of transitional calcite-magnetite ores at the phoscorite-carbonatite contact.

1.7 Literature review – Cape Verde carbonatites

The Cape Verdes are an archipelago of volcanic islands in the Eastern Atlantic Ocean (Fig. 1.18), and have been known to contain carbonatites for many years (Allegre et al., 1971; Le Bas 1984; Kogarko 1993). The discovery of carbonatites formed in oceanic environment such as Canary Island and Cape Verde (Allegre et al., 1971) changed the prevailing view of the occurrence of carbonatite as being formed in continental settings and associated with ring structures. To differentiate true carbonatite in oceanic setting from hydrothermal limestone, Allegre et al. (1971) developed specific criteria such as $^{87}Sr/^{86}Sr$ ratio. The value of this ratio is close to 0.703 for Cape Verde and Fuerteventura carbonatites (Hoernle et al., 2002; Wiedendorfer et al., 2016). The chondrite-normalised REE plot also differentiates a magmatic origin as igneous

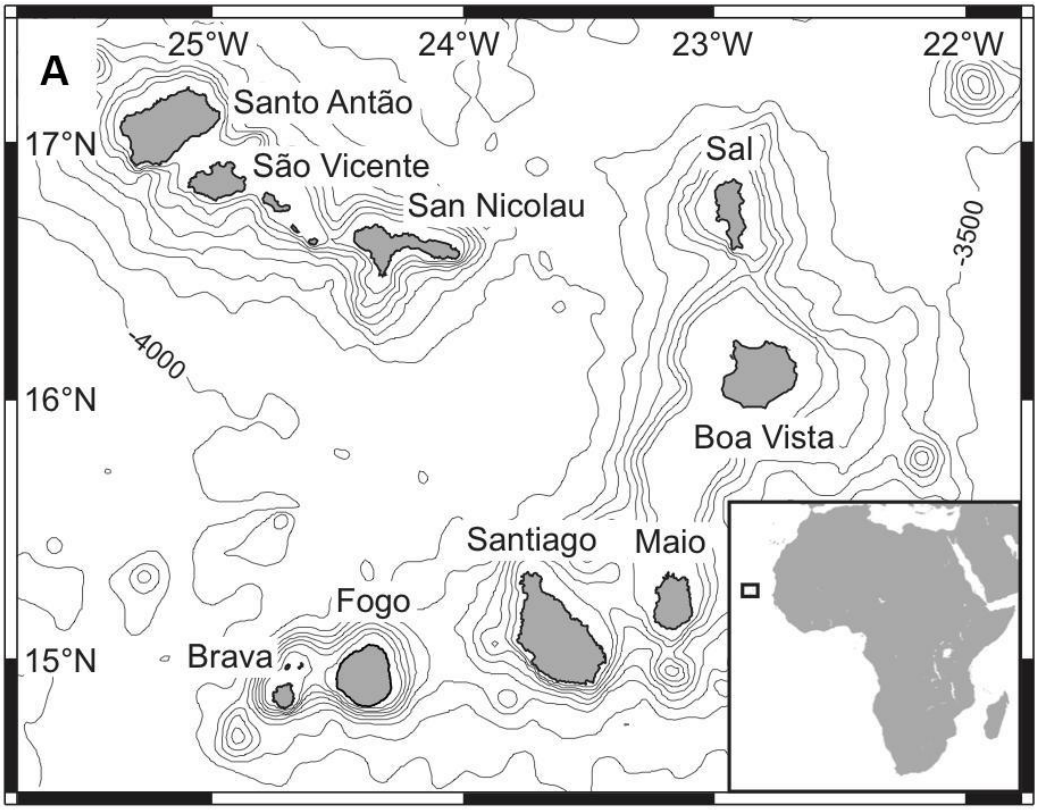

Fig. 1.18 Map of the Cape Verde Islands with 500m isobaths showing proximity of Fogo and Brava islands (after Klügel et al., 2020).

carbonatites are highly enriched in REEs compared to the lack of enrichment in limestone (Loubet et al., 1972). Le Bas (1984) recognised that the magmatic carbonatite-ijolite association exists commonly in the oceanic environment. He also noted that K-rich orthoclasites are dominant in fenites associated with continental carbonatites whereas

albitites are more dominant in oceanic fenites, possibly due to the involvement of Na-rich sea-water in the hydrothermal system. The association of Fogo calcio-carbonatites with nephelinites is apparent according to their similar Sr–Nd–Pb isotopic compositions (Hoernle and Tilton 1991).

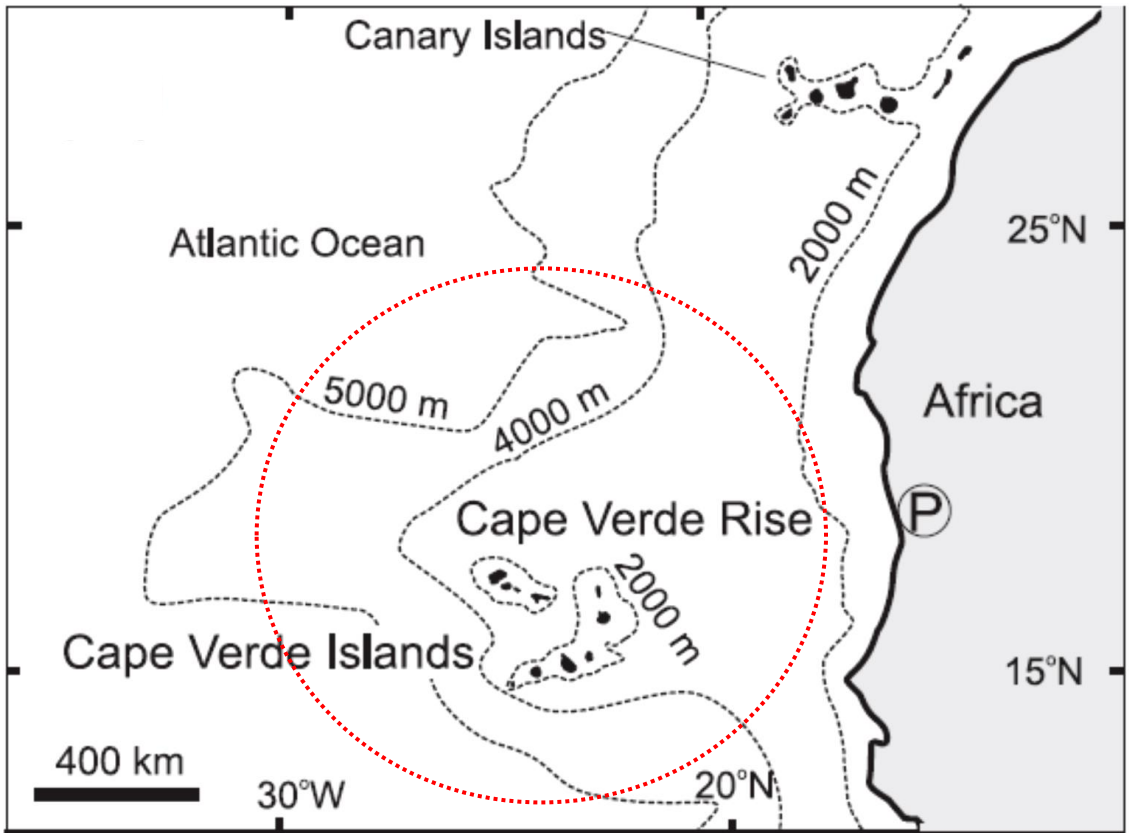

Fig.1.19 Location of the Cape Verde Islands, with the respect to Canary Islands and to the west coast of Africa with point P being the pole of rotation of the African plate. The hotspot is almost stationary, relative to the lithosphere, situated close to P (Pollitz, 1991; Holm et al., 2005). Possible position of the mantle plume beneath Cape Verdes is marked in the red circle.

Montelli et al. (2006) investigated tomographic images of the mantle beneath the islands (Figs. 1.18, 1.19 and 1.20) and deduced the existence of a deep mantle plume, which most likely originates below the upper mantle. The close proximity of the Canary Islands to the Cape Verde islands, their connection with the western coast of Africa (Fig. 1.20) and most of all the similarity in generation of carbonatites in oceanic setting is very appealing in postulating that similar mechanisms operate in the upper mantle to form these rock types.

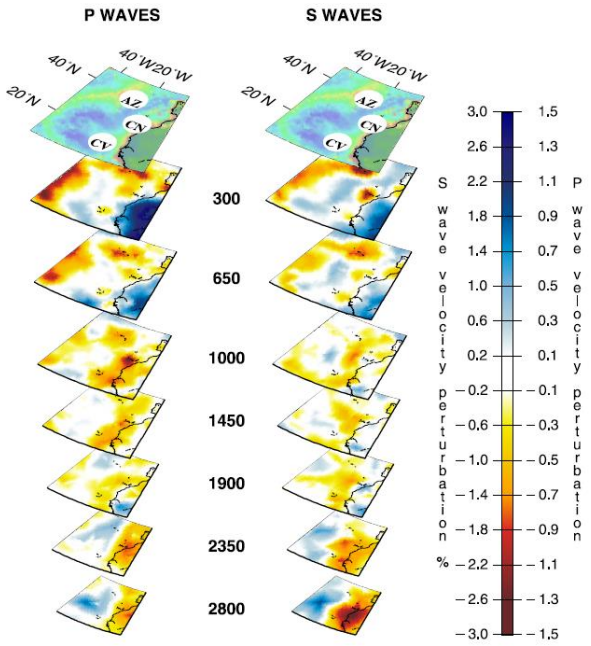

Fig. 1.20. 3-D representation of the (AZ) Azores, (CN) Canary Islands, and (CV) Cape Verde plumes in P- and S-wave tomographic models (Montelli et al., 2006). Only the S-wave tomographic images show the possibility of a deep-rooted plume.

Several researchers have previously investigated the carbonatites of the Cape Verdes. Kogarko (1993) studied both effusive and intrusive carbonatites and pointed out that carbonatites from Santiago, San Vincente and Sal islands are commonly enriched in SiO_2 up to 30%. She also suggested that silicate globules in carbonatites from Fogo and Brava islands were due to liquid immiscibility. According to Kogarko et al. (2009), Fogo calciocarbonatites can hold rare metal-bearing minerals that follow a crystallisation order: zirconolite→ pyrochlore→ pyrochlore group minerals→ Nb-Zr-Ti silicates→ zircon→ thorite. An alternative evolution sequence is: zirconolite→Th-calciobetafite→ betafite+Th-pyrochlore→thorite with Ti–Zr–Nb silicates+zircon.

SiO_2, $Ca(F,OH)_2$, and $Na_2Si_2O_5$ are the common components of fluids that coexist with carbonatite. Kogarko et al. (2009) concluded that "distribution and behaviour of rare and radioactive elements in oceanic carbonatites show the same tendencies as in continental carbonatites. The contents and distribution of Ti, Ta, and Th in zirconolites and pyrochlores from oceanic and continental carbonatites are different: the minerals of oceanic carbonatites are enriched in Ti and Th and strongly depleted in Ta".

Madeira at al. (2005) investigated shallow intrusive carbonatites from Fogo. They concluded that the extremely shallow location of the outcrops (heavily cross-cut by dykes) suggests that they are part of the common Basal Complex connecting Fogo, Brava and the Secos islets (north of Brava). The K/Ar age of the Fogo carbonatite is 3.2-5.1 Ma.

Mourão et al. (2012) analysed Brava's intrusive calciocarbonatites and silicate rocks of the Basal Complex. The K/Ar ages for carbonatite obtained by Madeira et al. (2005) places in an Early to Middle Pliocene (older than the Fogo volcanic building), thus indicating hypothesis of carbonatites being a part of an older basement which is responsible for the submarine platform connecting Fogo with Brava. Mourão et al. (2012) concluded that, due to the identical isotopic ratios of both rock types, carbonatites formed by silicate-carbonatite liquid immiscibility from a carbonated silicate magma generated by low degree of partial melting at the upper levels of the mantle. Also, Weidendorfer et al. (2016) stated that intrusive Brava carbonatites belong to a silica-undersaturated pyroxenite, ijolite, nephelinite, nepheline syenite, combeite–foiditite, carbonatite series. Their model of fractional crystallisation shows enrichment in alkalis and pushed the melt into the carbonatite–silicate miscibility gap. This model suggested that the carbonatites should have originally had a higher alkali content and the authors concluded that loss of alkali-rich CO_2 + H_2O fluids during final solidification was due to fenitization of adjacent rocks.

Finally, Marques et al. (2020) studied the mineralogy and chemistry of paleoweathering materials on top of Fogo carbonatites and concluded that weathered material differs from the fresh rock samples in having a higher concentration of mostly LREEs and MREEs.

1.8 Aims and objectives of PhD

The purpose of this thesis is to investigate the processes involved in the evolution of carbonatite magmas at shallow depths. Possibilities include primary processes such as shallow-level fractional crystallisation, magma mixing, assimilation of solid material from the silicate wall-rock, and liquid immiscibility, whereas secondary processes include phase replacement, deformation, hydrothermal circulation and fenitisation.

The study will investigate the detailed petrography of shallow intrusive carbonatites from an oceanic and a continental setting, focussing on textures that may indicate disequilibrium between minerals, magmas and fluids. The major element compositions and trace element contents in minerals from the selected carbonatites will be used to constrain which primary or secondary processes may have operated in the three different case studies.

- Case study 1 – Vuoriyarvi, Kola Peninsula, a continental environment with shallow intrusive sövite dykes. The carbonatites form part of a major alkaline/ultramafic complex, and show largely magmatic processes rather than post-magmatic ones. These include assimilation of xenocrysts and xenoliths of related host silicate rocks by carbonatite magmas. Studied samples are not typically found in Vuoriyarvi carbonatites as they belong to minority of specimens (10-20%) with unusual textures and mineralogy, helping to understand extremely early processes of carbonatite formation.
- Case study 2 – Cape Verde, an oceanic environment with shallow intrusive carbonatites forming the seamount rocks beneath the island of Fogo. Although the carbonatites have been investigated for K-Ar dating (Madeira et al., 2005), noble gas and carbon isotope signatures (Mata et al., 2010), radiogenic and oxygen isotope signatures and bulk rock geochemistry (Hoernle et al., 2002; Doucelance et al., 2010) and rare metal mineralisation (Kogarko et al., 2009), no detailed study has yet been made of their mineralogy and petrology. Also, the carbonatites show processes such as hydrothermal circulation and fenitization.
- Case study 3 – Brava, the adjacent island to Fogo, where carbonatite magmas have interacted extensively with the host (unrelated) silicate rocks, to form abundant fenites. They have not been studied for their mineralogy and petrology. They demonstrate processes such as fenitization, immiscibility, presence of ocelli, but also discovery of rare minerals.

Chapter 1 will give an introduction to carbonatites. Chapter 2 will describe the sampling and methodology.

Chapter 3 will give a detailed petrography of the Vuoriyarvi carbonatites. The purpose is to study the textures, to resolve the sequence of crystallisation and to determine whether minerals are in equilibrium. It will present major elements and in minerals including monticellite, pyroxene, garnet and phlogopite, as well as perovskite, calcite and apatite. It will compare the data to carbonatites from other localities, and to associated rocks from the Vuoriyarvi alkaline complex (such as pyroxenites, phoscorites and ijolites). It will also examine trace element distribution in Vuoriyarvi carbonatites in minerals such as perovskite, apatite, and calcite and in unusual minerals such as Zr-rich garnet, monticellite etc. Carbonatites contain the highest quantity of REEs amongst all igneous rocks, thus this information will

contribute to understanding the distribution of the elements amongst different minerals, and in some cases between different generations of the same mineral present in analysed sövite such as apatite or phlogopite.

Chapter 4 will examine petrography and geochemical data of constituent phases of major and trace elements of intrusive carbonatites of Fogo, Cape Verde and how trace elements are distributed in minerals crystallising in carbonatite magmas.

Chapter 5 will analyse petrography and geochemical data of constituent phases of major and trace elements of sövite and associated silicate rocks of Brava, Cape Verde. It will examine distribution of elements in minerals crystallising in carbonatite and associated silicate magmas. Chapter 6 will also answer the question “how is this distribution affected by processes such as immiscibility, fractionation, fenitization and hydrothermal alteration?”.

Chapter 6 will include a conclusion and a brief discussion of future work.

CHAPTER 2

SAMPLING AND METHODOLOGY

2.1 Sampling

2.1.1 Vuoriyarvi

The carbonatite complex in Vuoriyarvi is poorly exposed and all of the eight studied sövite samples were derived from the small hypabyssal body of Tukhta-Vara using drill core material from borehole “Vuoriyarvi 18” at depths of 248-254.5 m. They were collected form a stockwork of thin, slightly inclined dykes (Kapustin, 1975) which cross-cut an earlier apatite-bearing perovskite-magnetite-clinopyroxenite that forms the main body of the complex. Figure 2.1 shows the geological map of the Vuoriyarvi massif.

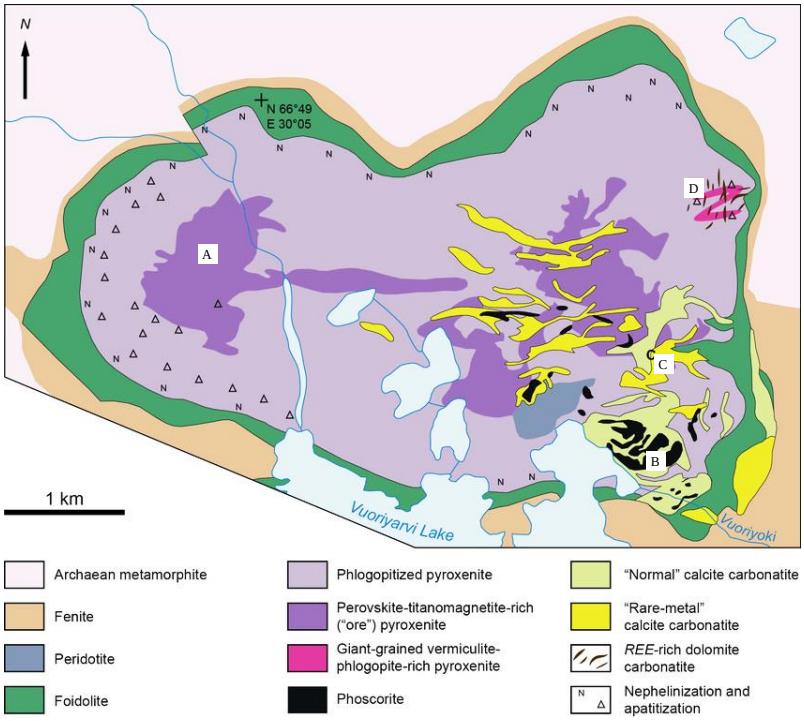

Fig. 2.1. The Vuoriyarvi foidolite-pyroxenite massif with carbonatite (Afanasyev, 2011). A) Western Vuoriyarvi perovskite-titanomagnetite (REE-Ti-Fe) deposit in ore pyroxenite; B) Tukhta-Vara baddeleyite-pyrochlore-magnetite-apatite (Zr-Ta-Nb-Fe-P) deposit in carbonatite and phoscorite; C) Neske-Vara apatite-magnetite-pyrochlore (P-Fe-Th-U-Ta-Nb) deposit in “rare-metal” carbonatite; D) Petyayan-Vara vermiculite-phlogopite-Zr-REE deposit.

Location B in the SE of the massif is the site from which samples of carbonatite analysed in this work were collected. They show a close spatial relation to phoscorites, which are silicate-apatite-magnetite ore bodies (Krasnova et al., 2004). Vuoriyarvi samples were collected, sectioned and numbered by the late Dr Elena Balaganskaya

at the Kola Science Centre, Apatity. Seven thick (100μm) and one thin 30μm (KR3) polished sections were analysed.

There is some confusion in sample numbering arising from a misunderstanding of the Russian letter “B” appears as “V” and the Russian letter Я (“Ya”) which sometimes appears as “2”. We keep the original numbering of the samples organised by Dr Balaganskaya starting with “BR”, “B2”, “BA” or “KR” which also applies in one case to the whole rock composition (BR18) as the mineralogy of studied sövites are from “Vuoriyarvi 18” borehole. Other authors such as Brassinnes et al. (2006) used Russian nomenclature of numbering, e.g., starting with VJA followed by 18 and so on (in his published thesis) but in Brassinnes et al. (2005) the numbering of rocks partially includes Brassiness method and partially that of the coauthor Balaganskaya, such as BR18, BR30, BR35 and BR64.

2.1.2 Fogo

Fogo carbonatites form part of the oldest unit on the island, the Basal Complex, which was formed during the seamount stage of oceanic island evolution (Day et al.,

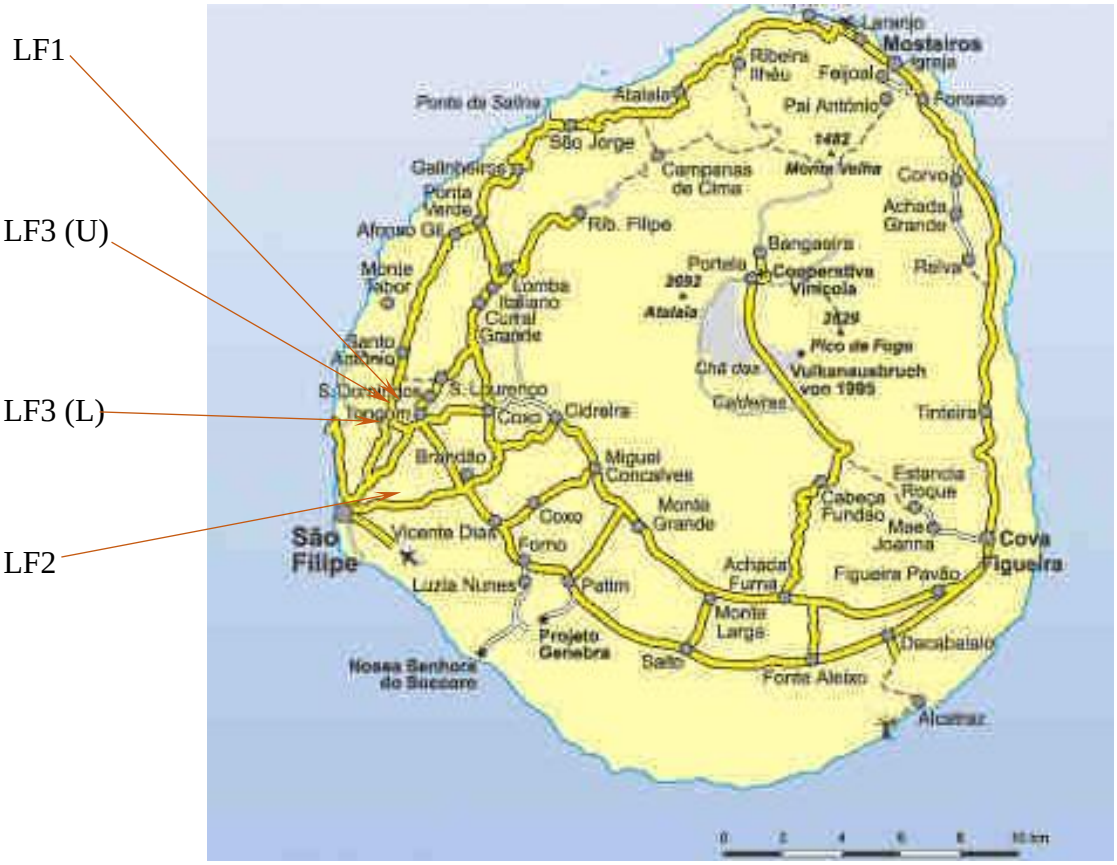

Fig. 2.2 Map of Fogo Island showing locations of LF1 (Ribeira de Almada), LF2 (Rib. Domingo Santo), LF3 (Monte Almada) (U) and LF3(L) showing where samples of intrusive carbonatite have been collected. U and L = Upper and Lower

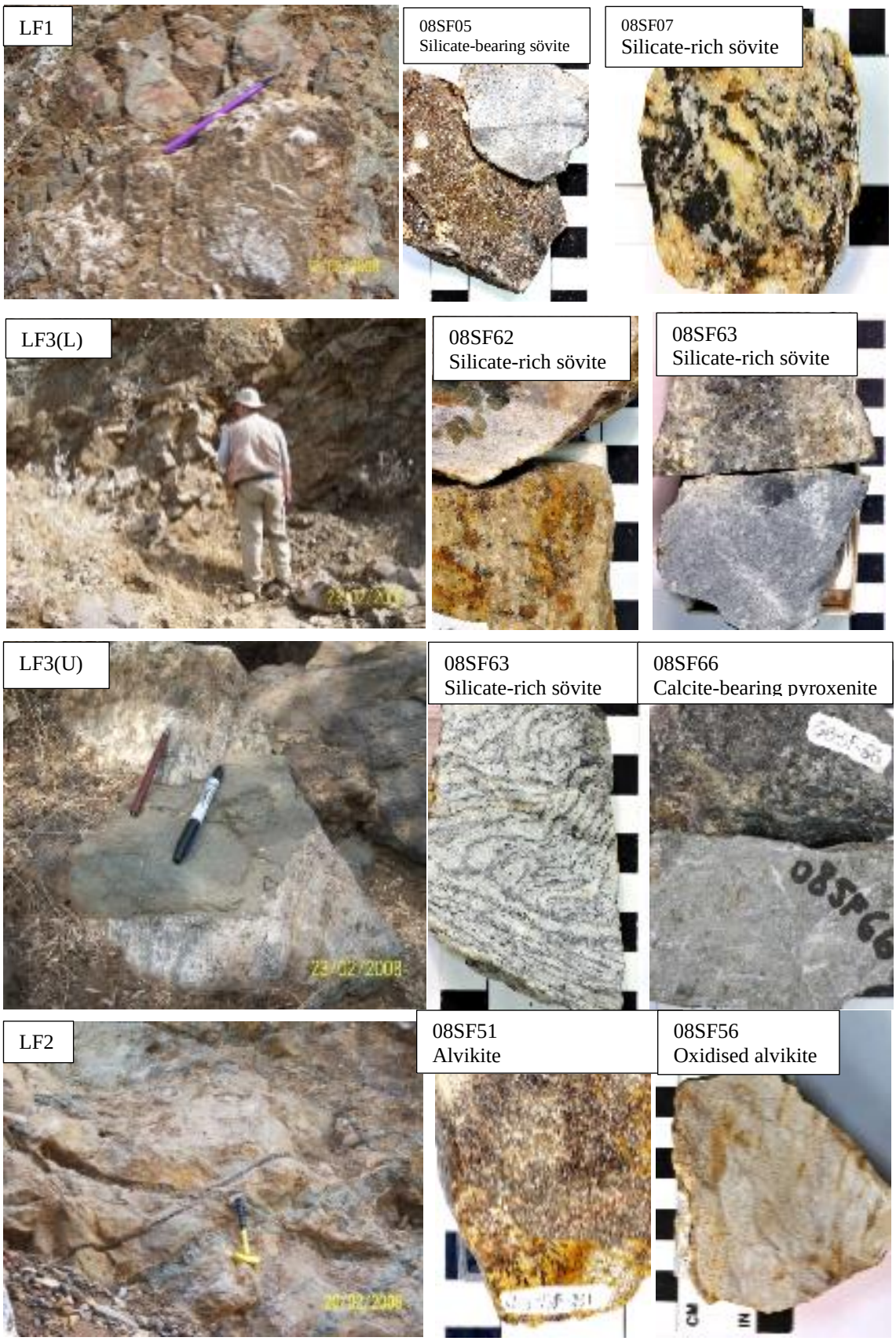

Fig. 2.3 Photographs of locations on Fogo, and representative hand specimens explained in later chapters.

1999). Three locations in the west of Fogo provided samples of intrusive carbonatite and associated rocks. The locations were referred to as LF1, LF2 and LF3 (Fig. 2.2). Outcrops are shown in Figure 2.3 together with representative hand specimens.

The LF1 site is well exposed in the Ribeira de Almada (Grid reference: 14.55.62N, 24.29.55W). It displays brecciated blocks of carbonatite, glimmerite, ijolite and syenite cut by several fine-grained green dykes. Samples 08SF01 to 08SF09 were collected from this locality. They were quite fresh due to recent quarrying (Fig. 2.4a).

The LF2 location is in Ribeira Domingo Santo (14.53.59N, 24.28.45W). It is cut by many slightly inclined subparallel thin (ca 5-10 cm) greenish basic dykes though now and again dykes are reaching 30 cm in thickness). Outcrop is highly oxidised and deformed. It provided samples 08SF51 to 08SF60, which are more weathered and stained by iron oxides with fewer mafic minerals.

Fig. 2.4 a**)** Sketch of location LF1 on Fogo from which hand specimens 08SF1 were collected. b) Picture of LF2 carbonatite outcrop highly oxidised, cut by multiply thin subparallel basic dykes slightly inclined.

The third location (LF3) is near Monte Almada and has been divided into two parts, denoted as the upper (U) and lower (L) parts. Site LF3(U), from which coarse-grained carbonatite samples 08SF61 and 08SF62 were obtained, lies at the top of the Monte Almada hill (14.55.06N, 24.29.17W), north of the valley where the lower site is situated. The LF3(L), in the valley bottom (outcrop approximately 30 x 30 m in size) (14.55.05N, 24.29.17W), exposed fairly fresh and white carbonatites. This outcrop is also cut by several basic green dykes, one of which cuts through the carbonatite with a shear zone. The shear zone is composed of distinct layers of two rock-types, which alternate on a mm to cm scale. The white-greyish layers are thicker and composed of coarse-grained calcite. The silicate-rich layers are thin, dark and rich in fine-grained pyroxene and amphibole with some feldspar. The thin silicate-rich layers enclose the thick calcite-rich layers and both parts show evidence of plastic deformation, cross-cutting and slight

folding. Four samples were collected here (08SF63 to 08SF66 – the latter being from one of the pyroxene-rich layers).

There is no evidence for intrusive carbonatites elsewhere on the island, including among the abundant xenoliths brought to the surface in shield stage lava flows. Ten representative samples were studied and detailed information and descriptions of the 15 remaining samples are provided in the Appendix.

2.1.3 Brava

Brava, the youngest westernmost position island of the southern group of the Cape Verde Islands, has the only known subaerial carbonatite volcanism on an oceanic island volcano (Hoernle et al. 2002; Faria and Fonseca 2014), as well as having intrusive carbonatite outcrops in its uplifted seamount complex (Fig. 2.5). Intrusive carbonatites on Brava are the oldest unit. The seamount itself which is now elevated above the sea level. The combination of intrusive alkaline units, such as pyroxenites and ijolites with cross-cutting and intrusive carbonatites is complex (Fig. 2.6). The intimate field relationship of ultramafic/mafic-carbonatite rocks, aided by the inhomogeneity of the collected samples, suggests a close relationship between both units and a complex magmatic evolution. Intrusive carbonatite on Brava in location L4 (Chão Preto 14º 49.609´ N, 24º 41.668´ W) hold sample 08SB38. Location L5 contain remaining samples from 08SB39 to 08SB47 (14º 49.641´ N, 24º 41.818´ W). The L5 site contain mostly silicate rocks with one sövite (08SB39).

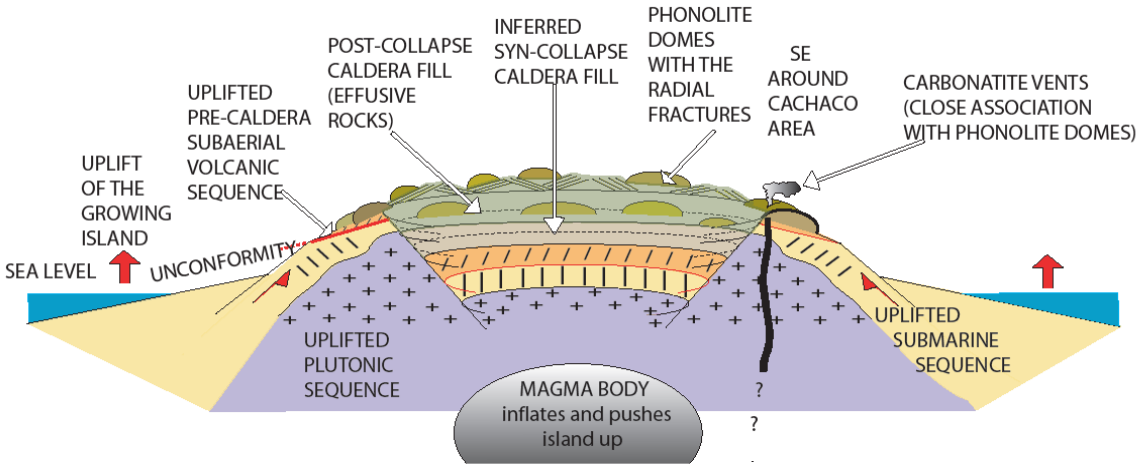

Fig. 2.5 Schematic geological cross-section through Brava Island, Cape Verdes, according to Dr Simon Day (UCL) (personal communication 2011).

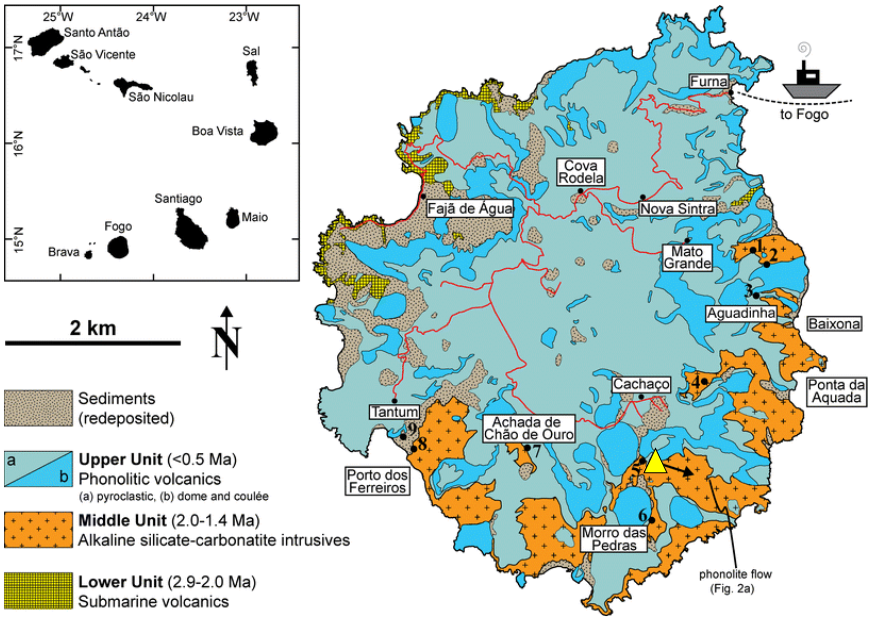

Fig 2.6 Geological map of Brava Island (Madeira et al. 2010) with stratigraphical Units: Lower submarine basalts, Middle intrusives and Upper phonolite domes and extrusives (with minor basalt flows). Yellow triangle represents the LF4 and LF5 sites where silicate–carbonatite samples were collected.

Fig 2.7 L4 and L5 sites with carbonatite and associated silicate rocks from Brava. The silicate rocks include zeolite-carbonatite syenite, calcite syenite, syenite cut by carbonatite, feldspar-feldspathoid syenitic dyke and others.

Eleven samples from this site were collected to perform detailed petrological and mineralogical study of the carbonatite-syenite complex on Brava. Fig. 2.7 demonstrates highly complicated association of carbonatites with silicate-rich rocks in a relatively small area (ca 50 m^2).

2.2 Sample preparation

Specific sites on Fogo and Brava were selected to obtain most representative parts from the collected rocks for sectioning and to save remaining material for further studies. In some cases, two thin sections were required from one rock sample cut at 90º to each other for investigation to a greater depth, e.g., layering investigated in the Fogo samples (08SF65 A and B).

As carbonatites are very fragile rocks, care was taken during grinding and polishing to achieve bubble-free samples. During preparation, water was used as a lubricant. Thin sections were used for mineral analysis by polarized light microscopy, Electron Microprobe and Laser Ablation Inductively-Coupled Mass Spectrometry. Sections were 30µm thick, thus being thin enough for light to pass through them for microscopy and have a polished surface for electron microprobe studies. Each thin section was petrographically analysed and described prior to further investigations. Photomicrographs were made of important textures and mineral relationships. Samples were carbon-coated prior to electron microprobe analysis.

2.3 Analytical methods – Electron Microprobe analysis

Prior to electron microprobe analyses examination of thin and thick sections of carbonatites and associated rocks occurred using an optical microscope during which all slides were studied in detail. Selected slides were used for the further analyses. Accordingly, A4 size scanned images of slides were made to navigate them on electron microprobe and to record sites of the analyses together with important textural and compositional annotations.

Polished thin sections were used to obtain major and minor element concentrations. Major elemental mineral analyses for the Vuoriyarvi samples were obtained using a Jeol 733 Superprobe with an Oxford Instrument INCA energy dispersive system (EDS), Birkbeck College. Data was collected at 15kV for 100 seconds count-time with a 2µm beam/spot diameter and corrected using a SEMQuant (ZAF4) program. The microprobe

was calibrated using Specpure Co metal (99.999 % Co) and profile standardisation material included natural and synthetic silicates and oxides. Total Fe is reported as FeO. The software was updated from INCA to Aztec, resulting in both being use in collecting probe data.

Additional major and minor element mineral analyses were obtained using the updated Jeol 8100 Superprobe (Wavelength Dispersive System - WDS), Birkbeck College, and were carried out using an accelerating voltage of 15 kV, current of 2.5 nA and a beam diameter of 1 μm. The analyses were calibrated against standards of natural silicates, oxides and Specpure metals with the data corrected using a ZAF program. Multiple analyses on a single homogeneous mineral grain revealed good reproducibility, with standard deviations for the major elements being included in relevant tables. Additional tables are included in the Appendices.

All major element mineral analyses for samples from Fogo and Brava were acquired at Birkbeck College using the further updated JEOL JXA-8100 electron microprobe with an Oxford Instrument AZtec microanalytical system (using EDS for most of the data), and were carried out using an accelerating voltage of 15-20 kV, current of 2.5 nA and a beam diameter of 1 μm. The analyses were calibrated against standards of natural silicates, oxides and Specpure metals with the data corrected using a ZAF program. The microprobe was calibrated using Specpure Co metal (99.999 % Co) and profile standardisation material included natural and synthetic silicates and oxides. Total Fe is reported as FeO. Numerous analyses on a single mineral presented good reproducibility, with standard deviations for the major elements being included in relevant tables.

Switching from using the WDS to using the EDS was due to practicality concerns, as the WDS is a longer process that usually runs overnight, and often resulted in a lack of useful data. Lack of control over gathering reliable data overnight became a problem. The complex nature of the samples required hands-on operator control and a more interactive approach to data gathering. Minerals such as xenolith phlogopite and calcite from the Vuoriyarvi carbonatite were analysed by both WDS and EDS resulting in good comparability (Table 2.3).

A drawback to using EDS was that mistakes could be encountered because of misidentification from the EDS software such as overlapping of the peaks of Si and Sr, resulting in Si being falsely identified in calcite. The problem is due to the overlap of the Si-K-alpha and Sr-L-alpha peaks (1.74 keV vs. 1.81 keV) (Fig. 2.8a). The Sr L-alpha is

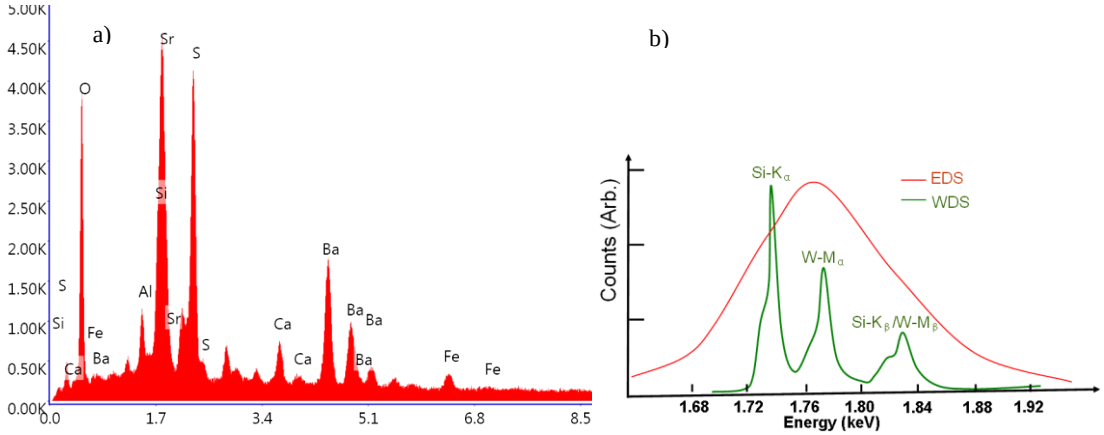

Fig. 2.8 a) EDS analysis showing spectra details for overlapping peaks of Si-K and Sr-L lines (Lang 2016) https://www.researchgate.net/post). b) Comparison between EDS vs WDS X-rays of Si. WDS is more efficient for the concentration of specific, known elements, though EDS is more efficient for an unknown specimen (Practical Electron Microscopy and Database (Liao 2006).

XENOLITH PHLOGOPITE	WDS B218	vs	EDS BR18_1	
	Ave n=23	St dev n=23	Ave n=15	St dev n=15
SiO_2	40.11	0.39	40.79	0.49
TiO_2	0.54	0.03	0.50	0.05
Al_2O_3	14.00	0.24	14.44	0.39
FeO	4.89	0.30	5.05	0.37
MnO	0.15	0.03	0.17	0.01
Cr_2O_3	0.04	0.01	0.01	0.00
MgO	24.97	0.17	24.40	0.82
CaO	0.04	0.03	0.02	0.01
Na_2O	1.05	0.02	1.04	0.05
K_2O	9.21	0.12	8.66	0.26
F	n/a	n/a	0.10	0.01
BaO	0.68	0.20	n/a	n/a
SrO	0.17	0.02	0.01	0.01
TOTAL	96.45	0.55	95.18	1.18
TiO_2+FeO	5.43	0.29	5.55	0.41
Si	5.670	0.033	5.784	0.038
Ti	0.057	0.003	0.053	0.006
Al	2.433	0.038	2.414	0.052
Fe^{2+}	0.578	0.036	0.599	0.051
Mn	0.018	0.003	0.020	0.001
Cr	0.004	0.001	0.001	0.001
Mg	5.260	0.035	5.155	0.118
Ca	0.006	0.005	0.003	0.002
Na	0.289	0.004	0.286	0.017
K	1.660	0.019	1.566	0.038
Ba	0.037	0.011	n/a	n/a
Sr	0.014	0.007	0.000	0.000
Total	16.028	0.014	15.882	0.030
mg#	0.901	0.006	0.896	0.010
Fe+Ti	0.636	0.035	0.652	0.055
Fe/(Fe+Mg)	0.099	0.006	0.104	0.010
Mg/Fe	9.123	0.653	8.670	1.011

	MONTICELLITE						
	WDS		**vs**		**EDS**		
	B218		KR3		BR18		BR18_1
	Ave	St dev	Ave	St dev	Ave	St dev	Ave
	n=10	n=10	n=19	n=19	n=16	n=16	n=12
SiO_2	*36.33*	*0.45*	*36.51*	*0.27*	*36.09*	*0.14*	*36.61*
TiO_2	*0.11*	*0.14*	*0.15*	*0.02*	*0.13*	*0.02*	*0.02*
FeO	*9.06*	*0.09*	*9.00*	*0.37*	*9.41*	*0.06*	*8.61*
MnO	*1.51*	*0.05*	*1.50*	*0.22*	*1.37*	*0.06*	*1.52*
MgO	*18.29*	*0.14*	*18.95*	*0.46*	*18.96*	*0.16*	*18.70*
CaO	*33.43*	*0.08*	*33.82*	*0.81*	*33.35*	*0.84*	*33.37*
TOTAL	*99.33*	*0.38*	*98.92*	*0.25*	*99.89*	*0.85*	*99.83*
Si	*1.000*	*0.007*	*1.002*	*0.006*	*1.000*	*0.003*	*0.997*
Ti	*0.003*	*0.003*	*0.003*	*0.000*	*0.003*	*0.000*	*0.000*
Fe^{2+}	*0.328*	*0.001*	*0.207*	*0.009*	*0.315*	*0.003*	*0.196*
Mn	*0.035*	*0.001*	*0.035*	*0.005*	*0.032*	*0.001*	*0.035*
Mg	*0.750*	*0.009*	*0.775*	*0.018*	*0.770*	*0.012*	*0.800*
Ca	*0.986*	*0.002*	*0.965*	*0.025*	*0.974*	*0.017*	*0.974*
Total	*2.997*	*0.005*	*2.985*	*0.005*	*2.993*	*0.001*	*3.002*
Fe/Mn	*6.383*	*0.207*	*6.026*	*1.126*	*6.815*	*0.359*	*5.610*
mg#	*0.771*	*0.003*	*0.789*	*0.011*	*0.782*	*0.000*	*0.803*
Mg/Fe	*3.371*	*0.056*	*3.756*	*0.244*	*3.590*	*0.009*	*4.085*

Table 2.3 Comparison of analysed minerals such as xenolith phlogopite and monticellite by WDS and EDS, displaying good agreement.

at 1.81 keV but is hidden by the large Si K-alpha peak at 1.74 keV. Although WDS would overcome this problem as is more accurate (Fig. 2.8b), it was not always possible to use this method due to the large amount of collected data.

According to collected data, out of 17 EDS analyses (two thin sections) Si was detected in calcite that apparently lacked Sr; out of 38 EDS analyses (four thin sections) Sr was detected in calcite without Si; out of 55 WDS analyses (three thin sections), Sr was detected in calcite and Si was absent. Thus, there is possibility that in 17 EDS spectra, the Sr peak has been wrongly identified as Si (Table 2.4).

	CALCITE								DOLOMITE (incl in mag)			
	BR18	BR18	ave	st dev	B218A	B218A	ave	st dev	B218A	B218A	ave	st dev
EDS	core (6)	rim (6)	n=12	n=12	core (6)	rim (6)	n=12	n=12	core (2)	rim (3)	n=5	n=5
SiO_2	**0.04**	**0.03**	*0.04*	*0.01*	**2.72**	**2.89**	*2.81*	*0.12*	0.02	0.08	*0.05*	*0.05*
TiO_2	0.16	0.18	*0.17*	*0.01*	0.27	0.07	*0.17*	*0.14*	0.05	0.06	*0.05*	*0.01*
FeO	0.01	0.12	*0.07*	*0.08*	0.06	0.31	*0.19*	*0.18*	0.96	0.60	*0.78*	*0.26*
MnO	0.07	0.05	*0.06*	*0.01*	0.00	0.00	*0.00*	*0.00*	1.80	2.26	*2.03*	*0.33*
MgO	0.12	0.05	*0.09*	*0.05*	0.14	0.15	*0.15*	*0.01*	18.74	18.48	*18.61*	*0.18*
CaO	53.78	53.87	*53.83*	*0.06*	52.21	51.57	*51.89*	*0.45*	29.40	29.39	*29.39*	*0.01*
SrO	**0.53**	**0.51**	*0.52*	*0.01*	**0.00**	**0.00**	*0.00*	*0.00*	n/a	n/a	*n/a*	*n/a*
TOTAL	54.71	54.81	*54.76*	*0.07*	55.40	54.99	*55.20*	*0.29*	50.96	50.86	*50.91*	*0.07*
Si	0.008	0.006	*0.007*	*0.001*	0.526	0.563	*0.544*	*0.026*	0.004	0.016	*0.010*	*0.009*
Ti	0.025	0.028	*0.026*	*0.002*	0.039	0.010	*0.025*	*0.021*	0.007	0.009	*0.008*	*0.002*
Fe^{2+}	0.002	0.021	*0.011*	*0.013*	0.010	0.050	*0.030*	*0.029*	0.156	0.097	*0.126*	*0.042*
Mn	0.012	0.009	*0.010*	*0.002*	0.000	0.000	*0.000*	*0.000*	0.295	0.372	*0.334*	*0.054*
Mg	0.037	0.015	*0.026*	*0.015*	0.040	0.044	*0.042*	*0.002*	5.417	5.356	*5.387*	*0.043*
Ca	11.821	11.827	*11.824*	*0.005*	10.819	10.760	*10.790*	*0.042*	6.111	6.124	*6.117*	*0.010*
Sr	0.063	0.061	*0.062*	*0.002*	0.000	0.000	*0.000*	*0.000*	n/a	n/a	*n/a*	*n/a*
Total	11.967	11.966	*11.967*	*0.001*	11.435	11.427	*11.431*	*0.005*	11.990	11.975	*11.982*	*0.010*
Ca/(Ca+Mg)	0.997	0.999	*0.998*	*0.001*	0.996	0.996	*0.996*	*0.000*	0.530	0.533	*0.532*	*0.002*

Table 2.4. Two samples (BR18 and B218A) where calcite analysis by EDS shows the presence of Si and lack of Sr which can be explained by EDS spectrum in which the Sr peak has been wrongly identified as Si. The other EDS and WDS analysed samples display presence of Sr and lack of Si in the calcite.

Minerals such as feldspars and feldspathoids can lose Na from their structure during electron microprobe analysis. To minimise this loss, the analysis time was shortened with the peak counting times 10 s on peak and 5 s for the background (from the peak counting times 20 s with a background measurement time of 10 s for most elements) and beam was spread from 1 μm to 10 μm.

In addition to mineral analyses by electron microprobe, many Back-Scatter Electron (BSE) images were taken to show the relationships between minerals and the internal textures of minerals. The most unusual areas in selected samples were also analysed using the electron microprobe to make false-colour X-Ray maps.

2.4 Laser Ablation Inductively Coupled Plasma Mass Spectometry

2.4.1 Vuoriyarvi samples

Laser Ablation Inductively Coupled Plasma Mass Spectrometer (LA-ICP-MS) was used for quantitative trace element analysis at Birkbeck College, London. New Wave Research UP213 laser aperture image frequency quintupled Nd:YAG solid state laser operating at 213 nm, coupled an Agilent 7500 a quadrupole ICP-MS system. Between every (approximately) ten analyses on Vuoriyarvi slides, the first two to three and the last two to three analyses in each run were made on the standard silicate glass reference material NIST 612 (National Institute of Standards Technology), for calibration. Spot ablation diameter was 50μm. The samples were ablated with pulses of 80mJ at a pulse repetition rate of 5Hz, over an ablation time of 20 s. Ablation was carried out in He mixed with Ar carrier gas before the plasma torch. The list of the elements and isotopes that were used for LA-ICPMS analyses is shown in Table 2.5.

The average concentration of Ca from the electron microprobe analysis in the particular mineral phase was used to calibrate the ICP-MS analyses. For minerals that did not contain sufficient Ca, such as olivine and phlogopite, values of Mn and Ti from the electron microprobe were used, respectively. For magnetite and ilmenite, the Ti values were used. Due to problems of identifying the reflected light image on the LA-ICP-MS with the BSE image from the electron microprobe, it was not always possible to use the same points for the trace element analyses, so they could be correlated exactly with the points analysed by microprobe. This may result in minor errors in quantification of the trace

elements. The GEMOC Glitter reduction software was used to process the raw data. It was also used to calculate the trace element concentrations normalised to chondrite values of Pearce et al. (1997). All values are reported in ppm.

^{24}Mg	^{59}Co	^{137}Ba	^{166}Er
^{27}Al	^{60}Ni	^{139}La	^{169}Tm
^{42}Ca	^{63}Cu	^{140}Ce	^{172}Yb
^{43}Ca	^{66}Zn	^{141}Pr	^{175}Lu
^{45}Sc	^{69}Ga	^{146}Nd	^{178}Hf
^{47}Ti	^{72}Ge	^{147}Sm	^{181}Ta
^{51}V	^{85}Rb	^{153}Eu	^{208}Pb
^{53}Cr	^{88}Sr	^{157}Gd	^{232}Th
^{55}Mn	^{89}Y	^{159}Tb	^{235}U
^{56}Fe	^{90}Zr	^{163}Dy	^{238}U
^{57}Fe	^{93}Nb	^{165}Ho	

Table 2.5 Table of elements and isotopes that were used for LA-ICPMS analyses in this study.

2.4.2 LA-ICP-MS Fogo samples

Trace element concentrations for minerals in Fogo samples were measured using the RESOlution M-50 193 mm ArF excimer laser coupled to an Aglient 7500ce/cs LA-ICP-MS system at Royal Holloway University of London (RHUL). Between every (approximately) twenty analyses on Fogo slides, including the first and the last one, analyses in each run were made on the standard silicate glass reference material NIST 612 and NIST 610 (National Institute of Standards Technology) for calibration.

All 5 thin sections were cleaned prior to laser-ablation analysis. Spot ablation diameter was 25µm. The samples were ablated with pulse repetition rate of 5Hz, over an ablation time of 40s, with 20s of counting time of the gas blank (background), which was then subtracted from the sample signal to correct for polyatomic interferences. Analyses were then calibrated to ^{29}Si or ^{44}Ca.

The data was exported as time-resolved ‘‘comma separated values’’ (.csv) files from the mass spectrometer, thus the concentrations in the analysed samples had to be recalculated. To process the raw data, a detailed methodology outlined by Dr Manning, Royal Holloway University of London, was used. Final values are reported in ppm and normalised to chondrite values of Pearce et al. (1997).

2.4.3 LA-ICP-MS Brava

As collected Brava samples contain scarce amounts of sensu stricto carbonatite, thus trace elements were collected to investigate calcite, apatite, amphibole phlogopite, orthoclase, albite, zeolite, hilairite and ilmenite from associated alkaline rock samples using LA-ICPMS. Unfortunately, some rare phases such as tazheranite, rhabdophane, parasite, törneboemite, lanthanite, burbankite and barite were too fine grained to be analysed. Laser Ablation Inductively Coupled Plasma Mass Spectrometer (LA-ICP-MS) at Birkbeck College (London) was used for quantitative trace element analysis in four silicate samples.

The sövite sample (08SB39) was analysed at Royal Holloway using the technique previously described. Between every (approximately) ten analyses on Brava slides, including the first and the last one, analyses in each run were made on the standard silicate glass reference material NIST 612 (National Institute of Standards Technology) for calibration. The average concentration from the electron microprobe analysis in the particular mineral phase was used to calibrate the ICP-MS analyses.

All 5 thin sections were cleaned prior to laser-ablation analysis. Spot ablation diameter was 25μm. Due to the difficulties, in some cases, of identifying the reflected light image on the LA-ICP-MS with the BSE image from the electron microprobe and extremely fine grain size, it was not always possible to use the same points for the trace element analyses so they could be correlated exactly with the points analysed by EMP.

2.5 Whole rock composition of Vuoriyarvi samples

Bulk rock chemical data for Dr Balaganskaya's Vuoriyarvi whole rock samples analysed by XRF at the University of Edinburgh includes carbonatites stage 1 and associated phoscorite also stage 1, accompanying by more evolved carbonatites stage 2 and stage 3, and other associated silicate rocks (Table 2.6).

depth in m			27-29	46-50	86.5	21-132	167-184	248-254.5
	cpxite (BR-45)	Alkaline silicate	amph/tetra ferriphl/calcite calcite carb (dol,pyroc)	phlogopite calcite carbonatite	calcite/dol carbonatite with qtz	tetraferriph/ cacl carbon	bt/amph/cal carbonatite	phlogopite mont-calc carbonatite
	(BR-45)	(BR-72)	(BR-30)	(BR-64)	(H-474)	(BR-49)	(BR-82)	(BR-18)
SAMPLE	**BYA45**	**BYA72**	**BYA 30**	**BYA 64**	**H 474**	**BYA 49**	**BYA 82**	**BYA 18**
SiO_2	36.800	35.130	2.220	1.210	20.770	1.060	14.130	6.220
Al_2O_3	6.070	15.140	0.210	0.450	0.410	0.390	4.090	0.700
Fe_2O_3	13.980	9.330	6.020	3.950	8.590	2.690	4.420	3.860
MgO	11.890	3.100	2.700	1.770	10.780	2.520	6.280	3.610
CaO	20.340	11.710	46.040	50.140	21.690	48.970	36.390	46.320
Na_2O	0.830	11.160	0.150	0.000	0.040	0.060	0.930	0.320
K_2O	1.351	0.439	0.272	0.192	0.236	0.186	2.171	0.451
TiO_2	4.826	5.295	0.375	0.080	0.789	0.074	0.164	0.243
MnO	0.182	0.212	0.306	0.141	0.379	0.255	0.173	0.203
P_2O_5	1.758	0.313	2.878	2.173	0.038	2.001	3.790	3.054
LOI	1.380	4.670	35.610	37.940	32.650	37.990	25.650	33.160
Total	99.407	96.499	96.781	98.046	96.372	96.196	98.188	98.141
Rb	34.5	6.5	8.5	5.2	bdl	2.6	34.8	8.7
Ba	793.0	148.0	1111.0	1041.0	2618.0	2270.0	1191.0	779.0
Th	20.0	18.8	12.4	bdl	83.9	117.6	1.7	14.6
K	11215.3	3644.4	2258.0	1593.9	1959.2	1544.1	18022.5	3744.0
Nb	387.0	1241.0	1791.0	24.0	353.0	922.0	43.0	100.0
La	285.0	267.0	522.0	209.0	632.0	366.0	178.0	359.0
Ce	522.0	651.0	1117.0	493.0	1336.0	793.0	335.0	755.0
Sr	612.7	924.6	8561.2	3812.0	11199.0	6869.0	3230.0	4686.4
Nd	229.0	331.0	438.0	213.0	745.0	318.0	128.0	326.0
P	7666.1	1364.9	12550.1	9475.8	165.7	8725.7	16527.0	13317.5
Zr	794.0	579.0	89.0	110.0	237.0	173.0	125.0	372.0
Ti	28931.8	31743.5	2248.1	479.6	4730.1	443.6	983.2	1456.8
Y	36.9	43.3	62.8	37.9	12.5	50.2	30.5	89.0
Cr	10.0	bdl	21.0	bdl	26.0	3.0	10.0	7.0
Zn	78.0	76.0	67.0	17.0	156.0	35.0	61.0	38.0
Cu	116.0	9.0	45.0	113.0	630.0	174.0	50.0	73.0
V	170.0	112.0	471.0	49.0	231.0	24.0	75.0	106.0
Ni	49.0	10.0	18.0	17.0	19.0	14.0	14.0	14.0
Sc	52.0	bdl	28.0	35.0	120.0	41.0	23.0	21.0
Pb	2.7	2.1	6.2	3.5	75.4	4.1	6.8	0.9

Table 2.6 Bulk rock chemical data for Dr Balaganskaya's Vuoriyarvi rock compositions from "Vuoriyarvi 18" borehole such as carbonatites and associated phoscorite and silicate rocks analysed by XRF at Edinburgh. Sampling includes carbonatite which has Russian number BYA 18 translated into English as BR18 and should not be confuse with the thick section sample also numbered as BR18. Also other rocks have both Russian and English numbering.

CHAPTER 3

PETROGRAPHY, CRYSTALLISATION ENVIRONMENT AND MINERAL COMPOSITIONS IN THE VUORIYARVI CARBONATITES

3.1 Petrography of Vuoriyarvi samples

The mineralogical assemblage for eight samples from the Vuoriyarvi borehole is summarised in Table 3.1 and shown in Fig. 3.1. The samples are silica-rich sövites, since calcite is the main mineral (up to 70% modal abundance). Modal distribution of calcite and silicate phases reflects the medium to coarse grained nature of these rocks, giving rise to an uneven distribution of minerals in thin-section. Consequently, some samples such as KR3 and BR18 contain a high percentage of calcite, whereas in others such as BA18A and B218A, silicate minerals are present in nearly equal abundance or even in slightly higher proportions. The main silicate phases are phlogopite and monticellite with subordinate olivine and clinopyroxene. Sample B218A is petrographically distinctly as it contains abundant phlogopite, lacks monticellite and has dolomite inclusions in magnetite.

Carbonate has recrystallised from originally magmatic tabular calcite to a granoblastic form with large and equant crystals which commonly show 120° triple junctions (Fig. 3.2). Apatite is the second dominant phase which is unevenly distributed either in small pockets or small vein-like bodies along calcite grain boundaries. Apatite crystals often display segregation, forming bands, lenses or irregular patches which probably crystallised together and accumulated in separate pockets. It also forms single subhedral crystals between the euhedral calcite crystals or occurs as small inclusions in monticellite, phlogopite and magnetite (Fig. 3.2). Features such as globules and dumbells of calcite and apatite are present mainly in monticellite crystals and in some cases in amphibole (Fig. 3.3).

Magnetite and pyrite form common minor components and are irregularly distributed. Magnetite appears in two forms: the first is fine-grained and associated with amphibole whereas the second forms large and often anhedral crystals full of apatite inclusions. Sample B218A contains magnetite with rare dolomitic inclusions.

Sample:	BA18A	B218	KR3	BR18	B218A	BR18_1	BR18_A	BR18_2
Rock type:	Silicate-rich Carbonatite	Silicate-rich Carbonatite	Silicate-rich Carbonatite	Silicate-rich Carbonatite	Silicate-rich Carbonatite	Silicate-rich Carbonatite	Silicate-rich Carbonatite	Silicate-rich Carbonatite
Mineral phase:								
Calcite	abundant	abundant	abundant	moderate	abundant	abundant	abundant	abundant
Phlogopite(xen)	minor	moderate	n/p	rare	moderate	minor	minor	minor
Phlogopite	abundant	moderate	moderate	moderate	moderate	moderate	moderate	moderate
Apatite	moderate	moderate	moderate	moderate	moderate	moderate	moderate	abundant
Magnetite	minor	minor	minor	abundant	minor	moderate	moderate	minor
Perovskite(xen)	n/p	rare	n/p	n/p	n/p	rare	rare	n/p
Zr-garnet(xen)	rare	rare	n/p	n/p	rare	n/p	rare	n/p
Monticellite	minor	moderate	minor	minor	n/p	moderate	moderate	moderate
Olivine	n/p	minor	n/p	n/p	minor	minor	minor	minor
Pyroxene(xen)	n/p	n/p	n/p	n/p	minor	minor	minor	minor
Amphibole	n/p	n/p	n/p	n/p	n/p	moderate	moderate	n/p
Dolomite	n/p	n/p	n/p	n/p	rare	n/p	n/p	n/p
Andradite	n/p	minor	n/p	n/p	n/p	minor	minor	n/p
Pyrite	minor	minor	minor	minor	minor	minor	minor	minor
Mafic area	n/p	n/p	n/p	n/p	n/p	fine grained: pyroxene-olivine-calcite	n/p	n/p

Table 3.1 Analysed samples from shallow intrusive carbonatitic dykes in Vuoriyarvi. Samples include uncommon varieties with more silicate minerals than normally found, thus they are considered to be silico-carbonatites according to their mineral assemblage, however some minerals are evidently xenocrystic in origin. Abbreviation: n/p=not present, xen=xenocryst

B218 silicate-rich carbonatite

BR18 silicate-rich carbonatite

B218A silicate-rich carbonatite

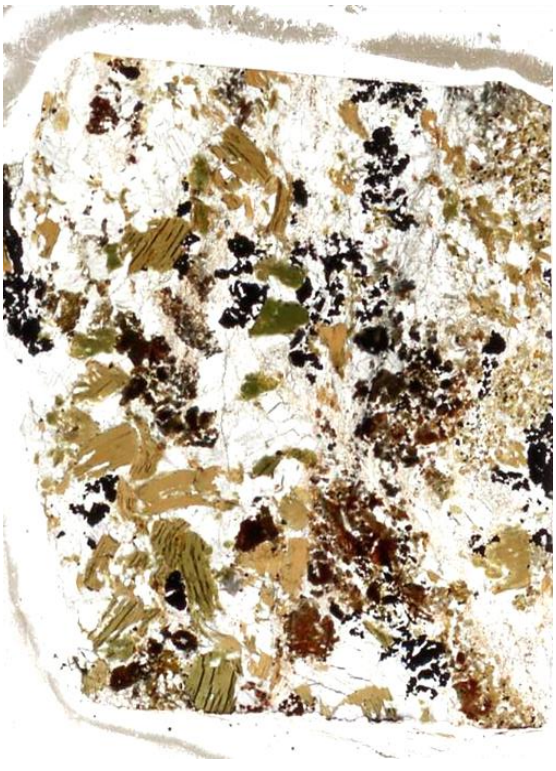

BA18A silicate-rich carbonatite

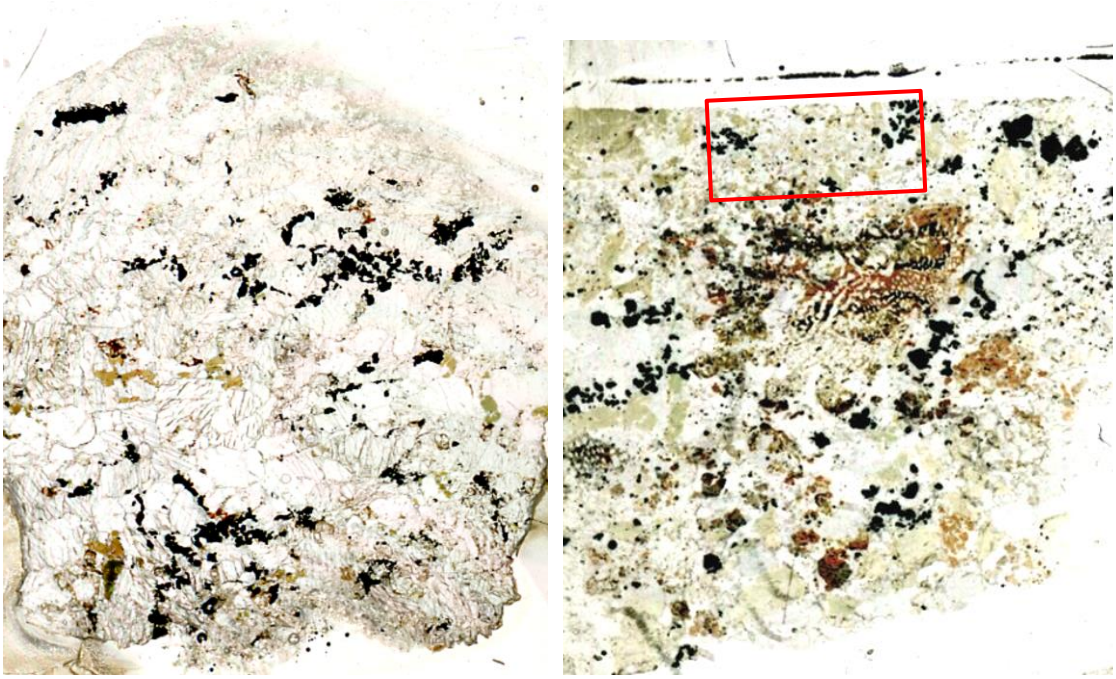

KR3 silicate-rich carbonatite

BR18_1 silicate-rich carbonatite

BR18_2 silicate-rich carbonatite

BR18_A silicate-rich carbonatite

2.5 cm

Fig. 3.1 Scanned images of thin-sections of Vuoriyarvi carbonatite samples, showing distribution of minerals: colourless calcite and some subordinate apatite; coloured ferromagnesian phases are phlogopite, monticellite and pyroxene; black oxides and pyrite are also present (the percentage of minerals is very variable – some sections are rich in ferromagnesian minerals; others are much richer in calcite and apatite). Red rectangular contains the mafic granular area discussed in the text.

Fine to medium grained monticellite exhibits an anhedral habit with characteristic embayments (in contact with calcite) and conchoidal fractures (Fig. 3.3). Round, fine

apatite and round or dumbell-like calcite grains form dense inclusions in monticellite (up to 25 modal %). Fine skeletal and dismembered olivine, often serpentinised, is sometimes strongly associated with monticellite (Fig. 3.3). This relict phase displays clear textural evidence of mineral replacement of olivine by monticellite.

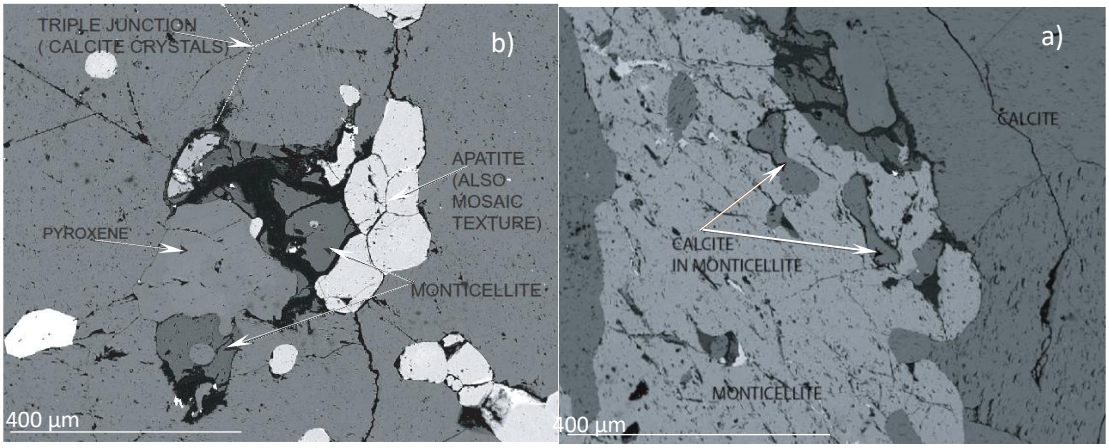

Fig. 3.2 BSE images of BR18_2 sample. (a) Mosaic texture of calcite (dark grey) and apatite (light grey) and small round apatite inclusions in calcite crystals. Darkest grey is monticellite separated by pyroxene (slightly lighter grey than calcite). Monticellite is intimately associated with (black) olivine. The embayed contact between pyroxene and monticellite is noticeable as well as a round calcite inclusions in monticellite. (b) Light grey monticellite with dumbell-like calcite inclusions (dark grey) and embayed contact.

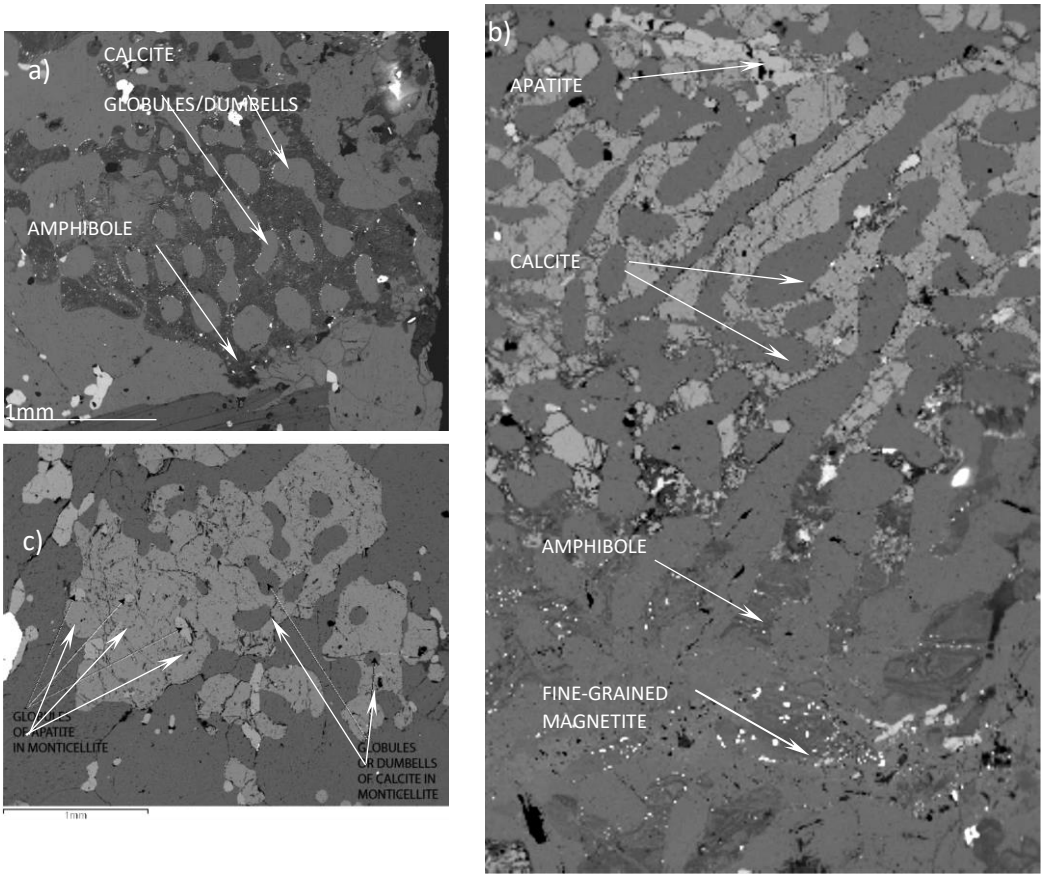

Fig. 3.3 BSE images of BR18_1 (a and b) and BR18_2. a) Amphibole-calcite association showing dumbell and semi-circular to elongated calcite. b) Monticellite-calcite intergrowth with embayed contact. Monticellite encloses dumbell-shaped or round calcite. Transformation from monticellite (upper part) into amphibole (lower part) occurs via olivine (black). c) Light grey monticellite with globule-like apatite inclusions and dumbell/globule-like calcite inclusions.

Another important petrographic feature is the formation of amphibole in sample BR18_1. This consists of a mat-like felt of fibres and in some cases is associated with abundant very fine apatite (Fig. 3.3). The transition from anhydrous monticellite into hydrous amphibole occurred via olivine (Fig. 3.3). Minor clinopyroxene (fine-grained diopside) is present in four samples (Table 3.1), where it forms embayed contacts with calcite and monticellite.

In some samples, e.g., B218, phlogopite takes two forms. One appears as large crystals typically up to 5-6 mm long (Fig. 3.4), but some crystals reach 10 mm in length. They are euhedral, taking a platy form that is often kinked and bent, typically showing brown to dark green pleochroism with pronounced opaque cleavage lines. These are interpreted as being xenocrysts. The second type forms much smaller, lighter brown flakes, full of apatite inclusions and is interpreted as being formed in equilibrium with the carbonatitic liquid (Fig. 3.4).

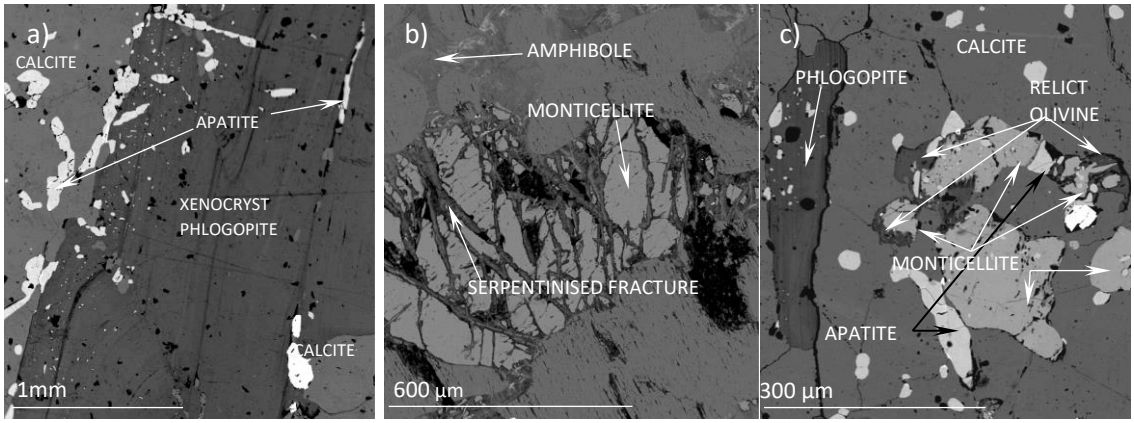

Fig. 3.4 BSE image of B218, BR18_1 and B218 respectively. a) Xenocryst phlogopite with rim full of apatite inclusions while core shows lack of inclusions. b) Monticellite with highly serpentinised conchoidal fractures. c) Monticellite/olivine transition with relict olivine.

Accessory minerals include Zr-rich garnet and perovskite (Fig. 3.5a, b). Perovskite is very rare, but typically contains numerous apatite and calcite inclusions, giving it an unusually spongy appearance (Fig. 3.5a). Nonetheless its sporadic presence in carbonatite and corroded appearance (of a formerly perfectly euhedral cubic form) is apparent. This textural evidence suggests the early crystallisation of perovskite in a more silica-rich environment (e.g., a clinopyroxenite or phoscorite magma) and the resorption feature indicates adaptation to a carbonatite-rich host liquid. Rare Zr-rich garnet occurs in Vuoriyarvi carbonatites (Fig. 3.5b) forming relatively large grains (up to 1mm) and shows a euhedral to anhedral habit with abundant apatite inclusions. The resorption texture could indicate adaptation to a carbonatite-rich magma.

The striking similarity of shape, size, occurrence and association with apatite inclusions could suggest that Zr-rich garnet and Nb-rich perovskite are related and perhaps crystallised under similar conditions. Phoscorites, according to Lee et al. (2003), strongly concentrate accessory Nb-Zr minerals. As the analysed samples are closely associated with phoscorite and/or pyroxenite, there is a strong possibility that the Zr-rich garnet and perovskite originated in these rocks.

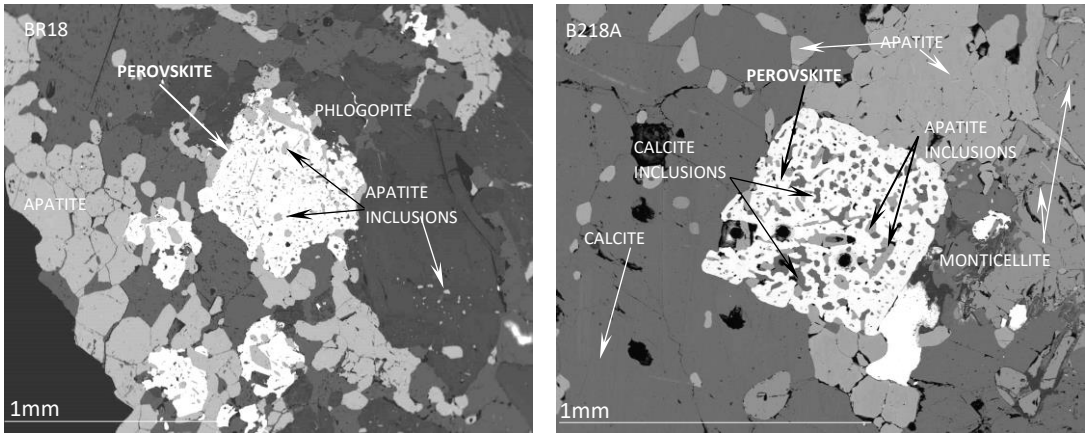

Fig. 3.5a BSE image showing the presence of rare perovskite in Vuoriyarvi carbonatite. The cubic form is still distinguishable with inclusions of apatite (light grey) and fewer inclusions of calcite (darker grey). Inclusions are forming either elongated needles or rounded to sub-rounded blebs.

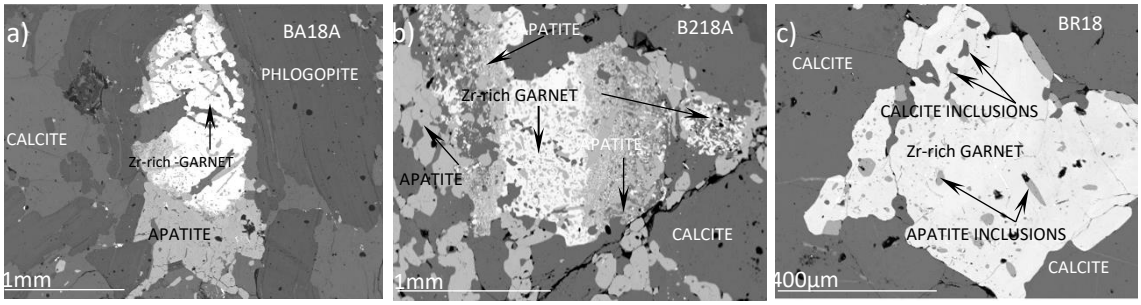

Fig 3.5b BSE images of Zr-rich garnet in BA18A, B218A and BR18 respectively. In (a) and (b) Zr-rich garnet (very light grey) is intimately associated with apatite (slightly darker grey). In BA18A Zr-rich garnet is physically pushed against phlogopite forcing mica-cleavage to wrap around garnet, this indicates that both minerals were not formed at the same time. (c) Zr-rich garnet in BR18 exhibits euhedral form with only few apatite inclusions.

Very rare andradite is usually associated with monticellite or olivine in Vuoriyarvi carbonatites and has a kidney-like appearance and in most cases fills cracks in monticellite crystals (Fig. 3.6). It is a secondary phase, possibly alteration after magnetite in the fractures of monticellite.

Another rare textural and mineralogical feature is areas which are rich in olivine, clinopyroxene and minor calcite with no monticellite and rare apatite. BR18_1 slide contains two such regions. One is roughly 0.5cm x 0.5cm of crudely layered minerals (Fig. 3.7) which are clearly different from the rest of the slide. The area is composed of finer-grained granular textured areas containing clinopyroxene, olivine, calcite and rare

apatite. Olivine appears to be slightly layered, so it is likely that the granular area came from a pre-existing layered rock.

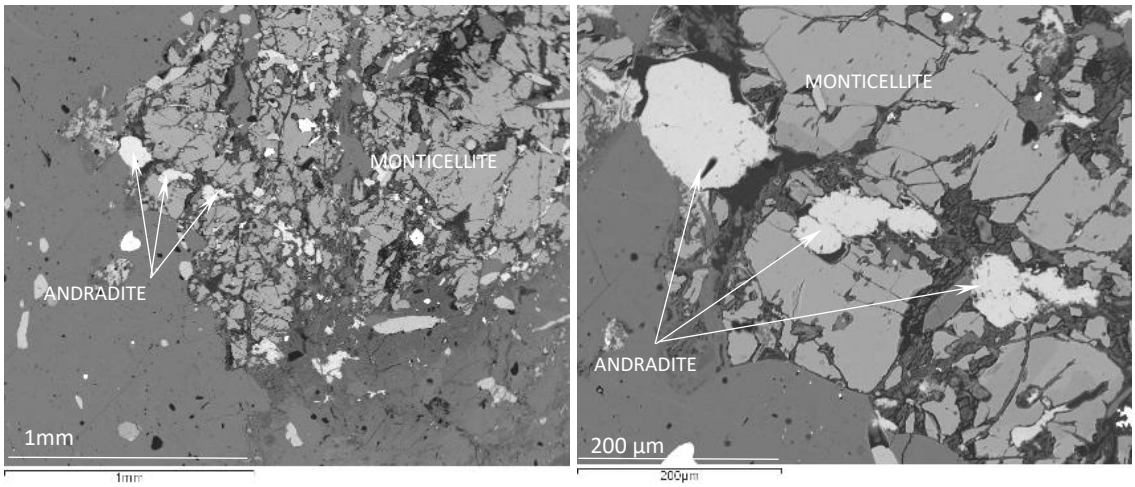

Fig 3.6 BSE image of BR18_1 showing monticellite hosting fine-grained andradite garnet. Higher magnification (right) revealed kidney-like form of andradite filling the fracture in monticellite.

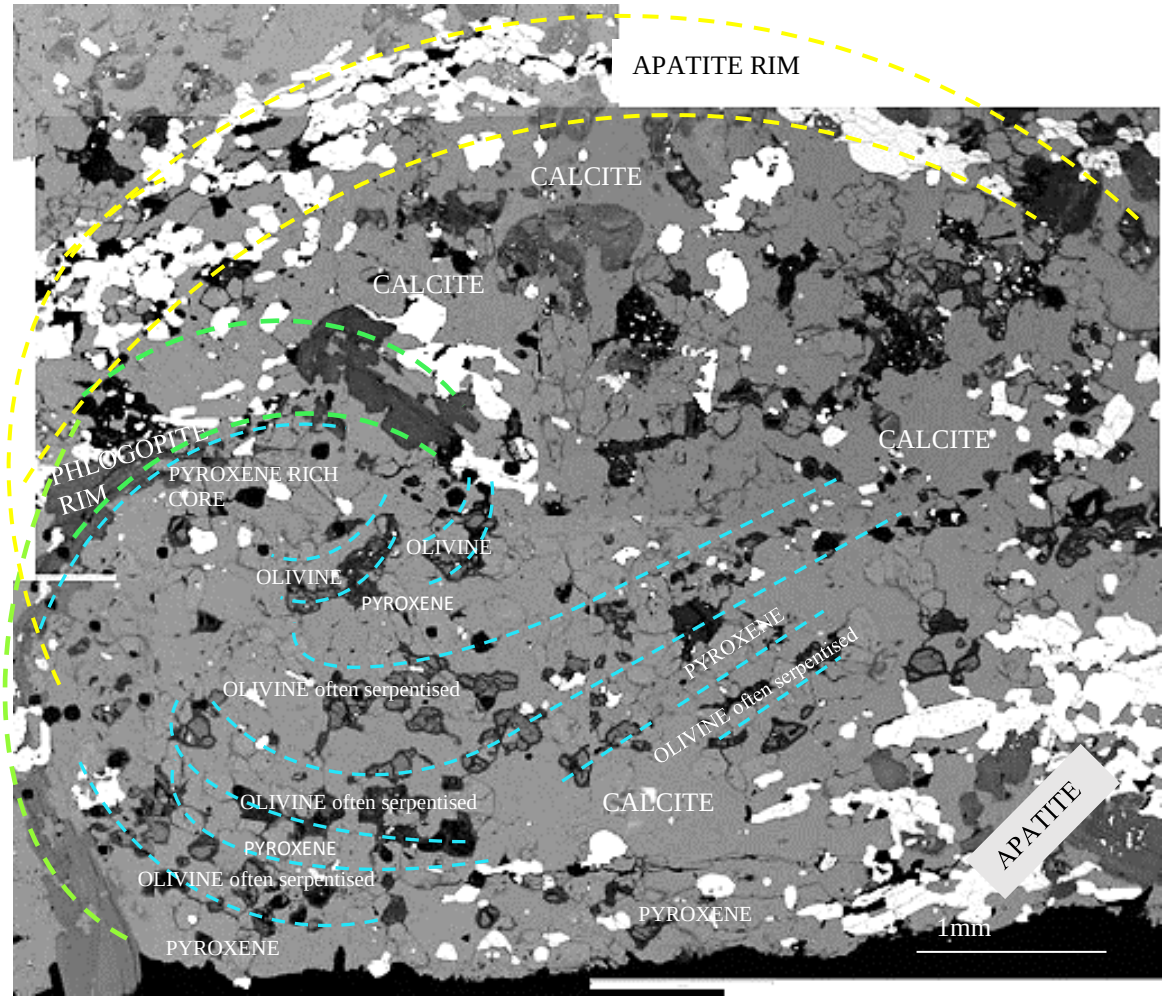

Fig 3.7 Montaged BSE image of mafic fine grained granular region in BR18_1 of olivine layers (dark mineral) separated by layer of pyroxene and some calcite (light grey). Patch is separated from the rest of the rock by phlogopite (green outline) and apatite (yellow outline). Regions separated by blue lines are rich in olivine (often highly serpentised). Large calcite is present. Overall clinopyroxene> olivine> calcite> apatite. The rounded nature of the area shows a spiral shape implying some rotation was induced by turbulent flow operating in carbonatite dykes on this xenolith entrained from the bordering clinopyroxenite.

3.2 Petrographic interpretation

The first generation of phlogopite have irregular boundaries that are often embayed. They are large, dark orange subhedral crystals, with deformed cleavage (bent or kinked) and partly resorbed crystal faces. Thus, they appear to be xenocrysts. Their cores lack inclusions but apatite inclusions are present in their rims, suggesting late-stage overgrowth during apatite crystallisation. Hence the probable succession of crystallisation started with incorporation of phlogopite xenocrysts. The abundance of phlogopite suggests crystallisation from a slightly hydrous magma. During fractional crystallisation, the water content would increase, allowing water-bearing minerals to crystallise. The phenocrysts form much smaller, lighter brown flakes, full of apatite inclusions and it is considered that they were formed in equilibrium with the carbonatitic magma in the early stages of crystallisation.

Perovskite appears as initially euhedral crystals which have been corroded by the carbonatite melt. They most likely formed in a neighbouring clinopyroxenite or phoscorite and were assimilated by the carbonatite magma, Some Vuoriyarvi clinopyroxenites contain 10-40 vol. % perovskite (Karchevsky and Moutte, 2004). Abundant apatite and calcite inclusions suggest simultaneous crystallisation of perovskite with apatite and calcite. Zr-rich garnet also contains fine inclusions of apatite and is closely associated with apatite (Figure 3.6a and b). It forms relatively large grains (up to 1mm) and has a euhedral to anhedral habit with abundant apatite inclusions. Like perovskite, it often appears to be corroded. It is often closely associated with apatite, which sometimes appears to be replacing it. The general lack of calcite inclusions which could indicate that Zr-rich garnet did not crystallise in its host sövite and may also be a xenocryst. It could have formed by early crystallisation in a silico-carbonate magma and incorporated from the country rock such as clinopyroxenites or phoscorite.

The small granular areas with high abundances of clinopyroxene + olivine + calcite (Fig. 3.7) are probably also resorbed fragments of a pre-existing rock, most likely pyroxenite. Low MnO contents of 0.50 wt% are found in olivine from pyroxenite in sample VJA60 (Brassinnes 2006) and (serpentised) olivine in the granular area in carbonatite BR18_1 also show low MnO (0.29-0.47 wt%). In contrast, olivine in carbonatite samples B218A, B218 and BR18A have high MnO contents (1.75-2.02 wt%), comparable to olivine in stage 1 carbonatite VIA18 (1.52-1.71 wt%). Pyroxene in the granular area has low MnO (0.19-0.23 wt%), which is in agreement with pyroxene from pyroxenite VJA60 (0.46-0.53 wt%). Monticellite is not present in the patch in BR18_1

but it is present in the main body of this sample with its high content of MnO of 1.28-1.80 wt%. Average values of MnO in monticellite in samples B218 is 1.80 wt%; in KR3 is 1.50 wt%; in BR18A is 1.46 wt% and in BR18 is 1.37 wt%. Carbonatite from VJA18 (Brassinnes, 2006) do not contain monticellite. Values of MnO in analysed olivine from Vuoriyarvi carbonatite samples: BR18A (1.75-1.93 wt%), B218A (1.90-2.02 wt%), B218 (1.75 wt%) is comparable with the high values of olivine in carbonatite VJA18 (1.66 wt%). Most of the analysed Vuoriyarvi samples contain both olivine and monticellite showing an unusual association not commonly occurring in Vuoriyarvi carbonatites analysed by other authors (including the presence of the granular area).

Karchevsky and Moutte (2004) mentioned the occurrence of monticellite associated with phlogopite in the Tukhta-Vara region of Vuoriyarvi, where monticellite and magnetite are skeletal or vermicular, or enclosed in calcite. These textures and mineralogy, the association of olivine with monticellite, its high MnO content, and proximity to clinopyroxenite and phoscorite dykes, all indicate an exceptionally early stages of carbonatite formation. Thus, the analysed olivine-monticellite assemblage in the Vuoriyarvi carbonatites represents an even earlier stages of development of carbonatites than recorded previously. These unusual samples therefore bring new evidence about very early formation processes of carbonatite.

Large rounded magnetite grains full of apatite and occasional calcite/dolomite inclusions could also be a relict phase from clinopyroxenites/phoscorites, since magnetite is a significant phase in these rock types. The second generation of magnetite is scarce and fine-grained without any inclusions, and may be related to crystallisation in the carbonatite.

Calcite inclusions occur mainly as rounded blebs in monticellite and perovskite. The coarse sövitic calcite groundmass has been affected by recrystallisation as it exhibits a granoblastic texture and not a primary tabular one. It is also mostly inclusion-free. Calcite forms an intergrowth texture with silicate phases such as monticellite or amphibole, leading to formation of globules, dumbbells and blebs.

Rare anhedral inclusion-free diopside shows embayed contacts with monticellite or/and calcite. Amphibole is present as a rare mat-like felt of fibres, occasionally associated with monticellite and olivine. Monticellite occurs in two forms: with or without inclusions. Formation of monticellite was confined to the early stages of sövite crystallisation. It is clearly related to calcite, apatite, and sometimes olivine, diopside and andradite. Inclusion-free monticellite, which is closely associated with olivine and serpentine, could be a recrystallisation feature after forsterite (or xenocrysts possibly

derived from clinopyroxenites). The second type of monticellite contains blebs and globules of calcite and apatite.

Apatite occurs in a range of sizes and different shapes; from euhedral to anhedral, granoblastic to acicular, minute to coarse. This is consistent with constant crystallisation throughout sövite formation. Inclusions of apatite are present in nearly all other minerals. Apatite itself contains only occasional inclusions such as carbonate. The second generation of phlogopite is full of tiny, mostly acicular, apatite inclusions. It was probably in equilibrium with the carbonatite melt.

Textural analyses of a small 2D section of intrusive carbonatites does not reveal all textural aspects of the carbonatite body that would be seen in hand specimen. Brooker and Kjarsgaard (2011) interpreted globular calcite as rounded crystalline calcite that precipitated from a silicate melt. Their interpretation is in agreement with Ionov and Harmer (2002) that rounded $CaCO_3$ originated as a solid phase during precipitation from a silicate melt. Therefore, the textural characteristics of the Vuoriyarvi (e.g., round or dumbbell-shaped calcite and apatite in monticellite) are most likely due to simultaneous crystallisation of minerals in fast upwelling carbonatite magma.

As sövites are often interpreted as cumulates, there is a question about their true origin. The polygonal calcite texture is often interpreted as a secondary post-magmatic recrystallisation feature (Aliev, 1966; Zhabin, 1971; Rosatelli et al. 2000). Hence different processes, operating at the same time or over a short period in the magma system, such as fractionation, crystal settling, deformation, devolatilisation and recrystallisation, could overprint the primary magmatic features. However, Mahotkin et al. (2003) argued that carbonatite dykes represent magmatic liquids rather than cumulates. The petrographic observations of the Vuoriyarvi sovites suggest that they were liquids, because they clearly incorporated xenoliths and xenocrysts from the surrounding rocks.

According to Haynes et al. (2003), crystallisation in carbonatite systems occurs over a range of temperature, and cooling rates are much higher than in large plutons. The presence of monticellite in Vuoriyarvi samples is significant in respect of high-temperature crystallisation of silicate-bearing carbonatite magma. Preservation of high temperature minerals supports the assumption of rapid cooling. Haynes et al. (2003) concluded that the high crystallisation temperature interval (750-550°C) is consistent with small and thin carbonatite dykes. The highest temperatures (745-770°C) were found for calcite–magnetite fractionation, whereas calcite–monticellite fractionation gave 700-

760°C. The Vuoriyarvi mineral assemblage and textural features suggest an early phase of carbonatite formation.

Figure 3.8 shows the general sequence of events deduced from the texture and mineralogy of the Vuoriyarvi carbonatites. The investigated samples of Vuoriyarvi carbonatites show varying textures, which suggest changeable conditions in the magma and probable interaction with the surrounding country rock. Entrainment of phlogopite and some magnetite xenocrysts from the phlogopite-magnetite-rich country rock occurred in the early stages, leading to some alteration of the liquid (slight zonation of the crystallising phenocrystic phlogopite). Perhaps the granular pyroxene-olivine-calcite area represents early sidewall crystallisation, or a resorbed xenolith of pyroxenite. The intergrowth between calcite and monticellite could be explained by trapped liquid rich in both components, leading to simultaneous crystallisation of both phases. Perovskite and Zr-garnet crystallization perhaps took place in an adjacent phoscorite or pyroxenite. The most probable interpretation for the dumbells/globules of calcite found in monticellite is solid-state precipitation of high temperature polymorph of calcite. In the mostly crystallised dyke, the magmatic textures were most likely modified by metamorphic recrystallisation to a granular/ granoblastic texture.

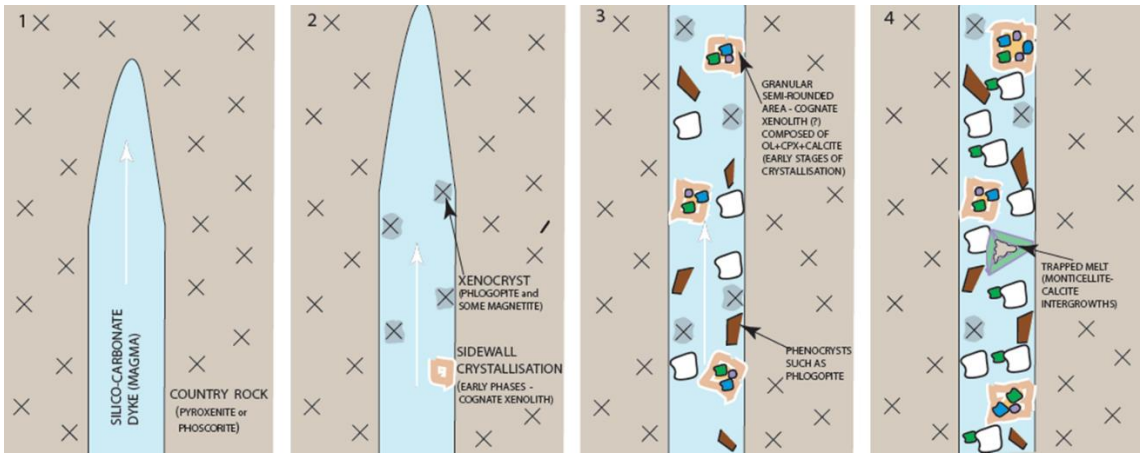

Fig.3.8 Sketch diagram showing possible emplacement of the Vuoriyarvi carbonatite dyke into country rock, just after the immiscibility, and the evolution trend of the dyke with justification of some peculiar texture (author's own interpretation using combined texture and geochemical data). Author's own diagram.

Figure 3.9 shows evidence of the petrographic interpretation of turbulent flow in the Vuoriyarvi carbonaitites, including crystallisation of coarse calcite (during turbulent upward flow) by replacing monticellite and forming "bulbous" texture.

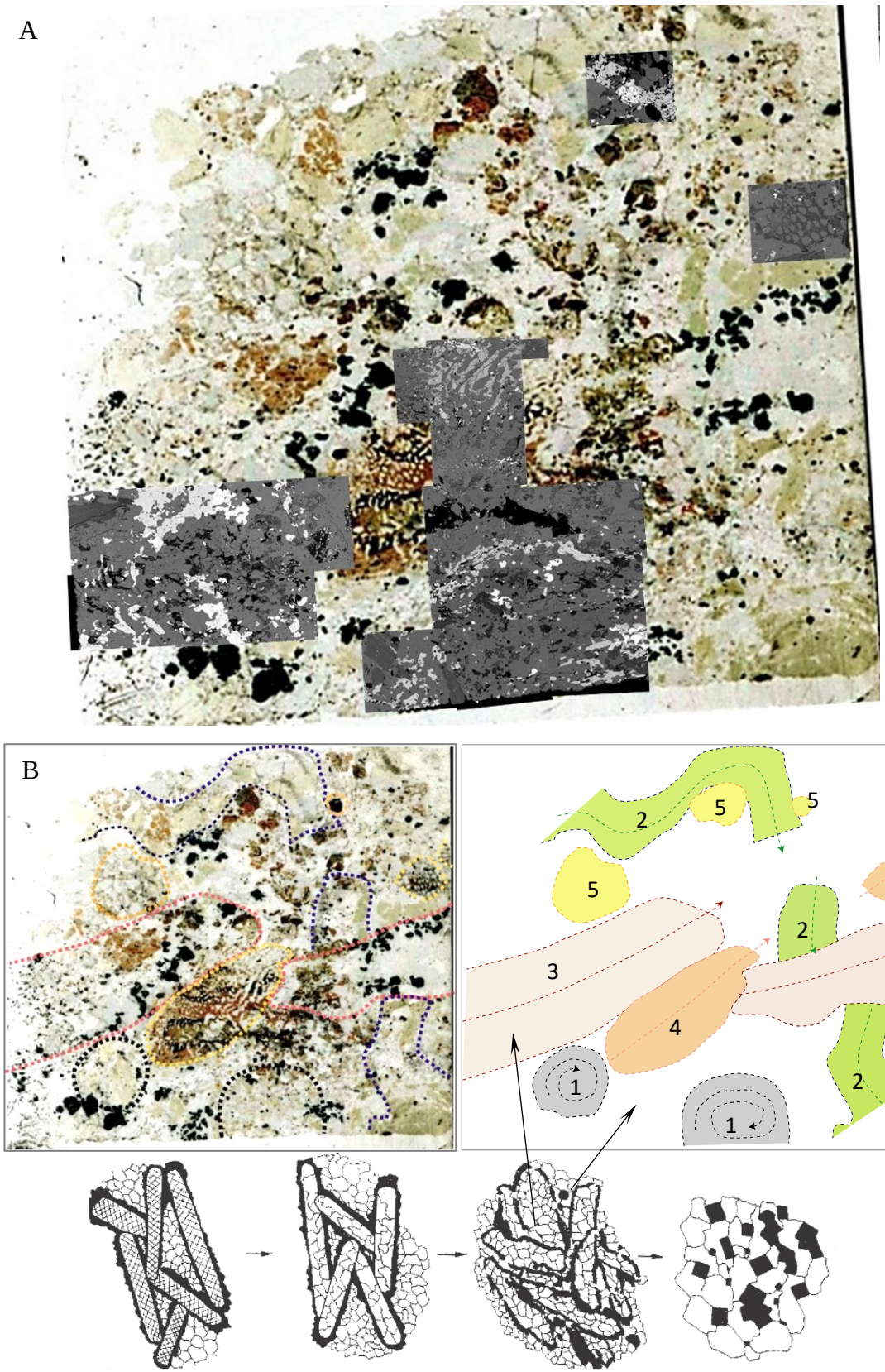

Fig. 3.9a Scanned image of BR18_1 with superimposed BSE images to show detailed texture of this sample. B) Texture of BR18_1 placing it on carbonatite evolution trend showing calcite in elongated areas, rounded pockets all set in areas composed of mafics, opaques, monticellite and apatite. 1. Circular pocket with serpentised olivine, clinopyroxene, calcite, apatite and phlogopite 2. Calcite rimmed by monticellite 3. Calcite, apatite and phlogopite 4. Fine grained calcite, monticellite, phlogopite, olivine and amphibole with elongated fine grained 5. Xenocrystic phases such as coarse xenocrystic phlogopite, perovskite and odd honeycomb texture of apatite.

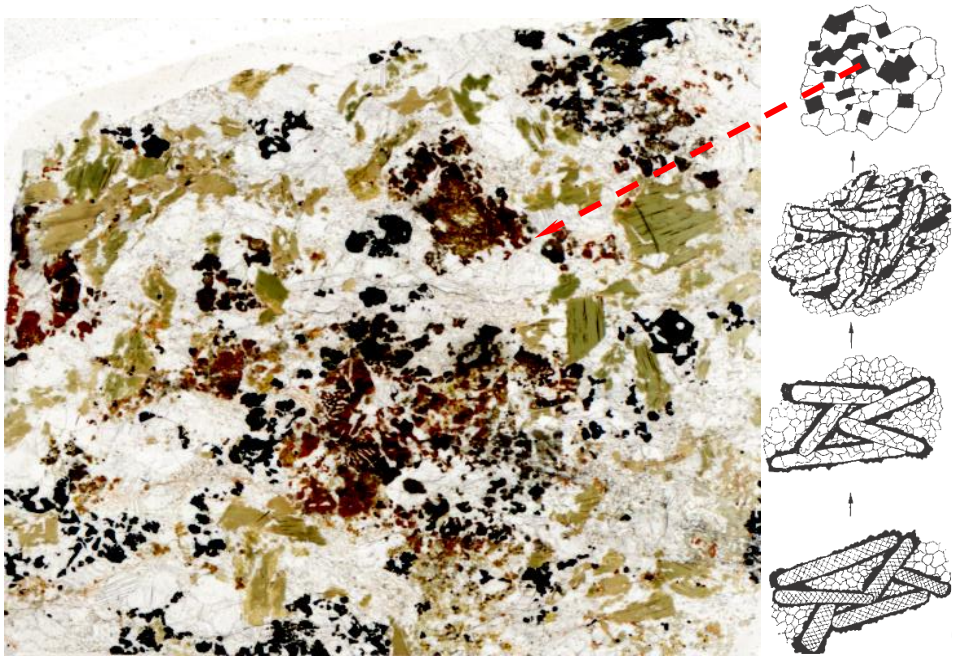

Fig3.9b. A more evolved sample with different texture (and chemistry) in calcite than in section BR18_1) having some coarse calcite overgrown by more equant mafics, opaques, silicates and apatite.

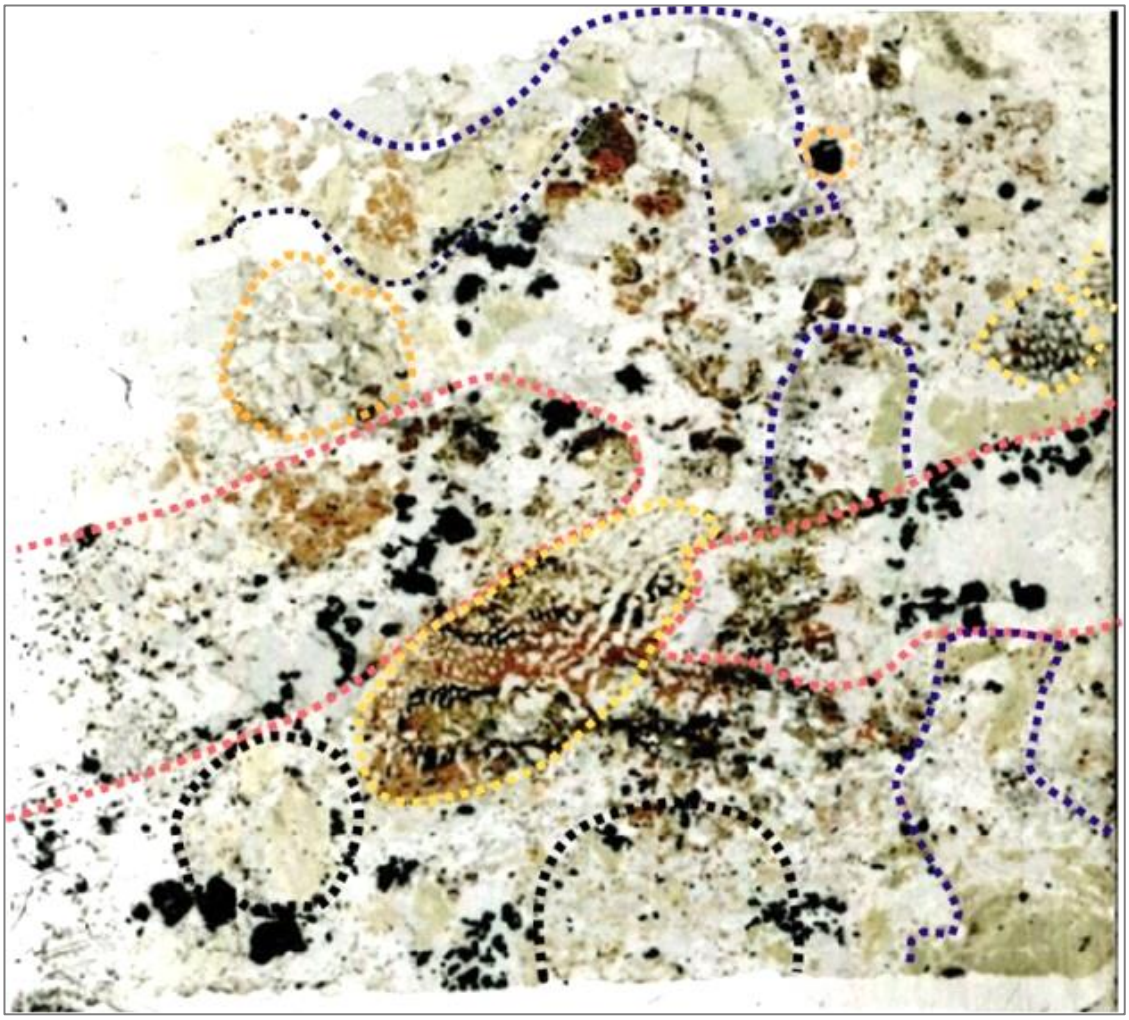

Fig. 3.9 c Interpretation of thin-section evidence for turbulent flow (Vuoriyarvi)

3.3 Major element compositions of minerals

3.3.1 Phlogopite

Major element data for phenocrystic and xenocrystic phlogopite in the studied Vuoriyarvi carbonatites are given in Table 3.2. Table 3.1d-f (Appendix 1) includes data for phlogopite from associated silicate and C1 carbonatite rocks from the same intrusion from Brassinnes (2006) and Karchevsky (2010). Figure 3.10 shows the classification of Vuoriyarvi phlogopite on an Al-Mg-Fe diagram. It is an aluminous mica with an average of 14.6 wt% Al_2O_3. According to Krasnova (2001), the maximum amount of Al_2O_3 in phlogopite from Kovdor is 14.3 wt%, which is also the case here. TiO_2 concentration (0.5-0.8 wt% TiO_2) is lower than phlogopite in Vuoriyarvi pyroxenites and ijolites (1.4-2.3 wt%) but higher than phlogopite in phoscorites (0.2-0.4 wt%) (Fig. 3.11). The low concentration of TiO_2 is also in agreement with an early stage of generation of phlogopite (Krasnova 2001). Hence the microprobe analyses of Vuoriyarvi phlogopite confirm its association with the early stage of carbonatite formation.

Average FeO in phlogopite phenocrysts varies from 4.9 wt% in cores to 4.3 wt% in rims, whereas FeO values in xenocrystic phlogopite cores are higher (5.2 wt%) with rim value of 5.6 wt%. Average MgO concentrations in xenocrysts are lower (rim 23.8 wt% and core 23.0 wt%, i.e., reverse zonation) than in the second generation of phlogopite (rim 24.4 wt% and core 23.9 wt%). The average mg# for phenocrystic phlogopite is 0.90 (0.88-0.92) whereas the average for xenocrystic phlogopite is 0.89 (0.87-0.91). Phenocrysts consistently show slightly higher mg# than xenocrysts.

Phlogopite phenocrysts have 9.1-9.7 wt% K_2O whereas xenocrysts have 8.7-9.2 wt%. Figure 3.9 shows clear core-rim differences (xenocryst and phenocryst phlogopite), demonstrating opposing Mg-Fe enrichment for each trend. The studied phlogopite lies in the field intersecting the trends of phlogopite in ijolite + pyroxenite and phoscorite (Fig. 3.10). Mica in phoscorites shows a negative correlation of Fe/(Fe+Mg) with Al, while mica in ijolites + pyroxenites shows a progressive decrease in Fe/(Fe+Mg) towards carbonatite at constant Al. The intersection between phlogopite from pyroxenite and carbonatite is defined by the xenocryst phlogopite and phenocrystic phlogopite core. In contrast, the phenocrystic phlogopite rims and most of the cores lie close to those from phoscorites. Decreasing Ti content in phlogopite reflects an evolution trend from pyroxenite to carbonatite, while in phoscorite mica Ti is rather uniform relative to the rapidly increasing Al content (towards carbonatite).

	Phenocryst PHLOGOPITE												Xenocryst PHLOGOPITE			
	EDS BA18A ave n=26	st dev n=26	EDS KR3 ave n=12	st dev n=12	EDS BR18 ave n=16	st dev n=16	EDS B218A ave n=12	st dev n=12	WDS B218_l-ge ave n=16	st dev n=16	WDS B218_l-ge ave n=44	st dev n=44	WDS B218 ave n=23	st dev n=23	EDS BR18 ave n=15	st dev n=15
SiO_2	39.72	*0.01*	39.18	*0.26*	39.60	*0.13*	39.12	*0.18*	40.08	*0.61*	40.44	*0.27*	40.11	*0.39*	40.79	*0.49*
TiO_2	0.79	*0.01*	0.50	*0.04*	0.57	*0.05*	0.50	*0.01*	0.59	*0.12*	0.50	*0.04*	0.54	*0.03*	0.50	*0.05*
Al_2O_3	13.97	*0.20*	14.16	*0.17*	14.44	*0.06*	13.87	*0.12*	14.90	*0.40*	14.56	*0.27*	14.60	*0.24*	14.44	*0.39*
FeO	4.42	*0.36*	4.19	*0.41*	4.71	*0.21*	4.29	*0.53*	4.91	*0.44*	4.55	*0.22*	4.89	*0.30*	5.05	*0.37*
MnO	0.17	*0.00*	0.21	*0.10*	0.21	*0.09*	0.08	*0.03*	0.16	*0.04*	0.13	*0.03*	0.15	*0.03*	0.17	*0.01*
Cr_2O_3	0.02	*0.01*	0.02	*0.00*	0.06	*0.06*	0.12	*0.04*	0.02	*0.03*	0.04	*0.01*	0.04	*0.01*	0.01	*0.00*
MgO	25.20	*0.40*	24.68	*0.21*	24.63	*0.16*	24.73	*0.47*	25.09	*0.54*	25.40	*0.13*	24.97	*0.17*	24.40	*0.82*
CaO	0.13	*0.10*	0.09	*0.04*	0.21	*0.28*	0.05	*0.07*	0.01	*0.01*	0.08	*0.06*	0.04	*0.03*	0.02	*0.01*
Na_2O	1.30	*0.01*	1.34	*0.13*	1.35	*0.04*	1.18	*0.03*	1.03	*0.02*	1.08	*0.03*	1.05	*0.02*	1.04	*0.05*
K_2O	9.73	*0.25*	9.10	*0.25*	9.16	*0.09*	9.14	*0.08*	9.14	*0.17*	9.25	*0.06*	9.21	*0.12*	8.66	*0.26*
BaO	n/a	*n/a*	0.74	*0.14*	0.73	*0.21*	0.69	*0.16*	0.90	*0.34*	0.66	*0.09*	0.68	*0.20*	n/a	*n/a*
SrO	n/a	*n/a*	0.24	*0.08*	0.23	*0.04*	0.28	*0.06*	0.16	*0.09*	0.12	*0.05*	0.17	*0.08*	0.01	*0.01*
TOTAL	95.44	*0.32*	94.43	*0.23*	95.87	*0.10*	94.02	*0.16*	96.99	*0.15*	96.80	*0.60*	96.45	*0.55*	95.18	*1.13*
TiO_2+FeO	5.21	*0.35*	4.69	*0.37*	5.28	*0.16*	4.79	*0.54*	5.50	*0.57*	5.05	*0.25*	5.43	*0.29*	5.55	*0.41*
Cations recalculated on the basis of 22 oxygens																
Si	5.662	*0.003*	5.661	*0.033*	5.648	*0.006*	5.676	*0.009*	5.640	*0.056*	5.683	*0.016*	5.670	*0.033*	5.784	*0.038*
Ti	0.085	*0.002*	0.054	*0.004*	0.061	*0.005*	0.055	*0.002*	0.063	*0.013*	0.053	*0.004*	0.057	*0.003*	0.053	*0.006*
Al	2.348	*0.031*	2.412	*0.031*	2.428	*0.015*	2.372	*0.028*	2.472	*0.079*	2.412	*0.033*	2.433	*0.038*	2.414	*0.052*
Fe^{2+}	0.526	*0.043*	0.506	*0.050*	0.562	*0.026*	0.520	*0.066*	0.578	*0.055*	0.534	*0.026*	0.578	*0.036*	0.599	*0.051*
Mn	0.021	*0.000*	0.026	*0.012*	0.025	*0.011*	0.010	*0.004*	0.019	*0.005*	0.016	*0.004*	0.018	*0.003*	0.020	*0.001*
Cr	0.002	*0.002*	0.002	*0.000*	0.006	*0.007*	0.013	*0.004*	0.002	*0.003*	0.004	*0.002*	0.004	*0.001*	0.001	*0.001*
Mg	5.352	*0.090*	5.315	*0.041*	5.234	*0.024*	5.348	*0.085*	5.261	*0.086*	5.319	*0.035*	5.260	*0.035*	5.155	*0.118*
Ca	0.020	*0.015*	0.013	*0.005*	0.032	*0.043*	0.008	*0.011*	0.002	*0.001*	0.013	*0.009*	0.006	*0.005*	0.003	*0.002*
Na	0.358	*0.002*	0.374	*0.038*	0.373	*0.011*	0.332	*0.007*	0.282	*0.003*	0.296	*0.011*	0.289	*0.004*	0.286	*0.017*
K	1.769	*0.045*	1.678	*0.045*	1.666	*0.020*	1.691	*0.019*	1.641	*0.023*	1.659	*0.014*	1.660	*0.019*	1.566	*0.038*
Ba	n/a	*n/a*	0.042	*0.008*	0.041	*0.012*	0.039	*0.009*	0.050	*0.019*	0.037	*0.005*	0.037	*0.011*	n/a	*n/a*
Sr	n/a	*n/a*	0.020	*0.007*	0.019	*0.004*	0.024	*0.005*	0.013	*0.007*	0.009	*0.004*	0.014	*0.007*	0.000	*0.000*
Total	16.142	*0.009*	16.104	*0.017*	16.094	*0.005*	16.088	*0.003*	16.022	*0.011*	16.034	*0.021*	16.028	*0.014*	15.882	*0.030*
mg#	0.910	*0.008*	0.913	*0.008*	0.903	*0.005*	0.911	*0.012*	0.901	*0.010*	0.909	*0.004*	0.901	*0.006*	0.896	*0.010*
Fe+Ti	0.611	*0.041*	0.560	*0.046*	0.622	*0.021*	0.575	*0.068*	0.641	*0.069*	0.587	*0.028*	0.636	*0.035*	0.652	*0.055*
Fe/(Fe+Mg)	0.090	*0.008*	0.087	*0.008*	0.097	*0.005*	0.089	*0.012*	0.099	*0.010*	0.091	*0.004*	0.099	*0.006*	0.104	*0.010*
Mg/Fe	10.210	*0.997*	10.551	*1.123*	9.328	*0.482*	10.376	*1.478*	9.151	*1.026*	9.976	*0.518*	9.123	*0.653*	8.670	*1.011*

Table 3.2 Electron microprobe data showing average values for phenocryst and xenocryst phlogopite in shallow intrusive carbonatites, Vuoriyarvi. Abbreviation n/a=not analysed, c=core, r=rim.

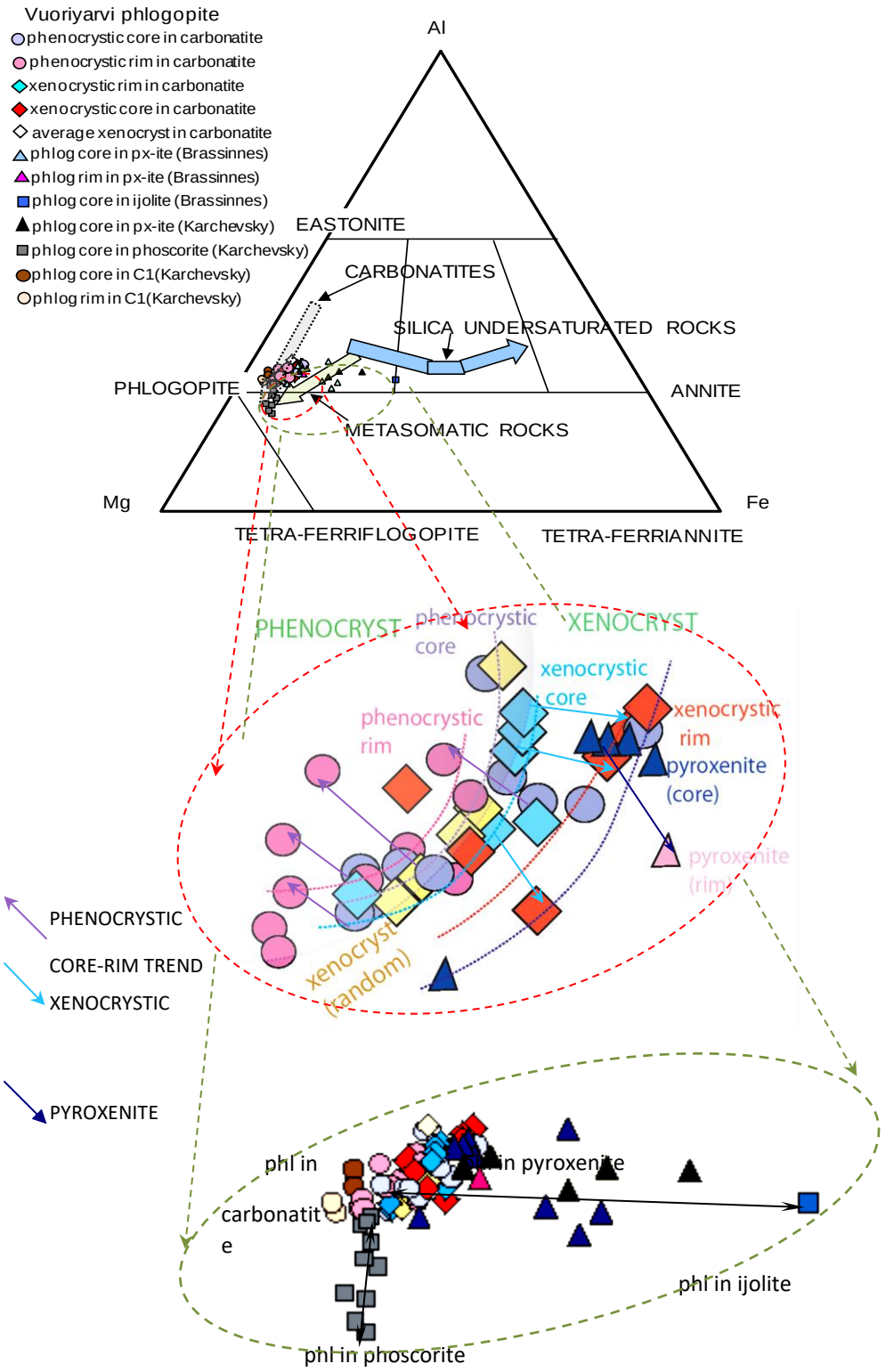

Fig.3.10 Classification of mica in Vuoriyarvi carbonatites according to Mg-Al-Fe components with the phenocryst-xenocryst distinction for the analysed phlogopite. Phlogopite from pyroxenites is included (Brassinnes, 2006) and core-rim trends (arrows) are plotted for the analysed phlogopite from the Vuoriyarvi carbonatites. Pyroxenites, ijolites, phoscorites and early carbonatites (C1) from the Vuoriyarvi complex are added (data from Brassinnes (2006) and Karchevsky (2010)). The main diagram is modified after Brod et al. (2001) showing composition of Jacupiranga micas (Al, Fe and Mg (p.f.u.)) as the evolution trend arrows (Fe obtained as Fe^{total} is recalculated to Fe^{2+}).

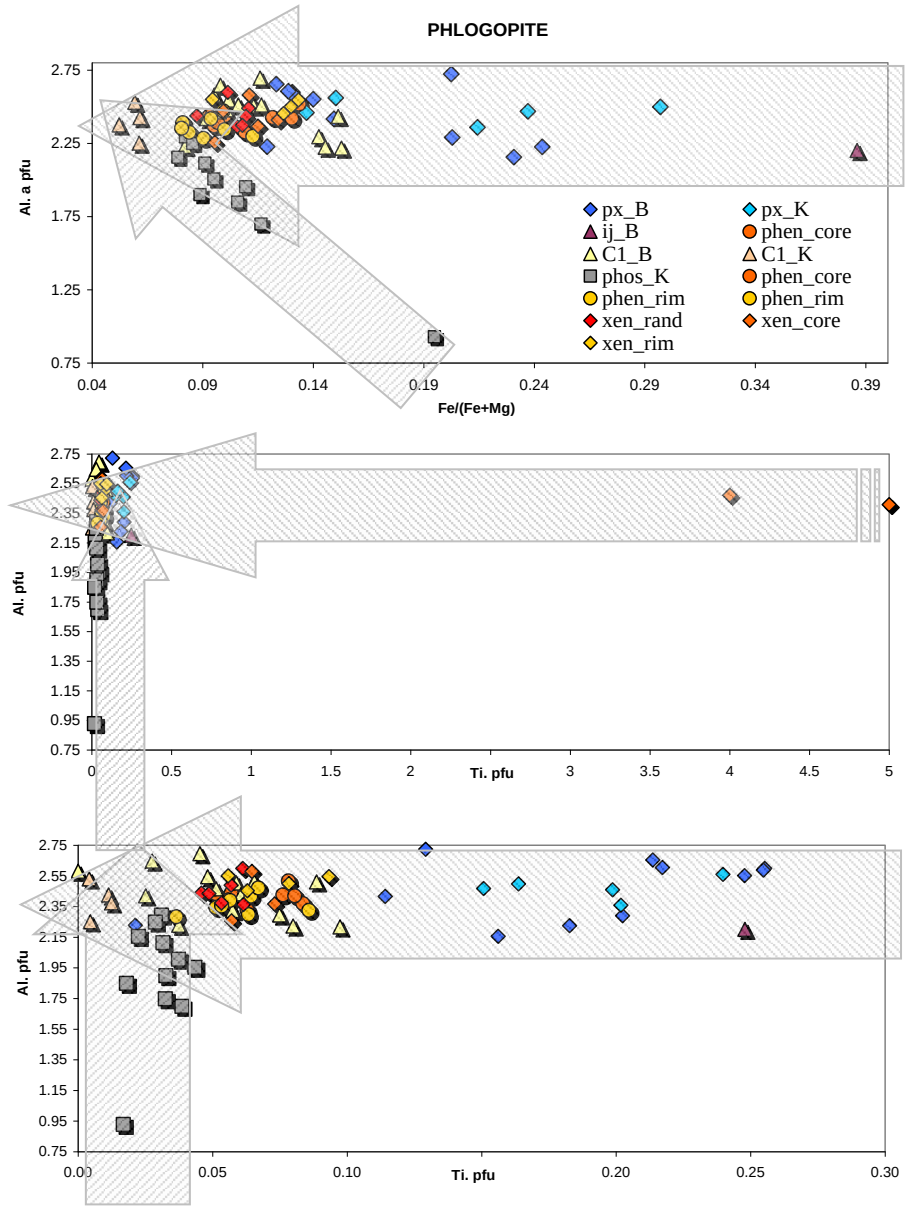

Fig.3.11 Variation diagram showing the chemical trends (Al vs. Fe/(Fe+Mg) and Al vs. Ti) for phlogopites from carbonatites and associated pyroxenites, phoscorites and ijolite from Vuoriyarvi. B in legend stands for the data from Brassinnes (2006), and K for the data from Karchevsky (2010).

3.3.2 Calcite and dolomite

Compositional data for coarse-grained calcite and fine-grained calcite inclusions in other phases are given in Table 3.3a-c. Table 3.3b distinguishes calcite as an inclusion or as a single crystal. Table 3.3d (Appendix 1) includes data for calcite from carbonatite from Oricola (Stoppa et al., 2005), and sövites from Kaiserstuhl, Oka and Almö (Horning-Kjarsgaard, 1998). CaO concentration in calcite varies with the lowest value in inclusions in magnetite (48 wt%), whereas granoblastic calcite contains 51.6-58.6 wt% CaO.

Dolomite inclusions in magnetite contain 24.4 wt% CaO. Dolomite is a primary mineral crystallised in the very early stage of carbonatite generation (Harmer and Gittins, 1998).

In most samples, calcite contains 0.3-0.6 wt% SrO (Table 3.3a) except for sample B218A, in which the calcite totally lacks SrO. Calcite inclusions in some magnetite crystals in sample B218 are also very poor in SrO (0.05 wt%). Calcite in B218A shows an apparent lack of SrO but a relatively high concentration of SiO_2 (2.7-3.1 wt%) which is due to misidentification of Sr for Si by the EDS software. In contrast, calcite with significant concentrations of SrO never appears to contain SiO_2.

Figure 3.12 shows the composition of Vuoriyarvi calcite on a diagram of MgO vs. SrO compared with calcite from worldwide carbonatite localities. It demonstrates a narrow variation in MgO for Vuoriyarvi calcite while Oricola calcite shows broad variation. The variation for SrO of Vuoriyarvi calcite is wide-ranging while Oricola calcite is more restricted. Some Vuoriyarvi calcite inclusions in apatite and all Vuoriyarvi calcite inclusions in magnetite show low SrO levels and high level of SiO_2, thus they are also affected by misidentification of Sr for Si. Figure 3.12 also shows uniform concentration of SrO with variable MgO in calcite from the associated rocks such as pyroxenite and phoscorite. Calcite from pyroxenite plots in the sövite field, meaning that it is closely related to the same phase in carbonatite

	Phenocryst PHLOGOPITE												Xenocryst PHLOGOPITE			
	EDS BA18A ave n=26	st dev n=26	EDS KR3 ave n=12	st dev n=12	EDS BR18 ave n=16	st dev n=16	EDS B218A ave n=12	st dev n=12	WDS B218_l-ge ave n=16	st dev n=16	WDS B218_l-ge ave n=44	st dev n=44	WDS B218 ave n=23	st dev n=23	EDS BR18 ave n=15	st dev n=15
SiO_2	39.72	*0.01*	39.18	*0.26*	39.60	*0.13*	39.12	*0.18*	40.08	*0.61*	40.44	*0.27*	40.11	*0.39*	40.79	*0.49*
TiO_2	0.79	*0.01*	0.50	*0.04*	0.57	*0.05*	0.50	*0.01*	0.59	*0.12*	0.50	*0.04*	0.54	*0.03*	0.50	*0.05*
Al_2O_3	13.97	*0.20*	14.16	*0.17*	14.44	*0.06*	13.87	*0.12*	14.90	*0.40*	14.56	*0.27*	14.60	*0.24*	14.44	*0.39*
FeO	4.42	*0.36*	4.19	*0.41*	4.71	*0.21*	4.29	*0.53*	4.91	*0.44*	4.55	*0.22*	4.89	*0.30*	5.05	*0.37*
MnO	0.17	*0.00*	0.21	*0.10*	0.21	*0.09*	0.08	*0.03*	0.16	*0.04*	0.13	*0.03*	0.15	*0.03*	0.17	*0.01*
Cr_2O_3	0.02	*0.01*	0.02	*0.00*	0.06	*0.06*	0.12	*0.04*	0.02	*0.03*	0.04	*0.01*	0.04	*0.01*	0.01	*0.00*
MgO	25.20	*0.40*	24.68	*0.21*	24.63	*0.16*	24.73	*0.47*	25.09	*0.54*	25.40	*0.13*	24.97	*0.17*	24.40	*0.82*
CaO	0.13	*0.10*	0.09	*0.04*	0.21	*0.28*	0.05	*0.07*	0.01	*0.01*	0.08	*0.06*	0.04	*0.03*	0.02	*0.01*
Na_2O	1.30	*0.01*	1.34	*0.13*	1.35	*0.04*	1.18	*0.03*	1.03	*0.02*	1.08	*0.03*	1.05	*0.02*	1.04	*0.05*
K_2O	9.73	*0.25*	9.10	*0.25*	9.16	*0.09*	9.14	*0.08*	9.14	*0.17*	9.25	*0.06*	9.21	*0.12*	8.66	*0.26*
BaO	n/a	*n/a*	0.74	*0.14*	0.73	*0.21*	0.69	*0.16*	0.90	*0.34*	0.66	*0.09*	0.68	*0.20*	n/a	*n/a*
SrO	n/a	*n/a*	0.24	*0.08*	0.23	*0.04*	0.28	*0.06*	0.16	*0.09*	0.12	*0.05*	0.17	*0.08*	0.01	*0.01*
TOTAL	95.44	*0.32*	94.43	*0.23*	95.87	*0.10*	94.02	*0.16*	96.99	*0.15*	96.80	*0.60*	96.45	*0.55*	95.18	*1.13*
TiO_2+FeO	5.21	*0.35*	4.69	*0.37*	5.28	*0.16*	4.79	*0.54*	5.50	*0.57*	5.05	*0.25*	5.43	*0.29*	5.55	*0.41*
Cations recalculated on the basis of 22 oxygens																
Si	5.662	*0.003*	5.661	*0.033*	5.648	*0.006*	5.676	*0.009*	5.640	*0.056*	5.683	*0.016*	5.670	*0.033*	5.784	*0.038*
Ti	0.085	*0.002*	0.054	*0.004*	0.061	*0.005*	0.055	*0.002*	0.063	*0.013*	0.053	*0.004*	0.057	*0.003*	0.053	*0.006*
Al	2.348	*0.031*	2.412	*0.031*	2.428	*0.015*	2.372	*0.028*	2.472	*0.079*	2.412	*0.033*	2.433	*0.038*	2.414	*0.052*
Fe^{2+}	0.526	*0.043*	0.506	*0.050*	0.562	*0.026*	0.520	*0.066*	0.578	*0.055*	0.534	*0.026*	0.578	*0.036*	0.599	*0.051*
Mn	0.021	*0.000*	0.026	*0.012*	0.025	*0.011*	0.010	*0.004*	0.019	*0.005*	0.016	*0.004*	0.018	*0.003*	0.020	*0.001*
Cr	0.002	*0.002*	0.002	*0.000*	0.006	*0.007*	0.013	*0.004*	0.002	*0.003*	0.004	*0.002*	0.004	*0.001*	0.001	*0.001*
Mg	5.352	*0.090*	5.315	*0.041*	5.234	*0.024*	5.348	*0.085*	5.261	*0.086*	5.319	*0.035*	5.260	*0.035*	5.155	*0.118*
Ca	0.020	*0.015*	0.013	*0.005*	0.032	*0.043*	0.008	*0.011*	0.002	*0.001*	0.013	*0.009*	0.006	*0.005*	0.003	*0.002*
Na	0.358	*0.002*	0.374	*0.038*	0.373	*0.011*	0.332	*0.007*	0.282	*0.003*	0.296	*0.011*	0.289	*0.004*	0.286	*0.017*
K	1.769	*0.045*	1.678	*0.045*	1.666	*0.020*	1.691	*0.019*	1.641	*0.023*	1.659	*0.014*	1.660	*0.019*	1.566	*0.038*
Ba	n/a	*n/a*	0.042	*0.008*	0.041	*0.012*	0.039	*0.009*	0.050	*0.019*	0.037	*0.005*	0.037	*0.011*	n/a	*n/a*
Sr	n/a	*n/a*	0.020	*0.007*	0.019	*0.004*	0.024	*0.005*	0.013	*0.007*	0.009	*0.004*	0.014	*0.007*	0.000	*0.000*
Total	16.142	*0.009*	16.104	*0.017*	16.094	*0.005*	16.088	*0.003*	16.022	*0.011*	16.034	*0.021*	16.028	*0.014*	15.882	*0.030*
mg#	0.910	*0.008*	0.913	*0.008*	0.903	*0.005*	0.911	*0.012*	0.901	*0.010*	0.909	*0.004*	0.901	*0.006*	0.896	*0.010*
Fe+Ti	0.611	*0.041*	0.560	*0.046*	0.622	*0.021*	0.575	*0.068*	0.641	*0.069*	0.587	*0.028*	0.636	*0.035*	0.652	*0.055*
Fe/(Fe+Mg)	0.090	*0.008*	0.087	*0.008*	0.097	*0.005*	0.089	*0.012*	0.099	*0.010*	0.091	*0.004*	0.099	*0.006*	0.104	*0.010*
Mg/Fe	10.210	*0.997*	10.551	*1.123*	9.328	*0.482*	10.376	*1.478*	9.151	*1.026*	9.976	*0.518*	9.123	*0.653*	8.670	*1.011*

Table 3.2 Electron microprobe data showing average values for phenocryst and xenocryst phlogopite in shallow intrusive carbonatites, Vuoriyarvi. Abbreviation n/a=not analysed, c=core, r=rim.

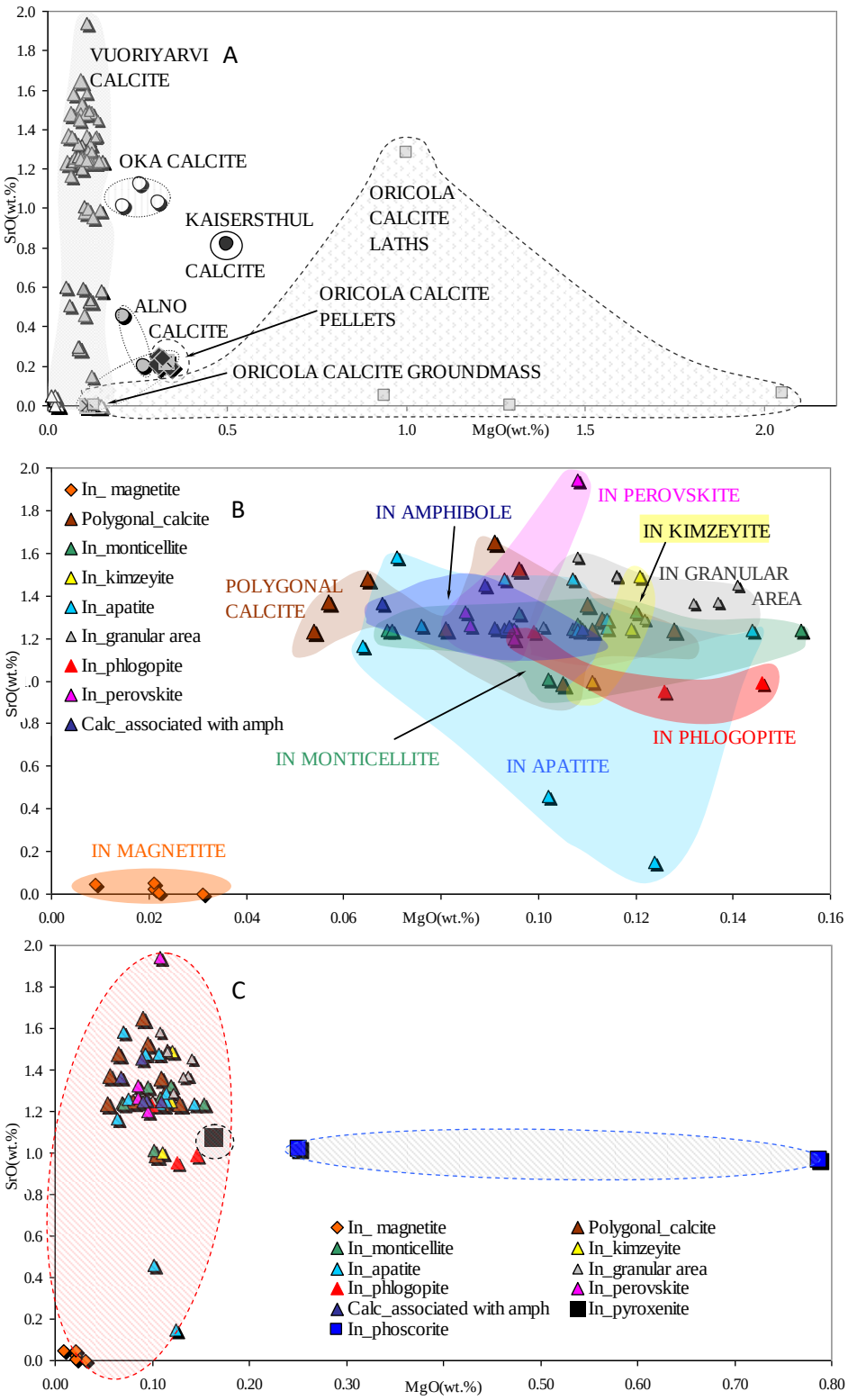

Fig.3.12A) Calcite composition expressed as MgO vs. SrO for Vuoriyarvi sövites and different carbonatite localities. Imported data from Hornig-Kjarsgaard, 1998, where calcite-bearing sövite rock types were selected to compare with the similar Vuoriyarvi specimens. Calcite from extrusive carbonatites from Oricola are considered to be of primary composition. B) Compositional fields of the Vuoriyarvi calcite as an inclusion in different phases and as a separate granular phase. C) Vuoriyarvi calcite from sövite vs. Vuoriyarvi calcite from pyroxenite and phoscorite (Karchevsky, 2010).

	CALCITE						DOLOMITE Inclusion in magnetite	
	BA18A		KR3		BR18		B218A	
	ave	st dev	ave	st dev	ave	st dev	ave	st dev
EDS	n=6	n=6	n=8	n=8	n=12	n=12	n=5	n=5
SiO_2	0.03	*0.04*	0.02	*0.03*	0.04	*0.01*	0.05	*0.05*
TiO_2	0.22	*0.10*	0.24	*0.03*	0.17	*0.01*	0.05	*0.01*
FeO	0.12	*0.09*	0.10	*0.04*	0.07	*0.08*	0.78	*0.26*
MnO	0.06	*0.03*	0.03	*0.04*	0.06	*0.01*	2.03	*0.33*
MgO	0.11	*0.06*	0.08	*0.04*	0.09	*0.05*	18.61	*0.18*
CaO	54.79	*0.06*	52.74	*0.48*	53.83	*0.06*	29.39	*0.01*
SrO	0.55	*0.05*	0.60	*0.01*	0.52	*0.01*	n/a	*n/a*
TOTAL	55.86	*0.24*	53.80	*0.52*	54.76	*0.07*	50.91	*0.07*
Si	0.006	*0.009*	0.004	*0.006*	0.007	*0.001*	0.010	*0.009*
Ti	0.033	*0.015*	0.038	*0.004*	0.026	*0.002*	0.008	*0.002*
Fe^{2+}	0.019	*0.015*	0.017	*0.006*	0.011	*0.013*	0.126	*0.042*
Mn	0.010	*0.005*	0.005	*0.007*	0.010	*0.002*	0.334	*0.054*
Mg	0.031	*0.019*	0.023	*0.011*	0.026	*0.015*	5.387	*0.043*
Ca	11.797	*0.031*	11.799	*0.010*	11.824	*0.005*	6.117	*0.010*
Sr	0.063	*0.006*	0.072	*0.000*	0.062	*0.002*	n/a	*n/a*
Total	11.961	*0.007*	11.958	*0.010*	11.967	*0.001*	11.982	*0.010*
Ca/(Ca+Mg)	0.997	*0.002*	0.998	*0.001*	0.998	*0.001*	0.532	*0.002*

Table 3.3a Electron microprobe data for calcite and dolomite in shallow intrusive carbonatites, Vuoriyarvi. Abbreviations: n/a=not analysed, n=number of analysis (some elements are below detection limit in some analyses). Cations recalculated on the basis of 12 oxygens.

	lge mosaic BR18A and BR18		inc in other phases BR18A and BR18							
	aver n=11	st dev n=11	aver n=11	st dev n=11	aver n=11	st dev n=11	aver n=11	st dev n=11	aver n=11	st dev n=11
SiO_2	0.02	*0.02*	0.02	*0.04*	0.02	*0.02*	0.01	*0.02*	0.02	*0.02*
FeO	0.00	*0.00*	0.01	*0.02*	0.00	*0.01*	0.00	*0.00*	0.00	*0.00*
MnO	0.02	*0.01*	0.01	*0.01*	0.01	*0.01*	0.02	*0.01*	0.01	*0.01*
MgO	0.09	*0.02*	0.11	*0.02*	0.10	*0.02*	0.12	*0.02*	0.09	*0.01*
CaO	53.66	*1.12*	53.49	*0.93*	53.52	*1.07*	53.52	*1.00*	53.17	*0.77*
SrO	1.33	*0.18*	1.24	*0.14*	1.14	*0.44*	1.32	*0.20*	1.34	*0.21*
TOTAL	55.12	*1.03*	54.88	*0.96*	54.79	*1.07*	54.99	*0.88*	54.64	*0.73*
Si	0.003	*0.004*	0.003	*0.004*	0.003	*0.005*	0.003	*0.004*	0.004	*0.005*
Fe^{2+}	0.001	*0.001*	0.003	*0.005*	0.001	*0.001*	0.000	*0.001*	0.000	*0.000*
ng	0.003	*0.002*	0.003	*0.003*	0.001	*0.002*	0.003	*0.002*	0.002	*0.002*
Mg	0.028	*0.008*	0.031	*0.007*	0.031	*0.007*	0.037	*0.005*	0.028	*0.003*
Ca	1.804	*0.028*	1.816	*0.029*	1.824	*0.054*	1.797	*0.024*	1.799	*0.031*
Sr	0.158	*0.023*	0.141	*0.028*	0.137	*0.053*	0.157	*0.026*	0.161	*0.026*
TOTAL	1.997	*0.004*	1.997	*0.004*	1.997	*0.005*	1.997	*0.004*	1.996	*0.005*
Ca/(Ca+Mg)	0.998	*0.001*	0.997	*0.001*	0.997	*0.001*	0.997	*0.000*	0.998	*0.000*

Table 3.3b Electron microprobe data for calcite as an inclusion in different phases in shallow intrusive carbonatites, Vuoriyarvi (some elements are below detection limit in some analyses).

3.3.3 Monticellite and olivine

Compositional data for major elements of monticellite, olivine and serpentine from Vuoriyarvi carbonatites are given in Table 3.4. Table 3.5c-d (Appendix 1) contains imported data for olivine in associated silicate and carbonatite rocks from the Vuoriyarvi

complex (Brasinness, 2006) and olivine from Kola peridotite xenoliths (Beard et al., 2007). Figure 3.13 shows the classification of phases on a Ca-Mg-Fe ternary plot.

Coexisting monticellite and olivine are present in samples B218, BR18_A, BR18_1 and BR18_2. They are part of Mg-Fe solid solution series with olivine mg# around 0.89-0.90. CaO content in monticellite is 32.7-33.9 wt%. MnO enrichment is evident from core (1.32 wt%) to rim (1.65 wt%) and shows normal zoning. Average FeO in monticellite is >9 wt% but reverse zoning is apparent. Increase in MgO from core to rim is not consistent but the average value is 19.3 wt%. Monticellite has a mg# 0.77-0.81, lower than olivine (Figures 3.13 and 3.14).

Olivine is rare and forms small relict crystals, often associated with monticellite, and is often heavily serpentinised. MnO contents from core to rim decrease from 2.0 wt% to 1.9 wt%. Olivine has a high mg# (0.90) which falls between that of olivine from a Vuoriyarvi carbonatite, and olivine from the Vuoriyarvi pyroxenites (Brassinnes, 2006) (Figure 3.13). There is a negative correlation when mg# is plotted against SiO_2. The Fe/Mn value also decreases with increasing SiO_2. Monticellite has lower SiO_2 values (36-37 wt%) and lower mg#.

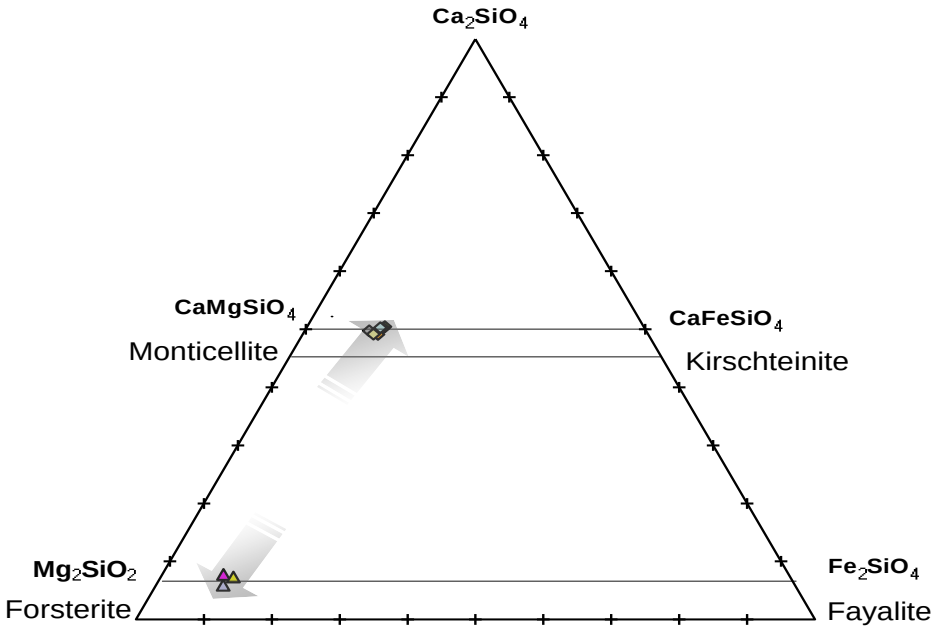

Fig.3.13 Diagram showing solid solution solution series between monticellite-kirschteinite forsterite-fayalite.

	MONTICELLITE								(Ca-)OLIVINE			SERPENTINE		SERPENTISED OLIVINE
	WDS						EDS		WDS		EDS	WDS		EDS
	B218		KR3		BR18		BR18A		B218A and B218		BR18A			BR18_1
	ave	st dev	ave	st dev	ave	st dev	ave	st dev	ave	st dev	ave	ave	st dev	ave
	n=10	n=10	n=19	n=19	n=16	n=16	n=12	n=12	n=6	n=6	n=1	n=3	n=3	rand (n=3)
SiO_2	36.33	*0.45*	36.51	*0.27*	36.69	*0.14*	36.61	*0.06*	41.12	*0.34*	40.32	42.80	*0.78*	45.44
TiO_2	0.12	*0.14*	0.15	*0.02*	0.13	*0.02*	0.02	*0.00*	0.08	*0.14*	0.00	0.07	*0.07*	0.01
FeO	9.66	*0.09*	9.00	*0.37*	9.41	*0.06*	8.61	*0.59*	9.82	*0.70*	10.27	5.43	*2.31*	3.45
MnO	1.51	*0.05*	1.50	*0.22*	1.37	*0.06*	1.52	*0.08*	1.89	*0.14*	1.91	0.65	*0.69*	0.35
MgO	18.29	*0.14*	18.95	*0.46*	18.96	*0.16*	19.70	*0.05*	46.46	*0.95*	47.53	35.42	*4.29*	40.32
CaO	33.43	*0.08*	32.82	*0.81*	33.35	*0.84*	33.37	*0.15*	0.55	*0.09*	0.58	0.22	*0.07*	0.13
TOTAL	99.33	*0.38*	98.92	*0.25*	99.89	*0.85*	99.82	*0.54*	99.92	*0.72*	100.61	84.59	*1.90*	89.70
Cations recalculated on the basis of 4 oxygens														
Si	1.000	*0.007*	1.002	*0.006*	1.000	*0.003*	0.997	*0.002*	1.015	*0.005*	0.991			
Ti	0.003	*0.003*	0.003	*0.000*	0.003	*0.000*	0.000	*0.000*	0.001	*0.003*	0.000			
Fe^{2+}	0.223	*0.001*	0.207	*0.009*	0.215	*0.003*	0.196	*0.013*	0.203	*0.017*	0.211			
Mn	0.035	*0.001*	0.035	*0.005*	0.032	*0.001*	0.035	*0.002*	0.039	*0.003*	0.041			
Mg	0.750	*0.009*	0.775	*0.018*	0.770	*0.012*	0.800	*0.004*	1.708	*0.018*	1.742			
Ca	0.986	*0.002*	0.965	*0.025*	0.974	*0.017*	0.974	*0.007*	0.014	*0.002*	0.015			
Total	2.997	*0.005*	2.985	*0.005*	2.993	*0.001*	3.002	*0.001*	2.981	*0.005*	3.000			
Fe/Mn	6.383	*0.207*	6.026	*1.126*	6.815	*0.359*	5.610	*0.088*	5.163	*0.686*	5.147			
mg#	0.771	*0.003*	0.789	*0.011*	0.782	*0.000*	0.803	*0.011*	0.896	*0.006*	0.892			
Mg/Fe	3.371	*0.056*	3.756	*0.244*	3.590	*0.009*	4.085	*0.290*	8.469	*0.770*	8.250			

Table 3.4. Electron microprobe data for monticellite, olivine and serpentine in shallow intrusive carbonatites, Vuoriyarvi. Abbreviations: n=number of analysis (TiO_2 is below detection limit in most analyses).

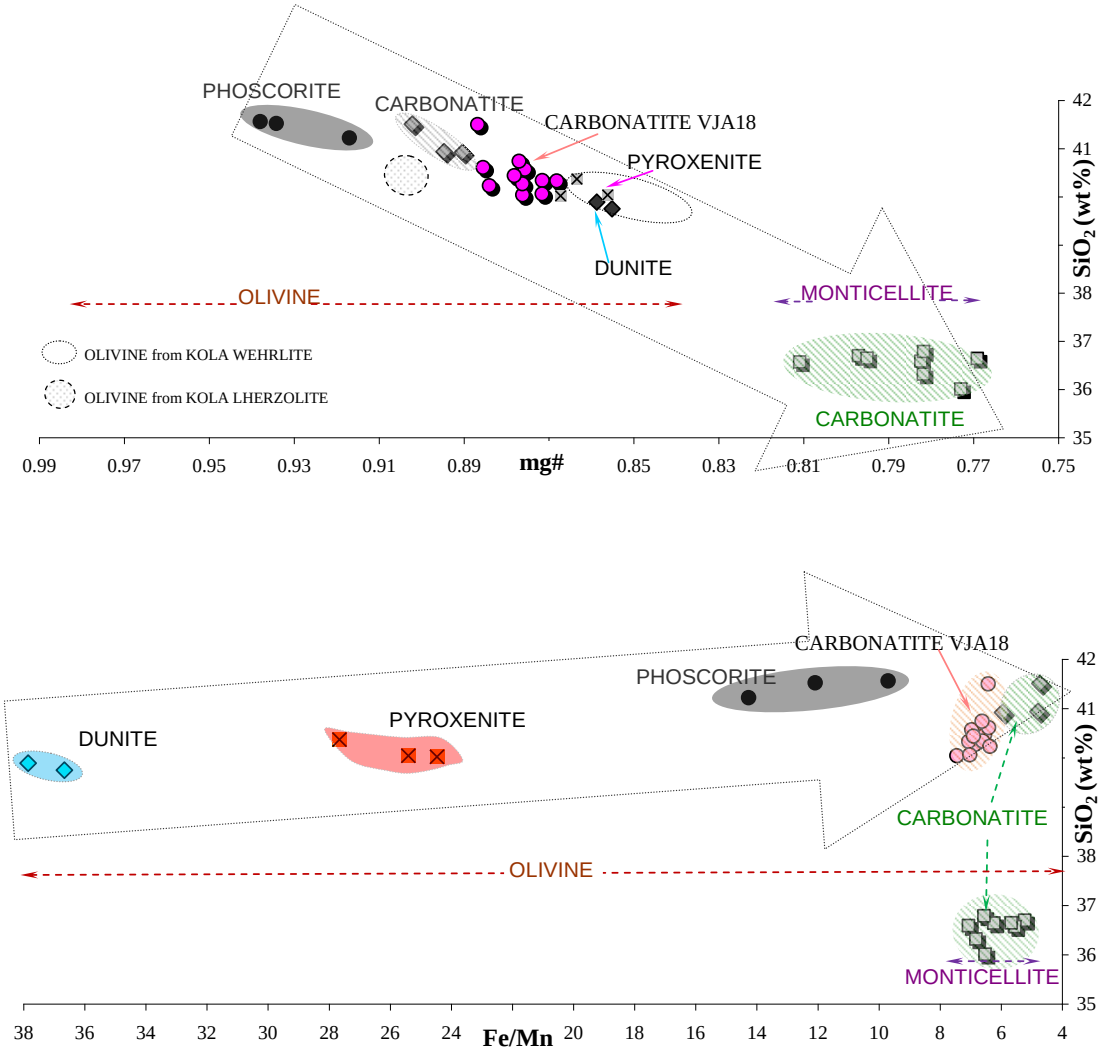

Fig.3.14 a) Olivine and monticellite in carbonatites from Vuoriyarvi and olivine from xenoliths from Kola Peninsula plotted on diagram SiO_2 versus mg#. Data includes also imported analyses from Brassinnes (2006) and Beard et al. (2007). b) Olivine and monticellite in carbonatites from Vuoriyarvi plotted on diagram SiO_2 versus Fe/Mn ratio with additional data from Brassinnes (2006).

3.3.4 Apatite

Compositional data for major elements of apatite from Vuoriyarvi carbonatites is given in Table 3.5. It contains 0.9-1.1 wt% F, so it is fluorapatite. Variation diagrams of major elements versus CaO in apatite are shown in Figure 3.15. This includes composition of apatite as inclusions in other minerals such as monticellite, phlogopite, Zr-rich garnet and amphibole.

There are two distinct levels of CaO in apatite; the higher content (54.5-56 wt%) is more common and the lower content (52-53.5 wt%) is less common. SiO_2 content reaches 2 wt% in all apatites and is slightly more enriched in cores (1.6-1.7 wt%) compared with rims (1.3-1.5 wt%). Sample B218A shows the opposite trend where the

	single apatite between large calcite grains		apatite from trail		hexagonals small ap in lge calcite		pocket's rim	in phlogopoite		many inclusion		n kimzeyit		in perovskite	with amph
	BR18_2		BR18A		BR18_2		BR18A	BR18_2		BR18_1		BR18A		BR18__1	BR18A
WDS	ave n=3	st dev n=3	ave n=3	st dev n=3	ave n=3	st dev n=3	ave n=1	ave n=4	st dev n=4	ave n=2	st dev n=2	ave n=2	st dev n=2	ave n=1	ave n=1
SiO_2	1.27	0.17	1.40	0.16	1.85	0.08	1.54	1.31	0.31	1.77	0.13	2.04	0.07	2.21	1.67
Al_2O_3	0.02	0.04	0.00	0.00	0.00	0.00	0.00	0.07	0.09	0.00	0.00	0.00	0.00	1.52	0.00
FeO	0.09	0.16	0.00	0.01	0.00	0.00	0.00	0.01	0.01	0.03	0.04	0.00	0.00	0.00	0.01
MnO	0.25	0.27	0.00	0.00	0.00	0.00	0.00	0.00	0.00	0.39	0.55	0.00	0.00	0.00	0.00
MgO	0.03	0.05	0.02	0.00	0.01	0.01	0.02	0.05	0.06	0.09	0.01	0.03	0.01	0.21	0.02
CaO	53.80	1.10	55.39	0.16	55.50	0.41	55.58	55.59	0.51	52.60	0.40	55.18	0.19	52.42	54.98
Na_2O	0.00	0.00	0.00	0.00	0.00	0.00	0.00	0.00	0.00	0.02	0.02	0.03	0.05	0.03	0.00
P_2O_5	42.21	0.78	41.22	0.05	40.79	0.65	40.93	40.93	0.71	42.29	0.15	40.24	0.15	41.61	40.47
SrO	0.29	0.17	0.36	0.11	0.15	0.04	0.12	0.27	0.12	0.53	0.02	0.13	0.01	0.15	0.21
La_2O_3	0.11	0.10	0.24	0.02	0.28	0.17	0.27	0.18	0.13	0.25	0.03	0.26	0.01	0.26	0.27
Ce_2O_3	0.51	0.12	0.61	0.02	0.60	0.26	0.73	0.37	0.26	0.51	0.18	0.72	0.18	0.65	0.57
F	1.01	0.04	1.03	0.06	1.05	0.03	1.07	0.92	0.09	1.00	0.01	1.01	0.01	0.96	0.98
Cl	0.01	0.01	0.01	0.00	0.01	0.00	0.00	0.01	0.00	0.01	0.01	0.00	0.00	0.02	0.01
TOTAL	99.61	0.36	100.29	0.11	100.24	0.28	100.28	99.72	0.57	99.48	0.41	99.65	0.17	100.09	99.20

	in Fe-Ti oxide		inside mafic granular area		small inclusions		in phlogopite		rounded apatite in amphibole		scarse inclusions	
	BR18_2 BR18A A BR18__1		BR18__1		BR18A		BR18_2 BR18A		BR18_2		BR18_2 BR18__1	
WDS	ave n=5	st dev n=5	ave n=4	st dev n=4	ave n=2	st dev n=2	ave n=3	st dev n=3	ave n=3	st dev n=3	ave n=2	st dev n=2
SiO_2	1.80	0.22	1.44	0.08	1.65	0.34	1.87	0.29	1.56	0.10	1.59	0.04
Al_2O_3	0.09	0.20	0.00	0.00	0.00	0.00	0.01	0.02	0.14	0.14	0.06	0.08
FeO	0.04	0.07	0.00	0.00	0.00	0.00	0.01	0.02	0.03	0.02	0.02	0.03
MnO	0.07	0.16	0.00	0.00	0.00	0.00	0.00	0.00	0.07	0.10	0.00	0.00
MgO	0.05	0.02	0.02	0.01	0.04	0.02	0.10	0.12	0.04	0.04	0.02	0.02
CaO	54.77	0.57	55.21	0.25	55.40	0.28	54.04	2.05	54.48	0.40	55.32	0.22
Na_2O	0.01	0.01	0.00	0.00	0.00	0.00	0.00	0.00	0.02	0.01	0.00	0.00
P_2O_5	40.81	0.48	40.73	0.51	40.48	0.14	41.38	1.25	41.33	0.28	41.04	0.03
SrO	0.37	0.13	0.17	0.06	0.11	0.03	0.62	0.41	0.36	0.21	0.20	0.07
La_2O_3	0.19	0.11	0.26	0.03	0.27	0.14	0.28	0.03	0.38	0.36	0.23	0.06
Ce_2O_3	0.65	0.18	0.59	0.01	0.65	0.15	0.62	0.07	0.41	0.09	0.73	0.12
F	1.01	0.06	1.04	0.04	1.11	0.08	0.91	0.22	0.98	0.11	1.04	0.07
Cl	0.00	0.00	0.01	0.01	0.01	0.01	0.01	0.01	0.01	0.01	0.01	0.00
TOTAL	99.87	0.43	99.47	0.16	99.80	0.67	99.91	0.63	99.81	0.73	100.26	0.05

Table 3.5 Electron microprobe data for apatite in the shallow intrusive carbonatites, Vuoriyarvi (some elements are below detection level in some analyses).

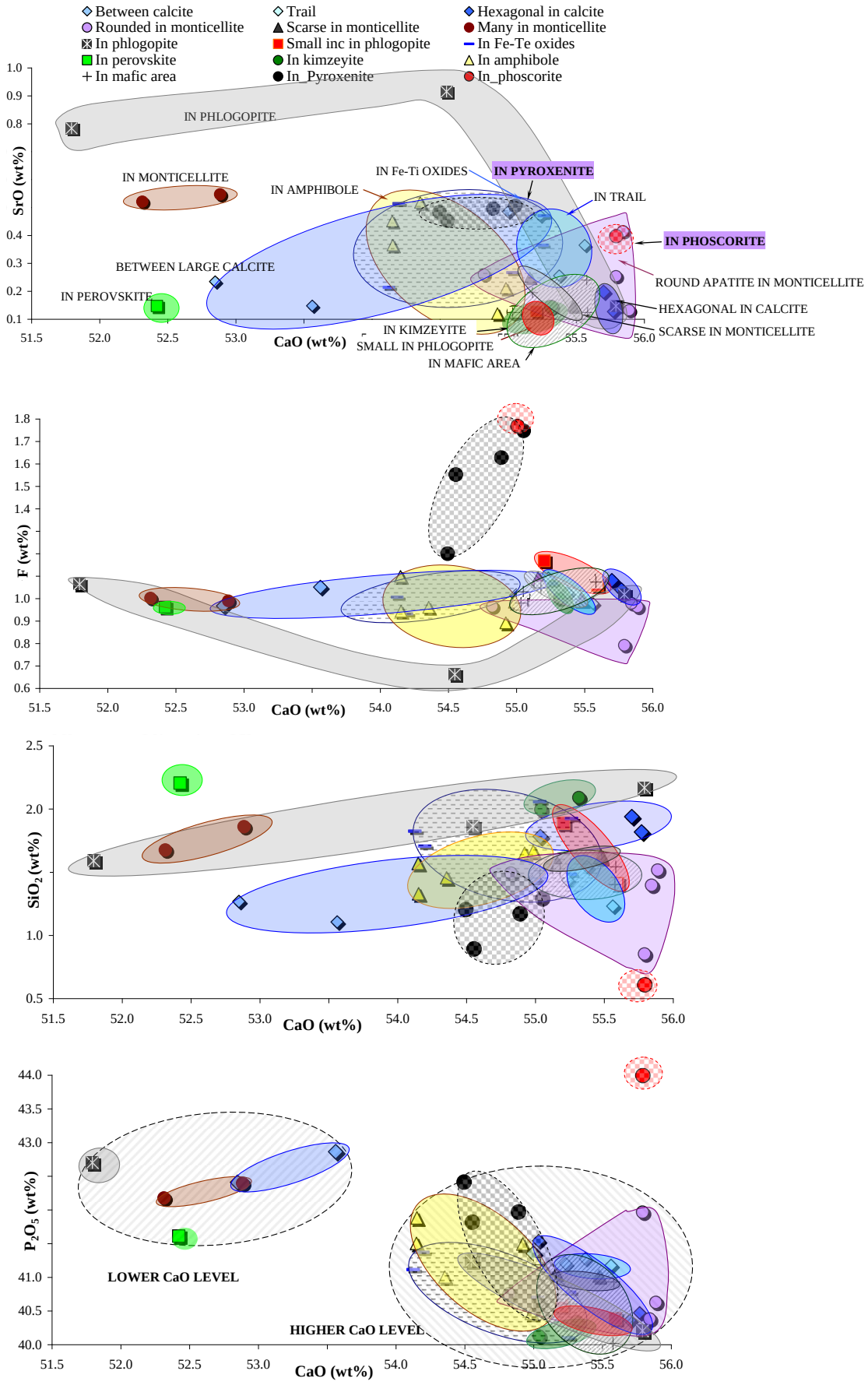

Fig 3.15 Variation diagram of major elements vs. CaO in apatite from Vuoriyarvi carbonatites. Inclusions of apatite found in different mineral phases and also taken from large single euhedral crystals are shown. Apatite from Vuoriyarvi pyroxenite and phoscorite is from Karchevsky (2010).

core contains 1.4 wt % SiO_2 and the rim 2.4 wt%. SrO concentration in apatite is variable but low (0.1-0.5 wt%) with only a few points close to 1 wt% from apatite inclusions in phlogopite. Apatite in sample B218A exhibits unusual enrichment in MgO from 0.15 wt % in the core to 1.06 wt% in the rim.

Figure 3.15 shows apatite from associated rocks such as phoscorite and pyroxenite (Karchevsky, 2010). Their SrO concentrations are within the range in apatite from Vuoriyarvi carbonatites, although those from pyroxenite reach higher levels similar to the numerous small apatite inclusions in monticellite and those from phoscorite are similar to the round/globule-like apatite in monticellite. Fluorine levels in apatite from associated silicate rocks are elevated above the concentration in apatite from carbonatites. SiO_2 in apatite from pyroxenite is low and similar to apatite occurring between large/rounded inclusions in monticellite. SiO_2 in apatite in phoscorite is similar to globule-like apatite inclusions in monticellite from carbonatite. Overall, the Vuoriyarvi pyroxenite shows a close relationship to apatite from the Vuoriyarvi carbonatite while apatite from the associated phoscorite differs.

3.3.5 Zr-garnet, perovskite and andradite

Vuoriyarvi carbonatites contain two types of garnet. The first one is Zr-rich and forms rare medium to fine grained crystals. Table 3.6 presents average and standard deviation values of major elements. They have a constant TiO_2 content (8.7-10 wt%; average 9.3 wt%). ZrO_2 concentration is high (11-14 wt%; average 12.7 wt%). Al_2O_3 content is fairly steady (1.4 wt%). The presence of a Zr- and Ti-rich garnet implies crystallisation from a magma enriched in both elements. Figure 3.16a shows that the Vuoriyarvi Zr-garnet is very similar in its Zr, Ti and Fe contents to those from Aillik Bay, whereas Zr and Ti concentrations for the Vuoriyarvi garnet are lower than those of Magnet Cove garnet. The second garnet, very small and rare, occurs in close association with monticellite and has a composition of nearly pure andradite (Table 3.7) ($Ca_3Fe^{3+}_2Si_3O_{12}$).

Perovskite is mainly composed of CaO, TiO_2 and Nb_2O_5 (2.6-9.6 wt%). Table 3.8 gives average and standard deviation values of major elements. Perovskite has the general formula ABX_3. The divalent A-site is occupied mainly by Ca in carbonatites (which is freely available in this system) but may also contain Sr or Ba, and the quadrivalent B-site can be filled by Ti, Th, Zr and Hf. Vuoriyarvi perovskite has numerous anhedral inclusions showing cognate crystallisation with apatite and calcite. It has petrographic

	Zr-GARNET							
	B218A		BA18A		BR18_A		B218	
	ave	st dev	ave	st dev	ave	st dev	ave	st dev
EDS	n=16	n=16	n=15	n=15	n=6	n=6	n=9	n=9
SiO_2	26.15	*0.38*	25.65	*0.51*	25.93	*0.28*	25.86	*0.35*
TiO_2	9.30	*0.31*	9.29	*0.32*	9.16	*0.27*	9.53	*0.37*
Al_2O_3	1.42	*0.10*	1.42	*0.11*	1.44	*0.05*	1.30	*0.09*
FeO	15.95	*0.27*	15.83	*0.27*	15.94	*0.26*	15.94	*0.23*
MnO	0.29	*0.12*	0.26	*0.10*	0.21	*0.14*	0.29	*0.13*
MgO	2.51	*0.11*	2.50	*0.13*	2.53	*0.07*	2.55	*0.12*
CaO	31.62	*0.55*	31.63	*0.28*	31.67	*0.26*	31.65	*0.23*
ZrO_2	12.19	*0.59*	12.95	*0.73*	13.00	*0.57*	12.55	*0.88*
TOTAL	99.43	*0.30*	99.54	*0.27*	99.87	*0.24*	99.68	*0.29*
ZrO_2+TiO_2	21.48	*0.58*	22.25	*0.74*	22.16	*0.56*	22.08	*0.58*
Recalculation on the basis of 12 oxygens		(Fe^{3+} based on stoichiometry)						
Si	2.379	*0.026*	2.341	*0.038*	2.356	*0.025*	2.370	*0.055*
Ti	0.636	*0.020*	0.638	*0.023*	0.625	*0.017*	0.652	*0.024*
Al	0.153	*0.011*	0.153	*0.012*	0.154	*0.006*	0.140	*0.010*
Fe^{3+}	1.213	*0.021*	1.208	*0.021*	1.211	*0.019*	1.213	*0.017*
Mn	0.022	*0.009*	0.020	*0.008*	0.016	*0.011*	0.022	*0.010*
Mg	0.341	*0.014*	0.340	*0.017*	0.343	*0.009*	0.346	*0.016*
Ca	3.082	*0.056*	3.092	*0.026*	3.083	*0.017*	3.085	*0.019*
Zr	0.541	*0.028*	0.576	*0.034*	0.576	*0.026*	0.557	*0.040*
Total	8.367	*0.031*	8.368	*0.016*	8.365	*0.009*	8.386	*0.047*
$Fe^{3+}/(Fe^{3+}+Mg)$	0.781	*0.007*	0.780	*0.009*	0.779	*0.006*	0.778	*0.008*
mg#	0.219	*0.007*	0.220	*0.009*	0.221	*0.006*	0.222	*0.008*

Table 3.6 Electron microprobe data for Zr-garnet in the shallow intrusive carbonatites, Vuoriyarvi.

	ANDRADITE					
	B218		BR18_1		BR18_A	
	ave	st dev	ave	st dev	ave	st dev
WDS	n=4	n=4	n=2	n=2	n=4	n=4
SiO_2	34.84	*0.54*	34.91	*0.42*	35.08	*0.41*
TiO_2	0.24	*0.15*	0.05	*0.01*	0.05	*0.03*
Al_2O_3	0.08	*0.12*	0.04	*0.01*	0.12	*0.08*
Fe_2O_3	25.01	*0.23*	25.27	*0.11*	24.79	*0.30*
FeO	4.24	*0.49*	4.69	*0.06*	4.73	*0.22*
MnO	0.29	*0.17*	0.09	*0.07*	0.07	*0.02*
MgO	1.12	*0.65*	0.48	*0.06*	0.51	*0.07*
CaO	32.64	*0.47*	33.53	*0.03*	33.15	*0.27*
Na_2O	0.07	*0.07*	0.02	*0.01*	0.02	*0.02*
K_2O	0.05	*0.06*	0.00	*0.00*	0.01	*0.01*
ZrO_2	0.05	*0.04*	0.01	*0.00*	0.00	*0.01*
BaO	n/a	*n/a*	0.02	*0.02*	0.01	*0.01*
TOTAL	98.61	*0.80*	99.08	*0.33*	98.54	*0.28*
Cations recalculated on the basis of 12 oxygens						
Si	3.011	*0.034*	3.012	*0.02*	3.035	*0.025*
Al^{iv}	0.007	*0.014*	0.002	*0.00*	0.000	*0.008*
Al^{vi}	0.001	*0.002*	0.003	*0.00*	0.013	*0.010*
Ti	0.016	*0.010*	0.003	*0.00*	0.003	*0.002*
Fe^{3+}	1.627	*0.016*	1.641	*0.02*	1.614	*0.025*
Fe^{2+}	0.306	*0.034*	0.339	*0.00*	0.342	*0.005*
Mn	0.021	*0.012*	0.007	*0.00*	0.006	*0.001*
Mg	0.145	*0.084*	0.061	*0.01*	0.068	*0.009*
Ca	3.023	*0.032*	3.099	*0.02*	3.073	*0.031*
TOTAL	8.157	*0.018*	8.164	*0.01*	8.150	*0.016*
Almandine	0	*0*	0	*0*	0	*0*
Andradite	99	*1*	100	*0*	99	*0*
Grossular	0	*0*	0	*0*	0	*0*
Pyrope	1	*1*	0	*0*	1	*0*
Spessartine	0	*0*	0	*0*	0	*0*
Uvarovite	0	*0*	0	*0*	0	*0*

Table 3.7 Electron microprobe data for andradite in the shallow intrusive carbonatites, Vuoriyarvi. FeO as FeO^{Total} recalculated to FeO and Fe_2O_3 some elements such as Na and K are below detection limit).

similarities to Zr-rich garnet but overall forms rather smaller crystals. It has a high and constant TiO_2 (47-49 wt%). Nb_2O_5 content varies from 5.5-9.1 wt% while Na_2O shows significant average value of 1.2 wt%, with constant FeO concentration (3 wt%). This Nb-rich variety contains an average of 48 wt% TiO_2. Na_2O is 0.7-1.2 wt% and levels of Ce_2O_3 are 2.3-3.1wt%.

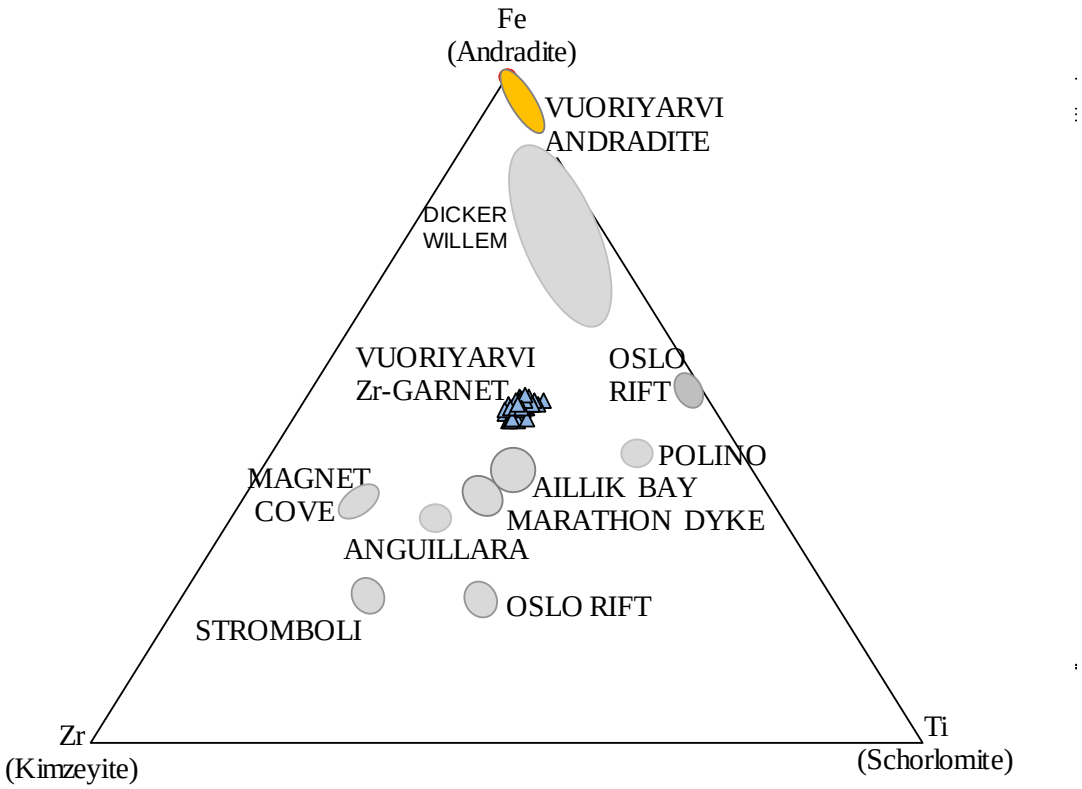

Fig. 3.16a Classification diagram for Fe- and Ti- and Zr-rich garnets of andradite-schorlomite-kimzeyite composition from Vuoriyarvi (Zr-garnet) and other localities such as Polino (Lupini et al. 1992), Oslo Rift (Jamtveit et al. 1997), Aillik Bay (Cooper and Reid, 1998), Dicker Willem (Cooper and Reid, 1998), Marathon Dyke (Platt and Mitchell, 1979), Magnet Cove (Milton et al. 1961), Diagram includes also kimzeyite found in volcanic rocks from Anguillara Sabazia and Stromboli (Italy) with high Zr content (24-27 wt% ZrO_2). Anguillara after Schingaro et al. (2001), Stromboli after Munno et al. (1980).

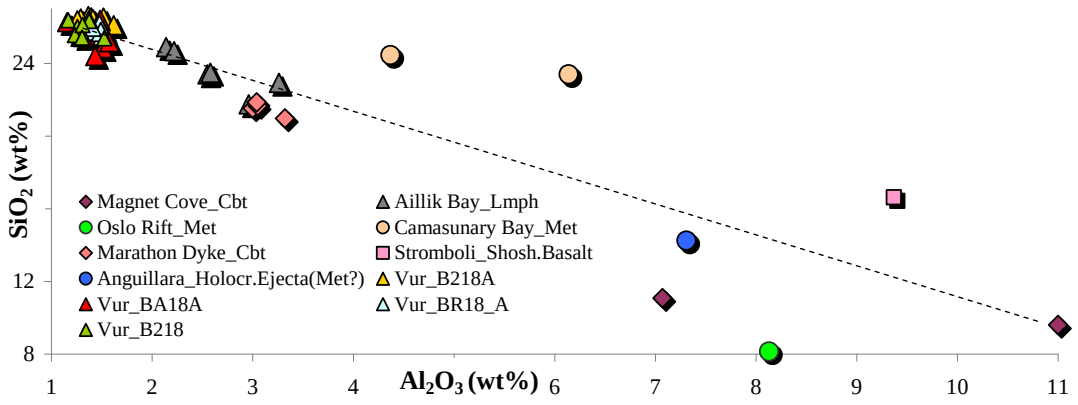

Fig. 3.16b Variation diagram SiO_2 versus Al_2O_3 for Zr-garnet from Vuoriyarvi carbonatites and other localities.

Zr-rich garnet contains a high amount of CaO (31.6 wt%), SiO_2 (26 wt%), FeO (16 wt%) and ZrO_2 (12-13 wt%). The variation diagram of SiO_2 vs Al_2O_3 for Zr-garnet from Vuoriyarvi carbonatites and other localities (Fig.3.16b) shows overall linear trend with Vuoriyarvi Zr-rich garnet being most enriched in SiO_2 while kimzeyite from Magnet Cove shows the lowest SiO_2 content (8 wt%), also Vuoriyarvi Zr-garnet contain lowest Al_2O_3 (1.5 wt%) while Magnet Cove kimzeyite has the highest content (11 wt%).

PEROVSKITE

	BR18_A		B218		BR18_1	
	ave n=6	st dev n=6	ave n=6	st dev n=6	ave n=4	st dev n=4
SiO_2	0.34	*0.05*	0.36	*0.09*	0.37	*0.03*
TiO_2	46.92	*0.12*	48.89	*1.16*	49.06	*2.12*
Al_2O_3	0.16	*0.07*	0.17	*0.04*	0.26	*0.10*
FeO	3.18	*0.14*	3.13	*0.40*	3.09	*0.12*
CaO	36.22	*0.19*	36.79	*0.53*	37.09	*0.24*
MgO	0.04	*0.04*	0.05	*0.05*	0.03	*0.05*
Na_2O	1.23	*0.08*	0.88	*0.14*	0.91	*0.17*
K_2O	0.03	*0.03*	0.04	*0.03*	0.04	*0.02*
SrO	0.12	*0.11*	0.08	*0.06*	0.16	*0.03*
Nb_2O_5	9.12	*0.26*	5.59	*1.71*	5.73	*2.33*
Ce_2O_3	2.39	*0.23*	3.14	*0.67*	2.78	*0.47*
Total	99.74	*0.22*	99.13	*0.53*	99.53	*0.31*
TiO +Nb_2O_5	56.04	*0.25*	54.48	*0.67*	54.79	*0.41*
Na_2O+Nb_2O_5	10.35	*0.29*	6.47	*1.84*	6.64	*2.50*
CaO+TiO_2	83.14	*0.28*	85.68	*1.62*	86.15	*2.16*
Cations recalculated on the basis of 3 oxygens						
Si	0.008	*0.001*	0.009	*0.002*	0.009	*0.001*
Ti	0.849	*0.002*	0.890	*0.022*	0.887	*0.037*
Al	0.004	*0.002*	0.005	*0.001*	0.007	*0.003*
Fe^{3+}	0.064	*0.003*	0.063	*0.008*	0.062	*0.002*
Mg	0.001	*0.002*	0.002	*0.002*	0.001	*0.002*
Ca	0.934	*0.004*	0.954	*0.014*	0.955	*0.003*
K	0.001	*0.001*	0.001	*0.001*	0.001	*0.001*
Na	0.057	*0.004*	0.041	*0.006*	0.042	*0.008*
Sr	0.002	*0.002*	0.001	*0.001*	0.002	*0.000*
Nb	0.099	*0.003*	0.061	*0.019*	0.062	*0.025*
Ce	0.021	*0.002*	0.028	*0.006*	0.024	*0.004*
TOTAL	2.021	*0.004*	2.028	*0.006*	2.029	*0.002*

Table 3.8 Electron microprobe data for perovskite in the shallow intrusive carbonatites, Vuoriyarvi.

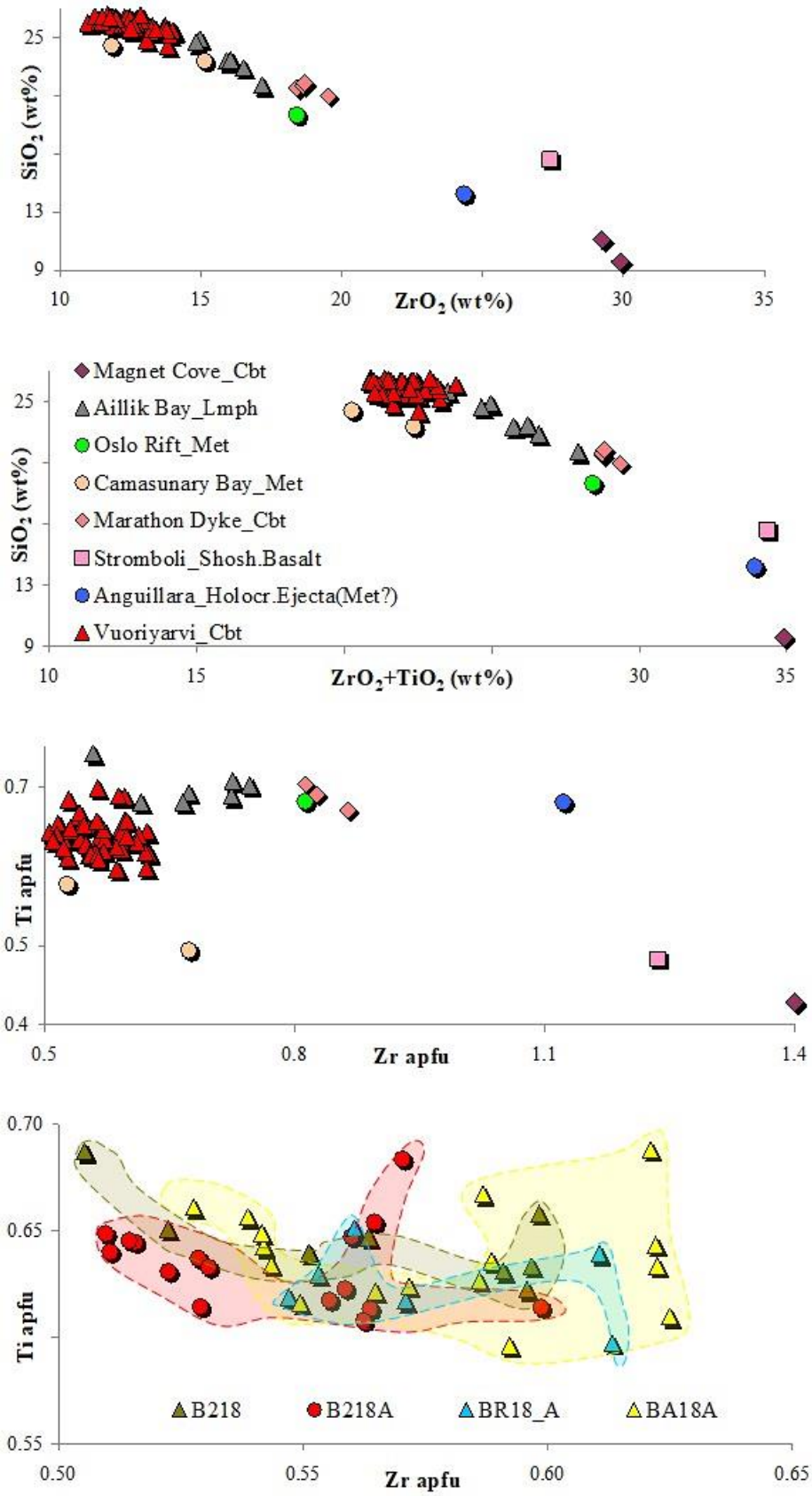

Fig.3.17 Variation diagrams (Ti versus Zr and SiO_2) for Ti-Zr-rich garnets composition from the Vuoriyarvi complex and other localities listed in Figure 3.8. Abbreviations: Cbt=carbonatites; Lmph=lamprophyric dyke; Met=metamorphic; Met?=possibly metamorphic.

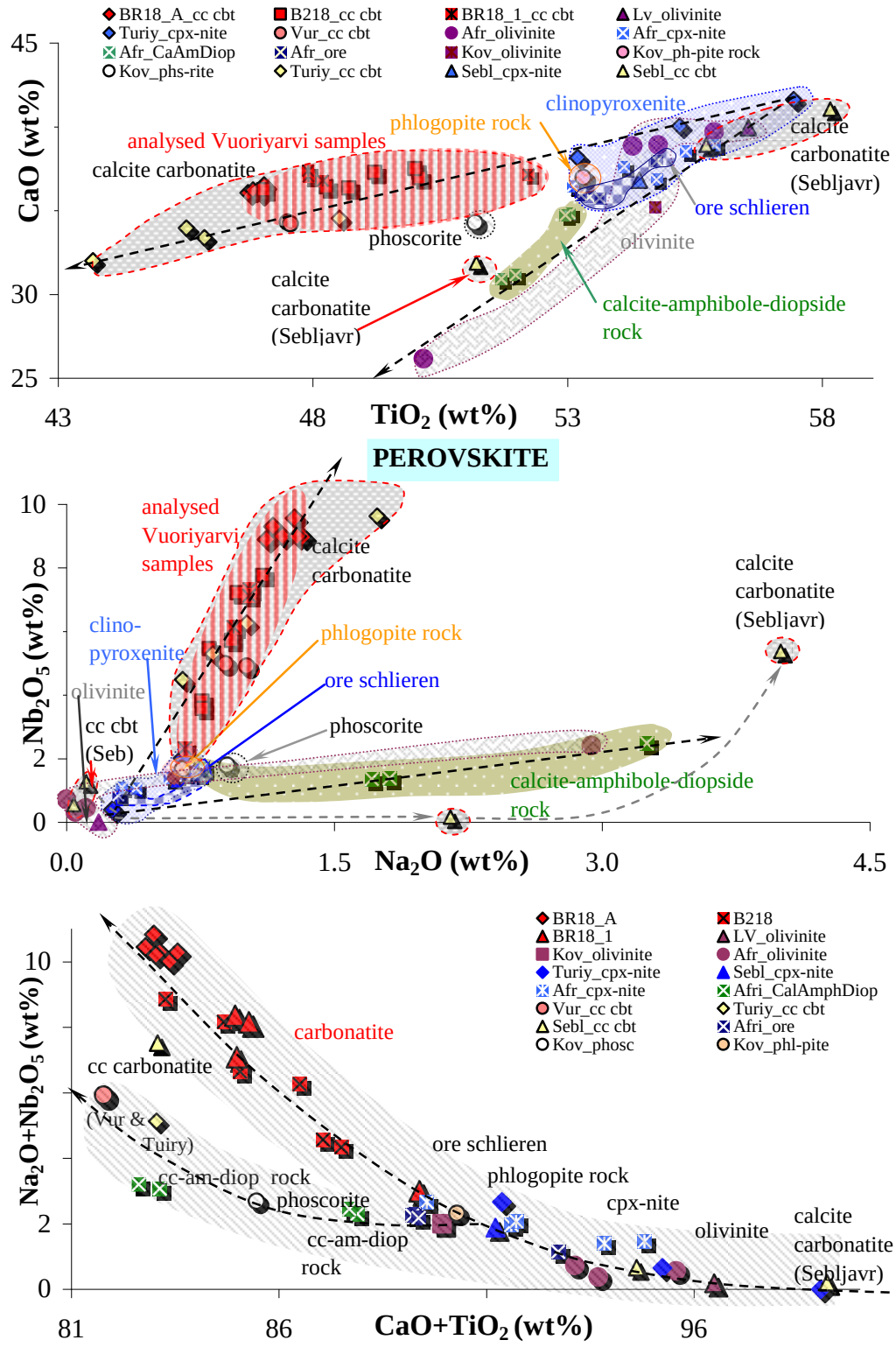

Fig.3.18 Variation diagrams wt%: TiO_2 versus CaO, Na_2O versus Nb_2O_5, and $Na_2O+Nb_2O_5$ versus $CaO+TiO_2$ for perovskite from the Vuoriyarvi complex and other carbonatite complexes of the Kola Alkaline Province (KAP), Russia. The authors data can be recognised by the names of slides (BR18_A, BR18_1 and B218). The perovskite-bearing rocks including: olivinite (Lesnaya Varaka, Tuiry, Kovdor, Afrikanda); clinopyroxenite (Turiy, Kovdor, Sebljavr); calcite-amphibole-diopside rock (veins emplaced in clinopyroxenite of the Afrikanda complex); ore schlieren (perovskite-titaniferous magnetite ore crystallised from Ca-Ti-Fe-rich liquid which was emplaced within cracks of ultramafic rocks of Afrikanda); calcite carbonatite (Tuiry, Kovdor, Afrikanda, and Vuoriyarvi). Data according to Chakhmouradian and Mitchell (1997).

According to Chakhmouradian and Mitchell (2000), variation in perovskite composition depends on the evolution of the host magma. As the crystallisation environment is Ca-rich, consequently the amount of CaO is high (37 wt%). Figure 3.17 expresses the positive relationship between CaO versus TiO_2 and Nb_2O_5 versus Na_2O, but at the same time shows a negative association between (CaO + TiO_2) versus (Nb_2O_5 + Na_2O). This implies that the lower content of Na and Nb in the Vuoriyarvi perovskite is compensated by a higher concentration of Ca and Ti. Concurrently, higher amount of Na in the Vuoriyarvi perovskite holds higher level of Nb and higher concentration of Ca is in accordance with higher level of Ti.

Figure 3.18 shows compositional trends of perovskite in carbonatites and associated rocks in KAP. The compositional evolution commences at clinopyroxenite field (highest TiO_2 and CaO) and divides into a lower trend which rapidly descends towards calcite-amphibolite-diopside and olivinite rocks, while the upper trend goes gently down towards carbonatites (including those from Vuoriyarvi). This partition into two evolutionary trends is consistent for perovskite in Nb_2O_5 vs. Na_2O diagram but it starts in the olivinite and clinopyroxenite fields, where the values are lowest. The first trend shows a strong linear increase towards the Vuoriyarvi carbonatites and the second one slightly rises towards calcite-amphibole-diopside and olivinite rocks. The summary of the compositional evolution of perovskite in Kola is underlined in the Nb_2O_5 + Na_2O vs. TiO_2 + CaO diagram (Fig. 3.18). Enrichment in Nb_2O_5 + Na_2O content increases gradually from: clinopyroxenite / Sebljavr carbonatite → olivinite → clinopyroxenite → phlogopite rock → ore schlieren to Vuoriyarvi carbonatites. Around phlogopite rock, the trend bifurcates towards: calcite-amphibole-diopside rock → phoscorite → Turiy carbonatites → Vuoriyarvi carbonatites (as analysed by Chakmouradian and Mitchell, 1997). Thus, the highest concentration of Nb and Na found in perovskite in Kola rocks is generally associated with carbonatites.

Vuoriyarvi perovskite exhibits an array of compositions, similar to those in Tuiry and Sebljavr calcio-carbonatites, which reflects complex evolution of this phase. It is xenocrystic in origin and assimilated from the associated pyroxenite.

3.3.6 Pyroxene and amphibole

Compositions of pyroxene are given in Table 3.9. The mg# is very close to 1, because FeO + Fe_2O_3 contents are very low (~2 wt%) and MgO is high (17-18.5 wt%), so the mineral is diopside. In the granular mafic area in BR18_1 Fe_2O_3 drops to about 1

wt%. The content of Al_2O_3 in pyroxene is very low, on average 0.4 wt%, being slightly higher in the mafic area (0.7 wt%). CaO concentration reaches 26 wt% and TiO_2 falls to < 0.3 wt%. The Wo-En-Fs diagram (Figure 3.18), presenting the composition of pyroxene from Vuoriyarvi carbonatites and associated pyroxenites, shows the same high Wo-component with clear evolution from pyroxenite towards carbonatite.

PYROXENE				in the mafic granular area		close association with olivin	
	B218A	BR18_1		BR18_1		BR18A	
WDS	diop (n=4)	ave n=4	st dev n=4	ave n=3	nst dev n=3	ave n=6	st dev n=6
SiO_2	50.76	53.85	*0.67*	53.66	*0.13*	54.19	*1.00*
TiO_2	0.25	0.11	*0.06*	0.23	*0.04*	0.13	*0.12*
Al_2O_3	0.45	0.34	*0.11*	0.61	*0.09*	0.36	*0.30*
FeO	-	0.45	*0.01*	1.12	*0.25*	0.46	*0.23*
Fe_2O_3	2.84	1.55	*0.41*	0.96	*0.10*	1.66	*0.59*
MnO	0.49	0.18	*0.02*	0.20	*0.02*	0.14	*0.06*
MgO	16.95	17.67	*0.34*	16.75	*0.03*	17.75	*0.70*
CaO	26.29	25.72	*0.11*	25.46	*0.07*	25.56	*0.17*
Na_2O	n/a	0.07	*0.02*	0.12	*0.01*	0.08	*0.04*
K_2O	0.08	0.00	*0.00*	0.01	*0.00*	0.02	*0.01*
TOTAL	98.10	99.73	*0.30*	99.13	*0.40*	99.83	*0.48*
Cations recalculated on the basis of 6 oxygens							
Si	1.894	1.961	*0.020*	1.972	*0.002*	1.969	*0.020*
Ti	0.007	0.003	*0.002*	0.006	*0.001*	0.004	*0.003*
Al	0.010	0.015	*0.005*	0.026	*0.004*	0.015	*0.013*
Fe^{3+}	0.069	0.040	*0.009*	0.026	*0.003*	0.044	*0.018*
Fe^{2+}	-	0.015	*0.000*	0.035	*0.007*	0.014	*0.009*
Mn	0.016	0.006	*0.001*	0.006	*0.001*	0.004	*0.002*
Mg	0.943	0.959	*0.019*	0.917	*0.005*	0.961	*0.031*
Ca	1.051	1.004	*0.006*	1.002	*0.005*	0.996	*0.004*
Na	0.004	0.005	*0.002*	0.009	*0.001*	0.006	*0.003*
TOTAL	3.99	4.00	*0.00*	4.00	*0.00*	4.00	*0.00*
fe#	0.07	0.05	*0.00*	0.06	*0.01*	0.04	*0.03*
mg#	0.93	0.95	*0.00*	0.94	*0.01*	0.96	*0.03*
en	45.37	47.59	*0.43*	46.16	*0.19*	47.94	*1.45*
wo	50.58	49.79	*0.34*	50.44	*0.17*	49.65	*0.18*
fs	4.05	2.63	*0.18*	3.39	*0.32*	2.41	*1.33*

Table 3.9 Electron microprobe data for pyroxene in the shallow intrusive carbonatites, Vuoriyarvi. FeO as FeOTotal recalculated to FeO and Fe_2O_3 (some elements are below detection limit).

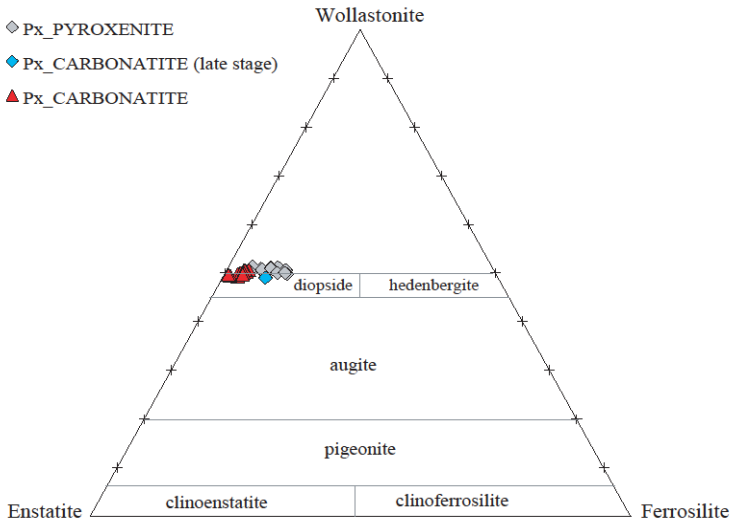

Fig.3.19 Wo-En-Fs diagram presenting the composition of pyroxene from the Vuoriyarvi carbonatites and from the associated pyroxenite (grey diamonds) and also from the late-stage carbonatite (blue diamonds) (Karchevsky, 2010).

Amphibole is restricted to just two samples (BR18_1 and BR18_A). Analyses (Table 3.10) plotted on a Ca+Al versus Si+Na+K diagram (Figure 3.19) show the principal trends for amphibole from carbonatites. The Vuoriyarvi amphibole falls in the field of edenite. CaO concentration is 15.6-17.3 wt% (calcic amphibole) and Na_2O reaches 2.7 wt%. The mg# is high (0.9) and lack of Al_2O_3 is noticeable. According to Hogarth (1989), early amphiboles can reach levels of 1 wt% TiO_2 but the Vuoriyarvi edenite displays very low TiO_2 content (0.05 wt%). MnO concentration is 0.58-0.64 wt%. Hogarth (1989) tabulated the constituents of amphiboles and stated that MnO in amphibole in carbonatites typically reaches <0.25 wt%, but maximum MnO is 0.58 wt%.

Development of minerals during fenitization depends on the host rock composition, as well as chemistry, temperature and pressure of the fenitizing fluid and also on the intensity of the process (Dawson, 1964; Heinrich, 1966; Le Bas, 1987; Platt, 1996). The unusual mat-like texture of the amphibole developed during low intensity Na-fenitization (close to the intrusion), most likely altering pyroxene as they are more susceptible to fenitization (Sutherland, 1969) and have a similar mg#.

Amph group	Ca	Na-Ca	Na-Ca	ave	st dev
WDS	BR18_1/1	BR18_1/2	BR18_1/3	n=3	n=3
SiO_2	50.22	50.91	52.65	*51.26*	*1.25*
TiO_2	0.05	0.08	0.08	*0.07*	*0.02*
FeO	4.11	4.14	4.42	*4.23*	*0.17*
MnO	0.64	0.58	0.59	*0.60*	*0.03*
MgO	20.81	20.76	20.34	*20.64*	*0.26*
CaO	17.26	15.92	15.57	*16.25*	*0.89*
Na_2O	1.92	2.70	2.56	*2.39*	*0.41*
K_2O	0.60	0.70	0.73	*0.67*	*0.07*
BaO	0.05	0.03	0.02	*0.03*	*0.01*
Total	95.66	95.82	96.95	*96.14*	
Cations recalculated on the basis of 23 oxygens					
Si	7.392	7.459	7.589	*7.480*	*0.100*
Ti	0.006	0.009	0.009	*0.008*	*0.002*
Fe^{3+}	0.000	0.000	0.000	*0.000*	*0.000*
Fe^{2+}	0.506	0.507	0.533	*0.516*	*0.015*
Mn	0.080	0.072	0.071	*0.075*	*0.005*
Mg	4.565	4.535	4.370	*4.490*	*0.105*
Ca	2.721	2.499	2.405	*2.542*	*0.163*
Na	0.548	0.766	0.714	*0.676*	*0.114*
K	0.112	0.132	0.133	*0.126*	*0.012*
Ba	0.003	0.002	0.001	*0.002*	*0.001*
Cl	0.002	0.000	0.000	*0.001*	*0.001*
OH*	1.998	2.000	2.000	*1.999*	*0.001*
Total	17.93	17.98	17.83	*17.91*	
$Mg/(Mg+Fe^2)$	0.900	0.899	0.891		
n=(Na+K)/(Na+K+Ca)	*23.726*	*34.526*	*33.905*		
$Ca+Al^{IV}$	*2.721*	*2.499*	*2.405*		
Si+Na+K	*8.052*	*8.357*	*8.437*		
m=(Mg:∑C ions)	*35.116*	*34.881*	*33.619*		
100Ca:(Na+K+Ca)	*80.476*	*73.574*	*73.938*		
100Fe/(Fe+Mg)	*9.985*	*10.055*	*10.875*		

Table 3.10 Electron microprobe data for amphibole in the shallow intrusive carbonatites, Vuoriyarvi,

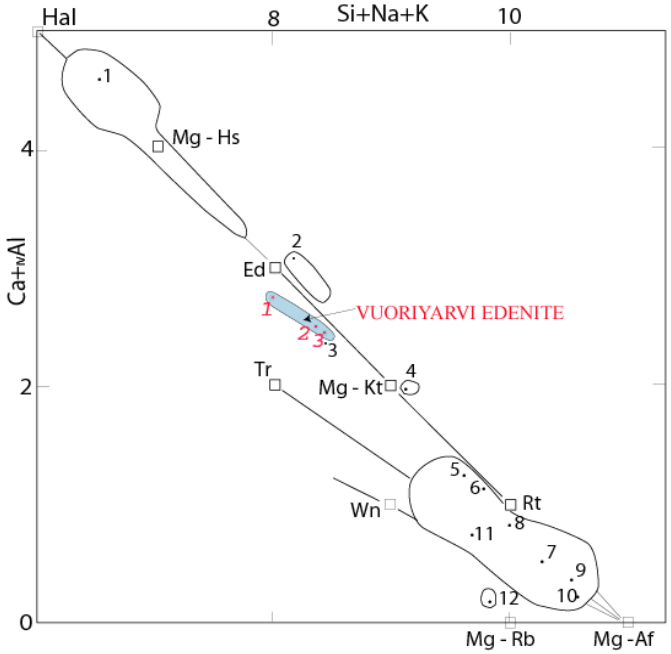

Fig.3.20 Ca + ^{IV}Al vs. Si + Na + K (apfu) diagram for amphibole in the Vuoriyarvi carbonatites after Hogarth (1989) and Giret et al. (1980). Data showing different fields taken from: winchite-richterite-magnesio-arfvedsonite (Fabries, 1978); magnesio-riebeckite (Samoylov, 1977); magnesio-katophorite (Samoylov, 1977); edenite (Vartiainen, 1980); magnesio-hastingsite (Samoylov, 1977); hornblende (Gold, 1966). Mineral abbreviations: Ed-edenite; Mg-Af-magnesio-arfvedsonite; Mg-Hs-magnesio-hastingsite; Mg-Kt-magnesio- katophorite: Mg-Rb- magnesio-riebeckite: Tr-tremolite; Wn- winchite; Hal-hypothetical compound $NaCa_2(Mg_3Fe_3^{2+})(Si_5Al_3)O_{22}(OH)_2$.

3.3.7 Magnetite

Magnetite (Table 3.11) contains variable concentrations of TiO_2 (1-5 wt%), MgO (0.5-5.0 wt%) and Al_2O_3 (0.2-4.7 wt%). Figure 3.21 displays compositional variation of magnetite from Vuoriyarvi carbonatites and associated pyroxenites and phoscorites (Karchevsky, 2010). Figure 3.22 includes data for magnetite from phoscorites and pyroxenites (Karchevsky, 2010). There is a positive correlation of TiO_2 against MgO and a negative one against wt % Fe_2O_3+FeO. As magnetite crystallised in the associated alkaline/ultramafic rocks, it can indicate the crystallisation trend for magnetite in Vuoriyarvi carbonatites and their related phoscorites and pyroxenites. The lowest MnO value in magnetite occurs in pyroxenites (0.3-0.6 wt%), the next occurs in phoscorites (0.7-1.1 wt%) and the highest value is associated with carbonatites (1.4-2.7 wt%). Magnetite associated with dolomite inclusions in B218A contains the highest levels of MgO amongst all of the analysed magnetite, implying that the magmatic liquid had higher levels of MgO. MnO concentration in magnetite (1.6-1.9 wt%) shows similar levels as the concentration of MnO in dolomite inclusions in magnetite (1.8-2.3 wt%) in the same B218A sample. Otherwise MnO values in calcite are negligible. Thus, the higher MnO concentration in magnetite is associated with formation of magnetite and dolomite.

MAGNETITE

	BA18								B218		BR18_1	
	ave	st dev	ave	st dev	ave	st dev	ave	st dev	ave	st dev	ave	st dev
EDS	n=3	n=3	n=4	n=4	n=4	n=4	n=4	n=4	n=5	n=5	n=2	n=2
SiO_2	0.17	*0.19*	0.13	*0.15*	0.14	*0.10*	1.08	*1.68*	0.18	*0.10*	0.03	*0.04*
TiO_2	2.74	*0.09*	2.96	*0.38*	2.37	*0.44*	2.47	*1.16*	2.28	*0.27*	1.54	*0.04*
Al_2O_3	0.30	*0.36*	0.39	*0.18*	0.67	*0.14*	1.23	*0.69*	0.27	*0.15*	0.94	*0.06*
Fe_2O_3	63.60	*0.74*	63.33	*1.00*	64.26	*0.71*	62.88	*0.31*	64.73	*0.64*	66.78	*0.00*
FeO real	27.44	*0.21*	26.78	*0.30*	26.82	*0.25*	25.28	*1.15*	26.83	*0.55*	24.20	*0.00*
CaO	0.23	*0.13*	0.13	*0.14*	0.26	*0.24*	0.80	*1.25*	0.25	*0.14*	0.16	*0.16*
MgO	2.32	*0.15*	2.52	*0.14*	2.70	*0.31*	3.55	*0.95*	2.24	*0.09*	4.02	*0.21*
MnO	2.34	*0.13*	2.96	*0.34*	2.05	*0.16*	1.85	*0.60*	2.71	*0.30*	2.10	*0.06*
Total	99.13	*0.36*	99.19	*0.14*	99.26	*0.39*	99.14	*1.74*	99.48	*0.36*	99.76	*0.17*
$Fe_2O+Fe_2O_3$	91.03	*0.66*	90.11	*0.97*	91.08	*0.48*	88.17	*1.46*	91.56	*0.47*	90.98	*0.00*
SPINEL recalculation formula to 4 oxygens and 3 cations												
Si	0.006	*0.007*	0.005	*0.006*	0.005	*0.004*	0.039	*0.061*	0.007	*0.004*	0.002	*0.000*
Ti	0.078	*0.002*	0.084	*0.011*	0.067	*0.012*	0.070	*0.033*	0.065	*0.007*	0.042	*0.000*
Al	0.013	*0.016*	0.017	*0.008*	0.030	*0.006*	0.054	*0.029*	0.012	*0.007*	0.039	*0.000*
Fe^{3+}	1.813	*0.027*	1.803	*0.029*	1.821	*0.029*	1.727	*0.084*	1.842	*0.021*	1.872	*0.000*
Fe^{2+}	0.869	*0.004*	0.847	*0.009*	0.845	*0.004*	0.822	*0.039*	0.848	*0.018*	0.754	*0.000*
Ca	0.009	*0.005*	0.005	*0.006*	0.011	*0.010*	0.032	*0.049*	0.010	*0.006*	0.011	*0.000*
Mg	0.131	*0.008*	0.142	*0.008*	0.151	*0.016*	0.197	*0.048*	0.126	*0.005*	0.215	*0.000*
Mn	0.075	*0.004*	0.095	*0.011*	0.065	*0.005*	0.059	*0.020*	0.087	*0.009*	0.065	*0.000*
Total	2.995	*0.009*	2.998	*0.002*	2.995	*0.003*	2.998	*0.001*	2.997	*0.002*	3.000	*0.000*
fe#	0.954	*0.003*	0.949	*0.003*	0.946	*0.006*	0.928	*0.018*	0.955	*0.002*	0.924	*0.000*

Table 3.11a Electron microprobe data for magnetite in the shallow intrusive carbonatites, Vuoriyarvi (some elements e.g., Si, are below detection limit).

	B218A								KR3					
	ave	st dev	ave	st dev	ave	st dev	ave	st dev	ave	st dev	ave	st dev	ave	st dev
	n=3	n=3	n=4	n=4	n=4	n=4	n=4	n=4	n=4	n=4	n=4	n=4	n=3	n=3
SiO_2	0.19	*0.29*	0.13	*0.12*	0.17	*0.20*	0.12	*0.11*	0.18	*0.15*	0.29	*0.14*	0.06	*0.06*
TiO_2	2.13	*0.86*	1.55	*0.70*	3.23	*0.47*	4.35	*0.60*	1.97	*0.44*	3.44	*0.65*	1.89	*0.65*
Al_2O_3	1.07	*0.10*	1.50	*0.81*	0.91	*0.33*	1.98	*0.86*	0.99	*0.84*	2.24	*1.69*	0.64	*0.09*
Fe_2O_3	64.48	*0.95*	65.21	*0.76*	61.60	*0.64*	59.52	*0.90*	64.48	*0.97*	60.57	*2.96*	65.27	*1.50*
FeO real	25.63	*1.44*	26.13	*1.34*	28.36	*2.54*	27.58	*1.19*	27.08	*0.39*	27.06	*0.88*	26.79	*0.54*
CaO	0.60	*0.47*	0.31	*0.34*	0.39	*0.16*	0.08	*0.11*	0.43	*0.46*	0.17	*0.24*	0.29	*0.22*
MgO	3.47	*1.06*	3.05	*1.28*	2.14	*1.35*	3.86	*0.58*	2.23	*0.52*	3.62	*0.57*	2.43	*0.21*
MnO	1.60	*0.87*	1.59	*0.36*	1.95	*1.00*	1.76	*0.84*	2.09	*0.17*	1.99	*0.19*	1.85	*0.10*
Total	99.17	*0.25*	99.48	*0.63*	98.74	*0.59*	99.24	*0.82*	99.46	*0.12*	99.37	*0.28*	99.22	*0.38*
$Fe_2O+Fe_2O_3$	90.11	*2.39*	91.34	*1.43*	89.96	*2.04*	87.10	*0.79*	91.56	*0.79*	87.63	*2.26*	92.07	*0.99*
SPINEL recalculation formula to 4 oxygens and 3 cations														
Si	0.007	*0.011*	0.005	*0.004*	0.006	*0.008*	0.005	*0.004*	0.007	*0.006*	0.011	*0.005*	0.002	*0.002*
Ti	0.060	*0.023*	0.043	*0.019*	0.092	*0.012*	0.121	*0.016*	0.056	*0.012*	0.096	*0.017*	0.054	*0.019*
Al	0.047	*0.004*	0.066	*0.036*	0.040	*0.014*	0.087	*0.038*	0.044	*0.037*	0.097	*0.072*	0.029	*0.004*
Fe^{3+}	1.810	*0.043*	1.833	*0.040*	1.759	*0.024*	1.659	*0.022*	1.828	*0.036*	1.687	*0.100*	1.859	*0.040*
Fe^{2+}	0.800	*0.052*	0.816	*0.051*	0.901	*0.094*	0.855	*0.040*	0.853	*0.011*	0.837	*0.024*	0.848	*0.018*
Ca	0.024	*0.019*	0.013	*0.014*	0.016	*0.006*	0.003	*0.004*	0.017	*0.019*	0.007	*0.009*	0.012	*0.009*
Mg	0.193	*0.058*	0.169	*0.069*	0.120	*0.074*	0.213	*0.031*	0.125	*0.029*	0.200	*0.030*	0.137	*0.012*
Mn	0.050	*0.027*	0.050	*0.011*	0.062	*0.032*	0.055	*0.026*	0.067	*0.006*	0.062	*0.006*	0.059	*0.003*
Total	2.991	*0.006*	2.996	*0.004*	2.996	*0.004*	2.997	*0.002*	2.998	*0.004*	2.997	*0.002*	2.999	*0.002*
fe#	0.931	*0.021*	0.940	*0.025*	0.957	*0.027*	0.922	*0.011*	0.955	*0.010*	0.927	*0.011*	0.952	*0.004*

Table 3.11b Electron microprobe data for magnetite in the shallow intrusive carbonatites, Vuoriyarvi (CaO is below detection limit in most analyses).

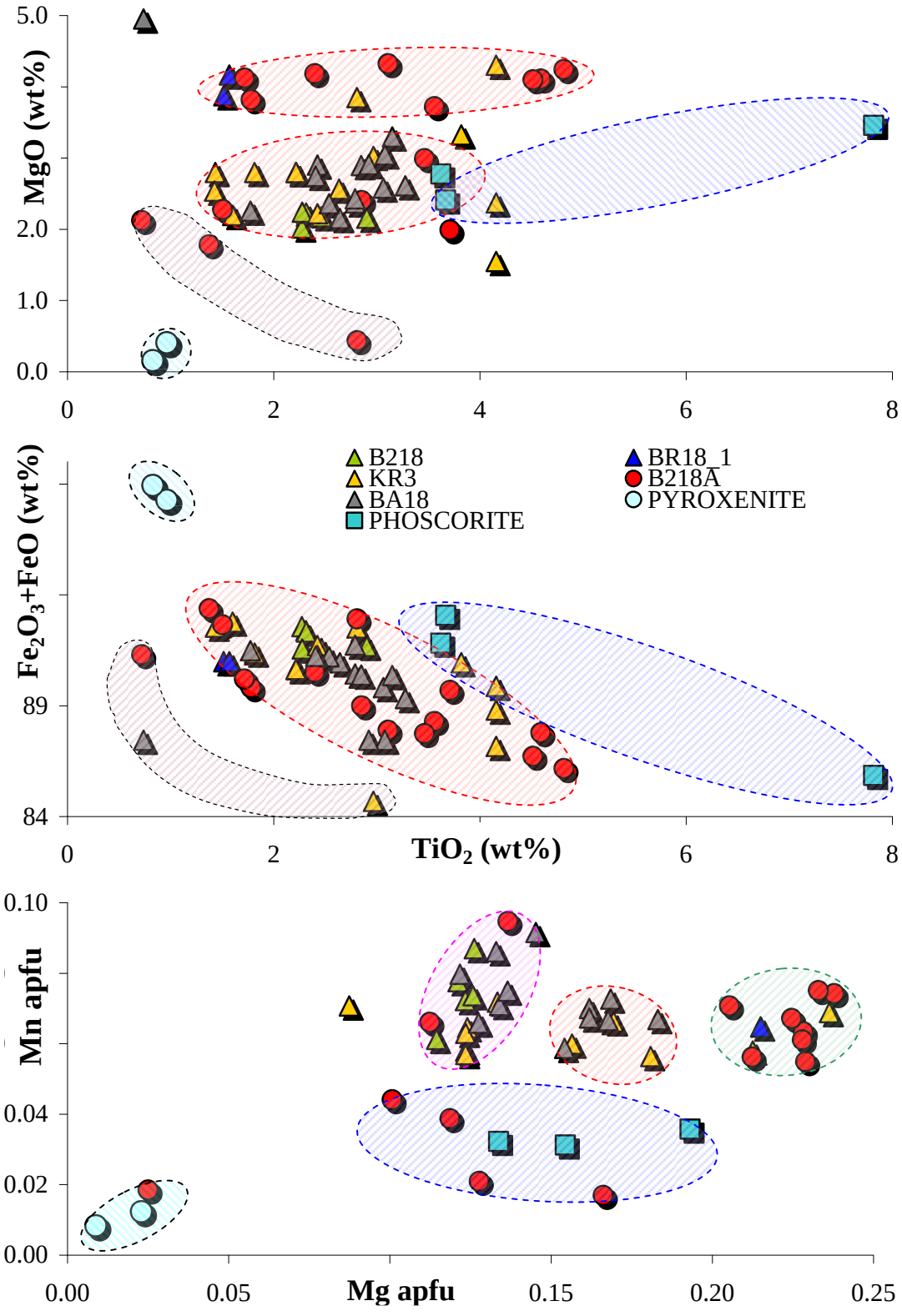

Fig.3.21 Composition of magnetite from Vuoriyarvi carbonatite and associated pyroxenite and phoscorite (Karchevsky, 2010). Magnetite from the B218A carbonatite sample shows similarity with that in pyroxenites and phoscorites.

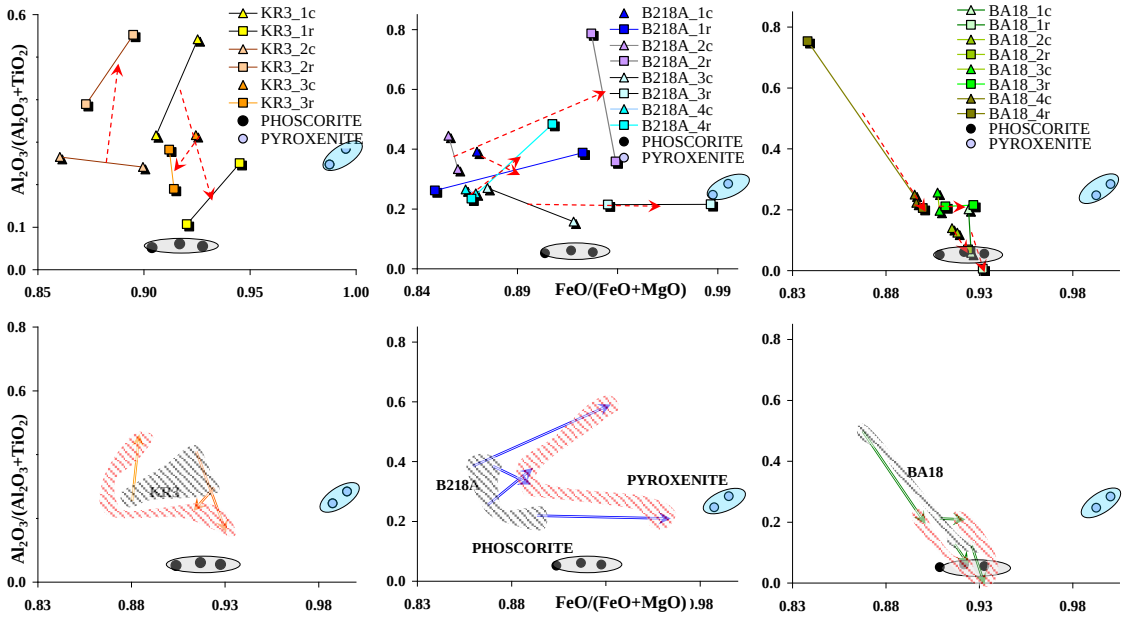

Fig.3.22 Composition of magnetite from Vuoriyarvi carbonatite distinguishing core and rim variation plotted on diagram FeO/(FeO+MgO) versus $Al_2O_3/(Al_2O_3+TiO_2)$. The red arrows show trend from core (black shaded areas) to rim (red shaded areas) and for better clarity only core-rim trend arrows are left in the lower diagram. Magnetite from Vuoriyarvi pyroxenite and phoscorite are from Karchevsky (2010).

3.4 Discussion of major elements

There are different generations of crystals in igneous systems (Erdmann et al., 2010; Clarke 2007; Streck 2008), such as primary, cognate magmatic, xenocrystic, derived from country rock, incorporated from magma mixing or inherited from the source, and crystals formed via secondary alteration. Woolley and Church (2005) recognised the possibility that relatively high SiO_2 content could be a primary characteristic of many carbonatite magmas. They suggested that many extrusive carbonatites have abundant cognate silicate phases which would drive the composition towards silica-rich carbonate rocks. In their view this could reflect the primary composition of typical carbonatite magmas and therefore the intrusive (often silica-free) carbonatites would not. However, in Vuoriyarvi carbonatites, there is abundant evidence that many of the silicate phases are xenocrystic and derived from surrounding silicate rocks, rather than being cognate.

Calcite from the analysed samples has a moderately high SrO concentration, typical for a primary carbonate phase crystallised from carbonatitic magma (Le Bas, 1981). Dolomite and calcite inclusions in magnetite are considerably enriched in FeO (0.90-0.85 wt%). Coarse calcite displays overall low levels of FeO, although B218A sövitic calcite rim is 5 times (up to 0.3 wt% FeO) enriched compared with its core. This elevated FeO concentration may result from higher concentration of FeO in the melt and

could suggest simultaneous crystallisation of magnetite with calcite and dolomite. If magnetite was incorporated from the associated clinopyroxenites, most likely different conditions were present during crystallisation of this phase and the chemical variation reflects higher concentration of MnO in the system and the ability to form dolomite. Or again there is the possibility of incorporation of xenoliths of pyroxenite (Mariano, 1989), preserving some of the primary geochemical information in the altered assemblage.

Fluorapatite is the second most abundant non-silicate constituent in Vuoriyarvi carbonatites and occurs as an inclusion in other phases. It does not show obvious zoning. Its major element geochemistry is typical for apatites from carbonatites and it shows a closer similarity to apatite from Vuoriyarvi pyroxenites than phoscorites (Figure 3.14).

There is a small difference between the mg# of xenocrystic phlogopite and phlogopite phenocrysts crystallised in equilibrium from their carbonatitic host. Variation of MgO is reverse, showing lower mg# for the earlier-formed xenocrystic crystals. Perhaps these xenocrysts were formed in an associated silicate magma, or they were the product of reaction with country rock such as pyroxenite. Mariano (1989) pointed out that pyroxenite xenoliths found in the Jacupiranga sövite are strongly altered around the margins to phlogopite, magnetite plus other mafic phases. As clinopyroxenites in Vuoriyarvi are found in close spatial association with the investigated carbonatite dykes, there is a strong probability that this is where the coarse phlogopite originated. Additionally, core-rim trends (Figure 3.9) for xenocryst phlogopite and phlogopite from Vuoriyarvi clinopyroxenites are similar.

Resorption of xenocrystic phlogopite would modify the carbonatitic liquid by increasing its SiO_2 content. This might have triggered growth of the second generation of phlogopite (crystallisation in equilibrium together with apatite inclusions in phlogopite). The second generation of phlogopite shows reverse zoning. Progressive incorporation and resorption of xenocrysts would also gradually increase the MgO component in the carbonatitic liquid; hence the MgO enrichment towards the rim. As the rim of the xenocrystic phlogopite is also rich in fine-grained apatite inclusions (strong resemblance to the second generation), it is likely to have crystallised at the same stage.

Only a small amount of olivine is present in analysed samples, mostly associated with serpentine plus monticellite. Vuoriyarvi clinopyroxenites are closely associated with carbonatites. Assuming that the complex represents a closed system, the liquid remaining after crystallisation and accumulation of minerals to form clinopyroxenite should be depleted in Mg and relatively enriched in Ca. So, assuming olivine is xenocrystic and probably crystallised at a higher temperature, after being mechanically assimilated from

clinopyroxenites to a Ca-rich magma, it would go through a reaction process and transform to monticellite. The mg# of olivine in Vuoriyarvi pyroxenites is 0.85, whereas mg# in olivine in associated carbonatites is higher (0.90). But monticellite, which contains some rounded calcite inclusions, is often highly abundant (up to 20%). Its *mg#* is slightly lower than in olivine. From the three coexisting mafic phases, diopside has the highest *mg#* (0.93-0.99), olivine slightly lower (0.89-0.90) and monticellite has the lowest *mg#* (0.77-0.81), thus these minerals show progressive Fe-enrichment (Figure 3.23).

Tracy et al. (1978) analysed an Adirondack marble which has a similar assemblage to the Vuoriyarvi carbonatites and also a comparable sequence of Fe-enrichment from diopside to olivine and monticellite. In the ternary system CaO-MgO-SiO_2, with excess CO_2, monticellite could be produced via the reaction:

diopside + forsterite + 2calcite = 3monticellite + $2CO_2$

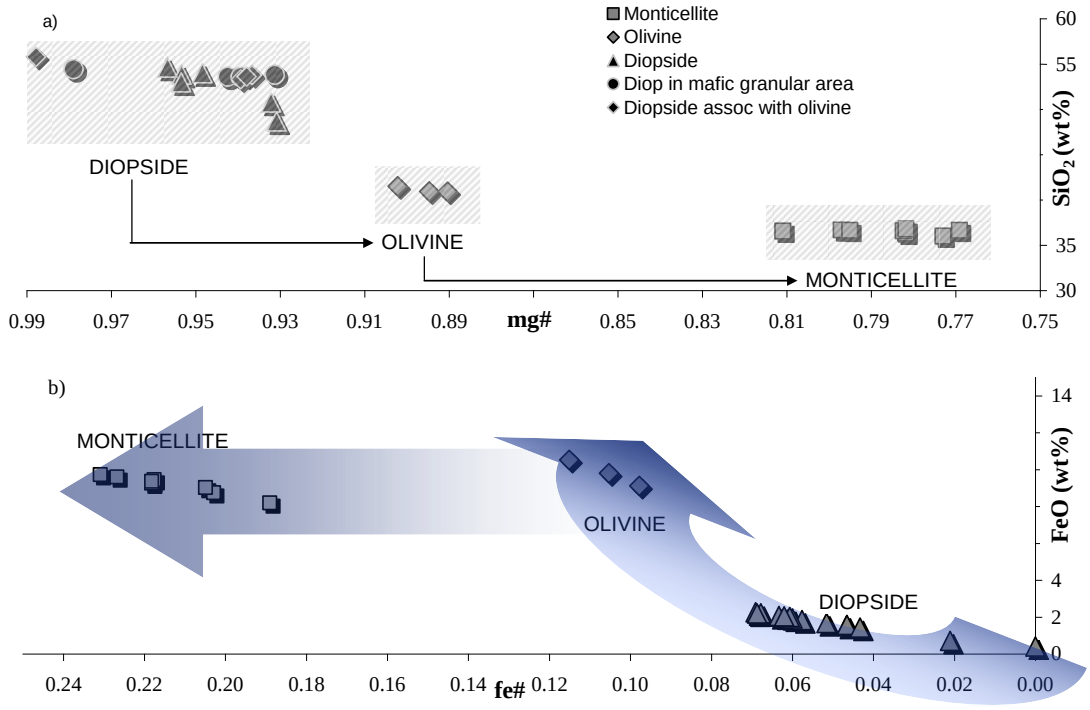

Fig.3.23a Diagram showing association between diopside-olivine-monticellite. (a) shows mg# versus SiO_2 of coexisting mafic phases in the Vuoriyarvi carbonatites with diopside having the highest mg#, olivine lower and monticellite lowest (negative trend with respect to SiO_2 meaning silica component is also decreasing). (b) shows fe# (Fe/(Fe+Mg)) vs. FeO of the same minerals giving the inside into increasing in Fe from diopside to olivine while FeO increases as well (positive trend) while olivine-monticellite having stable FeO concentration exhibits significantly increase in fe#.

Because of the compositional complexity of involved minerals, such as Fe/Mg variability, this simplified reaction is probably not adequate. Thus Tracy et al. (1978) expanded the graphical presentation to projection onto tetrahedron adding a FeO apex, thus the new figure would have projection from calcite onto SiO_2-FeO-MgO face (Figure 3.23b).

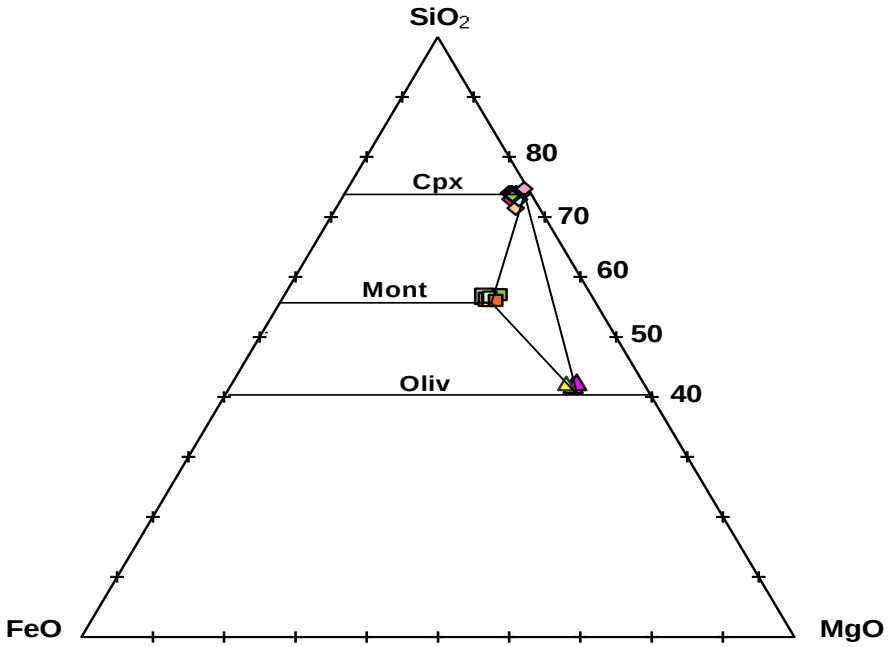

Fig.3.23b Ternary diagram of SiO_2-FeO-MgO with Vuoriyarvi diopside, olivine and monticellite plotted on CaO-SiO_2-FeO-MgO tetrahedron (projection from calcite with excess CO_2) to illustrate monticellite-forming reaction. Modified after Tracy et al., 1978.

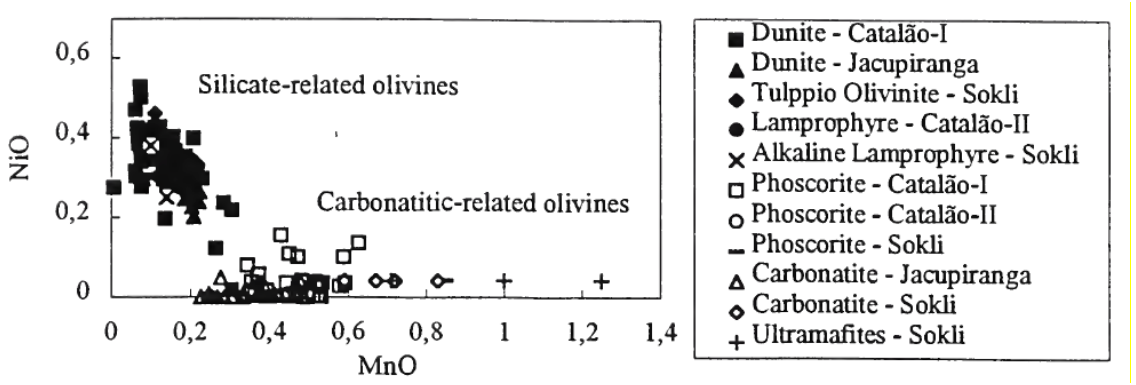

Fig.3.24 Olivine in carbonatitic and silicate rocks in carbonatite complexes (Gaspar et al., 1998). Two groups are present: one with high Ni and low Mn, and a second with low Ni and high Mn. The first group is found in dunite, olivinite and lamprophyre; the second is found in carbonatite and phoscorite. Olivine from carbonatite and phoscorite supports their genetic relationship (Lapin, 1982; Yegorov, 1983; Ericksson, 1989; Zaitsev and Bell, 1995, Araujo, 1996).

According to Gaspar at al, (1998) olivine in dunite contains 0.16-0.22 wt% MnO and 0.2-0.33 wt% NiO (Figure 3.24). In contrast, olivine from carbonatite shows higher MnO (0.23-0.49 wt%) and lower NiO (< 0.04 wt%). Rass et al. (2019) investigated phoscorite-carbonatite complex in Kovdor massif and concluded that the phosphate-carbonate melt separated from the alkaline-ultramafic silicate melt, followed by separation of the phosphate magma from the carbonate magma. Consequently, concentrations of Ni and Mn become varied within olivinite, carbonatite and phoscorite magmas. Thus, olivinites contain highest concentration of Ni (up to 840 ppm) than in phoscorites (up to 23 ppm) and carbonatites (up to 12 ppm). MnO is highest in phoscorite

(up to 0.46 wt%) than in olivinite (up to 0.38 wt%) and lowest in carbonatite (0.15 wt%). Olivine in olivinite shows the highest enrichment in MnO (0.56 wt%), with olivine in carbonatite being lower (0.40 wt% MnO) and least in phoscorite (0.37 wt% MnO). This is in agreement with the low concentration of Ni in olivine from the Vuoriyarvi carbonatite sample BR18_1 (2.4-8.3 ppm Ni).

The presence of rare olivine in Vuoriyarvi samples is important as it is not commonly found in carbonatites. According to Mikhailova et al. (2018), forsterite can be a key to understanding alkaline-ultrabasic massifs as it starts to crystallise in the peridotite intrusions and finishes in the late-stage carbonatites. Mikhailova et al. (2018) stated that because carbonate melts have low viscosity, they remain interconnected even when only 0.05 wt % melt is present. Also, "silicate melt selectively wets the grain-edge channels between solid phases, excluding the carbonate melt to the centre of melt pockets, away from grain edges". Thus "these features of carbonate melts enable to understand why forsterite grains can crystallise from carbonate-rich melt according to low-rate diffusion mechanism, and why they obtain predominant orientation in carbonate melt flow". Thus clinopyroxene was the solid phase incorporated into carbonatite magma which prepared the path for olivine to crystallise from carbonatite melt - sort of elder sister preparing the path for the younger sibling.

Monticellite exhibits reverse FeO chemical zoning, indicating changes of magma composition during crystallization. This could be influenced by the early resorption of magnetite xenocrysts which would cause higher FeO in the core and lower in the rim. The MgO component is generally higher in the rim than in the core. Perhaps these fluctuations of melt composition could be explained by corrosion and assimilation of xenocrystic phlogopite (the textural evidence of rim resorption is well preserved) and assimilation of clinopyroxene (diopside), hence redistribution of some major oxides (MgO, CaO, SiO_2) back into the melt. Veksler et al. (1998) stated that, in Kovdor, olivine would evolve with progressive fractionation towards forsteritic composition due to decrease of ferrous–ferric ratio in the residual melts of ultramafic alkaline magmas (suggested by the compositions of Mg-Fe silicates such as phlogopite), which means that Mg-rich olivine crystallised in the late stage of carbonatite formation and at lower temperatures. There is also compositional evolution (core-rim) towards MnO and SiO_2 enrichment. Quon and Heinrich (1965) noticed a similar MnO increase in calcite and dolomite grains from a study of world-wide occurrences and discussed its steady rise through the sequence calcite-dolomite-ankerite-siderite (>5%). Sample B218A contains both calcite (average MnO is 0.01 wt%) and dolomite (average MnO is 2.0 wt%). Concentration of MnO in

Vuoriyarvi monticellite is 1.5 wt%, in olivine 2 wt%. The slightly higher contents of MnO in olivine may be due to olivine being crystallised earlier and lower MnO contents in monticellite is the signature of the later evolving sequence. Fe/Mn ratio in olivine and monticellite in carbonatites from Vuoriyarvi plotted against SiO_2 (Figure 3.13) are very similar.

Guzmics et al. (2011) analysed melt and fluid inclusions in the Kerimasi calciocarbonatite with a similar assemblage to the Vuoriyarvi sövites and concluded that it crystallised from a carbonatite melt fraction with some dissolved silicate components, analogous to the crystallised silicate phases. Guzmics et al. (2011) estimated temperatures for the early stage of magma evolution (homogenization experiments of apatite-hosted carbonatite melt inclusions and forsterite–monticellite stability relations) as being in 900-1000 °C. These experiments could provide an answer to crystallisation of the Vuoriyarvi olivine (most probable in a MgO- and FeO-rich silicate melt) which occured during the very early stages of magma evolution. Thus, formation of monticellite in Vuoriyarvi could be associated with the silica-bearing carbonatite melt showing progressive enrichment in the CaO-component. During progressive exhaustion of the silicate component, monticellite is most likely to crystallise as this phase contains the highest amount of CaO (up to 35 wt%).

The crystallisation conditions of magnetite must have been changeable. According to Gaspar and Wyllie (1983), the importance of increasing concentration of FeO/(FeO+MgO) in magnetite reflects progressive crystallisation with decreasing temperature and increasing time. This consistency is established in Figure 3.25. Gaspar and Wyllie (1983) interpreted core variation as a result of constant crystallisation of magnetite, right throughout progressive evolution of carbonatite magma, thus generating gradually higher FeO/(FeO+MgO) core values (consistent in B218A and BA18). KR3 sample looks different which might reflect some local assimilation of the country rock or magnetite being incorporated after it started crystallisation elsewhere. Figure 3.22 illustrates the inconsistent behaviour of magnetite which could indicate the presence of several generations of xenocrysts. Magnetite in sample B218A shows a trend towards pyroxenite and in sample BA18 towards phoscorite.

Garnet occurs as an accessory constituent. Andradite lacks Al and Ti and Zr, whereas Zr-garnet is highly enriched in Ti+Zr (Figure 3.25). Both garnets coexist as separate phases, of which andradite is confined to monticellite fractures forming anhedral and very small grains (around 100 μm). Zr-rich garnet, on the other hand, can be either euhedral or subhedral situated between apatite and calcite phases. Furthermore, andradite

lacks zoning while Zr-rich garnet shows slight chemical variation though both garnets belong to the same andradite-schrolomite-Zr-garnet series (Figure 3.25). Thus, the secondary andradite most likely was formed as an alteration after magnetite (perhaps during a metasomatic event?).

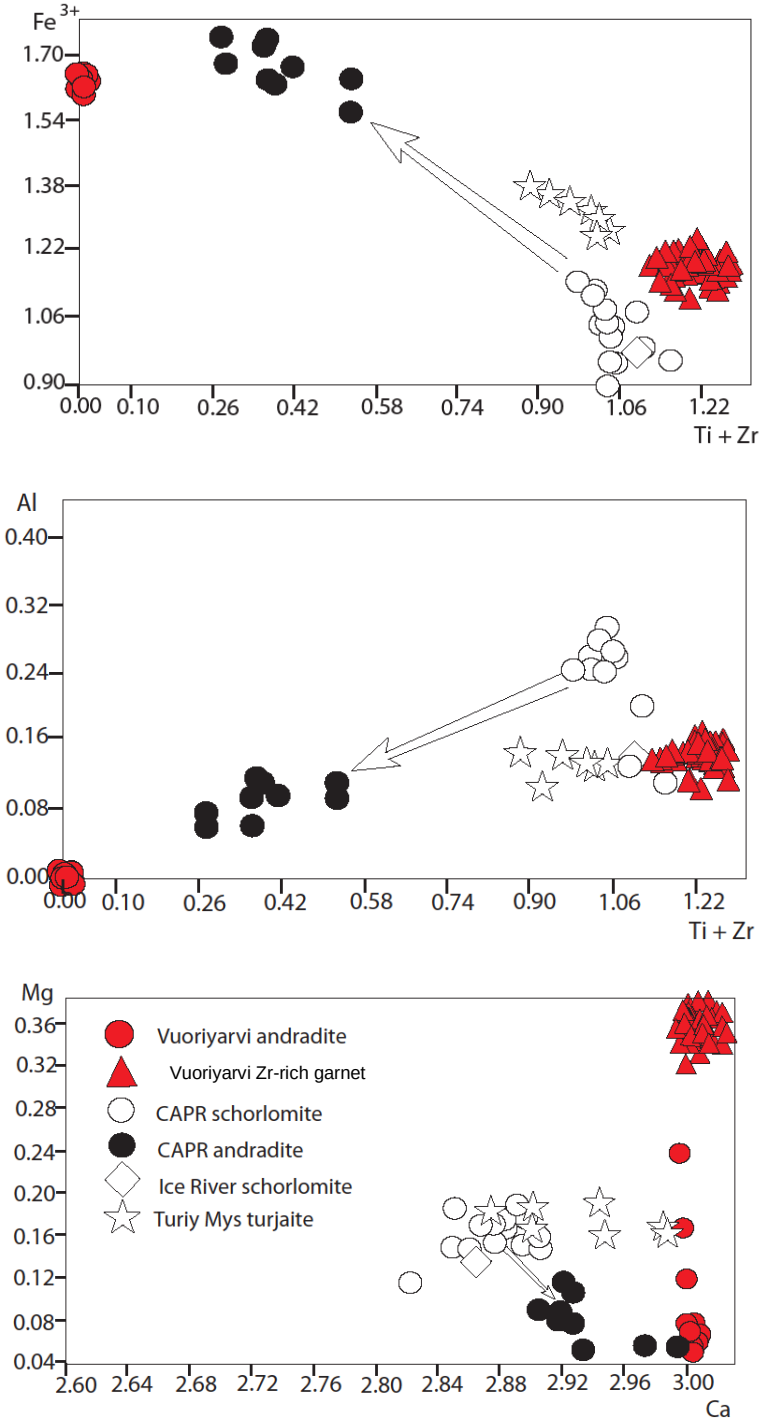

Fig.3.25 Variation diagrams, after Chakhmouradian and Zaitsev (2002), of major components (apfu) in the composition of Ti-rich garnets from calcite-amphibole-clinopyroxene rock from Africanda (analogous to silicocarbonatite) and for comparison from Ice River (Locock et al. 1995) and Turiy Mys (with Chakhmouradian and Zaitsev unpubl. data) with superimposed composition of garnets from Vuoriyarvi carbonatite.

Zr-rich garnet is very rare in carbonatites but are found in Magnet Cove (Milton et al., 1961). They are of great significance, as they are closely related to carbonatites and/or associated silicate rocks (Chakhmouradian and McCammon, 2005). The rare Vuoriyarvi garnets are small with their former euhedral shapes now partially resorbed. Providing that Zr-garnets formed as a liquidus phase, the textural evidence of numerous apatite and minor calcite inclusions illustrates that calcite and apatite crystallised prior to and during the crystallisation of garnets. All Zr-garnets are calcic (average CaO is 30 wt%), which agrees with the carbonatite-hosted environment, and relatively high in silica (25 wt% SiO_2), though very low in Al_2O_3 (1.2 wt%) and MgO (2.5 wt%).

Crystallisation of the Vuoriyarvi garnet was controlled by the higher concentration of CaO and SiO_2 (reflecting silicate-carbonatite magma association or carbonated silicate liquid on the verge of immiscibility), slight dominance of ZrO over TiO_2 and considerable amounts of FeO. This would indicate that the host liquid had to be enriched in CaO, SiO_2 and FeO and additionally would contain considerable amounts of Ti and Zr. Ti-bearing minerals such as Ti-magnetite, ilmenite and perovskite also form part of the mineral assemblage of associated pyroxenites and phoscorites.

The rarity of crystals and high volume of inclusions in perovskite could indicate crystallisation in the early stages of immiscibility or perhaps in an ultramafic magma or exotic system such as phoscorite, and later being incorporated into carbonatite (showing similarities to formation of Zr-garnet). Arzamastsev et al (2002) stated that perovskite is abundant in Vuoriyarvi pyroxenites up to 40 vol%. But there is a question of the high concentration of apatite inclusions as Arzamastsev et al. (2002) said that apatite is not so common in ultramafic rocks, with typical volumes of 3% in pyroxenite.

Hornig-Kjarsgaard (1998) established that the major element chemistry of perovskite in carbonatites is distinguished by high Nb, Fe^{3+} (and REE) due to a coupled substitution of $Na^{+} + RE^{3+}$ for Ca^{2+} and $Nb^{5+} + Fe^{3+}$ for Ti^{4+}. Elevated Ti activity in the system is confirmed by crystallisation of Ti-bearing phases. Mitchell and Chakhmouradian (1998) pointed out that perovskite is a stable phase on the liquidus of many magmatic rocks and, during subsolidus re-equilibration, it will be replaced by other Ti-rich minerals. In carbonatites, perovskite could be replaced by Mg- and Al-poor, Ti-rich garnet of schorlomitic or melanitic composition frequently accompanied by titanite:

$$\underset{\text{perovskite}}{CaTiO_3} + (SiO_2)_{aq} \rightarrow \underset{\text{titanite}}{CaTiSiO_5}$$

$$\underset{\text{perovskite}}{2CaTiO_3} + 3(SiO_2)_{aq} + Ca^{2+} + 3Fe^{3+} \rightarrow \underset{\text{schorlomite}}{Ca_3Ti_2Si_3Fe_3O_{12}}$$

Mitchell and Chakhmouradian (1998) stated that formation of silicate phases after perovskite is not commonly found in carbonatite rocks but they originate in silica-rich liquids such as phoscorite. In carbonatites, perovskite is unstable in the presence of CO_2-rich fluids (leaching of Ca^{2+}) and tends to be replaced by oxides such as Nb-pyrochlore induced by the increasing activity of volatiles. The presence of a Ti-rich silicate phase, together with Zr-garnet, in the Vuoriyarvi assemblage confirms high silica activity in the system, as does the presence of other silicates such as phlogopite, olivine, monticellite and diopside.

According to Zaitsev et al. (2010), Zr is a recurrent minor element in formation of andradite-melanite-schorlomite solid solution garnets and this type of garnet can accommodate up to 19.5 wt% ZrO_2. The incorporation of Zr is explained by Platt and Mitchell (1979) as involving the coupled substitution $^{[6]}Fe^{3+} + {}^{[4]}Si^{4+} \rightleftarrows {}^{[6]}Zr^{4+} + {}^{[4]}(Al,Fe)^{3+}$ (perhaps this is an explanation for the inverse SiO_2 versus Al_2O_3 correlation in Figure 3.26). Munno et al. (1980) studied kimzeyite and revised the formula as $Ca_3(Zr,Ti)_2(Si,Al,Fe^{3+})_3O_{12}$. Chakhmouradian and McCammon (2005) concluded that Zr is common substituent in Ti-rich garnets (although these garnets already show the complexity of Ti-substitution). Ito and Frondel (1967) researched the system andradite-shorlomite-kimzeyite, more precisely Ti- and Zr-rich synthetic garnets, concluding that a nearly complete solid solution between them was achieved at atmospheric pressure at 1050°C. Katerinopoulou et al. (2009) analysed Ti-Zr-Cr-rich garnets (solid solution andradite-uvarovite with considerable proportion of shorlomite-kimzeyite) from a high temperature melilitic skarn in Greece and concluded that the crystallisation conditions for the garnet (and other Ti-bearing minerals such as perovskite, andradite and titanite) reach temperatures up to 900°C. Katerinopoulou et al. (2009) also stated that the Ti-Zr-Cr-bearing garnet was formed due to the breakdown of titanite, ilmenite, magnetite and zircon under oxidizing conditions.

The analysed Zr-rich and Nb-rich phases show a linear relationship if Zr (in Zr-garnet) and Nb (in perovskite) are plotted against the Ti-component (Figure 3.26). Elevated concentration of Ti corresponds to lower concentration of Nb (perovskite side) and lower concentration of Ti is related to higher concentration of Zr (Zr-garnet sir garnete). This relation reflects close association between both phases. It is credible that some of perovskite, as an early fomed phase, survived in its original form while a number of crystals went through subsolidus alteration to form Ti-garnet (perhaps shorlomite) and consequently were further altered (via substitution Zr → Ti) to produce Zr-garnet.

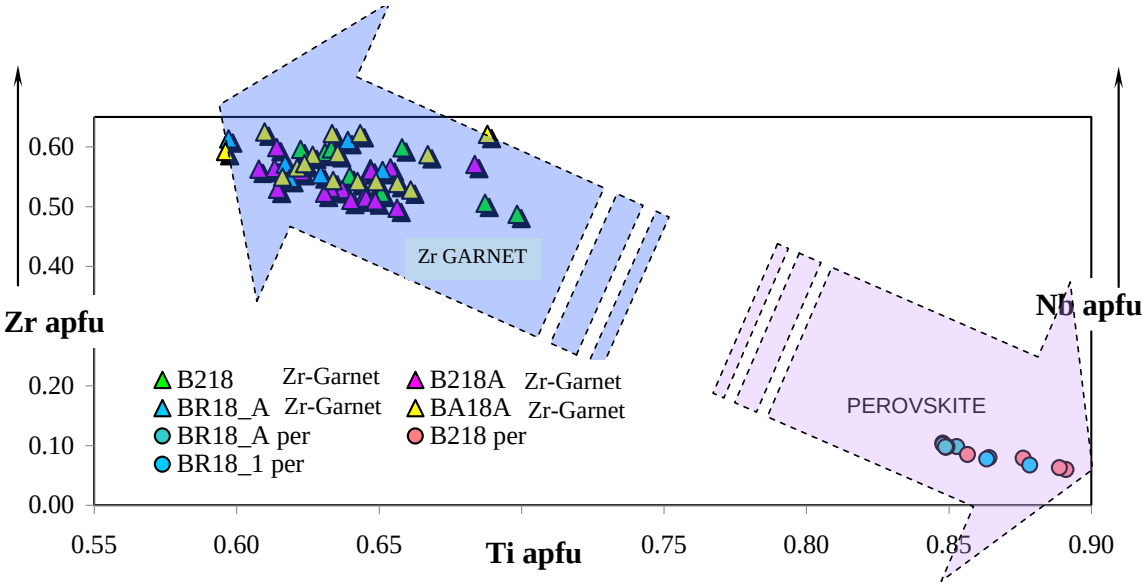

Fig.3.26 Variation diagram (Ti versus Zr (left hand side) or Nb (right hand side)) for Ti-Zr-Nb rich phases such as Zr-garnet and perovskite from Vuoriyarvi.

Xenocrystic clinopyroxene crystallised early in several samples. All pyroxenes are small and subhedral and form rounded crystals in contact with monticellite and calcite. According to the Wo-En-Fs diagram (Figure 3.27), they are diopsides and plot close to clinopyroxene from Vuoriyarvi pyroxenite which confirms they are xenocrystic in origin from pyroxenite. Similarity in composition indicates a close association such as evolution of diopside from clinopyroxenitic melts towards carbonatitic melts involving some Mg-enrichment. Diopside from more evolved Vuoriyarvi carbonatite (C3) shows slight Fe-enrichment and plots close to diopside from clinopyroxenite. The analysed diopside also demonstrates CaO-enrichment (ca. 50% Wo) and SiO_2-enrichment but very low Al_2O_3 and TiO_2 contents (Figure 3.27). According to Muñoz et al. (2003), the high Ca content coupled with significant substitution of Al by Si is characteristic of clinopyroxene in strongly alkaline series.

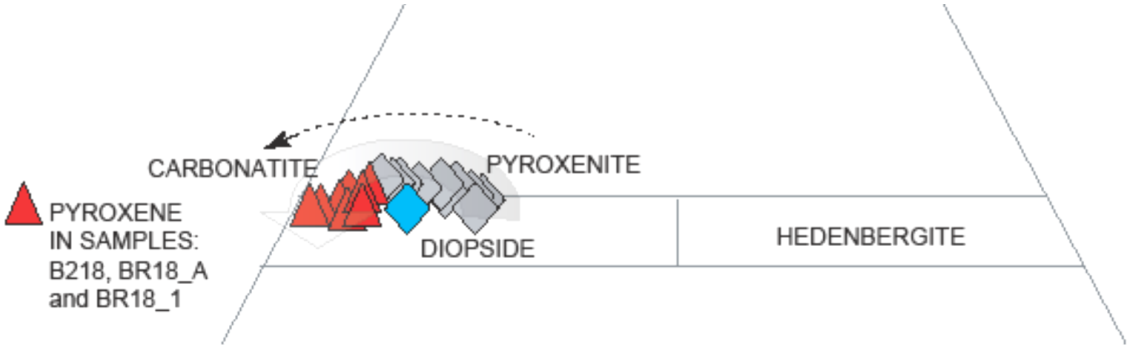

Fig.3.27 Wo-En-Fs diagram presenting the composition of pyroxene with pyroxenes from associated pyroxenite (grey diamonds) and late-stage carbonatite (blue diamonds) (Karchevsky, 2010.

Chakhmouradian and Zaitsev (2002) studied a calcite-amphibole-clinopyroxene rock (CAPR) from Afrikanda and established the low concentration of Al and Ti in diopside in these samples. According to the authors, the analysed rock is analogous to silicocarbonatite (the classification term not acknowledged by IUGS but it is close to silica-rich carbonatite classification), although the modal composition shows higher concentration of silicate phases over the carbonate ones. Chakhmouradian and Zaitsev (2002) noted that Al-poor diopside can be commonly found in carbonatites, however clinopyroxene with Al-Ti enrichment is distinctive from the ultramafic complexes (such as clinopyroxenite) as the authors found Ti-Al-rich xenocrystic clinopyroxene in CAPR rock. According to Chakhmouradian and Zaitsev (2002), diopside-bearing carbonatites (and phoscorites) are less common than forsterite-bearing varieties. Significantly, all those types are confined to the early stages of carbonatite genesis.

Amphibole from the Vuoriyarvi carbonatite is the reservoir for alkalis such as Na. Alkalis are prone to migrate to surrounding rock during fenitization. Thus, formation of the edenite confirms the availability of Na in carbonatitic fluid. Vuoriyarvi edenite and diopside are Al-poor, perhaps reflecting crystallization of Al-rich phlogopite. According to McCauley et al. (1986) “edenitic amphibole is stable only over a very limited temperature range in silica-undersaturated environments”.

3.5 Summary of major elements

1. Calcite with a moderately values of SrO is characteristic for a primary carbonate phase crystallised from carbonatitic magma. The same applies to fluorapatite formed as a primary mineral also with moderate SrO values.
2. Incorporation and resorption of xenocrystic phlogopite modified the carbonatitic liquid with respect to SiO_2 and MgO.
3. Complex core-rim zonation in the magnetite reflects variable condition in the system influenced by crystallisation, assimilation and perhaps post-solidus alteration.
4. Olivine contains 2.0 wt% MnO which is high and indicative of olivines which crystallised from a carbonatite melt **(**Gaspar et al. 1998). With progressively higher CaO-concentration, the relict olivine most likely switched to crystallisation of monticellite. The lower mg# of monticellite could reflect crystallisation of monticellite and transformation of olivine to monticellite which occurred over the same period.

5. Perovskite can represent the early precipitation of Nb-rich phases from the relatively silica-rich carbonate liquid during the early stages of separation, thus it is xenocrystic and derived from pyroxenite.
6. The complex history of the Vuoriyarvi carbonatite is highlighted by early stages of formation seen in xenocrystic Al-poor diopside which was entrained from pyroxenite followed by fenitization which formed Al-poor edenite.
7. Pure andradite is a secondary phase most probably alteration after magnetite, mostly found in the monticellite fractures.
8. The role of silicate phases in the Vuoriyarvi carbonatites is summarised in Figure 3.28 which shows the mg# of these minerals against their SiO_2 content. Earlier formed phases such as diopside and amphibole together with olivine exhibit highest mg# (0.97-0.90) while monticellite displays a lower mg# (~ 0.80). The trend descends in a linear manner towards the mg# of the bulk rock.

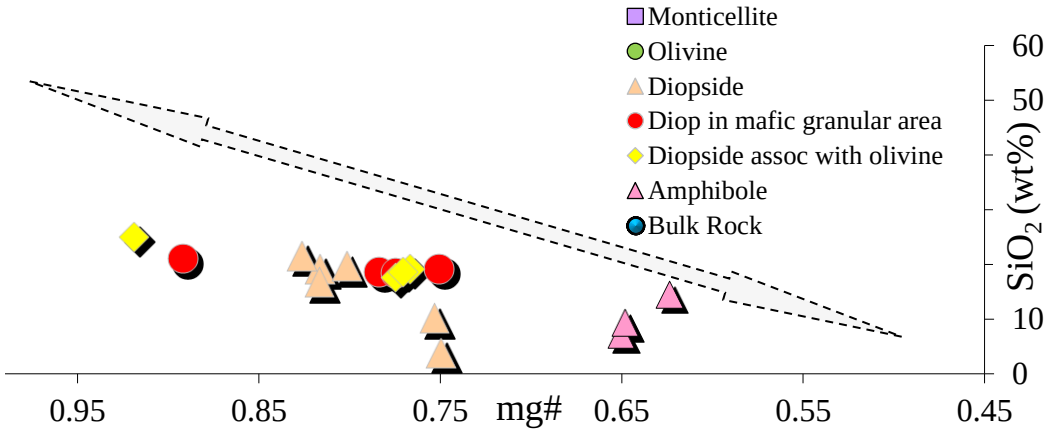

Fig.3.28 Plot of SiO_2 vs. mg# for diopside, olivine, amphibole, monticellite and bulk rock of the Vuoriyarvi carbonatite.

3.6 Trace elements for constituent minerals in Vuoriyarvi sövites

3.6.1 Calcite

Trace element compositions of Vuoriyarvi calcite are presented in Table 3.12. Calcite is rich in Sr and Ba, Y and REEs. La ranges from 40 to 120 ppm and Ce from 60 to 300 ppm (Figure 3.29). Most of the analysed samples show negative anomalies in trace elements like Rb, Th, U, Nb, Ta, Pb, Zr and Hf. The REE patterns in calcites are less steep than apatite and their profiles are sub-parallel to each other (Figure 3.29). La/Yb_{CN} ratio is 13-40. No Eu anomaly was detected except for a slight positive peak in BA18A

(Eu/Eu*=1.25). Ba and Nd developed peaks, also Sm and Y form peaks. Nb and Ta show troughs but U forms a small peak. Zr and Hf developed troughs attaining the same levels of concentration. Pb forms a trough but Ti, V and Sc developed the deepest troughs.

Trace elements in calcite were analysed in several carbonatite complexes (Chakmouradian et al. 2015) to determine degree of substitution of REEs and trace elements. It was concluded that REE contents and some REE ratios in calcite are mostly controlled by crystal fractionation of fluorapatite and monazite but also other minerals can be involved. Formation of some magmatic calcite, such as those containing around 2000 ppm of total REEs, is most likely controlled by coupled substitution including Na and P. Removal of HREEs from carbonatitic magma by crystallising garnet (e.g., in Magnet Cove) may be responsible for the steep negative REE slope.

Analyses of bulk rocks from Kola Alkaline Province (Zaitsev et al., 2016) revealed that they are characterised by low REE contents with a maximum of 1500-2200 ppm in carbonatites and the REEs are mostly concentrated in the major rock-forming minerals such as calcite and apatite. Overall calcite contributes from 9 to 48% to the whole-rock REEs budget (Reguir et al., 2012).

A different and much more unusual trace element composition of calcite was found in sample BR18_1. Although the REE are similar to the other analysed calcites, the high field strength elements are much more enriched. All HFSE are affected, including Zr, Hf, Nb, Ta and U and Th. Chakmouradian et al. (2015) stated that incorporation of large tetravalent cations such as Zr, Th and U would cause an “imbalanced distribution of bond valence and, hence, be less likely to occur”. They suggested that this is the reason why these elements are below detection limit (<<1 ppm) in most published analyses. Thus, in analysed Vuoriyarvi calcite, there is no crystallographic site for these elements, yet they appear to be present in quite significant concentrations. Although values of >1 ppm Th or Zr and >0.5 ppm U were reported by Xu et al. (2010), the HFSE in the analysed calcites in this sample are much higher.

Understanding the origin of this enrichment in HFSE in calcite in this single sample is beyond the scope of this thesis, but some suggestions could be investigated in the future. These include (a) the presence of tiny unseen inclusions of an extremely HFSE-rich phase or (b) exsolution of a mineral such as synchysite, which is a REE carbonate with a formula of $Ca(Ce/Nd/Y/REE)(CO_3)_2F$) which can contain Y, or thorbastnaesite which is a hydrated carbonate mineral with the formula $ThCa(CO_3)_2F_2 \cdot 3H_2O$.

3.6.2 Apatite

Trace element compositions of apatite are presented in Table 3.13. Apatites are characterised by high abundances of LREE, although the enrichment is very variable (up to two orders of magnitude) with the HREE concentrations rather fixed around 100 times chondrite, giving chondrite-normalised La/Yb ratios of 20-120. This indicates variable but overall strong LREE fractionation into apatite. No Eu anomaly was detected. Th together with U show high peaks (Figure 3.30). In contrast, Nb, Ta, Pb, Ti and Rb form troughs. Apatite is also highly enriched in Y, Sr, Th, U and moderately enriched in Zr. There is a positive correlation between Sr and REE content.

According to Reguir et al. (2012), the contribution of apatite to the whole-rock REE budget is variable with 51-86%. The REE content in apatite in analysed Vuoriyarvi samples ranges from 1100 to 30000 ppm with the highest value in BR18A and the lowest in B218. According to Zaitsev et al. (2016), rocks formed in the early stage such as calcite carbonatites and phoscorites are characterised by low REE contents (maximum approximately 1800-2000 ppm in phoscorites, and 1500-2200 ppm in carbonatites) although late-stage carbonatites are highly enriched up to 5.2 wt.% REE_2O_3. Zaitsev and Bell (1995) observed that REE concentrations in apatite increases from early to late formed carbonatites.

Laser-ICPMS analyses ppm CALCITE	KR3 aver n=5	st dev n=5	B218A aver n=3	st dev n=3	BR18 aver n=3	st dev n=3	BR18_A aver n=3	st dev n=3	B218 aver n=13	st dev n=13	BA18A aver n=9	st dev n=9
Sc	0.09	*0.03*	0.04	*0.01*	0.08	*bdl*	0.08	*bdl*	0.05	*bdl*	bdl	*bdl*
Ti	0.32	*0.22*	0.94	*0.86*	2.25	*bdl*	bdl	*bdl*	0.66	*0.30*	bdl	*bdl*
V	0.03	*0.02*	0.05	*bdl*	0.21	*bdl*	0.02	*bdl*	0.19	*0.24*	bdl	*bdl*
Cr	0.78	*0.18*	bdl	*bdl*	2.71	*bdl*	0.71	*0.03*	bdl	*bdl*	3.45	*bdl*
Mn	157	*29.0*	265	*20.6*	427	*24.0*	179	*21.7*	111	*26.5*	252	*29.1*
Co	0.25	*0.11*	0.15	*0.02*	0.06	*bdl*	0.03	*bdl*	bdl	*bdl*	bdl	*bdl*
Ni	0.97	*0.21*	0.26	*0.08*	0.71	*0.75*	0.13	*0.04*	0.15	*0.05*	bdl	*bdl*
Cu	0.10	*0.02*	0.03	*0.01*	0.37	*0.39*	0.10	*bdl*	7.57	*10.5*	bdl	*bdl*
Zn	1.19	*1.57*	0.16	*0.02*	1.35	*1.21*	bdl	*bdl*	2.34	*6.84*	bdl	*bdl*
Ga	5.85	*0.42*	7.38	*1.83*	13.0	*2.33*	3.27	*0.86*	2.65	*1.47*	1.35	*0.55*
Ge	0.69	*0.19*	0.93	*0.36*	1.52	*0.52*	0.22	*0.01*	0.24	*0.09*	0.94	*bdl*
Rb	0.01	*0.00*	0.05	*bdl*	0.12	*bdl*	0.04	*0.05*	0.06	*0.04*	bdl	*bdl*
Sr	5184	*80*	5823	*121*	14888	*1183*	5085	*109*	8739	*4318*	7855	*491*
Y	11.9	*1.97*	22.7	*7.59*	23.6	*6.43*	18.5	*3.44*	10.9	*5.92*	33.3	*10.4*
Zr	0.03	*0.01*	0.21	*0.24*	0.09	*0.05*	0.17	*0.19*	0.05	*0.06*	0.29	*bdl*
Nb	0.00	*0.00*	bdl	*bdl*	bdl	*bdl*	0.03	*0.03*	0.02	*0.01*	bdl	*bdl*
Ba	99.1	*6.25*	104	*31.8*	138	*17.4*	86.0	*22.6*	79.5	*30.4*	160	*39.9*
La	44.4	*8.19*	55.7	*29.6*	112	*36.8*	51.6	*14.7*	37.5	*17.8*	120	*41.2*
Ce	62.8	*13.6*	100	*57.7*	305	*139*	69.4	*20.8*	64.9	*33.1*	197	*74.7*
Pr	6.21	*1.40*	10.0	*5.26*	15.8	*5.33*	7.94	*2.00*	5.90	*2.98*	17.2	*6.74*
Nd	21.0	*4.72*	37.0	*18.6*	53.3	*16.4*	30.4	*8.42*	21.0	*10.6*	55.4	*21.5*
Sm	3.11	*0.69*	5.85	*2.71*	7.49	*2.87*	5.26	*1.35*	3.34	*1.69*	8.27	*3.27*
Eu	0.94	*0.24*	2.13	*0.96*	2.21	*0.81*	1.73	*0.41*	0.92	*0.49*	2.90	*0.96*
Gd	3.21	*0.62*	4.97	*1.83*	4.32	*1.47*	4.78	*1.14*	2.75	*1.37*	5.31	*1.93*
Tb	0.35	*0.06*	0.64	*0.24*	0.72	*0.21*	0.58	*0.12*	0.36	*0.22*	1.00	*0.34*
Dy	2.06	*0.27*	3.83	*1.24*	3.75	*1.21*	3.32	*0.67*	1.93	*1.08*	5.19	*1.80*
Ho	0.38	*0.06*	0.76	*0.24*	0.65	*0.18*	0.63	*0.15*	0.35	*0.21*	1.01	*0.34*
Er	1.03	*0.13*	1.93	*0.61*	1.67	*0.38*	1.53	*0.22*	0.91	*0.52*	2.39	*0.76*
Tm	0.14	*0.02*	0.26	*0.06*	0.19	*0.08*	0.22	*0.03*	0.11	*0.05*	0.33	*0.13*
Yb	0.86	*0.07*	1.73	*0.44*	1.18	*0.19*	1.36	*0.22*	0.71	*0.43*	1.79	*0.55*
Lu	0.13	*0.02*	0.25	*0.05*	0.17	*0.07*	0.21	*0.06*	0.10	*0.06*	0.33	*0.12*
Hf	0.00	*bdl*	0.01	*0.00*	bdl	*bdl*	0.04	*bdl*	0.01	*0.01*	0.14	*bdl*
Ta	0.00	*0.00*	0.00	*bdl*	bdl	*bdl*	0.00	*0.00*	0.01	*0.00*	bdl	*bdl*
Pb	0.37	*0.05*	0.64	*0.08*	0.52	*0.15*	0.48	*0.05*	0.32	*0.15*	0.81	*0.06*
Th	0.01	*0.01*	0.00	*0.00*	bdl	*bdl*	0.01	*0.00*	0.06	*0.05*	0.06	*0.02*
U	0.00	*0.00*	0.00	*bdl*	0.10	*bdl*	bdl	*bdl*	0.02	*0.03*	0.04	*bdl*

Table 3.12a Trace element contents of calcite (ppm) in the Vuoriyarvi carbonatites.

Laser-ICPMS CHONDRITE NORMALISED CALCITE	KR3 aver n=5	st dev n=5	B218A aver n=3	st dev n=3	BR18 aver n=3	st dev n=3	BR18_A aver n=3	st dev n=3	B218 aver n=13	st dev n=13	BA18A aver n=9	st dev n=9
La	121.1	*22.3*	151.7	*80.5*	305.7	*100.3*	140.6	*40.0*	102.3	*48.6*	326.8	*112.2*
Ce	65.64	*14.19*	104.5	*60.3*	318.9	*145.4*	72.5	*21.7*	67.8	*34.6*	206.2	*78.0*
Pr	45.31	*10.18*	73.1	*38.4*	115.1	*38.9*	57.9	*14.6*	43.1	*21.8*	125.7	*49.2*
Nd	29.58	*6.63*	52.01	*26.20*	75.00	*23.06*	42.82	*11.84*	29.59	*14.89*	77.99	*30.20*
Sm	13.47	*2.97*	25.32	*11.74*	32.42	*12.41*	22.77	*5.85*	14.44	*7.30*	35.80	*14.15*
Eu	10.76	*2.79*	24.46	*11.04*	25.44	*9.33*	19.84	*4.64*	10.55	*5.67*	33.30	*10.99*
Gd	10.49	*2.02*	16.23	*5.98*	14.12	*4.78*	15.61	*3.73*	8.98	*4.46*	17.35	*6.32*
Tb	6.11	*1.10*	10.98	*4.15*	12.37	*3.66*	10.04	*2.08*	6.21	*3.81*	17.25	*5.79*
Dy	5.39	*0.71*	10.05	*3.24*	9.86	*3.16*	8.72	*1.77*	5.07	*2.82*	13.61	*4.72*
Ho	4.50	*0.69*	8.96	*2.81*	7.67	*2.13*	7.38	*1.81*	4.09	*2.43*	11.87	*3.98*
Er	4.15	*0.53*	7.76	*2.43*	6.72	*1.50*	6.12	*0.89*	3.65	*2.09*	9.60	*3.04*
Tm	3.95	*0.68*	7.18	*1.75*	5.31	*2.23*	6.23	*0.84*	3.13	*1.50*	9.15	*3.70*
Yb	3.48	*0.29*	6.98	*1.77*	4.75	*0.76*	5.48	*0.88*	2.86	*1.71*	7.20	*2.22*
Lu	3.36	*0.41*	6.66	*1.34*	4.36	*1.76*	5.55	*1.54*	2.63	*1.66*	8.69	*3.24*

	KR3 aver n=5	st dev n=5	B218A aver n=3	st dev n=3	BR18 aver n=3	st dev n=3	BR18_A aver n=3	st dev n=3	B218 aver n=13	st dev n=13	BA18A aver n=9	st dev n=9
Rb	0.00	*0.00*	0.00	*0.01*	0.01	*0.02*	0.01	*0.01*	0.00	*0.01*	0.00	*0.00*
Ba	29.06	*1.83*	30.54	*9.32*	40.51	*5.10*	25.21	*6.62*	23.32	*8.92*	47.14	*11.71*
Th	0.10	*0.12*	0.02	*0.01*	0.00	*0.00*	0.22	*0.19*	0.56	*0.97*	0.30	*0.62*
U	0.21	*0.18*	0.05	*0.08*	2.81	*4.87*	0.00	*0.00*	0.74	*1.72*	0.32	*0.97*
Nb	0.00	*0.01*	0.00	*0.00*	0.00	*0.00*	0.06	*0.07*	0.02	*0.03*	0.00	*0.00*
Ta	0.02	*0.02*	0.01	*0.01*	0.00	*0.00*	0.12	*0.11*	0.11	*0.17*	0.00	*0.00*
La	121.1	*22.32*	151.7	*80.54*	305.7	*100.3*	140.6	*40.00*	102.27	*48.58*	326.8	*112.2*
Ce	65.64	*14.19*	104.5	*60.28*	318.9	*145.4*	72.52	*21.69*	67.82	*34.61*	206.2	*78.0*
Pb	0.10	*0.01*	0.17	*0.02*	0.14	*0.04*	0.13	*0.01*	0.09	*0.04*	0.22	*0.02*
Sr	435.6	*6.69*	489.3	*10.2*	1251	*99.4*	427.3	*9.13*	734.4	*362.8*	660.1	*41.23*
Nd	29.58	*6.63*	52.01	*26.20*	75.00	*23.06*	42.82	*11.84*	29.59	*14.89*	77.99	*30.20*
Zr	0.00	*0.00*	0.02	*0.04*	0.01	*0.01*	0.02	*0.03*	0.00	*0.01*	0.01	*0.02*
Hf	0.00	*0.01*	0.02	*0.02*	0.00	*0.00*	0.07	*0.12*	0.02	*0.04*	0.09	*0.26*
Sm	13.47	*2.97*	25.32	*11.74*	32.42	*12.41*	22.77	*5.85*	14.44	*7.30*	35.80	*14.15*
Ti	0.00	*0.00*	0.00	*0.00*	0.00	*0.00*	0.00	*0.00*	0.00	*0.00*	0.00	*0.00*
Y	5.29	*0.87*	10.09	*3.37*	10.50	*2.86*	8.21	*1.53*	4.83	*2.63*	14.79	*4.70*
V	0.00	*0.00*	0.00	*0.00*	0.00	*0.00*	0.00	*0.00*	0.00	*0.00*	0.00	*0.00*
Sc	0.01	*0.01*	0.00	*0.00*	0.00	*0.01*	0.00	*0.01*	0.00	*0.00*	0.00	*0.00*

Table 3.12b Chondrite-normalised trace element contents of calcite in the Vuoriyarvi carbonatites.

Laser-ICPMS analyses ppm CALCITE	BR18_1 aver n-5	in small xen st dev n-5	aver n-3	in small xen st dev n-3	aver n-5	st dev n-5	aver n-4	st dev n-4
Sc	1.08	0.41	2.32	1.36	0.98	0.21	0.96	0.13
Ti	2.38	0.22	2.04	0.48	2.13	0.40	2.29	0.21
V	0.50	0.30	0.30	0.04	0.43	0.12	0.35	0.04
Cr	0.01	0.01	0.00	0.01	0.01	0.00	0.01	0.00
Mn	0.39	0.53	0.44	0.30	0.11	0.02	0.10	0.02
Co	0.01	0.01	0.01	0.00	0.00	0.00	0.00	0.00
Ni	0.00	0.00	0.00	0.00	0.00	0.00	0.00	0.00
Cu	0.23	0.12	0.08	0.11	0.25	0.04	0.26	0.10
Zn	0.06	0.02	0.06	0.01	0.08	0.03	0.05	0.00
Ga	1.26	0.35	0.59	0.45	1.36	0.18	1.54	0.26
Ge	0.09	0.03	0.08	0.00	0.09	0.01	0.10	0.01
Rb	47.8	22.4	15.1	22.8	52.8	9.73	51.7	5.39
Sr	153	97.6	80.1	102	174	104	220	111
Y	11.9	2.00	8.79	1.90	12.8	7.57	10.7	1.20
Zr	67.0	17.3	62.2	27.5	60.1	12.3	68.5	7.13
Nb	117	41.4	35.2	48.8	116	21.4	123	11.7
Ba	175	24.9	49.4	74.5	157	24.8	171	18.7
La	122	28.4	77.8	59.0	206	190	115	16.1
Ce	91.7	25.9	78.1	51.3	254	280	81.6	21.8
Pr	68.5	19.4	60.4	27.4	209	326	64.2	17.8
Nd	46.0	13.6	47.4	18.5	94.5	101	44.7	7.02
Sm	26.0	9.86	28.6	4.93	46.3	52.3	24.8	6.45
Eu	22.4	8.44	22.2	4.45	41.4	37.5	32.6	31.4
Gd	17.4	4.72	17.9	2.95	27.1	29.7	16.7	4.53
Tb	12.2	5.00	16.4	4.65	21.3	22.4	13.0	2.50
Dy	12.2	3.18	11.8	1.34	17.9	19.0	9.96	0.98
Ho	11.1	2.30	9.69	0.93	12.5	10.5	8.95	0.57
Er	10.1	1.99	8.43	1.37	11.7	8.35	9.03	2.09
Tm	11.2	4.59	9.09	0.76	12.9	5.98	10.5	2.59
Yb	11.7	3.03	9.08	1.04	9.66	6.18	8.83	1.12
Lu	11.5	5.33	11.6	3.18	10.8	5.89	8.89	1.56
Hf	51.8	17.95	37.6	9.27	47.7	10.7	53.3	5.98
Ta	54.0	26.1	26.1	23.8	59.1	14.7	76.4	9.64
Pb	3.79	1.68	1.45	2.16	4.55	1.30	4.30	0.78
Th	151	30.0	54.3	64.2	397	464	226	132
U	327	150	151	210	502	199	517	106

Laser-ICPMS CHONDRITE NORMALISED CALCITE	BR18_1 aver n-5	in small xen st dev n-5	aver n-3	in small xen st dev n-3	aver n-5	st dev n-5	aver n-4	st dev n-4
La	122	28.4	77.8	59.0	206	190	115	16.1
Ce	91.7	25.9	78.1	51.3	254	280	81.6	21.8
Pr	68.5	19.4	60.4	27.4	209	326	64.2	17.8
Nd	46.0	13.6	47.4	18.5	94.5	101.1	44.7	7.02
Sm	26.0	9.86	28.6	4.93	46.3	52.3	24.8	6.45
Eu	22.4	8.44	22.2	4.45	41.4	37.5	32.6	31.4
Gd	17.4	4.72	17.9	2.95	27.1	29.7	16.7	4.53
Tb	12.2	5.00	16.4	4.65	21.3	22.4	13.0	2.50
Dy	12.2	3.18	11.8	1.34	17.9	19.0	9.96	0.98
Ho	11.1	2.30	9.69	0.93	12.5	10.5	8.95	0.57
Er	10.1	1.99	8.43	1.37	11.7	8.35	9.03	2.09
Tm	11.2	4.59	9.09	0.76	12.9	5.98	10.5	2.59
Yb	11.7	3.03	9.08	1.04	9.66	6.18	8.83	1.12
Lu	11.5	5.33	11.6	3.18	10.8	5.89	8.89	1.56
Rb	47.8	22.4	15.1	22.8	52.8	9.73	51.7	5.39
Ba	175	24.9	49.4	74.5	157	24.8	171	18.7
Th	151	30.0	54.3	64.2	397	464	226	132
U	327	150	151	210	502	199	517	106
Nb	117	41.4	35.2	48.8	116	21.4	123	11.7
Ta	54.0	26.1	26.1	23.8	59.1	14.7	76.4	9.64
La	122	28.4	77.8	59.0	206	190	115	16.1
Ce	91.7	25.9	78.1	51.3	254	280	81.6	21.8
Pb	3.79	1.68	1.45	2.16	4.55	1.30	4.30	0.78
Sr	153	97.6	80.1	102	174	104	220	111
Nd	46.0	13.6	47.4	18.5	94.5	101	44.7	7.02
Zr	67.0	17.3	62.2	27.5	60.1	12.3	68.5	7.13
Hf	51.8	17.9	37.6	9.27	47.7	10.7	53.3	5.98
Sm	26.0	9.86	28.6	4.93	46.3	52.3	24.8	6.45
Ti	2.38	0.22	2.04	0.48	2.13	0.40	2.29	0.21
Y	11.9	2.00	8.79	1.90	12.8	7.57	10.7	1.20
V	0.50	0.30	0.30	0.04	0.43	0.12	0.35	0.04
Sc	1.08	0.41	2.32	1.36	0.98	0.21	0.96	0.13

Table 3.12c Trace element contents of calcite (ppm) and chondrite-normalised abundances in BR18_1 sample.

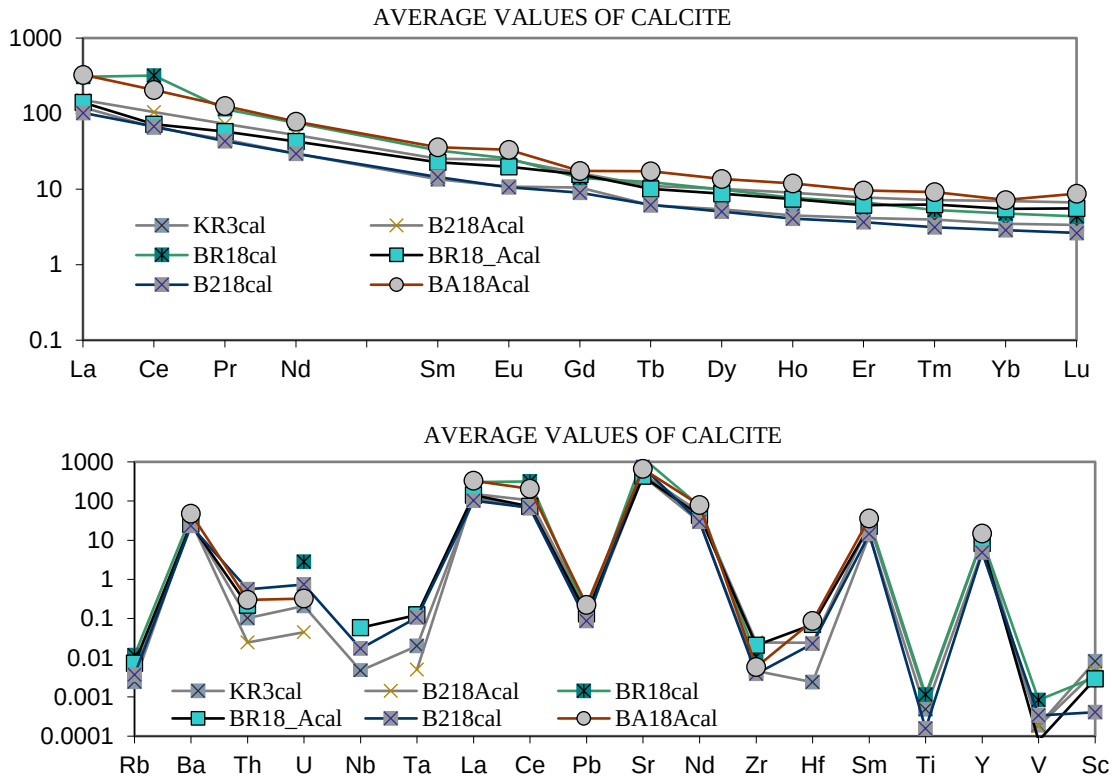

Fig.3.29a Chondrite-normalised average REE and trace element patterns of calcite in the Vuoriyarvi carbonatites

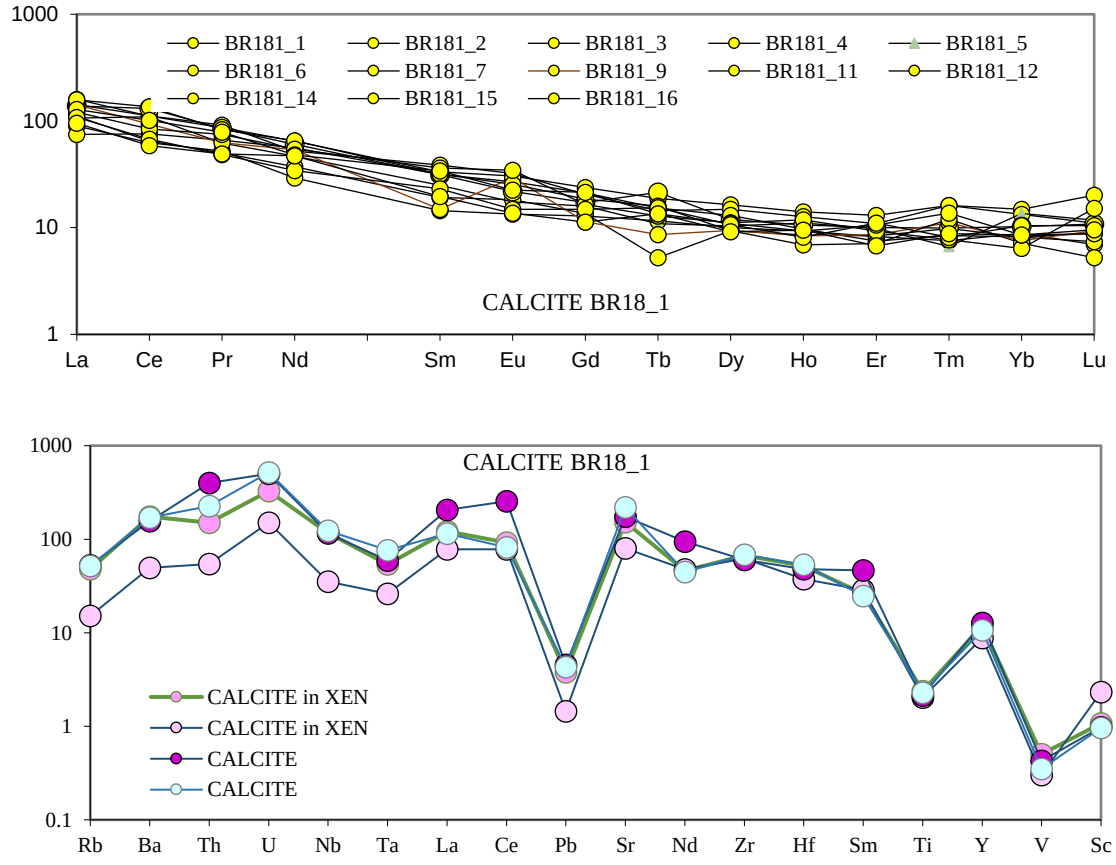

Fig.3.29b Chondrite-normalised average REE and trace element patterns of calcite in sample BR18_1.

Laser-ICPMS analyses ppm APATITE	B218 aver n=4	st dev n=4	KR3 aver n=3	st dev n=3	BR18 aver n=7	st dev n=7	B218A aver n=5	st dev n=5	BR18_1 aver n=11	st dev n=11	BR18A aver n=3	st dev n=3	BR18A aver n=10	st dev n=10
Sc	0.22	*0.05*	2.49	*1.94*	2.41	*2.08*	0.71	*0.41*	10.5	*1.42*	0.96	*0.10*	bdl	*bdl*
Ti	7.74	*1.68*	119.6	*26.5*	105	*26*	59.6	*22.3*	1809	*127*	58.2	*1.65*	32.5	*9.04*
V	321	*65.1*	129	*153*	336	*398*	234	*49*	65.8	*10.0*	275	*7.93*	404	*29.01*
Cr	69	*bdl*	bdl	*bdl*	7.47	*bdl*	8.1	*14.9*	54.4	*8.28*	bdl	*bdl*	bdl	*bdl*
Mn	58.4	*5.29*	14060	*12183*	15421	*14935*	519	*302*	477	*554*	106	*10.5*	161.7	*22.7*
Co	n/a	*n/a*	45.9	*40.6*	20.2	*20.0*	0.26	*0.13*	5.04	*3.83*	0.06	*bdl*	bdl	*bdl*
Ni	0.37	*0.03*	0.93	*0.35*	0.74	*0.79*	0.39	*0.53*	18.4	*5.65*	0.22	*0.00*	bdl	*bdl*
Cu	0.81	*0.87*	0.38	*bdl*	1.31	*0.78*	0.68	*1.16*	48.3	*19.6*	bdl	*bdl*	bdl	*bdl*
Zn	0.29	*0.09*	212	*186*	121	*115*	4.27	*4.98*	42.2	*33.4*	0.38	*0.06*	bdl	*bdl*
Ga	0.70	*0.16*	1.02	*1.02*	1.68	*1.59*	11.0	*13.1*	25.9	*2.10*	2.34	*0.05*	0.55	*0.13*
Ge	15.84	*2.33*	24.8	*26.1*	41.1	*46.4*	28.5	*6.36*	6.13	*1.44*	21.3	*1.08*	8.88	*0.55*
Rb	0.07	*0.01*	1.04	*1.02*	0.15	*0.08*	0.33	*0.25*	224	*21.4*	0.07	*0.05*	bdl	*bdl*
Sr	3792	*1252*	1437	*1576*	3656	*4082*	3056	*285*	1005	*228*	2803	*28.7*	4688	*293*
Y	666	*90.4*	379	*252*	1073	*779*	647	*112*	78.4	*21.0*	705	*7.94*	1281	*114*
Zr	69.6	*45.1*	33.7	*31.1*	70.8	*68.4*	95.5	*43.0*	455	*32.7*	90.6	*42.2*	164	*57.7*
Nb	2.28	*1.78*	1.31	*0.88*	2.18	*1.76*	5.26	*3.62*	55.9	*3.62*	1.99	*2.07*	5.55	*4.71*
Cs	0.02	*bdl*	n/a	*n/a*	n/a	*n/a*	n/a	*n/a*	2.51	*0.89*	bdl	*bdl*	n/a	*n/a*
Ba	3.78	*1.27*	3.48	*2.23*	4.83	*3.63*	196	*254*	657	*48.8*	5.73	*0.72*	28.0	*33.5*
La	3420	*1340*	968	*1126*	3610	*4294*	1965	*441*	242	*70.6*	2154	*57.2*	6372	*458*
Ce	7889	*2953*	2445	*2871*	8854	*10072*	4957	*1147*	771	*262*	4611	*174*	15212	*1140*
Pr	700	*124*	285	*331*	928	*1107*	564	*132*	81.2	*28.2*	588	*22.5*	1432	*104*
Nd	2605	*595*	1049	*1206*	3326	*3959*	2049	*445*	254	*69.1*	2519	*3.95*	4560	*294*
Sm	220	*61.4*	182	*199*	207	*215*	328	*71.6*	40.1	*10.9*	439	*13.77*	694	*46.2*
Eu	62.6	*20.3*	52.6	*55.1*	56.7	*56.5*	98.8	*23.9*	12.8	*2.64*	121	*1.60*	201	*14.4*
Gd	167	*45.4*	146	*148*	127	*122*	254	*53.9*	30.3	*10.8*	342	*5.57*	375	*22.2*
Tb	19.6	*6.58*	17.8	*15.7*	19.2	*16.0*	29.8	*6.33*	3.61	*0.83*	39.6	*0.31*	67.7	*4.09*
Dy	93.0	*27.9*	95.3	*73.0*	100	*70.77*	151	*30.1*	18.55	*5.16*	199	*2.64*	298	*20.2*
Ho	14.7	*5.40*	15.3	*10.1*	16.7	*9.69*	24.4	*4.55*	3.10	*0.90*	30.3	*0.15*	48.4	*3.77*
Er	30.0	*9.7*	35.6	*18.2*	39.1	*17.2*	50.6	*8.82*	6.48	*1.74*	62.7	*0.55*	99.2	*9.41*
Tm	3.13	*0.98*	4.32	*1.57*	4.39	*1.31*	5.45	*0.92*	0.87	*0.22*	6.84	*0.25*	11.3	*1.48*
Yb	15.6	*4.51*	24.9	*5.58*	24.8	*5.44*	29.0	*4.96*	4.63	*1.38*	34.5	*0.95*	52.1	*6.80*
Lu	1.74	*0.54*	3.30	*0.28*	3.52	*0.92*	3.45	*0.53*	0.75	*0.16*	3.92	*0.09*	7.34	*1.08*
Hf	0.40	*0.30*	0.16	*0.10*	0.39	*0.18*	0.34	*0.25*	12.01	*2.38*	0.39	*0.17*	0.74	*0.25*
Ta	0.06	*0.06*	0.03	*0.02*	0.06	*0.04*	0.06	*0.02*	2.35	*0.74*	0.05	*0.04*	0.27	*0.10*
Pb	2.67	*0.84*	2.30	*2.52*	2.60	*2.43*	3.74	*0.89*	21.0	*2.85*	2.84	*0.26*	5.77	*0.74*
Th	61.2	*20.5*	54.6	*67.3*	93.7	*93.7*	86.6	*19.6*	79.5	*141*	103	*10.5*	186	*26.1*
U	24.5	*10.7*	19.0	*22.5*	28.7	*28.0*	31.9	*8.15*	11.6	*2.10*	32.8	*0.35*	67.2	*6.21*

Table 3.13 Average trace element contents of apatite in the Vuoriyarvi carbonatites.

Laser-ICPMS CHONDRITE NORMALISED APATITE	B218 aver n=4	st dev n=4	KR3 aver n=3	st dev n=3	BR18 aver n=7	st dev n=7	B218A aver n=5	st dev n=5	BR18_1 aver n=11	st dev n=11	BR18A aver n=3	st dev n=3	BR18A aver n=10	st dev n=10
La	9320	3652	2637	3069	9837	11700	5354	1201	660	192	5870	156	17361	1248
Ce	8243	3086	2555	3000	9252	10525	5180	1198	806	274	4818	182	15896	1191
Pr	5111	904	2083	2418	6777	8082	4115	965	593	206	4290	164	10450	762
Nd	3664	837	1476	1696	4678	5569	2882	626	357	97.2	3543	5.56	6413	414
Sm	952	266	789	860	897	929	1420	310	174	47.1	1899	59.6	3006	200
Eu	720	233	605	633	652	650	1136	275	147	30.3	1389	18.4	2315	165
Gd	547	148	477	483	414	400	829	176	99.1	35.2	1119	18.2	1226	72.5
Tb	338	113	307	270	330	276	515	109	62.2	14.2	683	5.36	1166	70.5
Dy	244	73.2	250	192	262	186	397	78.9	48.7	13.5	521	6.92	783	53.0
Ho	173	63.4	180	118	196	114	286	53.4	36.4	10.5	356	1.73	569	44.3
Er	121	39.1	143	73.1	157	69.3	203	35.4	26.0	7.00	252	2.23	398	37.8
Tm	88.1	27.5	121	44.0	123	36.9	153	26.0	24.4	6.08	192	6.86	316.3	41.72
Yb	63.0	18.2	100	22.5	100	21.9	117	20.0	18.6	5.55	139	3.83	210.1	27.42
Lu	45.7	14.2	86.6	7.34	92.4	24.2	90.6	13.9	19.7	4.27	103	2.54	192.7	28.46
	B218 aver n=4	st dev n=4	KR3 aver n=3	st dev n=3	BR18 aver n=7	st dev n=7	B218A aver n=5	st dev n=5	BR18_1 aver n=11	st dev n=11	BR18A aver n=3	st dev n=3	BR18A aver n=10	st dev n=10
Rb	0.02	0.00	0.30	0.29	0.03	0.03	0.09	0.07	64.9	6.20	0.02	0.01	0.00	0.00
Ba	7.5	0.37	1.02	0.66	1.01	1.11	57.5	74.4	193	14.3	1.68	0.21	8.20	9.81
Th	1440	483	1284	1585	1890	2178	2037	462	1871	3312	2428	247	4378	614
U	2011	878	1554	1842	2014	2275	2615	668	954	172	2685	28.6	5504	509
Nb	6.09	4.75	3.49	2.35	5.81	4.69	14.0	9.64	149	9.66	5.32	5.53	14.8	12.6
Ta	1.73	2.11	1.32	0.86	0.66	1.32	2.24	0.74	90.3	28.5	1.27	1.49	2.09	4.58
La	9320	3652	2637	3069	9837	11700	5354	1201	660	192	5870	156	17361	1248
Ce	8243	3086	2555	3000	9252	10525	5180	1198	806	274	4818	182	15896	1191
Pb	0.73	0.23	0.63	0.69	0.61	0.66	1.02	0.24	5.74	0.78	0.78	0.07	1.58	0.20
Sr	319	105	121	132	307	343	257	23.9	84.5	19.1	236	2.42	394	24.6
Nd	3664	837	1476	1696	4678	5569	2882	626	357	97.2	3543	5.56	6413	414
Zr	12.6	8.15	6.09	5.62	12.8	12.3	17.2	7.77	82.1	5.91	16.3	7.61	29.7	10.4
Hf	1.68	1.76	0.60	0.65	1.54	1.34	1.93	1.39	67.1	13.31	2.18	0.96	3.31	2.15
Sm	952	266	789	860	897	929	1420	310	174	47.1	1899	59.6	3006	200
Ti	0.01	0.00	0.18	0.04	0.16	0.04	0.09	0.03	2.77	0.19	0.09	0.00	0.05	0.01
Y	296	40.2	168	112	477	346	287	49.9	34.8	9.32	313	3.53	569	50.8
V	3.78	0.76	1.52	1.80	3.96	4.68	2.75	0.57	0.77	0.12	3.24	0.09	4.76	0.34
Sc	0.02	0.01	0.29	0.23	0.28	0.24	0.08	0.05	1.22	0.16	0.11	0.01	0.00	0.00

Table 3.14 Chondrite-normalised trace element contents of apatite in the Vuoriyarvi carbonatites

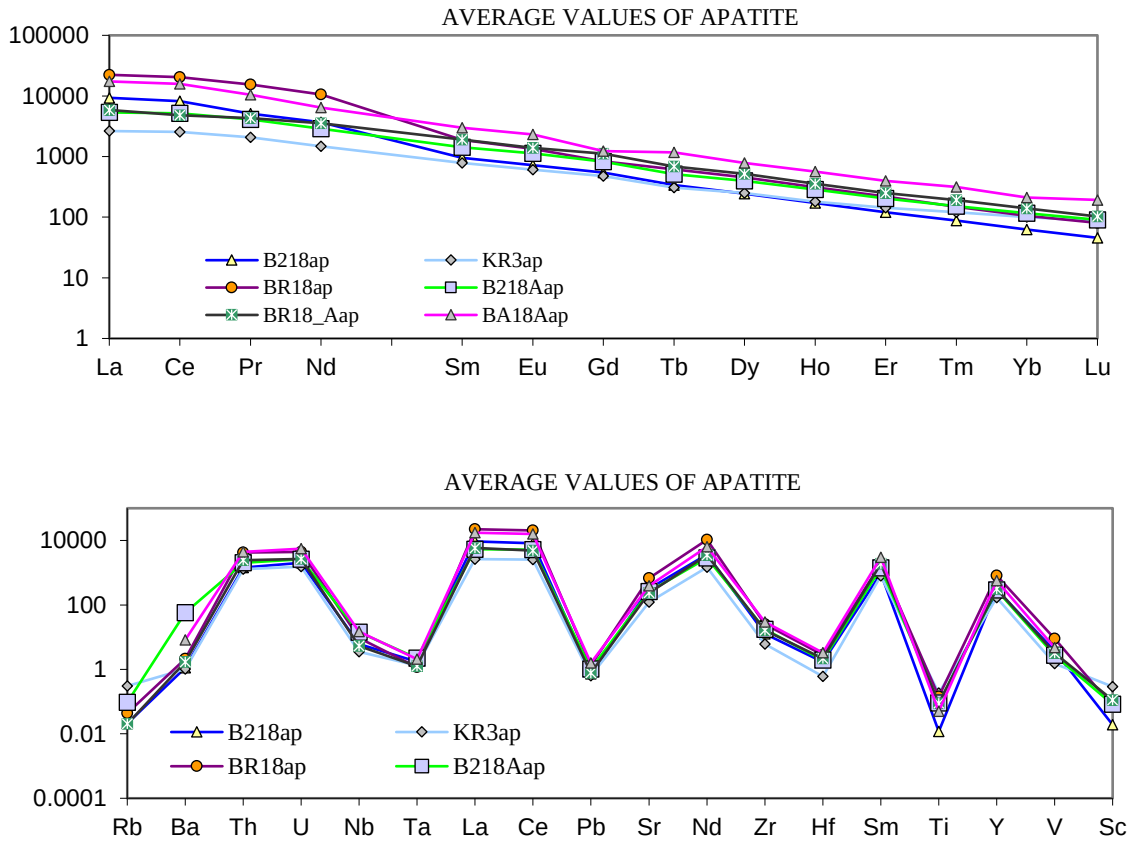

Fig.3.30 Chondrite-normalised average REE and trace element distribution patterns of apatite in the Vuoriyarvi carbonatites.

Chakmouradian et al. (2017) distinguished igneous apatite in carbonatites by using criteria such as being Cl-poor fluorapatite, which is in agreement with the analysed samples. Also, they should contain ≤1000 ppm Mn, whereas data in this study varies from 60 to 500 ppm though two samples (KR3 and BR18) show much higher contents, e.g., 14000-15000 ppm. Sr contents of apatite from Chakmouradian et al. (2017) are >2000 ppm, approximately in agreement with the samples in this study which contain 1000-4000 ppm. Apatite should also contain 200 ppm Ba on average and the analysed samples in this study either show low Ba contents (3-30 ppm) or high contents (200-700 ppm). The average value of Pb is 150 ppm (Chakmouradian et al., 2017) whereas Vuoriyarvi apatites are much lower 2-21 ppm (and some values are below detection limit). The analysed samples have 55-200 ppm Th, which is much lower than the 700 ppm Th of Chakmouradian et al. (2017), and U contents are also much lower (10-70 ppm compared with 150 ppm), as are V contents (40-400 ppm compared with 660 ppm V).

3.6.3 Phlogopite

The trace element compositions of phlogopite are presented in Table 3.14. The Vuoriyarvi phlogopites have low content of REEs, showing inclined REE patterns (the degree of enrichment of LREE to HREE defined by the chondrite-normalised La/Yb ranging 1.2-49.3) with distinct positive Eu anomaly (Eu/Eu*values ranging 1.17-10.14) (Figure 3.31). The phlogopites show high amounts of trace elements such as Ba (4314-20294 ppm), Rb (193-308 ppm), moderate amounts of Sr (92-158 ppm), Zr (45-86 ppm) and Nb (42-67 ppm). Nb together with Ta show high peaks (Figure 3.31). Elevated Ba in phlogopite confirms increased kinoshitalite component. U and Th show negative troughs with Pb having the deepest. This analysis shows that the Vuoriyarvi phlogopites can hold high content of some trace elements and significant concentration of the LREEs.

Figure 3.32 discriminates trace elements between core and rim of phlogopite and assesses possible differences between xenocryst and phenocryst phlogopite from the Vuoriyarvi carbonatite. Overall, the phlogopite rims show varied enrichment in REEs (chondrite-normalised La/Yb ranges 1-25) with phlogopite cores having higher variation (chondrite-normalised La/Yb ranges 1-61). The distribution of the REE in the core (either xenocryst or phenocryst) largely flank the rim values, perhaps reflecting relatively changeable conditions in the early stages of carbonatite formation affecting the initially formed (or entrained) phlogopite (crystallising cores), thus influencing varied trace element distributions. As conditions in the carbonatite magma was stabilising, the values of the rims attained more uniform values (Figure 3.32).

Reguir et al. (2009) investigated trace element compositions of mica as a petrogenetic indicator for carbonatites. Mica from carbonatite can be identified by trace element contents: ≤315 ppm Cr (Vuoriyarvi sample B218 contain 2.76 ppm or is bdl); ≤470 ppm Ni (0-259 ppm in analysed phlogopite); ≤34 ppm Co (analysed phlogopite varies from bdl to 30 ppm); up to 17200 ppm Mn (1138-1794 ppm in Vuoriyarvi); 1080 ppm Nb (analysed samples are 42-75 ppm), 830 ppm Sr (Vuoriyarvi samples are 92-246 ppm), 80 ppm Sc (Vuoriyarvi carbonatite micas contain 5-15 ppm), 105 ppm Zr (Vuoriyarvi values are 45-86 ppm), 27 ppm Cs (also lower 4.8-5.4 ppm) and 19 ppm Ta (also lower 1.9-2.8 ppm). Differences in some trace elements content in phlogopite in the Vuoriyarvi carbonatite compared to the data of Reguir et al. (2009) is most likely due to some phlogopite being xenocrystic and/or phenocrystic but also would depend on crystallisations of different phases during which depletion of some elements can occur prior to futher crystallisation of mica.

	KR3 xen aver n=4	st dev n=4	B218 xen aver n=2	st dev n=2	B218 xen aver n=2	st dev n=2	B218A xen1 aver n=4	st dev n=4	B218A phen1 aver n=5	st dev n=5
Sc	7.94	1.76	14.6	0.08	12.7	5.32	11.16	1.32	11.41	1.87
Ti	2998	0.00	4221	0.00	4221	0.00	4227	0.00	4736	0.00
V	39.0	3.26	55.9	3.50	53.3	11.4	54.1	5.91	63.2	3.56
Cr	bdl	bdl	bdl	bdl	2.76	bdl	bdl	bdl	bdl	bdl
Mn	1138	189	3714	219	3166	859	1523	227	1794	246
Co	17.2	1.85	bdl	bdl	bdl	bdl	23.9	3.37	29.6	4.33
Ni	0.35	0.07	259	13.2	251	49.2	0.25	0.05	0.39	0.12
Cu	0.82	0.85	bdl	bdl	bdl	bdl	0.37	0.14	0.90	1.07
Ga	293	26.9	434.5	63.6	366	11.8	621	63.0	718	185
Ge	2.40	0.59	3.9	0.96	3.23	0.33	3.39	0.22	4.21	0.27
Rb	193	10.7	302	23.3	308	42.9	287	35.0	391	59.7
Sr	92.1	37.5	148	15.6	148	5.49	158	30.0	246	188
Y	4.15	6.75	0.2	0.17	3.19	bdl	0.44	0.30	1.28	1.39
Zr	45.2	8.97	65.3	18.9	86.4	1.48	81.3	10.7	73.9	13.1
Nb	41.7	5.48	56.2	11.6	67.3	4.25	65.1	7.35	74.5	11.2
Cs	n/a	n/a	4.8	0.55	5.36	0.17	n/a	n/a	bdl	bdl
Ba	4314	430	20294	3942	18444	16440	7805	864	9441	2881
La	14.7	24.9	0.40	0.06	12.1	bdl	0.12	0.04	1.53	2.48
Ce	43.6	75.1	1.29	0.95	32.0	bdl	0.29	0.14	3.53	5.31
Pr	4.11	6.81	0.12	0.04	1.89	2.55	0.03	0.01	0.31	0.45
Nd	15.4	26.5	bdl	bdl	12.5	bdl	0.13	0.05	1.02	1.46
Sm	2.49	4.29	bdl	bdl	1.47	bdl	0.05	0.01	0.26	0.26
Eu	0.87	1.25	bdl	bdl	0.58	0.03	0.23	0.02	0.35	0.11
Gd	2.10	3.15	bdl	bdl	1.28	1.05	0.10	0.05	0.31	0.21
Tb	0.19	0.33	bdl	bdl	0.19	bdl	0.01	0.01	0.05	0.04
Dy	1.06	1.84	bdl	bdl	0.73	bdl	0.10	0.02	0.23	0.23
Ho	0.17	0.30	bdl	bdl	0.15	bdl	0.02	0.01	0.05	0.05
Er	0.33	0.57	0.06	bdl	0.26	bdl	0.06	0.04	0.11	0.12
Tm	0.05	0.07	0.01	bdl	bdl	bdl	0.01	0.00	0.02	0.02
Yb	0.21	0.35	0.03	bdl	0.34	bdl	0.07	0.03	0.14	0.12
Lu	0.03	0.04	0.02	bdl	0.06	bdl	0.02	bdl	0.02	0.02
Hf	0.70	0.18	0.70	0.51	1.10	0.14	0.84	0.13	0.99	0.20
Ta	1.88	0.33	2.75	0.33	2.85	0.45	2.36	0.10	2.69	0.43
Pb	0.32	0.08	0.46	0.08	0.71	0.17	0.59	0.14	1.14	0.93
Th	0.53	0.88	0.03	bdl	0.70	bdl	0.52	0.75	2.33	3.60
U	0.31	0.50	bdl	bdl	0.34	bdl	0.01	0.01	0.11	0.12

Table 3.15 Trace element contents (ppm) of phlogopite (xenocryst and phenocryst) in the Vuoriyarvi carbonatites.

	KR3 xen aver n=4	st dev n=4	B218 xen aver n=2	st dev n=2	B218 xen aver n=2	st dev n=2	B218A xen1 aver n=4	st dev n=4	B218A phen1 aver n=5	st dev n=5
La	61.8	105	1.68	0.27	51.2	bdl	0.49	0.15	6.47	10.45
Ce	71.2	123	2.11	1.55	52.3	bdl	0.47	0.24	5.76	8.68
Pr	43.2	71.7	1.23	0.38	19.9	26.9	0.35	0.13	3.27	4.78
Nd	32.9	56.7	bdl	bdl	26.7	bdl	0.27	0.11	2.18	3.12
Sm	16.3	28.1	bdl	bdl	9.59	bdl	0.31	0.08	1.72	1.70
Eu	15.1	21.5	bdl	bdl	9.95	0.56	3.93	0.31	6.09	1.95
Gd	10.2	15.3	bdl	bdl	6.21	5.13	0.49	0.22	1.49	1.00
Tb	5.10	8.79	bdl	bdl	5.20	bdl	0.40	0.14	1.37	1.10
Dy	4.18	7.25	bdl	bdl	2.89	bdl	0.40	0.10	0.92	0.89
Ho	2.99	5.21	bdl	bdl	2.64	bdl	0.34	0.20	0.89	0.89
Er	2.00	3.43	0.33	bdl	1.55	bdl	0.37	0.24	0.64	0.70
Tm	2.02	2.85	0.50	bdl	bdl	bdl	0.34	0.20	0.76	0.61
Yb	1.25	2.04	0.17	bdl	2.02	bdl	0.41	0.20	0.80	0.70
Lu	1.14	1.65	0.89	bdl	2.36	bdl	0.62	bdl	0.92	0.77
	aver n=4	st dev n=4	aver n=2	st dev n=2	aver n=2	st dev n=2	aver n=4	st dev n=4	aver n=5	st dev n=5
Rb	83.2	4.63	130	10.1	133	18.5	124	15.1	169	25.7
Ba	1790	179	8421	1636	7653	6822	3239	359	3918	1196
Th	18.4	30.3	1.18	bdl	24.3	bdl	17.9	25.9	80.2	124
U	39.1	62.6	bdl	bdl	43.0	bdl	1.62	1.12	13.5	14.8
Nb	170	22.3	228	47.3	274	17.3	265	29.9	303	45.5
Ta	134	23.8	196	23.3	204	32.3	168	7.07	192	30.7
La	61.8	105	1.68	0.27	51.2	bdl	0.49	0.15	6.47	10.5
Ce	71.2	123	2.11	1.55	52.3	bdl	0.47	0.24	5.76	8.68
Pb	0.13	0.03	0.19	0.03	0.3	0.07	0.24	0.06	0.46	0.37
Sr	12.7	5.17	20.4	2.14	20.3	0.76	21.8	4.13	33.9	25.9
Nd	32.9	56.7	bdl	bdl	26.7	bdl	0.27	0.11	2.18	3.12
Zr	11.7	2.32	16.9	4.89	22.3	0.38	21.0	2.75	19.1	3.37
Hf	6.52	1.68	6.59	4.76	10.3	1.33	7.84	1.26	9.25	1.89
Sm	16.27	28.1	bdl	bdl	9.6	bdl	0.31	0.08	1.72	1.70
Ti	4.58	0.00	6.45	0.00	6.45	0.00	6.46	0.00	7.24	0.00
Y	2.64	4.30	0.14	0.11	2.03	bdl	0.28	0.19	0.81	0.89
V	0.70	0.06	1.00	0.06	0.95	0.20	0.97	0.11	1.13	0.06
Sc	1.34	0.30	2.47	0.01	2.15	0.90	1.88	0.22	1.93	0.32

Table 3.16 Chondrite-normalised trace element contents of phlogopite (xenocryst and phenocryst) in the Vuoriyarvi carbonatites.

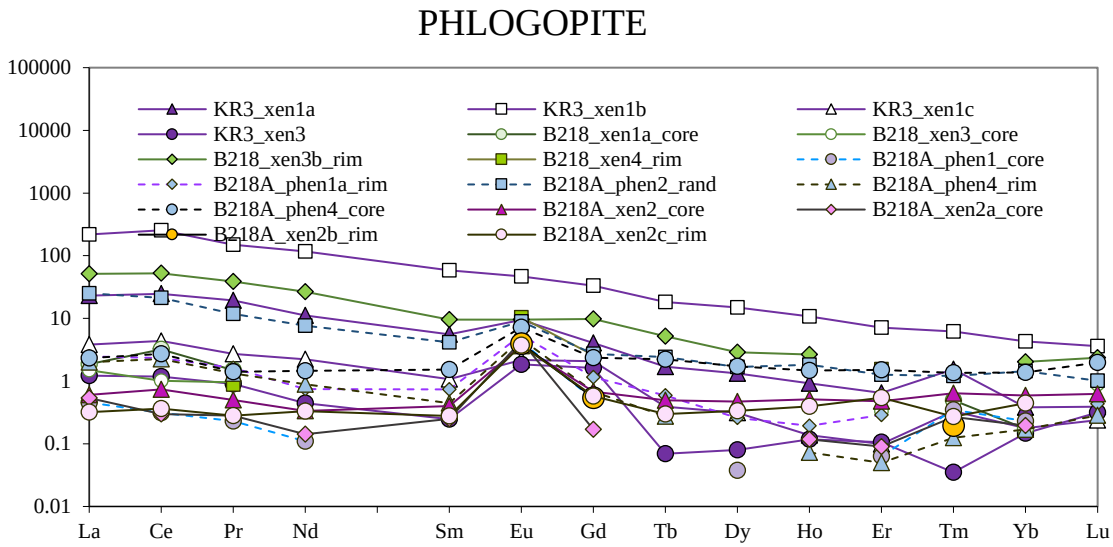

Fig.3.31a Chondrite-normalised REE patterns of phlogopite in the Vuoriyarvi carbonatites.

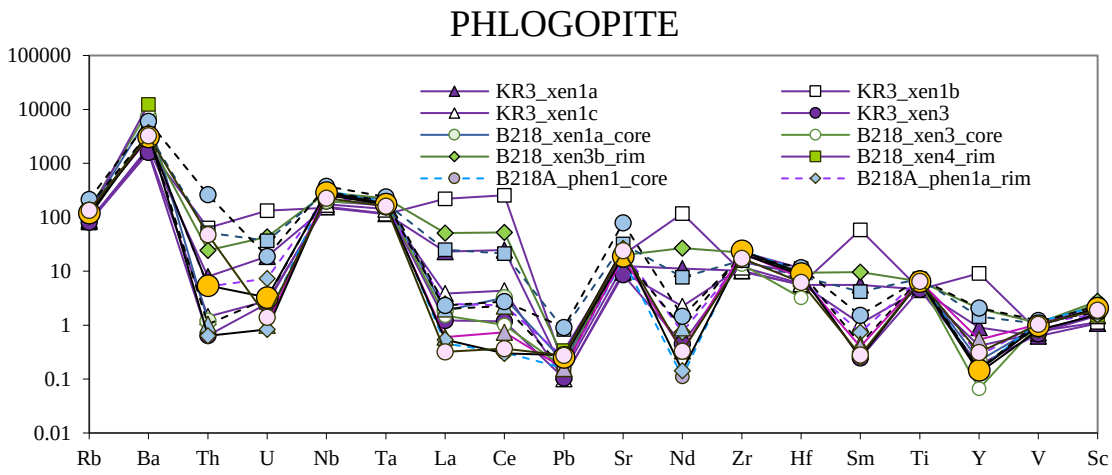

Fig.3.31b Chondrite-normalised trace element patterns of phlogopite in the Vuoriyarvi carbonatites.

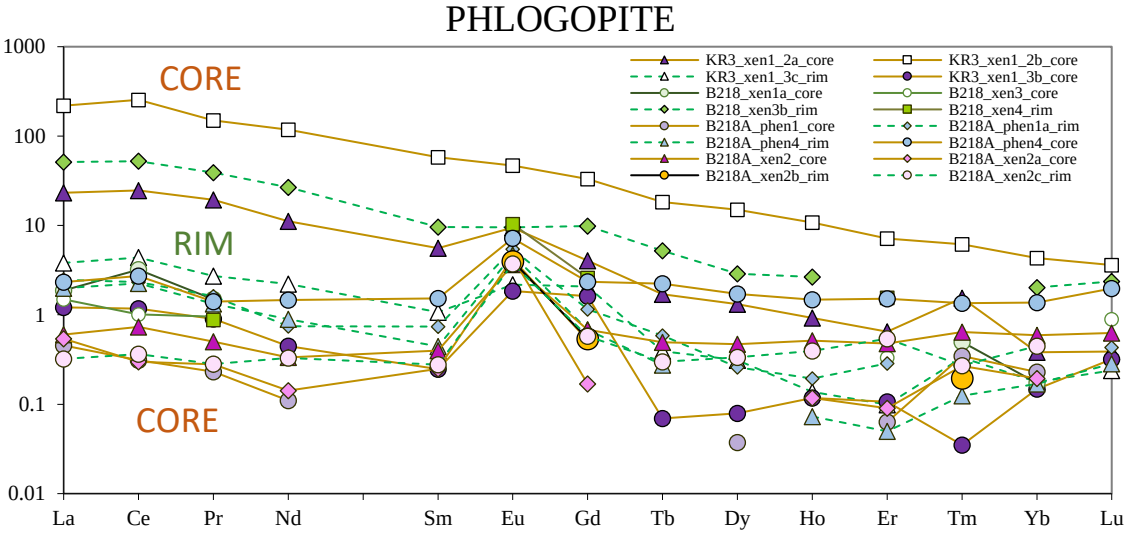

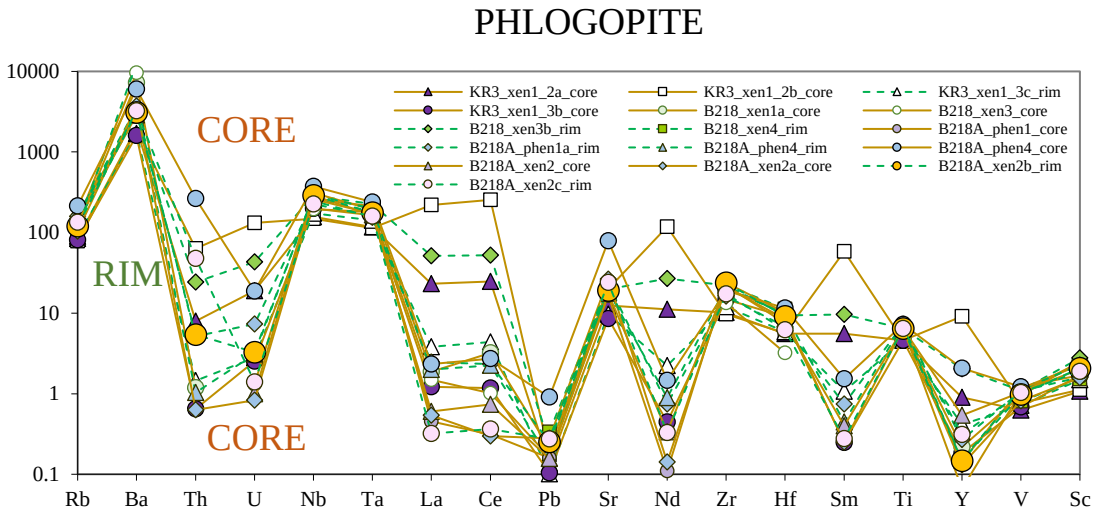

Fig.3.32 Chondrite-normalised REE and trace element patterns of phlogopite in the Vuoriyarvi carbonatites distinguishing phenocryst phlogopite (green) and xenocryst phlogopite (brown). The core is shown as a solid line and the rim as a dotted line. Finely dotted line represents composition of random phenocryst phlogopite.

3.6.4 Zr-rich garnet and perovskite

Trace element compositions of Zr-rich garnet and perovskite are presented in Tables 3.17 and 3.18, respectively. Their trace elements and REE concentrations are presented in Figure 3.33. The Zr-rich garnets are rich in REEs. The chondrite-normalised diagram displays a convex upward pattern showing a preference for the MREEs. It exhibits very high HFSE enrichment in Zr, Ti, Nb, Hf and Ta, Th and U, whereas Pb forms a deep trough. The contents of LILE such as Sr and Ba are much lower and the concentrations of Rb or Cs are negligible. Mn concentration is substantial, showing enrichment of 2000 ppm. This high concentration of the variable trace elements reflects the distribution coefficient for this unusual mineral phase which can accommodate REE, HFSE and some LILE.

Stifeeva et al. (2019) studied schorlomite–morimotoite–andradite garnets from the Vuoriyarvi and other Kola Alkaline Province massifs. REEs from pegmatoid pyroxenite show much lower enrichment compared to Vuoriyarvi carbonatites, although the trend is similar. Stifeeva et al. (2019) stated that Vuoriyarvi garnet shows high enrichment in MREE and much lower in HREE with $(La/Sm)_{CN}$ = 0.12-0.17. Vuoriyarvi Zr-garnet analysed in this study has a similar ratio $(La/Sm)_{CN}$ =0.19–0.30. Garnet from pegmatoid pyroxenite shows $(Gd/Yb)_{CN}$=1.22–1.92, one order higher, $(Gd/Yb)_{CN}$ ratio for analysed Zr-garnet shows values 2.26-2.52. Garnet from the pegmatoid pyroxenite shows enrichment of U in garnet from 4.82 to 8.02 ppm. The analysed xenocrystic Zr-garnet from the Vuoriyarvi carbonatite has a much higher U content (75-102 ppm).

Laser-ICPMS analyses ppm Zr-garnet	BA18A aver n=6	st dev n=6	B218A aver n=6	st dev n=6	B218 aver n=8	st dev n=8	BR18_A aver n=6	st dev n=6
Sc	526	*51.9*	528	*41.9*	465	*56.6*	545	*68*
Ti	53377	*5086*	54586	*3155*	55562	*3789*	48056	*6716*
V	308	*27.5*	312	*19.1*	315	*27.4*	264	*24.7*
Cr	2.23	*0.79*	bdl	*bdl*	bdl	*bdl*	0.57	*bdl*
Mn	2416	*109*	2434	*135*	2199	*130*	1988	*144*
Co	6.44	*0.35*	6.57	*0.37*	5.31	*0.52*	5.29	*0.53*
Ni	0.26	*bdl*	bdl	*bdl*	bdl	*bdl*	0.12	*0.02*
Cu	0.79	*0.82*	0.54	*0.13*	0.57	*0.06*	0.51	*0.17*
Zn	144	*48.4*	163	*13.5*	162	*20.8*	113	*12.4*
Ga	47.8	*3.89*	47.0	*3.93*	44.1	*4.97*	40.3	*4.21*
Ge	32.1	*5.79*	26.7	*2.20*	23.6	*3.05*	27.0	*1.62*
As	10.7	*6.20*	6.24	*0.59*	5.17	*0.55*	n/a	*n/a*
Rb	0.24	*0.09*	0.25	*0.16*	0.16	*0.01*	0.29	*0.10*
Sr	72.1	*24.5*	160	*92.2*	132	*186*	203	*143*
Y	1645	*305*	1985	*112*	1815	*101*	1844	*243*
Zr	81257	*15816*	90645	*7368*	80076	*10207*	78381	*10607*
Nb	2144	*402*	2880	*408*	2225	*589*	1950	*562*
Cs	0.01	*0.00*	0.02	*bdl*	0.01	*0.00*	0.02	*bdl*
Ba	27.2	*17.7*	48.7	*88.4*	2.57	*6.26*	22.0	*19.1*
La	126	*27.3*	234	*74.4*	148	*16.2*	205	*116*
Ce	683	*154*	926	*105*	820	*62.9*	785	*234*
Pr	172	*39.6*	218	*15.6*	200	*13.1*	183	*20.8*
Nd	1095	*234*	1340	*60.1*	1256	*86.6*	1176	*67.5*
Sm	421	*85.9*	490	*19.9*	479	*27.7*	456	*25.3*
Eu	158	*31.1*	182	*8.45*	180	*12.4*	166	*8.80*
Gd	499	*77.3*	581	*20.3*	563	*41.0*	539	*30.0*
Tb	81.6	*17.1*	97.9	*5.03*	92.5	*6.46*	89.1	*6.99*
Dy	503	*106*	608	*34.1*	570	*34.6*	573	*52.8*
Ho	89.7	*18.9*	109	*7.09*	101	*5.48*	102	*11.6*
Er	212	*43.1*	262	*23.4*	238	*15.0*	248	*32.1*
Tm	27.4	*5.78*	33.5	*2.94*	30.7	*1.65*	32	*5.15*
Yb	162	*30.6*	203	*25.9*	181	*10.7*	194	*39.6*
Lu	16.7	*3.83*	21.9	*2.94*	18.6	*0.94*	20.7	*4.96*
Hf	1038	*263*	1242	*132*	1075	*94.2*	1018	*120*
Ta	296	*73.2*	424	*35.6*	343	*50.3*	300	*36.6*
Pb	1.30	*0.62*	1.32	*0.14*	1.76	*0.39*	1.02	*0.28*
Th	36.0	*19.3*	40.9	*2.61*	52.2	*13.2*	39.3	*12.4*
U	86.0	*21.0*	102	*10.1*	96.0	*16.0*	75.2	*7.71*
CHONDRITE NORMALISED Zr-garnet	aver n=6	st dev n=6	aver n=6	st dev n=6	aver n=8	st dev n=8	aver n=6	st dev n=6
La	344	*74*	638	*203*	404	*44.0*	559	*317*
Ce	713	*161*	967	*110*	856	*65.8*	820	*245*
Pr	1256	*289*	1589	*114*	1460	*95.5*	1336	*152*
Nd	1540	*330*	1885	*84.5*	1766	*122*	1653	*95.0*
Sm	1822	*372*	2120	*86.2*	2074	*120*	1974	*109*
Eu	1816	*358*	2093	*97.2*	2070	*143*	1910	*101*
Gd	1630	*253*	1898	*66.2*	1839	*134*	1760	*98*
Tb	1407	*295*	1687	*86.8*	1595	*111*	1537	*121*
Dy	1320	*278*	1597	*89.6*	1497	*90.8*	1505	*139*
Ho	1054	*222*	1281	*83.4*	1189	*64.5*	1204	*137*
Er	853	*173*	1054	*93.8*	956	*60.3*	996	*129*
Tm	770	*162*	940	*82.6*	862	*46.5*	909	*145*
Yb	655	*123*	819	*104*	729	*43.2*	780	*160*
Lu	439	*101*	574	*77.1*	487	*24.7*	542	*130*
	aver n=6	st dev n=6	aver n=6	st dev n=6	aver n=8	st dev n=8	aver n=6	st dev n=6
Rb	0.07	*0.03*	0.07	*0.05*	0.05	*0.00*	0.08	*0.03*
Ba	5.31	*5.75*	14.3	*25.92*	0.66	*1.72*	6.46	*5.59*
Th	847	*454*	963	*61.5*	1228	*310*	924	*291*
U	7046	*1721*	8383	*827*	7865	*1315*	6166	*632*
Nb	5717	*1073*	7681	*1089*	5933	*1571*	5200	*1499*
Ta	11373	*2817*	16299	*1370*	13191	*1933*	11526	*1407*
La	344	*74.5*	638	*203*	404	*44.0*	559	*317*
Ce	713	*161*	967	*110*	856	*65.8*	820	*245*
Pb	0.35	*0.17*	0.36	*0.04*	0.48	*0.11*	0.28	*0.08*
Sr	6.06	*2.06*	13.4	*7.75*	11.1	*15.7*	17.02	*12.02*
Nd	1095	*234*	1340	*60.1*	1256	*86.6*	1176	*67.5*
Zr	81257	*15816*	90645	*7368*	80076	*10207*	78381	*10607*
Hf	5801	*1467*	6941	*737*	6003	*526*	5685	*669*
Sm	1822	*372*	2120	*86.2*	2074	*120*	1974	*109*
Ti	81.6	*7.77*	83.5	*4.82*	85.0	*5.79*	73.5	*10.3*
Y	731	*135*	882	*49.9*	807	*44.7*	820	*108*
V	3.63	*0.32*	3.67	*0.22*	3.71	*0.32*	3.10	*0.29*
Sc	60.9	*6.00*	61.1	*4.84*	53.8	*6.55*	63.1	*7.92*

Table 3.17 Average REE and trace element contents and chondrite-normalised abundances of Zr-rich garnet in the Vuoriyarvi carbonatites.

Laser-ICPMS analyses ppm PEROVSKITE	BR18_A aver n=3	st dev n=3	B218 aver n=2	st dev n=2	BR18_1 aver n=3	st dev n=3
Sc	3.44	0.38	1.32	0.37	3.82	0.89
Ti	281038	8301	286892	83927	203950	65039
V	217	3.22	216	5.96	161	33.5
Cr	bdl	bdl	bdl	bdl	12.5	6.60
Mn	301	221	n/a	n/a	909	738
Ni	0.18	0.07	81.3	21.0	3.58	1.54
Cu	2.21	0.27	2.30	bdl	11.8	4.91
Zn	4.78	0.12	6.62	2.88	14.1	4.18
Ga	6.90	1.03	1.77	0.33	12.9	2.29
Ge	64.1	2.27	40.8	10.1	29.7	7.43
Rb	0.09	0.06	bdl	bdl	54.3	28.0
Sr	1747	63.5	6690	436	1461	44.5
Y	346	40.6	376	6.88	339	73.0
Zr	2910	486	1598	612	1469	256
Nb	45782	7613	50163	10705	19152	6053
Cs	0.09	0.01	0.05	bdl	0.70	0.26
Ba	15.4	16.2	24.6	4.02	221	142
La	6390	320	15892	3427	5060	1355
Ce	17848	706	46693	11059	14304	4140
Pr	2172	84.2	5827	1389	1770	502
Nd	7856	301	20647	4971	6682	1709
Sm	1119	33.7	934	187	972	276
Eu	259	12.1	224	42.7	220	63.4
Gd	513	26.3	460	87.7	458	123
Tb	48.6	2.98	47.0	6.48	46.7	11.7
Dy	199	17.2	191	24.9	192	51.4
Ho	24.0	2.44	25.2	1.99	23.9	5.71
Er	40.5	4.69	44.2	3.66	41.2	10.2
Tm	3.47	0.51	4.05	0.09	3.82	0.92
Yb	14.3	2.64	16.0	0.08	15.7	3.25
Lu	1.18	0.30	1.53	0.08	1.42	0.31
Hf	50.1	2.58	37.3	9.70	33.5	4.41
Ta	3812	138	10406	2165	2762	911
Pb	23.6	1.69	43.9	12.8	26.2	3.06
Th	651	29.8	1030	200	553	100
U	154	5.59	193	55.0	155	46.7
CHONDRITE NORMALISED PEROVSKITE	aver n=3	st dev n=3	aver n=2	st dev n=2	aver n=3	st dev n=3
La	17410	871	43303	9339	13788	3693
Ce	18650	738	48792	11556	14947	4326
Pr	15855	615	42533	10139	12922	3664
Nd	11049	423	29039	6991	9399	2404
Sm	4843	146	4043	810	4206	1194
Eu	2973	139	2569	491	2534	729
Gd	1676	86.0	1503	287	1497	403
Tb	838	51.3	811	112	805	202
Dy	523	45.1	501	65.5	504	135
Ho	282	28.7	296	23.4	281	67.1
Er	163	18.8	177	14.7	165	40.9
Tm	97.5	14.2	114	2.62	107	26.0
Yb	57.5	10.6	64.7	0.31	63.5	13.1
Lu	31.0	7.96	40.2	2.17	37.4	8.0
	aver n=3	st dev n=3	aver n=2	st dev n=2	aver n=3	st dev n=3
Rb	0.02	0.02	0.00	0.00	15.7	8.11
Ba	4.53	4.75	7.21	1.18	64.9	41.5
Th	15323	702	24239	4699	13009	2361
U	12606	458	15786	4510	12676	3831
Nb	122085	20302	133768	28546	51072	16142
Ta	146610	5312	400213	83266	106218	35045
La	17410	871	43303	9339	13788	3693
Ce	18650	738	48792	11556	14947	4326
Pb	6.46	0.47	12.03	3.50	7.19	0.84
Sr	147	5.34	562	36.6	123	3.74
Nd	11049	423	29039	6991	9399	2404
Zr	525	87.6	288	110	265	46.2
Hf	280	14.4	208	54.2	187	24.6
Sm	4843	146	4043	810	4206	1194
Ti	430	12.7	439	128	312	99.4
Y	154	18.0	167	3.06	151	32.5
V	2.55	0.04	2.54	0.07	1.90	0.39
Sc	0.40	0.04	0.15	0.04	0.44	0.10

Table 3.18 Average REE and trace element contents of perovskite (chondrite-normalised and ppm) in the Vuoriyarvi carbonatites.

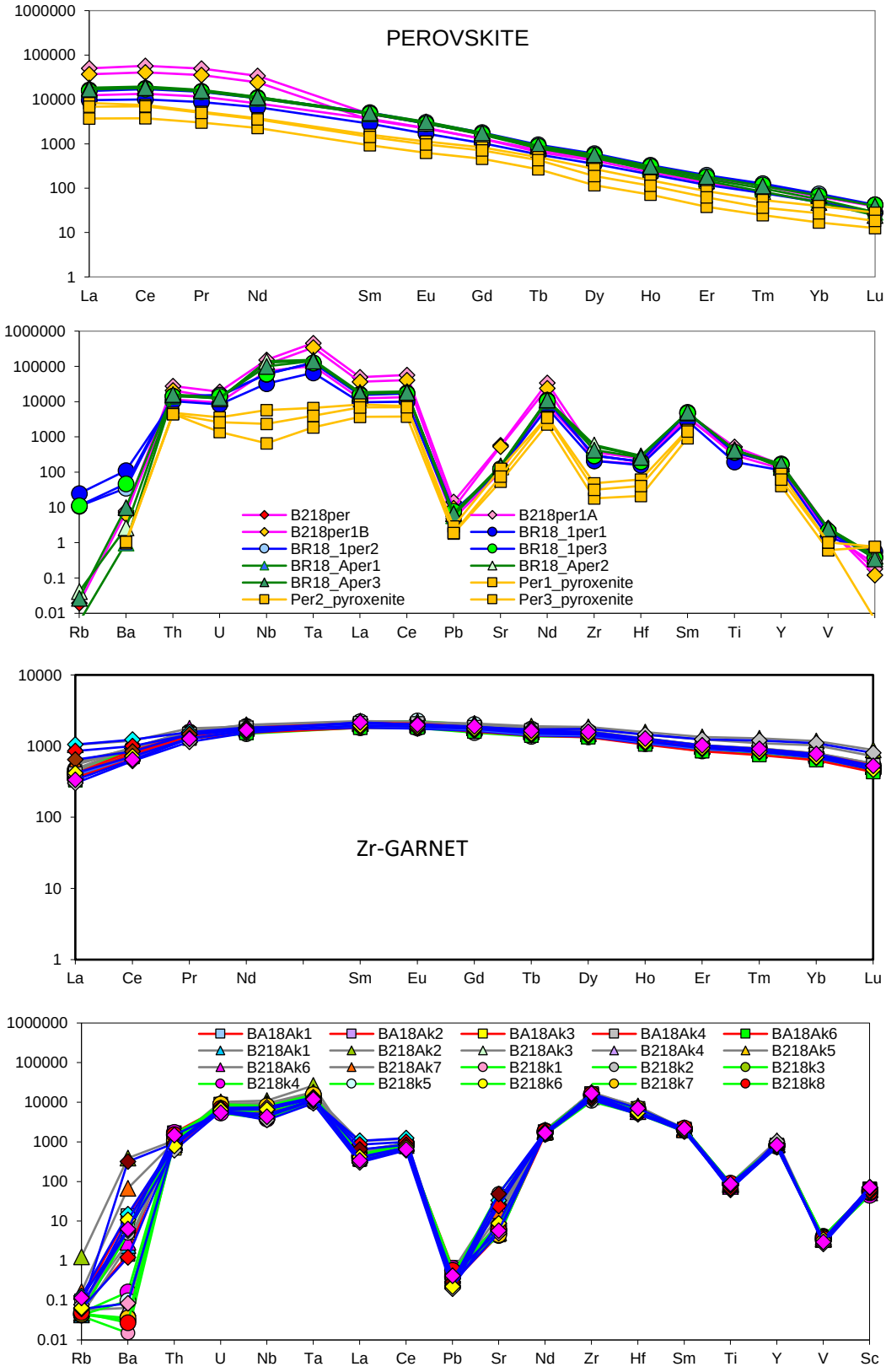

Fig.3.33 Chondrite-normalised average trace element and REE patterns of perovskite and Zr-rich garnet in Vuoriyarvi carbonatites.

Trace element compositions of perovskite are characterised by strong enrichment in LREE (Figure 3.33) with La/Yb_{CN} from 220 to 670. Perovskite shows high concentration

of HSFE such as Nb, Zr, Hf, Ta and Th (Figure 3.33). Th, Nd, Y and Sc also form peaks. U varies from 150 to 190 ppm. There is a relatively high Sr contents in perovskite as well as V, Y, Ba and Pb. U in perovskite forms a trough similar to that in the Zr-rich garnet. Pb again forms deep trough in perovskite. Average trace element concentrations of perovskite compared with Zr-rich garnet (Figures 3.33) shows great similarity in many respects but perovskite, being up to two orders elevated, forms a Zr-Hf negative anomaly while Zr-rich garnet shows a Zr-Hf peak.

Chakhmouradian et al. (2013) studied perovskite from kimberlites and other mantle-derived undersaturated alkaline silicate rocks. They determined that the LREE in perovskite shows high enrichment (La≥Nd>Pr>Sm) with La/Yb_{CN} being 245–3673 in the kimberlites and 1216 (±88) in the katungite. Analysed La/Yb_{CN} from Vuoriyarvi perovskite in this study falls in the lower part of kimberlite data (in BR18_1 is 369, in B218 is 1077, and in BR18_A is 562). Chakhmouradian et al. (2013) also studied Mn, Sr and V contents in perovskite (110–350, 1150–2020 and 80–160 ppm respectively) and concluded that they are not very significant. In contrast, Mn and V concentrations in Vuoriyarvi perovskite are higher (301-909 ppm Mn and 161-216 ppm V, and Sr content is also higher (1461-6690 ppm). It yields ratios such as Th/U=3.6-5.3, Nb/Ta=4.8-12, Y/Ho=14.2-14.9 and Zr/Hf=42.8-58.1, whereas Chakhmouradian et al. (2013) recorded these values as: Th/U=bdl-213, Nb/Ta=3.2-19.8, Y/Ho=16.4-16.9 and Zr/Hf=18.7-20.2. Thus these ratios infer that some trace elements ratios in perovskite from the Vuoriyarvi carbonatites are similar to those in alkaline silicate rocks, although the overall concentrations tend to be higher.

As perovskite in analysed samples is xenocrystic and was emplaced from the associated pyroxenite, it can be compared to perovskite in pyroxenite analysed by Arzamarstev et al. (2002) and shows the same trend of REE though slightly less enriched. HFSE such as Nb-Ta and Zr-Hf in perovskite from pyroxenite also have concentrations up to two orders lower. As the analysed perovskite originated in pyroxenite and exhibits lower enrichment of HFSE in pyroxenite perhaps higher concentrations in carbonatite was preserved in carbonatites and not so in pyroxenite as HFSE mobility is dependant on P-T condition, pH, and solution chemistry (Jiang et al., 2005) which carbonatite did not provide. Also the lack of minerals which can incorporate HFSE in carbonatites is obvious. Pyroxenite also host Zr-garnet which are highly enriched in HFSE.

3.6.5 Monticellite, pyroxene and amphibole

Monticellite (Table 3.19), pyroxene (Table 3.20) and amphibole (Table 3.21) all show rather low concentration in trace elements. Chondrite-normalised La/Yb in monticellite is 0.14-0.58, indicating depletion in LREE. Overall the REE pattern shows subparallel trends with HREE enrichment reaching slightly higher chondrite normalised levels. LREE concentrations are 10-100x chondrite (Figure 3.34) while HREE shows narrower range 40-105x. There is a significant, although variable, enrichment in Mn, Zr and Hf. Large Ion Lithophile Elements show variable concentration such as Ba (2-52 ppm), Rb 0.1-15.4 ppm and Sr 75-176 ppm and scattered pattern in Figure 3.34. Ba forms a peak as well as U, though Ba has higher level of enrichment. Nd and Y also developed peaks. The deepest trough is at Pb and V. Zr-Hf form distinct troughs showing variable concentrations in different thin sections.

Laser-ICPMS analyses ppm MONTICELLITE	BR18 aver n=6	st dev n=6	KR3 aver n=10	st dev n=10	BR18_1 aver n=10	st dev n=10	BR18_A aver n=4	st dev n=4
Sc	3.83	*2.22*	4.16	*2.76*	3.69	*0.75*	3.48	*0.84*
Ti	112	*28.4*	82.1	*46.0*	180	*41.2*	55.9	*13.4*
V	2.30	*1.19*	1.76	*2.46*	3.21	*0.74*	0.82	*0.16*
Cr	bdl	*bdl*	1.61	*0.69*	3.75	*1.12*	0.87	*bdl*
Mn	21831	*1194*	12275	*1138*	8692	*476*	8781	*789*
Co	31.0	*4.9*	37.6	*4.6*	29.7	*1.77*	30.8	*1.39*
Ni	0.38	*0.10*	0.79	*0.31*	1.46	*0.39*	0.23	*0.12*
Cu	7.56	*12.2*	3.43	*6.40*	3.40	*1.14*	0.22	*0.08*
Zn	222	*84.0*	188	*35.0*	136	*8.25*	132	*11.6*
Ga	0.26	*0.19*	0.90	*1.48*	2.11	*0.67*	0.73	*0.81*
Ge	2.82	*0.58*	2.55	*0.66*	2.06	*0.18*	2.61	*0.14*
Rb	0.10	*0.01*	3.93	*10.4*	15.4	*4.76*	0.83	*0.19*
Sr	92.8	*52.0*	176	*162*	111	*34.1*	74.8	*30.1*
Y	240	*153*	170	*100*	192	*27.0*	161	*39.2*
Zr	33.1	*24.4*	6.63	*6.69*	36.9	*12.2*	4.31	*4.57*
Nb	1.56	*0.88*	0.60	*0.45*	4.45	*1.41*	0.35	*0.25*
Ba	1.99	*1.94*	13.0	*21.3*	51.6	*14.9*	39.7	*9.28*
La	15.2	*9.25*	7.16	*4.22*	8.09	*1.49*	4.23	*1.53*
Ce	57.8	*31.0*	28.9	*13.9*	31.2	*5.78*	20.2	*6.98*
Pr	8.38	*4.00*	4.98	*2.38*	5.84	*1.17*	4.17	*1.30*
Nd	41.4	*19.0*	27.8	*13.9*	33.7	*7.10*	24.6	*7.33*
Sm	15.1	*6.99*	12.0	*6.42*	14.8	*3.57*	11.6	*3.31*
Eu	5.79	*2.53*	5.11	*2.86*	5.78	*1.13*	4.71	*1.37*
Gd	16.0	*6.91*	18.3	*10.7*	22.9	*4.07*	18.9	*5.27*
Tb	3.94	*1.79*	3.92	*2.19*	4.57	*0.73*	3.75	*1.08*
Dy	29.8	*12.7*	29.9	*17.1*	33.5	*5.01*	28.4	*7.41*
Ho	6.36	*2.71*	6.53	*3.70*	7.27	*1.04*	6.15	*1.73*
Er	18.1	*7.49*	20.0	*11.1*	22.4	*3.10*	18.5	*4.48*
Tm	2.64	*0.90*	3.10	*1.76*	3.43	*0.45*	2.93	*0.71*
Yb	17.7	*6.89*	21.3	*12.2*	23.0	*2.87*	19.5	*4.45*
Lu	2.79	*1.12*	3.29	*1.82*	3.49	*0.44*	2.92	*0.66*
Hf	0.43	*0.16*	0.08	*0.11*	0.85	*0.30*	0.04	*0.02*
Ta	0.21	*0.19*	0.03	*0.03*	0.19	*0.08*	0.01	*0.01*
Pb	0.26	*0.19*	0.25	*0.25*	1.37	*0.36*	0.04	*0.01*
Th	0.61	*bdl*	0.04	*0.04*	0.56	*0.17*	0.01	*0.00*
U	0.22	*0.06*	0.09	*0.11*	0.56	*0.14*	0.02	*0.02*

Table 3.19 Average trace element contents of monticellite in the Vuoriyarvi carbonatites

Laser-ICPMS CHONDRITE NORMALISED MONTICELLITE	BR18 aver n=6	st dev n=6	KR3 aver n=10	st dev n=10	BR18_1 aver n=10	st dev n=10	BR18_A aver n=4	st dev n=4
La	41.5	*25.2*	19.5	*11.5*	22.0	*4.05*	11.5	*4.16*
Ce	60.4	*32.4*	30.2	*14.5*	32.6	*6.04*	21.1	*7.30*
Pr	61.2	*29.2*	36.3	*17.3*	42.6	*8.57*	30.4	*9.45*
Nd	58.2	*26.7*	39.1	*19.6*	47.4	*9.99*	34.6	*10.3*
Sm	65.3	*30.3*	51.8	*27.8*	64.1	*15.5*	50.0	*14.3*
Eu	66.5	*29.1*	58.8	*32.9*	66.5	*13.0*	54.1	*15.8*
Gd	52.2	*22.6*	60.0	*35.1*	74.8	*13.3*	61.7	*17.2*
Tb	67.9	*30.8*	67.5	*37.7*	78.8	*12.6*	64.6	*18.6*
Dy	78.2	*33.5*	78.6	*44.8*	87.8	*13.2*	74.5	*19.4*

Ho	74.7	*31.9*	76.7	*43.4*	85.5	*12.3*	72.2	*20.3*
Er	72.7	*30.1*	80.4	*44.6*	89.9	*12.5*	74.2	*18.0*
Tm	74.1	*25.2*	87.0	*49.3*	96.3	*12.6*	82.2	*19.9*
Yb	71.2	*27.8*	86.0	*49.3*	92.8	*11.6*	78.6	*17.9*
Lu	73.2	*29.6*	86.3	*47.7*	91.7	*11.5*	76.7	*17.1*
	BR18		KR3		BR18_1		BR18_A	
	aver	st dev	aver	st dev	aver	st dev	aver	st dev
	n=6	n=6	n=10	n=10	n=10	n=10	n=4	n=4
Rb	0.02	*0.02*	*1.14*	*3.01*	4.46	*1.38*	0.12	*0.14*
Ba	0.49	*0.56*	*3.81*	*6.24*	15.1	*4.36*	5.82	*6.90*
Th	2.39	*5.86*	*0.76*	*0.92*	13.3	*3.94*	0.10	*0.12*
U	5.91	*9.43*	*7.15*	*9.15*	46.1	*11.7*	0.98	*1.56*
Nb	4.16	*2.33*	*1.61*	*1.20*	11.9	*3.77*	0.95	*0.67*
Ta	2.75	*5.36*	*1.04*	*1.17*	7.12	*3.06*	0.40	*0.33*
La	41.5	*25.2*	*19.5*	*11.5*	22.0	*4.05*	11.5	*4.16*
Ce	60.4	*32.4*	*30.2*	*14.5*	32.6	*6.04*	21.1	*7.30*
Pb	0.02	*0.04*	*0.07*	*0.07*	0.38	*0.10*	0.01	*0.00*
Sr	7.80	*4.37*	*14.8*	*13.63*	9.37	*2.87*	6.29	*2.53*
Nd	58.2	*26.7*	*39.1*	*19.6*	47.4	*10.0*	34.6	*10.3*
Zr	5.98	*4.40*	*1.20*	*1.21*	6.66	*2.20*	0.78	*0.83*
Hf	1.62	*1.44*	*0.41*	*0.59*	4.75	*1.65*	0.17	*0.14*
Sm	65.3	*30.3*	*51.8*	*27.8*	64.1	*15.5*	50.0	*14.3*
Ti	0.17	*0.04*	*0.13*	*0.07*	0.28	*0.06*	0.09	*0.02*
Y	107	*68.2*	*75.6*	*44.6*	85.2	*12.1*	71.5	*17.4*
V	0.03	*0.01*	*0.02*	*0.03*	0.04	*0.01*	0.01	*0.00*
Sc	0.44	*0.26*	*0.48*	*0.32*	0.43	*0.09*	0.40	*0.10*

Table 3.20 Trace element contents of monticellite chondrite-normalised in the Vuoriyarvi carbonatites.

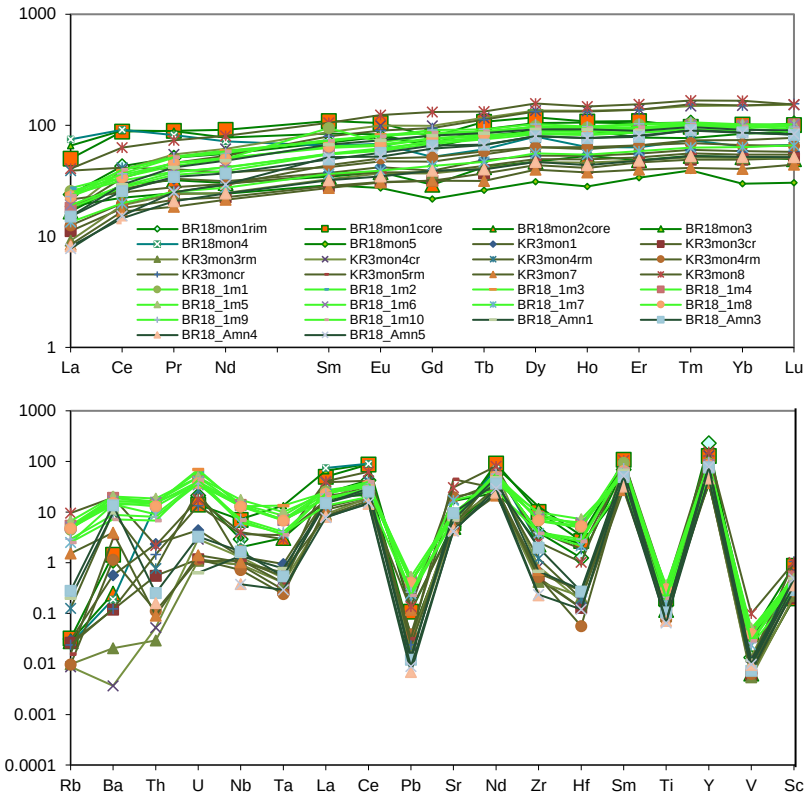

Fig.3.34 Chondrite-normalised average REE and trace element patterns of monticellite in the Vuoriyarvi carbonatites.

Pyroxene is similar in REE enrichment to monticellite, although is slightly less enriched in HREEs (Figure 3.35). There is considerable enrichment in HSFE such as Nb, Hf, Ta, also Zr, U and Th with pyroxene from the anomalous sample BR18_1showing highest HFSE enrichment. Ba (358 ppm) is highly enriched but Rb is only concentrated in values close to chondrite. The Sr content of pyroxene is 1370 ppm but does not form a

peak on the trace element diagram (Figure 3.35). U-Th concentrations is variable and forms anomalies some being up to 100 times enriched and others below the chondritic values. The second part of this diagram has a spiky appearance with an Y peak (also around 100 times chondrite).

Laser analyses of trace elements in pyroxene and olivine were collected from granular area which is separated from the rest of the section by phlogopite and apatite (Figure 3.37).

Laser-ICPMS analyses ppm PYROXENE	BR18_1 aver n=5	stdev n=5	B218A_core aver n=3	stdev n=3	B218A_rim aver n=2	stdev n=2
Sc	16.0	*9.89*	18.9	4.89	15.0	*5.13*
Ti	1223	*279*	1086	355	1101	*441*
V	25.6	*8.14*	18.8	2.84	19.4	*0.03*
Cr	n/a	*n/a*	bdl	bdl	bdl	*bdl*
Mn	1842	*1269*	1545	213	1582	*111*
Co	70.6	*96.1*	7.46	0.80	7.61	*0.51*
Ni	11.0	*9.8*	0.23	0.02	0.25	*0.01*
Cu	40.8	*39.0*	0.10	0.06	0.13	*0.04*
Zn	53.7	*51.6*	29.5	4.37	38.0	*1.22*
Ga	14.5	*10.0*	7.55	6.46	16.7	*12.2*
Ge	3.75	*1.46*	3.41	0.55	3.40	*1.00*
Rb	86.8	*78.9*	1.62	2.54	4.53	*5.80*
Sr	378	*157*	515	454	691	*673*
Y	17.9	*5.55*	11.0	4.13	8.87	*2.62*
Zr	307	*120*	320	104	253	*122*
Nb	18.2	*14.4*	1.09	0.98	1.06	*0.76*
Ba	438	*503*	60.5	94.0	181	*175*
La	18.5	*7.66*	7.73	5.11	8.58	*6.46*
Ce	42.8	*18.0*	22.7	9.16	23.3	*11.4*
Pr	5.60	*2.21*	3.32	0.93	3.04	*0.78*
Nd	21.5	*10.6*	15.3	3.60	12.6	*1.96*
Sm	4.28	*2.11*	3.49	0.89	2.79	*0.17*
Eu	1.35	*0.64*	1.17	0.28	1.00	*0.11*
Gd	4.05	*1.73*	3.13	0.80	2.37	*0.48*
Tb	0.60	*0.22*	0.42	0.14	0.34	*0.03*
Dy	3.58	*1.20*	2.70	0.79	1.96	*0.08*
Ho	0.70	*0.21*	0.48	0.17	0.34	*0.05*
Er	1.92	*0.67*	1.16	0.40	0.86	*0.26*
Tm	0.35	*0.19*	0.15	0.06	0.11	*0.02*
Yb	2.41	*1.18*	1.44	0.39	1.01	*0.12*
Lu	0.60	*0.38*	0.29	0.08	0.19	*0.02*
Hf	6.10	*1.16*	4.37	1.75	4.12	*2.29*
Ta	0.76	*0.41*	0.22	0.22	0.23	*0.17*
Pb	7.46	*6.27*	0.08	0.07	0.14	*0.08*
Th	2.85	*2.00*	0.02	0.01	0.02	*0.02*
U	2.48	*2.26*	0.01	0.01	0.04	*0.03*

Table 3.21 Average trace element contents of pyroxene in the Vuoriyarvi carbonatites.

Laser-ICPMS CHONDRITE NORMALISED PYROXENE	BR18_1 aver n=5	stdev n=5	B218A_core aver n=3	stdev n=3	B218A_rim aver n=2	stdev n=2
La	50.3	*20.9*	12.3	1.25	23.4	*17.6*
Ce	44.7	*18.9*	17.5	2.62	24.4	*11.9*
Pr	40.9	*16.1*	20.0	3.91	22.2	*5.72*
Nd	30.2	*15.0*	18.0	3.54	17.7	*2.76*
Sm	18.5	*9.13*	12.9	3.10	12.1	*0.73*
Eu	15.5	*7.32*	11.5	2.16	11.5	*1.29*
Gd	13.2	*5.66*	8.19	1.99	7.74	*1.56*
Tb	10.3	*3.80*	5.79	1.11	5.78	*0.57*
Dy	9.40	*3.15*	5.71	1.25	5.13	*0.20*
Ho	8.25	*2.54*	4.26	1.08	4.00	*0.65*
Er	7.72	*2.69*	3.42	0.71	3.46	*1.04*
Tm	9.85	*5.38*	3.22	0.58	3.19	*0.55*
Yb	9.72	*4.76*	4.52	0.71	4.09	*0.49*
Lu	15.7	*10.1*	5.84	1.40	4.86	*0.49*
	BR18_1 aver n=5	stdev n=5	B218A_core aver n=3	stdev n=3	B218A_rim aver n=2	stdev n=2
Rb	0.08	*0.03*	0.07	0.05	*1.31*	*1.68*
Ba	129	*148*	6.82	8.66	*53.0*	*51.2*
Th	67.0	*47.1*	0.34	0.26	*0.43*	*0.36*
U	203	*185*	0.81	0.33	*3.13*	*2.80*
Nb	55.5	*21.7*	3.86	2.27	*2.83*	*2.01*
Ta	29.2	*15.9*	11.6	7.81	*8.95*	*6.51*
La	50.3	*20.9*	12.3	1.25	*23.4*	*17.6*
Ce	44.7	*18.9*	17.5	2.62	*24.4*	*11.9*
Pb	2.04	*1.72*	0.00	0.01	*0.04*	*0.02*
Sr	25.2	*22.9*	20.4	6.25	*58.1*	*56.6*
Nd	30.2	*15.0*	18.0	3.54	*17.7*	*2.76*
Zr	7.94	*2.46*	61.2	17.8	*45.6*	*22.1*
Hf	34.1	*6.48*	28.4	9.6	*23.0*	*12.8*
Sm	18.5	*9.13*	12.9	3.10	*12.1*	*0.73*
Ti	1.87	*0.43*	1.99	0.38	*1.68*	*0.68*
Y	31.8	*13.2*	3.61	0.61	*3.94*	*1.17*
V	0.30	*0.10*	0.22	0.03	*0.23*	*0.00*
Sc	1.86	*1.15*	2.37	0.34	*1.73*	*0.60*

Table 3.22 Trace element contents of pyroxene chondrite-normalised in the Vuoriyarvi carbonatites.

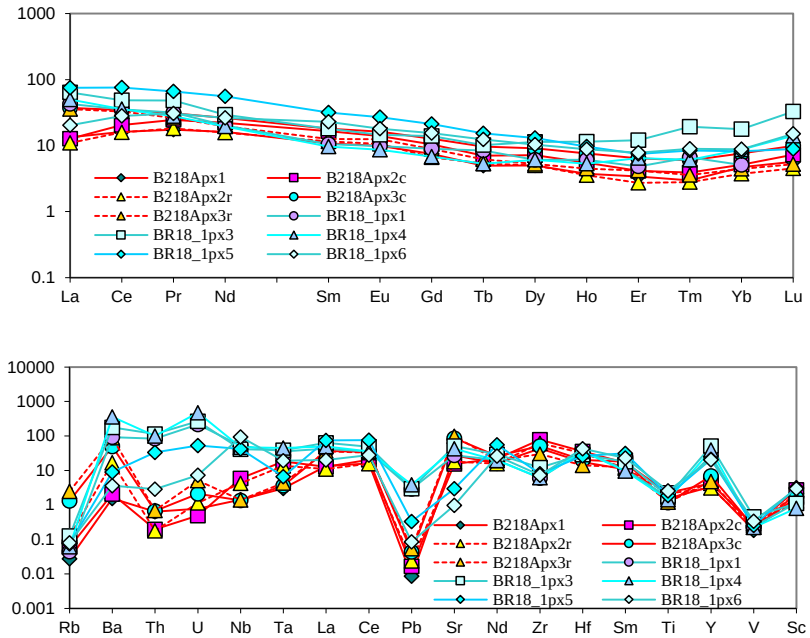

Fig.3.36 Chondrite normalised average REE and trace element patterns of pyroxene in the Vuoriyarvi carbonatites.

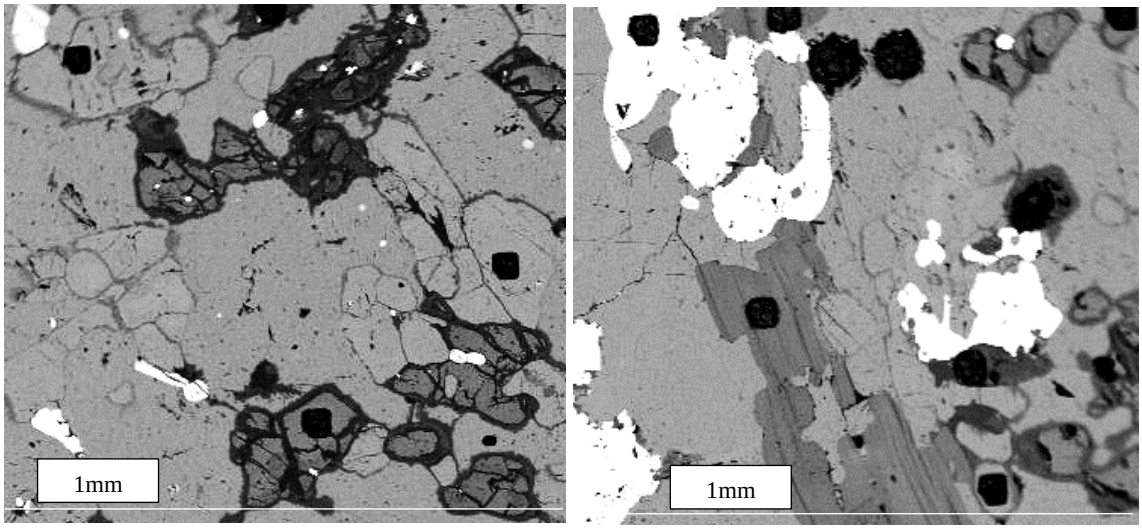

Fig. 3.37. BSE images of BR18_1 showing globular area containing fine-grained olivine highly serpentinised around the rim with occasional euhedral shape (dark grey); euhedral to subhedral clinopyroxene also serpentinised around the rim (light grey); f large phlogopite bordering granular area (darkish grey); large calcite infilling the space between silicate phases. Square black features are laser pits.

The REE chondrite-normalised pattern of amphibole (Figure 3.38) is very similar to that of calcite, although its concentration in REEs is one order lower. The La/Yb_{CN} ratio for amphibole is 24. In some aspects the amphibole trace element diagram also resembles the pyroxene one, mainly from the elements La to V (Figure 3.38). Positive anomaly in amphibole is shown by Y peak. Pb and Ti developed troughs.

Laser-ICPMS analyses ppm AMPHIBOLE	BR18_1 *aver* *n=4*	*stdev* *n=4*
Sc	1.72	*0.41*
Ti	192	*51.3*
V	8.47	*3.17*
Cr	3.96	*1.28*
Mn	3009	*671*
Co	12.3	*4.31*
Ni	1.43	*0.29*
Cu	4.98	*1.26*
Zn	30.4	*12.5*
Ga	3.70	*0.50*
Ge	1.57	*0.46*
Rb	19.8	*3.56*
Sr	236	*78.2*
Y	48.7	*19.1*
Zr	52.3	*12.1*
Nb	12.2	*5.42*
Cs	0.43	*0.24*
Ba	172	*25.0*
La	9.7	*1.41*
Ce	21.0	*2.26*
Pr	2.65	*0.44*
Nd	13.2	*4.31*
Sm	3.67	*1.17*
Eu	1.46	*0.43*
Gd	5.29	*1.86*
Tb	1.09	*0.44*
Dy	7.90	*3.24*
Ho	1.89	*0.79*
Er	6.07	*2.43*
Tm	1.09	*0.45*
Yb	7.89	*3.35*
Lu	1.36	*0.62*
Hf	0.96	*0.18*
Ta	0.26	*0.12*
Pb	1.83	*0.43*
Th	3.03	*0.81*
U	0.76	*0.27*

Laser-ICPMS CHONDRITE NORMALISED AMPHIBOLE	BR18_1 aver n=4	*stdev* *n=4*
La	26.3	*3.86*
Ce	22.0	*2.36*
Pr	19.3	*3.24*
Nd	18.5	*6.07*
Sm	15.9	*5.06*
Eu	16.8	*5.00*
Gd	17.3	*6.07*
Tb	18.7	*7.52*
Dy	20.7	*8.49*
Ho	22.2	*9.34*
Er	24.4	*9.76*
Tm	30.7	*12.7*
Yb	31.8	*13.5*
Lu	35.6	*16.3*

	BR18_1 aver n=4	*stdev* *n=4*
Rb	5.73	*1.03*
Ba	50.3	*7.3*
Th	71.4	*19.0*
U	62.1	*22.1*
Nb	32.4	*14.4*
Ta	9.88	*4.53*
La	26.3	*3.86*
Ce	22.0	*2.36*
Pb	0.50	*0.12*
Sr	19.8	*6.57*
Nd	18.5	*6.07*
Zr	9.44	*2.18*
Hf	5.35	*1.02*
Sm	15.9	*5.06*
Ti	0.29	*0.08*
Y	21.6	*8.47*
V	0.10	*0.04*
Sc	0.20	*0.05*

Table 3.23 Average trace element contents and chondrite-normalised abundances of amphibole in the Vuoriyarvi carbonatites

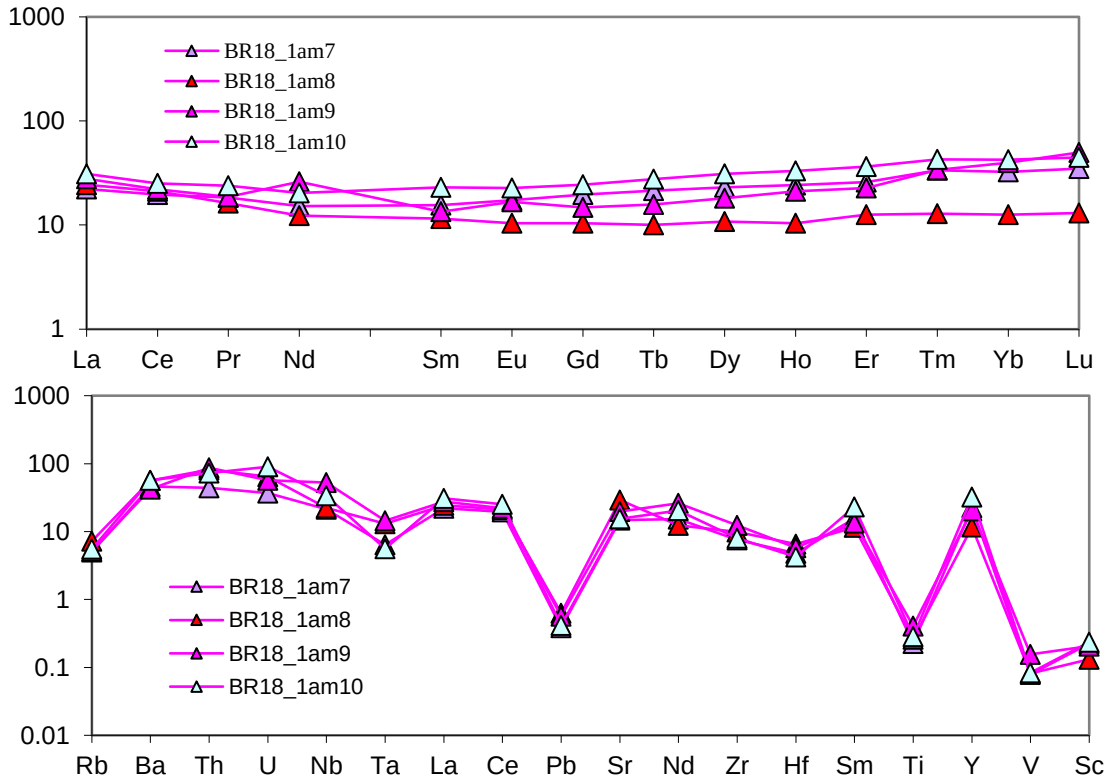

Fig.3.38 Chondrite normalised average REE and trace element patterns of amphibole in the Vuoriyarvi carbonatites

3.6.6 Olivine

Rare olivine was analysed in two slides: B218A and BR18_1 (Figures 3.37, 3.39, 3.40). Both sections contain fine-grained olivine though distribution differs. In BR18_1 olivine is restricted to granular area (Figure 3.37) whereas it is found in the main body of section in B218A (Figure 3.40). Its trace elements contents are shown in Table 3.24. High MnO content in olivine indicates formation from carbonatites. Chondrite-normalised value La/Yb in olivine is 1.8-3.3 (BR181) and 2.5-8.2 in B218A. Overall the REE pattern contain subparallel trends with HREE enrichment reaching slightly lower chondrite normalised levels. Trend of B218A is more elevated to compare to BR181 up to two orders in LREEs, one order in MREEs and meeting in HREEs.

To put analyses into Kola alkaline complex context, it is compared with olivine from a Kovdor dunite. Olivine in BR181 shows strong similarity in REE pattern to olivine from the Kovdor dunite (Figure 3.39). LREEs pattern in olivine from dunite fits between carbonatite samples and decreases towards the HREEs. The trace element trend of olivine in BR18_1 shows similarity to olivine from Kovdor dunite with the exception of Zr-Hf (negative trend in olivine from dunite and positive in olivine from carbonatites). Enrichment in HSFE including Nb, Hf, Ta, also Zr, U and Th is considerable. HFSE in

B218A shows higher enrichment compared to BR18_1 up to one order of magnitude mostly in Nd (137 ppm vs 8.57 ppm), Zr (2784 ppm vs 165 ppm), Hf (40.5 ppm vs 3.22 ppm) and in Sr (5825 ppm vs 352 ppm). Th (2.13 ppm) and U (2.42 ppm) is higher in BR18_1 than in B218A (0.20 ppm and 0.24 ppm respectively). Ba in B218A varies 53.4-3167 ppm. In BR18_1 the average value is 429 ppm. Rb is present in B218A and BR18_1 up to 10 times chondritic value. The trace element diagram has a spiky appearance with Y peak (around 100 times chondrite found in B218A and one order lower in BR18_1).

OLIVINE	BR181_ol1	BR181_ol2	BR181_ol3	*ave n=3*	st dev n=3
Sc	8.47	6.24	6.66	7.12	*1.18*
Ti	1496	624	421	847	*571*
V	70.2	14.2	9.41	31.3	*33.8*
Cr	18.7	7.96	10.2	12.3	*5.66*
Mn	2714	2709	2705	2709	*4.66*
Co	44.8	23.0	41.7	36.5	*11.8*
Ni	6.23	2.80	5.29	4.77	*1.77*
Cu	12.9	26.2	12.3	17.2	*7.85*
Zn	76.4	30.7	150	85.8	*60.3*
Ga	31.1	7.53	12.0	16.9	*12.5*
Ge	4.98	3.01	2.94	3.64	*1.16*
Rb	120	44.3	60.2	74.8	*39.9*
Sr	374	258	425	352	*85.7*
Y	16.7	11.6	7.84	12.0	*4.44*
Zr	147	253	94.1	165	*81.2*
Nb	44.3	8.17	11.6	21.4	*20.0*
Ba	458	202	625	429	*213*
La	11.0	9.5	7.64	9.35	*1.66*
Ce	22.2	21.7	13.3	19.1	*4.98*
Pr	2.49	3.01	1.57	2.36	*0.73*
Nd	9.46	11.0	5.29	8.57	*2.94*
Sm	1.99	2.58	1.18	1.92	*0.71*
Eu	0.75	0.65	0.39	0.59	*0.18*
Gd	2.24	2.58	0.98	1.93	*0.84*
Tb	0.50	0.43	0.20	0.37	*0.16*
Dy	2.99	2.37	1.18	2.18	*0.92*
Ho	0.75	0.43	0.39	0.52	*0.19*
Er	1.99	1.29	1.18	1.49	*0.44*
Tm	0.25	0.22	0.20	0.22	*0.03*
Yb	3.49	1.94	2.94	2.79	*0.79*
Lu	0.75	0.43	0.78	0.65	*0.19*
Hf	3.24	4.09	2.35	3.22	*0.87*
Ta	0.75	0.86	0.39	0.67	*0.24*
Pb	6.23	2.37	4.70	4.43	*1.94*
Th	3.74	1.08	1.57	2.13	*1.42*
U	4.23	1.08	1.96	2.42	*1.63*

NORMALISED	BR181_ol1	BR181_ol2	BR181_ol3	ave n=3	st dev n=3
La	29.9	25.8	20.8	25.5	*4.56*
Ce	23.2	22.8	14.1	20.0	*5.12*
Pr	17.9	21.5	11.4	16.9	*5.14*
Nd	13.4	15.5	7.55	12.1	*4.12*
Sm	8.91	11.0	4.70	8.21	*3.21*
Eu	7.87	8.47	3.37	6.57	*2.79*
Gd	7.57	8.28	3.25	6.37	*2.72*
Tb	7.35	6.11	2.37	5.27	*2.59*
Dy	7.67	6.00	3.04	5.57	*2.35*
Ho	7.74	5.53	3.68	5.65	*2.03*
Er	8.12	5.31	4.43	5.95	*1.93*
Tm	10.4	6.00	7.33	7.92	*2.28*
Yb	14.3	7.89	11.8	11.3	*3.21*
Lu	22.2	8.92	19.6	16.9	*7.02*
Rb	34.9	12.8	17.4	21.7	*11.6*
Ba	134	59.1	183	126	*62.6*
Th	86.2	26.0	35.1	49.1	*32.4*
U	348	90.9	153	197	*134*
Nb	119	21.5	31.0	57.0	*53.5*
Ta	24.4	34.6	16.5	25.2	*9.10*
La	29.9	25.8	20.8	25.5	*4.56*
Ce	23.2	22.8	14.1	20.0	*5.12*
Pb	1.72	0.64	1.27	1.21	*0.54*
Sr	31.4	21.7	35.7	29.6	*7.15*
Nd	13.4	15.5	7.55	12.1	*4.12*
Zr	26.6	45.8	17.1	29.8	*14.6*
Hf	17.9	23.0	13.1	18.0	*4.94*
Sm	8.91	11.0	4.70	8.21	*3.21*
Ti	2.29	0.95	0.64	1.30	*0.87*
Y	7.47	5.12	3.51	5.37	*1.99*
V	0.83	0.17	0.11	0.37	*0.40*
Sc	0.98	0.72	0.76	0.82	*0.14*

Table 3.23a Average trace element contents and chondrite-normalised values of olivine in the Vuoriyarvi carbonatites.

OLIVINE	B218A_ol1	B218A_ol3c	B218A_ol3r	B218A_ol2c	B218A_ol2r	ave n=5	st dev n=5
Sc	190	137	118	209	175	*166*	*37.6*
Ti	10267	7495	8207	12872	13308	*10430*	*2638*
V	158	189	202	186	183	*184*	*16.0*
Cr	bdl	bdl	bdl	bdl	bdl	*bdl*	*bdl*
Mn	14712	13512	15641	15641	15641	*15029*	*939*
Co	74.4	65.2	75.4	72.6	75.1	*72.5*	*4.26*
Ni	2.52	2.19	2.50	1.86	2.46	*2.31*	*0.28*
Cu	bdl	1.41	1.71	0.52	1.00	*1.16*	*0.51*
Zn	272	263	386	302	366	*318*	*55.5*
Ga	32.0	146	263	39.4	75.8	*111*	*96.2*
Ge	36.5	27.1	28.0	33.5	38.7	*32.8*	*5.10*
Rb	0.97	44.2	89.8	1.82	4.00	*28.2*	*39.0*
Sr	3295	10042	12140	1623	2024	*5825*	*4903*
Y	77.2	152	112	84.6	66.1	*98.2*	*34.3*
Zr	2422	2748	1726	3828	3194	*2784*	*792*
Nb	5.39	4.97	5.47	19.4	15.0	*10.0*	*6.71*
Ba	53.4	1645	3167	62.5	540	*1094*	*1328*
La	49.5	133	137	40.6	37.8	*79.5*	*50.6*
Ce	156	321	327	172	143	*224*	*91.9*
Pr	24.0	41.2	37.3	29.4	23.4	*31.0*	*7.95*
Nd	116	181	145	137	106	*137*	*29.4*
Sm	25.1	40.6	30.2	33.3	25.1	*30.9*	*6.46*
Eu	8.72	13.8	11.2	10.6	8.69	*10.6*	*2.10*
Gd	23.1	37.8	28.2	28.0	19.1	*27.2*	*6.99*
Tb	2.89	5.44	3.73	3.57	2.94	*3.71*	*1.03*
Dy	19.2	33.8	20.9	23.8	17.9	*23.1*	*6.36*
Ho	3.20	6.30	3.94	4.10	2.84	*4.08*	*1.35*
Er	8.50	15.59	10.86	9.03	6.38	*10.1*	*3.47*
Tm	1.07	2.07	1.32	1.21	0.94	*1.32*	*0.44*
Yb	11.8	18.3	11.4	11.1	8.74	*12.3*	*3.60*
Lu	2.19	3.68	2.07	2.43	1.62	*2.40*	*0.77*
Hf	31.4	35.2	26.0	55.7	54.1	*40.5*	*13.6*
Ta	0.80	0.91	1.17	4.16	3.32	*2.07*	*1.56*
Pb	0.32	1.56	2.04	0.53	0.82	*1.05*	*0.73*
Th	0.28	0.28	0.31	0.07	0.07	*0.20*	*0.12*
U	0.10	0.25	0.65	0.05	0.13	*0.24*	*0.24*

	B218A_ol1	B218A_ol3c	B218A_ol3r	B218A_ol2c	B218A_ol2r	ave n=5	st dev n=5
La	135	123	114	325	337	*207*	*114*
Ce	163	200	166	302	309	*228*	*72.3*
Pr	175	238	188	270	247	*224*	*40.3*
Nd	163	215	164	229	185	*191*	*29.9*
Sm	109	160	120	158	119	*133*	*24.2*
Eu	100	136	110	142	117	*121*	*17.6*
Gd	75.7	101.5	69.1	111	83.3	*88.1*	*17.7*
Tb	49.8	68.5	55.9	84.4	58.3	*63.4*	*13.5*
Dy	50.3	69.5	51.9	79.7	49.6	*60.2*	*13.6*
Ho	37.7	53.5	36.8	66.6	41.9	*47.3*	*12.7*
Er	34.2	40.3	28.3	56.3	39.5	*39.7*	*10.4*
Tm	30.0	37.8	29.1	52.3	33.6	*36.6*	*9.44*
Yb	47.4	50.0	38.9	66.5	41.8	*48.9*	*10.7*
Lu	57.6	71.1	46.9	86.8	49.0	*62.3*	*16.7*
Rb	0.28	0.59	1.28	11.5	23.5	*7.44*	*10.1*
Ba	15.6	20.4	175	434	841	*297*	*348*
Th	6.50	1.91	1.85	5.90	6.50	*4.53*	*2.43*
U	7.89	4.77	12.0	18.4	48.1	*18.2*	*17.5*
Nb	14.4	57.5	44.2	11.9	13.2	*28.2*	*21.2*
Ta	30.6	178	141.0	31.6	40.9	*84.4*	*69.8*
La	135	123	114	325	337	*207*	*114*
Ce	163	200	166	302	309	*228*	*72.3*
Pb	0.09	0.16	0.25	0.38	0.51	*0.28*	*0.17*
Sr	277	152	188	759	924	*460*	*356*
Nd	163	215	164	229	185	*191*	*29.9*
Zr	437	768	637	446	282	*514*	*190*
Hf	176	346	334	177	132	*233*	*99.6*
Sm	109	160	120	158	119	*133*	*24.2*
Ti	15.7	21.9	22.5	10.3	11.4	*16.3*	*5.70*
Y	34.4	41.8	32.5	60.6	44.9	*42.8*	*11.2*
V	1.86	2.43	2.38	2.00	2.15	*2.16*	*0.24*
Sc	22.1	26.8	22.4	14.3	12.4	*19.6*	*6.07*

Table 3.23b Trace trace element contents of olivine in B218A and chondrite-normalised trace element contents of olivine in the Vuoriyarvi carbonatites.

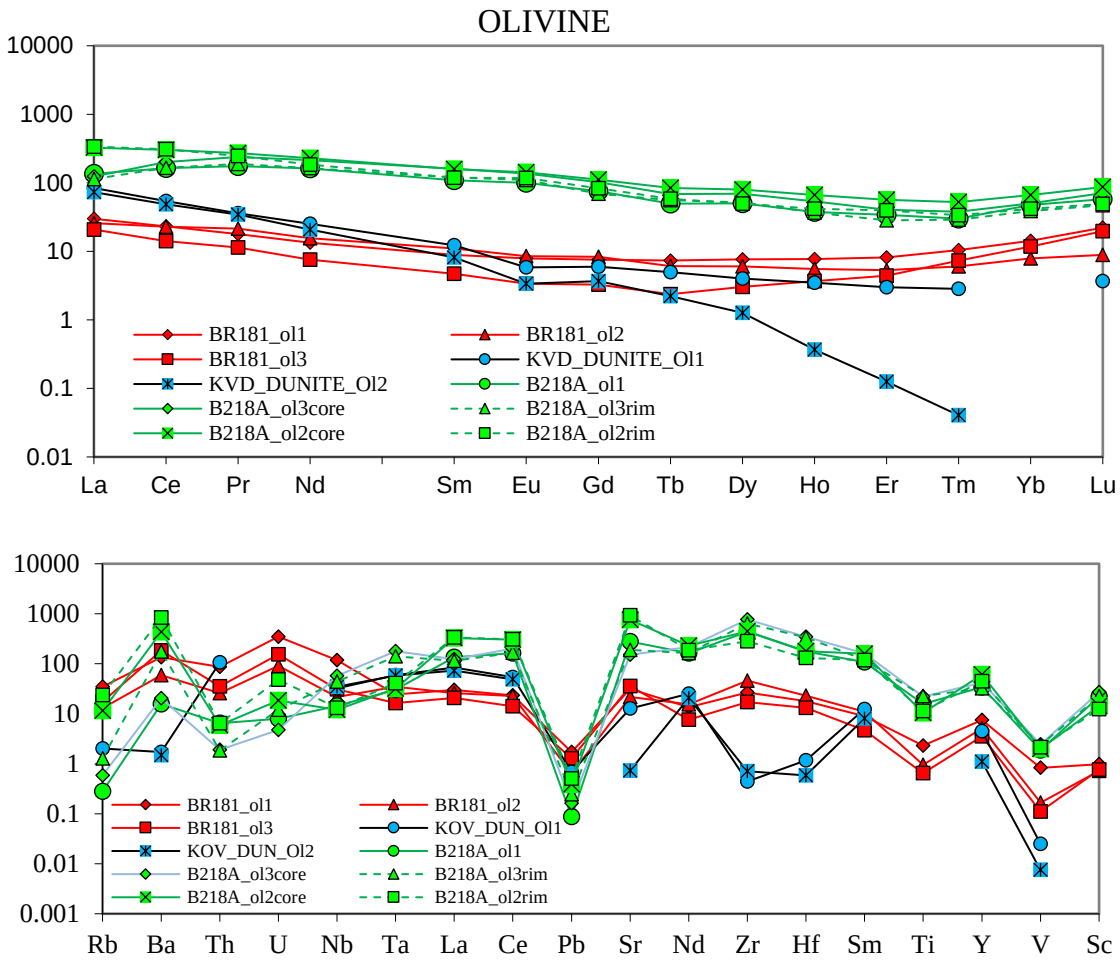

Fig.3.39 Chondrite normalised average REE and trace element patterns of olivine in the Vuoriyarvi carbonatites.

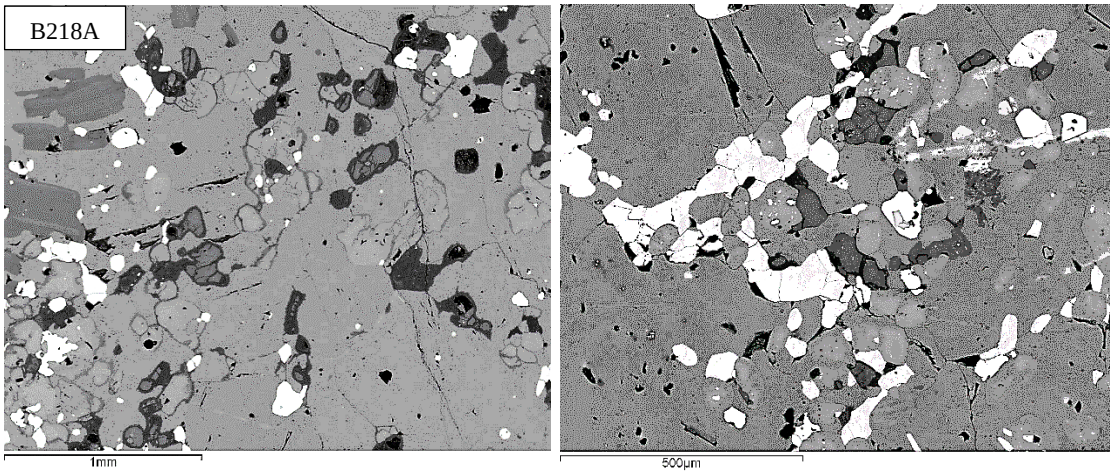

Fig.3.40 BSE images of B218A showing distribution of fine-grained olivine being highly serpentinised around the rim (A) showing anhedral shape associated with clinopyroxene (A) and rimming clinopyroxene (B) being less serpentised.

Trace element patterns in some of the less common minerals in carbonatites like monticellite, olivine, amphibole and pyroxene are summarised in Figure 3.41.

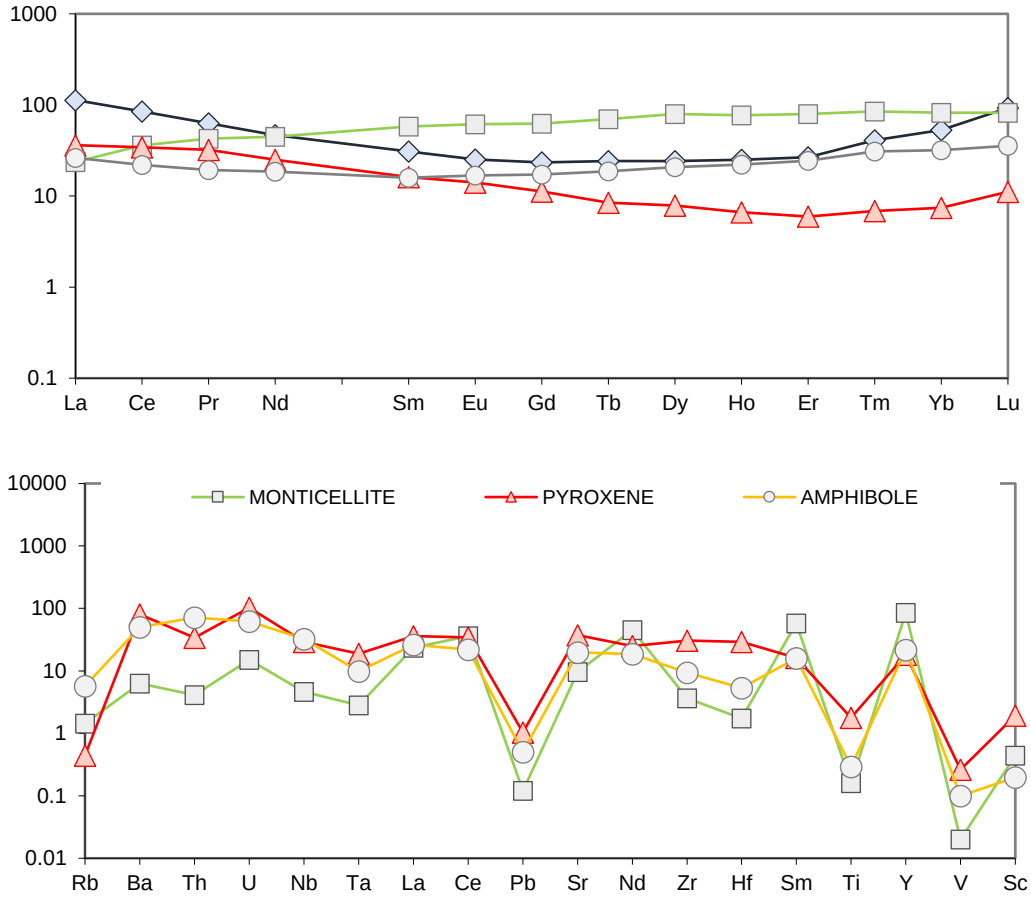

Fig.3.41 Chondrite-normalised average REE and trace element patterns of monticellite, olivine, pyroxene and amphibole in the Vuoriyarvi carbonatites.

Overall amphibole, monticellite and pyroxene contain similar quantity of REEs. The other phases can better accommodate trace and rare elements (Figure 3.41). The main minerals hosting these elements are perovskite and apatite, although apatite is more important due to its higher volumetric concentration. The same applies to calcite which is present in even higher percentages than apatite although it contains less trace and rare elements. Zr-garnet is a valuable candidate but occurs occasionally, thus it would account only for a very small fraction of these elements.

Fractionation of LREE over HREE in different minerals from the Vuoriyarvi carbonatites is represented by ∑LREE against ∑HREE in Figure 3.42. The highest ratio, controlled by fractionation of LREE over the HREE, is observed in perovskite, apatite and Zr-rich garnet. The other group, reaching the intermediate values, mainly belongs to calcite and silicate minerals such as monticellite, pyroxene and amphibole. The lowest ratio is observed in phlogopite.

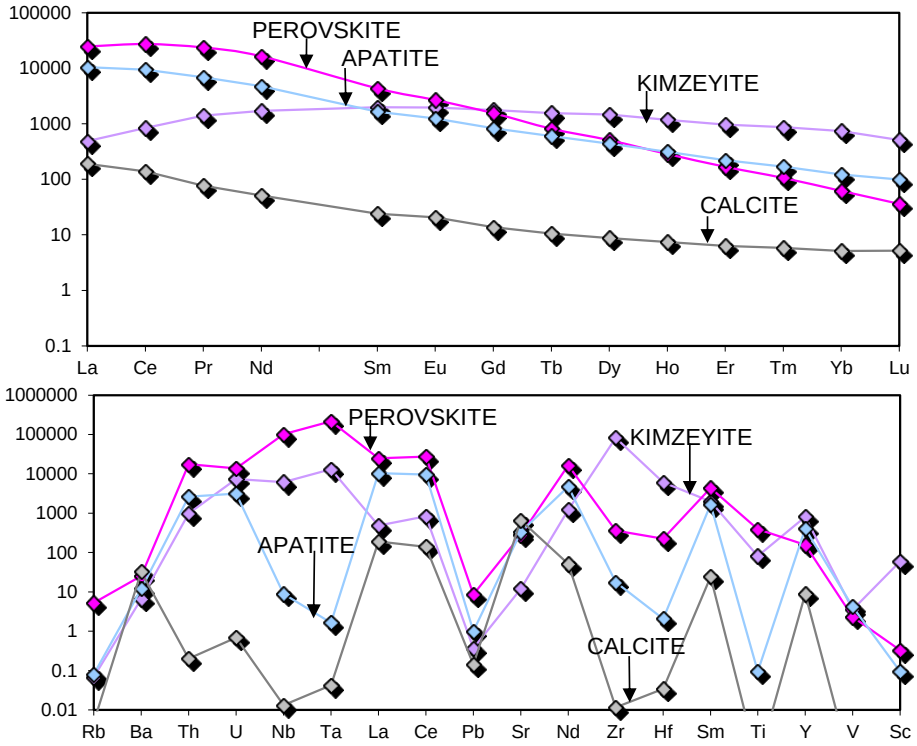

Fig 3.42 Chondrite normalised average REE and trace elements patterns of calcite, apatite, perovskite and Zr-rich garnet in the Vuoriyarvi carbonatites.

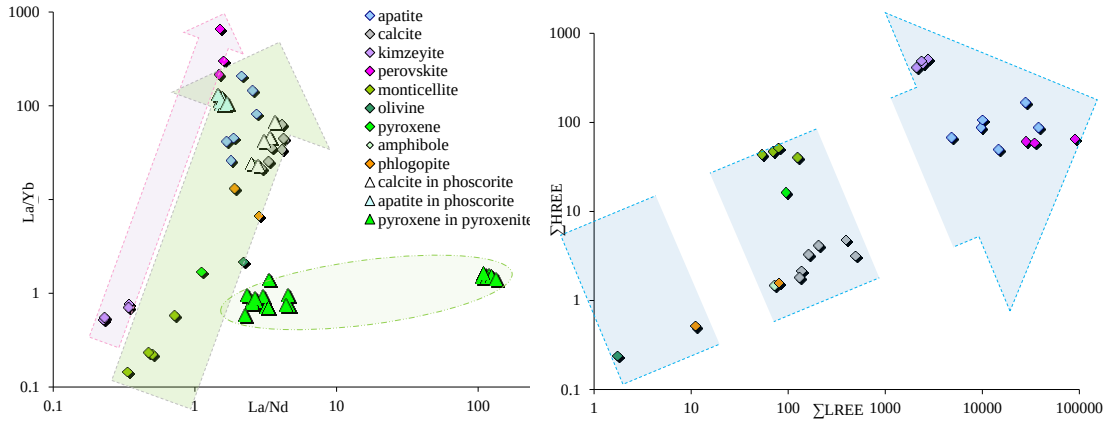

Fig.3.43 A plot of La/Yb vs. La/Nd and ∑LREE vs. ∑HREE for the Vuoriyarvi carbonatite phase. Pyroxene from associated pyroxenite and calcite/apatite from associated phoscorites is shown (Brassiness 2006).

Also REE fractionation, expressed by La/Yb over La/Nd, shows very narrow variation in La/Nd in carbonatites (ratio is low and similar for all the phases (Figure 3.43) but much wider variation in La/Yb. Thus monticellite and Zr-garnet have very low La/Yb falling below 1, calcite reaching 40, apatite 124, perovskite 670, suggesting that some phases in carbonatites have taken on important part in REE fractionation. La/Yb for pyroxene in the Vuoriyarvi carbonatite (>1) is slightly higher than for pyroxene in pyroxenite (average value <1). La/Nd variation for pyroxene is higher in pyroxenite (1-100) than in carbonatite (1). The concentration of SiO_2 influences the La/Yb and La/Nd

ratios. The average La/Yb ratio for calcite and apatite in carbonatite is comparable in associated phoscorite. The La/Nd in phoscorites is slightly higher than in carbonatites (Figure 3.41).

3.7. SUMMARY OF TRACE ELEMENTS

Perovskite and Zr-garnet accommodate many trace elements, consequently the partition coefficient for most of the trace elements shows strong compatibility. Apatite can favourably host LREE and some trace elements like Th, U, Y though Calcite (the major rock-forming mineral) can accommodate LREE (allowance of substitution Ca by LREE) and Sr, although the average D for the LREEs falls below 1 as the enrichment in LREEs is very variable (up to two orders of magnitude).

Phlogopite has a positive Eu anomaly and likes Ba, Nb, and Ta. Accommodation of Ba and Rb into phlogopite plays a significant role as D=100 and also the quantity of this phase in the Vuoriyarvi sövite is considerable. Mn in monticellite shows enrichment about 4 times more (on an average) than in pyroxene but 0.5 times of that in phlogopite. Lower REE contents were observed in the olivine in MREE and higher in LREE and HREE. Pyroxene, amphibole and partly monticellite (except HREEs) demonstrate incompatibility in REE, LIL and HFSE.

3.8 CONCLUSIONS

Vuoriyarvi carbonatites show various textures, which suggest highly changeable conditions in the upwelling magma and perhaps interaction with the surrounding country rock. Entrainment of phlogopite and some magnetite xenoliths from the phlogopite-magnetite-rich country rock occurred in the early stages, leading to some alteration of the liquid (slight zonation of the crystallising phenocrystic phlogopite). Perhaps the granular pyroxene-olivine-calcite area represents early sidewall crystallisation in a form of a cognate xenolith. The intergrowth between calcite and monticellite could be explained by trapped liquid rich in both components, leading to simultaneous crystallisation of both phases. Formation of perovskite and transformation to Zr-garnet took place during the early stages of crystallisation on a localized scale.

The most probable interpretation for the immiscibility-like texture, such as dumbells/globules of calcite found in monticellite, would be solid state precipitation of

high temperature polymorph of calcite from a silicate melt. In the course of the ascent of the (mostly crystallised) dyke, the magmatic textures of Vuoriyarvi sövites were most likely modified by metamorphic recrystallisation to a granular/ granoblastic texture.

The major elements suggest that formation of the Vuroriyarvi carbonatite happened just after immiscibility. Consequently Al-poor diopside and Al-poor edenite and perovskite (Nb-rich phase) precipitated from a silica-rich carbonatite. Subsolidus re-equilibration of perovskite to pyrochlore was blocked by insufficient concentration of F in the system. Thus, fluorapatite formed as a primary mineral with moderate F and SrO values. Calcite with moderate values of Sr is also characteristic of a primary carbonate phase. With progressively higher Ca-concentration, olivine most likely progressed to crystallisation of monticellite. The lower mg# of monticellite reflects the lower formation temperatures (around 760°C). Formation of Zr-rich garnet is characteristic of the complex substitution via Ti-rich phases. Incorporation of xenocrystic phlogopite modified the liquid in Si- and Mg- components. The core-rim zonation in magnetite reflects changeable state of the system subject to assimilation, crystallisation and post-solidus alteration, exemplified by the existence of pure andradite after magnetite found in monticellite fractures.

CHAPTER 4

PETROGRAPHY AND MINERAL CHEMISTRY OF CONSTITUENT PHASES IN INTRUSIVE CARBONATITES FROM FOGO, CAPE VERDE

4.1 Introduction to the Fogo carbonatite samples

Fogo, one of the westernmost islands of the southern group of the Cape Verde Islands (Figure 4.1), is well-known for its intrusive carbonatites (Assuncao et al., 1996; Kogarko 1993). These carbonatites form the part of the oldest unit on the island, the Basement Complex, which was formed during the seamount stage of oceanic island volcanic evolution (Day et al., 1999). Here they occur together with nephelinites (Hoernle et al., 2002). The biotite-bearing carbonatites are exposed in valleys cut into the lower flanks of the western part of the island. They are cut by basic dykes, and are overlain unconformably by lava flows from the main shield stage (Hoernle et al., 2002).

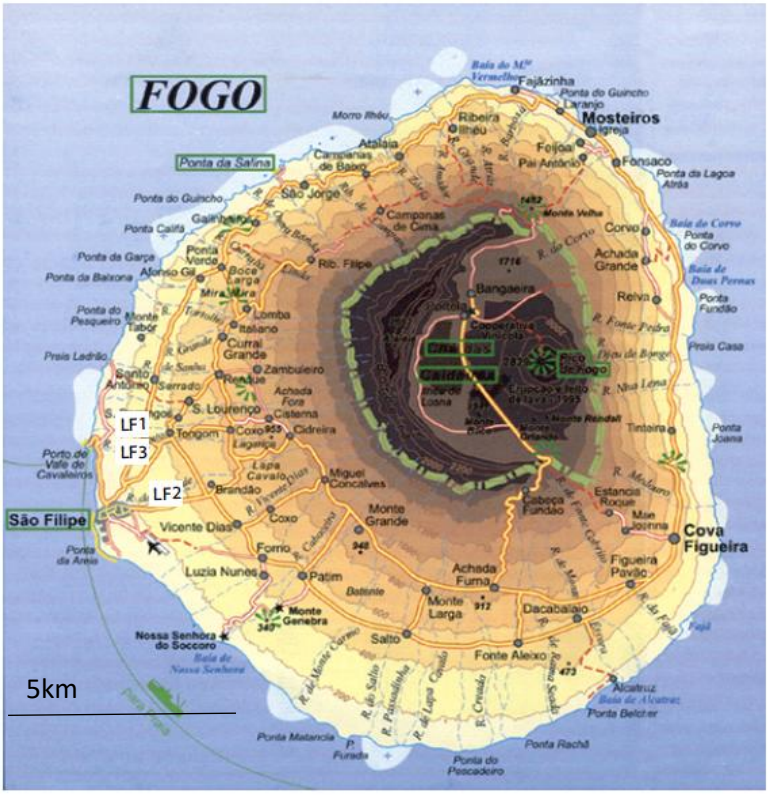

Fig 4.1 Map of Fogo Island showing carbonatite outcrops (LF1 = Ribeira de Almada, LF2 = Ribeira Santo Domingo and LF3 Monte Almada) from which samples were collected.

Although the carbonatites have been investigated for K-Ar dating (Madeira et al., 2005), noble gas and carbon isotope signatures (Mata et al., 2010), radiogenic and oxygen isotope values and bulk rock geochemistry (Hoernle et al., 2002; Doucelance et al., 2010), rare metal mineralisation (Kogarko et al., 2009) and even palaeoweathering (Marques et al., 2020), no detailed study has yet been made of their mineralogy and petrology.

Petrographic observations and mineral chemistry including trace elements determined by LA-ICP-MS are presented in this chapter. Since the carbonatites were emplaced within the seamount before the island emerged above sea-level (Day et al., 1999), particular importance will be placed on determining which minerals are primary and which are secondary. This chapter will show that the Fogo carbonatites had a long history including magmatic crystallisation, immiscibility between carbonatite melts and evolved Si-undersaturated alkaline melts, fenitisation under hydrothermal conditions, and late-stage haematisation.

4.2 Location of the Fogo carbonatite samples

Three locations in the west of Fogo provided samples of intrusive carbonatite and associated rocks. There is no evidence for intrusive carbonatites elsewhere on the island, including among the abundant xenoliths brought to the surface in shield stage lava flows. Ten representative samples analysed by microprobe are included here and detailed information and descriptions of the 24 samples are provided in the appendix.

The Ribeira de Almada site (originally called LF1) (Grid reference: 14.55.62N, 24.29.55W) displays brecciated blocks of carbonatite, glimmerite, ijolite and syenite cut by fine-grained green dykes. Samples 08SF01 to 08SF09 were collected here (Figure 4.2a). They were quite fresh due to recent quarrying. The second location was 0.5 km south of the Ribeira de Almada location, and lies south of Monte Almada (14.55.06N, 24.29.17W). It will be referred to here as “Monte Almada”, but was originally called LF3. It contained two sub-sites, the first (from which coarse-grained carbonatite samples 08SF61and 08SF62 were obtained) was at the top of the hill, north of the valley where the second site was situated (Figures 4.2b). The second site, in the valley bottom (outcrop approximately 30m x 30m in size) (14.55.05N, 24.29.17W), exposed fairly fresh and white carbonatites. This outcrop is cut by several basic green dykes. The carbonatite is composed of distinct layers of two rock-types, which alternate on a mm to cm scale. The

white-greyish layers are thicker and composed of coarse-grained calcite. The silicate-rich layers are thin, dark and rich in fine-grained pyroxene and amphibole with some feldspar. The thin silicate-rich layers enclose the thick calcite-rich layers and both parts show evidence of plastic deformation, cross-cutting and slight folding. Four samples were collected here (08SF63 to 08SF66 – the latter being from one of the pyroxene-rich layers). The third location is in Ribeira Domingo Santo (14.53.59N, 24.28.45W) about 2 km south of the other two locations. It provided samples 08SF51 to 08SF60, which are more weathered and stained by iron oxides with fewer mafic minerals (Figure 4.2c). The numbering of locations L1, L2 and L3 is due to the order of visiting the sites during fieldwork, although it was later understood that L1 and L3 belong to the same site.

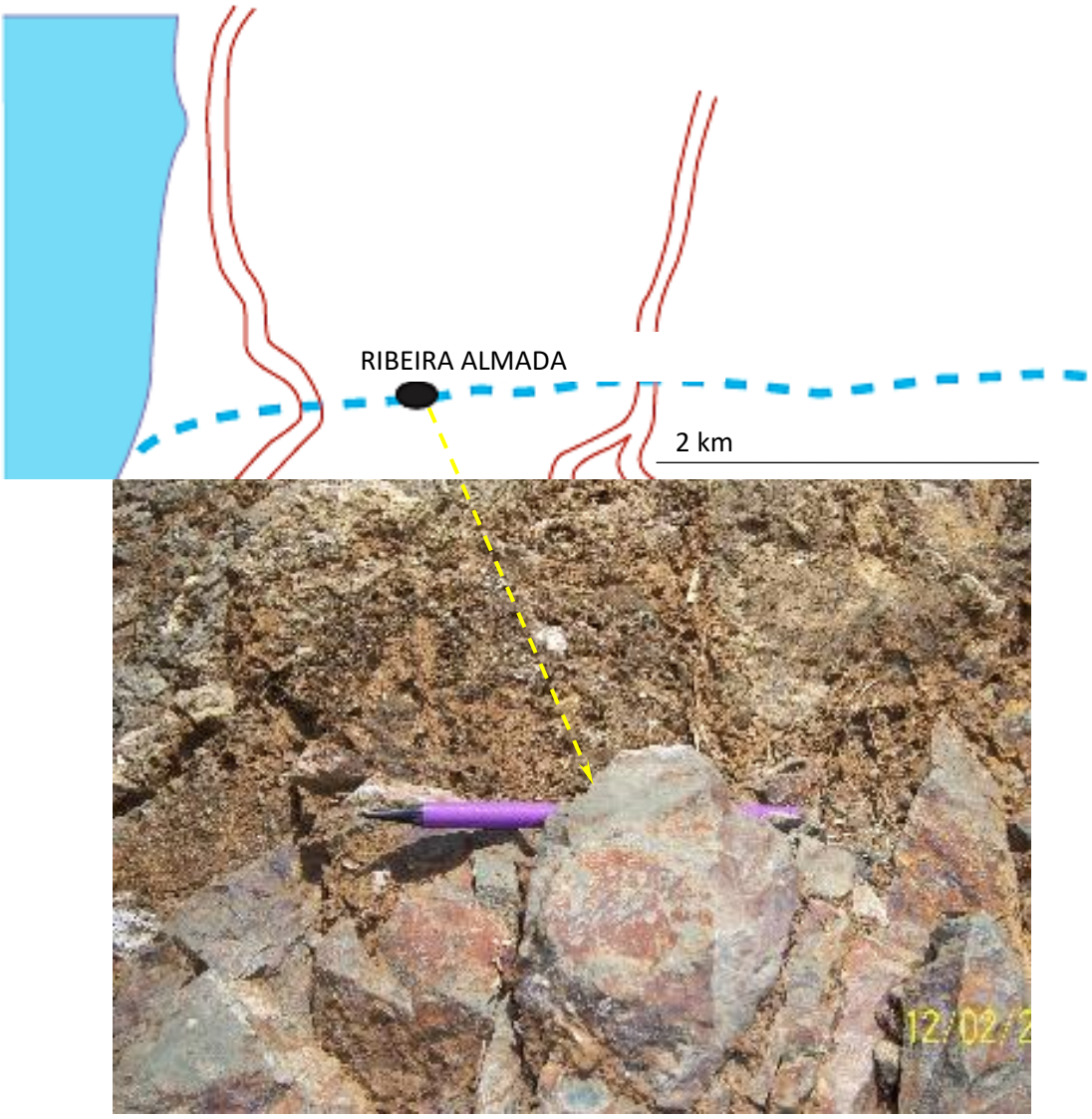

Fig 4.2a Location of LF1, Ribeira de Almada, showing picture of outcrop where samples of intrusive carbonatite has been collected samples from 08SF01 to 08SF09 of which SF01, SF03, SF05 and SF07 were analysed by electron microprobe.

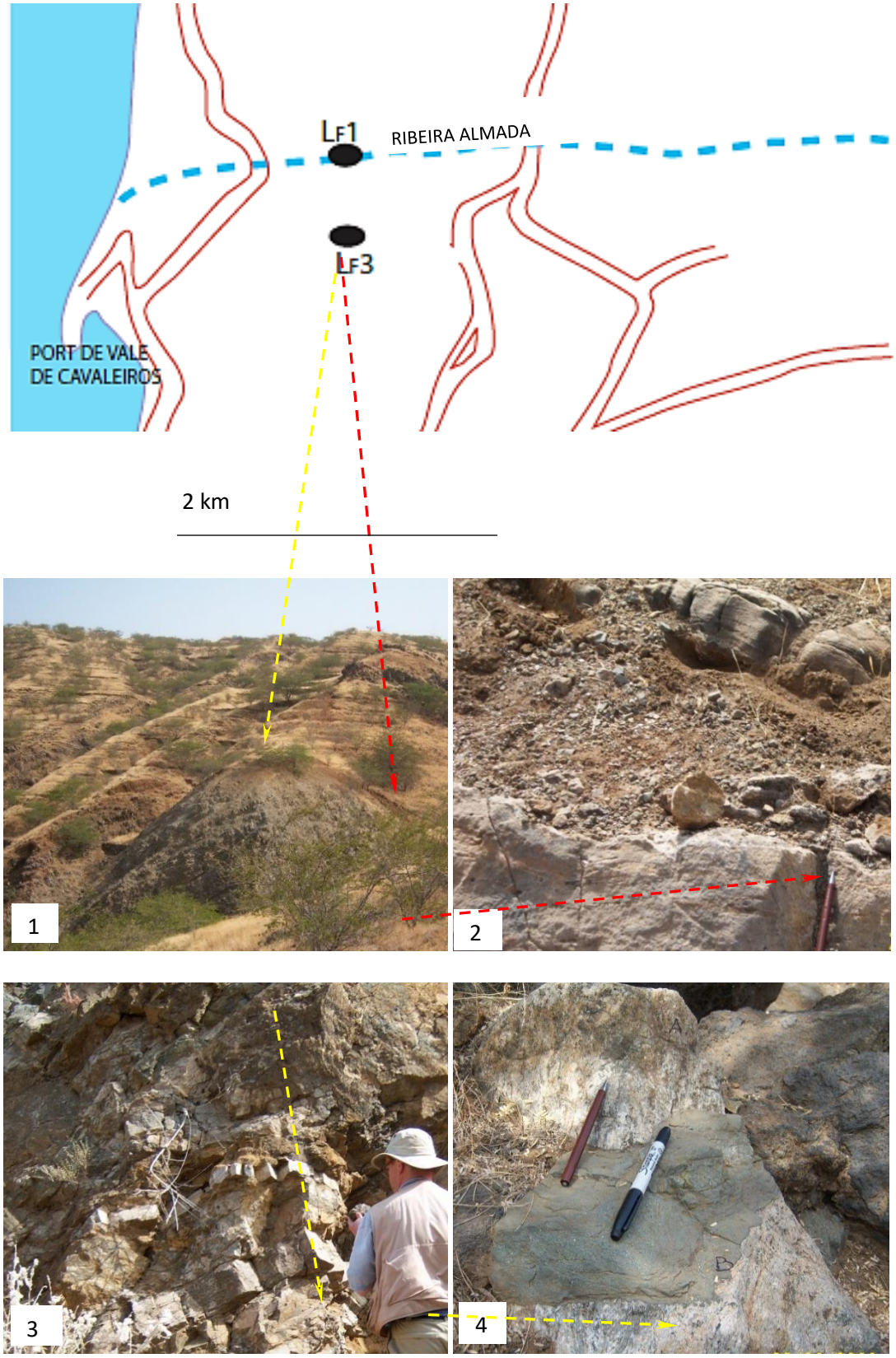

Fig 4.2b Location LF3, south of Monte Almada, is divided into two parts: the first one is the summit of the hill with coarse-grained sövite (pictures 1and 2) from which samples 08SF61and 08SF62 were obtained and thin-sections made; the second one is situated at the bottom of the valley (pictures 3 and 4) from which samples were collected and thin-section 08SF63, 08SF64, 08SF65 and 08SF66 were made.

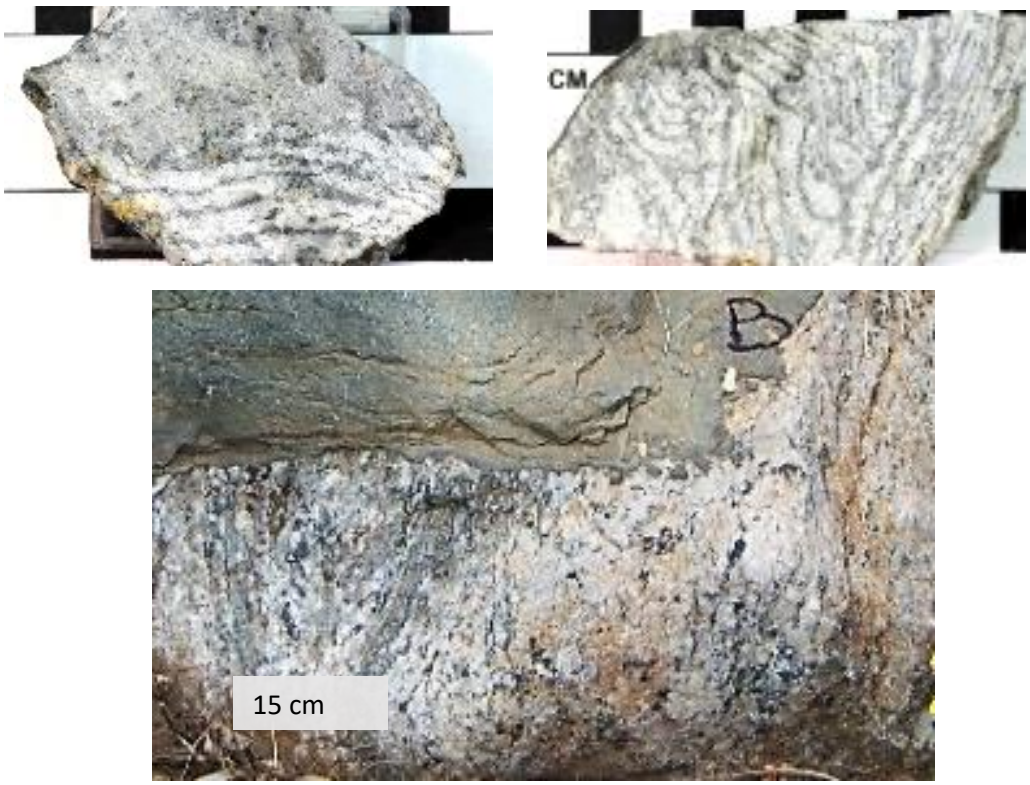

Fig 4.2b Texture of 08SF65 carbonatite with banding of two alternating layers: calcite-rich rimed by silica-rich. Lower picture shows association of sample with the cross-cutting mafic dyke on larger scale.

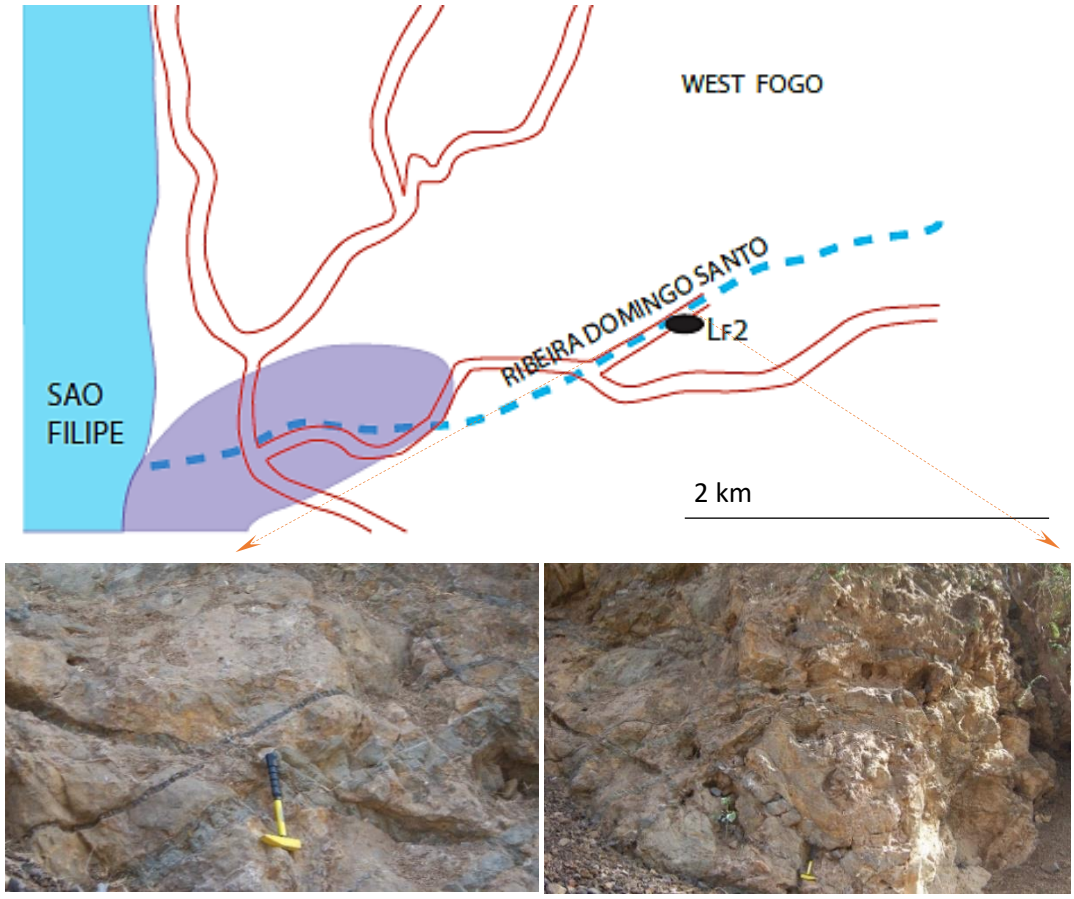

Fig 4.2c Locations LF2, Ribeira Domingo Santo, with pictures of outcrops from intrusive carbonatite where samples were collected, samples from 08SF51 to 08SF60 of which SF51, SF52, SF55 were analysed by electron microprobe.

4.3 Petrography of Fogo samples

Fogo carbonatite samples are mostly sövites and alvikites. They are silica-rich due to the presence of biotite, pyroxene, minor amphibole and rare feldspar. Accessory minerals include magnetite, titaniferous magnetite, titanite, Ti-rich garnet, zirconolite, zircon and other Ti-Zr-Nb-rich phases. The mineralogical assemblage for each section is summarised in Table 4.1 and whole-slide images are shown in Fig. 4.3. All investigated samples from Fogo are shown in Table 4.3.1a (Appendix) which also contains location with grid references, pictures of outcrops and collected hand specimens together with their brief descriptions, and scanned thin-sections with more detailed descriptions. One sample (08SF66 in appendix) is very rich in pyroxene and associated silicate phases with subordinate calcite; thus, it is a calcite-bearing pyroxenite. The coarse-grained nature of these rocks is reflected in the irregular modal distribution of calcite and silicate phases. Hand specimens and thin-sections show uneven concentrations of silica-rich areas, such as glimmerite, pyroxene/amphibole-rich, and regions rich in calcite and apatite. There is a difference between Rib. de Almada / Monte Almada and the Rib. Domingo Santo site. The latter contain rare fine-grained anhedral biotite set in even finer-grained carbonate groundmass. Rib. de Almada and Monte Almada locations have more abundant mica, forming coarser grained crystals often associated with other silicate minerals and apatite. Samples from Rib. de Almada and Monte Almada locations are considered together in the following description.

The Rib. de Almada samples are examples of the carbonatite-glimmerite association (Fig. 4.3a-g). Calcite has recrystallised to a granoblastic form with large crystals (up to 0.5cm) commonly exhibiting 120° triple junctions. The second dominant phase is apatite, which occurs as small (2-3 mm) crystals, often forming domains around large calcite crystals or silicate minerals. Subordinate silicates include biotite, pyroxene, amphibole and feldspar (Fig. 4.3a-n). Monte Almada provided mostly silica-rich sövites containing pyroxene, minor amphibole, biotite, feldspars, feldspathoids and zeolites (Fig. 4.3a-n), and the calcite-bearing pyroxenite. The Rib. de Almada sövite samples exhibit a coarse-grained texture with large calcite crystals (modal estimate 60-90%) often encircled by trails of apatite (formed before the hopper crystals), occasionally by pyroxene and also recrystallised granoblastic calcite (Fig. 4.3). Apatite concentration varies from 5 to 15%. Biotite occurs as both large porphyroclasts and a smaller second generation. Formation of hematite-rich net-veining and veinlets containing drusy rhombohedral calcite in 08SF03 (Fig. 4.3) is evidence of late-stage fluid circulation.

Sample:	LF1: 08SF01	LF1: 08SF03	LF1: 08SF07	LF2: 08SF51	LF2: 08SF52	LF2: 08SF55	LF3: 08SF62A	LF3: 08SF64A	LF3: 08SF65	LF3: 08SF66
Rock type	Mica-rich sövite	Silicate-rich sövite	Silicate-rich sövite	alvikite	alvikite	Highly hematised alvikite	Silica-rich sövite	Silicate-bearing sövite	Fenitic sövite	Calcite-bearing pyroxenite
Reference	GPS: 14 55.62 24 29.55			Grid: EAP 1979 07700 16486			Grid: EAP 1979 07690 16507			
Mineral phase:										
Calcite	abundant	abundant	abundant	abundant	abundant	abundant	abundant	abundant	abundant	fairly abundant
Apatite	abundant	abundant	fairly abundant	fairly abundant	minor	minor	minor	fairly abundant	abundant	fairly abundant
Plagioclase	n/p	n/p	minor	n/p	n/p	n/p	minor	n/p	n/p	n/p
K-feldspar	n/p	n/p	n/p	n/p	n/p	n/p	minor	n/p	fairy abundant	fairly abundant
Feldspathoid	n/p	n/p	minor	n/p	n/p	n/p	n/p	minor	n/p	fairly abundant
Pyroxene	n/p	fairly abundant	fairly abundant	n/p	n/p	rare	fairly abundant	minor	minor	very abundant
Titanite	n/p	fairly abundant	n/p	n/p	n/p	n/p	n/p	minor	minor	very rare
Magnetite	fairly abundant	minor	minor	fairly abundant	fairly abundant	abundant	n/p	minor	rare	minor
Ti-magnetite	n/p	minor	minor	n/p	n/p	n/p	fairly abundant	minor	n/p	minor
Melanite	n/p	n/p	n/p	n/p	n/p	n/p	n/p	minor	minor	minor
Ti-andradite	n/p	n/p	n/p	n/p	n/p	n/p	n/p	n/p	n/p	minor
Biotite/Phg	abundant	minor	n/p	rare	rare	rare	minor	minor	rare	minor
Zircon	minor	minor	n/p	n/p	n/p	n/p	n/p	n/p	n/p	n/p
Amphibole	n/p	n/p	n/p	n/p	n/p	n/p	n/p	minor	minor	minor
Zirconolite	n/p	minor	n/p	n/p	n/p	n/p	n/p	n/p	n/p	n/p
Monazite	n/p	n/p	n/p	rare	rare	rare	n/p	n/p	n/p	n/p
Pyrochlore	n/p	rare	n/p	n/p	n/p	n/p	n/p	n/p	n/p	n/p
Ferrihollandite	n/p	n/p	n/p	n/p	n/p	rare	n/p	n/p	n/p	n/p
Zeolite	n/p	n/p	minor	n/p	n/p	n/p	n/p	fairly abundant	minor	n/p

Table 4.1 Analysed intrusive carbonatites samples from localities from Fogo, Cape Verde. Sövite is a coarse-grained calcio-carbonatite, alvikite is fine-grained calcio-carbonatite. N/p stands for not present in analysed thin section, rare means present up to 1wt%, minor stands for being present up to 5 wt%.

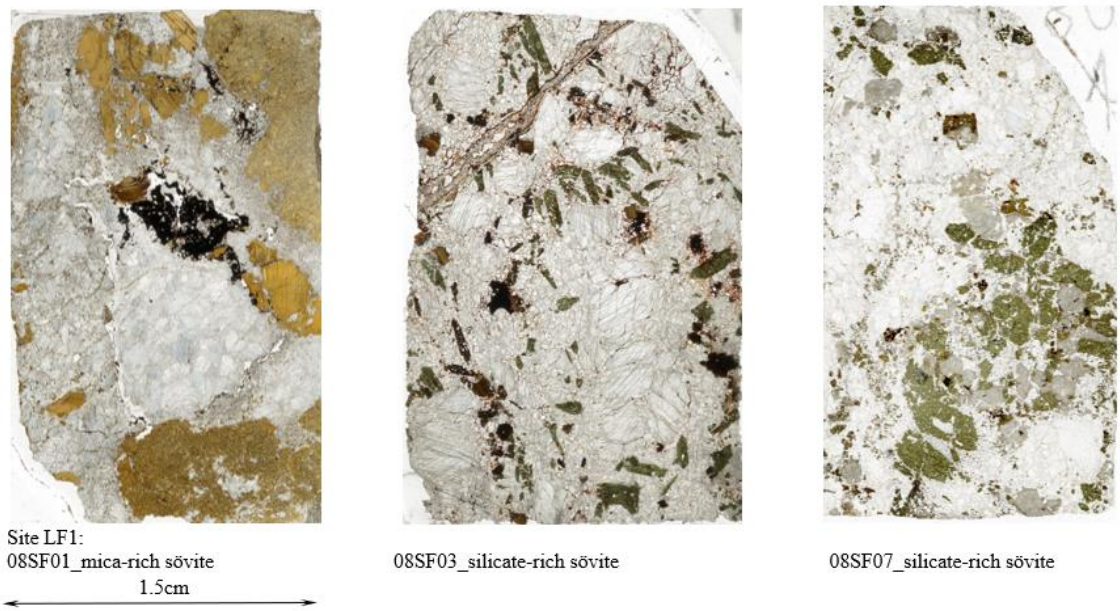

Figure 4.4a. Scanned images of thin-sections of LF1 (Rib. de Almada) Fogo carbonatite samples, showing distribution of minerasl (colourless/pinkish = calcite and some subordinate apatite; coloured ferromagnesian phases like biotite and amphibole; black oxides. In parts heavily stained by iron oxide. The 1.5 cm scale applies to all thin-sections.

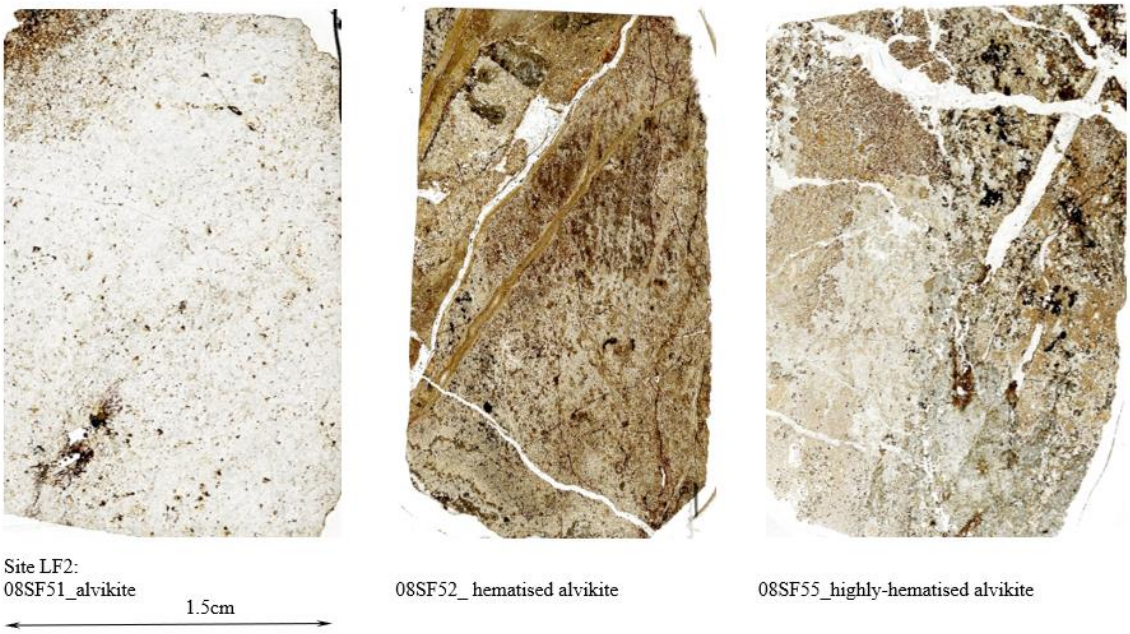

Figure 4.4b. Scanned images of thin-sections of LF2 (Rib. Domingo Santo) Fogo carbonatite samples, showing distribution of minerals (colourless/pinkish = calcite and some subordinate apatite; coloured ferromagnesian phases like biotite and amphibole; black oxides. In parts heavily stained by iron oxide. The 1.5 cm scale applies to all thin-sections.

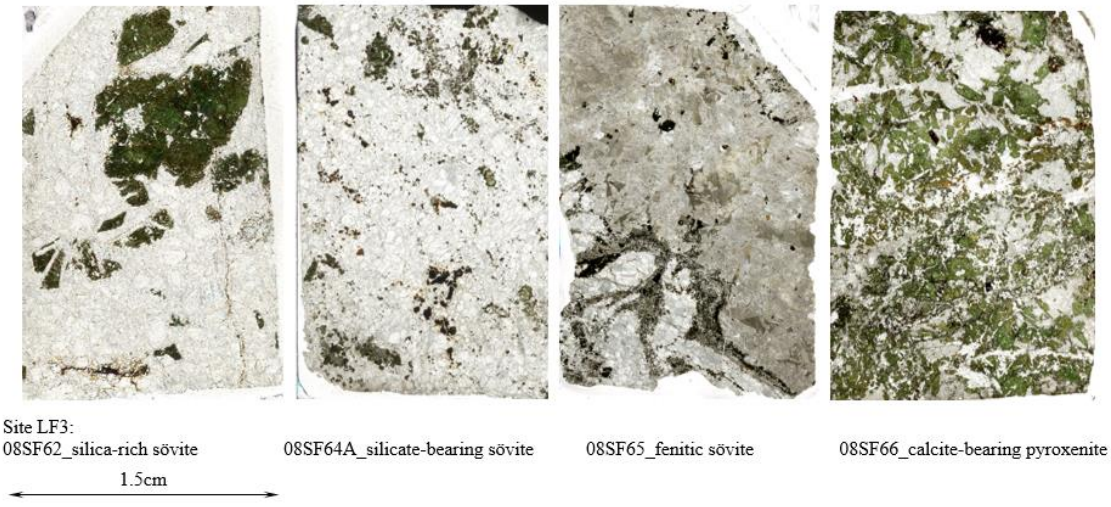

Figure 4.4c. Scanned images of thin-sections of LF3 (Monte Almada) Fogo carbonatite samples, showing distribution of minerasl (colourless/pinkish = calcite and some subordinate apatite; coloured ferromagnesian phases like biotite and amphibole; black oxides. In parts heavily stained by iron oxide. The 1.5 cm scale applies to all thin-sections.

Sample 08SF01 from Rib. de Almada has the highest concentration of mica (40-50%, Table 4.1). Inhomogeneity is demonstrated by formation of two distinct parts: one is mica-rich (with minor amounts of apatite) and the other is calcite-rich (with more apatite). Figure 4.4a shows calcite and mica varying from fine to coarse grained. Sometimes the contact between very coarse calcite and the finer one is separated by thin trail of “twisted”, elongated and fractured apatite. Thus, it is a glimmerite-carbonatite

rock and differs from other samples because of the lack of inclusions of calcite within mica; the mica concentrated separately from the carbonatite; areas with coarse-grained mica or fine-grained glimmerite separated by calcite-rich regions; predominantly monomineralic ultramafic silicate composition; highly deformed mica crystals. Biotite and phlogopite also vary in size from fine-grained to coarse-grained. They show slight chemical differences between the larger singular crystals (akin to biotite) and small glimmeritic mica (phlogopite). The glimmeritic regions contain fine-grained twisted, strained and broken crystals with small amounts of apatite and scarce calcite. The second form is coarse phlogopitic biotite, which shows straining or kinking. Both texture indicates deformation. Inclusions are not seen in the fine-grained mica but apatite inclusions are occasionally found in the coarse phlogopite.

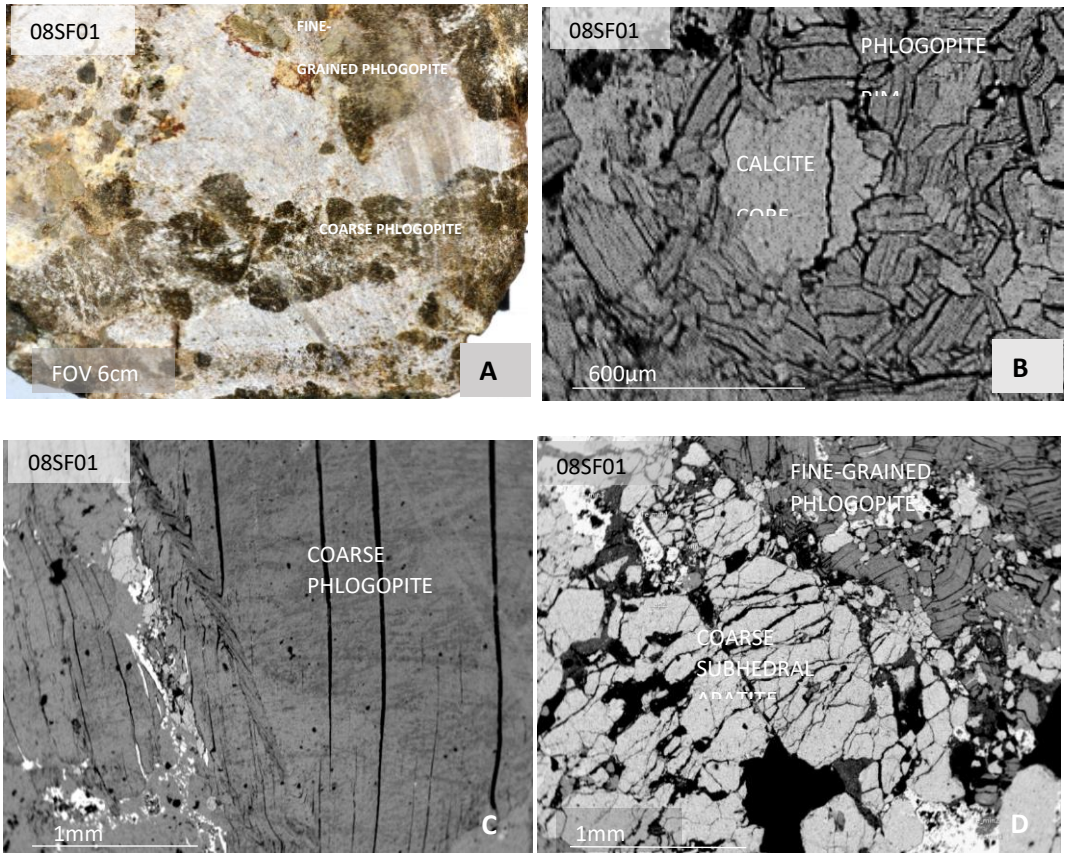

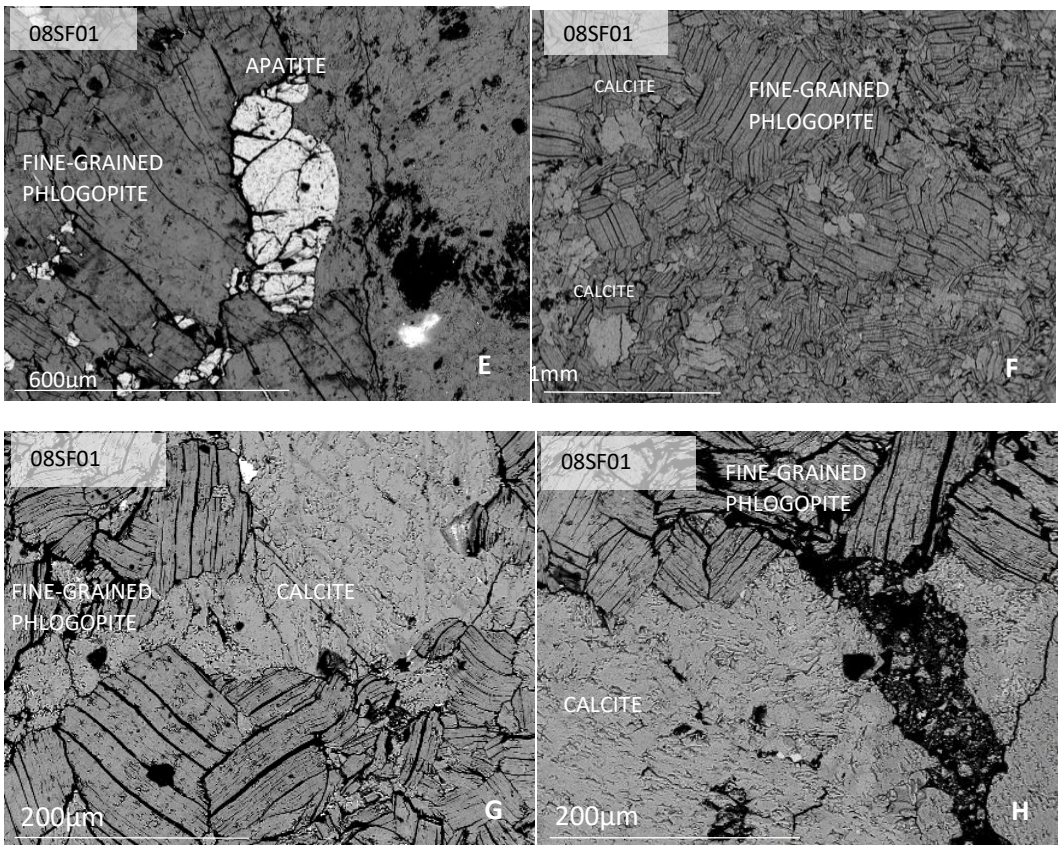

Fig. 4.4 A) Photomicrograph image of 08SF01 sample displaying photograph of hand specimen showing distinct banding (FOV 6cm) with enclave of fine-grained mica and coarse-grained mica; B) BSE image of ocelli-like features in glimmerite-rich part having carbonate core showing embayed edges (FOV 1mm); C) BSE image showing coarse kinked phlogopite with rare apatite inclusion; D) Coarse-grained apatite bordering glimmerite area; E) Small anhedral apatite in glimmerite; F) Texture of glimmerite region; G) Calcite spreading into glimmeritic area; H) V-shaped mica arrangement on the calcite-glimmerite border.

Rib. de Almada samples contain fractured subhedral to anhedral unzoned apatite microphenocrysts. Apatite sometimes contains inclusions of anhedral calcite, thus it crystallised early, just after calcite. Sample 08SF06 (appendix) displays a vein rich in small circular apatite crystals with hollow centres or calcite infills. As all crystals are thin, hollow and elongated, they are interpreted as hopper crystals.

Biotite and phlogopite vary in size ranging from fine-grained to coarse-grained in all samples (Fig. 4.5). There are areas where some fine-grained aggregates are present and developed glimmerite-rich regions, though in 08SF01 micas are forming subhedral and overall singular crystals of biotite often associated with apatite. Overall micas are inclusion-free though rare inclusions of calcite and apatite can be found in some samples.

Clinopyroxene displays a range of shapes (typically anhedral or subhedral and rarely euhedral) and sizes up to a few mm (Fig. 4.6 and 4.7). Most crystals are fractured. Large euhedral clinopyroxene (modal estimate 15-20% where present) is most commonly idioblastic or porphyroblastic within the matrix of granular apatite and fine-grained

calcite. It contains many calcite and apatite inclusions, so it crystallised late. The prevailing texture is fringing of pyroxene around coarse porphyroclastic calcite in a radiating manner (Fig. 4.6 a and b), while in 08SF07 the fringing involves an intergrowth of pyroxene with primary feldspar. Formation of sub-grains in 08SF03 around large calcite porphyroclasts and development of stress-induced lamellae in calcite sub-grains around prismatic pyroxene was caused by metamorphic deformation modifying the original igneous texture leading to formation of the bands (Fig. 4.7). Consequently, this carbonatite is interpreted to have experienced solid-state transformation and thus developed a gneissose texture.

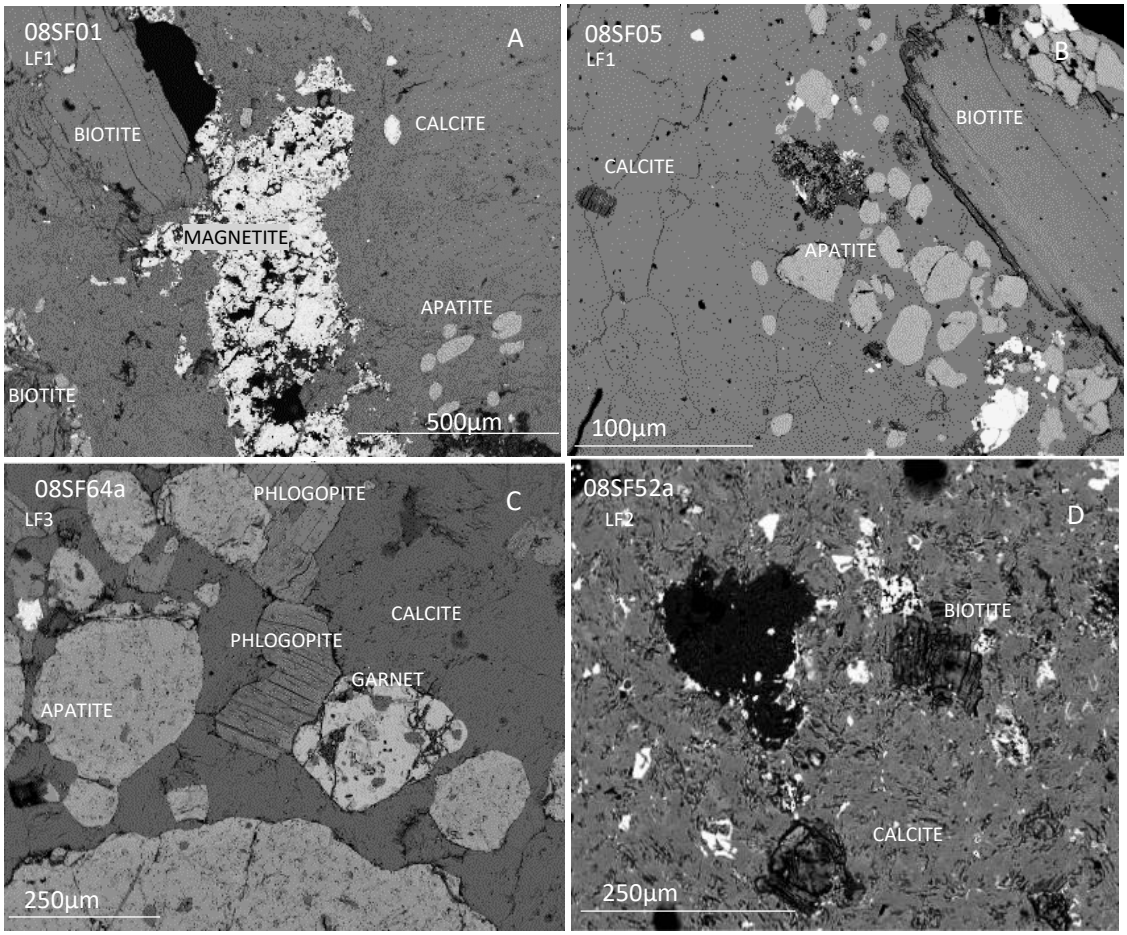

Fig.4.5 BSE images of Fogo samples containing biotite and phlogopite, varying from phenocrystic (B) to fine grained (A, C, D).

Pyroxene shows some alteration with the development of thick black rims and black cleavage lines (Fig. 4.6). Chakhmouradian et al. (2015) analysed a variety of post-magmatic textural variation of carbonatites including exsolution, subsolidus re-equilibration of igneous assemblage, hydrothermal crystallisation, recrystallisation and tectonic mobilisation in accordance with data from multiple localities. It was shown that, at higher temperatures, an onset of dynamic recrystallisation can be recognised by bulging

and migration of grain boundaries, subgrain rotation, formation of abundant small grains fringing porphyroclasts, some of which are seen in the analysed Fogo samples.

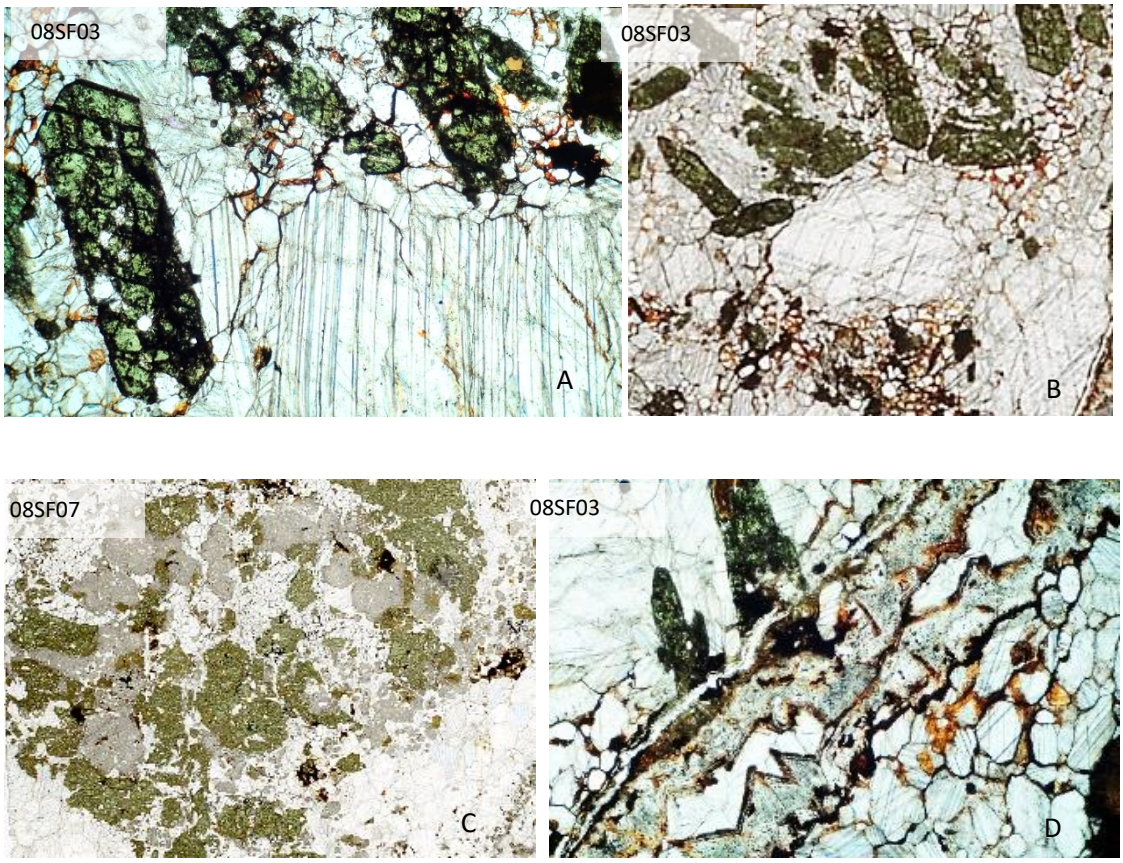

Fig.4.6. Photomicrographs (08SF03: A and D) and scanned thin section (08SF03: A, 08SF07: C) displaying radiating texture of pyroxene around porphyroclastic calcite suggesting some kind of deformation or radiating pyroxene intimately associated with feldspar. D) Secondary vein with rhombohedral calcite. FOV: A=0.25cm, B=0.5cm, C=0.25cm and D=0.15cm.

Slide 08SF03 exhibits a texture comprised of eliptical/rounded areas composed of porphyroclastic calcite rimmed by radiating, mostly euhedral, clinopyroxene (Figure 4.7). Modification of lamellae in small calcite grains encircling protruding pyroxene prisms is most likely associated with subsolidus plastic deformation (Figure 4.7). During this process, formation of a new sets of lamellae in calcite grains rimming the pyroxene occurred and created roughly convex upwards line around the prism (red dotted line in Figure 4.7). Overall pyroxene in 08SF03 is rimmed by clinopyroxene around the round to oval-shaped granoblastic calcite.

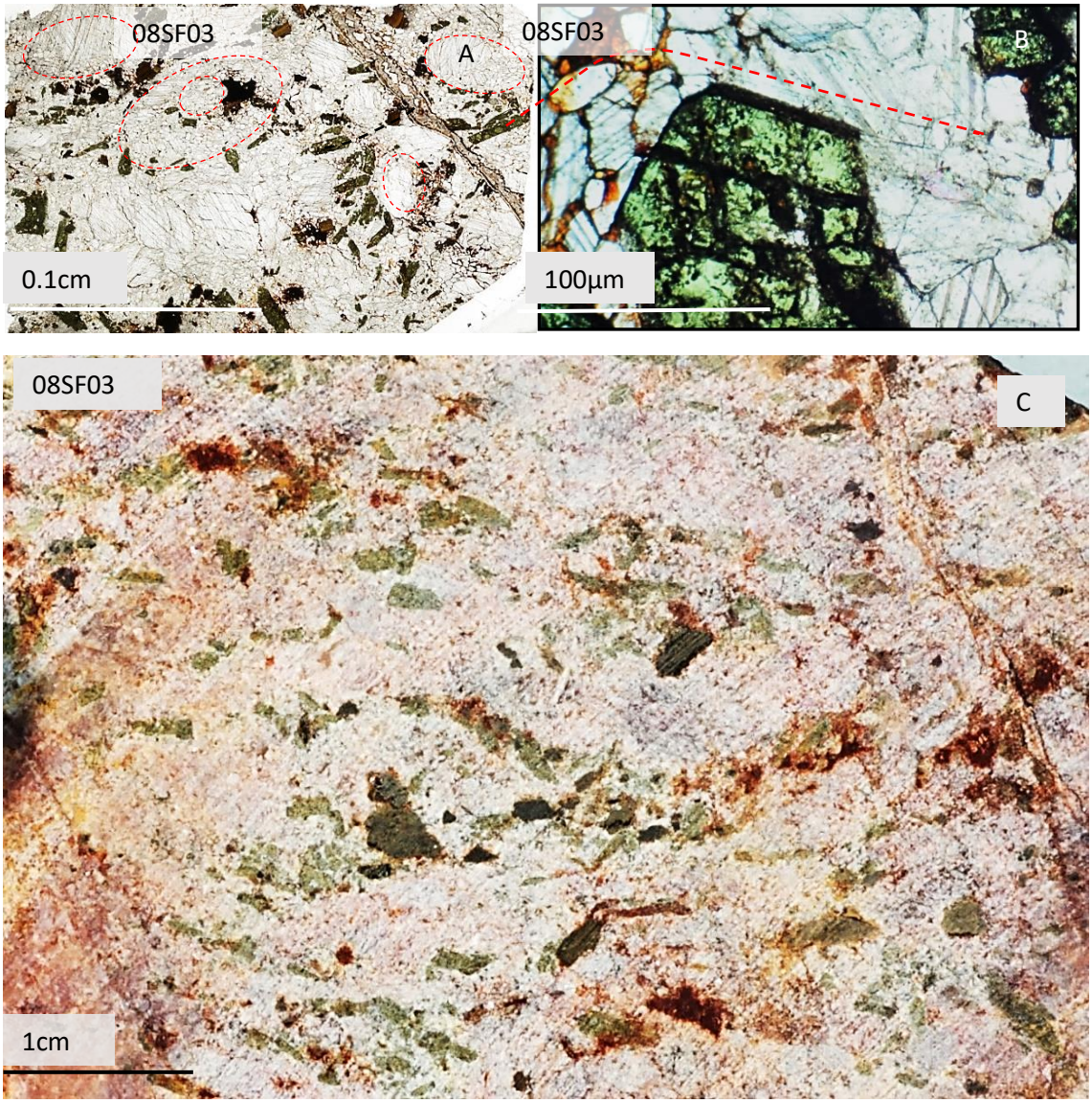

Fig.4.7 Development of gneissose texture in pyroxene-rich sövite in sample 08SF03 shown in thin-section (A and B) and hand specimen (C). Also, development of subsolidus plastic deformation seen in calcite grains (B).

Clinopyroxene displays a range of shapes (though rarely euhedral) and sizes up to few mm (Fig.4.8). Most of the crystals are fractured. In Rib. de Almada and Monte Almada, clinopyroxene looks unstable being highly cross-cut by multiply dark lines, internally having a granular assemblage and closely associated with fine-grained rounded apatite (Fig.4.8). Dark discolouration along the fractures is an alteration product such as zeolite. As in Rib. D. Santo, euhedral pyroxene is frequently linked to the rim of elliptical area of calcic composition. The growth of pyroxene occurs away from the vein which can be observed also on fine scale (Fig.4.8). Evidently the growth of pyroxene started from the veinlet and progressed away from it. Fig 4.8 demonstrates that such growth of pyroxene is common in the Rib. de Almada site. Both Rib. de Almada and Monte Almada

contain complex textures exhibiting rimming of pyroxene by feldspars, feldspathoids and apatite or an intimate association of those phases.

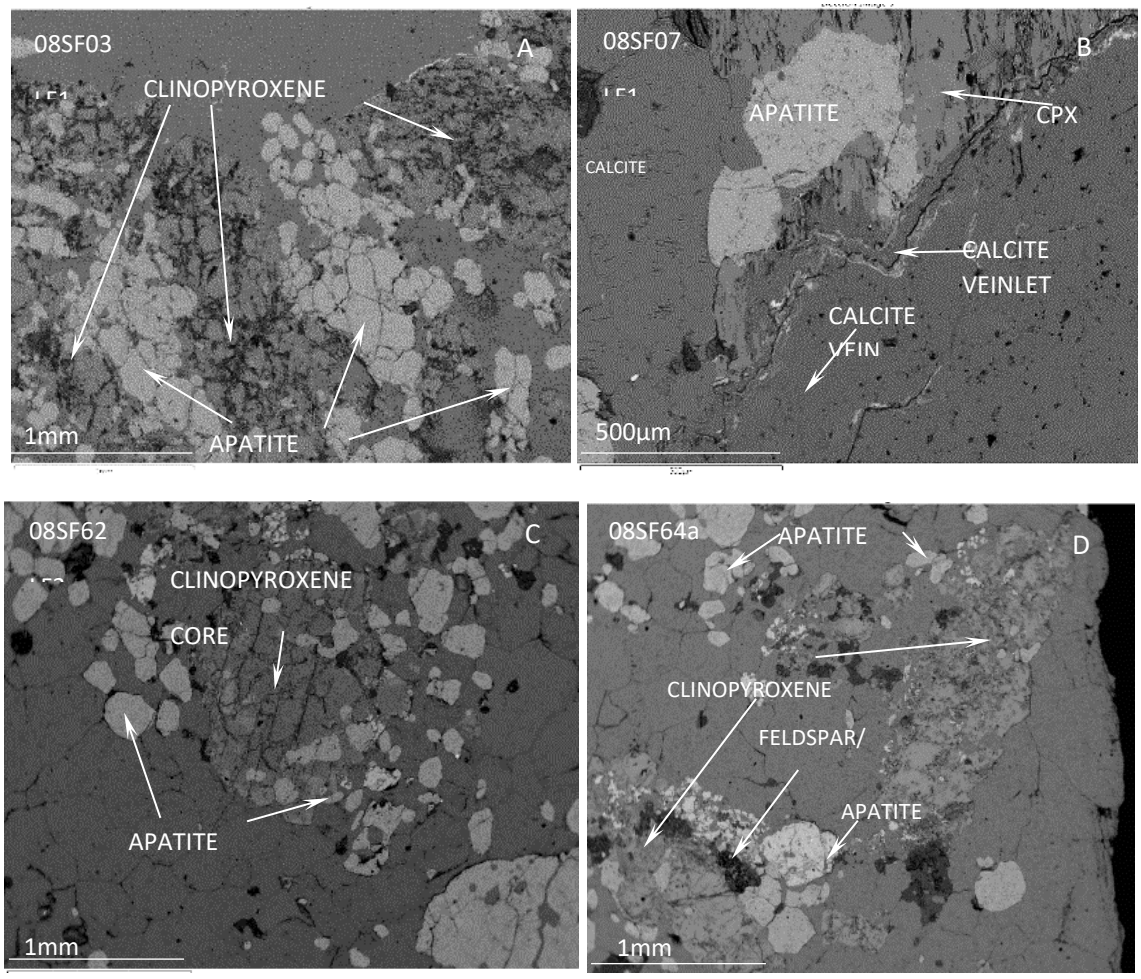

Fig.4.8 Back-scattered electron (BSE) images of the samples from Rib. de Almada and Monte Almada containing clinopyroxene demonstrating mostly anhedral (A, B) and subhedral (C, D) shape. Diopside appears broken up with many irregular cracks being regularly rimmed by granular apatite often associated with feldspar/feldspathoid.

Samples from Monte Almada (Fig.4.9) contain more abundant clinopyroxene than in samples from Rib. D. Santo. Clinopyroxene is euhedral though it is resorbed around the edges and highly fractured internally, showing a dismembered texture with multiple pyroxene grains. Sometimes calcite laths cross-cut pyroxene. It is sometimes associated with granular apatite that has been altered to feldspathoids. Pyroxenes lack zonation and are commonly highly fractured and strongly associated with felsic phases, apatite and calcite. This association implies that pyroxenes exerienced alteration, most likely during post-magmatic processes. The assemblage of pyroxene with associated phases forms an overall rounded to oval appearance.

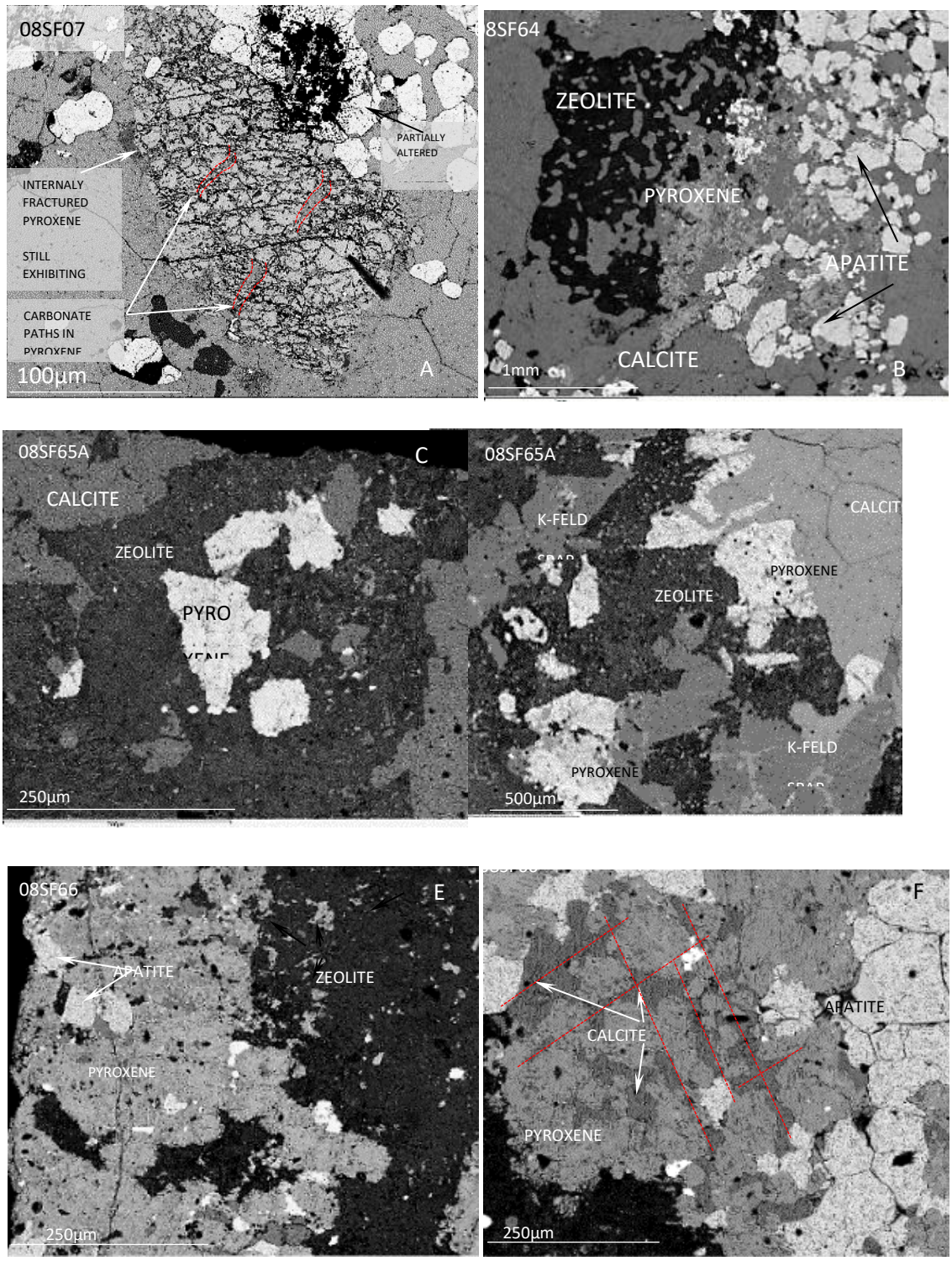

Fig.4.9 Back-scattered electron (BSE) image of 08SF07 sample containing in A) assemblage of calcite, pyroxene, apatite and zeolite (dark area close to the edge of pyroxene is zeolite associated with apatite). Samples from Monte Almada display in 08SF64 (B) calcite holding skeletal pyroxene being bordered by skeletal zeolite and granular apatite; in 08SF65a (C and D) display zeolite holding pyroxene and being bordered by alkali feldspar and in 08SF66 (E) intimate association of pyroxene and zeolite but also (F) pyroxene dismembered to granular subgrains rimmed by calcite (perhaps resorbtion of silicate phase during interaction with carbonatite fluid along the cleavage planes (?)) and it is cross-cut by apatite veinlet.

Rib. de Almada samples contain also rare feldspar crystals (Fig. 4.10). Modal estimation of feldspar and zeolite in 08SF07 is 10%. Compositionally these crystals are

not uniform. They contain mostly K-rich areas (orthoclase) with Na-rich regions which form a turbid texture. Feldspar in 08SF07 contains many calcite inclusions giving a spongy appearance (Fig. 4.10). One feldspar crystal retained its rectangular form but other feldspars (and zeolite) are anhedral, skeletal and have bimodal sizes.

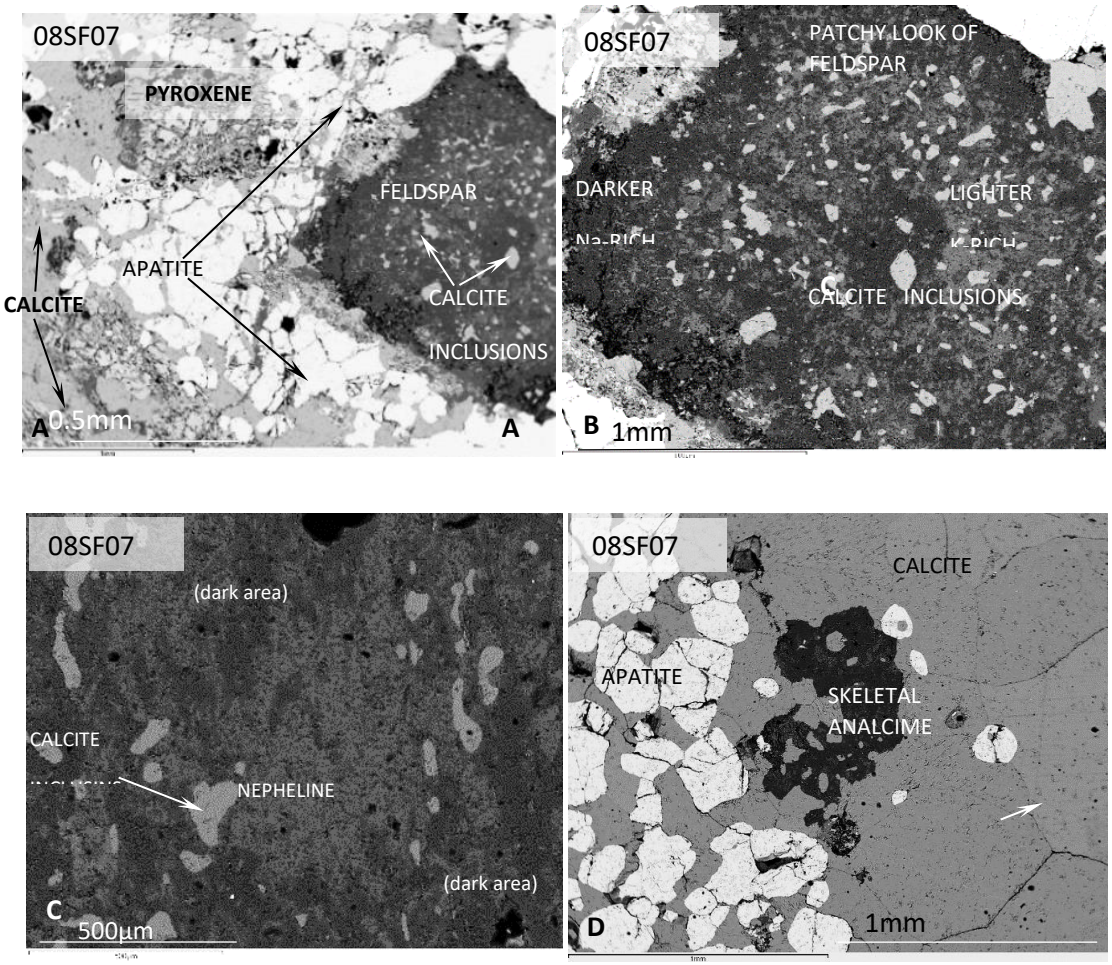

Fig.4.10 Back-scattered electron (BSE) images of 08SF07 sample displaying: A) Assemblage of calcite, apatite, pyroxene and feldspar showing dark areas of sodic composition (distributed close to the edge of feldspar) adjacent to apatite rim and light area of potassic composition (showing spongy dissolution texture containing fine calcite). B) Turbid feldspar with regions Na-rich and K-rich. C) Patchy looking altered feldspar with calcite inclusions. D) Embayed and skeletal patchy zeolite set in granoblastic calcite placed close to trail of anhedral and fractured apatite. E) Anhedral feldspar rimmed by feldspathoid and apatite. F) Fractured pyroxene still retaining euhedral form rimmed by zeolite which is overgrown by fractured apatite.

Associated zeolite and feldspar show first order grey colours: darker grey being Na-rich and lighter is K-rich. The euhedral rectangular feldspar (Figure 4.10) contains Na- and K-rich areas with K-rich region forming the inner part of the crystal while Na-rich part is near the rim. Na-rich rim shows a close association with fine-grained apatite encircling the crystal. Internally feldspar shows spongy dissolution texture (Fig. 4.10). Overall zeolites are anhedral and poikilitic, and always contain inclusions of calcite.

The texture shown in Fig. 4.11 is composed of oval shaped orthoclase rimmed by albite which also encircles a larger circular area containing calcite with a finely scattered orthoclase-albite assemblage. This unusual texture is analogous to rimmed ocelli formed during chemical and thermal disequilibrium during incomplete mixing (mingling) of carbonate and silicate magmas (Moore et al., 2009). Disequilibrium textures were preserved due to swift emplacement as enclaves.

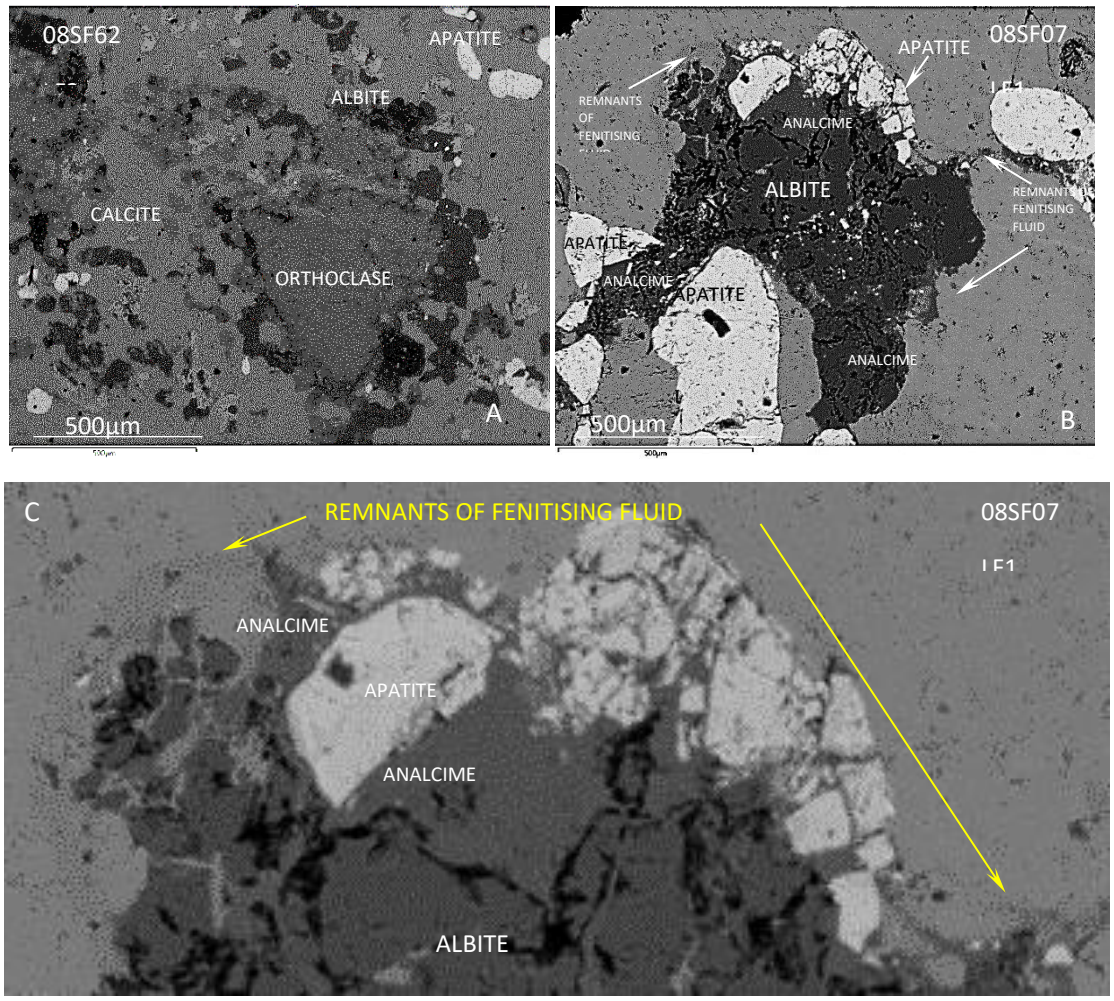

Fig 4.11 BSE images of sample from Monte Almada containing feldspars such as: (A) ocelli-like structure showing fine-grained albite encircling feldspar; (B) where fenitizing fluid flowed around the grain boundary of feldspar altering the rim of albite to feldspathoid and affecting associated apatite by forcing the path through it for analcime (lower left corner) or on fine scale opening many fine paths by dismembering apatite (top part). (C) Enhanced BSE image of 08SF07 displaying grainy areas encircling analcime which are most likely remnants of what was originally fenitising fluid.

Fig.4.11 displays fenitization showing alteration product of analcime around the albite while the central part is preserved. The lower large fractured apatite shows separation into two parts with the space being filled by analcime. The upper fine-grained apatite contains multiple fractures also infilled by analcime, a frequent feature in Fogo carbonatites. This agrees with Elliott et al. (2018) who reported that fenitizing fluids can flow along grain boundaries or/and around mineral cleavage planes (i.e., porous flow).

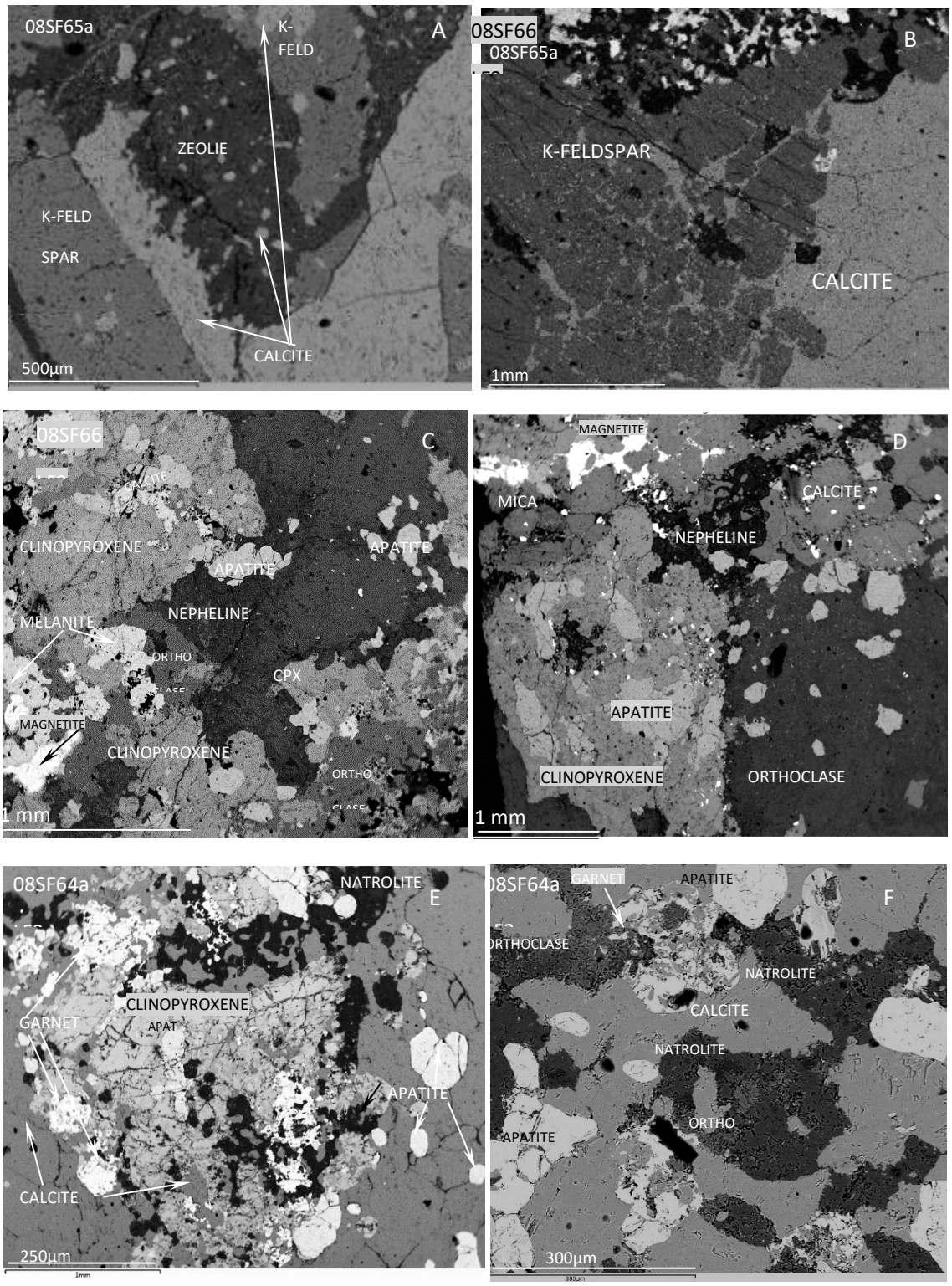

Fig 4.12 Back-scattered electron (BSE) images of the samples from Monte Almada site holding: A) K-feldspar rimming calcite which rims zeolite and k-feldspar both contain small calcite inclusion; B) Braking down K-feldspar associated with calcite which is also infilling the fractures in alakali feldspars; C) Clinopyroxene separated by nepheline-orthoclase contain also minor assemblage of apatite-calcite-garnet; D) Assemblage of pyroxene and orthoclase with minor calcite containing multiply apatite inclusions; E) Granoblastic calcite hosting anhedral and fractured pyroxene being partially infilled by natrolite, clinopyroxene is rimmed by garnet and apatite; E) Natrolite-orthoclase surrounded by calcite which hosting minor garnet and apatite.

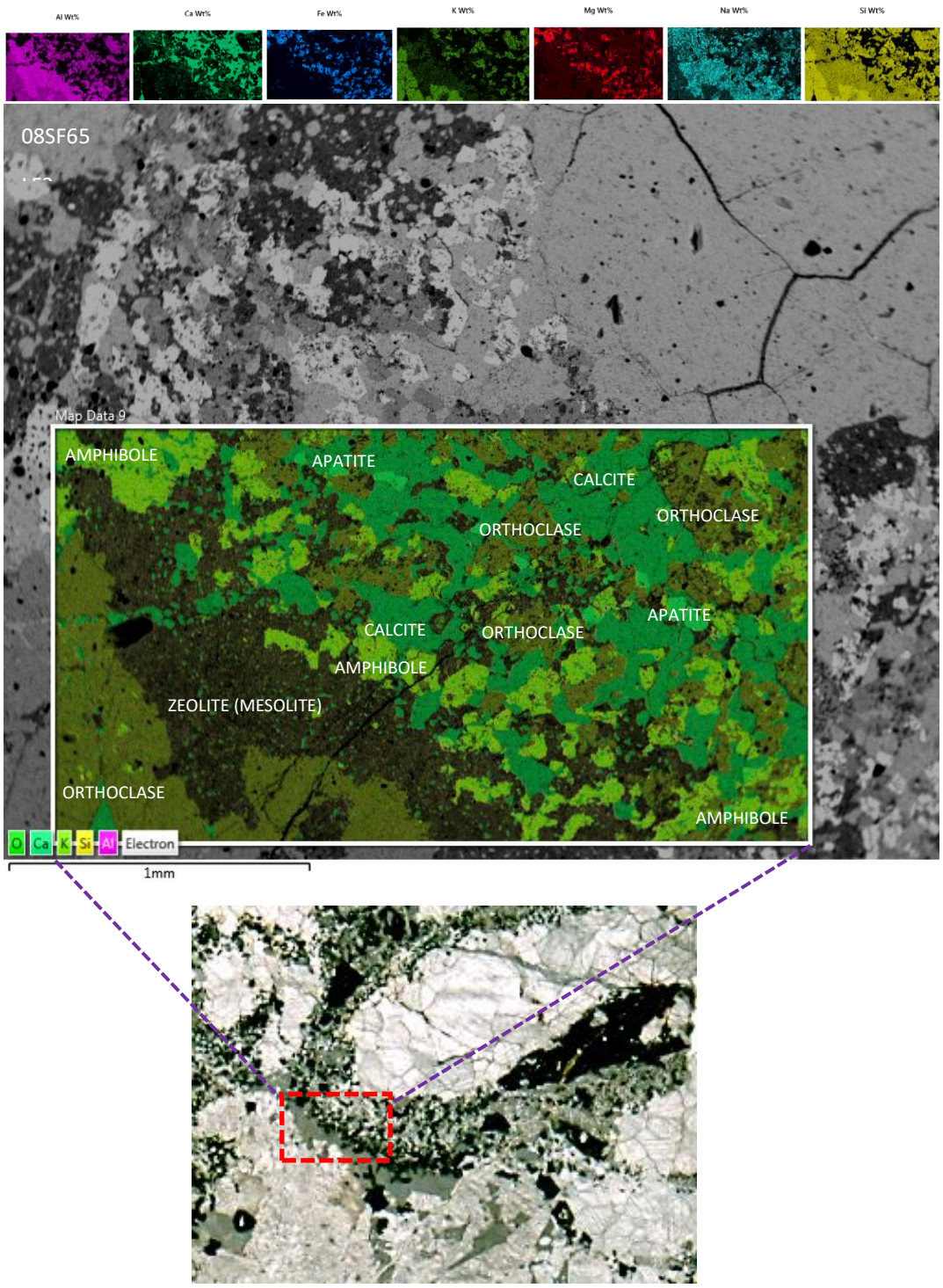

Fig 4.13 BSE image of SF0865 and false-coloured X-Ray map of 08SF65 showing elongated calcic area (calcic finger) rimmed by silicate assemblage such as zeolite-orthoclase-amphibole-apatite-calcite**.**

Feldspathoids and zeolites are present in samples from Monte Almada and are overall more abundant than in those from Rib. de Almada (Figs. 4.11, 4.12, 4.13). Nepheline is found in 08SF66. Zeolites such as natrolite are also present in Monte Almada. Zeolites and feldspathoids are absent in samples from the ridge of Monte Almada, though the lower outcrops contain zeolites. Here nepheline is found alongside

orthoclase though albite is absent. Overall, the complex turbid texture of feldspar, together with assemblage of pyroxene, apatite, garnet and calcite. In Fig.4.11 BSE images of samples from Monte de Almada site show calcite and silicates in 08SF65 and calcite-feldspar-zeolite in 08SF64 (F) by development of calcic areas. The calcic areas form fingers surrounded by silicate-rich rims (Fig.4.12). Textures in sample 08SF64(C) such as clusters of apatite and garnet encircling clinopyroxene, all set in calcite, perhaps indicate a late stage of crystallisation. The skeletal zeolite and pyroxene intergrowing with calcite and granoblastic apatite can be seen in 08SF65A (E). Large granoblastic calcite showing triple junction of 120° is overgrown by euhedral alkali feldspar (Fig.4.12), although the central part contains zeolite and alkali feldspar with small inclusion of calcite. In 08SF66 (C and D) pyroxene appears to be breaking up into smaller grains separated by nepheline or orthoclase with multiple calcite and/or apatite inclusions in pyroxene. Regular round apatite and garnet inclusions also occur in pyroxene in contact with calcite in 08SF64a (E).

In Fig. 4. 14, Monte de Almada section 08SF64 is enriched in apatite clusters with associated titanite set in granoblastic calcite (A) which indicates late-stage crystallisation. Abundant fine-grained apatite inclusions occur in granoblastic calcite with rare titanite (B). Late-forming subhedral garnet set in granoblastic calcite contains many inclusions of rounded calcite and oval apatite (C). Garnet is partially rimmed by zeolite. Skeletal zeolite (D) and skeletal clinopyroxene intergrown with fine-grained apatite are all set in granoblastic calcite. Sample 08SF65a from Monte Almada also contains zeolite though it is not skeletal. In both samples, zeolite is associated with pyroxene. Sample (E) is composed of anhedral zeolite with inclusions of medium grained clinopyroxene with fine-grained calcite and pyroxene, giving it speckled look. Zeolite is surrounded by granoblastic calcite. The second section (F) contains an assemblage of zeolite and alkali feldspar set in large granoblastic calcite showing 120° junctions. Clinopyroxene is also present, overgrown by zeolite and alkali feldspar. K-feldspar varies from euhedral to subhedral. Euhedral orthoclase displays a sharp contact with zeolite. Across the section, the orthoclase-zeolite contact is more complex forming S-shaped border. Zeolite contain multiple anhedral fine to medium grains of clinopyroxene inclusions.

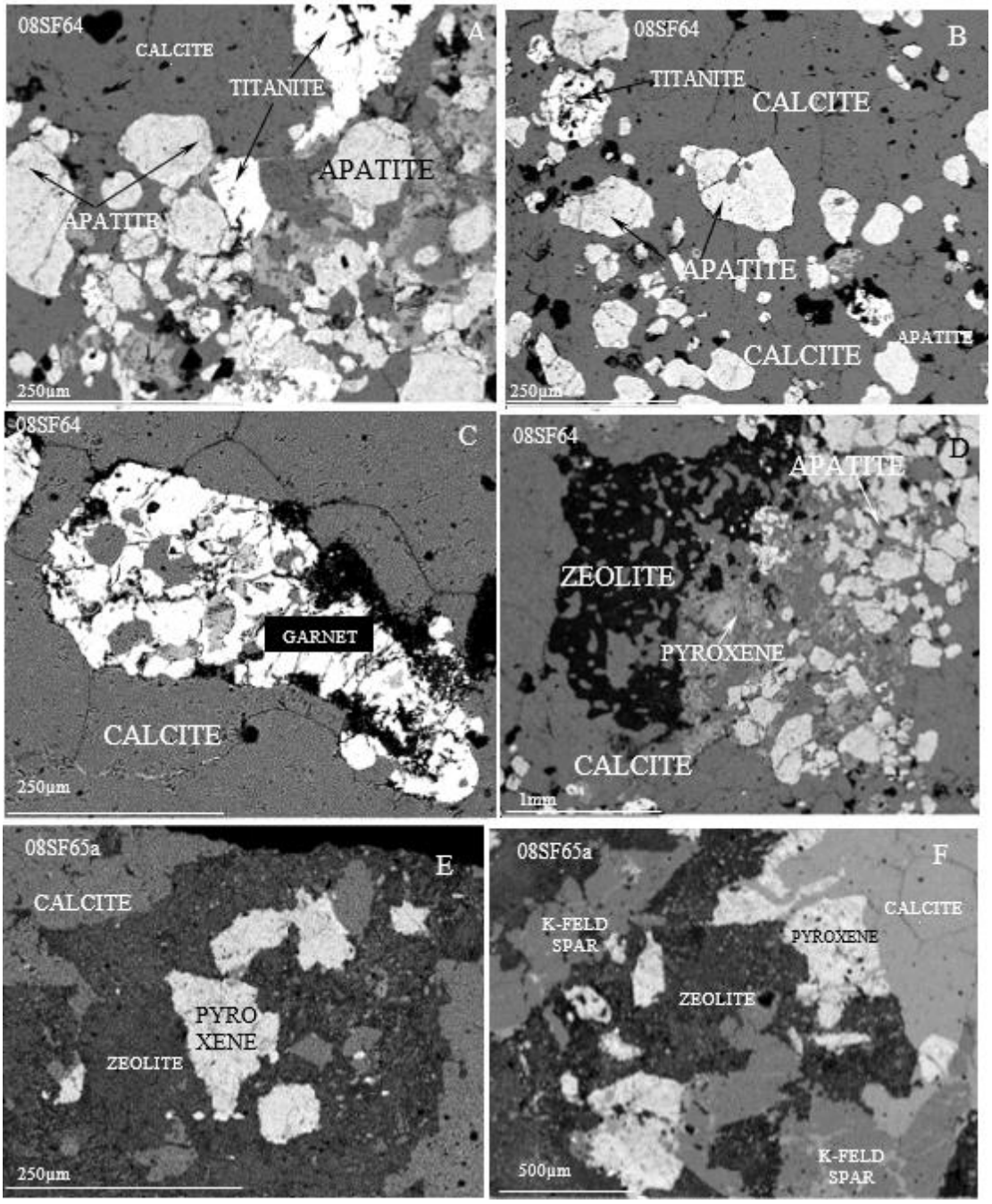

Fig 4.14 Back-scattered electron (BSE) images of samples from Monte de Almada showing calcite and silicates in 08SF64 and 08SF65a. Textures in sample 08SF64: A) Cluster of apatite and titanite in calcite (late stage of crystallization); B) Apatite inclusions in calcite; C) Late-forming garnet with inclusions of calcite and apatite; D) Skeletal zeolite and pyroxene intergrowing with calcite and granoblastic apatite. Sample 08SF65A: E) Zeolite with inclusion of pyroxene surrounded by calcite; F) Large granoblastic calcite showing triple junction of 120º overgrown by pyroxene and zeolite and alkali feldspar.

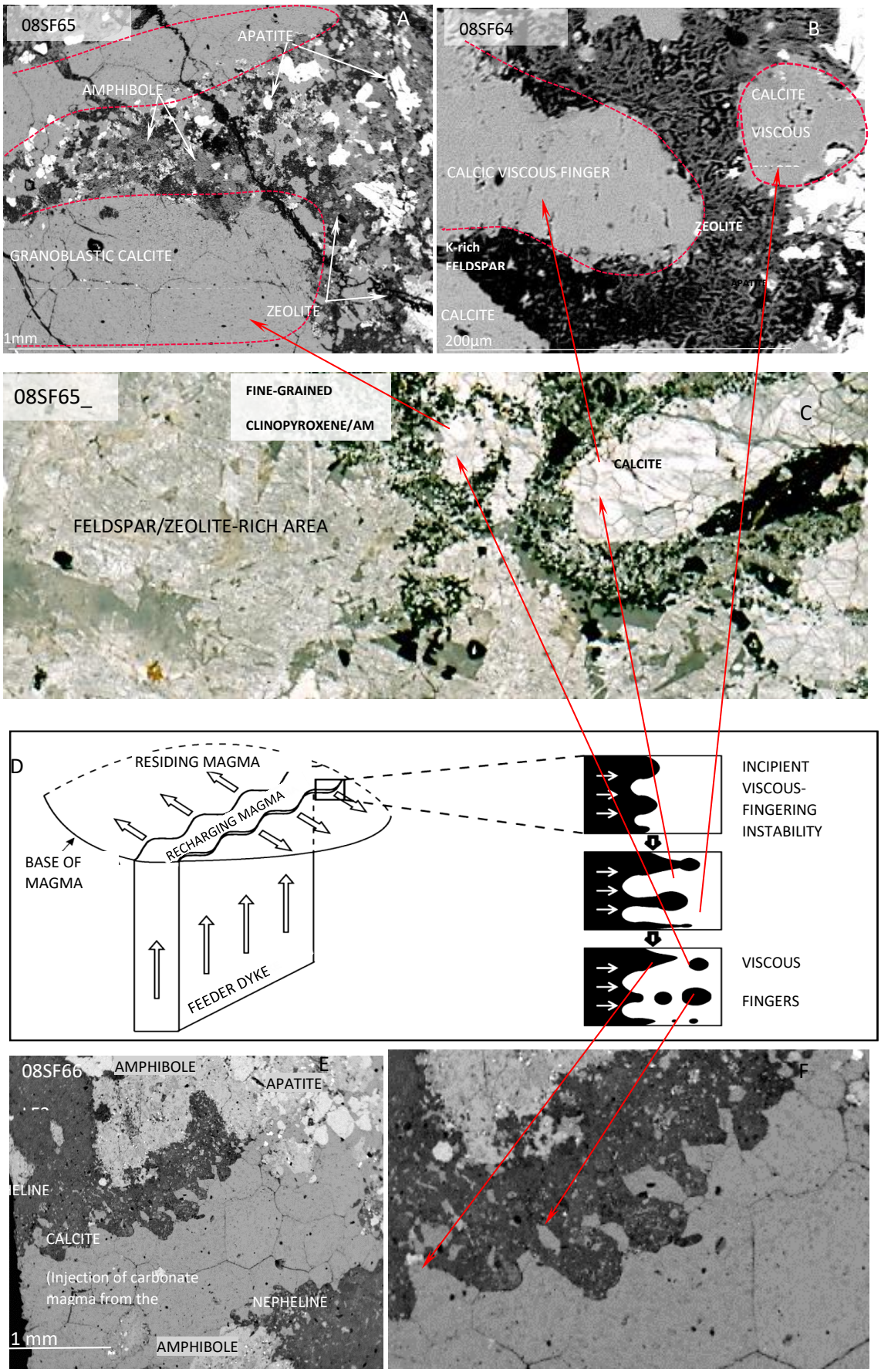

Fig.4.15 Photomicrograph and BSE images taken from the samples 08SF64 and 08SF65 collected in Monte de Almada showing areas such as granoblastic calcite being rimmed by silicate assemblage of amphibole and/or feldspar, feldspathoids with apatite and iron oxide (A, B, C, E and F). Figure D according to Valentini et al. (2010) represents formation of viscous fingering and viscous fingers break-up

Slides 08SF65 and 08SF66 (Figure 4.14) contain an important texture composed of elongated carbonate areas rimmed by feldspar/fedspathoids together with other silicate phases such as clinopyroxene, amphibole, garnet and also apatite. According to Valentini et al. (2010), this texture can be explained by formation and breakup of viscous fingers. Figure 4.15a,b represents incipient viscous-fingering instability and interruption of viscous fingers during the injection of a recharging magma. Fig. 4.15c demonstrates development of this texture on larger scale and Fig. 4.15d,e shows formation of viscous fingers and viscous fingers breakup in great detail. The viscous fingers are of carbonate composition, rimmed by an assemblage of feldspars, feldspathoids, zeolite and Na-silicates indicative of a metasomatic assemblage formed during secondary processes.

Carbonatites from Rib. de Almanda and Monte Almada are rich in pyroxene, amphibole, biotite and feldspars so they are silica-rich sövites. They also contain apatite, garnet, titanite, zircon and zirconolite (Fig. 4.16). Zirconolite is found in sövite 08SF03. It is euhedral showing nearly perfectly developed faces although most specimens display fracturing (Fig. 4.16a and b). Cluster of zirconolite crystallised together from one point forming a radiating texture (Fig. 4.16b). Thus, this type of zirconolite is primary. Anhedral zirconolite is present in 08SF03, intimately associated with niobian ilmenite and set in titanite (Fig. 4.16c). Samples from Rib. de Almada show two different titanite textures. One occurs as an anhedral phase intergrown with Nb-Zr minerals (Fig. 4.16c) but, more commonly, titanite is present in euhedral/subhedral form in association with apatite (Ribeira de Almada, Fig. 4.3.11 (a and b)) or melanite is intergrown with apatite, calcite, titanite and pyroxene. Skeletal form involved rapid growth towards the edges enveloping melt at the ends, thus trapping the liquid and crystallising the calcite-apatite-titanite assemblage. Zircon exhibiting skeletal texture is also present in Rib. de Almada samples (Fig. 4.15e and f). Lack of zonation of anhedral zircon is apparent (Fig. 4.16 a and b). Here zircon exhibits skeletal form, intergrown with titanite and apatite. BSE image of zircon associated with glimmerite shows anastomosing veinlets filled with zircon, thus providing passage for mineralising fluid from which secondary zircon crystallised.

Figure 4.17 exhibits a more complex association with titanite-zirconolite-pyrochlore set in phlogopite which is bordered by large calcite crystals and rounded apatite. Mica forms an intimate assemblage with titanite-zirconolite-pyrochlore and zircon, in which mica crystallised prior to zircon. Figure 4.18 summarizes the main petrographic features of accessory pyrochlore, titanite, zirconolite and zircon.

As this assemblage is set mostly in glimmerite and some calcite, mica probably originally provided the passage via anastomosing veinlets and also provided the space (together with calcite) for newly crystallising phases. Mobilized fluid could travel mostly via grain boundary/cleavage planes of mica.

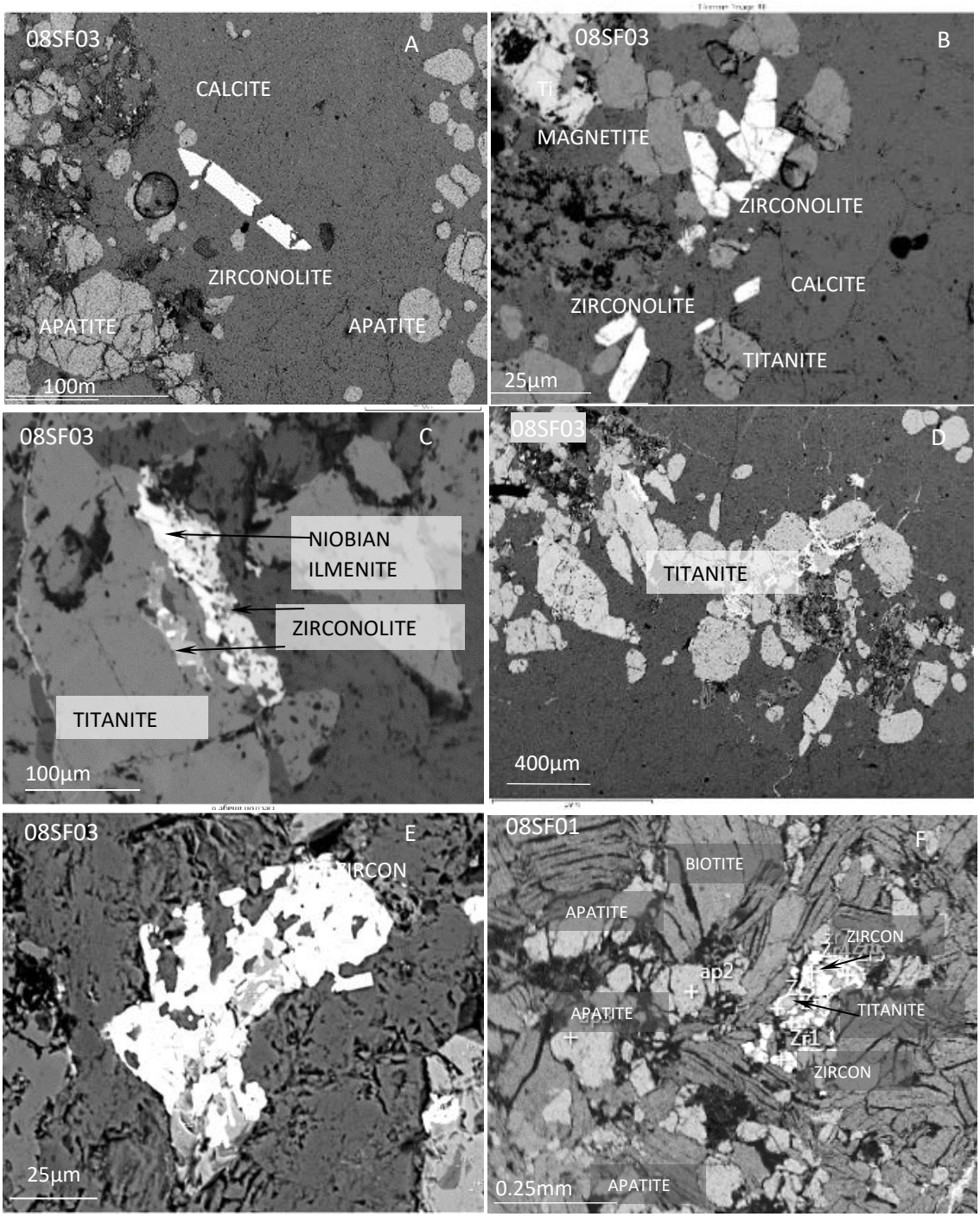

Fig. 4.15. Back-scatter electron (BSE) images from LF1 of 08SF01 and 08SF03 samples displaying accessory phases such as zircon, zirconolite, titanite and Nb-ilmenite and association with other phases.

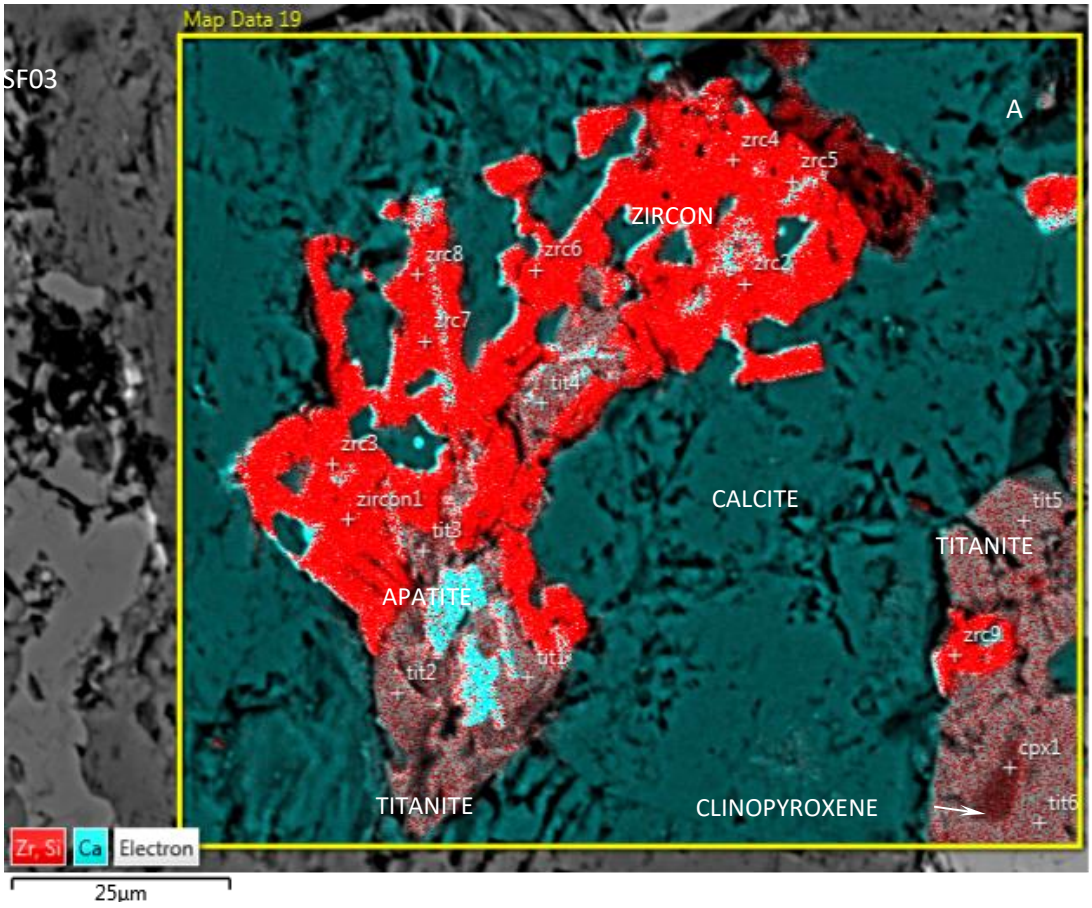

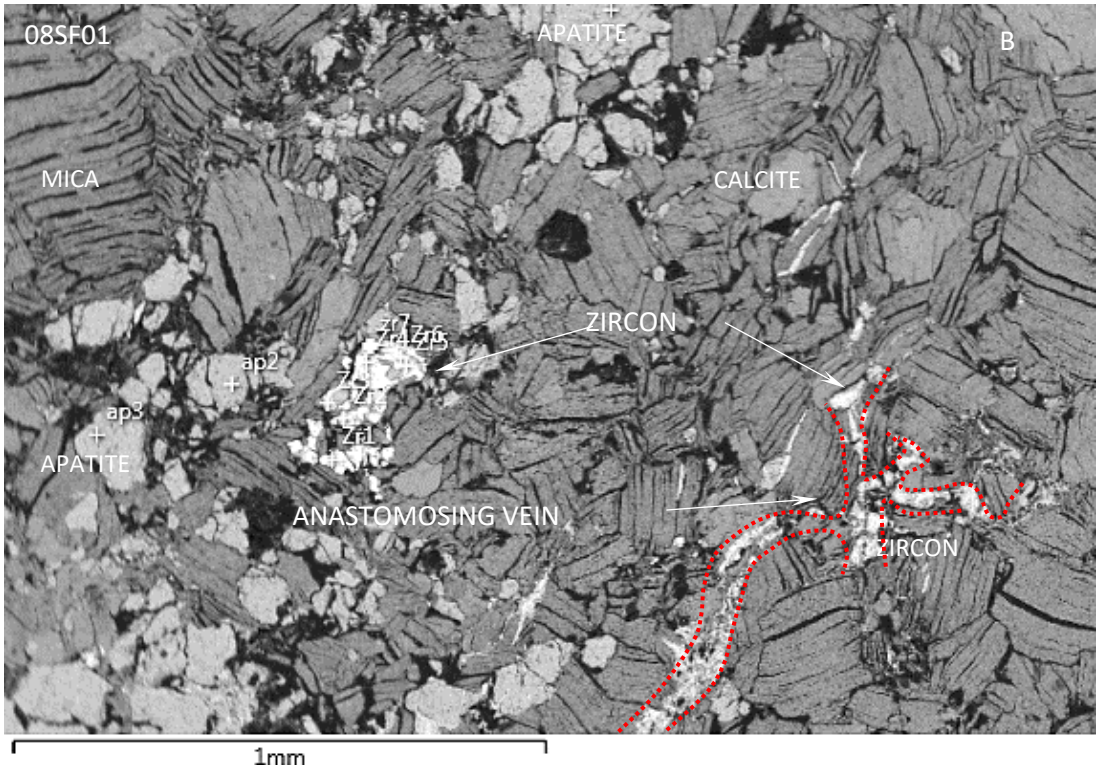

Fig.4.16 Back-scattered electron (BSE) images from Rib. de Almada sample 08SF03 (a) and 08SF01 (b) samples displaying accessory zircon associated with titanite, apatite and calcite. False-coloured X-Ray map of 08SF03 (a) from Rib. de Almada displaying zircon.

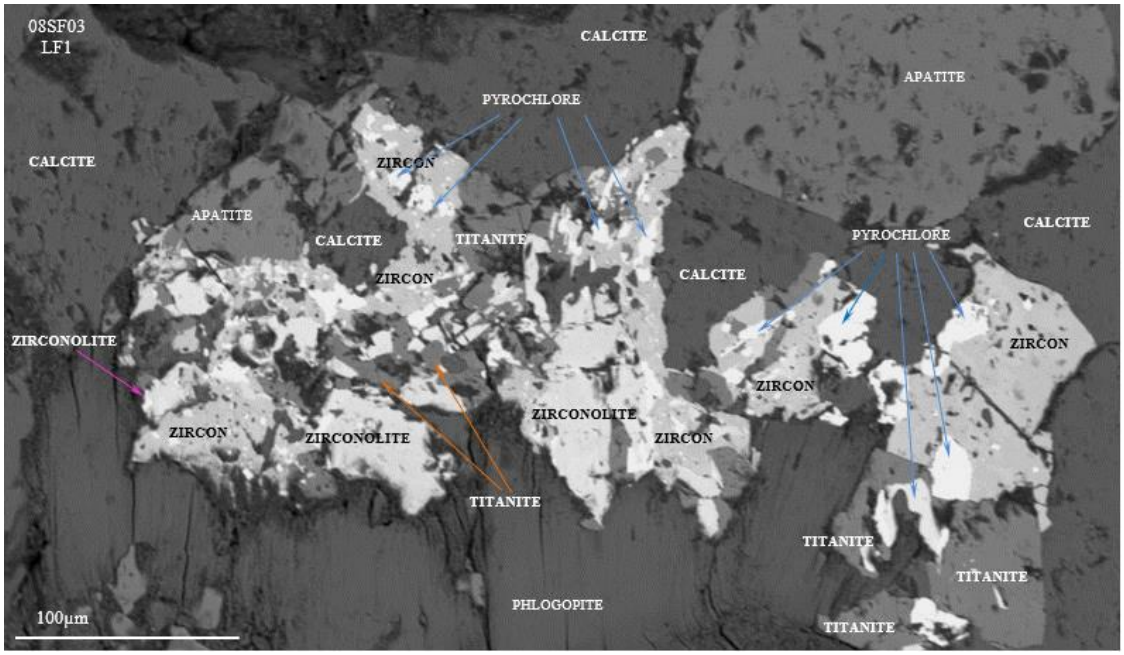

Fig. 4.17 Back-scattered electron (BSE) images of 08SF03 sample displaying accessory phases and complicated association between phlogopite and accessory minerals such as zircon, zirconolite, titanite and radioactive pyrochlore.

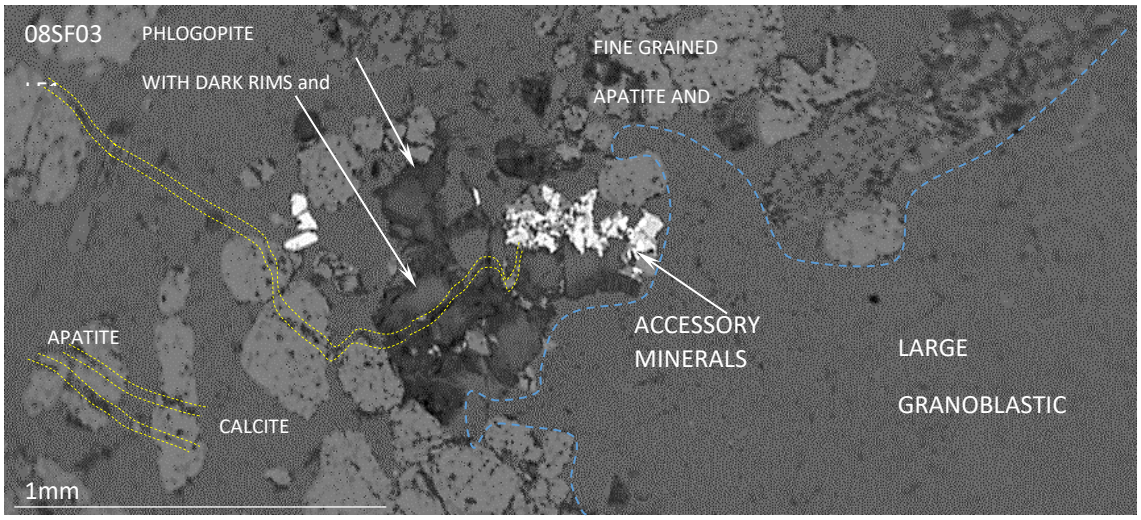

Fig 4.18 Backscattered electron image of 08SF03 from Rib. de Almada, displaying phlogopite associated with titanite-zircon-zirconolite-pyrochlore (bright white colour). This unusual intimate assemblage set in phlogopite is bordered by apatite (lighter grey) and calcite (slightly darker grey). Growth of accessory minerals occurred close to granoblastic calcite which is free from other minerals. Possible paths for fluid invoved in crystallising accessory minerals is highlighted by yellow dotted lines.

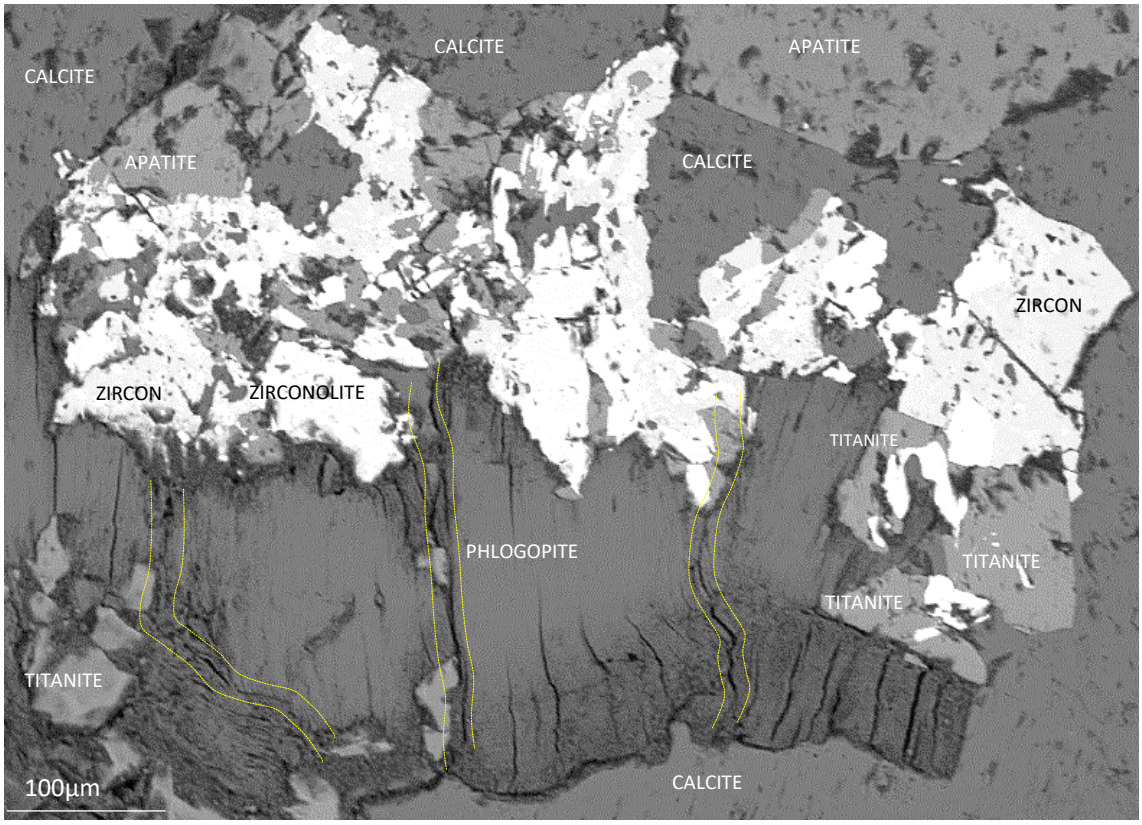

Fig. 4.19 BSE image of 08SF03 from Rib. de Almada showing mica holding rare minerals, all set in fine-grained matrix composed of calcite and apatite. Yellow lines represent remnants of anastomosing veinlets that delivered the fluid to crystallise titanite, zircon, zirconolite and pyrochlore.

In Figure 4.16b the anastomosing vein is composed of zircon, though in Figure 4.17 this assemblage is more complex as zircon/zirconolite/titanite/pyrochlore crystallised. In these places, mica shows darker coloration in BSE image, perhaps implying it was affected by the upwards moving fluid, accomodated newly formed phases together with calcite, as they most likely crystallised from the hydrothermal fluid which traveled along the mica cleavages.

In 08SF03 (Fig.4.18 and Fig.4.19), this process shows the preferential association of mica holding those accessory minerals within the fine-grained calcite-apatite (Fig.4.18) which borders granoblastic calcite. Accessory minerals are preferentially positioned in the upper part of the phlogopite to which fluid traveled through possible paths from the lower part of phlogopite (denoted here by the yellow dotted line, Figure 4.19). Probable paths for the fluid derived from calcite-apatite to phlogopite can also be seen by fractures infilled by dark inclusions in apatite and calcite (Fig.4.18) highlighted by yellow dotted line. Overall, the texture of cluster of

phlogopites can be divided into: darker grey (nearly black) colouration around the phlogopite rims and lighter grey inner semi-circular inner regions (Fig. 4.18). Thus, the fluid derived from the calcite/apatite region moved around phlogopite cluster composed of semicircular phlogopites. Fig. 4.19 followed possible distribution paths highlighted by yellow dotted lines. It seems that fluid circulated around the phlogopites altering their rims (dark grey). The fluid also used internal passages within phlogopite seen as dark grey subparallel streaks position within light grey area.

Overall accessory minerals are associated with upper part of phlogopite/calcite area which is close to the granoblastic calcite. Darker grey rim of phlogopite looks highly strained and joined by many dark streaks (Fig.4.19). The cores of the mica appear strain-free though under higher magnification dark streaks can be seen which lead from the lower to upper part where accessory minerals are seen. Thus, crystallisation of titanite, zircon, zirconolite and pyrochlore happened through anostomosing veinlets (darker streaks) carrying fluid. This resembles the process that formed zircon in glimmerite in 08SF01. As phlogopite is set in fine-grained calcite-apatite where apatite shows multiple fracturing (numerous dark lines), it points to sourcing the fluid from this side associated with plastically deformed calcite-rich areas. Described texture of accessory minerals might suggest formation during intercumulus infill during which fluid was obtained from deformed calcite-apatite part (being fine grained vs nearby coarse granoblastic).

Fogo carbonatites contain garnet. Garnet is usually fine to medium grained and overall anhedral and skeletal, sometimes composed of cluster of rounded grains (Fig.4.20a-d) or even finer rounded granules encircling oval shaped clinopyroxene (Fig.4.20b). Occasionally the rims of garnet are overgrown by other phases such as titanite (Figure 4.22). Garnet is patchily zoned; in BSE images, garnet is generally bright along the rims, with darker centres, however, patches of bright garnet are also observed within the darker central parts, reflecting elevated Fe content. Garnet texture and morphology suggest porphyroblastic growth of the mineral.

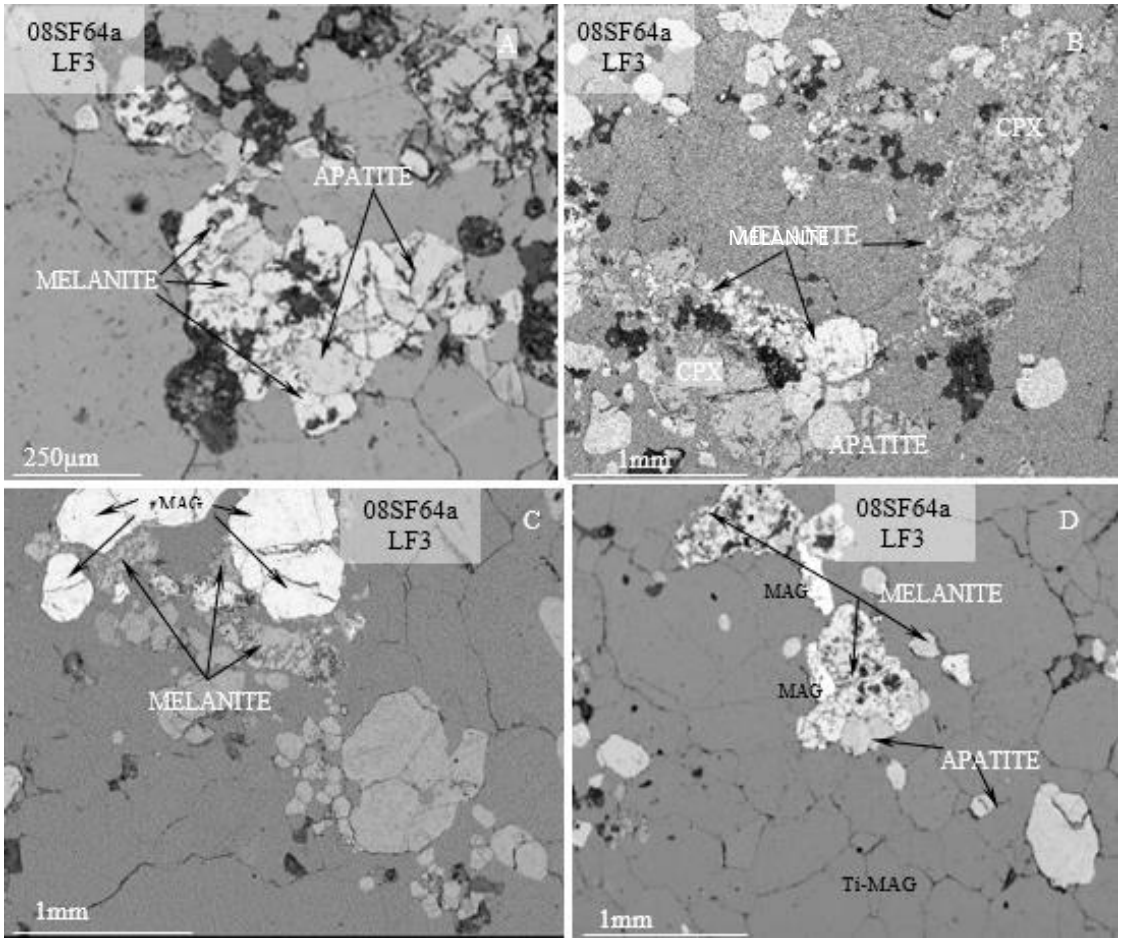

Fig.4.20 Back-scattered electron (BSE) images of the samples from Monte Almada 08SF64a containing the Ti-rich garnet melanite. Anhedral garnet displays internally granular texture. It is also intimately associated with other phases such as apatite or magnetite.

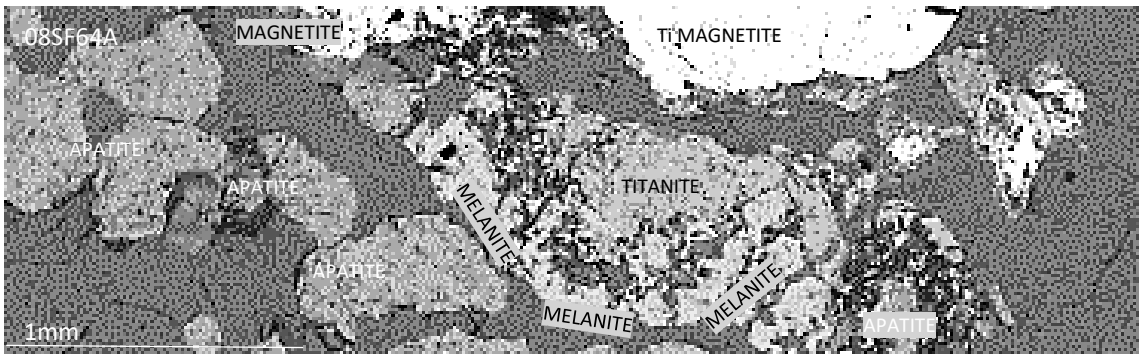

Fig 4.21. Backscattered electron image of 08SF64a from Monte de Almada, displaying anhedral titanite overgrown by melanite rim.

Fig.4.22 Photomicrograph of 08SF63 (FOV 3cm) displaying in upper part calcite-apatite-feldspar (gray), clinopyroxene (green)-rich area separated by fine-grained garnet-titanite from the lower part which contains calcite with minor pyroxene.

Figure 4.23 shows the association of magnetite-titanomagnetite and granet with their alteration minerals. Rare magnetite also displays an irregular distribution. Size and texture of titanomagnetite is variable but generally shows anhedral crystals that are often embayed, indicating marginal resorption. Internally titanomagnetite shows multiple fractures perhaps providing paths for resorbed fluid or liquid enriched in elements such as Ti. Titanomagnetite is often associated with other Ti-bearing minerals. In Monte Almada samples, fluid circulation is demonstrated by magnetite adjacent to titanomagnetite as well as melanite bordering titanite and was perhaps responsible for alteration of ilmenite and/or melanite to titanite.

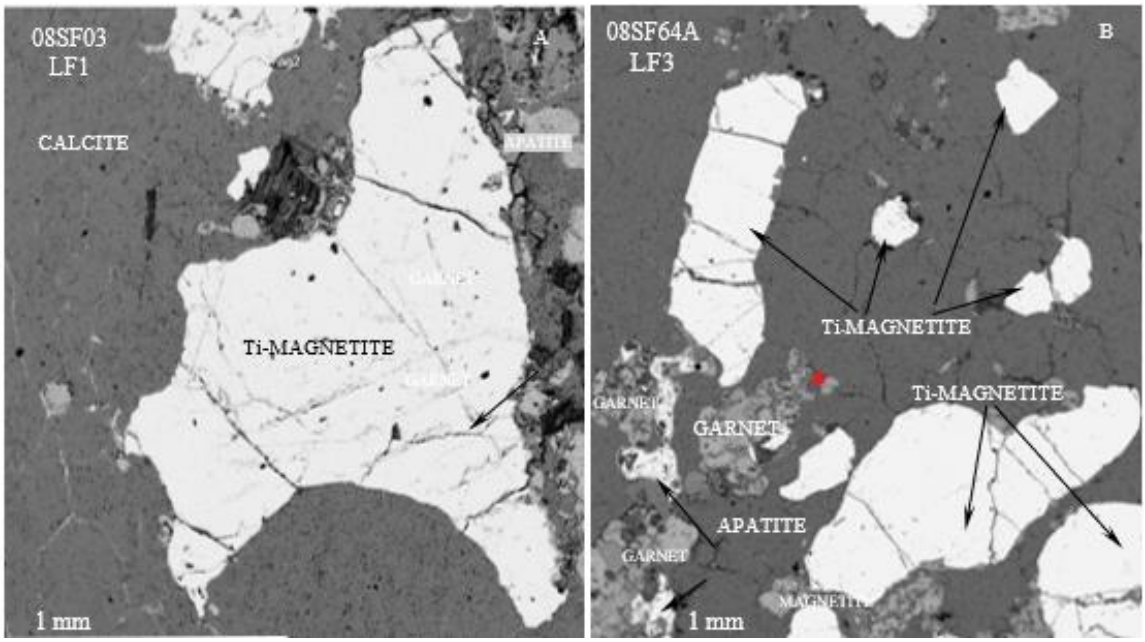

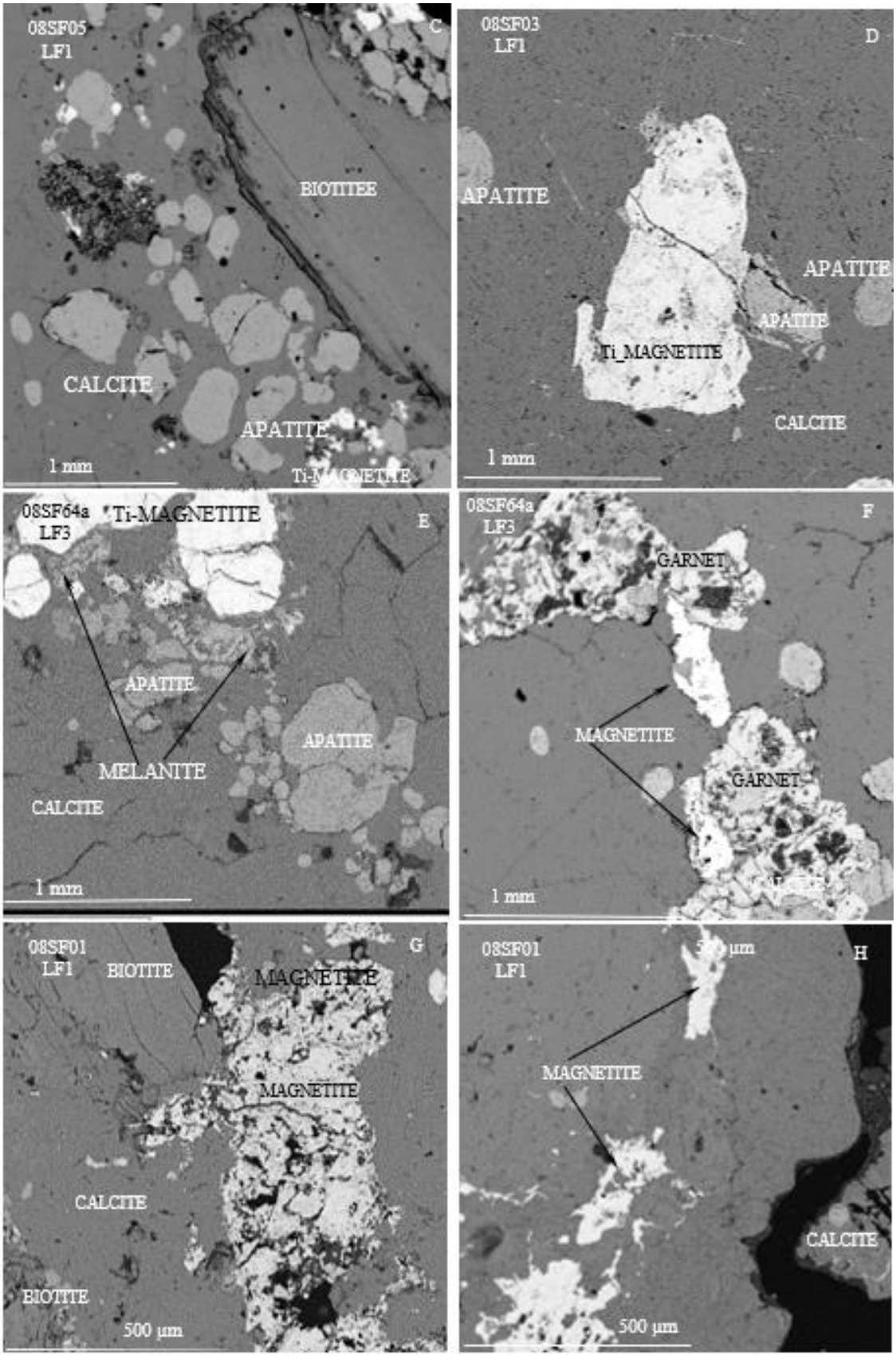

Fig. 4.23 Backscattered electron image of 08SF03, 08SF05 and 08SF64a from Rib. de Almada and Monte Almada, displaying titanomagnetite and displaying magnetite. BSE image I shows association of magnetite-titanomagnetite-melanite-titanite.

Samples from Rib. D. Santo (LF2) are fine to medium-grained alvikites, in parts heavily stained by iron oxide and cut by secondary calcite veins (Figure 4.24 a-c). They are mostly composed of recrystallised calcite with subordinate apatite.

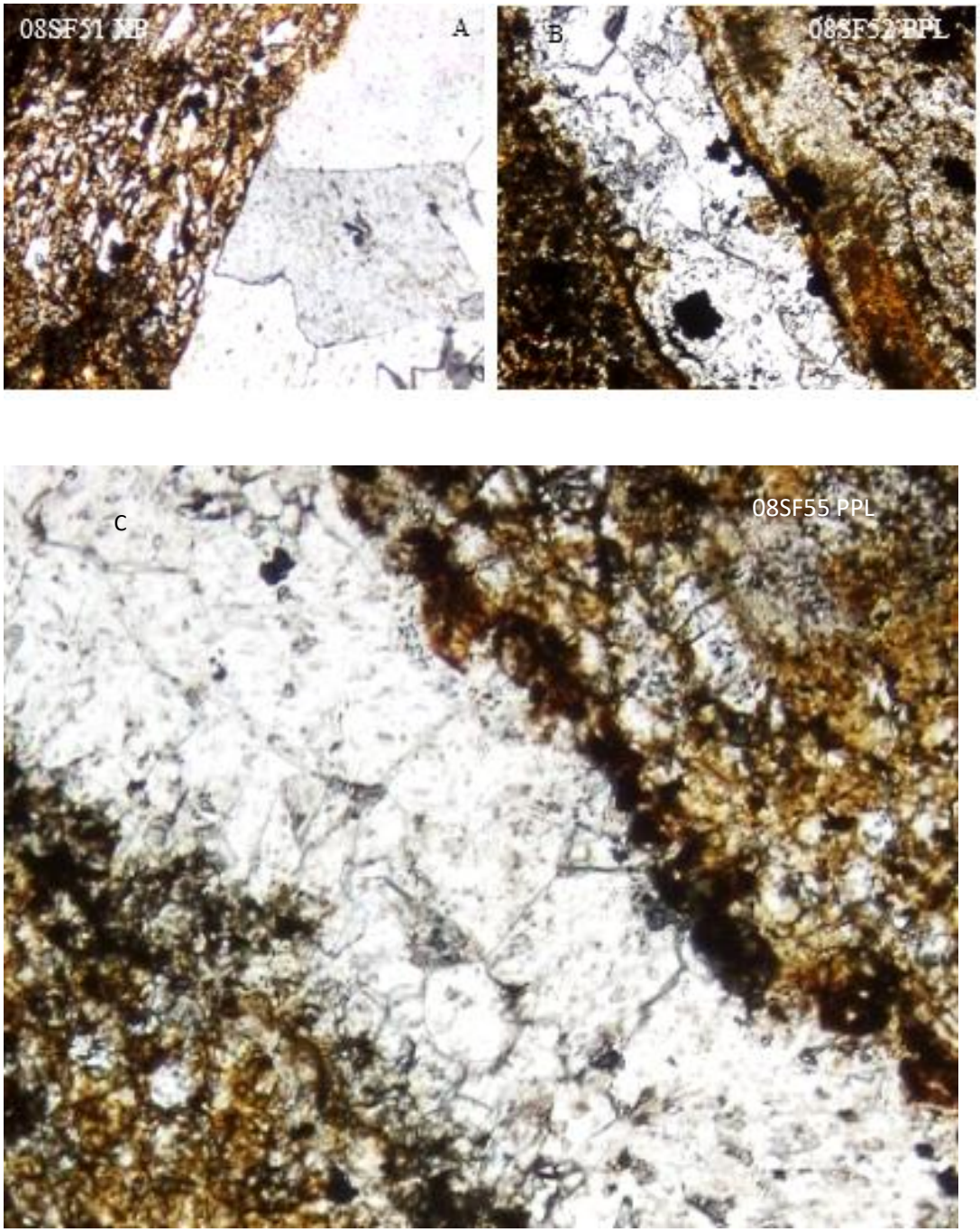

Fig.4.24 Photomicrographs taken from the samples collected in Rib. Dom. Santo area such as 08SF51 with highly stained carbonatite by iron oxide; 08SF52 showing secondary calcite veining; 08SF055 revealing highly iron oxide staining of carbonatite with cross-cutting by secondary calcite veins. Field of view 1.2mm.

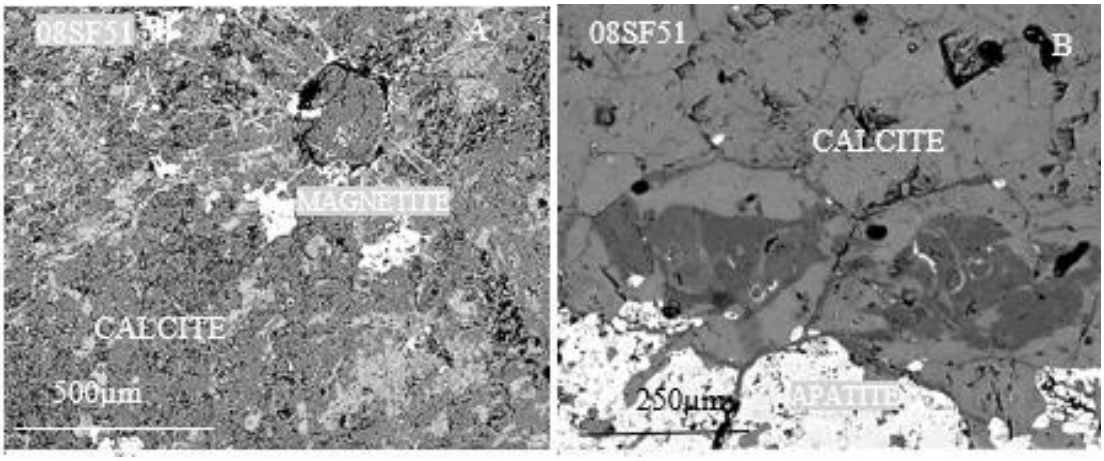

Fig.4.25a Back-scattered electron (BSE) images of samples from Rib. Domingo Santo site. Sample 08SF51: A) Round calcite rimmed by magnetite which also radiates into main body of carbonatite; B) Granoblastic calcite showing triple junction with dark grey areas (MnO-rich) and some apatite (light grey).

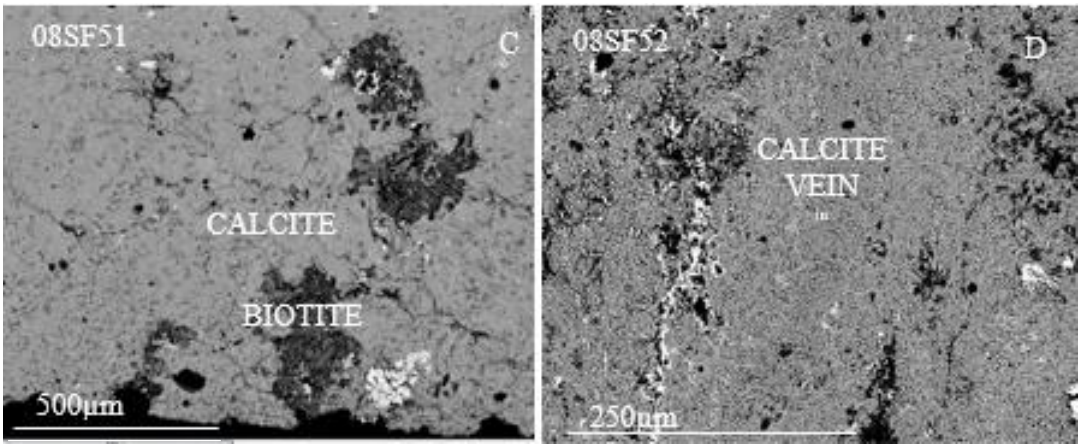

Fig.4.25b Back-scattered electron (BSE) images of samples from Rib. Domingo Santo site. Sample 08SF51: C) Mostly calcite with small amount of apatite and the darkest grey represents biotite clusters. Sample 08SF52: D holds secondary calcite vein rimmed by magnetite.

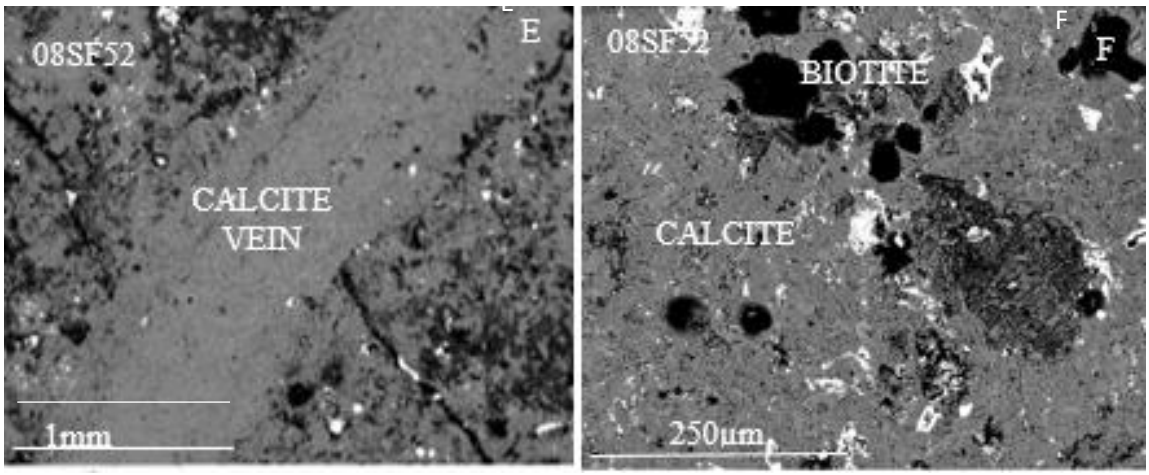

Fig.4.25c Back-scatter electron (BSE) images of samples from Rib. Domingo Santo site. Sample 08SF52: E) Secondary calcite veins; F) Mostly calcite with some biotite cluster and magnetite.

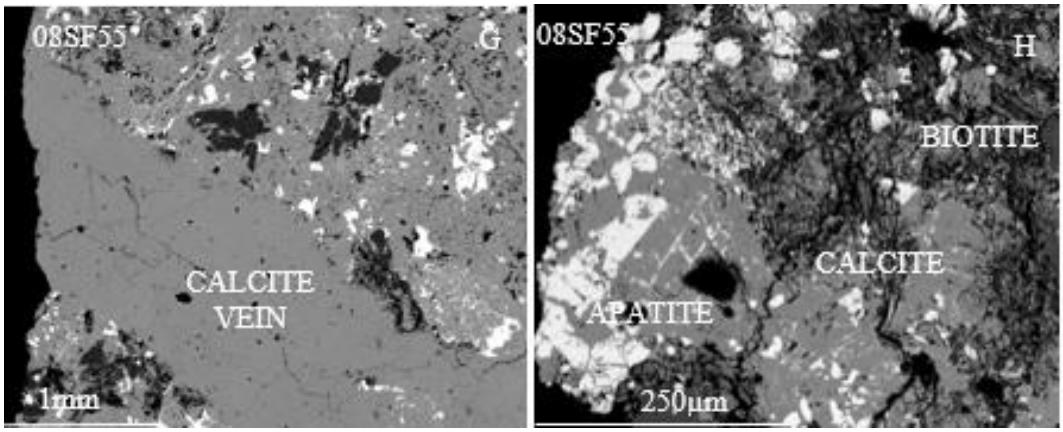

Fig.4.25d Back-scatter electron (BSE) images of samples from Rib. Domingo Santo site. Sample 08SF55: G) Calcite vein displacing carbonatite full of tiny magnetite and pyroxene; H) Light grey apatite set in calcite with some biotite.

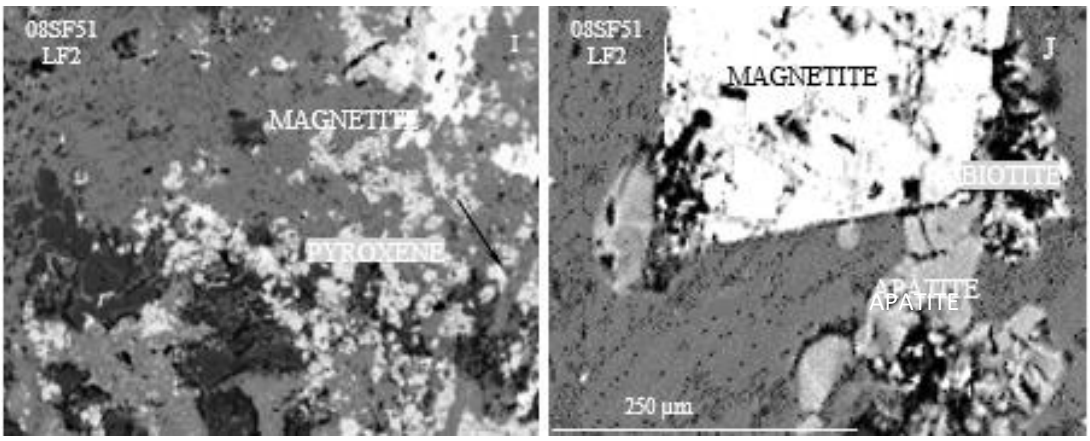

Fig. 4.25e Back-scattered electron (BSE) images of samples from Rib. Domingo Santo. Sample 08SF51: I) Calcite vein displacing carbonatite full of tiny magnetite and pyroxene; H) Magnetite and light grey apatite set in calcite with some biotite

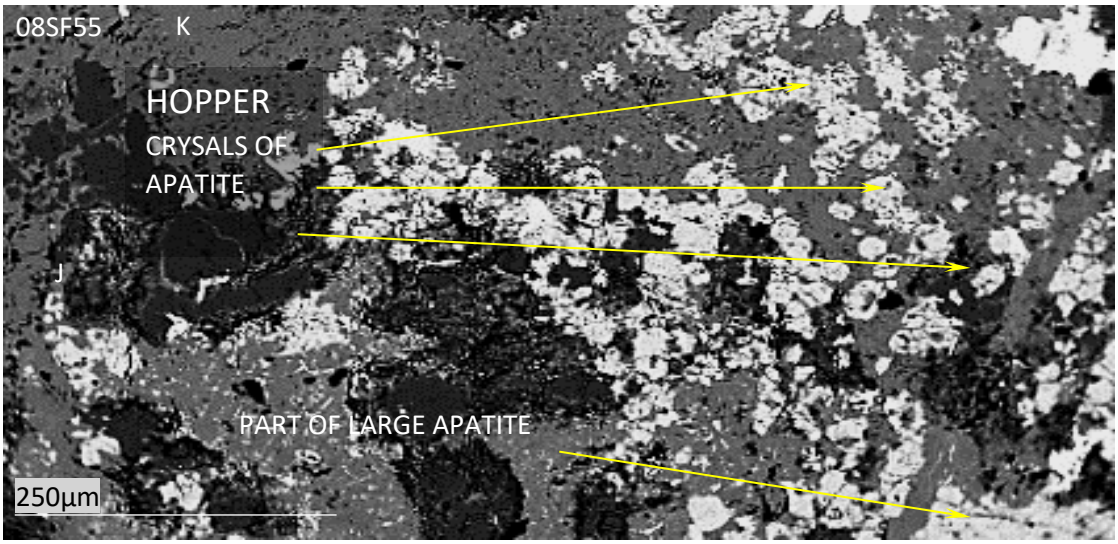

Fig. 4.25f Back-scattered electron (BSE) images of samples from Rib. D. Santo site. Sample 08SF51: two types of apatite are present here such as primary large apatite quenched apatite exhibiting hopper texture.

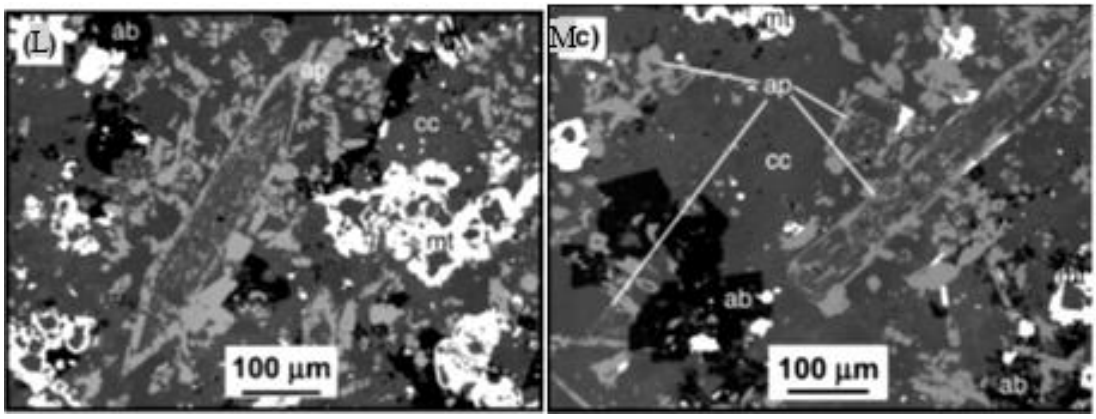

Fig.4.25g Back-scatter electron (BSE) images of hopper crystals of apatite from the Triassic Chagatai Complex, Uzbekistan (Moore et al., 2009).

Ferromagnesian phases like biotite and amphibole are scarce but magnetite is common. The alvikites (Fig.4.25) are composed of a preferentially orientated fine-grained calcite and apatite matrix, with rare calcite porphyroclasts, heavily veined and stained by iron oxide. Accessory phases include ferrihollandite and magnetite. The pattern of accumulation of fine-grained calcite in lozenge-like areas resembles the recrystallisation texture of augen porphyroclasts. Two populations of apatite can be recognised. The first forms larger anhedral grains and the second one forms fine-grained subhedral crystals which show hopper texture and is highly comparable to images of hopper crystals of apatite from the Triassic Chagatai Complex, Uzbekistan (Moore et al., 2009). Isolated plagioclase and fairly large euhedral alkali feldspar can be distinguished here. Secondary calcite veining is common.

4.4 Interpretation of petrography

In the Rib. de Almada locality, an intrusive carbonatite body was affected by metamorphism and deformation leading to formation of porphyroclastic calcite while surrounding grains have undergone grainsize reduction during deformation (recrystallisation). Strain was triggered most likely by uplift, and continuous strain persisted until uplift ceased. Consequently, progressive deformation led to development of gneissic texture, which gave rise to formation of subparallel bands encompassing preferentially aligned elliptical calcite porphyroclasts rimmed by prismatic clinopyroxene. Subsequently separate glimmeritic sheets were emplaced within the carbonatitic body as shown by the presence of ocelli with calcite cores,

monomineralic composition, and highly deformed mica with an inclusion-free texture. In response to brittle stress, under probably low T and P, fractures developed leading to veining and consequently to infiltration by hydrothermal fluids, hence the evidence of oxidation. Occurrence of hydrothermal conditions led to interaction with the carbonatite and fenitization and formation of feldspar encircling calcite porphyroclasts, while developing an intimate association with pyroxene. Crystallisation of accessory zircon, zirconolite, pyrochlore, titanite was also associated with circulation of hydrothermal fluids. Late-stage fluid circulation led to formation of hematite-rich net-veining and veinlets containing drusy rhombohedral calcite.

Much of the carbonatite from the Monte Almada location has a peculiar texture, consisting of alternating subparallel layers of coarse-grained calcite surrounded by a fine-grained assemblage of clinopyroxene, calcite, apatite, zeolite and alkali feldspar/feldspathoid. These layers later went through plastic deformation. This site could represent a body of sövite with preserved (to some degree) primary calcite texture though modified by post-magmatic processes. Approximately 80% of pure calcite is tightly packed in layers, often being in contact with feldspar-rich rock. Assuming that originally primary calcite would have crystallised tabular lath-like coarse crystals, with time these elongated crystal internally recrystallised to polycrystalline granoblastic calcite. The rim of the calcitic layer is Na-rich, as is composed of sodic zeolite (after feldspathoids/plagioclase?) and clinopyroxene/amphibole, and K-rich due to presence of alkali feldspar and feldspathoids. Thus, it is highly suggestive of Na-K-fenitisation. Most likely metasomatic rims formed around elongated calcite preserving the original shape (calcite laths). The layers subsequently went through plastic deformation as they show structural features such as folding, complex cross-cutting and could be explained by the post-emplacement changes including sheet closure at waning magma pressure, sagging and partial backflow after injection, and show signs of persistent recrystallisation (following interpretation of Andersson et al., 2016). 08SF62 sövite found at higher elevation does not show this texture and also has different assemblage including albite, orthoclase and pyroxene set in Sr-rich calcite and apatite (more pristine mineral chemistry). This variation might represent different parts of a fenite-carbonatite unit with more intense metasomatism affecting the lower part.

In carbonatites from the Rib. Doming Santo, crystallisation of calcite and apatite occurred in the early stages. Overall, this site is devoid of mafic silicates

typically found in other Fogo sites, thus this carbonatite indicates a reduced activity of silica. Two populations of apatite are present, of which primary happened earlier and crystallised larger crystals, then mode switched to form fine hopper crystals tightly packed in parallel bands (rapidly formed hopper apatite). Consequently, this site is characterised by a magmatic body showing condition of rapid cooling with instantaneous drop in pressure. The strong foliated texture influenced by metamorphism was induced by shearing, which provided passage to REE-rich hydrothermal fluids and altered the early-formed phases. Highly oxidised state points to low temperature hydrothermal alteration. Most likely circulation of hydrothermal fluids led to staining by iron oxide and further fracturing led to formation of veins. Alteration processes induced by circulation of these fluids produced late-stage phases such as hollandite.

4.5 Major element compositions of constituent phases in intrusive carbonatites from Fogo

Tables 6.4.1a to 6.4.1i (Appendix 2b) provide in detail major element composition of calcite from intrusive carbonatite specimens from Fogo, while Table 4.2a,b outlines average and standard deviation of major elements of calcite. The lowest concentration of CaO in primary calcite amongst three locations is 50 wt% and the highest (Rib. Domingo Santo) reaches 61.5 wt%.

Calcite in all locations originated as a primary phase with considerable Sr content but then secondary calcite can be found in veins, infilling the voids, forming inclusions in feldspar and present as a patches within primary calcite. It can be recognised by its low to negligible SrO content (highest value 0.16 wt%). The Monte Almada site contains calcite with the highest concentration of SrO (up to 1.6 wt%), and Rib. Domingo Santo has the lowest SrO concentration (0.8 wt%). Consequently, Fogo primary calcite is enriched in SrO with average values 0.7-1.5wt%, near the top end of the array of worldwide carbonatites (0.2-1.4 wt%, Hornig-Kjarsgaard, 1998).

	LF1 EDS PRIM SF01		EDS PRIM SF05		EDS PRIM SF03		EDS PRIM SF07		LF2 WDS PRIM SF51		EDS PRIM SF51		LF3 EDS PRIM SF61		EDS PRIM SF62		EDS PRIM SF64		EDS PRIM SF64		EDS PRIM SF64		EDS PRIM SF64	
	ave n=5	st dev n=5	ave n=14	st dev n=14	ave n=2	st dev n=2	ave n=4	st dev n=4	ave n=4	st dev n=4	ave n=3	st dev n=3	ave n=12	st dev n=12	ave n=20	st dev n=20	ave n=8	st dev n=8	ave n=4	st dev n=4	ave n=11	st dev n=11	ave n=11	st dev n=11
SiO_2	0.15	0.07	0.05	0.04	0.02	0.03	0.06	0.09	0.01	0.01	0.22	0.30	0.09	0.10	0.06	0.08	0.04	0.05	0.21	0.32	0.04	0.05	0.04	0.05
Al_2O_3	0.25	0.15	0.13	0.18	0.05	0.07	0.02	0.01	n/a	n/a	0.26	0.41	0.81	1.06	0.44	0.89	n/a	n/a	0.22	0.30	n/a	n/a	n/a	n/a
FeO	0.73	0.69	0.10	0.10	0.26	0.28	0.17	0.28	0.54	0.20	0.67	0.60	0.17	0.11	0.13	0.10	0.06	0.06	0.20	0.28	0.06	0.06	0.06	0.06
MnO	0.39	0.10	0.22	0.08	0.07	0.09	0.30	0.06	1.37	0.32	1.15	0.38	0.15	0.10	0.18	0.10	0.12	0.07	0.21	0.06	0.12	0.07	0.12	0.07
MgO	0.24	0.10	0.16	0.04	0.18	0.04	0.14	0.09	0.60	0.16	0.67	0.13	0.13	0.05	0.12	0.06	0.05	0.03	0.07	0.04	0.05	0.03	0.05	0.03
CaO	50.61	0.78	52.68	0.72	51.99	0.33	52.65	1.17	58.31	1.63	52.20	1.82	51.22	1.34	52.19	1.27	52.82	0.93	51.84	1.55	52.82	0.93	52.82	0.93
Na_2O	n/a	n/a	n/a	n/a	n/a	n/a	n/a	n/a	n/a	n/a	0.05	0.06	0.07	0.07	0.05	0.05	n/a	n/a	0.07	0.05	n/a	n/a	n/a	n/a
K_2O	n/a	n/a	n/a	n/a	n/a	n/a	n/a	n/a	n/a	n/a	0.04	0.04	0.05	0.04	0.05	0.04	n/a	n/a	0.05	0.04	n/a	n/a	n/a	n/a
BaO	0.05	0.03	0.15	0.11	0.11	0.09	0.04	0.05	0.32	0.08	0.38	0.12	0.09	0.10	0.15	0.12	0.12	0.11	0.21	0.11	0.12	0.11	0.12	0.11
P_2O_5	0.17	0.10	0.05	0.06	0.06	0.06	0.03	0.04	0.03	0.01	0.08	0.02	0.11	0.09	0.07	0.07	0.02	0.04	0.01	0.01	0.02	0.04	0.02	0.04
La_2O_3	0.12	0.16	0.07	0.09	0.02	0.02	0.17	0.15	n/a	n/a	0.04	0.05	0.08	0.08	0.07	0.08	0.13	0.15	0.11	0.12	0.13	0.15	0.13	0.15
SrO	1.17	0.17	1.39	0.09	1.30	0.14	1.29	0.03	0.77	0.07	1.32	0.18	1.22	0.16	1.37	0.15	1.54	0.07	1.43	0.09	1.54	0.07	1.54	0.07
F	0.43	0.11	0.38	0.09	0.10	0.11	0.08	0.07	n/a	n/a	0.11	0.11	0.31	0.11	0.34	0.12	n/a	n/a	0.02	0.02	n/a	n/a	n/a	n/a
Total	54.29		55.37		54.14		54.96		61.95		57.19		54.49		55.20		54.90		54.64		54.90		54.90	
Si	0.006	0.006	0.009	0.008	0.020	0.002	0.012	0.019	0.002	0.002	0.043	0.060	0.007	0.009	0.013	0.016	0.009	0.010	0.043	0.065	0.009	0.010	0.009	0.010
Al	0.042	0.067	0.032	0.043	0.002	0.003	0.006	0.003	n/a	n/a	0.062	0.098	0.190	0.243	0.104	0.205	n/a	n/a	0.053	0.074	n/a	n/a	n/a	n/a
Fe	0.012	0.015	0.016	0.017	0.020	0.029	0.029	0.047	0.082	0.031	0.112	0.100	0.029	0.018	0.023	0.017	0.011	0.011	0.035	0.048	0.011	0.011	0.011	0.011
Mn	0.043	0.013	0.037	0.013	0.010	0.009	0.053	0.008	0.213	0.052	0.192	0.062	0.027	0.007	0.032	0.018	0.021	0.013	0.037	0.011	0.021	0.013	0.021	0.013
Mg	0.049	0.016	0.048	0.012	0.054	0.052	0.044	0.028	0.163	0.045	0.198	0.037	0.039	0.015	0.036	0.017	0.016	0.010	0.021	0.012	0.016	0.010	0.016	0.010
Ca	11.507	0.126	11.543	0.093	11.832	0.067	11.752	0.116	11.426	0.127	11.083	0.274	11.302	0.415	11.441	0.342	11.728	0.025	11.516	0.303	11.728	0.025	11.728	0.025
Na	n/a	n/a	n/a	n/a	n/a	n/a	n/a	n/a	n/a	n/a	0.018	0.025	0.029	0.026	0.021	0.019	n/a	n/a	0.027	0.020	n/a	n/a	n/a	n/a
K	n/a	n/a	n/a	n/a	n/a	n/a	n/a	n/a	n/a	n/a	0.010	0.009	0.014	0.009	0.013	0.009	n/a	n/a	0.012	0.011	n/a	n/a	n/a	n/a
Ba	0.011	0.008	0.012	0.009	0.000	0.000	0.003	0.004	0.023	0.005	0.029	0.009	0.007	0.008	0.012	0.009	0.009	0.008	0.017	0.009	0.009	0.008	0.009	0.008
P	0.008	0.010	0.009	0.010	0.009	0.001	0.006	0.006	0.002	0.001	0.014	0.003	0.019	0.016	0.012	0.012	0.002	0.003	0.002	0.003	0.002	0.003	0.002	0.003
La	0.007	0.006	0.005	0.007	0.007	0.000	0.013	0.012	n/a	n/a	0.003	0.004	0.006	0.006	0.005	0.006	0.005	0.006	0.009	0.010	0.005	0.006	0.005	0.006
Sr	0.068	0.009	0.082	0.005	0.075	0.006	0.078	0.003	0.082	0.008	0.152	0.020	0.073	0.010	0.082	0.009	0.185	0.006	0.172	0.011	0.185	0.006	0.185	0.006
F	0.272	0.058	0.247	0.059	0.006	0.009	0.052	0.043	n/a	n/a	0.000	0.000	0.199	0.069	0.218	0.076	n/a	n/a	0.000	0.000	n/a	n/a	n/a	n/a
Total	12.026		12.041		12.037		12.048		11.994		11.917		11.951		12.012		11.986		11.943		11.986		11.986	

Table 4.2a Electron microprobe data for primary calcite in the intrusive carbonatite found in Fogo, Cape Verde. Abbreviations: st dev=standard deviation, ave=average, prim=primary. Cations recalculated on the basis of 12 oxygens. Some elements in some analyses are below detection limit.

	LF1 EDS ASS with FRAC SF01		EDS ASS with FRAC SF01		EDS VEIN SF03		EDS DNC in FELD SF07		LF2 WDS SECOND SF51		EDS SECOND SF51		WDS SECOND SF52		WDS SECOND SF52		EDS SECOND SF52		LF3 EDS SECOND SF61	WDS SECOND SF64		
	ave n=4	st dev n=4	ave n=7	st dev n=7	ave n=6	st dev n=6	ave n=5	st dev n=5	ave n=6	st dev n=6	ave n=1		ave n=5	st dev n=5	ave n=7	st dev n=7	ave n=3	st dev n=3	ave n=1	ave n=9	st dev n=9	
SiO_2	0.10	0.07	0.07	0.05	0.08	0.04	0.08	0.05	0.03	0.03	0.03		0.02	0.02	0.07	0.04	0.08	0.11	0.00	0.03	0.05	
Al_2O_3	0.21	0.01	0.05	0.08	0.11	0.10	0.06	0.10	n/a	n/a	4.00		n/a2	n/a	n/a	n/a	0.33	0.50	0.05	n/a	n/a	
FeO	0.29	0.23	0.20	0.18	0.30	0.14	0.18	0.12	0.14	0.09	0.51		0.52	0.28	1.32	0.24	0.65	0.88	0.08	0.15	0.14	
MnO	0.13	0.06	0.10	0.13	0.07	0.04	0.07	0.05	0.08	0.09	0.00		1.32	0.06	0.24	0.20	0.35	0.35	0.06	0.20	0.03	
MgO	0.21	0.03	0.25	0.10	0.32	0.09	0.26	0.13	0.35	0.14	0..29		0.62	0.31	0.18	0.09	0.21	0.24	0.13	0.03	0.02	
CaO	52.24	0.65	53.97	1.27	53.25	0.67	54.18	1.44	60.02	1.13	55.36		58.20	1.26	57.92	1.40	51.56	3.13	53.69	59.18	1.79	
Na_2O	n/a	n/a	n/a	n/a	n/a	n/a	n/a	n/a	n/a	n/a	0.03		n/a	n/a	n/a	n/a	0.05	0.06	0.06	n/a	n/a	
K_2O	n/a	n/a	n/a	n/a	n/a	n/a	n/a	n/a	n/a	n/a	0.00		n/a	n/a	n/a	n/a	0.05	0.01	0.01	n/a	n/a	
BaO	0.06	0.07	0.03	0.05	0.05	0.06	0.04	0.06	0.06	0.10	0.30		0.02	0.04	0.03	0.05	0.15	0.14	0.00	0.10	0.09	
P_2O_5	0.22	0.08	0.05	0.04	0.02	0.02	0.03	0.03	0.09	0.04	0.00		0.07	0.02	0.08	0.05	0.09	0.08	0.05	n/a	n/a	
La_2O_3	0.16	0.14	0.08	0.07	0.05	0.05	0.06	0.05	n/a	n/a	0.00		n/a	n/a	n/a	n/a	0.07	0.13	0.00	n/a	n/a	
SrO	0.11	0.09	0.03	0.04	0.03	0.03	0.02	0.02	0.00	0.00	0.08		0.00	0.00	0.00	0.00	0.03	0.04	0.02	0.02	0.04	
F	0.41	0.12	0.07	0.07	0.09	0.06	0.06	0.06	n/a	n/a	0.14		n/a	n/a	n/a	n/a	0.05	0.05	0.20	n/a	n/a	
Total	54.13		54.90		54.35		55.04		60.77		56.72		61.03		59.84		53.68		54.35	59.70		
Si	0.010	0.008	0.014	0.009	0.013	0.015	0.016	0.010	0.005	0.006	0.006		0.006	0.004	0.014	0.007	0.017	0.022	0.000	0.005	0.009	
Al	0.016	0.011	0.031	0.032	0.006	0.005	0.015	0.023	n/a	n/a	0.009		n/a	n/a	n/a	n/a	0.081	0.123	0.103	n/a	n/a	
Fe	0.027	0.023	0.024	0.019	0.032	0.031	0.031	0.020	0.022	0.014	0.085		0.047	0.043	0.208	0.037	0.115	0.155	0.036	0.023	0.022	
Mn	0.030	0.018	0.029	0.016	0.032	0.025	0.012	0.008	0.013	0.015	0.000		0.007	0.008	0.037	0.033	0.063	0.063	0.002	0.032	0.004	
Mg	0.050	0.007	0.066	0.032	0.071	0.038	0.078	0.039	0.095	0.038	0.086		0.099	0.083	0.050	0.024	0.068	0.078	0.032	0.009	0.004	
Ca	11.581	0.064	11.630	0.108	11.757	0.082	11.763	0.089	11.839	0.016	11.765		11.821	0.107	11.658	0.068	11.519	0.412	11.562	11.916	0.040	
Na	n/a	n/a	n/a	n/a	n/a	n/a	n/a	n/a	n/a	n/a	0.012		n/a	n/a	n/a	n/a	0.020	0.025	0.000	n/a	n/a	
K	n/a	n/a	n/a	n/a	n/a	n/a	n/a	n/a	n/a	n/a	0.000		n/a	n/a	n/a	n/a	0.012	0.002	0.025	n/a	n/a	
Ba	0.012	0.013	0.009	0.007	0.003	0.004	0.003	0.005	0.004	0.007	0.023		0.001	0.003	0.003	0.004	0.013	0.011	0.011	0.007	0.007	
P	0.014	0.015	0.002	0.003	0.005	0.005	0.005	0.004	0.007	0.003	0.000		0.005	0.001	0.007	0.005	0.016	0.014	0.013	n/a	n/a	
La	0.000	0.000	0.004	0.006	0.008	0.010	0.004	0.004	n/a	n/a	0.000		n/a	n/a	n/a	n/a	0.005	0.009	0.000	n/a	n/a	
Sr	0.006	0.005	0.002	0.002	0.002	0.002	0.001	0.001	0.000	0.000	0.009		0.000	0.000	0.000	0.000	0.004	0.005	0.159	0.002	0.004	
F	0.222	0.064	0.156	0.101	0.044	0.042	0.039	0.040	n/a	n/a	0.000		n/a	n/a	n/a	n/a	0.000	0.000	0.000	n/a	n/a	
Total	11.967		11.966		11.974		11.969		11.985		11.995		11.986		11.976		11.933		11.942	11.995		

Table 4.2b Electron microprobe data for secondary calcite in the intrusive carbonatite found in Fogo, Cape Verde. Abbreviations: st dev=standard deviation, ave=average, second=secondary, prim=primary, ass-associated, frac=fracture. Cations recalculated on the basis of 12 oxygens.

The MnO content of calcite is overall lower in Rib. de Almada than Monte Almada. In Rib. Domingo Santo 2 (08SF51) two population of calcite is detected with Mn-rich calcite being also Sr-rich and Mn-poor calcite also Sr-poor. Low silica content in calcite links the origin of Fogo carbonatites to evolution from silica-undersaturated liquids and considerable level of SrO is characteristic for primary calcite crystallisation from carbonatitic magma. Narrow variation in MgO (0.1-0.6 wt%) and lack of dolomite suggest sövitic composition. Calcite in Rib. Domingo Santo samples, mainly 08SF52, show considerable enrichment in FeO with an average of 0.5-1.3 wt%.

Detailed microprobe analyses of apatite are presented in Table 6.4.3a, 6.4.3b, 6.4.3c and 6.4.3d (Appendix 2b). Average compositions of apatite, with their standard deviations, is given in Table 4.3. Apatite forms an essential constituent of the Fogo carbonatites (up to 15%). The average values of CaO in apatite, from all locations, do not vary significantly (52.0-52.8 wt%). P_2O_5 concentration shows little variation (average 42 wt% P_2O_5). SiO_2 content reaches 1 wt% in Monte Almada but is lower in Rib. de Almada (0.70 wt%) and even lower in LF2 (0.33 wt%). SrO concentration in apatite shows slight variation (1.04-1.26 wt% for Rib. de Almada and Monte Almada) though in Rib. Domingo Santo higher values are detected (1.25-1.85 wt%). FeO, Al_2O_3 and Na_2O concentrations are below 0.5 wt%. Apatite also contains 1.1-2 to 4 wt% F and is thus fluorapatite.

	EDS													
	LF1		LF1		LF1		LF1		LF2		LF3		LF3	
	08SF01		08SF07		08SF03		08SF05		08SF51		08SF61		08SF64	
	ave n=16	st dev	ave n=3	st dev	ave n=7	st dev	ave n=5	st dev	ave n=2	st dev	ave n=16	st dev	ave n=13	st dev
SiO_2	0.72	0.14	0.82	0.06	0.86	0.19	0.58	0.11	0.33	0.16	0.65	0.27	1.02	0.37
TiO_2	0.06	0.06	0.12	0.06	0.07	0.06	0.01	0.01	0.02	0.03	0.01	0.03	0.03	0.06
FeO	0.24	0.37	0.18	0.15	0.09	0.06	0.01	0.01	0.29	0.41	0.06	0.12	0.13	0.20
MnO	0.05	0.07	0.02	0.03	0.01	0.03	0.06	0.04	0.03	0.04	0.04	0.05	0.03	0.04
MgO	0.03	0.04	0.02	0.02	0.02	0.03	0.02	0.03	0.07	0.00	0.03	0.07	0.02	0.03
CaO	52.08	0.56	51.97	0.15	52.84	0.46	52.87	0.64	51.36	0.62	52.12	0.52	52.80	0.76
Al_2O_3	0.13	0.12	0.09	0.03	0.13	0.24	0.06	0.06	0.69	0.91	0.09	0.11	0.15	0.29
Na_2O	0.31	0.16	0.19	0.03	0.26	0.06	0.23	0.06	0.38	0.06	0.18	0.07	0.12	0.06
P_2O_5	41.77	0.60	42.68	0.20	42.32	0.49	42.52	0.73	41.63	0.16	42.13	0.57	41.56	0.79
SrO	1.23	0.20	1.04	0.02	1.22	0.13	1.11	0.13	1.85	0.11	1.24	0.14	1.25	0.17
BaO	0.07	0.12	0.09	0.16	0.07	0.12	0.15	0.12	0.00	0.00	0.13	0.12	0.06	0.10
Cl	0.04	0.02	0.05	0.01	0.00	0.00	n/a	n/a	0.02	0.02	n/a	n/a	0.03	0.03
F	1.99	0.59	1.12	0.26	1.44	0.19	2.42	0.31	2.43	0.30	2.11	0.30	1.32	0.16
TOTALS	99.12	0.64	99.22	0.53	100.04	0.53	100.10	0.91	99.86	0.06	99.84	0.56	99.73	0.43
Si	0.115	0.023	0.135	0.008	0.139	0.030	0.093	0.018	0.053	0.029	0.106	0.043	0.167	0.062
Ti	0.008	0.009	0.014	0.010	0.008	0.008	0.001	0.002	0.002	0.003	0.002	0.003	0.004	0.006
Fe^{+2}	0.021	0.016	0.025	0.020	0.012	0.011	0.001	0.002	0.039	0.033	0.008	0.016	0.019	0.027
Mn	0.008	0.010	0.002	0.004	0.002	0.004	0.009	0.005	0.003	0.005	0.006	0.007	0.004	0.005
Mg	0.008	0.012	0.006	0.005	0.005	0.007	0.004	0.006	0.017	0.000	0.008	0.017	0.004	0.007
Ca	9.089	0.213	9.106	0.080	9.181	0.097	9.045	0.132	8.890	0.082	9.162	0.089	9.271	0.098
Al	0.024	0.021	0.017	0.006	0.025	0.046	0.011	0.010	0.131	0.172	0.016	0.022	0.029	0.056
Na	0.091	0.042	0.059	0.008	0.080	0.017	0.070	0.015	0.119	0.027	0.057	0.022	0.039	0.017
P	5.748	0.076	5.909	0.014	5.810	0.041	5.747	0.044	5.692	0.019	5.741	0.033	5.765	0.090
Sr	0.115	0.018	0.099	0.001	0.114	0.013	0.103	0.012	0.173	0.010	0.116	0.013	0.119	0.017
Ba	0.005	0.008	0.006	0.010	0.005	0.007	0.010	0.008	0.000	0.000	0.008	0.008	0.004	0.006
Cl	0.011	0.007	0.015	0.005	0.000	0.000	n/a	n/a	0.004	0.006	n/a	n/a	0.008	0.008
F	1.035	0.310	0.588	0.132	0.751	0.095	1.250	0.136	1.273	0.138	1.096	0.133	0.693	0.084
OH	-0.040	0.307	0.397	0.131	0.249	0.095	-0.250	0.136	-0.278	0.164	-0.096	0.133	0.298	0.087
TOTALS	16.256	0.213	16.402	0.102	16.407	0.084	16.095	0.132	16.143	0.082	16.229	0.177	16.466	0.052

Table 4.3. Electron microprobe data for apatite in the intrusive carbonatite found in Fogo, Cape Verde. Abbreviations: st dev=standard deviation, ave=average. Complete tables in Appendix 2.

The two populations of apatite distinguished in Rib. Domingo Santo samples by texture and grain size also differ in chemistry. The early anhedral, large crystals have

lower SrO content (1.77 wt%) and minor Ce_2O_3 content (0.59 wt%). The smaller euhedral hopper crystals have higher SrO concentration (1.92 wt% - the highest analysed on Fogo) and significant 0.98 wt% Ce_2O_3 (Table 6.4.3b, Appendix 2b).

4.5.1 Interpretation of calcite and apatite

Samples from Rib. de Almada are composed of large calcite crystals some of which show strain in the form of thick and curved lamellae twins. A few smaller calcite crystals are strain-free. This might imply two generation of crystallisation. Initially it could occur during upward movement of magmatic body in a form of crystalline mush, hence bending/straining of crystals. The second stage could happen after the magmatic body come to a halt and interstitial liquid was able to crystallise strain-free calcite alongside apatite. However, the possibility of post-magmatic recrystallisation of large strained calcite is more plausible as the strain-free crystals tend to be smaller and both types of calcite do not show chemical variation (Figure 4.26). Lack of zoning in apatite in Rib. de Almada and Monte Almada samples is clear though in Rib. Sato Domingo samples the presence of small hopper crystals of apatite is evident alongside anhedral larger ones (Figure 4.27). Apatite crystallised after initial calcite and continuous crystallisation of apatite followed. Although solubility of P_2O_5 in carbonatitic magma is low, crystallisation of apatite persisted until the final solidification as P saturation is relatively continuous due to precipitation of carbonate minerals (Gittins, 1989). Hopper crystals are more enriched in LREEs than the large anhedral crystals, as they crystallisation was more rapid (preference of Ce over other LREEs). Concentration of SrO in the apatite and primary calcite is similar and shows on average >1wt%. According to Chakhmouradian (2002) strontium is incorporated into the apatite structure through substitutions (Pushcharovskii et al. 1987, Rakovan and Hughes 2000): $Ca^{2+} \Leftrightarrow Sr^{2+}$ (solid solution toward strontium-apatite) or $3Ca^{2+} + 2Ca^{2+} \Leftrightarrow 3Sr^{2+} + Na^{1+} + LREE^{3+}$ (solid solution toward belovite). Also examined data show that the solid solution between apatite and strontium-apatite is continuous. Chakhmouradian (2002) concluded that Sr-apatite (Lovozero and Murun) is formed by reaction of the primary fluorapatite with deuteric fluids (late-stage) and involves progressive evolution towards enrichment in Sr and LREE.

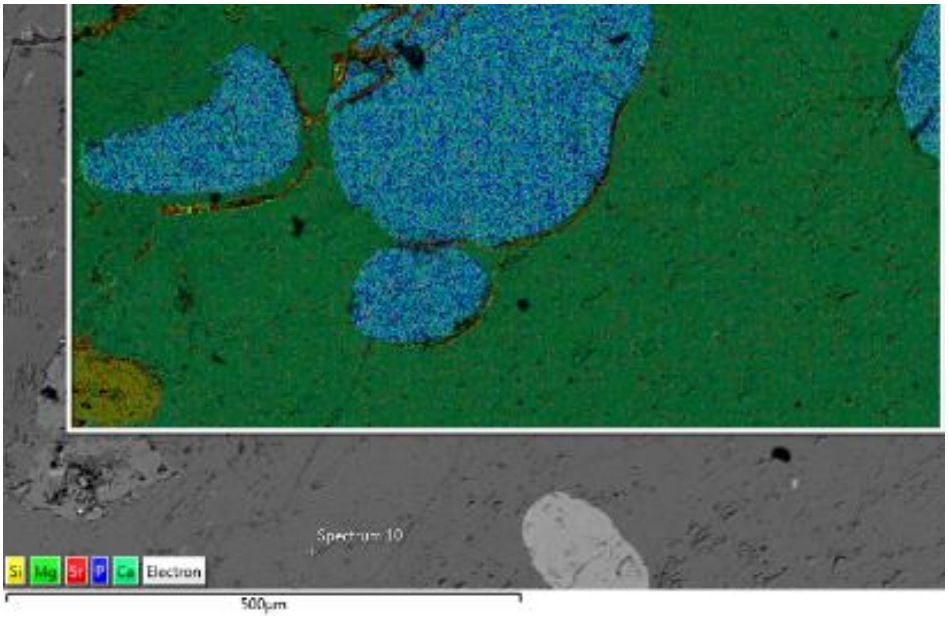

Fig.4.26 Back-scattered electron (BSE) images of the samples from Rib. de Almada containing apatite and calcite, with superimpose false-colour X-Ray map equally showing absence of zoning. Also shows Sr concentration in both phases.

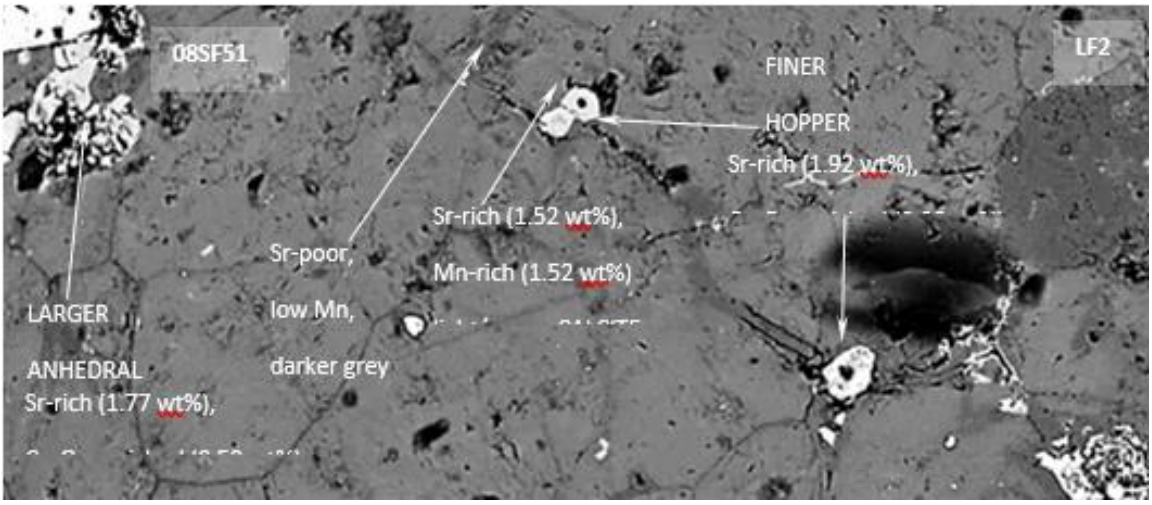

Fig.4.27 BSE image from Rib. Domingo Santo showing hopper texture of apatite set in granoblastic calcite in 08SF51.

Representative compositions of mica from the Fogo intrusive carbonatite are given in Tables 6.4.5a, 6.4.5b, 6.4.5c and 6.4.5d (Appendix 2.b). The average figures with their standard deviation for the mica is presented in Table 4.4.

Mica occurs as both phlogopite and biotite in Fogo carbonatites (Figure 4.28). Substitution of Fe for Mg forms biotite (average FeO for phlogopite is 11.36 wt% (Rib. de Almada) and 10.05 wt% (Rib. Santo Domingo)), then average FeO in biotite increases to 13.6-15.1 wt% (Rib. de Almada) and up to 21.2 wt% in Monte Almada. Mica is the second main potassium-bearing phase (after feldspar) with values reaching

9.38 wt% K_2O. Fogo mica has a substantial content of TiO_2 from 1.06 wt% (Rib. Santo Domingo phlogopite to 3.04 wt% in (Rib. de Almada biotite. This reflects evolution of the carbonatite magma from low to high TiO_2. Mica in the studied carbonatites is aluminous, with an average value close to 12 wt%, but reaching a maximum of 15 wt% Al_2O_3. The lowest average SiO_2 from Monte Almada biotite (36.7 wt%) and the highest by Rib. Santo Domingo phlogopite (42.9 wt%).

	EDS LF1 08SF01	PHLOG small in glimmerite		larger single crystals	EDS LF1 08SF03	large rim	core		EDS LF1 08SF03	small PHLOG	WDS LF1 08SF03	PHLOG	EDS LF1 08SF05	one large BIOT	EDS LF2 SFS2a	PHLOG	EDS LF3 08SF64a	BIOT
	ave n=10	st dev n=10	ave n=5	st dev n=5	ave n=9	st dev n=9	ave n=7	st dev n=7	ave n=21	st dev n=21	ave n=9	st dev n=9	ave n=10	st dev n=10	SFS2a pb2	ave n=1	ave n=4	st dev n=4
SiO_2	40.25	*0.83*	40.77	*0.51*	36.26	*0.61*	35.97	*0.50*	38.48	*0.73*	38.37	*1.11*	36.88	*0.44*	42.29	42.29	35.40	*0.25*
TiO_2	1.76	*0.17*	2.19	*0.37*	3.36	*0.17*	3.62	*0.17*	2.89	*0.18*	2.96	*0.52*	3.07	*0.29*	1.04	1.04	2.32	*0.11*
Al_2O_3	10.99	*0.18*	11.98	*0.94*	13.82	*0.65*	13.80	*0.49*	12.91	*0.50*	14.70	*0.60*	13.46	*0.61*	11.94	11.94	11.95	*0.04*
FeO	11.31	*0.51*	14.66	*0.61*	13.56	*0.37*	14.73	*0.53*	12.40	*0.52*	13.82	*1.02*	14.85	*0.78*	10.41	10.41	21.96	*0.38*
MnO	0.26	*0.07*	0.27	*0.06*	0.35	*0.09*	0.36	*0.11*	0.28	*0.09*	0.35	*0.07*	0.53	*0.08*	0.00	0.00	0.86	*0.13*
MgO	18.54	*0.22*	16.52	*0.50*	16.33	*0.52*	15.43	*0.25*	18.65	*0.41*	16.09	*1.35*	15.90	*0.60*	19.35	19.35	10.87	*0.20*
CaO	0.47	*0.21*	0.48	*0.11*	0.43	*0.09*	0.32	*0.29*	0.34	*0.13*	0.50	*0.14*	0.36	*0.14*	1.10	1.10	0.48	*0.19*
Na_2O	0.27	*0.03*	0.25	*0.01*	0.31	*0.04*	0.30	*0.02*	0.26	*0.05*	0.30	*0.08*	0.37	*0.05*	0.29	0.29	0.23	*0.02*
K_2O	8.78	*0.41*	8.19	*0.11*	8.37	*0.20*	8.29	*0.20*	9.23	*0.34*	8.06	*0.14*	9.38	*0.24*	7.90	7.90	8.83	*0.25*
BaO	0.11	*0.11*	0.09	*0.05*	0.81	*0.12*	0.94	*0.13*	0.20	*0.18*	0.14	*0.10*	0.32	*0.21*	0.06	0.06	0.48	*0.13*
F	0.48	*0.15*	0.41	*0.03*	0.04	*0.00*	0.06	*0.03*	0.05	*0.03*	0.07	*0.02*	0.04	*0.04*	0.00	0.00	0.00	*0.00*
HfO_2	n/a	*n/a*	n/a	*n/a*	0.78	*0.11*	0.68	*0.12*	0.71	*0.17*	n/a	*n/a*	n/a	*n/a*	n/a	n/a	n/a	*n/a*
TOTAL	93.20	*1.37*	95.82	*1.01*	94.81	*0.61*	94.93	*1.29*	96.72	*1.24*	95.36	*1.33*	95.15	*0.54*	94.38	94.38	93.37	*0.29*
TiO_2+FeO	13.08	*0.61*	16.85	*0.37*	16.92	*0.50*	18.34	*0.66*	13.19	*0.50*	16.78	*2.34*	17.92	*0.95*	11.45	11.45	24.28	*0.31*
Si	3.027	*0.026*	3.008	*0.038*	2.746	*0.029*	2.734	*0.019*	2.822	*0.031*	2.828	*0.051*	2.784	*0.025*	3.075	3.075	2.841	*0.012*
Ti	0.100	*0.009*	0.122	*0.020*	0.192	*0.011*	0.207	*0.007*	0.159	*0.010*	0.164	*0.029*	0.174	*0.016*	0.057	0.057	0.140	*0.007*
Al	0.974	*0.013*	1.041	*0.076*	1.234	*0.054*	1.236	*0.040*	1.116	*0.044*	1.277	*0.047*	1.198	*0.055*	1.023	1.023	1.131	*0.007*
Fe^{2+}	0.712	*0.034*	0.905	*0.041*	0.859	*0.028*	0.936	*0.024*	0.761	*0.033*	0.853	*0.125*	0.938	*0.050*	0.633	0.633	1.474	*0.028*
Mn	0.016	*0.004*	0.017	*0.004*	0.022	*0.006*	0.023	*0.007*	0.017	*0.005*	0.022	*0.004*	0.034	*0.005*	0.000	0.000	0.058	*0.009*
Mg	2.079	*0.025*	1.816	*0.046*	1.843	*0.047*	1.748	*0.033*	2.038	*0.031*	1.767	*0.137*	1.789	*0.066*	2.097	2.097	1.300	*0.022*
Ca	0.038	*0.017*	0.038	*0.009*	0.035	*0.008*	0.027	*0.024*	0.027	*0.010*	0.039	*0.011*	0.029	*0.011*	0.086	0.086	0.041	*0.016*
Na	0.039	*0.005*	0.035	*0.001*	0.045	*0.006*	0.045	*0.003*	0.037	*0.008*	0.043	*0.011*	0.054	*0.009*	0.041	0.041	0.035	*0.003*
K	0.842	*0.034*	0.771	*0.016*	0.808	*0.013*	0.803	*0.021*	0.864	*0.032*	0.758	*0.023*	0.903	*0.022*	0.733	0.733	0.904	*0.024*
Ba	0.003	*0.003*	0.003	*0.002*	0.024	*0.004*	0.028	*0.004*	0.006	*0.005*	0.004	*0.003*	0.010	*0.006*	0.002	0.002	0.015	*0.004*
F	0.113	*0.033*	0.096	*0.008*	0.009	*0.008*	0.015	*0.007*	0.011	*0.007*	0.015	*0.004*	0.009	*0.009*	0.000	0.000	0.000	*0.000*
Hf	n/a	*n/a*	n/a	*n/a*	0.020	*0.003*	0.017	*0.003*	0.017	*0.004*	n/a	*n/a*	n/a	*n/a*	n/a	n/a	n/a	*n/a*
TOTAL	7.94		7.75		7.85		7.84		7.89		7.77		7.92		7.74	7.74	7.92	
mg#	0.75		0.67		0.68		0.65		0.73		0.67		0.66		0.77	0.77	0.47	
Fe+Ti	0.81		1.03		2.70		2.68		2.80		1.02		1.11		0.69	0.69	1.61	
Fe/(Fe+Mg)	0.25		0.33		0.32		0.35		0.27		0.33		0.34		0.23	0.23	0.53	
Mg/Fe	2.93		2.01		2.15		1.87		2.69		2.13		1.92		3.31	3.31	0.88	

Table 4.4 Electron microprobe data for mica in the intrusive carbonatite found in Fogo, Cape Verde. Abbreviations: st dev=standard deviation, ave=average, n/a=not analysed. Cations recalculated on the basis of 11 oxygens. Complete tables supplied in Appendix 2b.

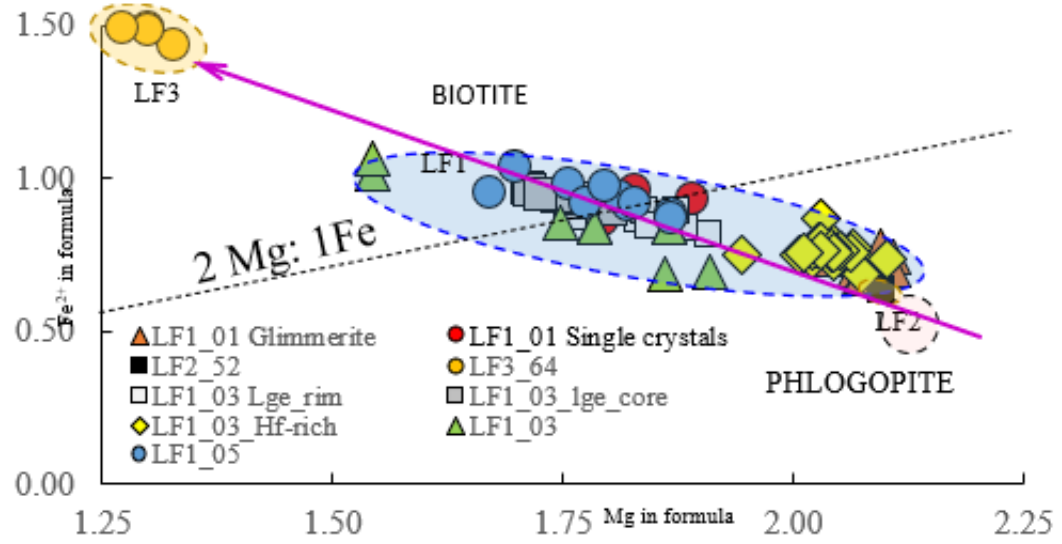

Fig.4.28 Diagram of Fogo mica with plot Mg vs Fe revealing phlogopite and biotite fields. Magmatic evolution trend goes from LF2 (Rib. Santo Domingo) phlogopite to LF3 (Monte Almada) biotite.

Biotite and phlogopite vary from fine-grained to coarse-grained (Figure 4.29). There are areas where fine-grained aggregates are present and developing glimmeritic

regions (Figure 4.29f). In 08SF01 slight chemical differences are detected between the larger singular crystals (akin to biotite) and small glimmeritic mica (phlogopite). Both are inclusion-free. Rare inclusions of calcite and apatite are present in other Fogo samples.

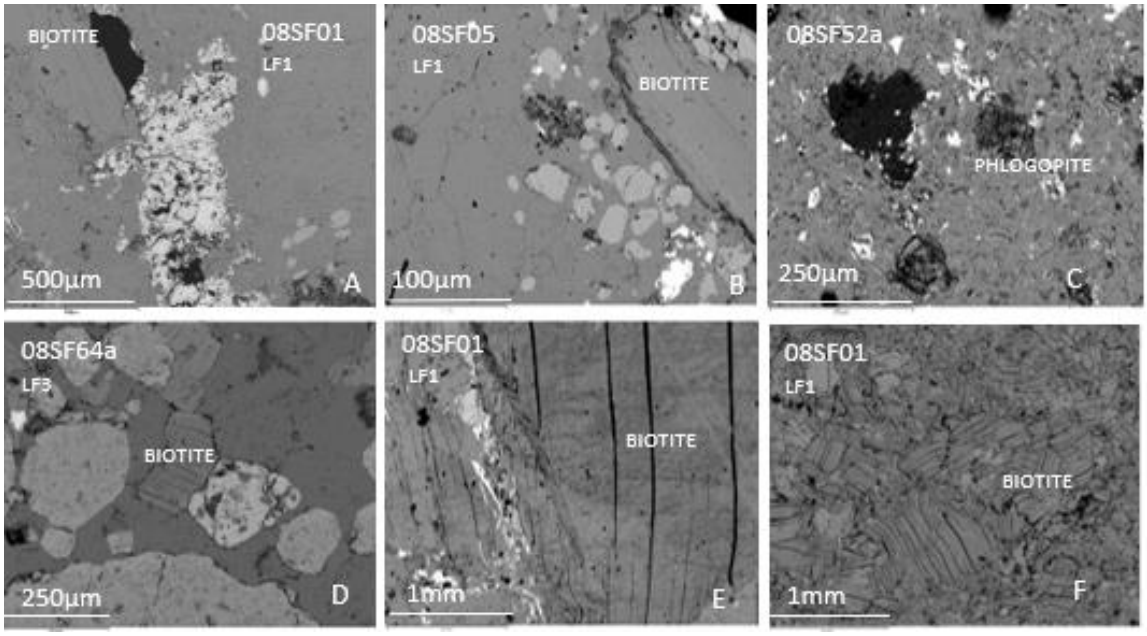

Fig.4.29 BSE images of the samples from Fogo containing biotite and phlogopite. Biotite-phlogopite varies from being phenocrystic (B and E) to fine grained (A, C, D and F) and in some cases the whole area is composed of aggregate of biotite (glimmerite), which shows kinked and broken up texture of crystals due to high straining (F).

Figure 4.30 (after Deer et al., 1966) reveals a steady increase Al_2O_3 as mg# increases, reflecting crystallisation of phlogopite-biotite series. The low-Al crystallised phlogopite was found in Rib. Santo Domingo samples and some from Rib. de Almada. Mica progressively changed to more aluminous biotite, found also in Rib. de Almada. It gradually increased to form highly Al-rich biotite in Monte Almada (Figure 4.30). This trend reflects evolution of carbonatititic magma from being low-Al, progressively achieving higher Al concentrations, with increasing Fe at the same time.

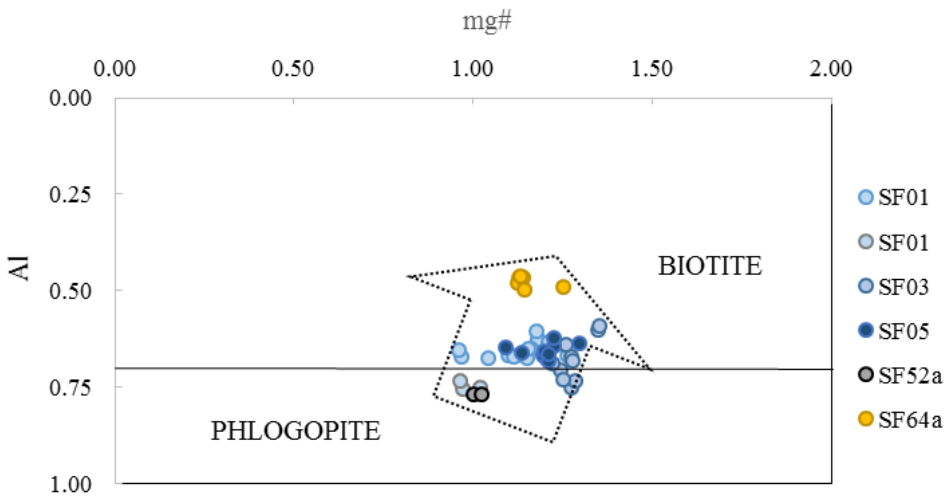

Fig.4.30 Al-mg# plot of phlogopite and biotite across the 3 locations of the Fogo intrusive carbonatites containing analysed mica. It shows progressive compositional variation from phlogopite to biotite. Diagram after Deer et al., 1966

A single, near-euhedral, phlogopite flake from 08SF03 (Rib. de Almada) was checked for core-rim zonation (Figure 4.31). It is a microphenocryst as it is larger than the surrounding crystals, thus crystallised at an early stage of carbonatite formation. Early crystallisation is reflected in the iron/magnesium content. The core is slightly more enriched in FeO than the rim, whereas MgO content shows opposite variation. TiO_2 is also slightly higher in the core than in the rim. BaO is to be lower in the rim. According to Le Bas (2008), Ba is a common in carbonatite mica. The compositional range Mg vs Fe of mica is obvious (Figure 4.32), as phlogopitic mica evolved towards biotite. Hf is present in detectable amounts.

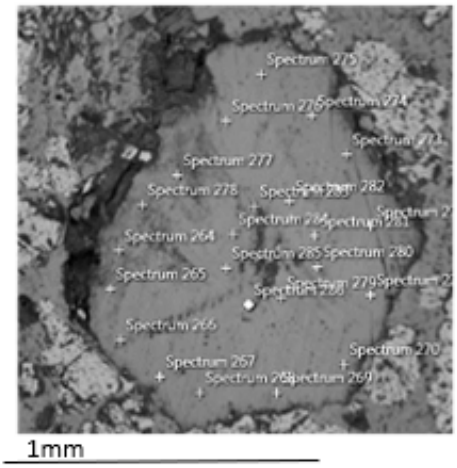

	rim		core	
	ave n=9	st dev n=9	ave n=7	st dev n=7
SiO_2	35.48	*1.45*	35.97	*0.56*
TiO_2	3.24	*0.28*	3.62	*0.17*
Al_2O_3	15.19	*2.63*	13.80	*0.49*
FeO	13.14	*0.79*	14.73	*0.53*
MnO	0.35	*0.08*	0.36	*0.11*
MgO	16.02	*0.68*	15.43	*0.25*
CaO	0.49	*0.17*	0.32	*0.29*
Na_2O	0.30	*0.04*	0.30	*0.02*
K_2O	8.17	*0.36*	8.29	*0.26*
ZrO_2	0.01	*0.02*	0.00	*0.00*
BaO	0.75	*0.21*	0.94	*0.13*
HfO_2	0.77	*0.15*	0.68	*0.12*
ThO_2	0.03	*0.04*	0.03	*0.05*
UO_2	0.00	*0.00*	0.00	*0.00*
TOTAL	94.35	*1.12*	94.92	*1.31*

Fig.4.31 Back-scattered electron (BSE) image of the phlogopite from the 08SF03 sample. The phlogopite flake exhibiting semi-hexagonal shape, which being singled out for the analyses on possible core-rim zonation.

Mica forms an intimate assemblage with titanite-zirconolite-pyrochlore and Hf-poor zircon (mica crystallised prior to zircon) (Figure 4.32). Overall mica in 08SF03 is associated with the rim of the oval-shaped granoblastic calcite which is also composed of pyroxene, apatite, iron oxide and fine-grained calcite. Here prismatic pyroxene shows a radiating texture. It is possible that the space between large calcite crystals was penetrated by hydrothermal fluid and consequently influenced/modified crystallised minerals (mobilisation of rare elements).

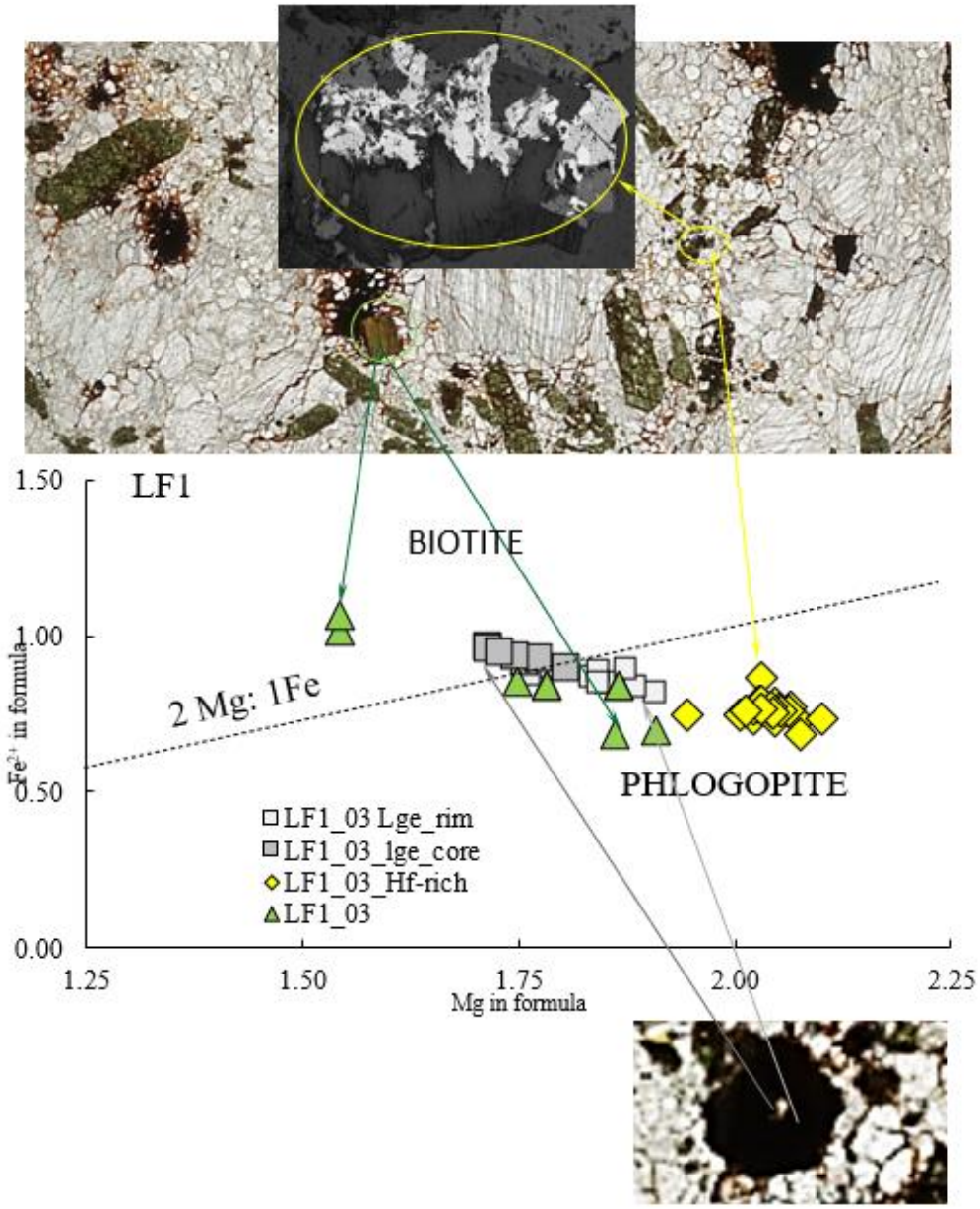

Fig.4.32 Combined BSE images, photomicrographs and diagram Mg vs Fe showing compositional variation of mica in 08SF03. Hf-REEs-rich mica associated with pyrochlore has been mostly Mg-enriched placing it in phlogopite field, single hexagonal flake shows revers core-rim Mg-enrichment as well as the second single crystals which also exhibits compositional variation from biotite to phlogopite (progressive phlogopitization).

According to Reguir et al. (2009), micas are very sensitive to changes such as temperature, pressure and chemistry of their crystallisation environment. Peculiarity of Hf-bearing phlogopite (Figure 4.32) lies in association with not only unusual accessory minerals but also with zircon which is Hf-poor. It suggests partitioning of Hf into phlogopite which means that most of the accessory minerals must have crystallised before the zircon, so when zircon crystallised, there was no Hf left in the system. Hydrothermal fluids must have been enriched in heavy rare earth elements implying remobilization of these elements. Texture of phlogopite also proves the formation of mica prior to crystallisation of titanite, zirconolite, zircon and pyrochlore. Accessory minerals invade phlogopite alongside the rim and cleavage. Phlogopite shows high strain around the lower rim which could occur during metamorphic event (shearing).

Compositions of pyroxene are given in Table 6.4.7a-f (Appendix 2b). Table 4.5 shows the average values with their standard deviations. They vary from diopside to aegirine-augite. Samples from Rib. de Almada contain a small proportion of pyroxene (diopside) but from Monte Almada clinopyroxene (diopside and aegirine-augite) is more abundant. Clinopyroxene displays a range of shapes (though rarely euhedral) and sizes up to few mm (Figure 4.33). Most of the crystals are fractured. Dark discolouration along the fractures is an alteration product.

According to its mg#, two varieties of pyroxene can be distinguished. The Rib. de Almada samples show higher mg# (0.70) but in Monte Almada samples mg# is much lower (0.42-0.57), reflecting the increase from the average value of 9 wt% FeO in Rib. de Almada to 17 wt% in Monte Almada. Wo-En-Fs diagram (Figure 4.34) displays the composition of pyroxene from both locations. Clinopyroxene from Rib. de Almada and one sample from Monte Almada falls in the middle of the diopside field, while Monte Almada plots on the border of diopside-hedenbergite field, exhibiting a clear evolution of carbonatite from Rib. de Almada towards Monte Almada. Consequently Rib. de Almada pyroxene is more primitive, whereas Monte Almada is relatively more evolved, consistent with the trend seen in mica. Pyroxene from Monte Almada located at higher elevation largely falls in diopside field akin towards hedenbergite but samples from Monte Almada from the valley show lower Ca and higher Fe values trending towards aegirine-augite composition, thus the pyroxene is more evolved.

	DIOP EDS SF01		WDS SF03		EDS SF07		WDS SF07		EDS SF62a		HED EDS SF62a		AUG EDS SF62a		DIOP WDS SF64a		WDS SF66		EDS SF66	
	ave. n=6	st.dev n=6	ave. n=15	st.dev n=15	ave. n=14	st.dev n=14	ave. n=6	st.dev n=6	ave. n=8	st.dev n=8	ave. n=8	st.dev n=8	ave. n=8	st.dev n=8	ave. n=3	st.dev n=3	ave. n=2	st.dev n=2	ave. n=13	st.dev n=13
SiO_2	50.11	1.67	52.02	1.02	50.24	1.27	50.92	1.38	51.90	0.44	50.74	0.40	51.87	0.30	50.48	0.65	51.83	3.04	52.74	0.87
TiO_2	0.68	0.37	0.54	0.27	0.62	0.27	0.47	0.27	0.36	0.13	0.32	0.00	0.29	0.13	n/a	n/a	n/a	n/a	0.22	0.13
Al_2O_3	1.46	0.85	1.71	0.61	1.64	0.71	1.80	0.68	0.72	0.19	0.53	0.00	0.86	0.22	2.06	0.47	1.60	0.71	0.85	0.29
FeO	9.43	1.40	9.01	0.90	10.71	1.45	11.96	0.35	15.24	0.83	17.54	0.29	16.93	0.39	16.75	2.73	14.06	0.67	12.61	1.52
MnO	0.53	0.06	0.47	0.11	0.58	0.09	0.72	0.09	1.20	0.12	1.20	0.11	1.16	0.26	0.78	0.13	0.78	0.14	1.10	0.24
MgO	11.43	0.75	11.82	0.66	10.77	0.96	9.88	0.14	8.16	0.59	6.88	0.05	7.49	0.16	6.88	1.45	8.25	0.08	9.57	0.89
CaO	21.56	0.51	22.03	1.23	21.43	0.52	21.19	1.02	20.33	0.78	20.07	0.11	18.27	0.39	19.23	2.16	20.72	0.19	20.34	0.67
Na_2O	1.24	0.31	1.85	0.84	1.56	0.51	2.58	0.79	2.03	0.39	1.91	0.08	3.05	0.14	3.36	1.32	2.42	0.11	2.03	0.24
TOTAL	96.74	0.16	99.47	0.54	97.56	1.85	99.51	1.01	99.93	0.39	99.18	0.08	99.92	0.14	99.54	0.78	99.64	1.42	99.46	0.94
Si	1.946	0.053	1.941	0.034	1.936	0.043	1.913	0.029	1.983	0.002	1.983	0.001	1.987	0.008	1.924	0.014	1.969	0.093	2.002	0.015
Ti	0.020	0.011	0.015	0.008	0.018	0.008	0.013	0.008	0.010	0.004	0.009	0.000	0.008	0.004	0.000	0.000	0.000	0.000	0.006	0.004
Al	0.067	0.039	0.075	0.027	0.075	0.032	0.080	0.030	0.032	0.009	0.024	0.000	0.039	0.010	0.093	0.021	0.072	0.033	0.038	0.013
Fe^{2+}	0.095	0.041	0.136	0.062	0.134	0.072	0.121	0.057	0.132	0.024	0.136	0.007	0.200	0.012	0.226	0.008	0.277	0.136	0.305	0.031
Fe^{3+}	0.201	0.013	0.145	0.072	0.196	0.048	0.255	0.064	0.356	0.006	0.422	0.012	0.320	0.013	0.307	0.089	0.170	0.163	0.095	0.032
Mn	0.018	0.002	0.015	0.003	0.019	0.003	0.023	0.003	0.039	0.004	0.040	0.003	0.038	0.008	0.025	0.004	0.025	0.004	0.035	0.008
Mg	0.661	0.040	0.658	0.036	0.619	0.060	0.553	0.009	0.464	0.030	0.401	0.000	0.428	0.009	0.391	0.084	0.467	0.010	0.541	0.046
Ca	0.897	0.024	0.881	0.052	0.885	0.023	0.854	0.048	0.832	0.029	0.840	0.002	0.750	0.015	0.785	0.092	0.843	0.017	0.827	0.022
Na	0.093	0.023	0.134	0.060	0.116	0.036	0.188	0.055	0.151	0.029	0.145	0.005	0.227	0.011	0.248	0.096	0.178	0.010	0.150	0.019
TOTAL	4.000	0.000	4.000	0.000	4.000	0.000	4.000	0.000	4.000	0.000	4.000	0.000	4.000	0.000	4.000	0.000	4.000	0.000	4.000	0.000
Wo	0.510	0.016	0.481	0.016	0.522	0.026	0.475	0.015	0.504	0.002	0.505	0.003	0.501	0.005	0.455	0.029	0.475	0.170	0.459	0.007
En	0.376	0.015	0.359	0.015	0.364	0.019	0.308	0.008	0.281	0.010	0.241	0.002	0.286	0.004	0.226	0.038	0.263	0.001	0.300	0.023
Fs	0.114	0.007	0.160	0.017	0.115	0.026	0.217	0.009	0.216	0.009	0.254	0.005	0.214	0.009	0.319	0.067	0.262	0.003	0.240	0.029
mg#	0.767	0.014	0.700	0.031	0.762	0.045	0.596	0.007	0.566	0.018	0.487	0.007	0.572	0.014	0.423	0.091	0.512	0.009	0.575	0.051

Table 4.5 Electron microprobe data for pyroxene in the intrusive carbonatite found in Rib. de Almada and Monte Almada, Fogo, Cape Verde. Abbreviations: st dev=standard deviation, ave=average. Complete tables supplied in Appendix.

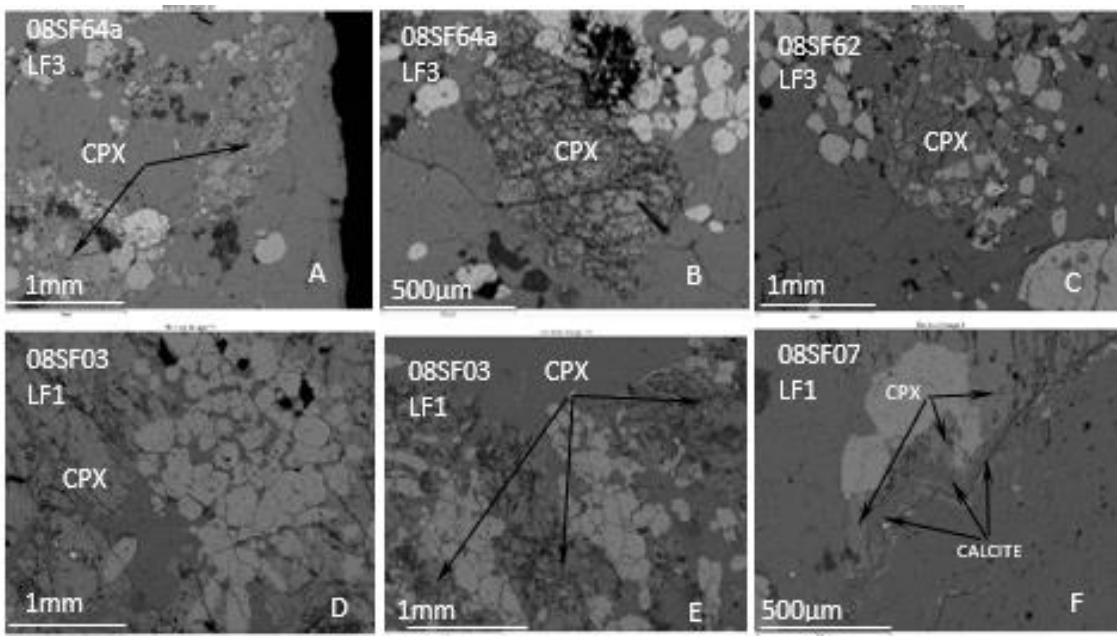

Fig.4.33 Back-scattered electron (BSE) images of the samples from Rib. de Almada and Monte Almada containing clinopyroxene demonstrating euhedral (E), subhedral (B) and anhedral (A, C, D and F) shape. Diopside appears broken up with many irregular cracks.

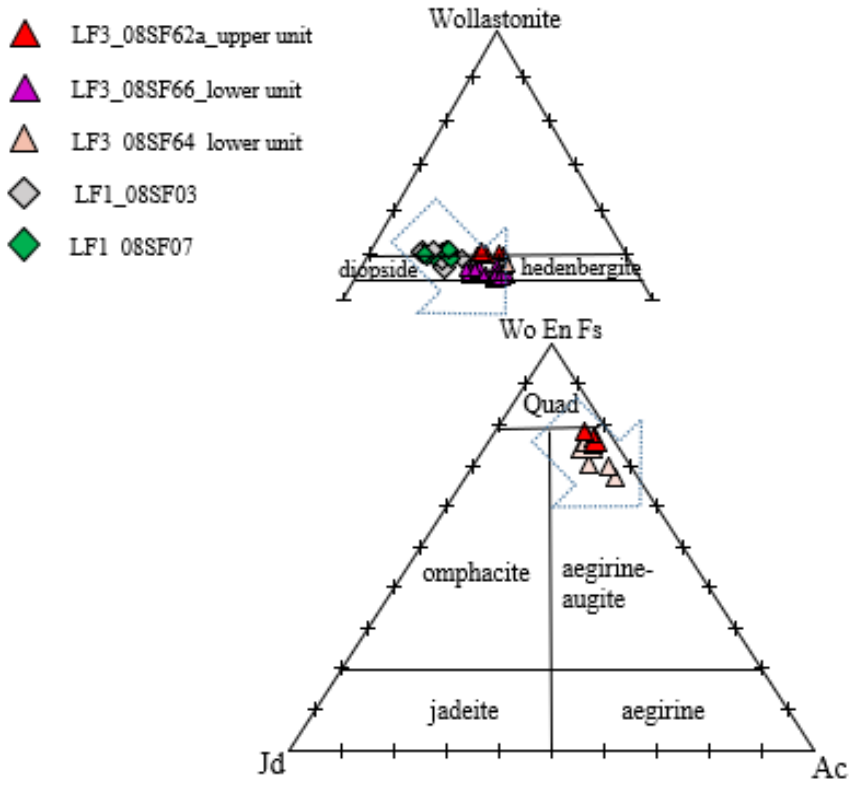

Fig.4.34 Wo-En-Fs and WoEnFs-Jd-Ac diagrams presenting the composition of pyroxene from the Fogo carbonatites differentiating two locations as Rib. de Almada (diamonds) and Monte Almada (triangles). The arrow shows the trend of evolution of carbonatite (originally less iron-rich) thus crystallising diopside (position in the middle of the diopside field) and shifting composition of clinopyroxene towards more Fe-rich side (hedenbergite field) and consequently moving towards aegirine-augite composition.

The complete electron microprobe data for amphibole from the Fogo carbonatites is given in Appendix 2b in Table 6.4.9a,b and c. Average figures with their standard deviations are given in Table 4.46.

According to the IMA classification (2012) the amphibole is classified as ferro-richterite and calcian-ferro-eckermannite, which are alkali amphiboles. Amphibole, found only in LF3, has a low TiO_2 content (0.48 to 2.03 wt%). It is Mg-poor (2.7-4.9 wt%) and its Al_2O_3 falls below 1.73 wt%. Substantial amount of FeO is present (average concentration of 22.17 wt%). CaO varies between 5.40 and 12.20 wt%. Na_2O (but not K_2O) is present (5.9 to 9.9 wt%). The amount of MnO varies from 0.50 to 1.04 wt%.

As both types of amphiboles (richterite and eckermannite) were found in a single crystal (Figure 4.35), the amphibole internally displays inhomogeneity (Figure 4.36). The main factor of heterogeneity is interaction with alkaline fluid, as the affected area of amphibole is in contact with nepheline. Less sodic part of amphibole

(7.06-7.76 wt% Na_2O) and more calcium-rich (7-89-8.53 wt% CaO) is richterite. In the rim region the amphibole, in close proximity to nepheline (13 wt% Na_2O), forms the more sodium-rich eckermannite. As Hawthorne and Oberti (2007) observed that the substitution of Na for Ca (B), seen in Figure 4.36, can be coupled with Na entering A site in richterite, thus pushing the composition towards eckermannite. According to Anderson (1989), large scale fenites (in the Fen complex) originated by release of fluids from alkaline silicate magmas such as ijolite or syenite, prior to emplacement of carbonatites. The petrographic observation of amphibole from the Fogo carbonatite, together with geochemical data, argues for possible metasomatic alteration associated with movement of alkalis in carbonatites.

LF3 08SF66	FERRO-RICHTERITE		CALCIAN-FERRO-ECKERMANNITE		one crystal_1		one crystal_2	
	ave n=5	st dev n=5	ave n=9	st dev n=9	ave n=5	st dev n=5	ave n=5	st dev n=5
SiO_2	53.38	0.44	52.58	0.83	53.20	0.77	53.64	0.27
TiO_2	0.61	0.13	1.11	0.43	0.71	0.19	0.80	0.17
Al_2O_3	0.96	0.10	1.05	0.07	1.05	0.14	1.20	0.32
Fe_2O_3	0.00	0.00	0.00	0.00	0.00	0.00	0.00	0.00
FeO	20.67	1.46	22.10	0.69	21.88	0.43	23.23	0.60
MnO	0.93	0.09	0.74	0.18	0.70	0.11	0.58	0.09
MgO	4.61	0.76	3.15	0.25	3.84	0.44	3.18	0.37
CaO	9.78	1.69	6.93	0.99	7.86	0.46	6.64	0.89
Na_2O	7.00	0.74	8.22	0.30	7.78	0.46	8.40	0.41
K_2O	0.02	0.02	0.03	0.02	0.03	0.03	0.04	0.04
F	0.00	0.00	0.00	0.00	0.00	0.00	0.00	0.00
Cl	0.00	0.00	0.00	0.00	0.00	0.00	0.00	0.00
H_2O	1.98	0.02	1.93	0.02	1.95	0.02	1.96	0.01
O=F,Cl	0.00	0.00	0.00	0.00	0.00	0.00	0.00	0.00
TOTAL	99.93	1.13	97.83	0.72	99.01	1.15	99.66	0.31
Si	8.099	0.045	8.177	0.072	8.161	0.025	8.195	0.023
Ti	0.070	0.015	0.129	0.050	0.082	0.022	0.092	0.019
Al	0.171	0.018	0.192	0.012	0.190	0.024	0.216	0.057
Fe^{3+}	0.000	0.000	0.000	0.000	0.000	0.000	0.000	0.000
Fe^{2+}	2.624	0.197	2.875	0.079	2.807	0.039	2.968	0.074
Mn	0.119	0.011	0.098	0.025	0.091	0.014	0.075	0.011
Mg	1.041	0.167	0.729	0.059	0.880	0.106	0.724	0.085
Ca	1.589	0.265	1.155	0.172	1.293	0.085	1.086	0.147
Na	2.060	0.229	2.479	0.085	2.313	0.119	2.489	0.121
K	0.004	0.004	0.007	0.004	0.005	0.006	0.007	0.009
F	0.000	0.000	0.000	0.000	0.000	0.000	0.000	0.000
Cl	0.000	0.000	0.000	0.000	0.000	0.000	0.000	0.000
TOTAL	15.777	0.057	15.841	0.059	17.822	0.020	17.852	0.026

Table 4.6 Electron microprobe data for amphibole in the intrusive carbonatite found in 08SF66 from Monte Almada, Fogo, Cape Verde. Abbreviations: st dev=standard deviation, ave=average. Complete tables supplied in Appendix 2b (F and Cl were below detection limit in all analyses).

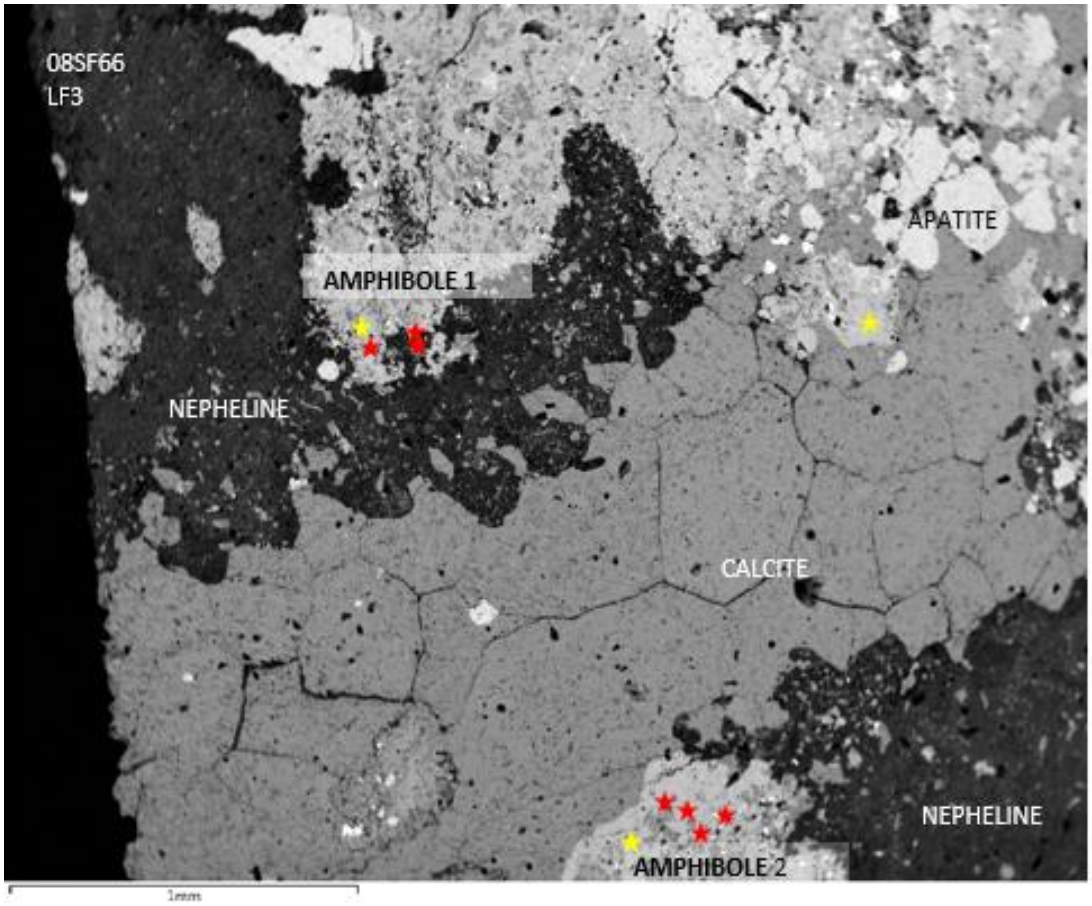

Fig.4.35 Back-scattered electron (BSE) image of the samples 08SF66 from Monte Almada containing inhomogeneous amphibole (yellow star=ferro-richterite, red star=calcian-ferro-eckermmanite). Association with nepheline is apparent. Calcite vein cross cutting feldspathoid/amphibole assemblage. The calcite vein is composed of mostly euhedral crystals showing triple junctions

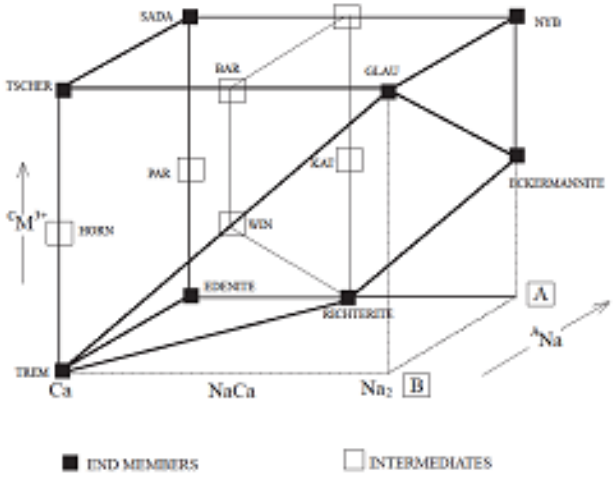

A: $NaNa_2Mg_5(Si_8Al_1)O_{22}(OH)_2$ B: $Na_2Mg_5(Si_{10}Al_1)O_{22}(OH)_2$

Fig. 4.36 The plane outlined by the heavy line containing end members of Trem-Richterite-Eckermennite-Glaucophane-Win-Trem showing the compositional limits of amphibole. A-B-C is compositional space for amphiboles (only Ca and Na as B cations). Compositions shown as white squares are a 50:50 combination of the end-member, e.g. hornblende can be represented as 0.50 tremolite and 0.50 tschermakite, Diagram after Hawthorne and Oberti, 2007.

Some intrusive carbonatites from Monte Almada location contain minor garnets (samples 08SF64 and 08SF66). Compositions of garnet are given in Table 6.4.11a and b (Appendix 2a) and the average values in Table 4.7. The CaO content is considerable and fairly constant (31.5 wt%). Al_2O_3 content varies from 0.9-2.4 wt%. Concentration of SiO_2 is more variable in SF64 from 29.1 to 37.3 wt% and less in SF66 (34.5 wt%). The garnet has a significant amount of TiO_2 (2.8-8.8 wt%) so it is Ti-rich.

	MELANITE 08SF64A ave n=16	st dev n=16	Ti-ANDRADITE 08SF66 ave n=13	st dev n=13
SiO_2	32.35	*1.96*	34.49	*0.66*
TiO2	5.95	*1.58*	3.53	*0.90*
Al_2O_3	1.66	*0.52*	1.20	*0.28*
Fe_2O_3	22.45	*2.35*	25.77	*1.19*
FeO	1.87	*1.95*	1.37	*0.80*
MnO	0.55	*0.15*	0.63	*0.10*
MgO	0.59	*0.21*	0.37	*0.09*
CaO	31.27	*0.75*	31.72	*0.32*
ZrO_2	0.33	*0.31*	0.66	*0.39*
TOTAL	97.53	*1.04*	99.73	*0.76*
Cations recalculated on the basis of 25 oxygens				
Si	2.812	*0.116*	2.919	*0.042*
Ti	0.382	*0.108*	0.225	*0.057*
Al	0.164	*0.048*	0.119	*0.028*
Fe^{+3}	1.473	*0.161*	1.642	*0.086*
Fe^{+2}	0.135	*0.137*	0.096	*0.056*
Mn	0.042	*0.011*	0.045	*0.007*
Mg	0.074	*0.024*	0.047	*0.011*
Ca	2.908	*0.057*	2.877	*0.028*
Zr	0.012	*0.010*	0.028	*0.016*
TOTAL	8.00	*0.00*	8.00	*0.00*
almandine	4.29	*3.91*	3.12	*1.80*
pyrope	2.34	*0.77*	1.52	*0.37*
grossular	7.51	*2.25*	5.64	*1.30*
spessartine	1.30	*0.35*	1.45	*0.22*
uvarovite	0.00	*0.00*	0.21	*0.25*
andradite	67.31	*6.65*	77.53	*3.80*
Ca-Ti Gt	17.20	*4.12*	10.58	*2.50*

Table 4.7 Electron microprobe data for garnet in the intrusive carbonatite found in 08SF64 and 08SF66 from Monte Almada, Fogo, Cape Verde. Abbreviations: st dev=standard deviation, ave=average. Complete tables supplied in Appendix 2b

Garnet in 08SF64 is 50-75% andradite (Table 4.7). The second most abundant component is Ca-Ti garnet (12 to 25%). The third constituent is almandine from 0 to 17%. The garnet in 08SF66 contains higher content of andradite than in 08SF64 from 69.2 to 82.2% (Table 6.4.11b). The next important component, as previously, is Ca-Ti garnet with a lower and more limited compositional range (8.4 to16.0%). The third

abundant component is grossular (3.3-6.6%). Almandine is present only between 0 and 5.3%. According to Fig 4.37, the garnet is Ti-rich almandine/ melanite (after Chen et al., 2016; Ray et al., 2011). According to Deer et al. (1982), if the TiO_2 is below 15 wt% it is melanite/ Ti-andradite. Consequently, sample 08SF66 contains melanite, while sample 08SF64 contains a combination of melanite and Ti-rich andradite.

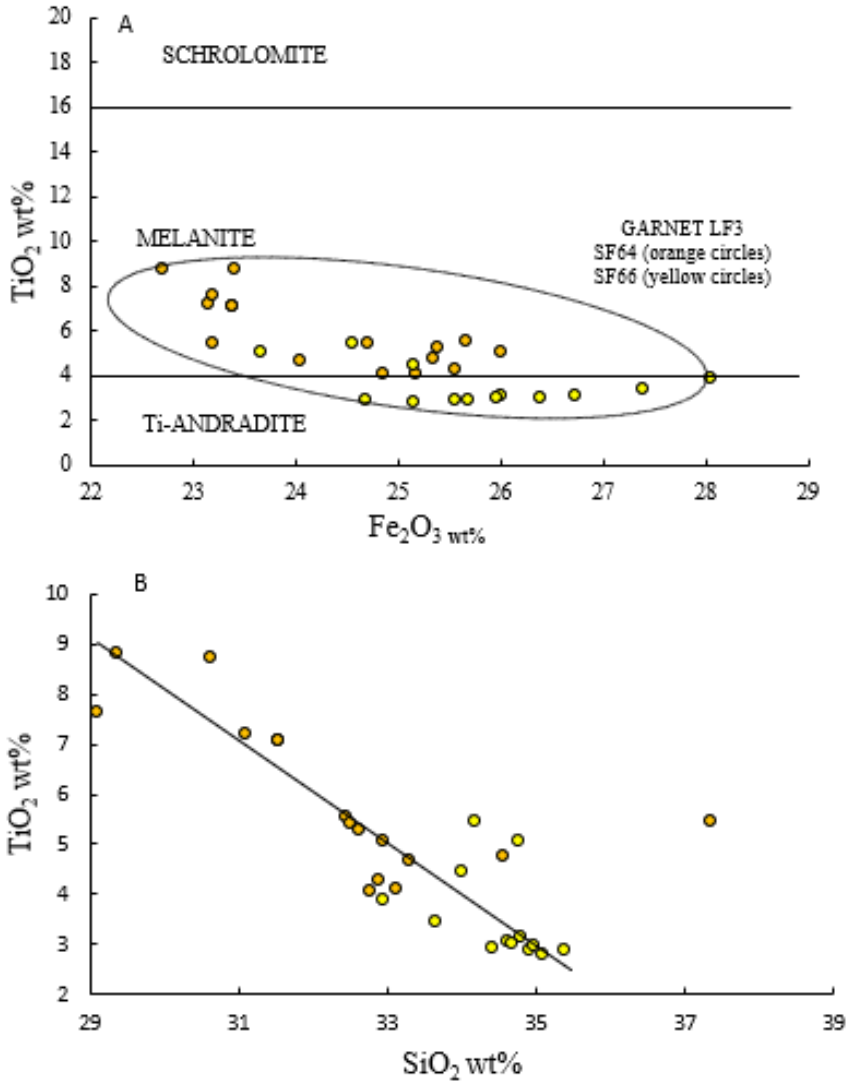

Fig.4.37 The major element variation diagram for garnet. Diagram showing Fe_2O_3 and SiO_2 vs TiO_2. Different compositional fields highlight schrolomite, melanite and Ti-andradite (Ray et al., 2011).

Garnets occur as rare, small and anhedral crystals, often intimately associated with apatite or titanite (Figure 4.38) but also magnetite (Figure 4.39). Single grains of Ti-andradite/melanite are zoned in Ti, Fe and Al content. Essentially the core of the garnet has higher concentration of TiO_2 than the outer parts of the crystal.

According to Chakhmouradian and McCammon (2005) and Dunworth and Bell (2003), the formation of melanite arises with substitution of Ti, Al and Fe in the

tetrahedral site which preferentially incorporates $Al \geq Fe^{3+} \geq Ti$. A diagram of Fe_2O_3 vs TiO_2 (Figure 4.37a) shows an overall negative slope, which could validate the substitution trend. However, Huggins et al. (1977b) and Armbruster et al. (1998) indicated that the main substitution would be Ti-Si exchange. The good negative correlation on the SiO_2 vs TiO_2 diagram (Figure 4.38b) demonstrates substitution of Ti for Si. The availability of TiO_2 in Fogo carbonatites is documented by crystallisation of Ti-rich phases such as titanite or Ti-magnetite (Figure 4.38).

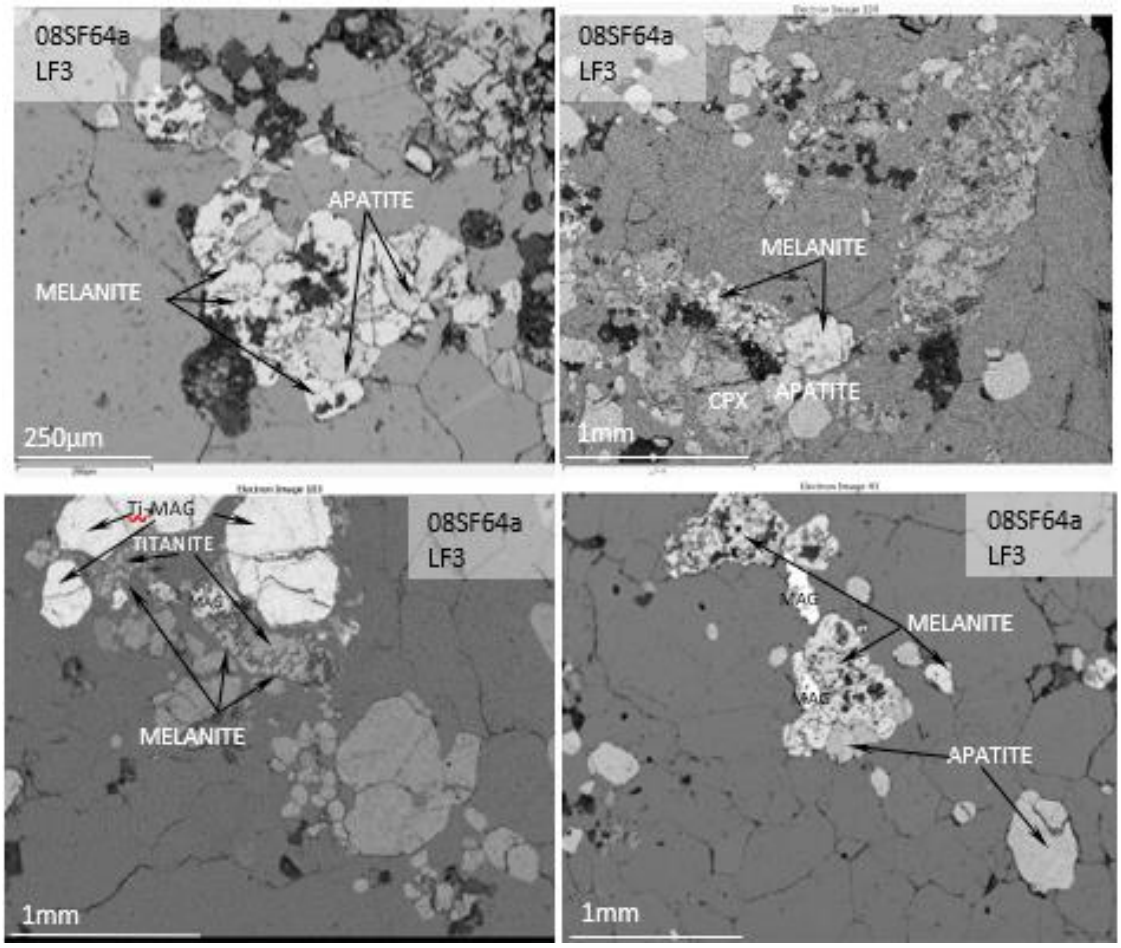

Fig.4.38 Back-scattered electron (BSE) images of samples from Monte Almada containing Ti-rich garnet melanite. Anhedral garnet displays internally granular texture. It is also intimately associated with apatite or titanite

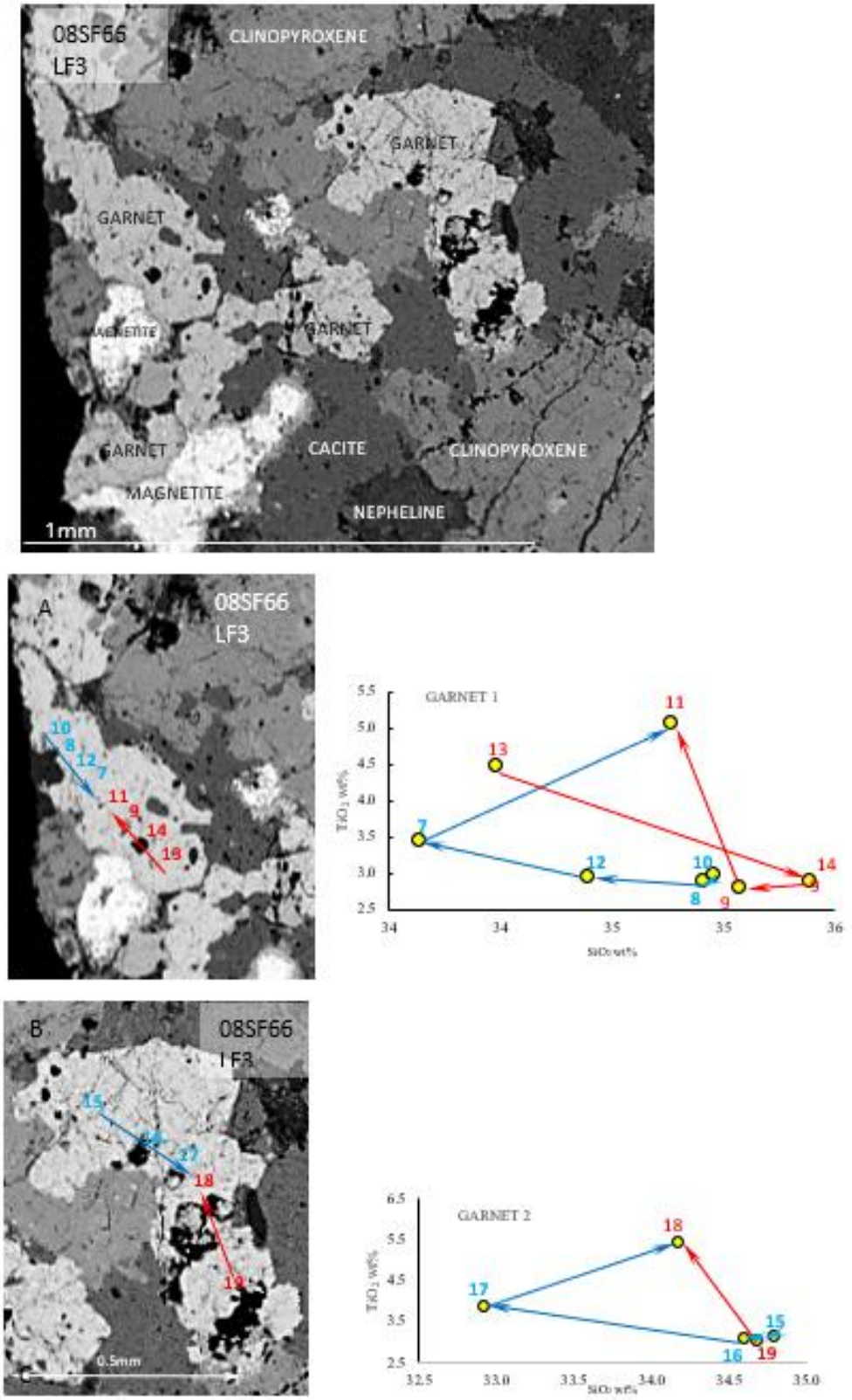

Fig.4.39 BSE images of 08SF66 from Monte Almada. A) Ti-rich garnet exhibiting intimate association with Ti-poor magnetite. Anhedral garnet displays intergrowing texture with calcite (inclusions of calcite present in the garnet). B) and C) single garnets with plotted points, investigated for variation in Ti concentration. Plot SiO_2 vs TiO_2 reveals enrichment in Ti (and to some point in silica) in the core. Arrows present the enrichment path towards the central point of the grain. Complexity of the path reflects problem with other phases crystallising from the magma at the same time and competing for Si and Ti.

Major element compositions of plagioclase are given in Table 6.4.13a-b (Appendix 2b). Table 4.8 shows the average values with their standard deviation. Albite occurs in samples from Monte Almada and Rib. de Almada. Plagioclase in the upper unit of Monte Almada is closer to the Ab end-member (Ab_{98}) (Figure 4.40). The Al_2O_3 content is variable 20-30 wt% (more variable in Rib. de Almada samples as alteration to zeolite is more common). The concentration of Na_2O is fairly constant with average values of 9.1-9.9 wt%.

Albite in the two samples exhibit slightly different petrographic features (Figure 4.41). In Rib. de Almada it forms euhedral to anhedral crystals and is intimately associated with apatite. Alteration of albite to zeolite is common. The upper Monte Almada site contains albitic plagioclase which does not show alteration to zeolite though an association with orthoclase is apparent. Thus, the topographically higher rocks are not so intensely fenitized as the lower outcrops where plagioclase is altered to zeolite.

	LF1 08SF07				LF3 08SF62A	
ALBITE	ave n=6	st dev n=6	ave n=3	st dev n=3	ave n=11	st dev n=11
SiO_2	57.69	*3.79*	66.46	*1.43*	68.73	*0.46*
Al_2O_3	29.56	*1.82*	19.11	*0.06*	19.68	*0.19*
FeO	0.05	*0.03*	0.02	*0.02*	0.14	*0.08*
CaO	0.32	*0.53*	0.17	*0.14*	0.16	*0.05*
Na_2O	9.73	*2.33*	9.05	*0.33*	9.94	*0.10*
K_2O	0.15	*0.09*	0.35	*0.21*	0.18	*0.05*
BaO	0.01	*0.02*	0.01	*0.02*	0.07	*0.08*
TOTAL	97.50	*3.25*	95.20	*1.42*	99.45	*0.62*
Si	10.389	*0.277*	12.080	*0.071*	11.955	*0.035*
Al	6.279	*0.261*	4.094	*0.077*	4.035	*0.032*
Fe	0.007	*0.005*	0.004	*0.003*	0.021	*0.012*
Ca	0.060	*0.099*	0.033	*0.028*	0.029	*0.010*
Na	3.438	*0.973*	3.189	*0.069*	3.351	*0.024*
K	0.035	*0.021*	0.081	*0.049*	0.039	*0.011*
Ba	0.001	*0.001*	0.001	*0.002*	0.005	*0.005*
TOTAL	20.208	*0.696*	19.504	*0.045*	19.714	*0.032*
Or	1.090	*0.850*	2.440	*1.470*	1.14	*0.33*
Ab	96.810	*4.590*	96.560	*2.250*	98.01	*0.37*
An	2.100	*3.760*	1.010	*0.830*	0.85	*0.29*

Table 4.8 Electron microprobe data for plagioclase in the intrusive carbonatite found in Rib. de Almada (08SF07) and Monte Almada (08SF62), Fogo, Cape Verde. Abbreviations: st dev=standard deviation, ave=average. Complete tables supplied in Appendix 2b. Low totals in albite from 08SF07 reflects alteration process such as Na-fenitization.

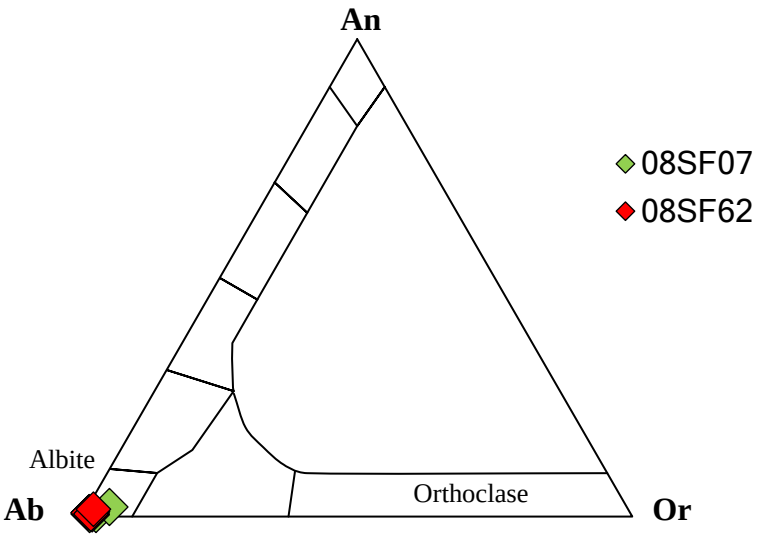

Fig.4.40 An-Ab-Or diagram presenting composition of albite from the Fogo carbonatites from Rib. de Almada (08SF07) and Monte Almada (08SF62).

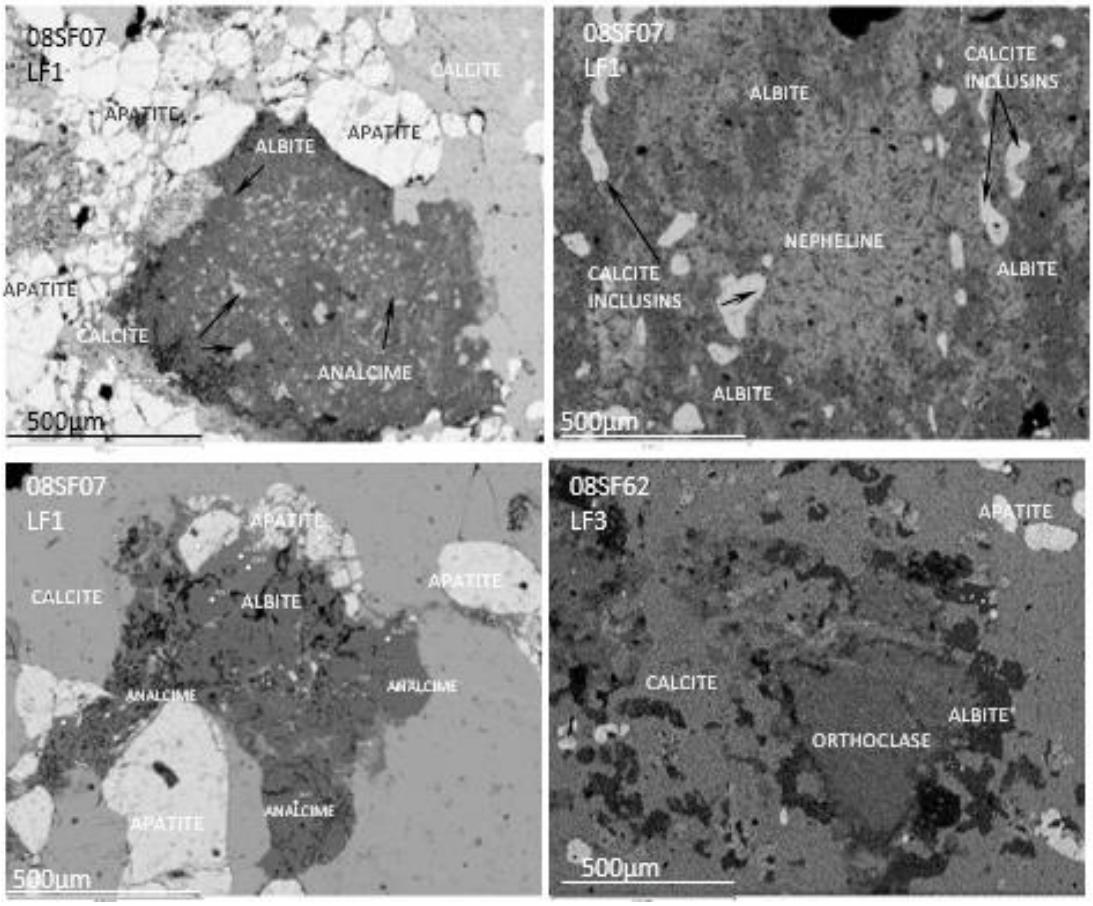

Fig 4.41 Back-scattered electron (BSE) images of the samples from Rib. de Almada (08SF07) and Monte Almada (08SF62), Fogo, Cape Verde, containing albite. LF1 site holds subhedral to ahedral albite containing calcite inclusions and showing alteration to zeolite analcime. It is also intimately associated with apatite. Monte Almada sample has fine-grained albite encircling feldspar.

Table 4.9 shows the average major elements values with their standard deviation. The average composition of orthoclase varies from Or_{73} to Or_{87} (Figure 4.42). Alkali feldspar occurs only in Monte Almada and is present in both upper and lower units (Figure 4.43). Alkali feldspar in the upper unit of Monte Almada is close to the Or end-member, while samples from the lower unit have slightly lower Or-component (Figure 4.43). Fogo orthoclase has low Na_2O, ranging from 1.6 to 2.1 wt%, with varied K_2O concentration (5.6-14.4 wt%).

	08SF62 EDS		08SF66 EDS		08SF65 WDS	
ORTHOCLASE	ave n=11	st dev n=11	ave n=9	st dev n=9	ave n=4	st dev n=4
SiO_2	63.06	*0.71*	64.52	*0.68*	63.95	*8.59*
TiO_2	0.06	*0.05*	0.17	*0.10*	n/a	*n/a*
Al_2O_3	18.27	*0.32*	18.41	*0.26*	23.66	*7.82*
FeO	0.30	*0.12*	0.36	*0.11*	0.90	*1.18*
CaO	0.15	*0.05*	0.08	*0.05*	0.08	*0.13*
Na_2O	1.31	*0.18*	2.06	*0.38*	1.35	*0.46*
K_2O	14.41	*0.25*	13.30	*0.70*	5.65	*1.55*
BaO	1.03	*0.30*	n/a	n/a	0.21	*0.16*
TOTAL	98.97	*0.94*	98.91	*0.94*	95.80	*1.52*
Si	11.807	*0.042*	11.949	*1.035*	11.620	*1.390*
Ti	0.008	*0.007*	0.024	*0.014*	n/a	*n/a*
Al	4.032	*0.047*	4.020	*0.036*	5.100	*1.800*
Fe	0.047	*0.019*	0.056	*0.018*	0.140	*0.190*
Ca	0.030	*0.010*	0.016	*0.011*	0.020	*0.030*
Na	0.476	*0.063*	0.739	*0.135*	0.470	*0.160*
K	3.443	*0.090*	3.142	*0.172*	1.310	*0.360*
Ba	0.075	*0.022*	n/a	n/a	0.020	*0.010*
TOTAL	20.121	*0.036*	20.005	*0.191*	18.720	*0.360*
Or	87.17	*1.68*	81.64	*4.84*	72.75	*1.85*
Ab	12.06	*1.58*	17.70	*5.33*	25.76	*3.00*
An	0.77	*0.25*	0.66	*0.85*	1.49	*2.61*

Table 4.9 Electron microprobe data for orthoclase in the intrusive carbonatite in 08SF62, 08SF665 and 08SF66 found in Monte Almada, Fogo, Cape Verde. Abbreviations: st dev=standard deviation, ave=average. Complete tables supplied in Appendix 2b.

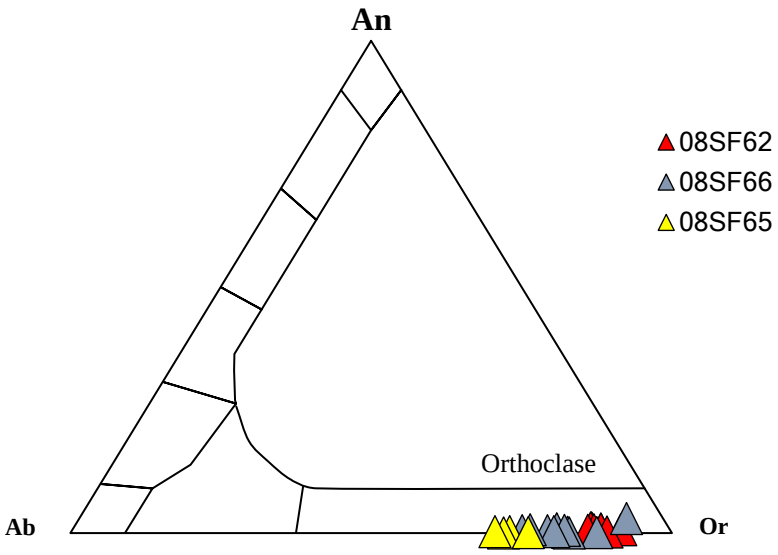

Fig.4.42 An-Ab-Or diagram presenting composition of orthoclase from carbonatites from Monte Almada divided into upper unit (08SF62) and lower unite (08SF65 and 08SF66).

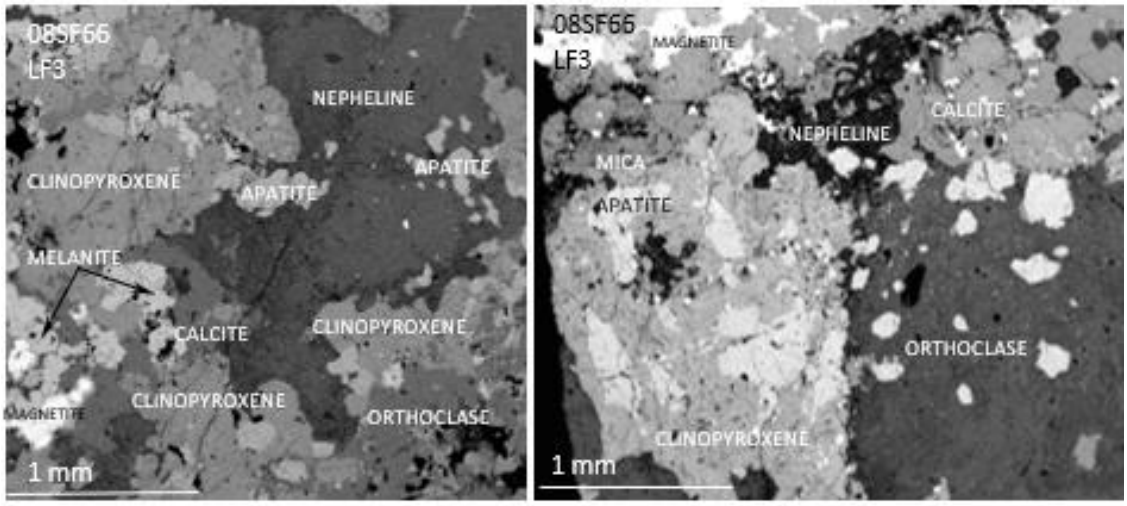

Fig 4.43 Backscattered electron image of 08SF66 containing alkali feldspars from Monte Almada, Fogo, Cape Verde. This sample exhibits turbid texture on K-rich feldspar with Na-rich areas. Turbid regions also contain abundant inclusions.

Feldspathoids and zeolites are present in samples from Rib. de Almada and Monte Almada. Nepheline is found in 08SF66 while leucite in 08SF07. The main difference between these feldspathoids is the presence of K_2O in leucite and its absence in nepheline. Zeolites such as natrolite, analcime and mesolite are also present in Rib. de Almada and Monte Almada. Difference in zeolites lies in amount of Na_2O, Al_2O_3 and in presence of CaO (such as in mesolite). Composition of feldspathoids and zeolites is given in Table 6.4.13f-h (Appendix 2b). Table 4.10 shows the average values with their standard deviation for the major elements from analysed feldspathoids and zeolites from Fogo. Chemical and petrographic study of zeolites and

feldspathoids in LF3 samples (Figure 4.44) suggest that zeolites were derived from hydration and alteration of existing phases such as feldspathoids like leucite or nepheline. Natrolite is probably a product of hydrothermal alteration after sodalites.

Zeolites and feldspathoids are not present in samples from the ridge of Monte Almada, although the lower outcrops contain zeolites. Here nepheline is found alongside orthoclase though albite is absent. Only albite and orthoclase werefound in the upper unit of Monte Almada. Leucite, nepheline and albite is present in Rib. de Almada. Overall, the complex turbid texture of feldspar, together with assemblage of alkali amphibole/pyroxene, apatite, garnet and calcite, indicates that these sites underwent alteration by alkali-rich fluids leading to modification in texture and chemistry of the minerals. The summary of occurrence of feldspars, feldspathoids and zeolites is presented in Table 4.11.

	08SF86 NEPHELINE WDS		08SF86 NEPHELINE EDS		08SF07 ALTERED EDS		08SF07 LEUCITE WDS		08SF07 NATROLITE WDS		08SF64A NATROLITE WDS
	ave n=2	st dev n=2	ave n=13	st dev n=13	ave n=5	st dev n=5	ave n=4	st dev n=4	ave n=2	st dev n=2	SF64A n=1
SiO_2	45.79	1.42	43.51	1.18	45.06	0.71	60.23	0.82	52.60	2.56	59.28
Al_2O_3	34.45	0.16	33.48	0.44	34.53	1.27	30.44	1.83	27.79	0.54	28.54
FeO	0.90	0.36	0.73	0.20	1.23	0.27	0.05	0.04	0.06	0.05	0.09
CaO	0.06	0.05	0.74	0.62	0.42	0.14	0.43	0.71	0.09	0.05	0.23
Na_2O	13.60	0.09	13.44	0.70	0.69	0.28	8.42	1.54	12.35	2.19	12.54
K_2O	5.50	0.74	6.68	0.69	9.15	0.86	0.18	0.12	0.10	0.01	0.11
BaO	0.13	0.04	n/a	n/a	0.15	0.11	0.01	0.03	0.00	0.00	0.00
TOTAL	100.42	0.40	98.60	0.93	91.25	1.09	99.77	0.78	92.97	0.29	100.79

Cations recalculated on the basis of 32 oxygens								08SF07 ANALCIME WDS		08SF65 MESOLITE EDS	
								ave n=4	st dev n=4	ave n=4	st dev n=4
Si	8.620	0.150	8.920	0.170	9.002	0.207	SiO_2	53.30	0.33	47.61	3.39
Al	7.640	0.070	5.160	0.080	8.128	0.229	Al_2O_3	22.48	0.29	34.15	1.34
Fe	0.140	0.060	0.120	0.030	0.205	0.043	FeO	0.06	0.04	0.19	0.11
Ca	0.010	0.010	0.160	0.140	0.090	0.031	CaO	0.16	0.12	5.89	1.03
Na	4.960	0.100	5.350	0.310	0.267	0.111	Na_2O	9.66	0.41	3.09	1.38
K	1.320	0.200	1.750	0.170	2.331	0.216	K_2O	0.10	0.06	0.26	0.24
Ba	0.010	0.000	0.000	0.000	0.012	0.009	BaO	0.03	0.07	0.01	0.02
TOTAL	22.710	0.260	21.460	0.240	20.229	0.139	TOTAL	85.78	0.48	91.19	2.62

Table 4.10 Electron microprobe data for feldspathoid and zeolite in the intrusive carbonatite in 08SF07 (Rib. de Almada) and 08SF64A, 08SF65 (Monte Almada), Fogo, Cape Verde. Abbreviations: st dev=standard deviation, ave=average. Complete tables supplied in Appendix 2b.

		ALBITE	ORTHOCLASE	FELDSPATHOID	ZEOLITE
LF1	08SF07	V	-	V	V
LF3 (U)	08SF62	V	V	-	-
LF3 (L)	08SF64	-	-	-	V
LF3 (L)	08SF65	-	V	-	V
LF3 (L)	08SF66	-	V	V	-

Table 4.11 Occurrence of albite, orthoclase, feldspathoid and zeolite in the intrusive carbonatite in 08SF07 (Rib. De Almada) and 08SF62, 08SF64, 08SF65and 08SF66 (Monte Almada).

Elliot et al. (2018) stated that distribution of the fenitic fluid can lead to macrotextures which can either be pervasive or closely associated with veins, as a response to circulation of fluid in the host rock (Figure 4.45).

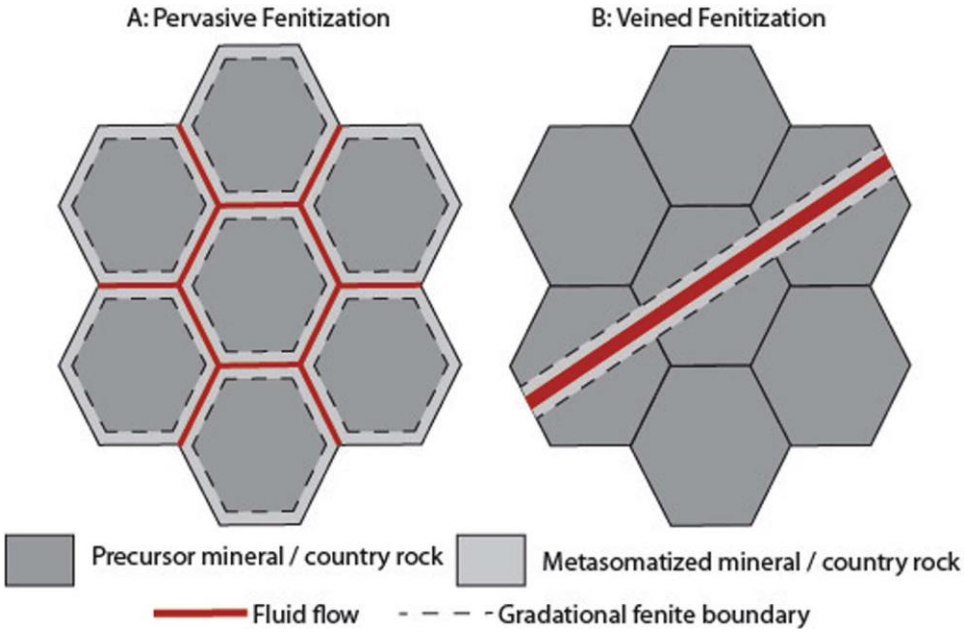

Fig 4.45 Schematic diagram illustrates the difference between pervasive and veined fenitization. In first case fluid interacts with a larger volume of country rock during diffuse porous flow than fluid flowing through fracture (second case). According to Elliot et al. (2018).

BSE images and maps of 08SF65 (Figure 4.46 and 4.47) provide insight into the distribution of the metasomatic fluid and its effect on texture and mineral chemistry. Figure 4.46 displays pervasive fenitization with alkali fluid having circulated around elongated calcite fingers (most likely originally tabular calcite crystals recrystallised to granoblastic texture). The outer rim is zeolite-rich (mesolite) and is fringed by orthoclase, whereas an assemblage of fine-grained alkali amphibole-calcite-apatite forms the inner rim next to the calcite finger. This structure and assemblage are repeated around elongated calcite regions. In contrast Figure 4.47

shows the process of veined fenitization. A fracture that cross-cuts the rock provided the path for metasomatic fluid which formed the zeolite-rich mineral. Multiple fine veinlets protrude from the main fracture forming net-veining of zeolite-rich composition. Fenitization of the host rock occurs close to veins.

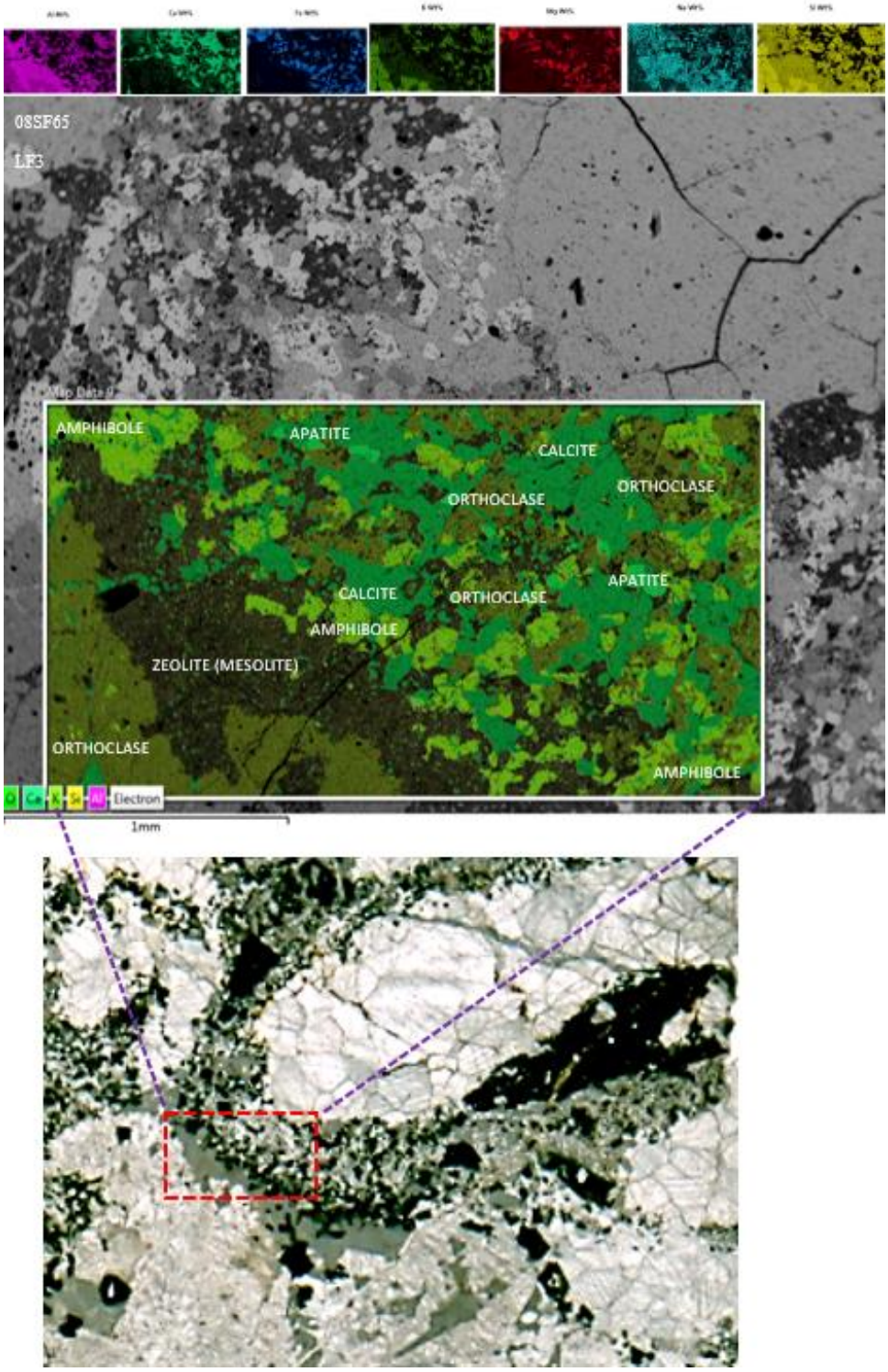

Fig 4.46 BSE image and false-coloured X-Ray map of 08SF65 from Monte Almada showing pervasive fenitization around calcic "finger" rimmed by assemblage of zeolite-orthoclase-amphibole-apatite-calcite

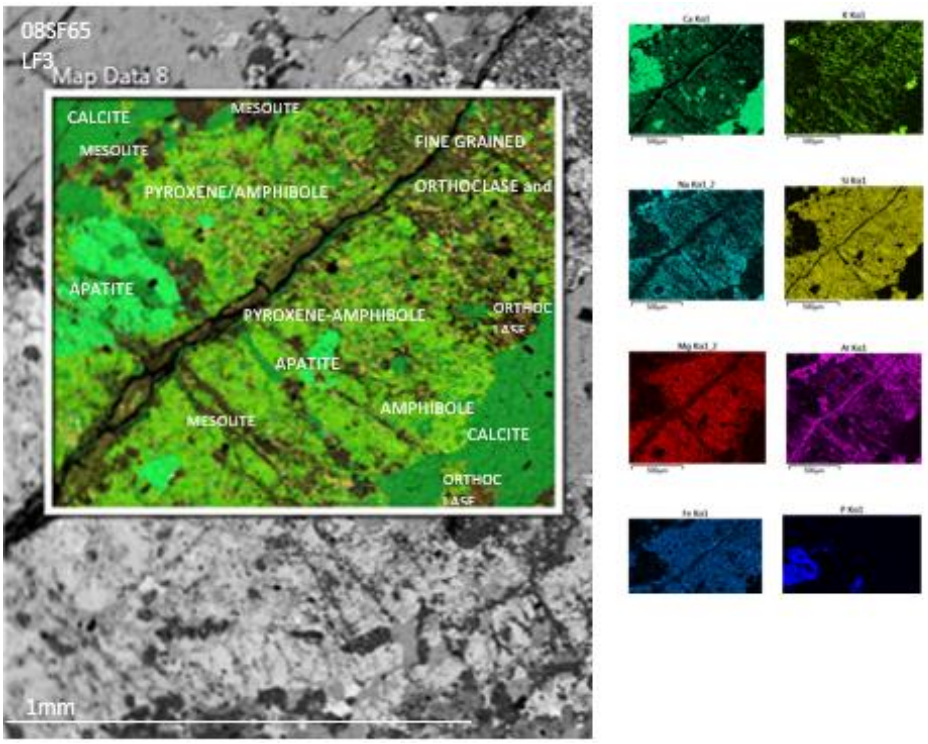

Fig 4.47 BSE image and false-coloured X-Ray map of 08SF65 from Monte Almada, Fogo, Cape Verde, displays veined fenitization. Fractures forming net-veining provide paths for hydrothermal fluids and over time become infilled by secondary zeolite. Progressive alternation of primary assemblage (plagioclase and/or feldspathoids) to secondary one affects the rock through planes of weakness.

Zr-Nb-Ti-rich minerals such as zircon, zirconolite, pyrochlore, titanite and Ti-magnetite are minor phases mostly found in Rib. de Almada samples (08SF03 and 08SF01), and sporadically in Monte Almada. These rare phases are good indicators of the source of particular late-stage REE-enrichment after emplacement in highly evolved parts of intrusion characteristic of fenitization.

Two Rib. de Almada samples (08SSF01 and 08SF03) contain zircon while zirconolite was detected only in 08SF01. Compositional data for zircon is given in Table 6.4.15a-d (Appendix 2b). The average values and standard deviation are shown in Table 4.12. Hafnium, Th and Nb contents in zircon differs between the two samples. 08SF01 shows average of 0.44 wt% whereas 08SF03 has <0.04 wt%. In contrast ThO_2 content is significantly higher in 08SF03 zircon (0.98-1.94 wt%) than in 08SF01 (0.21 wt%). Nb_2O_5 content is overall similar but some values are higher in 08SF03 leading to wider range (0.8-3.3 wt%) while values in 08SF01 have narrower range (0.7-1.3 wt%). TiO_2 is absent in zircon from 08SF01 but in 08SF03 it is up to 2.2 wt% though the average value is low (0.3 wt%).

	ZIRCON SF03 ave n=7	st dev n=7	ave n=18	st dev n=18	ave n=18	st dev n=18	SF01 ave n=7	st dev n=7
SiO_2	31.10	*0.78*	32.21	*0.95*	32.50	*0.46*	31.36	*1.38*
TiO_2	0.20	*0.41*	0.47	*0.59*	0.15	*0.17*	0.05	*0.06*
FeO	0.14	*0.11*	0.17	*0.16*	0.09	*0.09*	0.55	*0.44*
MnO	0.03	*0.04*	0.44	*0.37*	0.16	*0.13*	0.02	*0.04*
CaO	0.55	*0.31*	n/a	*n/a*	n/a	*n/a*	0.26	*0.11*
Al_2O_3	0.04	*0.04*	n/a	*n/a*	n/a	*n/a*	0.39	*0.32*
BaO	0.04	*0.07*	n/a	*n/a*	n/a	*n/a*	0.22	*0.13*
Nb_2O_5	1.66	*0.69*	1.53	*0.59*	1.36	*0.31*	1.08	*0.20*
ThO_2	0.98	*0.87*	1.20	*1.17*	1.84	*1.63*	0.21	*0.25*
ZrO_2	63.33	*1.93*	63.46	*1.71*	63.49	*1.81*	63.79	*1.27*
HfO_2	0.01	*0.03*	0.04	*0.07*	0.03	*0.06*	0.44	*0.17*
La_2O_3	0.02	*0.06*	0.12	*0.11*	0.12	*0.14*	0.12	*0.12*
Ce_2O_3	0.10	*0.15*	0.14	*0.15*	0.12	*0.14*	0.01	*0.03*
SrO	0.76	*0.12*	n/a	*n/a*	n/a	*n/a*	0.88	*0.14*
F	0.47	*0.14*	n/a	*n/a*	n/a	*n/a*	0.40	*0.09*
TOTAL	99.43	*0.51*	99.77	*0.72*	100.00	*0.53*	99.78	*0.36*
Cations recalculated on the basis of 4 oxygens								
Si	0.961	*0.016*	0.872	*0.173*	1.000	*0.008*	0.961	*0.034*
Ti	0.005	*0.010*	0.010	*0.012*	0.003	*0.004*	0.001	*0.001*
Fe	0.003	*0.003*	0.005	*0.006*	0.002	*0.002*	0.014	*0.011*
Mn	0.001	*0.001*	n/a	*n/a*	n/a	*n/a*	0.000	*0.001*
Ca	0.018	*0.010*	0.016	*0.015*	0.005	*0.004*	0.008	*0.004*
Al	0.001	*0.002*	n/a	*n/a*	n/a	*n/a*	0.014	*0.012*
Ba	0.001	*0.001*	n/a	*n/a*	n/a	*n/a*	0.003	*0.002*
Nb	0.023	*0.010*	0.023	*0.010*	0.019	*0.004*	0.009	*0.004*
Th	0.007	*0.006*	0.014	*0.015*	0.013	*0.012*	0.001	*0.002*
Zr	0.954	*0.023*	1.052	*0.151*	0.952	*0.018*	0.954	*0.027*
Hf	0.000	*0.000*	0.001	*0.001*	0.000	*0.001*	0.004	*0.002*
La	0.000	*0.001*	0.002	*0.002*	0.001	*0.002*	0.002	*0.002*
Ce	0.002	*0.003*	0.003	*0.003*	0.001	*0.002*	0.000	*0.001*
Sr	0.014	*0.002*	n/a	*n/a*	n/a	*n/a*	0.016	*0.003*
F	0.046	*0.013*	n/a	*n/a*	n/a	*n/a*	0.039	*0.009*
TOTAL	2.035	*0.009*	2.012	*0.010*	2.000	*0.003*	2.046	*0.014*

Table 4.12 Electron microprobe data for zircon in the intrusive carbonatite in 08SF01 and 08SF03 (Rib. de Almada), Fogo, Cape Verde. Abbreviations: st dev=standard deviation, ave=average. Complete tables supplied in Appendix 2b.

Figure 4.48 summarises the main petrographic features of accessory zircon in Rib. de Almada. Zircon exhibits skeletal texture and is intergrown with apatite, calcite, titanite and pyroxene. Skeletal form involves rapid growth towards the edges enveloping melt at the ends, thus trapping the liquid and crystallising the calcite-apatite-titanite assemblage. In 08SF01 zircon is strongly associated with glimmeritic part of the sövite, which most likely reflects the zircon geochemistry as it contains some minor quantity of FeO and lacks TiO_2. Zircon in 08SF03 (Figure 4.49 and 4.50) exhibits a more complex association with titanite-zirconolite-pyrochlore set in phlogopite which is bordered by large calcite crystals and rounded apatite. Texture and geochemistry of all associated minerals in 08SF03 is more complex than in

08SF01 as it suggests simultaneous crystallisation. Also, solid state alteration by hydrothermal fluids would lead to development of patchiness, which is not seen.

Zircon is uncommon in carbonatites as requires a relatively high silica activity (O'Brien et al., 2015). Thus, the presence of zircon (and titanite) reflects higher local silica saturation in the melt. Thus, the unusual assemblage most likely formed during hydrothermal dissolution of original phase(s) and reprecipitation of dissolved minerals with modified composition by incorporating elements from the hydrothermal fluid.

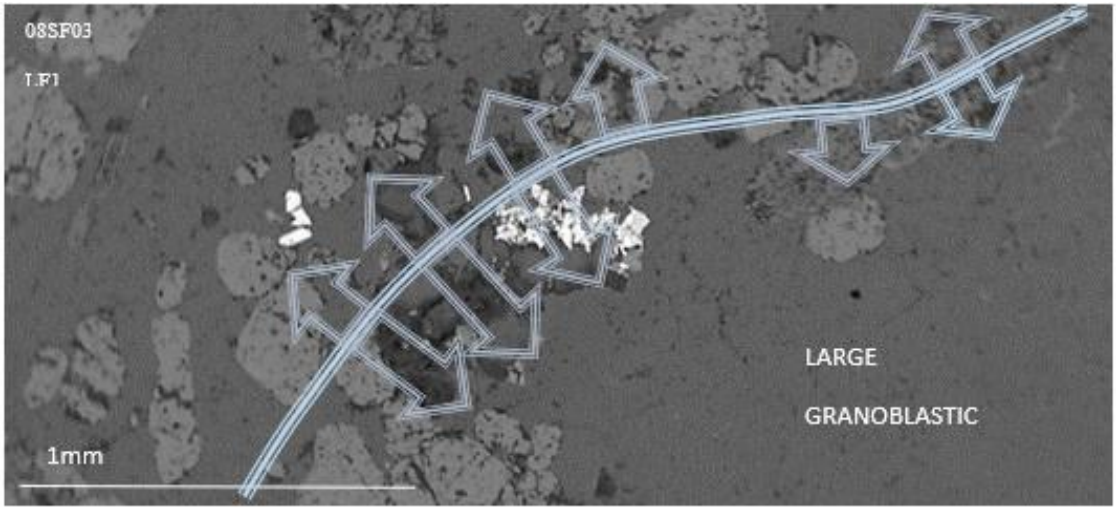

Fig 4.49 BSE image of 08SF03 from Rib. de Almada, displaying phlogopite hosting titanite-zircon-zirconolite-pyrochlore. Assemblage is set in phlogopite bordered by apatite (lighter grey) and calcite (darker grey). Growth of secondary minerals occurred around large granoblastic calcite representing passage for hydrothermal fluids (blue dotted line and arrows show possible paths of penetration by hydrothermal fluids).

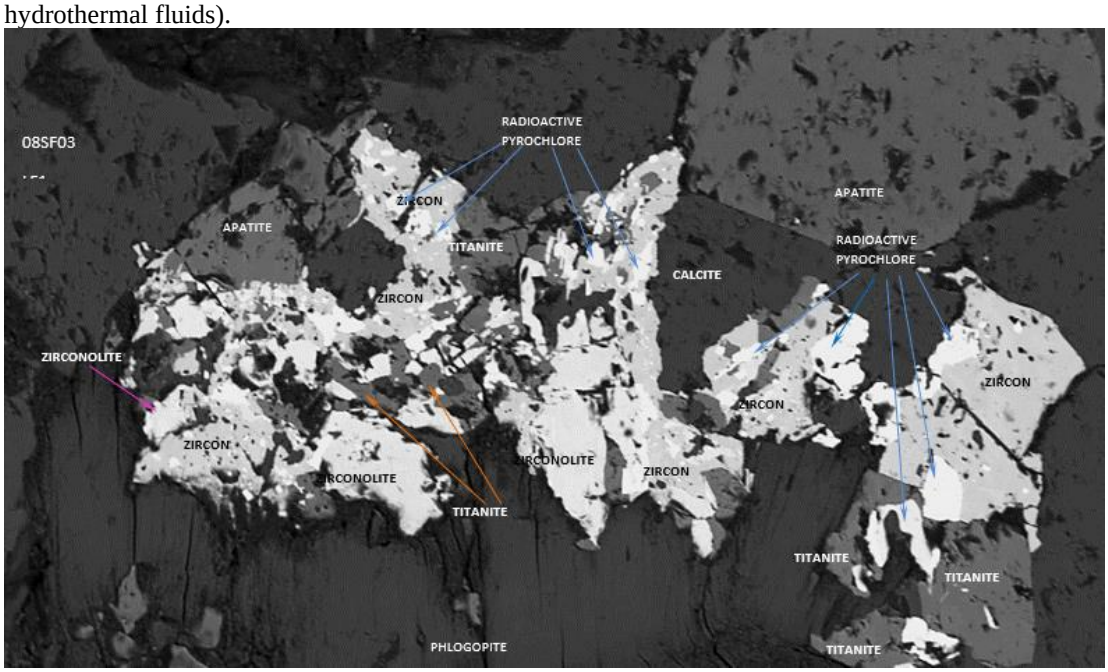

Fig.4.50 Back-scattered electron (BSE) image of phlogopite from 08SF03 exhibiting intimate association with zircon, zirconolite, titanite and pyrochlore

According to Sheard et al. (2012), the Nechalacho layered alkaline suite was affected by primary magmatic REE mineralisation resulting from gravity settling of eudialyte and zircon (accountable for ~7 wt% REE_2O_3 and ~3 wt% REE_2O_3, respectively). Williams-Jones (2012) stated that hydrothermal fluids remobilised REEs and reprecipitated them as fergusonite-(Y), secondary zircon, allanite-(Ce), bastnäsite-(Ce) and monazite-(Ce). Significantly the HREEs were deposited near its predecessor while the LREEs were deposited several metres away. The REE mineralisation occurred during the final stages of crystallisation in fluorine-rich magma enriched in incompatible elements (such as REEs). Analyses on fluid inclusion revealed that the remobilisation occurred in 350 ºC to < 150 ºC. According to Salvi and Williams-Jones (1996) these process involved interaction of sodic magmatic brines with lower-temperature calcic brines. Thus, the HREE enrichment can arise because they are less mobile and the LREEs having higher mobility and can be removed further away. In the Fogo samples phlogopite shows alteration and partial dissolution around the rim and cleavages. Also mica contains highest HfO_2 concentration in analysed assemblage (average of 0.7 wt%), which indicates enrichment in HREEs while zircon, zirconolite and titanite lack HfO_2 as there was no more Hf left in the system during final crystallisation.

Compositional data for zirconolite is given in Table 6.4.17a-c (Appendix 2b). The average values and standard deviation is shown in Table 4.13. The enrichment in TiO_2 is considerable and constant (25.4-26.6 wt%) as well as ZrO_2 content (31.2-35.5 wt%). Concentrations of Nb_2O_5 and CaO are similar around 12 wt%, whereas ThO_2, ranges from 2.2 to 6.8 wt%. The total average concentration of La_2O_3, Ce_2O_3, Nd_2O_3 and UO_2 in zirconolite which is intimately associated with pyrochlore and zircon, is 5 wt%, though in euhedral grains these values are much lower with exception of Ce_2O_3.

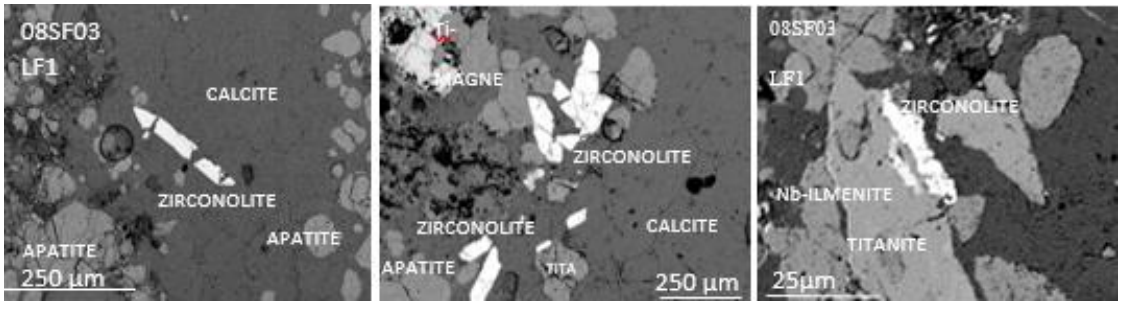

Fig 4.51 Backscattered electron image of 08SF03 from Rib. de Almada, Fogo, Cape Verde, displaying euhedral zirconolite and anhedral associated with titanite which is also hosting Nb-ilmenite

ZIRCONOLITE	Anhedral associated with pyrochlore-zircon-titanite		Euhedral single grain		Euhedral single grain	
	ave n=10	st dev n=10	ave n=17	st dev n=17	ave n=13	st dev n=13
SiO_2	0.33	0.07	0.73	0.99	0.26	0.08
TiO_2	26.64	1.40	25.44	0.80	25.75	0.71
Al_2O_3	0.46	0.60	0.45	0.36	0.33	0.17
FeO	7.41	0.29	6.88	0.25	6.74	0.28
MnO	0.35	0.11	0.19	0.11	0.15	0.13
CaO	12.49	0.62	11.79	0.37	12.05	0.3
BaO	n/a	n/a	0.53	0.42	0.62	0.3
F	n/a	n/a	0.16	0.15	0.13	0.12
SrO	n/a	n/a	0.18	0.13	0.14	0.11
Nb_2O_5	11.60	0.51	11.12	0.58	11.36	0.45
ThO_2	4.48	1.41	5.34	1.00	4.76	0.84
ZrO_2	31.18	0.98	34.97	1.11	35.47	0.89
HfO_2	0.04	0.06	0.16	0.12	0.15	0.12
La_2O_3	0.79	0.35	0.09	0.11	0.24	0.26
Ce_2O_3	1.27	0.30	0.85	0.30	0.94	0.18
Nd_2O_3	1.05	0.30	n/a	n/a	n/a	n/a
UO_2	2.00	0.60	n/a	n/a	n/a	n/a
TOTAL	100.07	0.66	98.85	1.21	99.08	0.18
Cations recalculated on the basis of 7 oxygens						
Si	0.021	0.004	0.046	0.061	0.020	0.010
Ti	1.268	0.044	1.218	0.042	1.150	0.340
Al	0.034	0.045	0.034	0.027	0.120	0.330
Fe	0.393	0.018	0.366	0.016	0.360	0.020
Mn	0.019	0.006	0.010	0.006	0.010	0.010
Ca	0.847	0.028	0.804	0.020	0.830	0.020
Ba	n/a	n/a	0.013	0.010	0.010	0.010
F	n/a	n/a	0.033	0.030	0.020	0.020
Sr	n/a	n/a	0.007	0.005	0.010	0.000
Nb	0.332	0.020	0.320	0.017	0.330	0.010
Th	0.065	0.021	0.077	0.015	0.070	0.010
Zr	0.963	0.019	1.085	0.039	1.110	0.020
Hf	0.001	0.001	0.003	0.003	0.000	0.000
La	0.032	0.014	0.004	0.005	0.010	0.010
Ce	0.052	0.013	0.035	0.013	0.020	0.010
Nd	0.026	0.013	0.000	0.000	n/a	n/a
U	0.028	0.009	n/a	n/a	n/a	n/a
TOTAL	4.083	0.010	4.053	0.018	4.050	0.010

Table 4.13 Electron microprobe data for zirconolite in the intrusive carbonatite in 08SF03 (Rib. de Almada). Abbreviations: st dev=standard deviation, ave=average. Complete tables in Appendix 2b.

Rare fine-grained pyrochlore, closely associated with phlogopite, forms an intergrowth texture with Zr-rich phases (typically zircon and zirconolite) and infrequently with Ti-rich phase such as titanite. Table 4.14 provides its major element compositions of pyrochlore. Significant range of Nb_2O_5 (29 wt% to 34 wt%) and CaO (9 wt% to 10 wt%) is coupled with high contents of ThO_2 (16-22 wt%), UO_2 (8-17 wt%) and TiO_2 (15-17 wt%). Significant amount of REEs such as La_2O_3, Ce_2O_3 and Nd_2O_3 were also detected. Analysed pyrochlore gives average value of 2.3 wt% SiO_2.

EDS	SF03 pyr_6	SF03 pyr_7	SF03 pyr_8	SF03 pyr_9	SF03 pyr_10	ave n=5	st dev n=5
Na_2O	1.49	1.35	1.95	1.63	1.23	*1.53*	*0.28*
CaO	10.21	8.31	8.74	8.74	9.07	*9.01*	*0.72*
MnO	0.41	0.00	0.26	0.45	0.33	*0.29*	*0.18*
La_2O_3	1.25	0.77	1.38	0.63	0.31	*0.87*	*0.44*
Ce_2O_3	2.97	2.13	2.09	1.89	2.06	*2.23*	*0.42*
Nd_2O_3	1.16	0.11	0.94	0.80	0.83	*0.77*	*0.39*
ThO_2	21.63	16.31	19.54	16.52	19.33	*18.67*	*2.24*
UO_2	8.47	13.28	14.64	16.59	13.14	*13.22*	*3.00*
HfO_2	0.24	0.04	0.00	0.11	0.04	*0.09*	*0.09*
SiO_2	1.33	2.93	2.41	2.90	2.11	*2.34*	*0.66*
TiO_2	15.77	14.16	16.76	15.85	16.16	*15.74*	*0.97*
ZrO_2	0.00	1.13	0.67	0.18	1.68	*0.73*	*0.69*
FeO	1.02	1.37	1.08	1.04	1.38	*1.18*	*0.18*
Nb_2O_5	28.69	33.57	30.43	29.02	31.38	*30.62*	*1.97*
TOTAL	94.64	95.46	100.89	96.35	99.05	*97.28*	*2.61*
Formulae based on 2 B-site cations, apfu							
Na^{+}	0.214	0.172	0.252	0.219	0.157	*0.203*	*0.036*
Ca^{2+}	0.810	0.585	0.624	0.648	0.639	*0.661*	*0.086*
Mn^{2+}	0.026	0.000	0.015	0.026	0.018	*0.017*	*0.011*
La^{3+}	0.034	0.019	0.034	0.016	0.008	*0.022*	*0.012*
Ce^{3+}	0.080	0.051	0.051	0.048	0.050	*0.056*	*0.014*
Nd^{3+}	0.031	0.003	0.022	0.020	0.019	*0.019*	*0.010*
Th^{4+}	0.364	0.244	0.296	0.260	0.289	*0.291*	*0.046*
U^{4+}	0.139	0.194	0.217	0.255	0.192	*0.200*	*0.042*
Hf^{4+}	0.006	0.001	0.000	0.003	0.001	*0.002*	*0.002*
$\sum A$	*1.698*	*1.267*	*1.512*	*1.493*	*1.372*	*1.468*	*0.162*
Si^{4+}	0.098	0.192	0.161	0.201	0.139	*0.158*	*0.042*
Ti^{4+}	0.878	0.699	0.840	0.825	0.799	*0.808*	*0.067*
Zr^{4+}	0.000	0.036	0.022	0.006	0.054	*0.024*	*0.022*
Fe^{3+}	0.063	0.075	0.060	0.060	0.076	*0.067*	*0.008*
Nb^{5+}	0.960	0.997	0.917	0.908	0.933	*0.943*	*0.036*
$\sum B$	*1.999*	*2.000*	*2.000*	*2.000*	*2.000*	*2.000*	*0.000*
TOTAL O	6.595	6.080	6.350	6.340	6.205	*6.314*	*0.192*

Table 4.14 Electron microprobe data for pyrochlore in intrusive carbonatite SF03 from Rib. de Almada Fogo, Cape Verde. Analysed pyrochlore is associated with phlogopite and zircon-titanite assemblage. Abbreviations: st dev=standard deviation, ave=average. Formulae based on 2 B-site cations, a.p.f.u.

Pyrochlore is intergrown with silica-rich phases and shows homogenous chemistry. It has a a high average UO_2+ThO_2 (32 wt%), while associated zirconolite has the second highest amount of UO_2+ThO_2 (6 wt%). Thus, both pyrochlore and zirconolite incorporated Th and U. The other minerals in the assemblage do not hold substantial amounts of these elements. According to Lumpkin et. al (2014) "pyrochlore is a derivative of the fluorite structure and corresponds to the general formula $A_2B_2X_6Y$, and "zirconolite is a derivative of the fluorite structure type and can be considered as a condensed version of pyrochlore". Pyrochlore and zirconolite can incorporate some silica in the presence of SiO_2-bearing aqueous fluids. Kogarko et al. (2009) found in Fogo calcite carbonatite very similar assemblage (to data obtained by the author) composed of zirconolite, pyrochlore and zircon concluding that the evolution from zirconolite to Th-pyrochlore occurred during increase F and

SiO_2 activity destabilizing zirconolite and forming secondary zircon and pyrochlore. Fogo pyrochlore is enriched more in Th than U reflecting the average value of Th/U=1.5 and as well as zirconolite showing higher ratio of 2.3, thus both phases are the major hosts for incompatible HFS-elements.

Mitchell and Kjarsgaard (2004) studied conditions for pyrochlore solubility in carbonatitic melts. Authors confirmed that stability of this type of pyrochlore depends on F-bearing system. In an F-poor system, early crystallisation of Ta-rich pyrochlore will occur. The Fogo pyrochlore is Nb-rich and also belongs to thorian-uranpyrochlore variety. Nasraoui and Bilal (2000) investigated pyrochlore of magmatic origin, hydrothermally altered and the weathered variety (supergene alteration leading to Nb mineralization forming niobian titanite and diverse Nb–Zr-silicates) from the Lueshe syenite-carbonatite complex, DRCongo. Figure 4.52 shows that Fogo pyrochlore falls at the top-end of hydrothermal nature and close to supergene species. In most cases hydrothermal alteration affects the rim of mineral during the reaction between mineral and fluid, while the core should not be affected showing still magmatic composition. Analysed Fogo specimens do not show such alteration. Thus, the possibility of localised dissolution by hydrothermal fluids (most likely enriched in Nb, Th and U) of Zr-rich precursor mineral(s) and recrystallisation into currently found in Fogo carbonatite assemblage is conceivable.

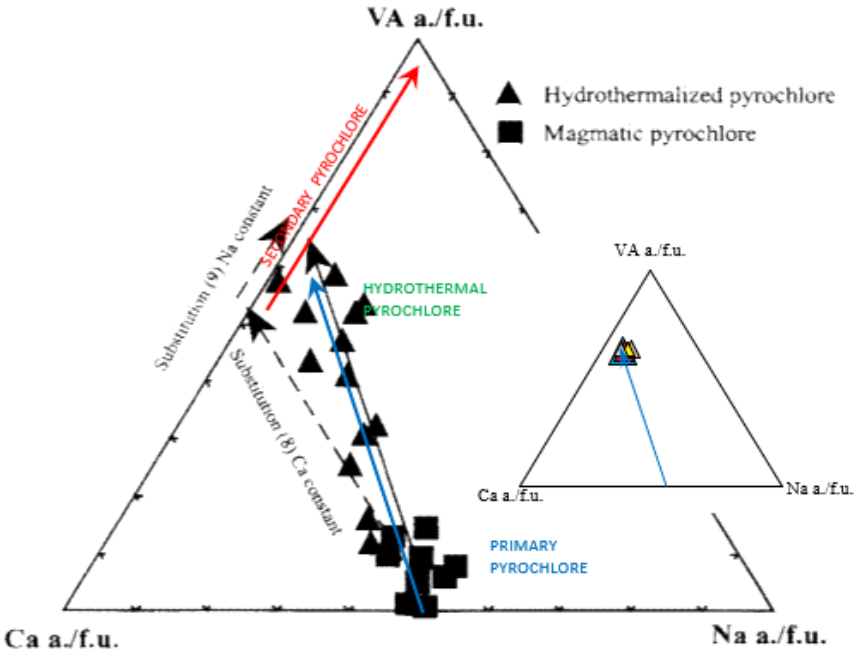

Fig 4.52 Ternary plot of Ca, Na and A-site vacancies (a./f.u.) showing the trends of magmatic and hydrothermal pyrochlores of the Lueshe complex (large triangle) and Fogo pyrochlore plot showing hydrothermal nature of analysed phase (small triangle). Diagram after Nasraoui and Bilal (2000). Red arrow represents the trend for supergene pyrochlore.

Rare ilmentite and titanite were found in 08SF03 (Rib. de Almada). Ilmenite forms an inclusion in titanite. Titanite is present in Rib. de Almada and Monte Almada. Compositional data for Nb-ilmenite and Nb-titanite are given in Table 6.4.20a and 6.4.22a-d (Appendix 2b). Average values and standard deviation are shown in Table 4.15 and 4.16, respectively. Fogo ilmenite lacks in MgO (average MnO concentration is 0.8 wt%). TiO_2 varies from 34 wt% to 50 wt% as well as significant concentration of Nb_2O_5 (1.2 wt% to 6.5 wt%). Niobium has a tendency to enter the structure of ilmenite as a trace element (Gaspar and Wyllie 1983). Both ilmenite and titanite contain substantial amounts of Nb_2O_5 from 2.5 to 4 wt%. The average concentration of ZrO_2 varies between 0.8-2.2 wt%. HfO_2 is only found in titanite associated with pyrochlore-zircon-zirconolite assemblage, having an average value of 0.2 wt%. LREEs can be detected in titanite being enriched up to 1 wt%.

Nb-ILMENITE	08SF03	
	ave n=4	st dev n=4
SiO_2	1.06	*1.44*
TiO_2	45.99	*6.16*
Al_2O_3	0.14	*0.14*
Fe_2O_3	1.74	*3.48*
FeO	40.31	*4.95*
MnO	0.83	*0.28*
MgO	0.02	*0.03*
CaO	1.13	*1.10*
Na_2O	0.57	*0.09*
K_2O	0.01	*0.02*
BaO	0.97	*0.36*
Nb_2O_5	3.13	*2.36*
Total	95.90	*3.25*
Cations recalculated on the basis of 3 oxygens		
Si	0.029	*0.040*
Ti	0.945	*0.114*
Al	0.005	*0.005*
Fe^{+3}	0.037	*0.073*
Fe^{+2}	0.921	*0.101*
Mn	0.019	*0.006*
Mg	0.001	*0.001*
Ca	0.034	*0.033*
Na	0.030	*0.005*
K	0.000	*0.001*
Ba	0.010	*0.004*
Nb	0.044	*0.034*
TOTAL	2.024	*0.002*

Table 4.15 Electron microprobe data for Nb-ilmenite in the intrusive carbonatite found in 08SF03 from Rib. de Almada, location LF1. Abbreviations: st dev=standard deviation, ave=average.

The Rib. de Almada samples show two different titanite textures. One occurs as anhedral intergrowing phase with Nb-Zr minerals (Figure 4.53) but more commonly titanite is present as euhedral/subhedral form in association with apatite (Rib. de Almada) or melanite (Monte Almada). Both types of titanite were influenced by metasomatic fluid. According to Chakhmouradian et al. (2003), igneous titanite rarely

crystallises in early formed carbonatites due to low activity of silica but is most commonly found in late-stage carbonatites as a result of interaction of deuteric fluids with precursor minerals (Ti-rich) at relatively low temperature and pressure. Chakhmouradian et al. (2003) stated that titanite in carbonatites is an important sink for HFSE, such as Nb and Zr, and if compositional zoning is present, it can give evidence of mobility of these elements and also provide the order of crystallisation of the associated mineral phases. Thus, titanite in Rib. de Almada occurred after formation of Nb-Zr phases seen in Rib. de Almada (relic zirconolite and Nb-ilmenite in titanite but also assemblage of pyrochlore -zirconolite-zircon set in phlogopite).

	SINGLE GRAINS		SINGLE GRAINS		TITANITE INTERGROWING WITH PYROCH/ZIRCON/ZIRCONOLITE		SINGLE GRAINS		SINGLE GRAINS			
	LF1										LF3	
	EDS		EDS		EDS		EDS		EDS		WDS	
	SF03		SF03		SF03		SF03		SF07		SF64a	
TITANITE	ave n=9	st dev n=9	ave n=9	st dev n=9	ave n=10	st dev n=10	ave n=10	st dev n=10	ave n=8	st dev n=8	ave n=6	st dev n=6
SiO_2	29.80	*0.22*	29.72	*0.66*	29.99	*0.48*	30.42	*0.44*	29.43	*0.22*	29.70	*0.69*
TiO_2	33.54	*0.68*	34.60	*1.04*	33.62	*1.45*	34.03	*2.28*	34.88	*0.89*	33.11	*1.01*
FeO	1.43	*0.22*	1.36	*0.25*	1.47	*0.24*	1.48	*0.41*	1.29	*0.20*	1.97	*0.52*
CaO	27.07	*0.29*	26.90	*0.75*	26.17	*0.58*	26.63	*0.80*	26.78	*0.29*	26.74	*0.38*
Al_2O_3	0.67	*0.14*	0.48	*0.26*	1.32	*1.57*	0.42	*0.21*	0.53	*0.16*	0.63	*0.22*
Na_2O	0.14	*0.06*	0.23	*0.15*	0.46	*0.26*	0.48	*0.24*	0.09	*0.04*	0.16	*0.07*
BaO	0.98	*0.31*	0.53	*0.48*	n/a	*n/a*	n/a	*n/a*	0.92	*0.53*	0.71	*0.29*
F	0.42	*0.10*	0.36	*0.12*	n/a	*n/a*	n/a	*n/a*	0.03	*0.03*	0.00	*0.00*
Nb_2O_5	2.43	*0.78*	2.47	*0.76*	3.97	*1.94*	4.06	*2.46*	2.55	*0.55*	3.05	*1.02*
ThO_2	0.07	*0.10*	0.19	*0.20*	0.05	*0.08*	0.11	*0.09*	0.00	*0.00*	n/a	*n/a*
ZrO_2	2.24	*0.36*	1.68	*0.85*	1.06	*0.68*	0.78	*0.73*	2.04	*0.60*	1.85	*0.50*
HfO_2	0.01	*0.03*	0.01	*0.03*	0.22	*0.13*	0.08	*0.08*	0.00	*0.00*	n/a	*n/a*
La_2O_3	0.54	*0.29*	0.23	*0.30*	0.57	*0.17*	0.67	*0.33*	0.50	*0.39*	0.17	*0.14*
Ce_2O_3	0.12	*0.20*	0.15	*0.23*	0.38	*0.29*	0.34	*0.35*	0.07	*0.07*	0.05	*0.07*
TOTAL	99.47	*0.33*	99.01	*1.19*	99.27	*0.91*	99.49	*0.51*	99.09	*0.56*	98.13	*0.89*
Cations recalculated on the basis of 5 oxygens												
Si	1.001	*0.006*	1.000	*0.010*	1.008	*0.015*	1.021	*0.009*	0.995	0.009	0.987	*0.013*
Ti	0.847	*0.016*	0.880	*0.030*	0.850	*0.039*	0.859	*0.053*	0.886	0.020	0.828	*0.031*
Fe	0.040	*0.006*	0.040	*0.010*	0.041	*0.007*	0.042	*0.012*	0.036	0.006	0.055	*0.014*
Ca	0.974	*0.009*	0.970	*0.020*	0.942	*0.020*	0.957	*0.023*	0.970	0.011	0.953	*0.024*
Al	0.026	*0.005*	0.020	*0.010*	0.052	*0.061*	0.017	*0.008*	0.021	0.006	0.025	*0.009*
Na	0.009	*0.004*	0.010	*0.010*	0.030	*0.017*	0.031	*0.016*	0.006	0.003	0.010	*0.004*
Ba	0.013	*0.004*	0.010	*0.010*	n/a	*n/a*	n/a	*n/a*	0.012	0.007	0.009	*0.004*
F	0.045	*0.011*	0.040	*0.010*	n/a	*n/a*	n/a	*n/a*	0.003	0.003	0.000	*0.000*
Nb	0.037	*0.012*	0.040	*0.010*	0.060	*0.030*	0.062	*0.038*	0.039	0.008	0.046	*0.015*
Th	0.001	*0.001*	0.000	*0.000*	0.000	*0.001*	0.001	*0.001*	0.000	0.000	0.000	*0.000*
Zr	0.037	*0.006*	0.030	*0.010*	0.017	*0.011*	0.013	*0.012*	0.034	0.010	0.030	*0.008*
Hf	0.000	*0.000*	0.000	*0.000*	0.002	*0.001*	0.001	*0.001*	0.000	0.000	0.000	*0.000*
La	0.007	*0.004*	0.000	*0.000*	0.007	*0.002*	0.008	*0.004*	0.006	0.005	0.002	*0.002*
Ce	0.001	*0.002*	0.000	*0.000*	0.005	*0.004*	0.004	*0.004*	0.001	0.001	0.001	*0.001*
Total	3.044		3.040		3.015		3.014		3.016		3.034	

Table 4.16 EDS data for titanite in the intrusive carbonatite found in SF03 Rib. de Almada, location LF1. Titanite is associated with phlogopite and zircon-zirconolite-pyrochlore assemblage. Abbreviations: st dev=standard deviation, ave=average. Cations recalculated on the basis of 5 oxygens.

Ti-rich garnet forms over a wide P-T range (Gwalani et al., 2000) and can involve metasomatic reactions between pyroxene or/and amphibole and late-stage fluids. Association of melanite with titanite in Monte Almada can be explained by a reaction involving introduction of Ti (at the expense of Si) observed by Huggins et al.

(1977b) and Armbruster et al. (1998). Thus, formation of rare titanite can occur in late stages due to metasomatic processes. If the late-stage processes produce oscillatory zoning on titanite, it would show reverse zonation to compare to the primary purely igneous specimen, such as increase in Zr content and decrease in Nb content towards the rim. This shift can be explained by co-crystallisation of rival phases (within phlogopite) in competition for HFSE such as pyrochlore (incorporation of Nb) and consequently formation of zircon-zirconolite. In 08SF03 instead of zoning, an intimate crystallisation of pyrochlore-zirconolite-zircon and titanite provides evidence for metasomatic reactions leading to alteration of Fogo carbonatite (Figure 4.54).

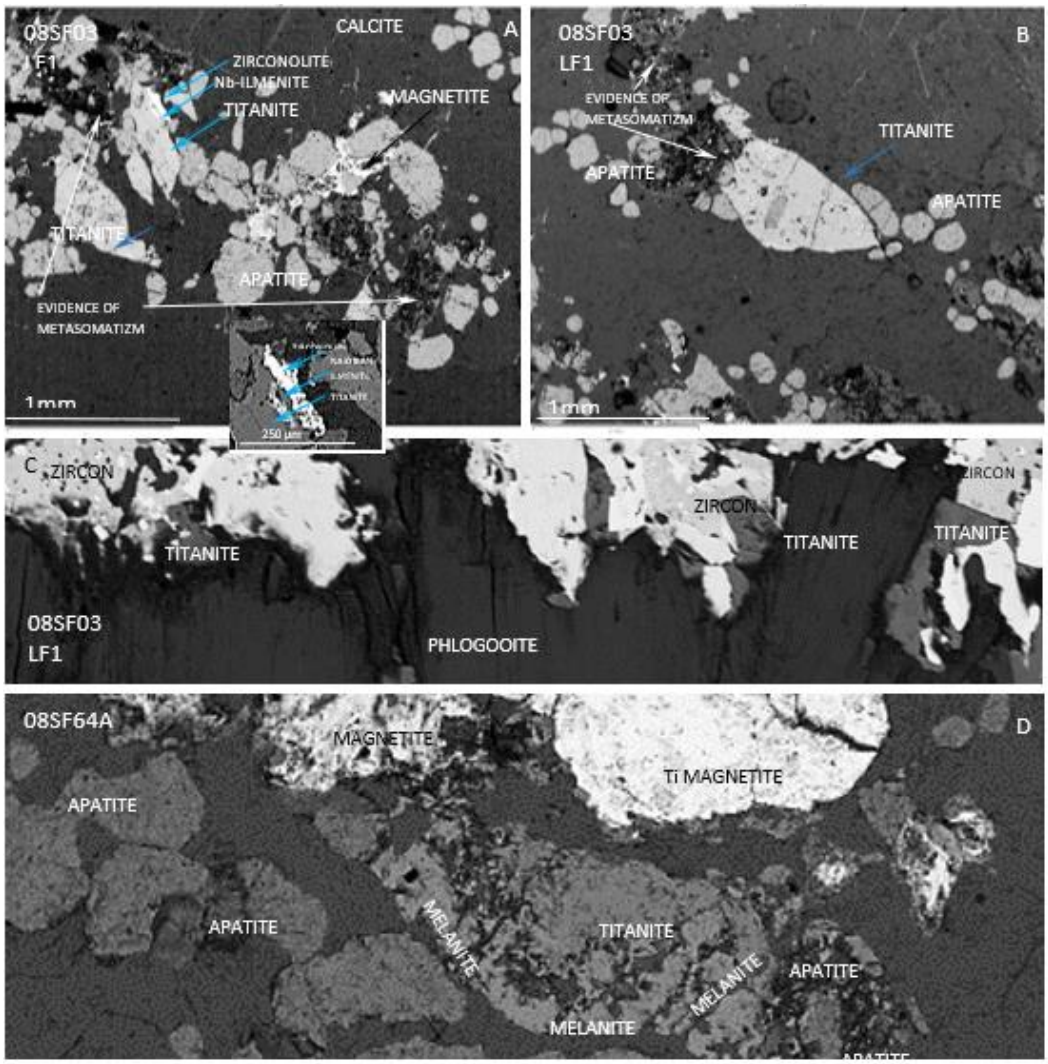

Fig4.53 Backscatter electron image of 08SF03 from Rib. de Almeda, Fogo, Cape Verde, displaying titanite with subhedral texture roughly diamond in shape (A and B), intergrowing texture with Zr-Ti-rich accessory minerals (C) and anhedral titanite being overgrown by melanite rim (D).

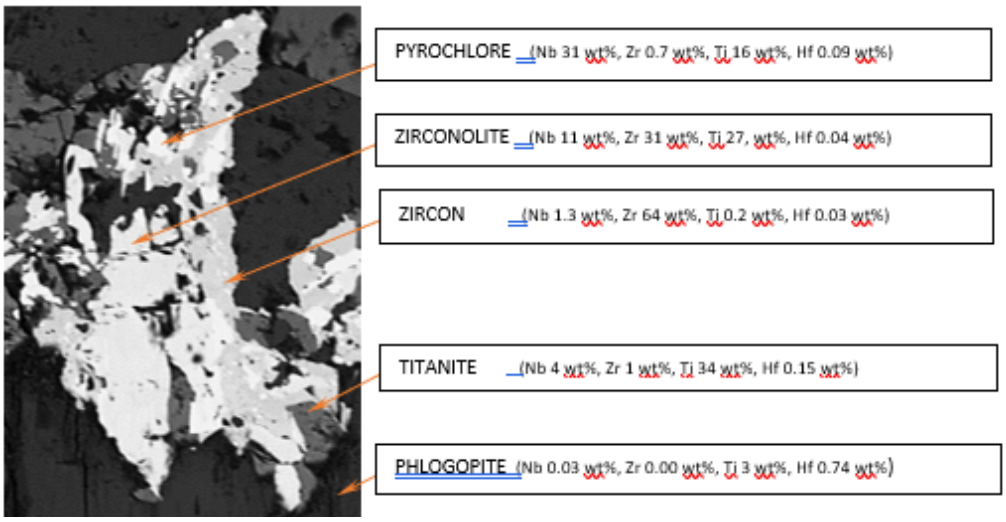

Fig 4.54 BSE image of 08SF03 from Rib. de Almada, displaying intergrowing texture of Zr-Ti-rich accessory minerals with geochemical data for Nb, Zr, Ti and Hf contents.

Fe-Ti-oxides are present in all three locations though titanomagnetite is more commonly found in the Almada locations while magnetite is also present in Rib. Domingo Santo. Compositional data for Fe-Ti-oxides is present in Table 6.4.24a-e (Appendix 2b) and Table 4.17a-b shows average values with standard deviation.

	LF1 WDS SF03		LF1 EDS SF03		LF3 EDS SF64a		LF3 EDS SF66	
TITANOMAGNETITE	ave n=4	st dev n=4	ave n=4	st dev n=4	ave n=4	st dev n=4	ave n=5	st dev n=5
SiO_2	0.31	0.29	0.05	*0.05*	0.38	*0.15*	0.51	*0.82*
TiO_2	2.86	0.31	2.07	*0.77*	2.30	*0.51*	3.62	*0.62*
Al_2O_3	0.66	0.90	0.18	*0.08*	0.47	*0.17*	0.47	*0.36*
Fe_2O_3	60.94	2.73	60.58	*1.28*	59.41	*0.79*	56.99	*2.06*
FeO	32.09	0.51	29.59	*0.54*	30.52	*0.70*	31.45	*1.57*
MnO	0.90	0.09	1.37	*0.32*	1.23	*0.14*	1.40	*0.20*
MgO	0.38	0.08	0.10	*0.07*	0.13	*0.06*	0.34	*0.17*
TOTAL	98.245	1.471	94.452	*0.627*	94.790	*0.612*	95.236	*1.545*
Cations recalculated on the basis of 4 oxygens								
Si	0.012	*0.011*	0.002	*0.002*	0.015	*0.006*	0.020	*0.032*
Ti	0.084	*0.010*	0.063	*0.023*	0.070	*0.015*	0.109	*0.018*
Al	0.030	*0.041*	0.009	*0.004*	0.022	*0.008*	0.022	*0.016*
Fe^{3+}	1.776	*0.068*	1.854	*0.048*	1.801	*0.028*	1.712	*0.075*
Fe^{2+}	1.040	*0.022*	1.006	*0.013*	1.028	*0.019*	1.049	*0.043*
Mn	0.030	*0.003*	0.047	*0.011*	0.042	*0.005*	0.047	*0.006*
Mg	0.022	*0.005*	0.006	*0.005*	0.008	*0.004*	0.020	*0.010*
TOTAL	2.998		3.015		3.014		3.012	

Table 4.17a Electron microprobe data (EDS and WDS) for titanomagnetite in the intrusive carbonatite found in LF1 and LF3 Fogo, Cape Verde. Abbreviations: st dev=standard deviation, ave=average. Cations recalculated on the basis of 4 oxygens.

	EDS		EDS	EDS		WDS		WDS	
	SF64a		SF66	SF51		SF01		SF07	
MAGNETITE	ave n=3	st dev n=3	ave n=1	ave n=3	st dev n=3	ave n=4	st dev n=4	ave n=4	st dev n=4
SiO_2	1.19	*1.08*	0.30	0.23	*0.09*	3.75	*0.90*	5.64	*0.50*
TiO_2	0.04	*0.04*	0.10	0.08	*0.07*	0.01	*0.01*	0.03	*0.04*
Al_2O_3	0.94	*0.81*	0.47	0.10	*0.03*	0.58	*0.32*	0.26	*0.20*
Fe_2O_3	59.06	*4.46*	65.27	63.46	*0.86*	56.10	*2.52*	51.95	*0.56*
FeO	29.72	*0.75*	30.34	28.34	*0.27*	33.14	*1.14*	35.19	*1.24*
MnO	0.02	*0.03*	0.00	0.24	*0.05*	0.20	*0.05*	0.08	*0.06*
MgO	0.05	*0.05*	0.00	0.07	*0.02*	0.47	*0.10*	0.61	*0.23*
CaO	0.26	*0.26*	0.20	0.48	*0.03*	0.35	*0.12*	0.58	*0.08*
Na_2O	0.19	*0.06*	0.10	0.19	*0.04*	0.09	*0.04*	0.06	*0.05*
K_2O	n/a	*n/a*	0.08	0.05	*n/a*	0.03	*0.02*	0.03	*0.03*
BaO	n/a	*n/a*	n/a	n/a	*n/a*	0.01	*0.02*	0.03	*0.02*
TOTAL	91.47	*1.65*	96.86	93.22	*1.22*	94.72	*0.42*	94.47	*1.19*
Cations recalculated on the basis of 4 oxygens									
Si	0.050	*0.045*	0.012	0.010	*0.004*	0.148	*0.035*	0.222	*0.017*
Ti	0.001	*0.001*	0.003	0.002	*0.002*	0.000	*0.000*	0.001	*0.001*
Al	0.046	*0.040*	0.022	0.005	*0.001*	0.027	*0.015*	0.012	*0.009*
Fe^{3+}	1.848	*0.128*	1.945	1.967	*0.001*	1.672	*0.085*	1.539	*0.036*
Fe^{2+}	1.034	*0.032*	1.005	0.976	*0.003*	1.098	*0.032*	1.158	*0.026*
Mn	0.001	*0.001*	0.000	0.008	*0.002*	0.007	*0.002*	0.003	*0.002*
Mg	0.003	*0.003*	0.000	0.004	*0.001*	0.028	*0.005*	0.036	*0.014*
Ca	0.012	*0.012*	0.008	0.021	*0.002*	0.015	*0.005*	0.025	*0.003*
Na	0.015	*0.005*	0.008	0.015	*0.003*	0.007	*0.003*	0.005	*0.004*
K	n/a	*n/a*	0.004	0.001	*n/a*	0.002	*0.001*	0.002	*0.002*
Ba	n/a	*n/a*	n/a	n/a	*n/a*	0.000	*0.000*	0.001	*0.000*
TOTAL	3.009		3.007	3.010		3.005		3.004	

Table 4.17b Electron microprobe data (EDS and WDS) for magnetite in the intrusive carbonatite found in Fogo, Cape Verde. Abbreviations: st dev=standard deviation, ave=average. Cations recalculated on the basis of 4 oxygens. Some elements are below detection limit.

Titanomagnetite shows similar values regarding FeO^T, on average 90 wt%, slightly varying content of TiO_2 from 1.2 to 4 wt% and MnO from 1 to 1.8 wt%. The higher concentration TiO_2 is associated with the lower FeO^T, thus substitution of Fe for Ti is apparent. Magnetite from Fogo carbonatites is depleted in TiO_2, with low MnO (up to 0.2 wt%), variable Al_2O_3 (0.03-1.94 wt%) and detectable amounts of SiO_2 (0.2 to 5.6 wt%). MgO is low (average 0.5 wt%) and found only in Rib. de Almada.

Compositions of the Fe-Ti oxides are plotted on the TiO_2–FeO–Fe_2O_3 ternary diagram (Figure 4.55), and show a transition from magnetite towards titanomagnetite and futher into ilmenite. Titanomagnetite is more commonly found than magnetite and shows a close association with Ti-rich minerals such as melanite and titanite, implying access of Ti in the system.

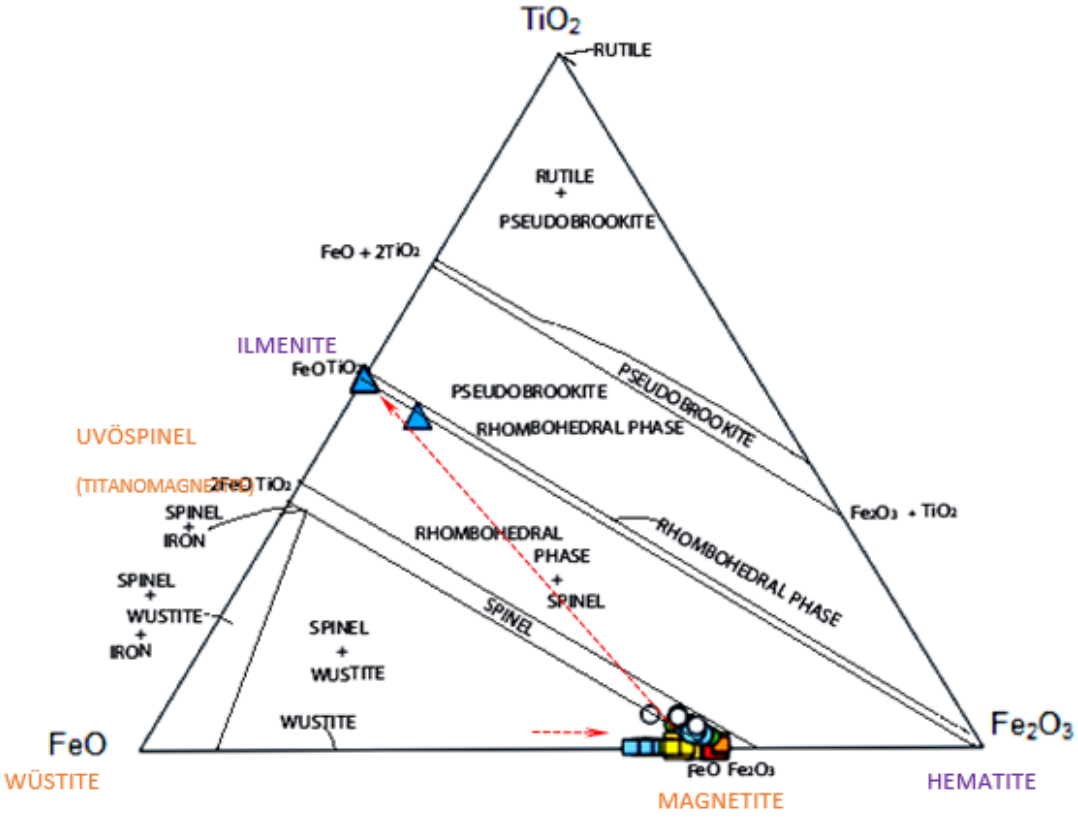

Fig 4.55 TiO_2–FeO–Fe_2O_3 ternary diagram (Fleischer, 1965) showing compositions of FeTi-oxide minerals such as titanomagnetite-ilmenite-magnetite solid solution series are indicated.

Figure 4.56 shows magnetite-titanomagnetite association (and other minerals). Size and texture of titanomagnetite is variable but generally shows anhedral crystals that are often embayed, indicating marginal resorption. Internally mineral shows multiple cracks perhaps providing paths for resorbed fluid or liquid enriched in elements such as Ti. Titanomagnetite is often associated with Ti-bearing minerals. In

Figure 4.56 (BSE image I) position of magnetite close to titanomagnetite as well as melanite bordering titanite demonstrates fluid circulation and metasomatism responsible for increasing activity of silica which allows ilmenite and/or melanite to alter to titanite. The post-magmatic changes in the system in Fogo carbonatites, due to involvement of metasomatic fluids, produced gradual assemblage composed of magnetite→ titanomagnetite→ ilmenite→ garnet→ titanite.

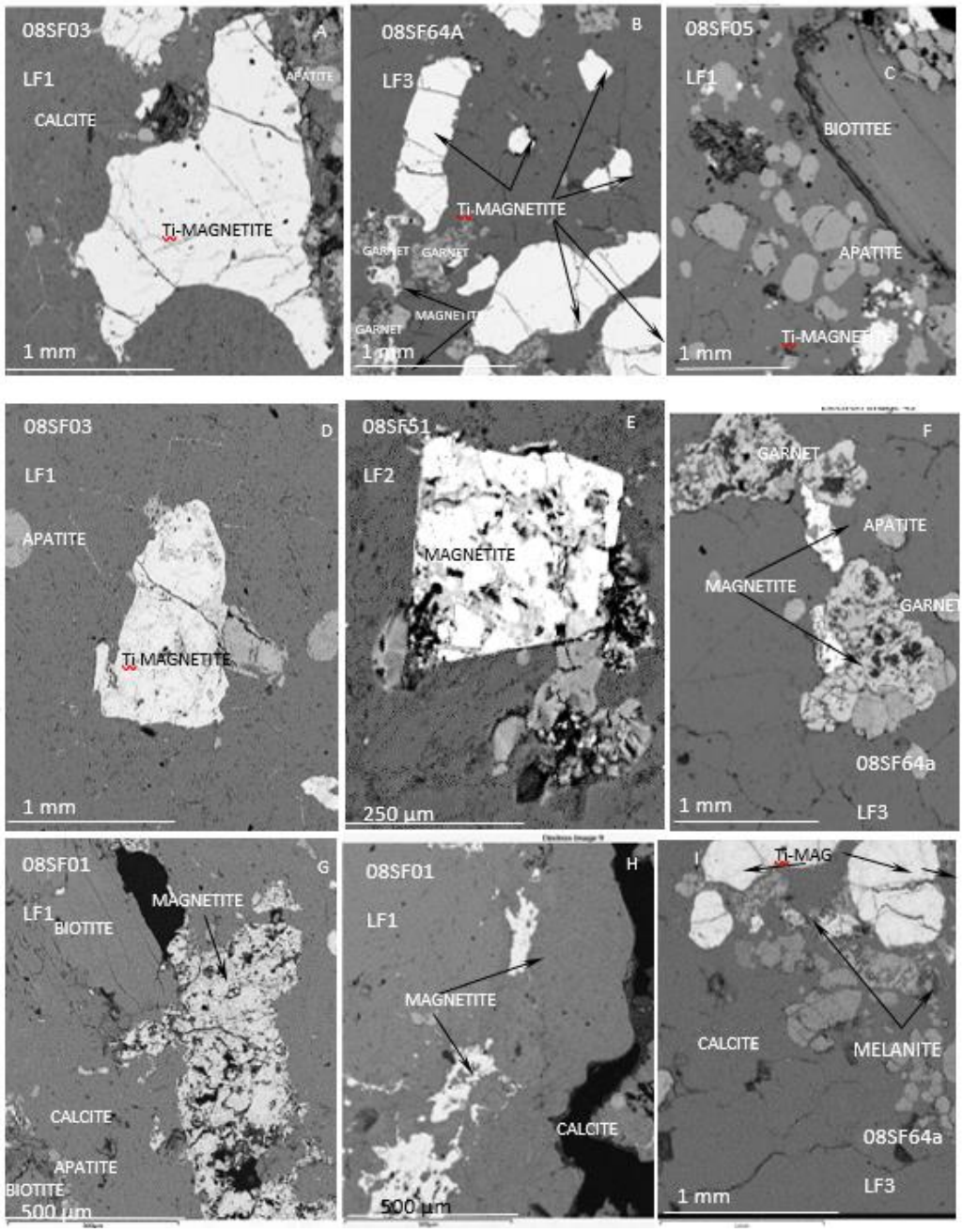

Fig 4.56 Backscatter electron image of 08SF03 and 08SF05 from Rib. de Almada and 08SF64A from Monte Almada, Fogo, Cape Verde, displaying titanomagnetite (A, B, C, and D). Backscatter electron image of 08SF01 from Rib. de Almada, 08SF51 from Rib. Domingo Santo and 08SF64A from Monte Almada, displaying magnetite (F, G, H). BSE image I presenting association of magnetite-titanomagnetite-melanite-titanite.

4.6 Summary of major elements and petrography

- Calcite in all locations originated as a primary phase, though secondary calcite can be found in veins, voids, forming inclusions in feldspar and patches in primary calcite -Two populations of apatite are distinguished according to texture, grain size and chemistry. The first is anhedral, larger with lower Sr content and minor Ce content. The hopper crystals are smaller, euhedral with higher SrO concentration and significant Ce_2O_3. The hopper apatite is set between Mn-Sr-rich granoblastic calcite and in close association with cross-cutting veins.
- Crystallisation of apatite persisted until the final solidification. Hopper crystals exist alongside the larger anhedral specimens though more enriched in LREEs than as they crystallisation was more rapid (preference of Ce over other LREEs).
- Rib. de Almada pyroxene is more primitive and Monte Almada is relatively more evolved. This trend is consistent with the trend seen in most mica as Rib. de Almada has more primitive phlogopite and Monte Almada mica is more evolved biotite.
- Rib. de Almada has a mineral assemblage of calcite and phlogopite reflecting emplacement of a potassic body (glimmeritic sheets) into the intrusive carbonatite. Stress-related fractures provided paths for hydrothermal fluids (fenitization) also aiding crystallisation of accessory minerals.
- Rib. Santo Domingo site represents highly oxidised carbonatite, which is devoid of mafic silicates typically found in Rib. de Almada and Monte Almada (reduced activity of silica). Monazite (Ce, La, Nd, and Th-rich phase) most likely formed as a replacement of apatite. The preferred orientation influenced by metamorphism was induced by shear zone, which provided passage to REE-rich hydrothermal fluids and altered early formed phases. Highly oxidised state points to low-temperature hydrothermal alteration.
- Monte Almada contains amphiboles which are not found in Rib. de Almada and Rib. Santo Domingo. This reflects K-fenitization, typically formed in the upper levels of sövitic intrusions.
- Texture of some phlogopite, showing intimate association with rare phases, provides insight into crystallisation of titanite, zirconolite, zircon and pyrochlore. Enrichment of phlogopite in Hf arises from condition of lower mobility of HREEs while LREEs can be removed further away from the system. Zircon, zirconolite and titanite lack Hf there was no more Hf left in the system during final crystallisation of those phases.

- The presence of amphibole together with geochemical data arguments for possible metasomatic alteration associated with movement of alkalis in carbonatite (amphibole formed in expense of pyroxene).
- Study of zeolites and feldspathoids in Monte Almada led to conclusion that the zeolites were derived from the hydration and alteration of pre-existing feldspathoids. Natrolite probably is a product of hydrothermal alteration after sodalites.
- Complex turbid texture of feldspar together with assemblage of alkali amphibole/pyroxene, apatite, garnet and calcite indicates that fenitization controlled modification of texture and chemistry.
- Investigation into distribution of the metasomatic fluid and its effect on texture and chemistry of the minerals led to conclusion that two types of fenitization took place: pervasive (alkali fluid circulating around phases) and veined (fractures running through the phases providing paths for metasomatic fluids).
- The the presence of zircon which is rare in carbonatites reflects high localised silica saturation in overall undersaturated carbonatite.
- Zirconolite in association with titanite-niobian ilmenite differs from the association with zircon-pyrochlore-titanite (intergrowing with each other).
- Nb-pyrochlore which is Th-U-rich has hydrothermal origin reflecting localised dissolution of Zr-rich precursor mineral(s) by hydrothermal fluids, enrichment in Nb/Th/U and recrystallisation into Nb-Th-U-rich assemblage. Thus late-stage metasomatic processes operating profoundly depend on precursor minerals, which can be resorbed and incorporate back to the system.
- Textural evidence reflects late formation of melanite during metasomatic stage, which was further influenced by metasomatic reactions leading to formation of titanite (Monte Almada) by reactions involving introduction of Ti in expense of Si.
- Post-magmatic changes due to involvement of metasomatic fluids gradually altered the assemblage: magnetite→ titanomagnetite→ ilmenite→ garnet→ titanite.

4.7 Trace element distribution in carbonatites and pyroxenite from Fogo

REE and trace element contents were analysed in calcite, apatite, pyroxene, amphibole, phlogopite-biotite, orthoclase, nepheline, zeolite, garnet and titanite. Compositional data for calcite and apatite are given in Table 6.5.1a-b and 6.5.3a-c

respectively (Appendix 2b). Average values and standard deviation shown in Tables 4.18a-b and 4.19. The REEs and trace elements diagrams for calcite and apatite are presented in Figure 4.57 and 4.58.

CALCITE

ppm

	SF03_aver1		SF03_aver2		SF03_aver3		SF03_aver4		SF01_aver		SF65_aver		SF66_aver	
	ave n=8	dev n=8	ave n=8	dev n=8	ave n=8	dev n=8	ave n=2	dev n=2	ave n=3	dev n=3	ave n=13	dev n=13	ave n=3	dev n=3
Sc	0.681	0.098	0.005	0.004	0.020	0.012	0.034	0.013	bdl	bdl	8.454	14.97	0.072	bdl
Ti	bdl	bdl	bdl	bdl	0.000	0.000	0.000	0.000	0.000	0.000	0.011	0.013	0.011	0.013
V	0.095	0.051	0.004	bdl	0.214	0.300	2.169	0.270	bdl	bdl	1.990	2.629	31.38	6.399
Cr	32.23	6.003	0.309	bdl	0.436	0.274	0.412	0.259	44.467	3.332	227.7	531.3	3.748	3.012
Mn	0.381	0.059	0.006	0.000	0.003	0.003	0.003	0.001	1.228	0.205	7.965	18.692	0.152	0.071
Co	0.114	0.008	0.009	0.010	0.002	0.001	0.049	0.022	bdl	bdl	1.577	3.363	53.98	39.25
Ni	0.733	0.534	0.039	bdl	0.021	0.027	0.024	0.004	1.213	0.693	44.13	95.12	4.855	3.969
Cu	0.154	0.025	0.002	bdl	0.011	0.008	0.082	0.044	0.436	0.152	4.057	5.854	285.6	97.92
Ga	17.356	2.630	0.258	0.011	0.005	0.005	0.055	0.015	28.692	1.650	278.8	674.2	28.96	6.512
Ge	11.394	0.012	0.167	bdl	0.042	0.038	0.135	0.153	23.791	2.409	211.4	522.3	2.572	0.828
Rb	bdl	bdl	bdl	bdl	0.005	0.005	0.060	bdl	0.096	0.021	2.485	2.990	41.8	33.5
Sr	28794	1477	438.7	12.79	13.20	9.324	14.66	3.434	52674	4353	650194	1596185	1239	1212
Y	267.4	27.37	4.310	0.024	0.641	0.700	2.065	0.442	442.0	52.76	4608	11209	50.87	8.832
Zr	bdl	bdl	bdl	bdl	0.076	0.055	0.589	0.149	bdl	bdl	22.35	bdl	4.929	2.874
Nb	bdl	bdl	bdl	bdl	bdl	bdl	0.049	0.049	0.042	0.029	1.278	1.829	2.315	0.245
Cs	bdl	bdl	bdl	bdl	0.003	0.004	0.000	bdl	0.035	0.049	1.376	1.858	7.927	13.27
Ba	1795	389.3	26.39	0.491	0.138	0.248	3.055	1.217	2764	222.7	24233	62146	139.8	129.3
La	702.8	69.5	11.46	0.393	0.137	0.100	2.160	0.475	1089	100.6	12708	31781	120.9	19.06
Ce	1327	159.9	20.24	1.078	0.035	0.048	2.364	0.559	2142	189.0	21312	53684	318.4	49.40
Pr	147.9	31.64	2.111	0.145	0.019	0.017	0.404	0.105	235.3	24.48	2052	5111	27.08	3.076
Nd	526.5	47.49	7.880	0.527	0.089	0.074	1.634	0.407	900.9	96.35	7723	19400	97.22	8.698
Sm	86.38	10.94	1.229	0.094	0.018	0.013	0.272	0.062	147.3	17.54	1217	3107	13.72	1.156
Eu	22.30	1.863	0.345	0.022	0.007	0.005	0.080	0.013	40.26	4.080	321.4	810.4	3.464	0.378
Gd	66.66	4.845	0.924	0.055	0.031	0.017	0.239	0.018	112.3	15.97	1072	2787	10.46	1.150
Tb	8.607	0.914	0.121	0.004	0.004	0.002	0.035	0.000	14.39	1.541	139.9	358.2	1.320	0.236
Dy	49.98	4.932	0.698	0.050	0.031	0.019	0.223	0.005	81.24	8.726	871.1	2230	7.463	1.045
Ho	9.015	0.167	0.129	0.015	0.008	0.006	0.048	0.004	15.27	2.045	160.2	387.3	1.490	0.246
Er	24.75	3.583	0.379	0.044	0.025	0.020	0.145	0.013	39.21	4.931	414.2	986.2	4.333	0.547
Tm	3.053	0.082	0.048	0.005	0.004	0.002	0.020	0.003	5.27	0.422	58.68	130.2	0.570	0.122
Yb	18.22	2.116	0.300	0.004	0.024	0.016	0.139	0.028	32.40	3.578	337.7	792.9	3.657	0.781
Lu	2.499	0.145	0.038	0.002	0.004	0.003	0.022	0.006	4.373	0.411	37.36	86.61	0.465	0.159
Hf	0.024	0.006	bdl	bdl	0.000	0.000	0.002	0.001	0.008	0.005	0.861	1.384	0.079	0.069
Ta	bdl	bdl	bdl	bdl	bdl	bdl	0.002	bdl	0.009	0.010	0.020	0.008	0.014	0.001
Pb	8.989	2.267	0.117	0.009	0.002	0.001	0.022	0.011	14.353	1.093	341.8	823.8	287.0	77.96
Th	bdl	bdl	bdl	bdl	bdl	bdl	0.022	bdl	bdl	bdl	2.863	5.683	0.391	0.307
U	bdl	bdl	bdl	bdl	0.000	bdl	0.001	bdl	bdl	bdl	0.212	0.477	5.053	1.972

Table 4.18a Average and standard deviation values of trace element contents (ppm) of calcite in the Fogo mica-rich sövite 08SF01, silicate-rich sövite 08SF03, fenitic sövite 08SF65) and calcite-bearing pyroxenite (08SF66).

CALCITE normalised to chondrite

	SF03_aver1		SF03_aver2		SF03_aver3		SF03_aver4		SF01_aver		SF65_aver		SF66_aver	
	ave n=2	dev n=2	ave n=2	dev n=2	ave n=2	dev n=2	ave n=8	dev n=8	ave n=3	dev n=3	ave n=13	dev n=13	ave n=3	dev n=3
Rb	bdl	bdl	bdl	bdl	0.026	bdl	0.002	0.002	0.041	0.009	1.071	1.289	18.04	14.43
Ba	744.7	161.5	10.95	0.204	1.267	0.505	0.057	0.103	1147	92.40	10055	25787	58.00	53.65
Th	bdl	bdl	bdl	bdl	0.748	bdl	bdl	bdl	bdl	bdl	98.74	196.0	13.50	10.58
U	bdl	bdl	bdl	bdl	bdl	bdl	bdl	bdl	bdl	bdl	26.47	59.63	631.6	246.5
Nb	bdl	bdl	bdl	bdl	0.199	0.201	bdl	bdl	0.172	0.119	5.194	7.435	9.410	0.995
Tm	123.6	3.334	1.940	0.202	0.822	0.135	0.152	0.095	0.622	0.741	1.409	0.594	1.028	0.105
La	2965	293.4	48.36	1.657	9.116	2.003	0.578	0.422	4595	424.6	53622	134097	510.4	80.41
Ce	2169	261.3	33.07	1.762	3.863	0.914	0.057	0.078	3501	308.8	34824	87720	520.2	80.72
Pb	3.639	0.918	0.048	0.004	0.009	0.005	0.001	0.000	5.811	0.443	138.4	333.5	116.2	31.56
Sr	3966	203.4	60.43	1.761	2.019	0.473	1.818	1.284	7255	599.6	89558	219860	170.6	166.9
Nd	1127	101.7	16.87	1.128	3.499	0.872	0.190	0.158	1929	206.3	16537	41543	208.2	18.62
Zr	bdl	bdl	bdl	bdl	0.152	0.039	0.020	0.014	bdl	bdl	5.776	bdl	1.274	0.743
Hf	0.227	0.057	bdl	bdl	0.018	0.011	0.001	0.001	0.073	0.051	8.080	12.98	0.741	0.648
Sm	564.6	71.50	8.034	0.612	1.776	0.408	0.116	0.084	962.8	114.7	7952	20309	89.70	7.559
Ti	bdl	bdl	bdl	bdl	0.006	0.006	0.000	0.000	0.002	0.003	0.145	0.175	0.153	0.174
Y	170.3	17.44	2.745	0.015	1.315	0.281	0.408	0.446	281.5	33.60	2935	7140	32.40	5.625
V	0.002	0.001	0.000	bdl	0.039	0.005	0.004	0.005	bdl	bdl	0.036	0.047	0.560	0.114
Sc	0.115	0.017	0.001	0.001	0.006	0.002	0.003	0.002	bdl	bdl	1.428	2.529	bdl	bdl
	ave n=2	dev n=2	ave n=2	dev n=2	ave n=2	dev n=2	ave n=8	dev n=8	ave n=3	dev n=3	ave n=13	dev n=13	ave n=3	dev n=3
La	2965	293.4	48.36	1.657	9.116	2.003	0.578	0.422	4595	424.6	53622	134097	510.4	80.41
Ce	2169	261.3	33.07	1.762	3.863	0.914	0.057	0.078	3501	308.8	34824	87720	520.2	80.72
Pr	1557	333.0	22.22	1.523	4.257	1.106	0.204	0.176	2477	257.6	21602	53802	285.0	32.38
Nd	1127	101.7	16.87	1.128	3.499	0.872	0.190	0.158	1929	206.31	16537	41543	208.2	18.62
Sm	564.6	71.50	8.034	0.612	1.776	0.408	0.116	0.084	962.8	114.7	7952	20309	89.70	7.559
Eu	384.5	32.11	5.941	0.386	1.382	0.216	0.113	0.084	694.2	70.35	5541	13973	59.73	6.519
Gd	324.4	23.57	4.496	0.268	1.165	0.088	0.150	0.082	546.6	77.71	5215	13564	50.92	5.594
Tb	230.1	24.44	3.237	0.101	0.941	0.013	0.111	0.062	384.9	41.22	3741	9577	35.29	6.308
Dy	196.8	19.42	2.746	0.196	0.877	0.019	0.124	0.075	319.8	34.35	3429	8780	29.38	4.114
Ho	159.3	2.950	2.276	0.264	0.844	0.077	0.140	0.101	269.8	36.14	2830	6842	26.33	4.341
Er	149.6	21.65	2.287	0.267	0.874	0.079	0.154	0.118	236.9	29.79	2503	5959	26.18	3.304
Tm	123.6	3.334	1.940	0.202	0.822	0.135	0.152	0.095	213.2	17.08	2376	5271	23.06	4.947
Yb	107.2	12.45	1.767	0.022	0.819	0.168	0.142	0.095	190.6	21.05	1986	4664	21.51	4.596
Lu	98.37	5.706	1.503	0.069	0.864	0.222	0.156	0.113	172.1	16.186	1471	3410	18.30	6.274

Table 4.18b Average and standard deviation values of trace element contents of calcite in the Fogo carbonatites (mica-rich sövite 08SF01, silicate-rich sövite 08SF03, fenitic sövite 08SF65) and calcite-bearing pyroxenite (08SF66)).

Average Sr contents in calcite in sövites vary from very high (600000 ppm in 08SF65) to intermediate (50000-30000 ppm in 08SF01 and 08SF03 respectively) and low (500-10 ppm in 08SF03). It is also low in pyroxenite 08SF66 (1000 ppm). Ba

concentrations are also variable with highest average concentrations in sövite 08SF65 (25000 ppm), intermediate in sövites 08SF01 and 08SF03 (3000-2000 ppm) and lowest in 08SF03 and 08SF01 (23-0.1 ppm). Calcite in pyroxenite 08SF66 has low Ba (140 ppm). Sr and Ba contents in apatites vary: highest in pyroxenite 08SF66 (600000 and 6000 ppm respectively), intermediate in sövite 08SF01 (70000 and 200 ppm) and lowest in sövite 08SF03 (300 and 12 ppm). Calcite in sövites contains significant amounts of Y, being highest in 08SF65 (5000 ppm), low in 08SF01 (400 ppm) and variable in 08SF03 (300-1 ppm). Calcite from pyroxenite 08SF66 has a low Y content (50 ppm). The Y contents in apatite varies, being significantly higher in pyroxenite 08SF66 and lower in sövites 08SF01 and 08SF03.

APATITE	08SF66		08SF03		08SF01	
	wv n=7	st.dev n=7	wv n=7	st.dev n=7	wv n=9	st.dev n=9
Sc	37.51	40.54	0.024	0.012	709.4	bdl
Ti	0.008	0.005	0.000	0.000	0.011	0.012
V	8276	9427	5.384	3.931	689.0	551.1
Cr	198.1	211.9	0.411	0.360	26.82	19.14
Mn	1.764	1.849	0.003	0.002	0.417	0.239
Co	2.334	4.508	0.004	0.005	1012	bdl
Ni	4.932	4.143	0.019	0.010	3.871	5.477
Cu	4.866	3.099	0.004	0.004	13.40	20.99
Ga	3152	3045	1.119	0.625	373.3	244.2
Ge	2164	2094	0.944	0.481	326.1	196.6
Rb	12.17	20.86	0.006	0.003	2.526	3.699
Sr	636499	647042	278.9	98.982	75140	42166
Y	22983	23619	14.27	7.458	3341	2275
Zr	1054	1269	0.590	0.402	48.47	60.85
Nb	191.9	180.8	0.093	0.058	21.53	24.93
Cs	6.599	8.855	0.003	0.003	0.661	0.602
Ba	6345	7134	8.023	12.40	223.3	168.8
La	128349	119686	37.64	19.38	10691	6597
Ce	268548	254975	82.75	45.97	27135	18029
Pr	29232	27979	9.563	5.490	3327	2247
Nd	114608	110001	39.04	22.86	13926	9526
Sm	16498	16529	6.741	4.030	2312	1604
Eu	3954	3895	1.859	1.096	590.3	396.3
Gd	10991	11195	5.211	3.063	1595	1095
Tb	1068	1062	0.631	0.369	180.1	121.4
Dy	5079	5150	3.244	1.844	874.3	582.9
Ho	780.8	810.0	0.535	0.298	139.6	93.66
Er	1664	1708	1.217	0.644	291.1	182.1
Tm	179.8	176.3	0.135	0.069	33.02	21.98
Yb	955.8	978.9	0.720	0.345	146.5	91.93
Lu	93.38	96.33	0.079	0.034	15.84	9.804
Hf	1.763	2.680	0.000	0.001	0.225	0.158
Ta	0.586	0.735	0.000	0.000	0.242	0.185
Pb	176.9	174.6	0.064	0.036	11.15	4.605
Th	17469	17628	3.388	1.122	1186	1345

APATITE	08SF66		08SF03		08SF01	
	wv n=7	st.dev n=7	wv n=7	st.dev n=7	wv n=9	st.dev n=9
Rb	5.246	8.990	0.003	0.001	1.089	1.594
Ba	2633	2960	3.329	5.146	92.64	70.06
Th	602371	607876	116.8	38.69	40908	46380
U	287011	288990	84.53	6.491	9001	13740
Nb	780.1	735.0	0.377	0.237	87.53	101.3
Ta	41.83	52.51	5.467	2.778	17.29	13.21
La	541556	505846	158.8	81.75	45110	27837
Ce	438803	416626	135.2	75.11	44337	29459
Pb	71.61	70.70	0.026	0.015	4.515	1.864
Sr	87672	89124	38.42	13.63	10350	5808
Nd	245414	235547	83.60	48.96	29819	20399
Zr	272.4	327.9	0.182	0.083	12.53	15.72
Hf	16.53	25.14	0.006	0.003	2.112	1.482
Sm	107831	108032	44.06	26.34	15109	10481
Ti	0.103	0.063	0.000	0.000	0.170	0.162
Y	14639	15044	9.088	4.750	2128	1449
V	147.8	168.3	0.096	0.070	12.30	9.842
Sc	6.336	6.848	0.004	0.002	119.8	bdl
	wv n=7	st.dev n=7	wv n=7	st.dev n=7	wv n=9	st.dev n=9
La	541556	505846	158.8	81.75	45110	27837
Ce	438803	416626	135.2	75.11	44337	29459
Pr	307703	294519	100.7	57.79	35022	23653
Nd	245414	235547	83.59	48.96	29819	20399
Sm	107831	108032	44.06	26.34	15109	10481
Eu	68180	67162	32.05	18.90	10178	6833
Gd	53486	54479	25.36	14.90	7761	5330
Tb	28547	28404	16.86	9.877	4815	3245
Dy	19997	20276	12.77	7.259	3442	2295
Ho	13796	14310	9.455	5.270	2466	1655
Er	10052	10319	7.353	3.893	1759	1101
Tm	7279	7140	5.467	2.778	1337	889.9
Yb	5622	5758	4.236	2.028	861.8	540.8
Lu	3676	3793	3.129	1.353	623.7	386.0

Table 4.19 Average and standard deviation values of trace element in ppm and chondrite-normalised contents of apatite in the Fogo mica-rich sövite (08SF01) and calcite-bearing pyroxenite (08SF66).

REE concentrations in apatite are higher than in calcite however both phases show substantial variation. The average LREEs in calcite in sövite range for La 0.1-13000 ppm and Ce 0-20000 ppm. In pyroxenite the La concentration is 120 ppm and Ce is 300 ppm. Apatite exhibits higher values; pyroxenite 08SF66 shows an average of 100000 ppm La and 200000 ppm Ce. In sövite 08SF03 apatite La and Ce values are 40 and 80 ppm and in 08SF01 are 10000 and 30000 ppm.

The degree of enrichment of LREE to HREE is expressed by the chondrite-normalised La/Yb ratio. It is typically 28 for Fogo calcite (though some of 08SF03

show lower values 4-11). Apatites La/Yb range is broader than in calcite 53-96 with pyroxenite exhibiting highest values.

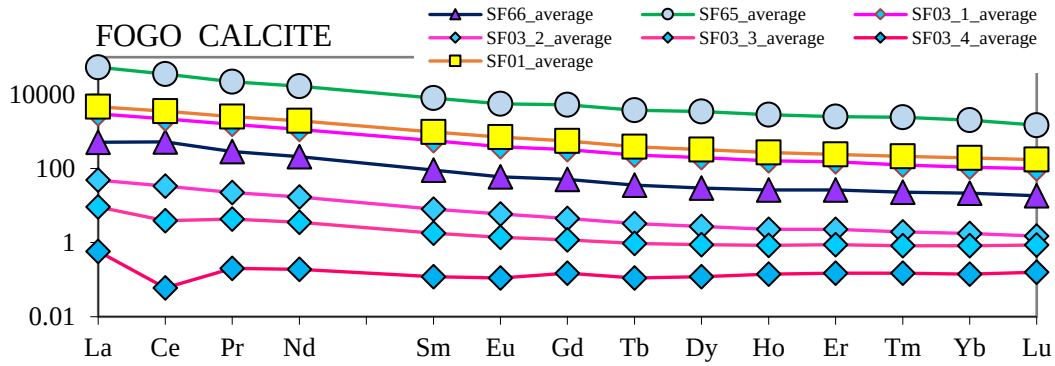

Fig 4. 57 Chondrite-normalised REE and trace element patterns of calcite in Fogo carbonatites (mica-rich sövite 08SF01, silicate-rich sövite 08SF03 and fenitic sövite 08SF65) and calcite-bearing pyroxenite (08SF66).

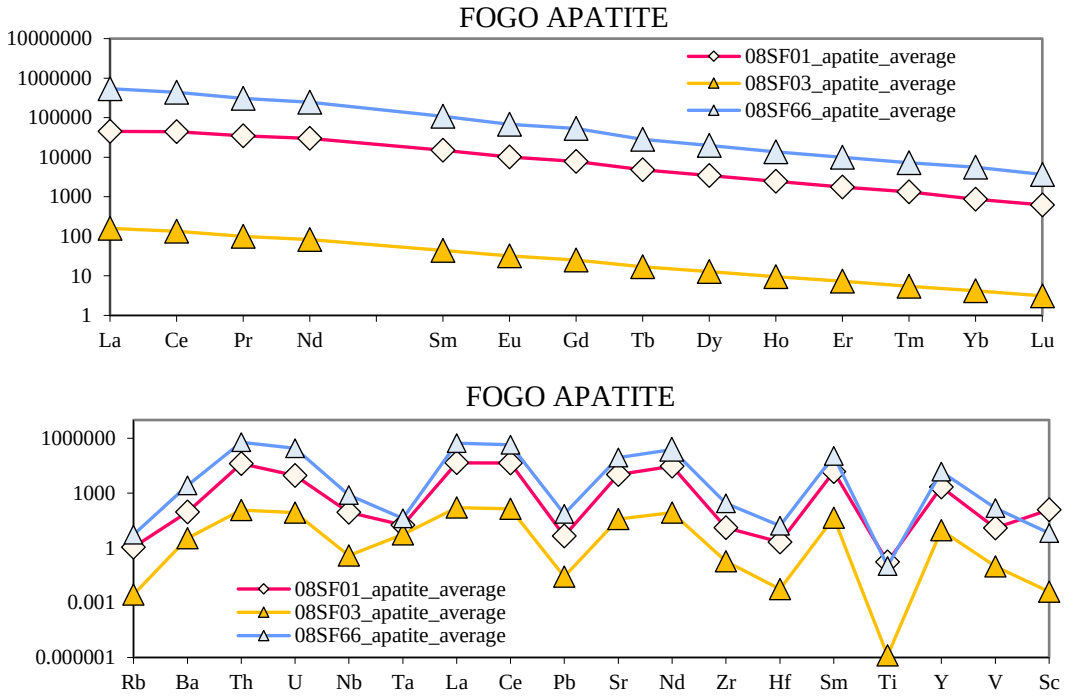

Fig 4.58 Chondrite-normalised REE and trace element patterns of apatite in the Fogo mica-rich sövite (08SF01) and calcite-bearing pyroxenite (08SF66).

The REEs in calcite from Fogo have less-steep patterns than in apatite. The profiles in apatite and calcite are sub-parallel to each other (Figure 4.57 and 4.58), though apatite has higher REE content with LREE being more enriched relative to HREEs. Apatite is REE-enriched by one order of magnitude to calcite. This points to variable but largely stronger LREE fractionation into apatite. A positive correlation between the high Sr content and the high REE content in both calcite and apatite is

apparent. Calcite and apatite show negative anomalies in Rb, Ta, Pb and Hf. Additionally calcite is depleted in Zr and apatite is depleted in Nb and Ti. Apatite shows enrichment in Th and U in pyroxenite 08SF66 and in sövites 08SF01 though the sövite 08SF03 lacks these enrichments. Apatite displays high Zr enrichment in pyroxenite 08SF66 (1000 ppm), moderate in sovite 08SF01 (50 ppm) and low sovite 08SF03 (0.6 ppm).

Compositional data for pyroxene and amphibole are given in Table 6.5.5a-d (Appendix 2b), with the average values and standard deviation in Table 4.20. The REEs and trace elements diagram for pyroxene and amphibole with the average values is presented in Figure 4.59.

	AMPHIBOLE (ppm)				PYROXENE (ppm)			
	08SF03 amph		08SF66 amph		08SF65 px		08SF66 px	
	ave.n=6	sl dev n=6	ave.n=2	sl dev n=2	ave.n=6	sl dev n=6	ave.n=10	sl dev n=10
Sc	0.375	0.084	2.558	0.912	3.350	3.039	0.622	0.302
Ti	0.083	0.039	0.177	0.064	0.083	0.024	0.112	0.045
V	40.81	9.075	299.18	68.33	130.9	50.13	114.2	58.17
Cr	0.110	0.034	0.951	0.513	6.304	5.059	0.598	0.269
Mn	0.053	0.004	0.132	0.009	0.169	0.037	0.195	0.025
Co	0.916	0.099	1.300	0.054	1.451	0.495	3.699	1.027
Ni	0.016	0.007	0.136	0.015	0.348	0.277	0.198	0.085
Cu	0.135	0.106	0.153	0.008	0.420	0.647	0.153	0.080
Ga	3.815	0.884	6.446	0.738	5.944	4.250	7.416	1.813
Ge	0.305	0.043	0.709	0.036	7.958	10.38	0.459	0.150
Rb	0.196	0.130	0.056	bdl	2.633	2.604	2.962	4.354
Sr	31.867	1.729	22.37	3.072	95.63	70.40	106.1	46.75
Y	1.276	0.297	0.580	0.360	2.385	1.168	2.017	0.995
Zr	95.27	21.85	756.10	121.74	788.8	331.5	343.1	196.8
Nb	0.625	0.642	1.179	1.385	1.146	0.763	2.305	1.610
Cs	0.010	0.009	0.003	bdl	0.828	1.075	0.100	0.164
Ba	0.694	0.425	0.303	0.356	6.084	3.837	17.20	17.16
La	0.650	0.184	0.142	0.009	2.506	1.799	2.533	1.213
Ce	1.876	0.368	0.472	0.082	5.502	3.601	5.712	2.113
Pr	0.285	0.047	0.076	0.016	0.645	0.346	0.699	0.231
Nd	1.408	0.187	0.393	0.119	2.465	1.404	2.939	0.940
Sm	0.345	0.048	0.127	0.047	0.476	0.202	0.557	0.190
Eu	0.107	0.015	0.040	0.018	0.159	0.093	0.166	0.064
Gd	0.297	0.047	0.112	0.056	0.419	0.267	0.415	0.172
Tb	0.045	0.007	0.017	0.009	0.061	0.040	0.055	0.024
Dy	0.265	0.050	0.112	0.060	0.469	0.304	0.328	0.153
Ho	0.048	0.010	0.022	0.015	0.089	0.062	0.064	0.033
Er	0.133	0.018	0.094	0.071	0.410	0.226	0.208	0.111
Tm	0.024	0.003	0.031	0.022	0.120	0.050	0.048	0.023
Yb	0.237	0.030	0.437	0.302	1.388	0.610	0.488	0.227
Lu	0.054	0.006	0.132	0.094	0.366	0.140	0.114	0.056
Hf	0.342	0.103	8.727	1.755	12.14	8.136	3.582	2.470
Ta	0.036	0.046	0.018	0.022	0.019	0.015	0.035	0.021
Pb	0.023	0.008	0.003	0.002	0.186	0.210	0.422	0.450
Th	0.056	0.054	0.046	0.049	0.157	0.099	0.438	0.319
U	0.017	0.019	0.002	bdl	0.075	0.090	0.083	0.077

Table 4.21 Average and standard deviation values of trace element contents (ppm) of clinopyroxene and amphibole in Fogo carbonatites (silicate-rich sövite 08SF03 and fenitic sövite 08SF65) and calcite-bearing pyroxenite (08SF66).

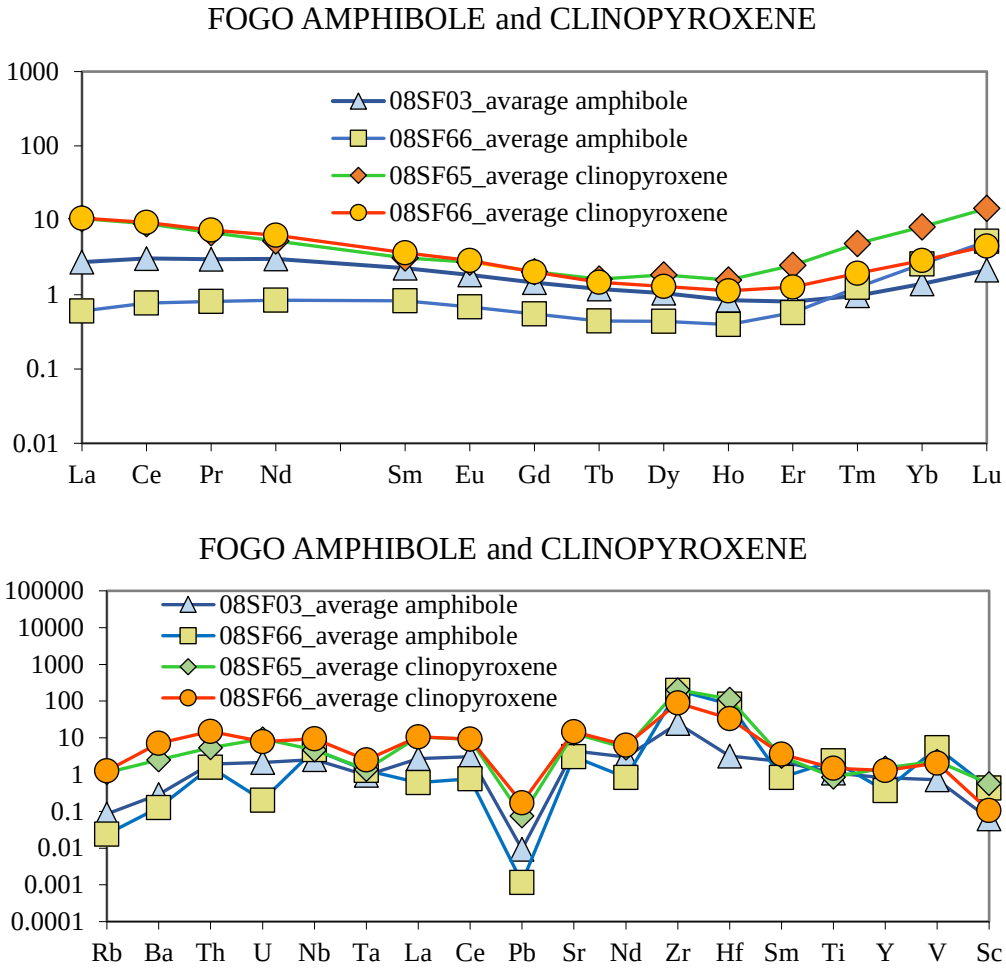

Fig 4.59 Chondrite-normalised REE and trace element patterns of pyroxene and amphibole in the Fogo carbonatites (silicate-rich sövite 08SF03 and fenitic sövite 08SF65) and calcite-bearing pyroxenite (08SF66).

Pyroxene and amphibole show rather low levels of trace elements. The pyroxene REE pattern is similar to amphibole, although amphibole is not as enriched (Figure 4.59). The total average REE in amphibole from sövite 08SF03 is 5.8 ppm. In pyroxenite 08SF66 it is 2.2 ppm. The total average REE in pyroxene in sövite 08SF65 is 15.1 ppm. In pyroxenite 08SF66 it is 14.3 ppm.

The REE chondrite-normalised pattern of the amphibole and clinopyroxene from pyroxenite 08SB66 (Figure 4.59) has concave downward pattern with LREE being one order higher than HREEs for pyroxene, while amphibole is one order lower. The HREEs for both minerals are fixed at the same point, just above the chondritic value. Thus, pyroxene shows preferred LREEs enrichment over amphibole. HREEs from pyroxenite shows lack of preference in both phases. There is considerable enrichment in Hf in amphibole from pyroxenite (8.7 ppm) and to lesser degree in

sövite (0.34 ppm). The Hf enrichment in pyroxene shows the opposite trend, having a higher concentration in sövite (12.1 ppm) and lower in pyroxenite (3.58 ppm). The highest Zr concentration occurs in clinopyroxene from sövite 08SF65 (789 ppm) and amphibole in pyroxenite 08SF66 (768 ppm). The lower concentration was detected in pyroxene from pyroxenite (343 ppm) and lowest is found in amphibole from sövite 08SF03. The Sr content is higher in pyroxene than in amphibole. On the trace element diagram (Figure 4.59) HFSE such as Nb, U and Th form positive anomalies in clinopyroxene though amphibole shows values lower than chondritic. LILE elements such as Rb and Ba, show great similarity in their trends between pyroxene and amphibole. However, Rb and Ba in pyroxene have higher than chondritic values while in amphibole both elements fall below chondritc values.

In most aspects the trace element diagram of amphibole resembles the pyroxene trend although clinopyroxene shows slightly higher enrichment. Also, minerals in clinopyroxenite exhibit higher trace elements contents than in the sövite.

Trace elements of phlogopite-biotite were analysed in sövite 08SF03 and pyroxenite 08SF66. The data are presented in Table 6.5.7a-c (Appendix 2b) and average values are shown in Table 4.22. The REEs and trace elements diagram for mica is given in Figure 4.60.

Fogo micas shows a low content of REEs with rather flat REE patterns, to some extent oscillating around chondritic values (Figure 6.60) yet showing a positive Eu anomaly. The LREE in the pyroxenite have higher abundances than in the sövite.

The micas show high amounts of trace elements such as Ba (1200-4000 ppm), Rb (1600-2000 ppm) and Nb (300-500 ppm), moderate amounts of Sr (110-140 ppm) and low to moderate Zr (2.5-50 ppm). Phlogopite-biotite in silicate-rich sövite (08SF03) shows slight enrichment in Hf (above chondritic value) while in calcite-bearing pyroxenite (08SF66) it does not, which is in agreement with previous observation suggesting remobilization of heavy rare earths. The above analyses show that the Fogo mica can hold high content of some trace elements and significant concentration of the LREEs. Sövite shows higher enrichment than pyroxenite though values are somewhat variable.

PHLOGOPITE-BIOTITE (ppm)

	08SF03		08SF66	
	av. n=15	s.dev n=15	av. n=5	s.dev n=5
Sc	1.969	1.890	0.943	0.241
Ti	7.088	0.683	6.458	0.382
V	664.5	84.04	306.1	68.64
Cr	7.533	5.977	10.24	4.110
Mn	0.707	0.080	1.859	0.063
Co	55.91	5.278	81.57	3.819
Ni	4.853	3.616	15.52	3.343
Cu	2.509	1.556	3.189	1.669
Ga	222.1	24.49	241.9	18.34
Ge	1.771	2.038	3.730	0.758
Rb	2062	624.9	1640	62.20
Sr	139.2	47.35	110.8	132.0
Y	0.121	0.089	0.509	0.207
Zr	50.23	9.060	2.428	1.696
Nb	337.1	45.61	516.0	125.8
Cs	16.17	3.51	28.48	2.968
Ba	3899	710.1	1203	168.6
La	0.142	0.123	0.943	0.918
Ce	0.447	0.838	0.836	0.420
Pr	0.022	0.020	0.078	0.045
Nd	0.112	0.149	0.362	0.201
Sm	0.106	0.115	0.073	0.036
Eu	0.064	0.050	0.042	0.010
Gd	0.087	0.112	0.061	0.036
Tb	0.005	0.007	0.009	0.006
Dy	0.133	0.182	0.064	0.021
Ho	0.007	0.012	0.019	0.008
Er	0.019	0.024	0.036	0.029
Tm	0.002	0.005	0.005	0.004
Yb	0.038	0.043	0.047	0.033
Lu	0.006	0.011	0.004	0.003
Hf	0.139	0.079	0.057	0.026
Ta	3.884	0.619	2.882	1.099
Pb	0.291	0.198	0.720	0.416
Th	0.783	bdl	0.048	0.038
U	0.564	bdl	0.053	0.036

PHLOGOP-BIOT (normalised to chondrite)

	08SF03		08SF66	
	av. n=15	s.dev n=15	av. n=5	s.dev n=5
Rb	888.9	269.36	707.1	26.81
Ba	1618	294.64	499.3	69.96
Th	27.00	bdl	1.661	1.327
U	70.56	bdl	6.657	4.508
Nb	1370	185.4	2098	511.3
Tm	0.286	0.251	205.9	78.54
La	0.599	0.518	3.981	3.872
Ce	0.730	1.369	1.366	0.687
Pb	0.118	0.080	0.291	0.168
Sr	19.17	6.522	15.27	18.19
Nd	0.240	0.319	0.776	0.431
Zr	12.98	2.341	0.627	0.438
Hf	1.308	0.745	0.534	0.247
Sm	0.693	0.751	0.477	0.237
Ti	94.66	9.118	86.24	5.107
Y	0.077	0.057	0.324	0.132
V	11.865	1.501	5.466	1.226
Sc	0.333	0.319	0.159	0.041

	av. n=15	s.dev n=15	av. n=5	s.dev n=5
La	0.599	0.518	3.981	3.872
Ce	0.730	1.369	1.366	0.687
Pr	0.230	0.213	0.816	0.475
Nd	0.240	0.319	0.776	0.431
Sm	0.693	0.751	0.477	0.237
Eu	1.098	0.865	0.728	0.166
Gd	0.424	0.545	0.296	0.177
Tb	0.143	0.189	0.250	0.148
Dy	0.523	0.715	0.252	0.083
Ho	0.132	0.210	0.331	0.140
Er	0.115	0.148	0.220	0.175
Tm	0.286	0.251	0.222	0.175
Yb	0.225	0.250	0.277	0.195
Lu	0.299	0.438	0.200	0.085

Table 4.22 Average and standard deviation values of trace element contents (ppm) and chondrite-normalised contents of phlogopite-biotite in the Fogo carbonatites (silicate-rich sövite 08SF03 and calcite-bearing pyroxenite (08SF66).

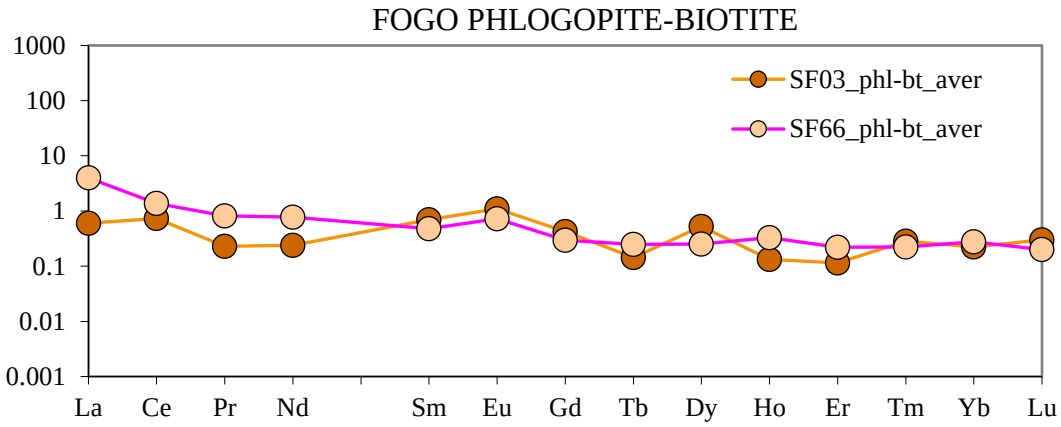

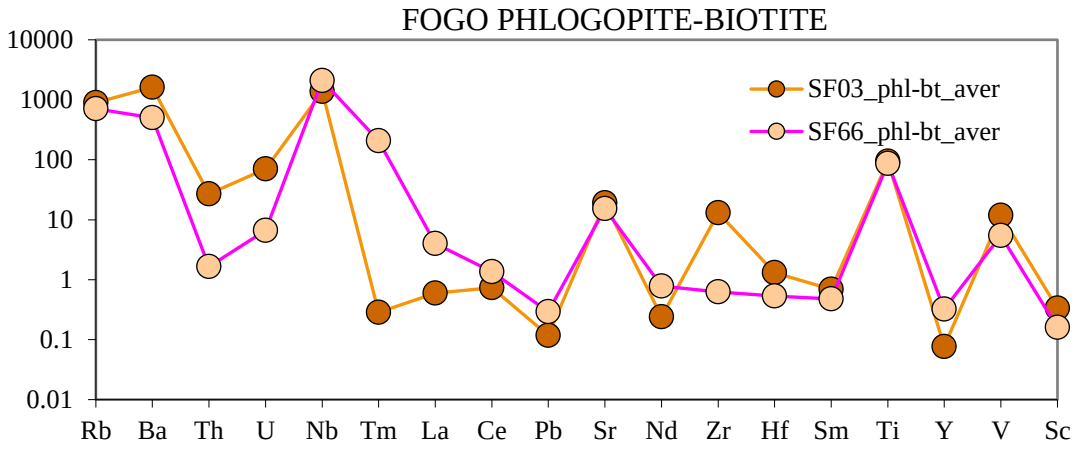

Fig 4.60 Chondrite-normalised REE and trace element patterns of phlogopite-biotite in the Fogo silicate-rich sövite (08SF03) and calcite-bearing pyroxenite (08SF66).

Feldspar and zeolite in sövite 08SF65 and feldspathoids from pyroxenite 08SF66 were analysed for trace elements (Table 6.5.9a-c, Appendix 2b) and average values are shown in Table 4.23.

	08SF65 ORTHOCLASE		08SF66 NEPHELINE		08SF65 ZEOLITE	
	ave n=4	st dev n=4	ave n=3	st dev n=3	ave n=7	st dev n=7
Sc	10.97	*bdl*	1.270	*0.571*	2.102	*2.348*
Ti	0.077	*0.035*	0.022	*0.004*	0.011	*0.003*
V	53.63	*30.63*	18.10	*4.524*	1.789	*1.613*
Cr	23.92	*2.750*	9.193	*3.773*	66.51	*65.37*
Mn	0.039	*0.013*	0.108	*0.115*	0.045	*0.067*
Co	0.966	*0.349*	14.933	*2.981*	0.151	*0.139*
Ni	12.65	*5.56*	8.173	*3.505*	5.554	*4.542*
Cu	14.30	*6.37*	35.96	*6.862*	2.148	*1.957*
Ga	83.87	*27.99*	128.1	*12.81*	45.50	*27.12*
Ge	4.836	*4.035*	7.607	*10.07*	19.48	*19.40*
Rb	122.7	*31.35*	46.66	*5.609*	309.1	*134.1*
Sr	1877	*696.4*	11925	*3161*	1819	*2788*
Y	11.06	*9.120*	39.18	*32.01*	20.03	*27.89*
Zr	1103	*621.1*	31.47	*11.07*	16.88	*19.38*
Nb	38.86	*10.90*	3.509	*0.356*	2.083	*3.442*
Cs	4.101	*2.805*	7.402	*1.497*	2.860	*1.192*
Ba	492.5	*108.2*	682.7	*374.0*	2172	*1107*
La	24.68	*20.38*	65.07	*84.62*	28.27	*47.24*
Ce	36.75	*23.50*	102.5	*132.8*	55.42	*82.40*
Pr	5.054	*4.197*	10.86	*12.77*	5.661	*7.931*
Nd	19.62	*18.08*	38.15	*43.78*	21.17	*29.09*
Sm	4.002	*4.633*	6.168	*6.222*	3.632	*4.797*
Eu	1.334	*1.317*	1.765	*1.595*	1.091	*1.221*
Gd	2.882	*2.730*	5.635	*5.627*	3.249	*4.318*
Tb	0.401	*0.316*	0.778	*0.738*	0.560	*0.737*
Dy	2.732	*2.067*	4.989	*4.603*	3.320	*3.841*
Ho	0.425	*0.327*	1.134	*1.121*	0.668	*0.832*
Er	1.243	*1.225*	3.059	*2.991*	2.171	*3.151*
Tm	0.147	*0.074*	0.429	*0.409*	0.350	*0.502*
Yb	1.379	*1.136*	2.913	*2.955*	1.766	*2.539*
Lu	0.473	*0.449*	0.308	*0.339*	0.266	*0.317*
Hf	12.098	*5.802*	0.490	*0.413*	0.372	*0.193*
Ta	0.390	*0.274*	0.020	*0.008*	0.055	*0.039*
Pb	4.035	*1.245*	12.641	*3.075*	2.073	*1.662*
Th	1.174	*0.513*	0.245	*0.175*	0.520	*0.324*
U	0.927	*0.468*	0.478	*0.123*	0.260	*0.337*

	08SF65 ORTHOCLASE		08SF66 NEPHELINE		08SF65 ZEOLITE	
	ave n=4	st dev n=4	ave n=3	st dev n=3	ave n=7	st dev n=7
Rb	52.90	*13.51*	20.11	*2.418*	133.2	*57.8*
Ba	204.3	*44.88*	283.3	*155.2*	901.3	*459.5*
Th	40.47	*17.71*	8.461	*6.050*	17.94	*11.16*
U	115.9	*58.53*	59.69	*15.41*	32.56	*42.09*
Nb	157.98	*44.32*	14.264	*1.445*	8.467	*13.99*
Ta	27.85	*19.57*	1.408	*0.577*	3.955	*2.783*
La	104.12	*85.98*	274.5	*357.1*	119.3	*199.3*
Ce	60.05	*38.41*	167.5	*217.0*	90.6	*134.6*
Pb	1.634	*0.504*	5.118	*1.245*	0.839	*0.673*
Sr	258.6	*95.92*	1642.6	*435.4*	250.6	*384.0*
Nd	42.01	*38.71*	81.69	*93.75*	45.34	*62.29*
Zr	285.1	*160.5*	8.133	*2.860*	4.363	*5.008*
Hf	113.5	*54.43*	4.593	*3.876*	3.492	*1.810*
Sm	26.16	*30.28*	40.32	*40.67*	23.74	*31.36*
Ti	1.023	*0.468*	0.293	*0.056*	0.141	*0.042*
Y	7.046	*5.809*	24.95	*20.39*	12.76	*17.77*
V	0.958	*0.547*	0.323	*0.081*	0.032	*0.029*
Sc	1.852	*bdl*	0.214	*0.096*	0.355	*0.397*

	ave n=4	st dev n=4	ave n=3	st dev n=3	ave n=7	st dev n=7
La	104.1	*85.98*	*274.5*	*357.1*	119.3	*199.3*
Ce	60.05	*38.41*	*167.5*	*217.0*	90.55	*134.64*
Pr	53.20	*44.18*	*114.3*	*134.4*	59.59	*83.48*
Nd	42.01	*38.71*	*81.69*	*93.75*	45.34	*62.29*
Sm	26.16	*30.28*	*40.32*	*40.67*	23.74	*31.36*
Eu	23.01	*22.70*	*30.43*	*27.50*	18.81	*21.05*
Gd	14.03	*13.28*	*27.42*	*27.38*	15.81	*21.01*
Tb	10.73	*8.449*	*20.80*	*19.73*	14.97	*19.71*
Dy	10.76	*8.139*	*19.64*	*18.12*	13.07	*15.12*
Ho	7.513	*5.778*	*20.04*	*19.80*	11.79	*14.69*
Er	7.509	*7.401*	*18.48*	*18.07*	13.12	*19.04*
Tm	5.937	*3.011*	*17.36*	*16.54*	14.16	*20.32*
Yb	8.114	*6.683*	*17.14*	*17.38*	10.39	*14.94*
Lu	18.60	*17.67*	*12.13*	*13.34*	10.45	*12.47*

Table 4.23 Average and standard deviation values of trace element contents (ppm) and chondrite-normalised contents of orthoclase, nepheline and zeolite in the Fogo fenitic sövite 08SF65) and calcite-bearing pyroxenite (08SF66).

The average REEs and trace elements diagram for these phases are shown in Figure 4.61. Feldspar and zeolite show strong similarities in the REE and trace element patterns but the orthoclase trends are slightly different (Figure 4.61). Nepheline from pyroxenite has the highest REE contents but lack the positive Eu anomaly. The degree of enrichment, expressed by the chondrite-normalised La/Yb ratio, is 22.7. Zeolite from carbonatites has the ratio of 15.9 and orthoclase from sövite has the lowest ratio of 5.6. The total average REE in nepheline is highest (244 ppm), in zeolite is much lower (128 ppm) and in orthoclase is lowest REE contents (101 ppm).

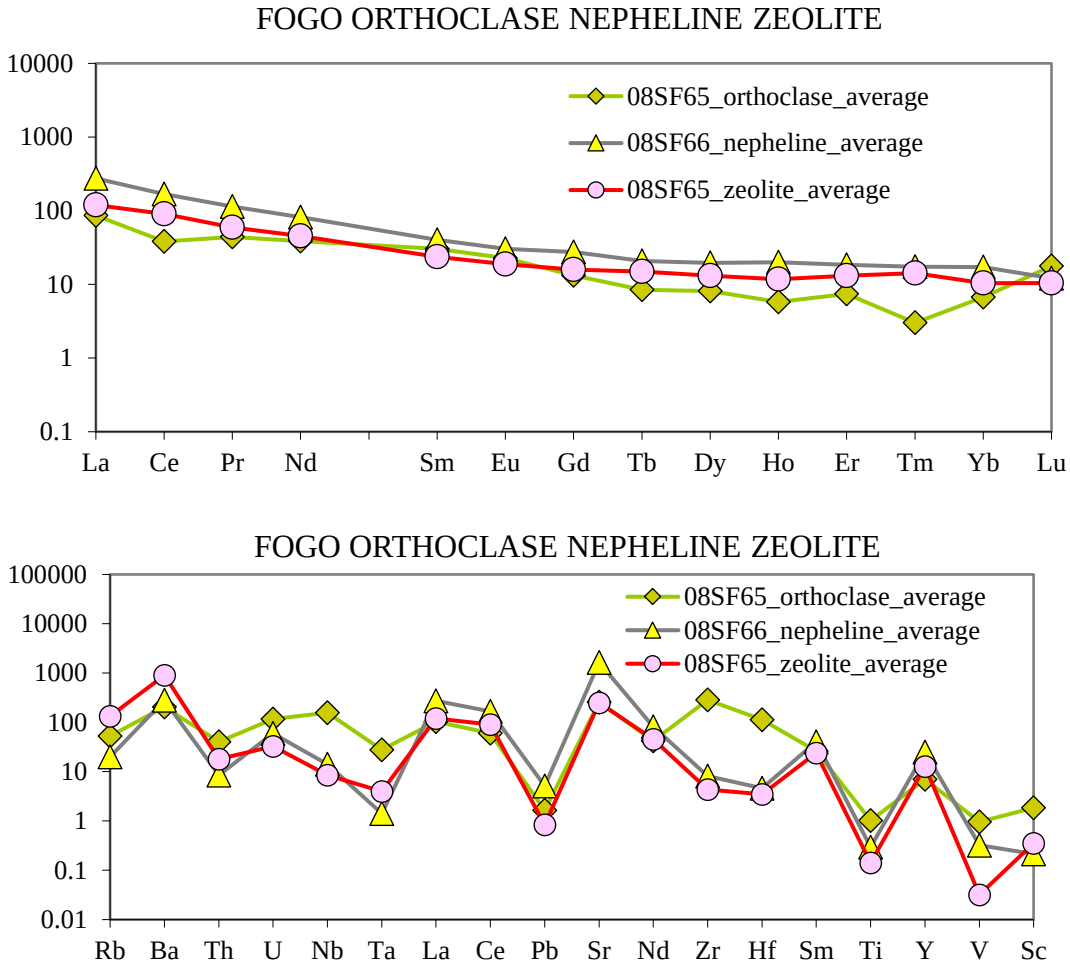

Fig 4.61 Chondrite-normalised REE and trace element patterns of orthoclase, nepheline and zeolite in the Fogo fenitic sövite 08SF65) and calcite-bearing pyroxenite (08SF66). Tm anomaly in orthoclase could be a detection limit problem

Nepheline has higher content of Sr (10000 ppm) than orthoclase and zeolite, which are both equally enriched in range of 2000 ppm. Zeolite contain highest concentration of Rb and Ba (300 ppm and 2000 ppm respectively) while orthoclase concentration is lowest in Ba (500 ppm) with nepheline being lowest in Rb (50 ppm). Orthoclase from carbonatite is characterised by high content of Zr (1000 ppm). It

contains also higher amount of Hf (12 ppm) and Nb (40 ppm). Also, Th and U are one order higher (1 ppm) in orthoclase than in nepheline and zeolite (0.2-0.5 ppm).

The REE contents in zeolite are higher than those in the coexisting orthoclase in 08SF65 carbonatite. Nepheline, orthoclase and zeolite is lacking in Eu anomaly (either negative or positive) meaning that Eu concentration in analysed phases are either not enriched or depleted relative to chondrite.

The chemical compositions of garnet and titanite are presented in Table 6.5.11a-b (Appendix 2b) and average values are shown in Table 4.24. The REEs and trace elements diagram for garnet and titanite is given in Figure 6.62.1 (Appendix 2b), with the average values presented in Figure 4.62.

	08SF66 GARNET		08SF03 TITANITE	
	ave n=2	st dev n=2	ave n=3	st dev n=3
Sc	2.272	0.065	28.24	17.92
Ti	1.916	0.063	3.919	2.470
V	577.8	97.58	18.80	12.00
Cr	0.370	0.378	bdl	bdl
Mn	0.205	0.013	0.050	0.029
Co	0.966	0.478	0.405	0.038
Ni	0.121	0.093	0.042	bdl
Cu	0.613	0.834	0.060	0.043
Ga	21.15	1.214	27.16	16.43
Ge	3.589	0.271	25.86	15.80
Rb	7.221	10.18	0.275	0.264
Sr	31.78	17.52	122.3	174.1
Y	150.5	81.34	751.0	460.6
Zr	2278	141.7	32186	20414
Nb	270.9	97.15	10219	6687
Cs	0.148	0.206	0.022	0.003
Ba	1.479	1.783	6.918	11.62
La	13.90	8.890	174.1	103.5
Ce	75.05	25.53	1238.7	763.8
Pr	14.96	2.681	215.7	130.9
Nd	91.63	4.245	1230.5	745.8
Sm	30.07	4.539	342.7	206.6
Eu	9.958	2.363	104.6	62.34
Gd	29.53	9.115	271.2	164.2
Tb	4.55	2.010	42.24	25.50
Dy	28.51	14.43	246.2	149.1
Ho	5.475	3.239	42.76	25.99
Er	15.13	10.12	103.1	62.77
Tm	2.172	1.445	12.57	7.774
Yb	13.34	9.225	67.44	41.94
Lu	1.761	1.141	7.098	4.426
Hf	20.31	1.590	62.20	39.86
Ta	7.416	1.647	362.0	240.0
Pb	0.378	0.066	2.873	1.671
Th	7.751	3.071	5078	3437
U	6.801	0.798	1995	1384

	08SF66 GARNET		08SF03 TITANITE	
	ave n=2	st dev n=2	ave n=3	st dev n=3
Rb	3.113	4.389	0.119	0.114
Ba	0.613	0.740	2.870	4.822
Th	267.3	105.892	175120	118507
U	850.1	99.750	249411	172946
Nb	1101	394.903	41541	27183
Ta	529.7	117.613	508.8	314.7
La	58.65	37.511	734.5	436.8
Ce	122.6	41.720	2024	1248
Pb	0.153	0.027	1.163	0.676
Sr	4.377	2.413	16.85	23.98
Nd	196.2	9.091	2635	1597
Zr	588.5	36.625	8317	5275
Hf	190.5	14.920	583.4	373.9
Sm	196.5	29.667	2240	1350
Ti	25.59	0.836	52.34	32.99
Y	95.87	51.807	478.3	293.4
V	10.32	1.742	0.336	0.214
Sc	0.384	0.011	4.770	3.028

	ave n=2	st dev n=2	ave n=3	st dev n=3
La	58.65	37.51	734.5	436.8
Ce	122.6	41.72	2024	1248
Pr	157.5	28.22	2271	1378
Nd	196.2	9.091	2635	1597
Sm	196.5	29.67	2240	1350
Eu	171.7	40.74	1804	1075
Gd	143.7	44.36	1320	799.2
Tb	121.8	53.76	1129	681.9
Dy	112.2	56.81	969.2	586.9
Ho	96.73	57.22	755.4	459.2
Er	91.45	61.17	623.0	379.3
Tm	87.93	58.50	508.8	314.7
Yb	78.46	54.26	396.7	246.7
Lu	69.31	44.91	279.4	174.3

Table 4.24 Average and standard deviation values of trace element contents (ppm) and chondrite-normalised contents of garnet and titanite in the Fogo silicate-rich sövite (08SF03) and calcite-bearing pyroxenite (08SF66).

The garnet and titanite are rich in REEs. The chondrite-normalised diagram displays a convex upward pattern which show some preference for the MREEs over LREEs and HREEs. Garnet and titanite exhibit medium to high HFSE enrichment in Zr (2300-32000 ppm respectively), Nb (270 ppm and 10000 ppm), Hf (20 ppm and 60 ppm) and Ta (7 ppm and 360 ppm). Also garnet and titanite contain a fair quantity of Th (40 ppm and 50 ppm respectively) and U (75 ppm and 100 ppm). Garnet and titanite contain also Sr though the contents of other LILE such as Ba and Rb are much lower and Cs concentration are insignificant. There is also considerable amount V in garnet (577 ppm) and Ga in garnet and in titanite (21 ppm and 27 ppm respectively). Overall titanite contain higher concentration of trace elements than garnet. Distribution of these elements reflects involvement of the less common phase, which can accommodate fair amount of REE, HFSE and some of LILE.

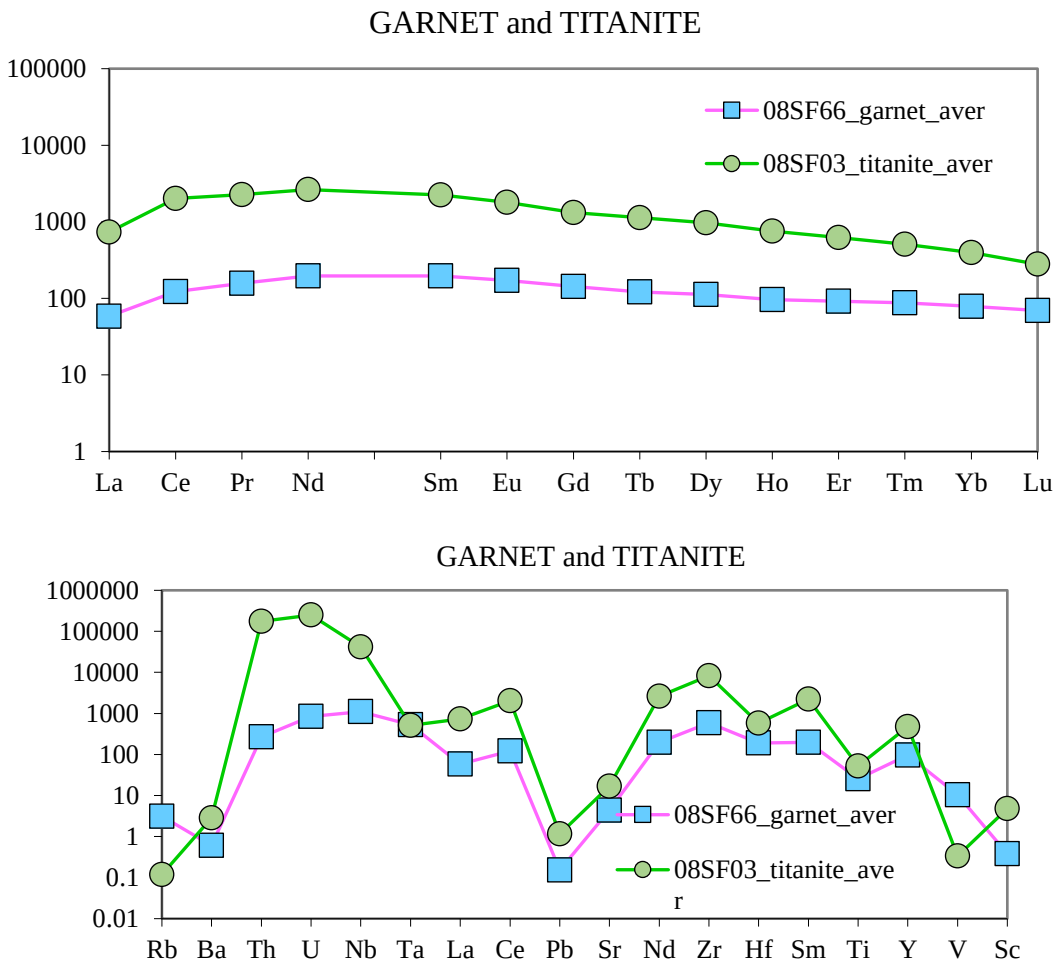

Fig 4.62 Chondrite-normalised REE and trace element patterns of garnet and titanite in the Fogo silicate-rich sövite (08SF03) and calcite-bearing pyroxenite (08SF66).

4.8 Summary of trace elements

-Calcite in fenitic sövite 08SF65 displays the highest enrichment in trace elements. The next most highly enriched calcite though one order below 08SF65, is in silicate-rich sövite 08SF03_1 which also shows elevated values of Th, U, Nb and Ta. Calcite in this sample has been divided into four groups according to trace element reflecting the inhomogeneity of this phase. Calcite-rich pyroxenite 08SF66 also decreases one degree in enrichment with La and Ce showing equal level of enrichment. The silicate-rich sövite 08SF03_2 to 08SF03_4 displays progressively less trace element enrichment in calcite to the point of falling below the chondritic values. Development of negative Ce anomaly is most likely associated with detection limit.

- Apatite is REE-enriched by one order of magnitude higher than calcite. It displays highest REE enrichment in pyroxenite 08SF66, lesser in sövite 08SF03 and the lowest level is detected in mica-rich 08SF01. Apatites La/Yb range is higher and broader than in calcite which indicates stronger LREE fractionation into apatite. Apatite shows enrichment in Th and U in pyroxenite and sövites 08SF01, though the sövite 08SF03 lacks thie enrichment. Zr enrichment in apatite is the highest in pyroxenite 08SF66, moderate in sovite 08SF01 and negligible sövite 08SF03.

- The concentration of trace elements in pyroxene and amphibole is rather low. The chondrite-normalised diagram for pyroxene and amphibole displays convex downward patterns with equally-enriched preference for the LREEs and HREEs over MREEs. Both phases show high similarity in REEs and trace element distribution patterns with pyroxene being one order more enriched than amphibole (though amphibole is depleted in LILE such as Rb and Ba, showing a strong connection between both phases.

- The phase which can accommodate only restricted contents of trace elements.in its structure is mica. Phlogopite-biotite is present in calcite-rich pyroxenite 08SF66 and silicate-rich sövite 08SF03. The REE pattern of mica fluctuates close to chondritic values though some trace elements such as LILE (Rb and Ba) and HFSE (mostly Nb and in some cases Ta) together with Sr and Zr can be partitioned into mica.

- The Fogo feldspar, feldspathoid and zeolite have REE and trace element patterns which arevery similar mostly in nepheline from pyroxenite and zeolite from fenitic sövite. Orthoclase differs in having negative Ce and Tm anomaly (detection limit

problem). Also, orthoclase displays higher enrichment in HFSE and positive Zr-Hf pattern, while nepheline together with zeolite display negative Zr-Hf anomaly. Consequently, some trace elements between orthoclase and nepheline-zeolite are distributed differently as zeolite can accumulate moderate amounts of Zr and Hf.

- Accessory minerals such as garnet from calcite-rich pyroxenite 08SF66 and titanite from silicate-rich sövite 08SF03 show similar trace element patterns with titanite being more enriched largely in REEs and HFSE such as Th, U and Nb. As post-magmatic metasomatic fluids played a major role in Fogo carbonatites and associated rocks leading to alteration of pre-existing assemblages (in this case garnet to titanite), the process can also be seen in enrichment in REEs and HFSE.
- Analysed samples from Kola carbonatite does not contain so many post-magmatic phases as ones found in the Fogo carbonatites, however xenocrystic phlogopite is commonly present in the Vuoriyarvi samples.
- Vuoriyarvi perovskite and Zr-garnet accommodate many trace elements so does Fogo garnet and titanite. Fogo calcite and apatite is more variable and reaching higher LREEs values than the same phases found in the Vuoriyarvi carbonatite. Fogo clinopyroxene and amphibole is one order less enriched than from Vuoriyarvi carbonatite.

CHAPTER 5

PETROGRAPHY AND MINERAL CHEMISTRY OF CONSTITUENT PHASES IN INTRUSIVE CARBONATITE-SILICATE ROCKS FROM BRAVA, CAPE VERDE

5.1 Location of the Brava carbonatite-silicate samples

Brava, the westernmost island of the southern group of the Cape Verde Islands (Figure 5.1), has the only known subaerial carbonatite volcanism on an oceanic island volcano (Hoernle et al. (2002) Faria and Fonseca (2014)), as well as having intrusive carbonatite outcrops in its uplifted seamount complex. Intrusive carbonatite on Brava

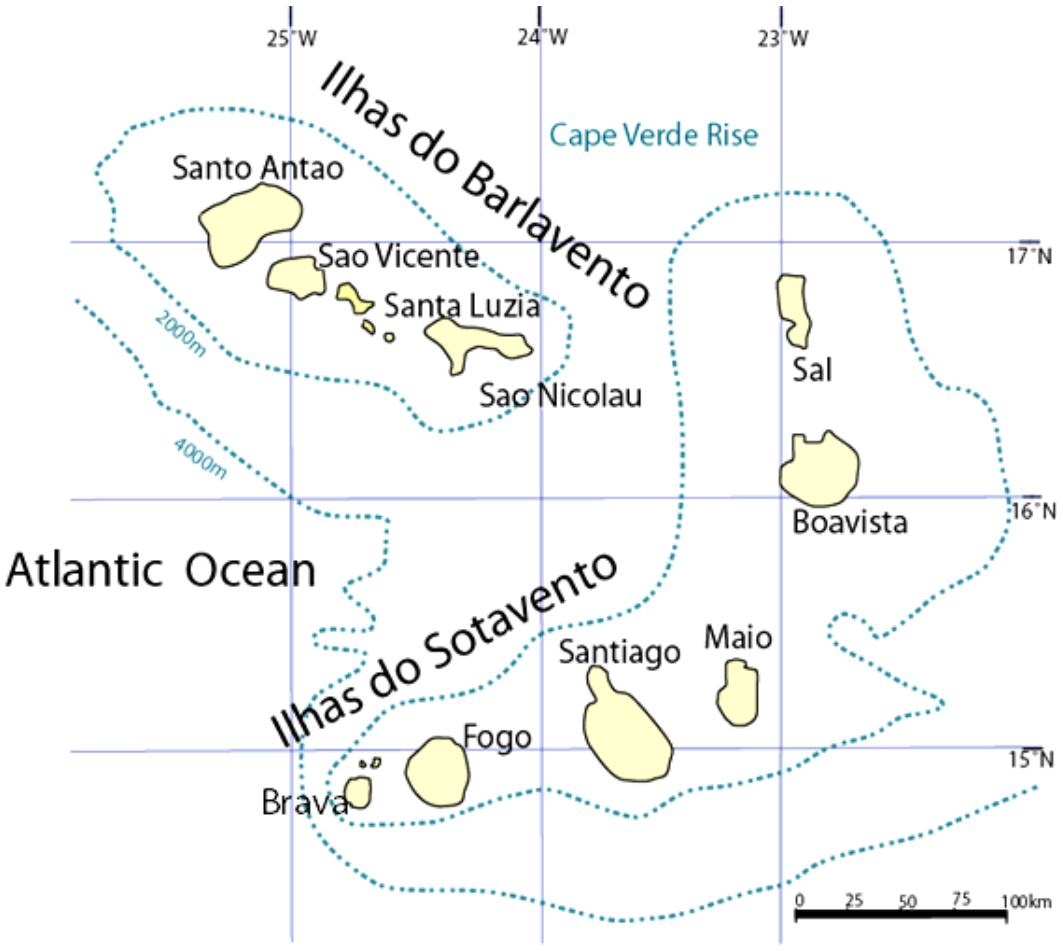

Fig.5.1 Sketch map of the Cape Verde Islands, showing location of Brava

.

(Chão Preto 14º 49.609´ N, 24º 41.668´ W sample 08SB38; 14º 49.641´ N, 24º 41.818´ W remaining samples), location L5 in Figure 5.2) is associated with the

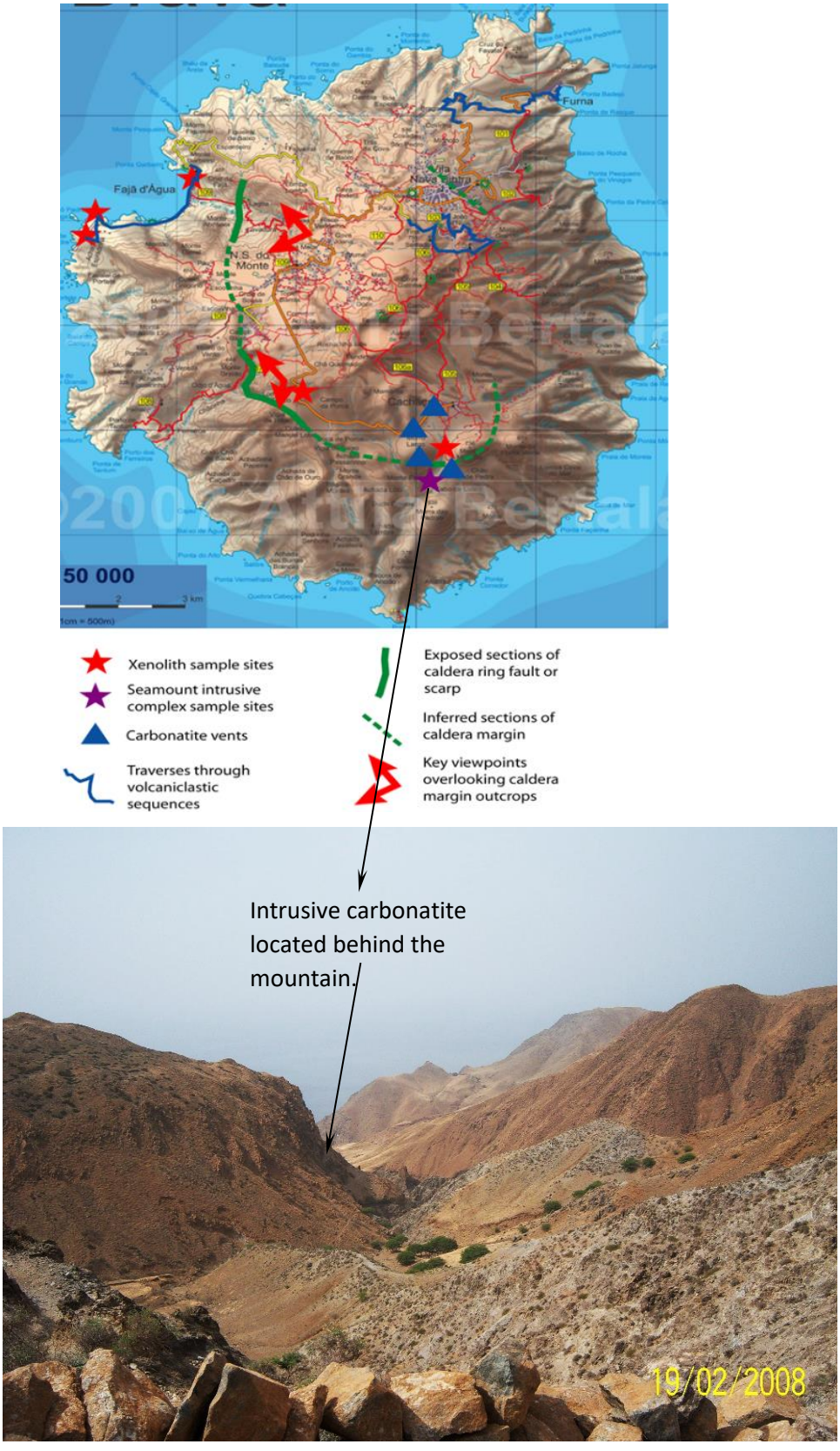

Fig.5.2 Brava Island. General view of difficulty associated with reaching localities by foot. The area contains intrusive carbonatite in the form of thick veins and pegmatites deformed together with the host seamount rock during the uplift.

oldest unit the seamount itself which is now elevated above the sea level. The combination of intrusive alkaline units, such as pyroxenites and ijolites with cross-cutting and intrusive carbonatites is complex and access, finding outcrops and sampling was difficult. The intimate field relationship of ultramafic/mafic-carbonatite rocks, aided by the inhomogeneity of the collected samples, suggests a close relationship between both units and a vastly complex magmatic evolution.

5.2 Petrography of silica-bearing sövite, alvikite and associated silicate rocks from Brava

The set of samples from L5 location is presented in Table 7.1 (Appendix 2), which contains location, pictures of outcrops and hand specimens. Scanned thin sections are included also with brief descriptions. Table 5.2 provides the mineralogy of thin sections and the appropriate names of the rocks. Analysed samples include one alvikite and one sövite, plus composite samples such as glimmerite-syenite-carbonatite, carbonatite-zeolite and feldspar-feldspathoid (part of dyke or vein). Most abundant samples are of syenitic composition, which vary in the amount of calcite, amphibole, pyroxene, feldspar/feldspathoid and zeolite.

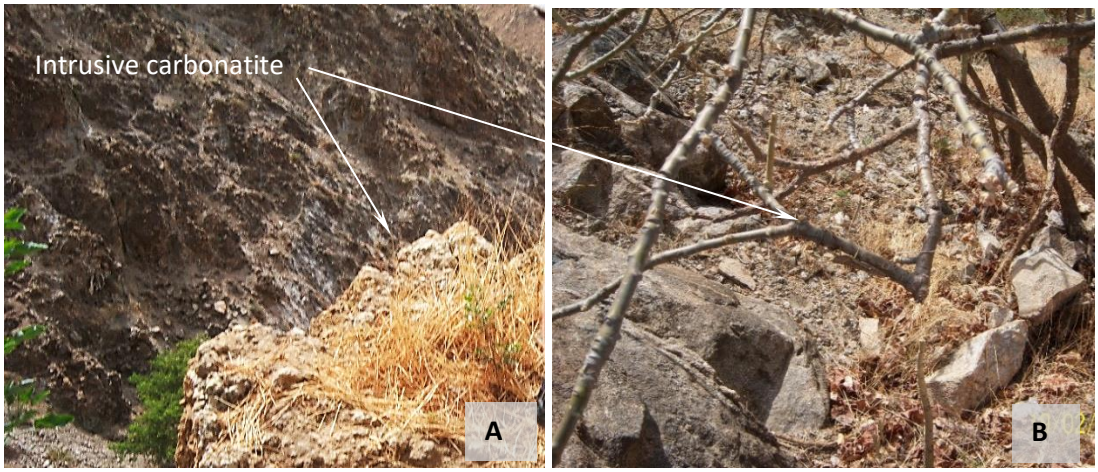

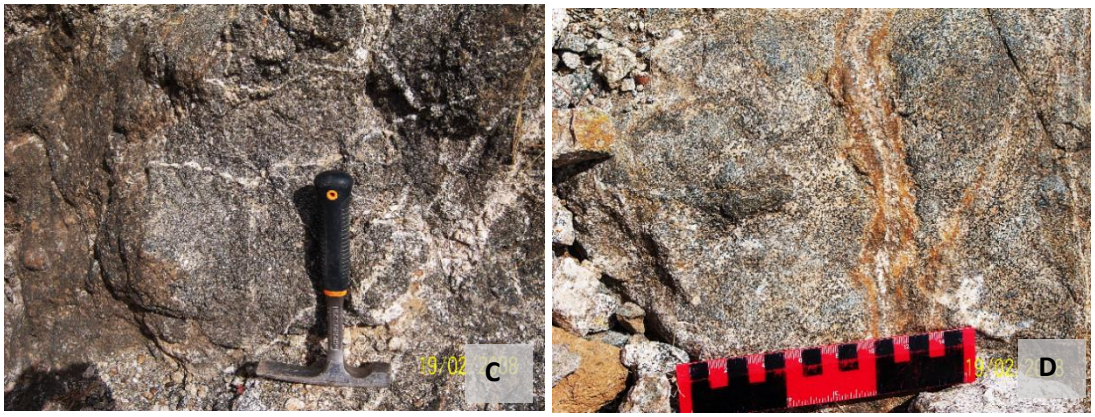

Fig.5.3 Locations L5 with pictures of outcrops from intrusive carbonatite and silicate rocks where relevant samples have been collected. Brava, Cape Verde, samples from 08SB38 to 08SB50 of which 10 were analysed on the electron microprobe (Table 5.1).

Sample:	L5: 08SB38	L5: 08SB39	L5: 08SB40	L5: 08SB43	L5: 08SB44	L5: 08SB45	L5: 08SB46	L5: 08SB47	L5: 08SBF48	L5: 08SB49	L5: 08SB50
Rock type	Silcate-bearing	Silcate-bearing	Glimmerite-syenite-carbonatite composite rock	Carbonate Zeolite vein	Zeolite-carbonatite vein with minor syenite	Calcite-enriched sodic-amphibole syenite	Calcite-enriched syenite	Syenite-cut by carbonatite vein	Syenite cut by alkali-feldspar vein	Feldspar-feldspathoid pegmatitc (altered) dyke/vein	Syenite-calcite vein composite rock
Mineral phase:	alvikite	sövite									
Calcite	abundant	abundant	abundant	abundant	abundant	minor	abundant	abundant	minor	minor	abundant
Apatite	minor	minor	minor	minor	minor	minor	minor	abundant	n/p	minor	minor
Albite	n/p	n/p	abundant	n/p	n/p	n/p	altered	n/p	minor	altered	altered
Orthoclase	n/p	minor	n/p	n/p	n/p	abundant	altered	altered	abundant	altered	altered
Amphibole	minor	abundant	minor	n/p	abundant	abundant	minor	minor	minor	minor	minor
Pyroxene	minor	n/p	n/p	n/p	n/p	n/p	abundant	minor	abundant	n/p	n/p
Rutile	n/p	minor	minor	n/p	n/p	n/p	n/p	n/p	minor	n/p	n/p
Ti-mag	n/p	minor	minor	minor	minor	minor	n/p	n/p	minor	minor	monor
Magnetite	minor	minor	minor	minor	abundant	minor	minor	abundant	minor	minor	minor
Biotite/Phlg	minor	minor	abundant	n/p	minor	n/p	minor	minor	minor	n/p	minor
Pyrochlore	minor	minor	n/p	n/p	n/p	n/p	n/p	minor	minor	n/p	n/p
Zeolite	n/p	minor	n/p	abundant	minor	n/p	n/p	n/p	minor	n/p	n/p
REE-phases	n/p	minor	n/p	minor	n/p	n/p	n/p	n/p	minor	n/p	n/p
Na-K carbonate	n/p	minor	n/p	n/p	n/p	n/p	n/p	n/p	n/p	n/p	n/p
Strontianite	n/p	minor	n/p	n/p	n/p	n/p	n/p	minor	n/p	n/p	n/p
Barite	minor	n/p	n/p	n/p	n/p	n/p	n/p	n/p	minor	n/p	n/p
Hollandite	n/p	n/p	minor	n/p	n/p	n/p	n/p	n/p	n/p	n/p	n/p
Foid	n/p	n/p	n/p	n/p	n/p	n/p	minor	minor	n/p	n/p	n/p
Mn chlorite	n/p	n/p	n/p	n/p	n/p	n/p	n/p	n/p	minor	n/p	n/p

Table 5.2 Analysed samples from L5 localities from Brava, Cape Verde, representing intrusive carbonatite-silicate complex. Sövite stands for coarse-grained calcio-carbonatite, alvikite stands for medium-grained calico-carbonatite, syenite for coarse grained rock composed of feldspar and ferromagnesian mineral, composite zeolite-calcite is coarse grained rock representing part of the vein. N/p stands for not present or not detected in analysed thin section.

Samples from Brava alkaline-carbonatite suite show extremely complex relationships between silico-carbonatites and associated alkaline rocks such as syenite. All collected samples show their alkaline relationship either directly by being intruded into syenite, or indirectly by being metasomatised (e.g., exhibiting degrees of albitization) and/or hydrothermally altered during which the host rock was affected by geochemical reaction of circulated fluids released from associated rocks (depletion of elements from one site and redeposition in surrounding rocks, leading to replacement of primary igneous assemblage with secondary minerals). Also texture of the rocks and minerals is affected (multiple veinlets which cross-cut the rock, alteration of minerals, fast growth from a focal point forming bow-tie specimens, formation of

hopper crystals, crystallisation of new phases stable in new conditions etc.). Remobilised fluids can circulate along a network of fractures and faults. Hydrothermal alteration depends on specific conditions such as temperature and pressure.

The field association of carbonatite (white-coloured dykes) and alkaline rocks (dark-coloured) is presented in Figure 5.3. Eleven samples from L5 site were selected for mineralogical analyses. Scanned images of the studied slides are provided in Figure 5.4. The colourless carbonate mineral is calcite and colourless silicate mineral is orthoclase, green colour represents pyroxene or amphibole, and light-grey represents feldspar (or alteration after feldspar to clay mineral). The coarse- to medium-grained nature of these rocks varies. Brief descriptions of analysed thin sections show the complexity of the association between different rock types, as follows:

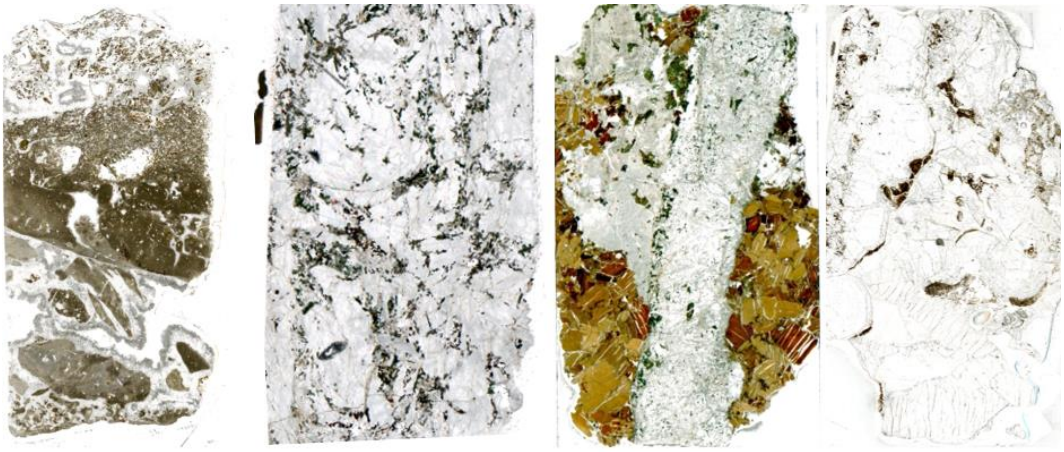

08SB38_alvikite 08SB39_ sövite 08SB40_ veined composite rock (glim/crbt/syen) 08SB43_carbonate zeolite vein

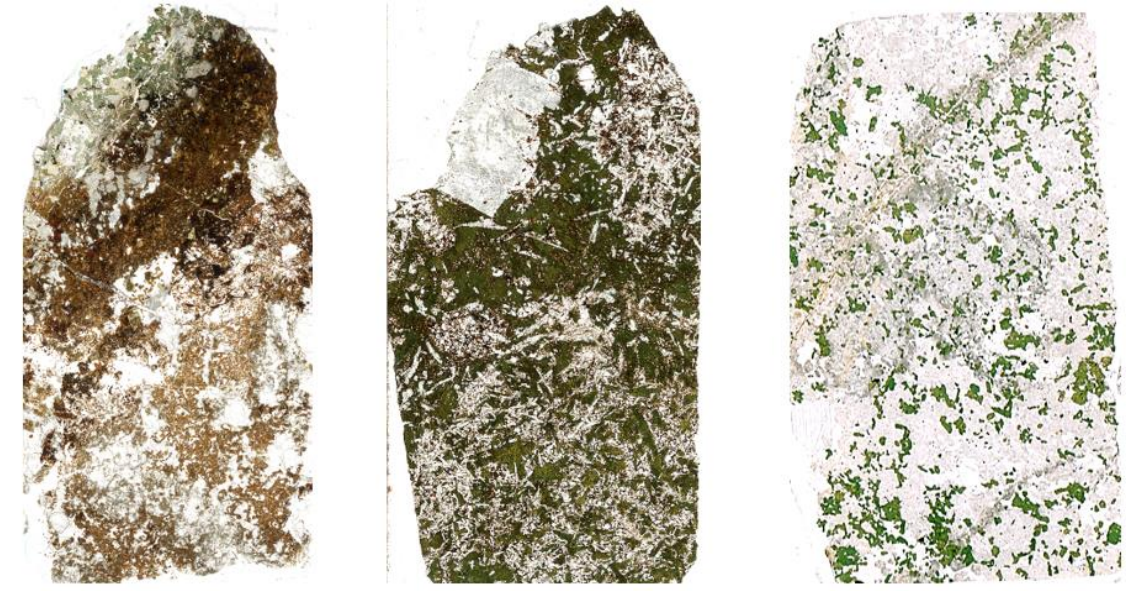

08SB44_zeolite carbonatite syenite vein 08SB45_amphibole calcite syenite 08SB46_calcite syenite

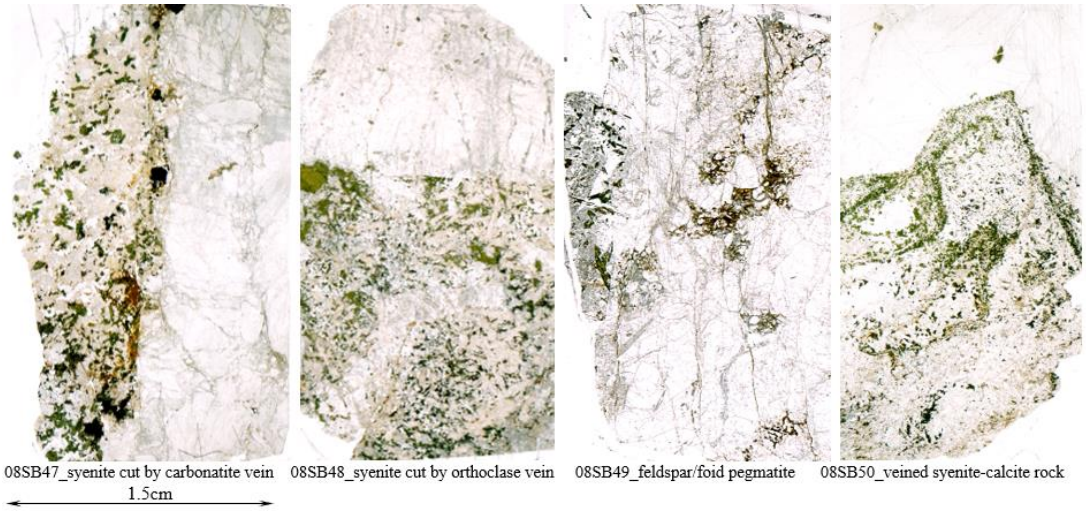

Fig.5.4 Scanned images of thin-sections of Brava intrusive carbonatite samples, showing distribution of minerals: colourless/ pinkish calcite and some subordinate apatite; grey colour represents feldspars/feldspathoids, coloured are ferromagnesian phases like biotite and amphibole; black oxides. In parts heavily stained by iron oxide. The 1.5cm scale applies to all thin-sections.

08SB38 sample is inhomogeneous having calcite as a main component with minor clinopyroxene, amphibole, biotite, apatite and magnetite. Three generations of calcite can be recognised. The first one is fine-grained forming "islands". The second generation is medium-grained calcite surrounding these "islands". The third generation is post-emplacement calcite which forms veins and commonly displays sparry texture bonding the rock together. Sample shows a porphyroclastic texture with vast invasion by hydrothermal Ca-rich fluid, from which sparry calcite crystallised. It is a silica-enriched alvikite with a metamorphic overprint that occured during uplift.

08SB39 sample is largely composed of areas rich in coarse-grained calcite. The rims of these calcic-regions contain apatite, amphibole, feldspar and hopper magnetite generally forming bow-tie assemblages. Crystallisation of acicular fanning crystals and skeletal magnetite most likely implies a fast-cooling environment or pressure-induced recrystallisation. Concentration of K-Na-rich silicate phases around calcite clusters suggest small scale regional fenitization. It is a silica-rich sövite.

Sample **08SB40** is a composite rock. The first rock type is a glimmerite containing highly kinked phlogopite with inclusions of rutile and opaque. Mica cleavage shows invasions by calcite. Glimmerite has been cross-cut by a feldspar-rich syenite formed of albite, fine-grained amphibole/clinopyroxene and coarse-grained anhedral feldspar. An embayed margin with the glimmerite implies a reaction or corrosion of mica during emplacement of the syenite liquid. Syenite is affected by

albitization (Na-fenitization?). The third rock type is calcite carbonatite showing a thin margin of fine-grained amphibole and pyroxene at the contact with the syenite or glimmerite. Multiple calcite veins cross-cut all associated lithologies. Thus, it is glimmerite invaded by albitized syenite and subsequently by carbonatite from which many veinlets were derived and heavily infiltrated all associated rock types.

About one third of sample **08SB43** is composed of calcite carbonatite while the rest contains euhedral zeolite. There is an evidence of recrystallisation of the large calcite specimen to polycrystalline smaller calcite aggregates. Zeolite grew very fast replacing other phases, such as feldspathoid or feldspar, and/or invading the fractures. Triple junctions are present between the calcite crystals showing the equilibrium state. Net-veining formed during the last stages (remobilisation of calcite). This is zeolite-carbonatite vein.

Sample **08SB44** contains moderate amounts of calcite, amphibole, skeletal apatite and minor titanite and phlogopite. It is heavily affected by hematisation. Numerous fine rhomboidal hematitised crystals are stained zeolites. Large euhedral hexagonal zeolites cluster together. The specimen displays strong fabric as a result of shearing. The brown vein-like part of the sample contains remnants of biotite within hematite (conduit for hydrothermal fluid). Thus, the rock is a hydrothermally altered syenite associated with a zeolite-carbonatite vein.

Sample **08SB45** contains abundant medium-grained prismatic feldspar and commonly radiating acicular amphibole implying fast crystallisation from a focal point. The amphibole is often intergrown with feldspar. Apatite and calcite are minor components. Medium/fine-grained calcite is anhedral and closely associated with amphibole and both minerals are highly hematised. Pools of hematite are present within the calcite-rich areas, while amphibole-rich area is heavily cross-cut by multiple hematite veins. The main body of syenite rock is cross-cut by pegmatite orthoclase.

The **08SB46** sample consists of calcite (some crystals being very coarse), displaying triple junctions with altered feldspar and pyroxene. Smaller anhedral calcite grains show a close association with pyroxene forming rims around calcite-feldspar regions. It is possible that metamorphism caused the texture, perhaps during uplift of the seamount. The subparallel cracks, having preferred orientation, provided conduits for hydrothermal fluids as clay minerals tend to accumulate along these veins. The

veins are also hematised. The sample is thus a hydrothermally altered calcite-rich syenite.

Sample **08SF47** consists of calcite- and silica-rich parts. Syenite is cross-cut by calcite vein/dyke. The calcite-rich part is monomineralic containing large crystals that are elongated along the boundary with silica-rich part. It shows strain and recrystallisation to fine-grained calcite and partial hematisation occurred during shearing (uplift of the seamount or emplacement of calcite-rich vein/dyke). Invasion by an Fe-rich fluid caused distribution of hematite along the planes of weakness. The silica-rich sample consists mainly of clinopyroxene and altered feldspar with small amount of mica, apatite, calcite, Ti-rich magnetite and brown pyrochlore.

Sample **08SB48** is also formed of two parts. The monomineralitic pegmatitic alkali feldspar (orthoclase) displays a sharp contact with syenite (feldspar and clinopyroxene). Contact is faulted and hematised. It is evident that silica-rich part was affected by hydrothermal alteration and oxidation. The rock is syenite cut by feldspar-pegmatite vein.

08SB49 is a highly altered feldspar pegmatite with a small portion of altered syenite. Multiple linear and subparallel fractures recorded the process of shearing. The fractures are outlined by brown iron oxide (conduit for hydrothermal fluids expanding in places into spider-web like style). Fluid invasion explains high alteration of feldspar.

08SB50 is composed of two parts. The first is coarse-grained calcite-rich vein with occasional inclusions of fine amphibole. The vein is emplaced into syenite showing a sharp contact underlined by small amphiboles. The silicate part is composed mostly of feldspar (altered to clay mineral), fine-grained apatite, oxides (Ti-magnetite and magnetite) and commonly amphibole. Calcite is responsible mostly for the vein-part but to some degree can be found in silicate part.

From the field relationship (Figure 5.3) and studied thin sections, it is obvious that carbonatites were emplaced as the last intrusive event forming multiple dykes, often cross-cutting other rock-types and each other.

All silicate samples contain calcite, although its modal distribution is variable. Calcite in alvikite sample 08SB38 is inhomogeneous, exhibiting a patchy look. Patches contain Mg-poor calcite which form sub-rounded areas surrounded by Mg-rich calcite (Figure 5.4A, B, C and D). The glimmerite-syenite-carbonatite sample (08SB40) contains calcite in all interconnected parts. Calcite forms net-veining which

cross-cuts the glimmerite and syenite. Calcite veinlets are very intense and penetrative Figure 5.4E and F. They invaded previously formed silicate rocks, exploiting the planes of weakness in the mica-cleavage in the glimmerite (Figure 5.4G). Veinlets from the glimmerite continue into the syenite. Fracturing of albite crystals, infilled by calcite, is apparent (Figure 5.4H). Sub-parallel net veining implies shearing probably associated with uplift of the seamount complex and possibly the late-stage emplacement of carbonatite dykes.

Samples 08SB43 and 08SB44 contain moderate amounts of calcite, both primary Sr-rich and secondary Sr-poor. Secondary calcite is strongly associated with zeolite (analcime) forming a calcite-zeolite rock (vein?). Zeolite occurs as coarse-grained euhedral crystals (Fig.5.4I and G), suggesting that they crystallised from a fluid (metasomatic perhaps?) and, according to their Si-Al-Na-rich chemistry, they were derived from alteration of feldspar/feldspathoids. Interstitial calcite, filling the space between zeolite crystals and forming interlocking texture with zeolites, also points to a strong connection to hydrothermal fluids, probably released from the earlier formed carbonatite, eventually leading to late-stage calcite-zeolite veining. As the calcite is interstitial, it crystallised after the zeolite, or the two phases simultaneously started to crystallise together but zeolite formed earlier (faster rates of crystallisation controlled by higher temperatures) thus it crystallised larger euhedral crystals. In Fig. 5.4L there is textural evidence of calcite-analcime separation into analcime-rich area and calcite-rich region. The difference in grain size and intense hematisation between samples 08SB43 and 08SB44 which contain zeolite, leads to the conclusion that calcite-zeolite crystallisation occurred in both samples in different environments. The former shows a higher oxidation state and more complex invasion by fluids.

Calcite in the syenites (08SB45 and 08SB46) is strongly associated with the Ca-rich silicate minerals (calcian-eckermannite and diopside, respectively). In both samples the intimate association expresses itself by Sr-rich calcite forming part of the amphibole or pyroxene (Figure 5.4 P, R and S). In 08SB46 there is an evidence of secondary recrystallisation to sparry calcite (Mg-enriched and Sr-poor) showing growth of concentric zones (crystallisation in voids as seen in Figure 5.4T). Sample 08SB47 (carbonate-syenite rock) shows another site of calcite crystallisation in the Brava intrusive complex as primary calcite has the highest Sr-enrichment (up to 4 wt% SrO). It forms anhedral regions between silicate phases and sometimes shows internal inhomogeneity as Sr-poor streaks are separated from Sr-rich areas (Figure 5.4U).

Calcite in sample 08SB48 crystallised in close vicinity to rare phases such as pennantite or parisite (Figure 5.4X and Y). Calcite in 08SB49 is secondary (Sr-poor) (Figure 5.4Y1) and in 08SB50 it is primary, being Sr-rich (Figure 5.4Y2, Y3 and Y4).

Calcite in the sövite 08SB39 sample has a patchy look (Figure 5.4bZ1 and Z2) with dark and light grey areas. The light-grey patches represent primary Sr-rich calcite. Darker regions denote Sr-poor calcite. The bright speckles are fine-grained Sr-rich carbonates. Thus, crystallisation of carbonate minerals reflects migration of Sr from Sr-rich calcite, depleting areas surrounding bright areas rich in Sr and forming Sr-poor calcite islands.

Apatite is not as common as calcite and is a minor or accessory constituent. Scarce anhedral apatite crystals are mostly fractured, fine-grained and associated with clinopyroxene or amphibole (Fig. 5A, B and C). Sample 08SB44 contains clustered anhedral apatites rimmed by iron oxide (Fig. 5.5D). Two types of apatite crystals were found in 08SB47. The first is subhedral, partially resorbed showing embayment, perhaps formed during alteration as it is set in altered feldspar (Figure 5.5E). The other apatite contains multiple fractures, some being sub-parallel and perhaps related to shearing. Apatite shows a strong association with Nb-rich pyrochlore, implying simultaneous crystallisation (Fig. 5.5F). Apatite in 08SB49 shows an association with Zr-rich tazheranite (Fig. 5.5G, G1) and in Figure 5.5H skeletal apatite is associated with calcite. This unusual apatite-calcite/pyrochlore/tazheranite relationship implies complex crystallisation, which involved localised enrichment in rare elements and/or post-magmatic alteration (partial replacement by interaction with fluids?). Sample 08SB50 (syenite cross-cut by carbonate vein) contains a greater amount of apatite, which varies in shape. Apatite in sövite (08SB39) occur as euhedral-subhedral and mostly fine-grained crystals with characteristic fractures (Fig. 5.5 L, M, N, O). Clustering of apatites or formation of single crystals is infrequent (Fig. 5.5 L, O), while radiating aggregates in association with silicate phases are common (Fig. 5.5 M, N). In the radiating aggregates, acicular/skeletal apatite is intergrown with orthoclase and the orthoclase-apatite assemblage is flanked by amphibole, which often exhibits curved texture (Fig. 5.5 N). As sövite 08SB39 is composed of large calcite-rich regions fringed by fine/medium-grained radiating minerals, rich in silicate-phosphate phases, this texture might reflect metamorphic recrystallisation associated with uplift. Circulation of fluid is also apparent as altered plagioclase, often flankd/infiltrates the assemblage. Net-veining provided the path for the circulating fluid (Fig. 5.5 L, M).

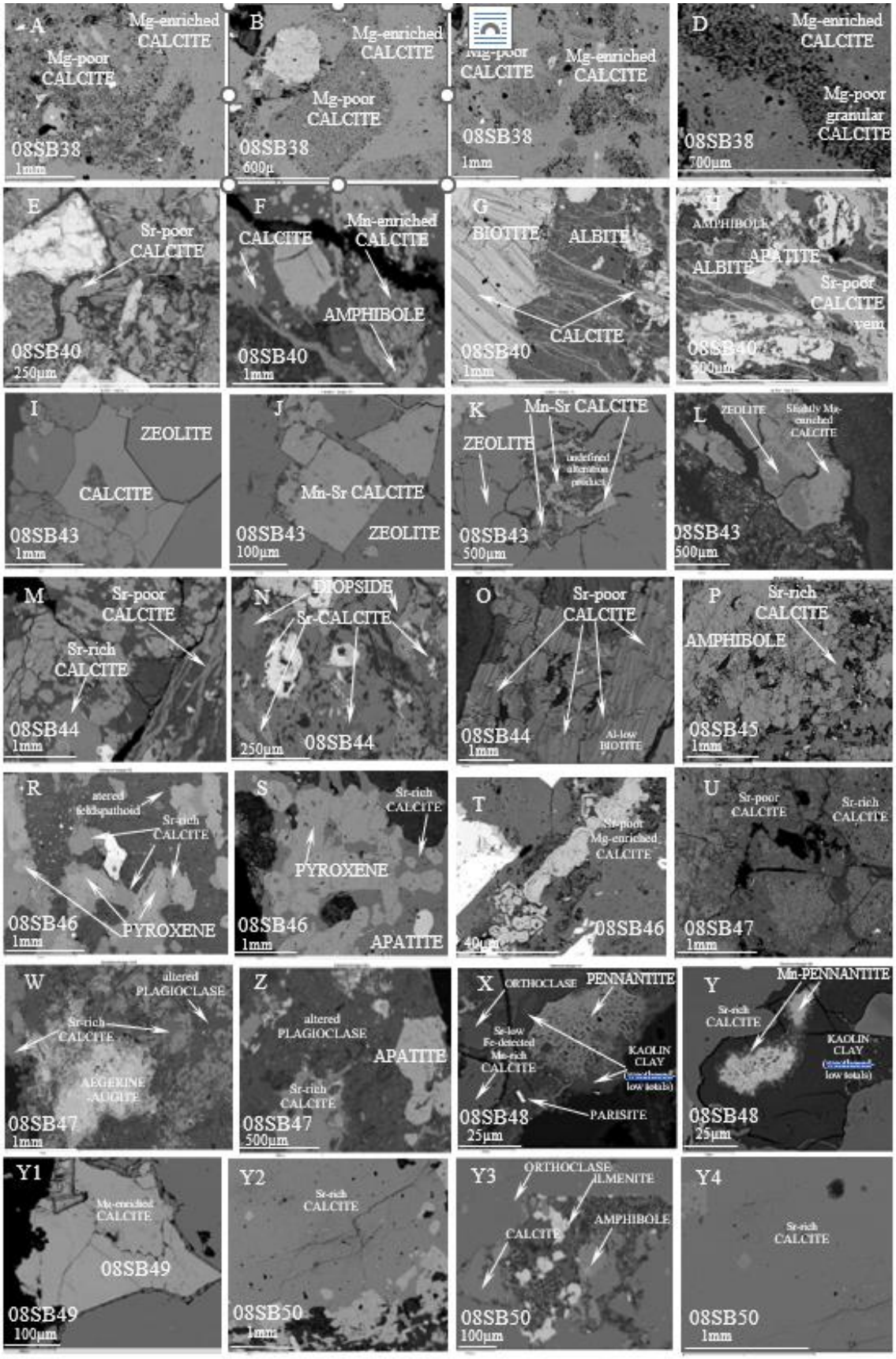

Fig.5.4a Backscatter electron images of alvikite and silicate rocks associated with carbonatite showing textural differences between calcite from analysed thin sections from L5 location, Brava, Cape Verde

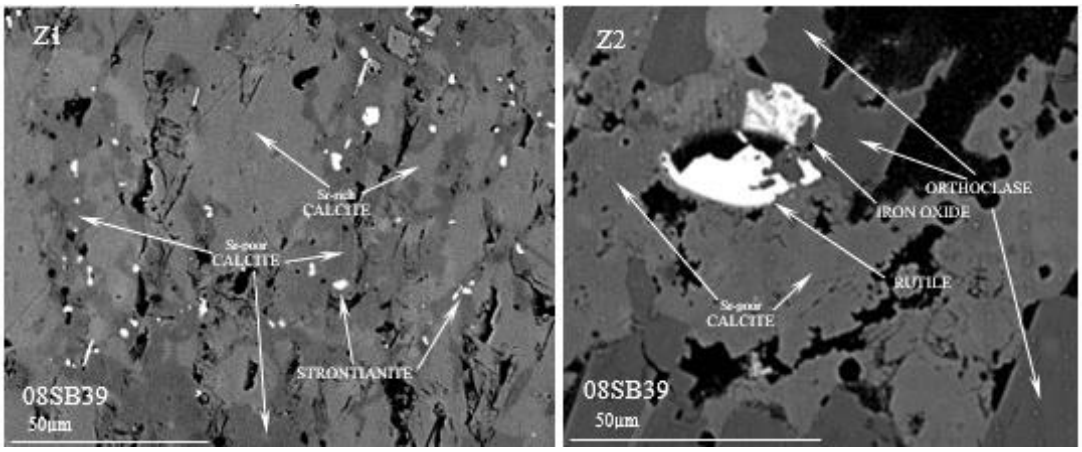

Fig.5.4b Backscatter electron image of sövite showing textural differences between calcite from analysed thin sections from L5 location, Brava, Cape Verde.

Pyroxene and amphibole are the two principal mafic silicate constituents in the Brava intrusive complex. The minority of samples holding exclusively pyroxene are 08SB44, 08SB46 and 08SB44. In two samples (08SB38 and 08SB47) both mafic phases coexisting with amphibole being more abundant than pyroxene. Amphibole-bearing samples have higher abundances of these phase than the one just containing pyroxene, where pyroxene is rather infrequent. Amphibole-rich samples are 08SB39, 08SB40, 08SB45, 08SB49 and 08SB50. Overall amphibole is found in higher quantity than pyroxene.

Pyroxene and amphibole can co-exist as a minor or as a major phase in most samples except 08SB43. Minor amphibole is found in several thin sections (Figure 5.6). All these rocks are strongly associated with pegmatite feldspar or calcite veining (Figure 5.4). Amphibole is anhedral, zoned, and intimately associated with calcite and plagioclase, often cross-cut by secondary calcite veining (Figure 5.6. A1 to E4). In two samples (08SB38 and 08SB47) remnants of rare clinopyroxene were found (Figure 5.6A3, A4, C1 and C2). Texture of amphiboles leads to the conclusion that alteration of pyroxene took place during fluid-flow or fenitization.

In syenite 08SB45 sodic amphibole is abundant. The main body of the syenite displays a sharp contact with an orthoclase pegmatite (or vein). In close proximity to the orthoclase pegmatite a high concentration of large amphiboles is found (Figure 5.7). Away from the orthoclase intrusion, crystallisation of fine-grained prismatic orthoclase/amphibole occurred. Prismatic orthoclase is often hollow and radiating from a central point (Figure 5.7A, B). Also amphibole used the meeting point of two prisms to start crystallisation, forming a fan texture (Fig. 5.7B, C). The texture implies

fast crystallisation. Figure 5.8A, B and C respectively demonstrate (in greater detail) texture such as bending of acicular crystals, fanning of amphibole and high concentration of large amphibole (internally intruded by streaks of orthoclase), in close vicinity to alkali feldspar. Amphibole together with feldspar crystallised as primary phases. The syenite is enriched by secondary Mn-calcite, which intensely infiltrates the whole rock.

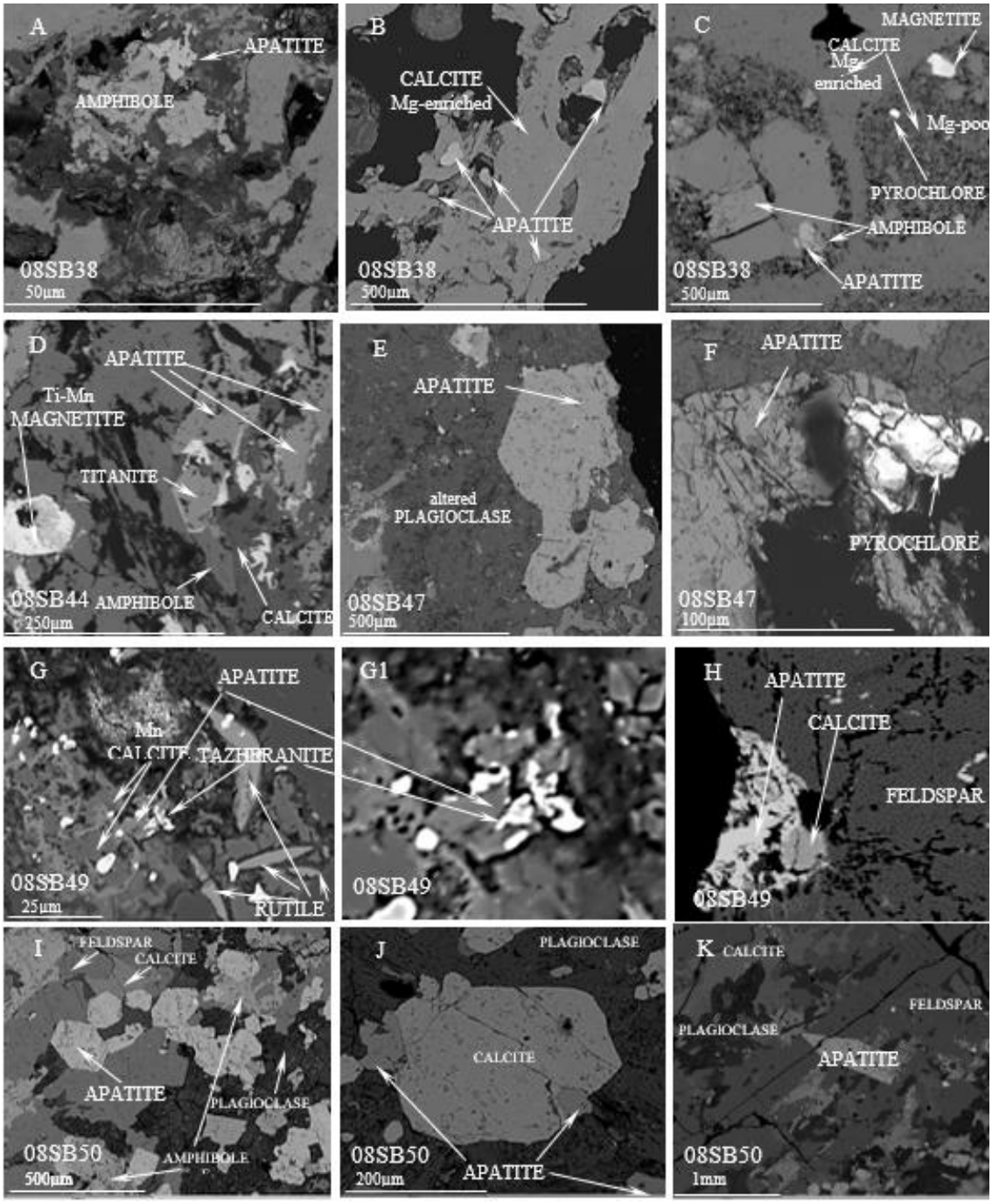

Fig 5.5a Backscatter electron image of alvikite and silicate rocks associated with carbonatite showing textural differences between apatite from analysed thin sections from L5 location, Brava, Cape Verde

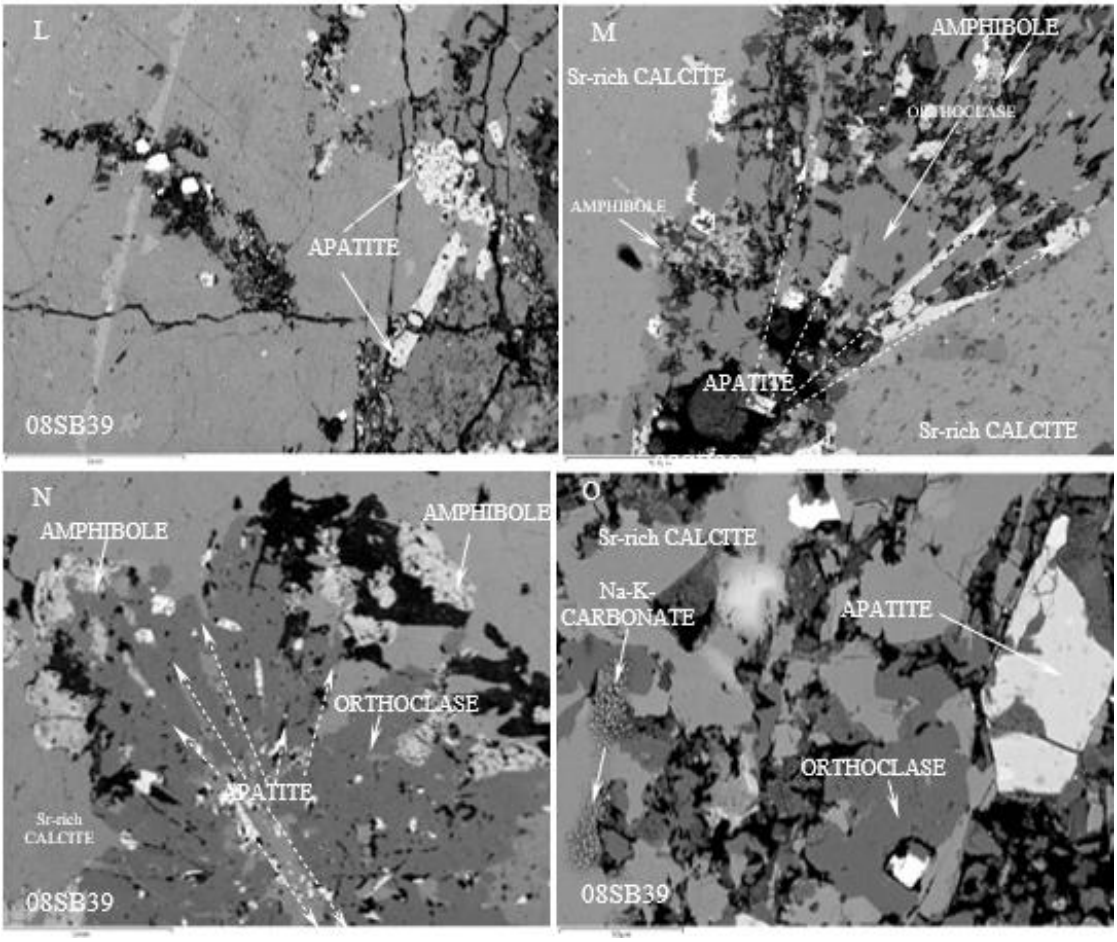

Fig 5.5b Backscatter electron image (BSE) of sövite showing textural differences between apatite from analysed thin sections from L5 location, Brava, Cape Verde

Amphibole in sövite (Figure 5.9) is mostly altered along the cleavage planes, which have been invaded by fluid where partial alteration to clay mineral occurred. Wherever fast crystallisation occured (fanning texture), alteration between the cleavage planes is intense (Figure 5.9A and D), otherwise it is minor (Figure 5.9B and C). Crystallisation of silicate phases was introduced on the margins of calcic-regions (Figure 5.10). Calcite-rich elliptical areas were formed most-likely during a pressure-induced metamorphic event (shearing during uplift) leading to fast co-crystallisation of silicate phases, such as amphibole and orthoclase, forming fanning aggregates including acicular amphibole crystals (silica-rich metasomatic margins?).

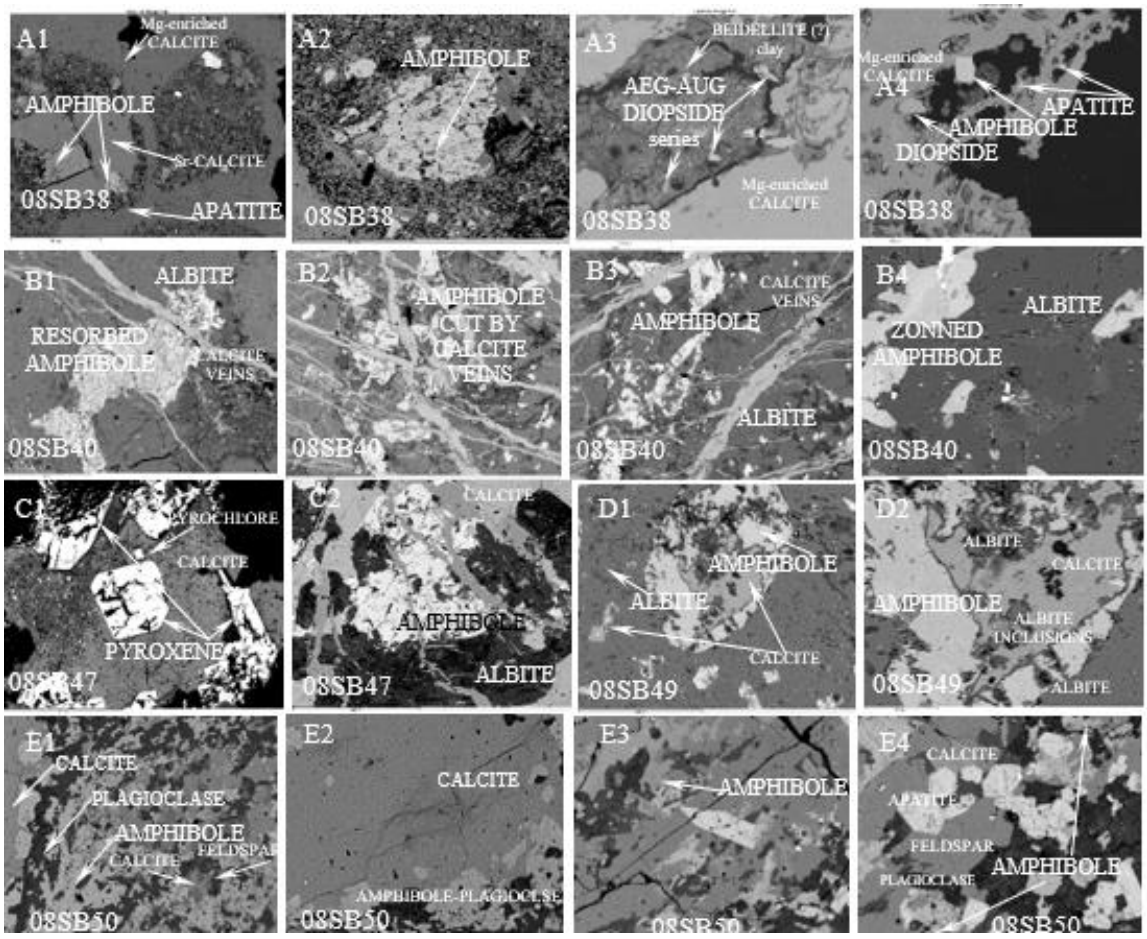

Fig 5.6 Backscatter electron images of intrusive rocks containing minor amphibole (and rare pyroxene) with associated phases in 08SB38, 08SB40, 08SB47, 08SB49 and 08SB50 thin sections from L5 location, Brava, Cape Verde.

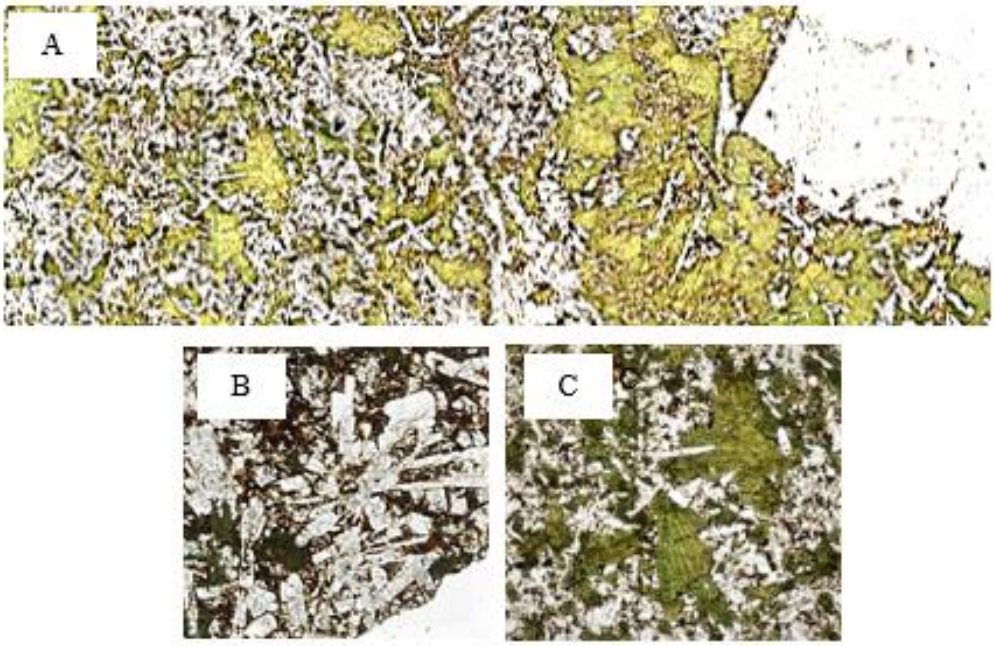

Fig 5.7 Scanned thin section of 08SB45. A) Extreme sharpness and contrast applied to emphasise some features such as varying distribution and texture of amphibole close to orthoclase and away from the large orthoclase. B) Radiating small euhedral orthoclase. C) Radiating amphiboles

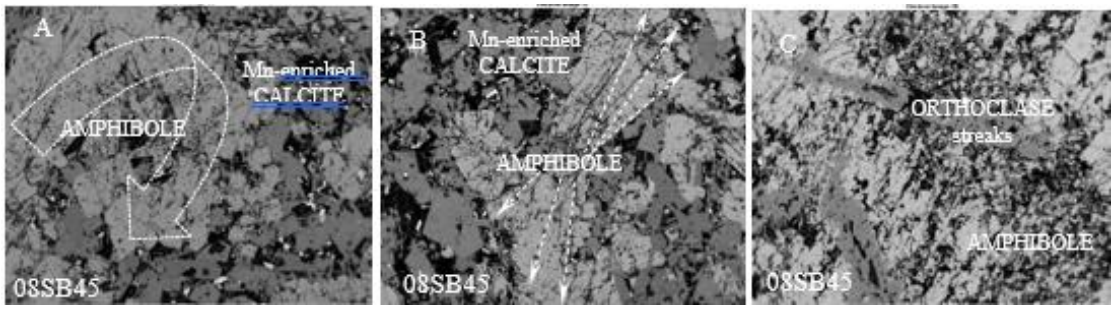

Fig 5.8 Backscatter electron image of 08SB45 associated with carbonatite containing high concentration of sodic amphibole from L5 location, Brava, Cape Verde.

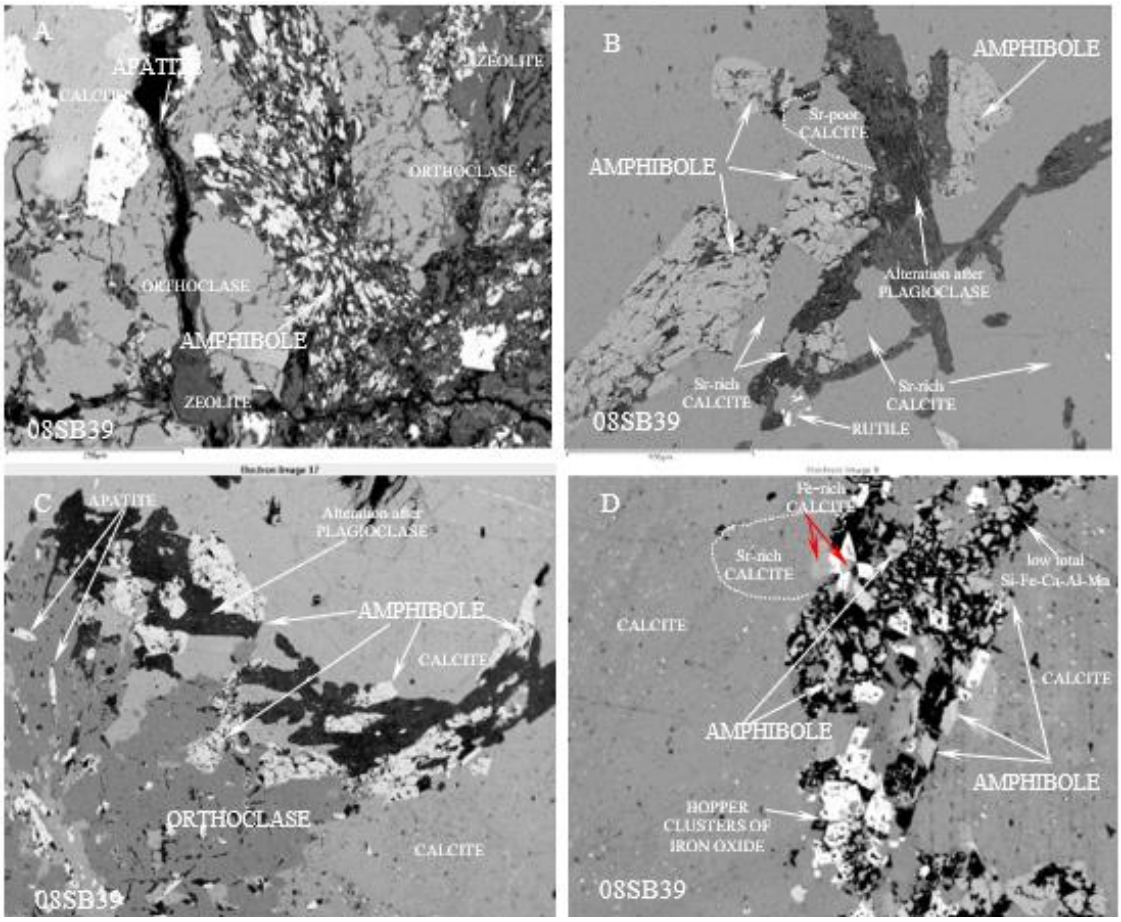

Fig 5.9 Backscatter electron image of sövite containing sodic amphibole from L5 location, Brava, Cape Verde.

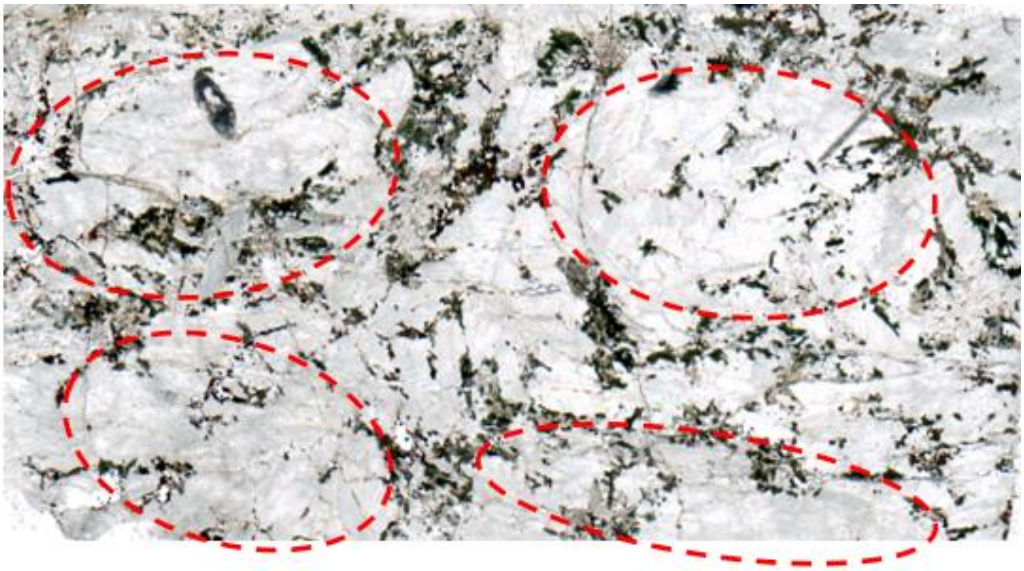

Fig. 5.10 Scanned thin section of sövite 08SB39. Emphasis placed on formation of calcic-regions (metamorphic effect) with their margins co-crystallising radiating amphibole and orthoclase.

Figure 5.11 highlights rimming by multiple clinopyroxene around the oval regions containing feldspars/feldspathoids, seen in 08SB46. Similar rimming occurs in sample 08SB48. The mafic-rich part of sample 08SB44 is moderately rich in pyroxene (Figure 5.12A, B and C). Pyroxene shows alteration to clay minerals and displays an association with titanite (Figure 5.12 A1, A2, A3 and B3). Pyroxene in 08SB46 is also anhedral, set in Sr-rich calcite (Figure 5.12B1 and B2). Overall sodic clinopyroxene is intimately associated with calcite and shows an unusual feature of rimming around the rounded regions rich in feldspathoids (Figure 5.12B1and B2). Composite sample 08SB48 containing syenite intruded by a calcite-rich body (vein?) is enriched in clinopyroxene varying from coarse-grained to fine lath-like crystals (Figure 5.12C1, C2 and C3). Its shape varies from multitudes of lath-like crystals encircling round zeolite or euhedral crystal breaking into ilmenite.

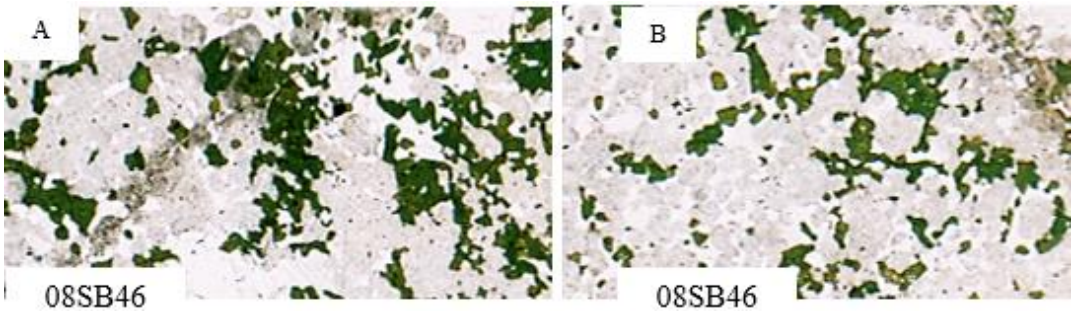

Fig 5.11 Scanned thin section of 08SB46 showing feldspathoid regions (grey) internally invaded by calcite (white) and surrounded by pyroxene (green). Anhedral fine-grained pyroxene holds also calcite forming kind of rim around feldspathoid

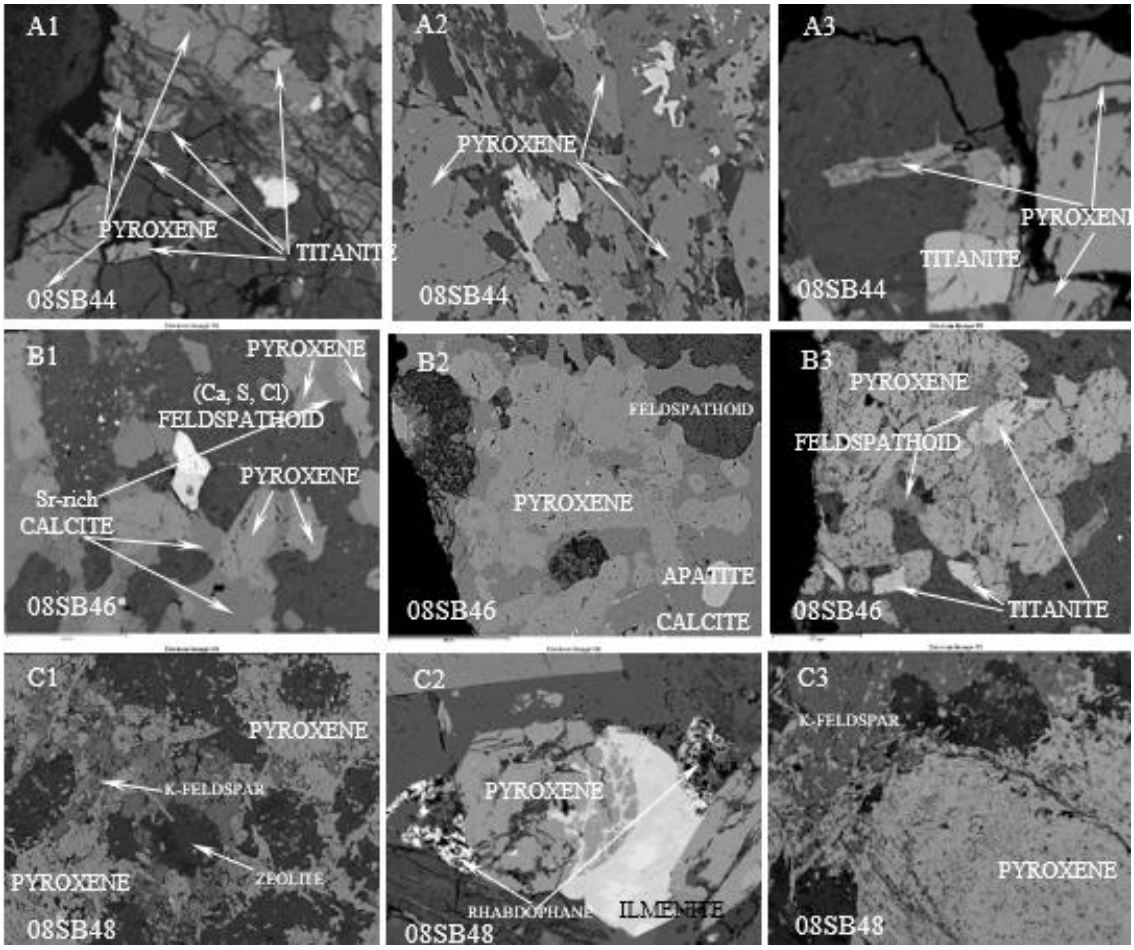

Fig 5.12 Backscatter electron image of intrusive silicate rocks associated with carbonatite containing high concentration of sodic pyroxene from L5 location, Brava, Cape Verde.

Feldspar and feldspathoid can be found frequently in analysed samples. Fresh albite was found in 08SB40 and 08SB48, whereas the other specimens display alteration to clay mineral. Sample 08SB40 contains a moderate amount of albite, which is found between the glimmerite and calcite-rich parts of the sample. The contact with the glimmerite is distinctive showing multiple embayments (partial resorption of biotite/phlogopite-rich side) filled by albite. Calcite veins are very invasive and cross-cut all rock-types in a subparallel manner. There is a thin layer of calcite between albite and mica along the marginal alteration, thus calcite has also invaded the contact between mica and albite. As the calcite veins show parallel alignment, there is a likelihood of a shearing zone nearby (Figure 5.13A and B). Equally sample 08SB48 (Figure 5.13C) shows albitization probably associated with the fenitization stage of the intrusive complex.

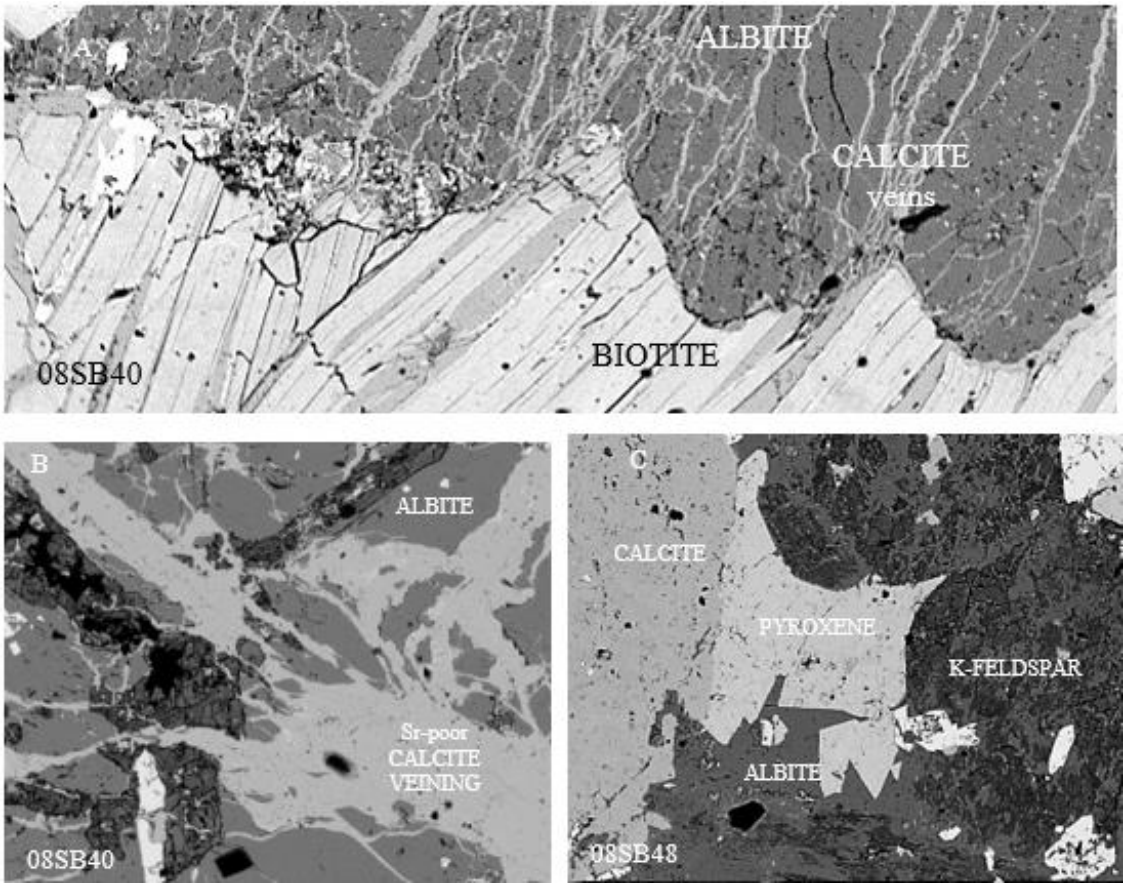

Fig 5.13 Backscatter electron image of intrusive silicate rocks 08SB40 and 08SB48 from L5 location, Brava, Cape Verde containing abundant albite.

Alkali feldspars are present as two types: coarse varieties which perhaps originated as alkalic pegmatites (Figure 5.14A and C) and smaller prismatic crystals forming part of the syenitic intrusion (Figure 5.14B and D). In most cases alkali feldspar has been altered but rare unaltered specimens can be defined as an orthoclase. Inhomogeneous alkali feldspar contains darker patches (Figure 5.13C and 5.14). Feldspars are often turbid with uneven distribution of elements. Examination of different areas in turbid-feldspar revealed that in very close proximity different types of cancrinite subgroup feldspathoids are present such as: S-pitiglianoite, Cl-pitiglianoite, Ca/S-pitiglianoite (Figure 5.13E and F). According to Pekov and Olysch (2011), cancrinite-subgroup minerals form in alkaline intrusive complexes only under low activity of CO_2. The rarity of this mineral is affected by competition with formation of Na-aluminosilicates (without additional anions) such as albite, nepheline and zeolites which have a wider field of thermodynamic stability.

Sövite in sample 08SB39 is moderately enriched in orthoclase. Pristine plagioclase is not present but alteration after albite to clay mineral and zeolite (analcime) is found in moderate amount (implication of fluid circulation).

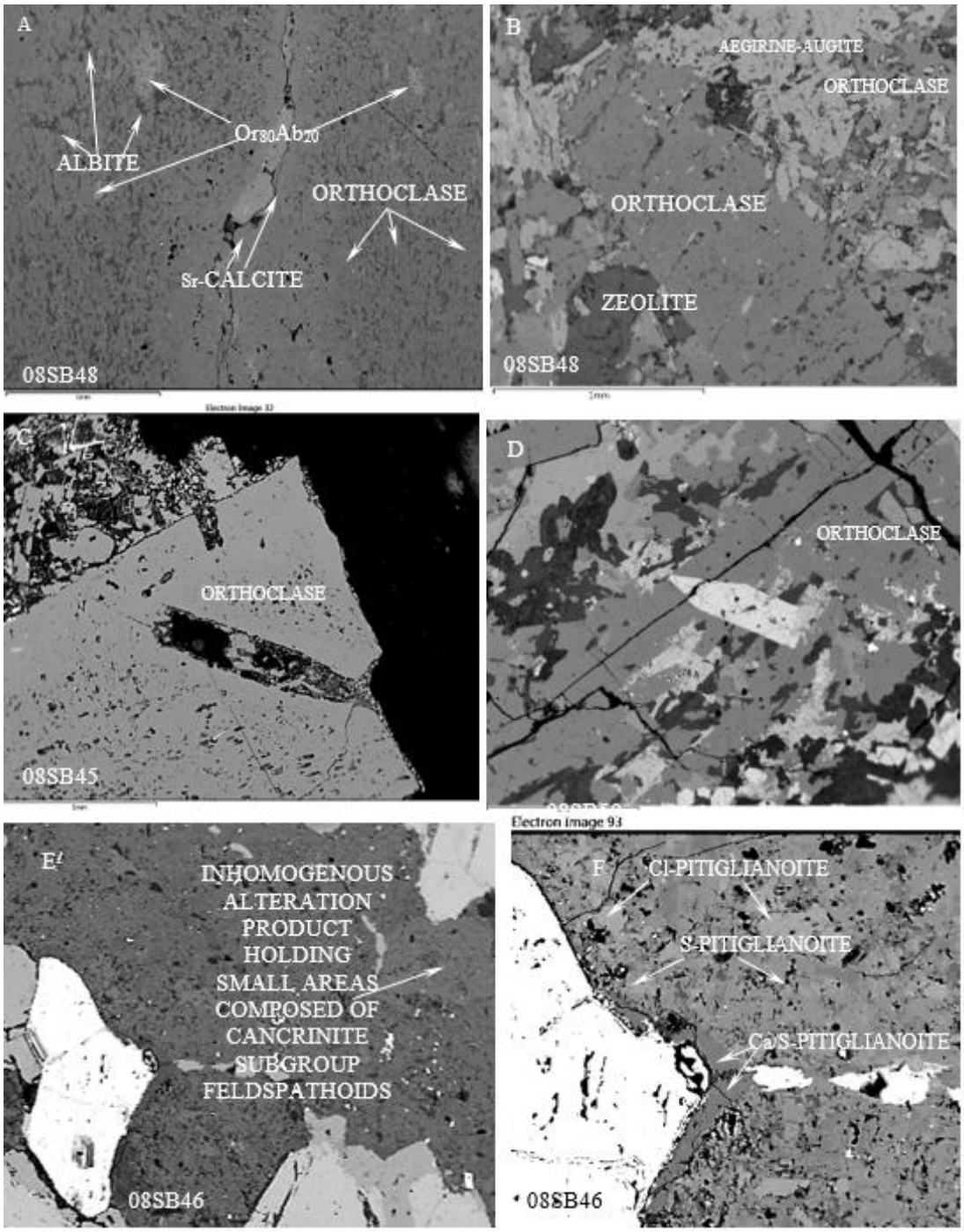

Fig 5.14a Backscatter electron image of intrusive silicate rocks associated with carbonatite intrusion such as 08SB48, 08SB45, 08SB50 and 08SB43 containing alkali feldspars and feldspathoid from L5 location, Brava, Cape Verde.

Orthoclase sometimes forms an unusual assemblage showing a single elongated crystal radiating from the central point composed of calcite (Figure 5.14G). Orthoclase is rather uniform in composition though it can have mineral inclusions such as apatite, iron oxide and rare phases (Figure 5.14H). Radiating orthoclase forms an intimate assemblage with amphibole, mostly bordering feldspars. Thus K-rich phases concentrate on the inside whereas more mobile Na-rich phases (sodic amphibole) on the outside (small scale K-Na fenitization?).

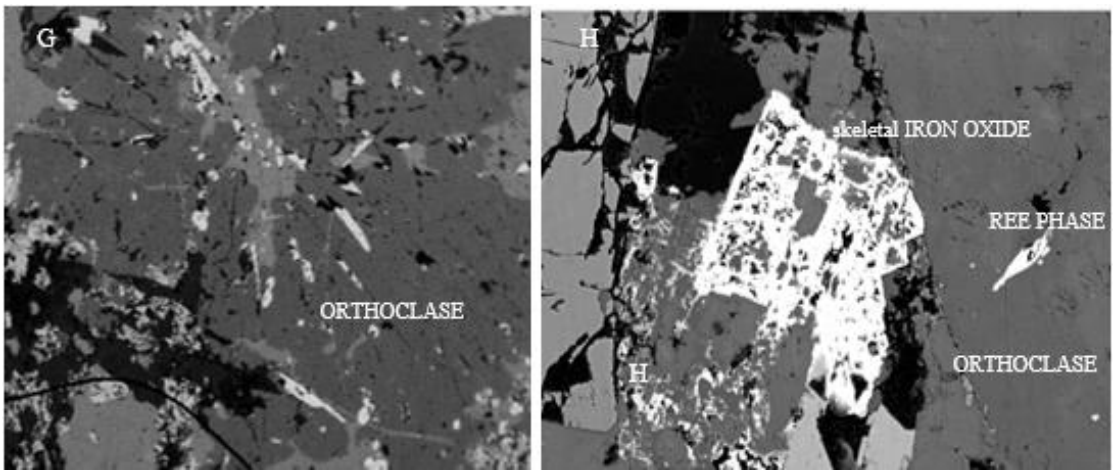

Fig 5.14b Backscatter electron image of sövite 08SB39 containing alkali feldspars from Brava

Three samples 08SB43, 08SB44. 08SB7 and 08SB48 contain zeolite, which is analcime in composition (Figure 5.15). Coarse-grained analcime mostly exists in 08SB43 forming euhedral crystals with an interlocking structure filling one side of the specimen (vein-type space). Often, much smaller euhedral-anhedral crystals of zeolite are found intimately associated with calcite and/or clinopyroxene (Figure 5.15). Remobilisation of Si and Al can be attained by process of post-emplacement metasomatism (Stemprok (1987); Elliot et al., 2018), which can be preceded or followed by potassic or sodic alteration. Released fluids, enriched in Si- and Al-ions, most-likely triggered crystallisation of zeolites. Thus, zeolites precipitated during the hydrothermal stage and crystallised as euhedral-subhedral crystals sometimes forming honeycombed structure, at times flanking calcite (Figure 5.15E) and at times partially replacing calcite along cleavage planes (Figure 5.15B). Analcime in 08SB43A encloses zoned secondary calcite. According to Chackmouradian et al. (2015), the formation of late-stage calcite is associated with hydrothermal fluids and production of rhombohedral zoned crystals projecting into fractures/voids, often accompanied by late-forming zeolites.

Mica is scarce in the Brava intrusive complex samples, with the exception of the glimmerite sample (08SB38). Compositionally it varies from phlogopite to biotite, but some samples contain Al-low biotite and phengite. This wide variety suggests a fenitic origin or alteration induced by metasomatism. In the zeolite-rich sample (08SB44), mica is low-Al biotite (Figure 5.16A and B). Anhedral crystals bordering analcime display undulating margins, texture very similar to mica-albite marginal contact in the glimmerite. The close association of analcime (Al-rich) with Al-low biotite reflects distribution of Al by related fluids, and crystallisation of zeolites at the expense of biotite. Phengitic mica is present in 08SB47 and 08SB48 (Figure 5.16C and D). In 08SB47 fine-grained phengite exhibits a radiating texture but also a decussate texture with chaotic orientation of elongated crystals. It seems that rapid crystallisation occurred in voids and is of secondary origin.

Alteration of phlogopite to phengite is linked to fractures in phlogopite and around it, allowing fluid to invade and partially modify the original mineral composition. Approximately one third of sample 08SB40 is composed of biotite (glimmeritic side) heavily intruded by calcite along the cleavage planes, and to lesser extent by albite. As biotite is cross-cut by albite and subsequently by calcite, the first event which took place was Na-fenitization followed by carbonatite veining.

Mica in sövite 08SB39 is also scarce. The rare mica in sövite is phlogopite and shows intense alteration alongside the bent part of the crystal. Breakage of the highly strained part of crystal led to invasion by albite which was then transformed to clay. The alteration process formed intense embayments on phlogopite in the heavily altered part, similar to glimmerite-albite embayment in the alvikite (08SB38). Bending of the crystal is caused by destruction of the already formed crystal by upward (?) movement of the carbonatite.

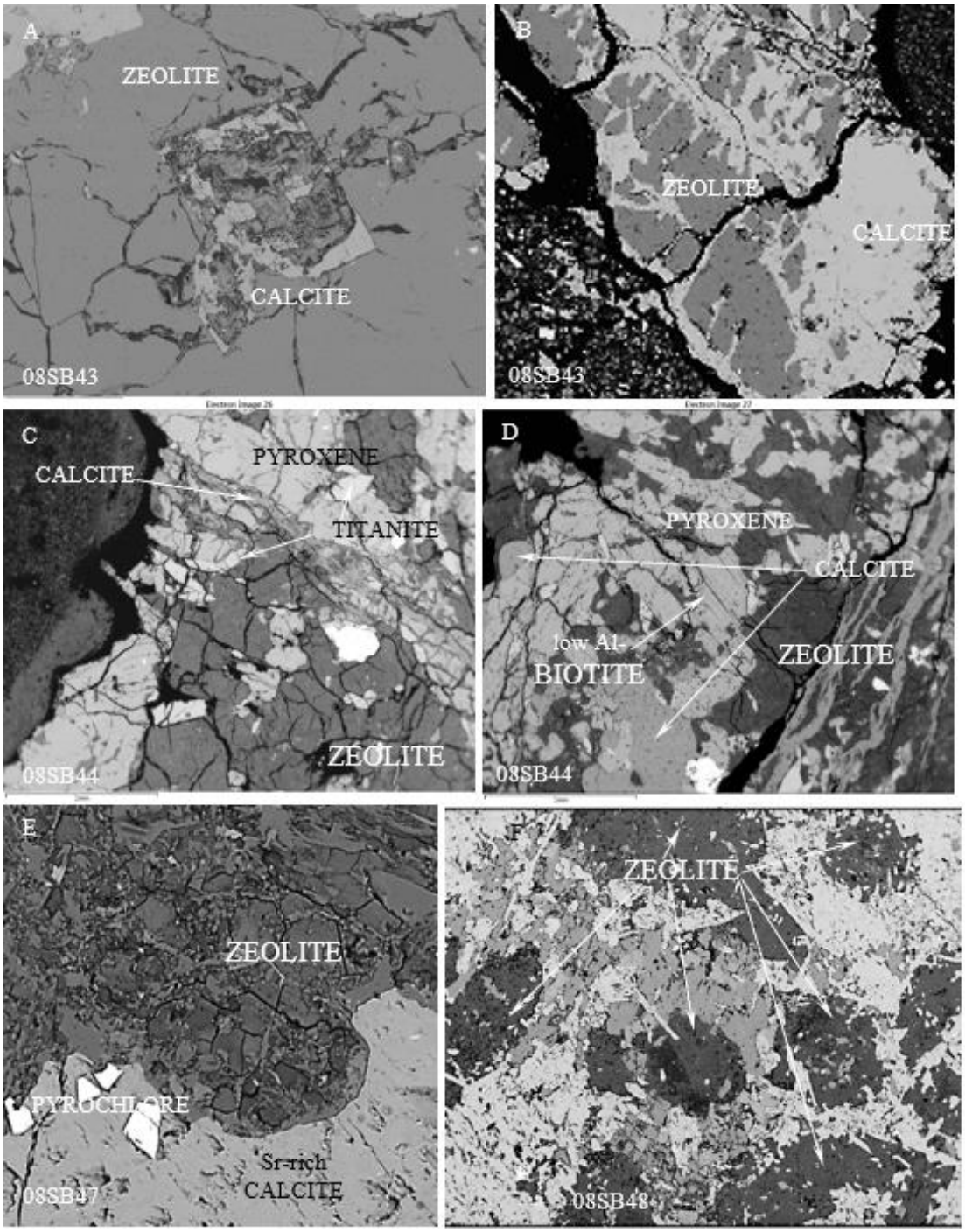

Fig 5.15 Backscatter electron image of intrusive silicate rocks associated with carbonatite intrusion such as 08SB43, 08SB47 and 08SB48 containing zeolite from L5 location, Brava, Cape Verde.

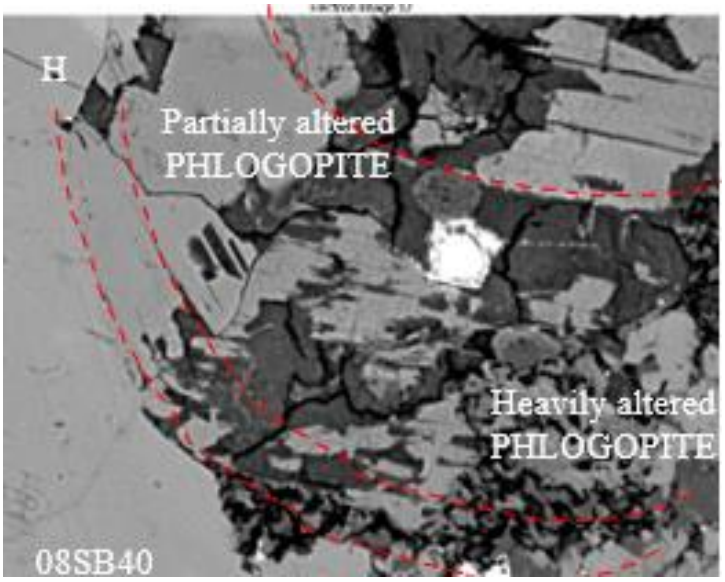

Fig 5.16b Backscatter electron image of sövite 08SB39 containing phlogopite crystal from L5 location, Brava

Some analysed samples contain accessory minerals, which are important as crystallisation of these rare specimens can lead to a better understanding of post-magmatic processes affecting the intrusive alkaline rocks on Brava. Ti-rich minerals are present in most samples in the form of titanite, ilmenite and titanomagnetite, but sporadic rutile was also detected in samples 08SB40, 08SB48 and 08SB49. In 08SB47 there is rare henrymeyerite, a hollandite-type Ba–Fe titanite, showing close association with Ba-La titanite and ilmenite (Figure 5.17A). Sample 08SB48 contains the widest spectrum of Ti- and Zr-phases with Mn-ilmenite and Nb-rutile. Overall titanomagnetite is more commonly found than magnetite.

Sample 08SB40 contains a cluster of Zr-rich phases varying from Ti-Zr-magnetite through Ti-rich zirconosilicates (catapleiite and hilairite) to Zr-rich ilmenite (Figure 5.17B). In 08SB43 (Figure 5.17C) an intimate association is seen between Mn- and Zr-rich phases, such as hollandite and penninite, rimmed by zirconosilicate. Hilairite is present in 08SB49 as well as Zr-rich tazherainite (Figure 5.17D). Tazherainite crystallised in close proximity to rutile and/or tends to associate with Sr-poor calcite. The localised availability of Nb reflects formation of pyrochlore in three samples (08SB38, 08SB47 and 08SB48).

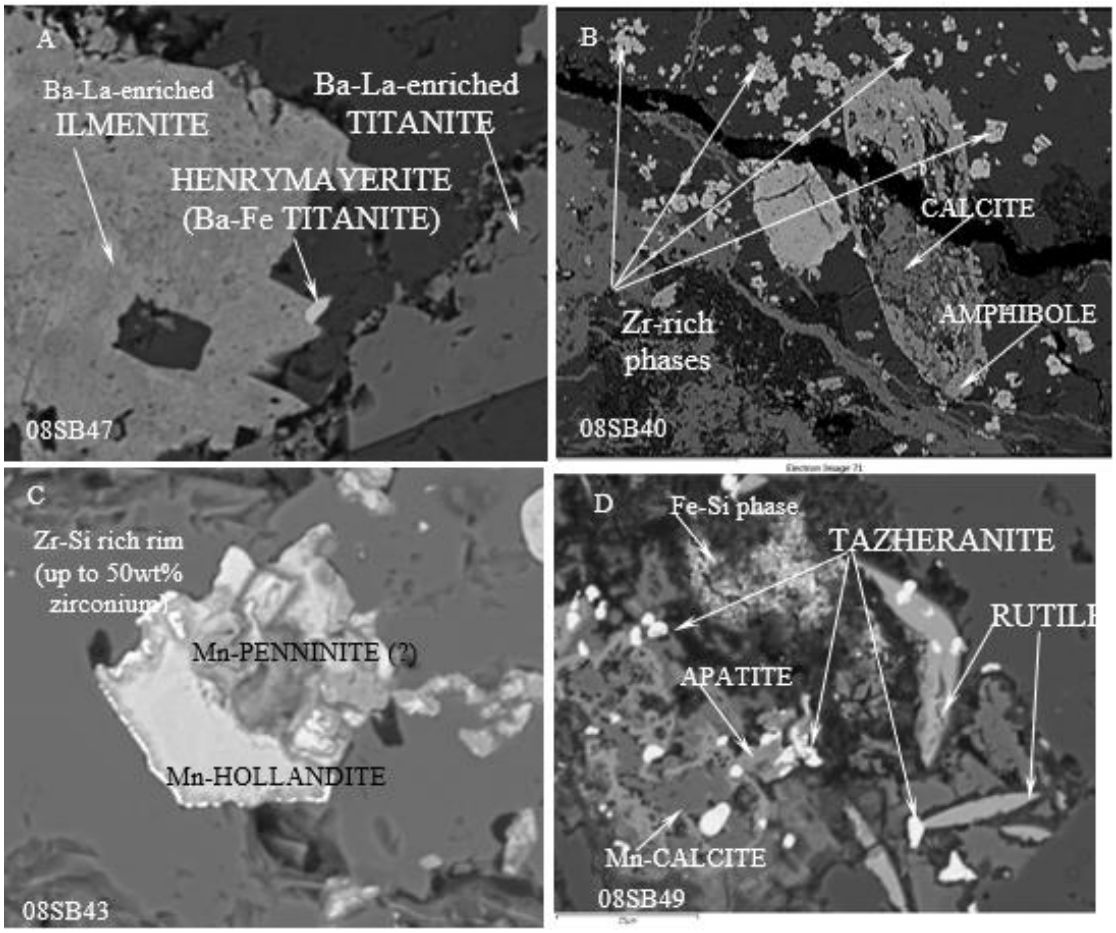

Fig 5.17 BSE images of intrusive silicate rocks associated with carbonatite intrusion containing rare Ti-, Zr- phases in 08SB47, 08SB40, 08SB43 and 08SB49 from L5 location, Brava, Cape Verde.

Pyrochlore tends to have a euhedral to subhedral shape, often clustering and displaying concentric zoning (Figure 5.18A, B, C and D). The subhedral form most likely is linked to post-crystallisation resorption and fracturing (Figure 5.18B and D) due to changing conditions (fluctuation of hydrothermal fluids and their chemistry) and shearing during uplift and/or veining.

Iron oxide is commonly found in sövite 08SB39 (Figure 5.19A, B). This kind of texture of rhomboidal/octahedral crystals is not unusual in magnetite (or hematite after magnetite). The hopper crystal growth indicates rapid crystallisation. Thus growth of the iron oxide was rapid. The brownish look of this phase indicates that it is hematite, which points to fluid circulation. In the silicate part of the intrusive alkaline complex, a wide range of Ti-Fe phases was detected. Oddly, analysed sövite is limited to magnetite/hematite or rutile and no other Ti-rich intermediate phases were found (Figure 5.19C,D). Rutile is very rare. Another accessory phase pyrochlore crystallised

small and subhedral specimens to some degree resorbed on one side (Figure 5.19E, F). BSE images do not reveal zonation like in silicate rocks (Figure 5.18B, D).

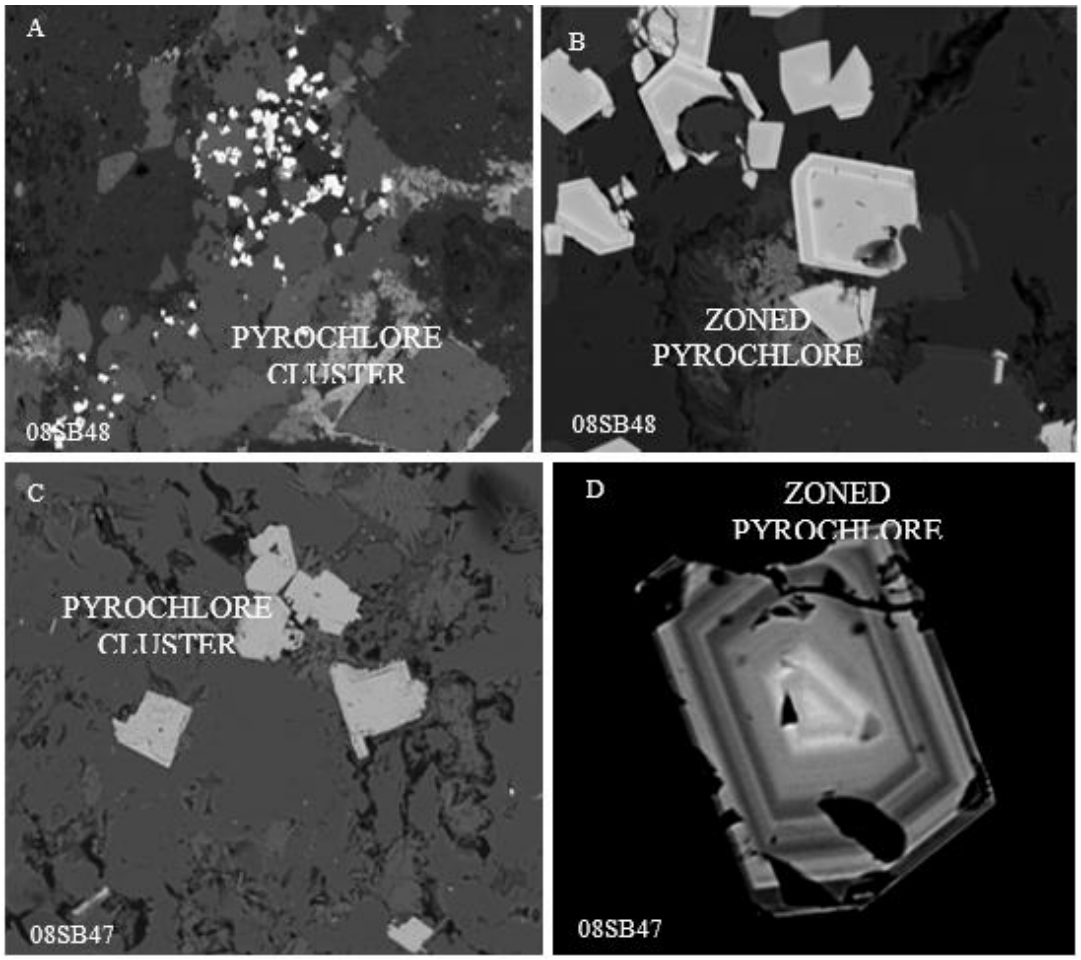

Fig 5.18 Backscatter electron image of intrusive silicate rocks associated with carbonatite intrusion containing pyrochlore from L5 location, Brava, Cape Verde

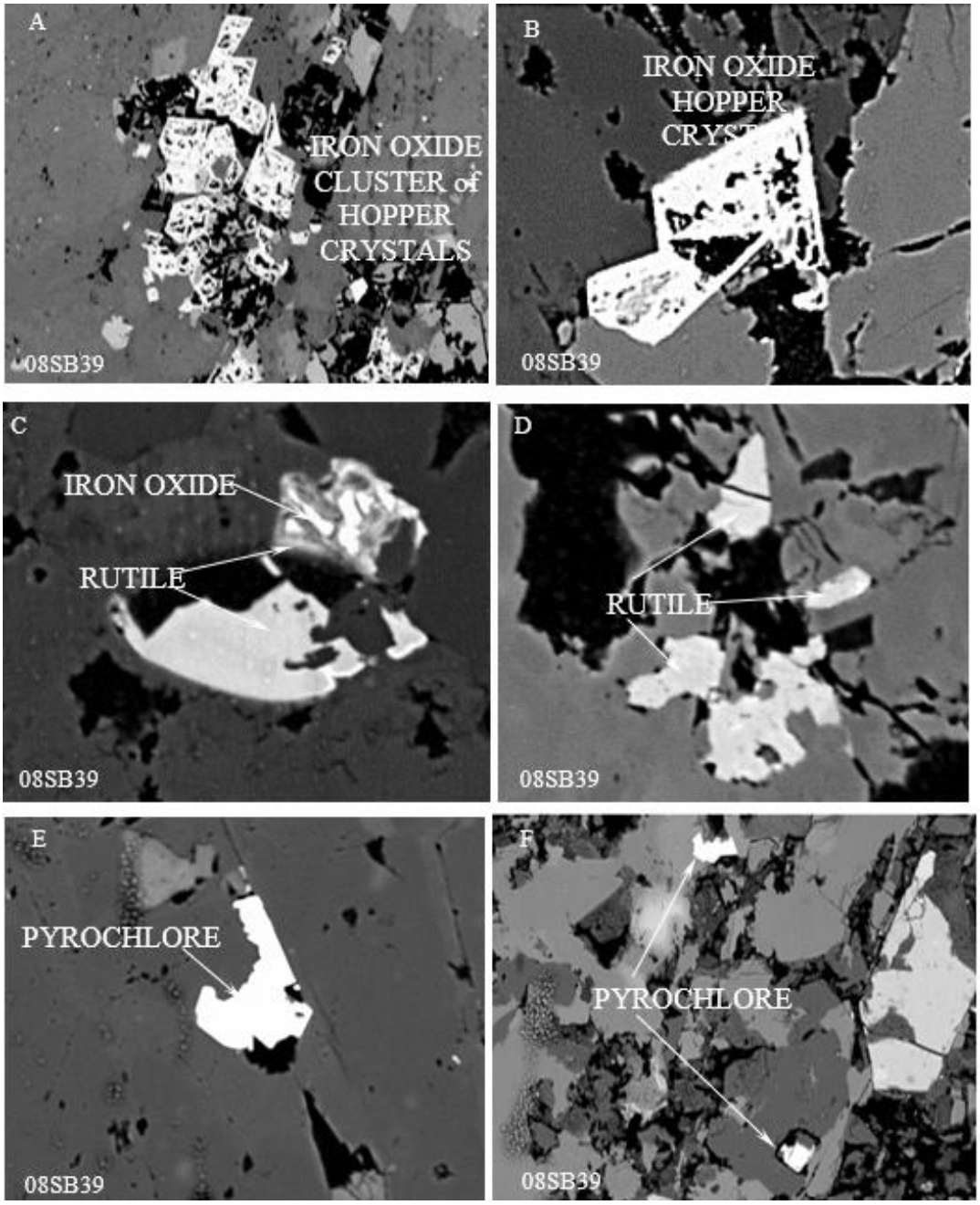

Fig 5.19 BSE image of sövite 08SB39 containing iron oxide, rutile and pyrochlore from L5 location, Brava

Unusual carbonate and silicate REE-minerals were identified by electron microprobe as they are extremely fine-grained and form odd shapes. Sample 08SB48 is richest in rare phases, where La-Ce-rich minerals can be recognised such as rhabdophane, parisite-synchysite and torneböhmite (Figure 5.20A, B, C and D). Phases rich in Sr include the carbonate burbankite (Figure 5.20E and F), containing varying content of Ba.

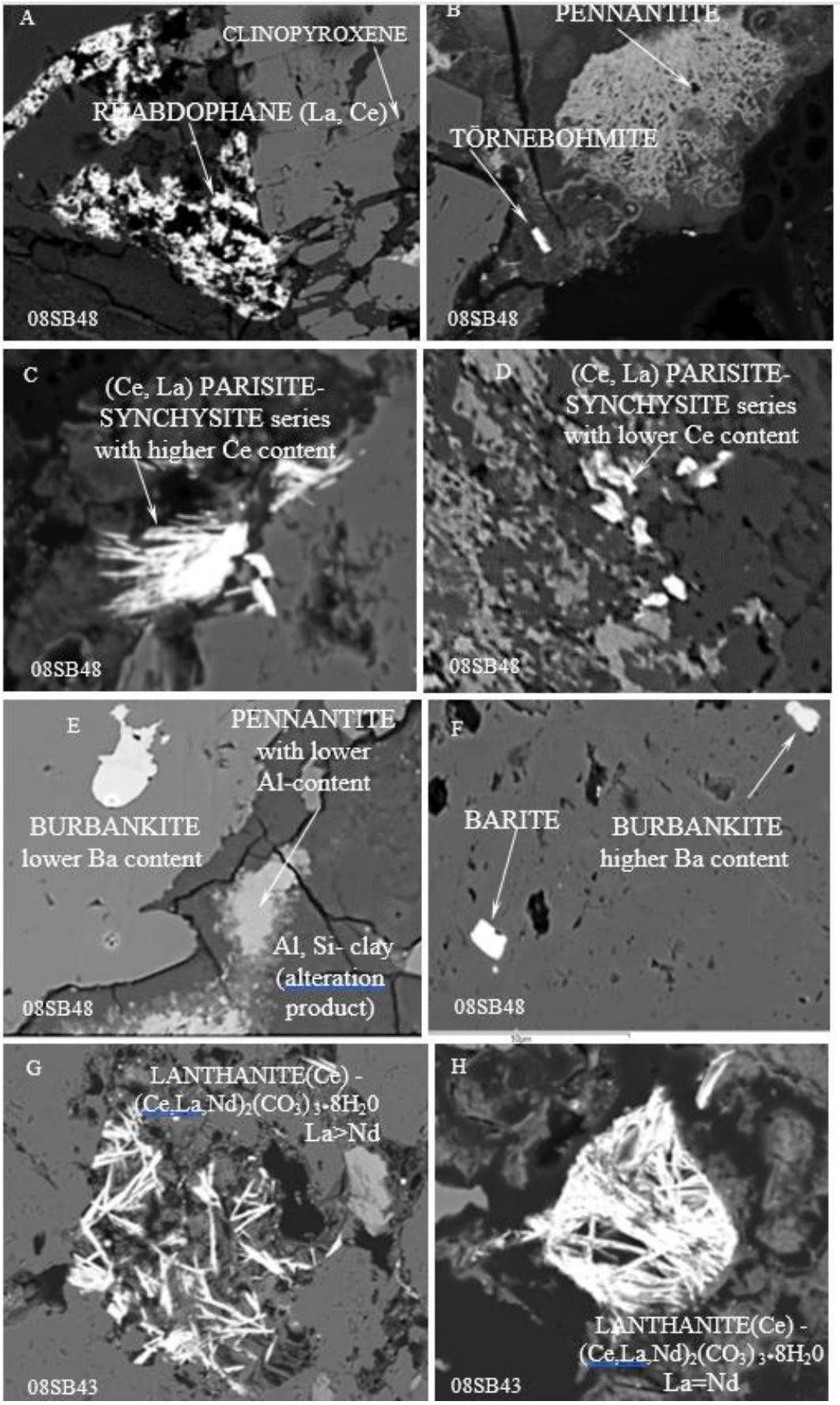

Fig 5.20 Backscatter electron image of intrusive silicate rocks associated with carbonatite intrusion containing rare phases enriched in REE and other rare elements in 08SB48 and 08SB43 from L5 location, Brava, Cape Verde.

Manganese forms pennantite mesh-like structure (Figure 5.20B) and also varies in chemistry as it can crystallise a low-Al variety (Figure 5.20F) most probably because they are associated with Al-rich clay mineral (Figure 5.20E). Barium occasionally can form its own phase such as barite (Figure 5.20F). In addition to REE minerals in 08SB48, another sample yielded lanthanite-phases (Figure 5.20G and H). Both analysed species are La-Ce-Nd-rich and slightly differ in chemistry according to La and Nd content.

Analysed sövite 08SB39 is also enriched in REE phases such as parisite-synchysite, carboceranite, calcian strontianite and strontian calcite (Figure 5.21). Fine grained carbonate forms bands intensly populated by star-like carbonate grains, rich in K and Na (Figure 5.21D and E). Sr-rich phases crystallised from the Sr-rich calcite (primary), depleting surrounding area in Sr-content, leading to form of dark-grey blotches in calcite full of bright spots of strontian calcite, calcian strontianite or carboceranite (Figure 5.21C and F). The light-grey areas are untouched by Sr depletion thus they are Sr-rich calcite (Figure 5.21F).

In summary the Brava samples are enriched in REEs, Nb, Ba, Sr which is reflected in crystallisation of unusual and uncommon phases. Deformation, induced by uplift of the seamount complex, could be responsible for the shearing, which regulated development of net-veining. Shear zones and veins, acting as conduits, spread hydrothermal fluids derived from the surrounding rocks (perhaps late-magmatic fluids or/and metamorphic fluids). Remobilisation of elements, mainly REEs but also others such as Sr, Ba, Mn, followed by interaction with surrounding rocks thus altering the chemistry and texture of the rocks.

5.3 Summary from petrology

Sövite samples were very rare in the L5 site, reflecting the field relationship as only a small amount of carbonatite is present in the basal complex. Also the lack of pristine silicate samples associated with carbonatites makes it more problematic to resolve the problem of assessing the processes involved in formation of the Brava alkaline intrusive complex. But the effect of carbonatite melts and fluids and associated processes can be detected by analysing petrography and features (primary followed by secondary) such as:

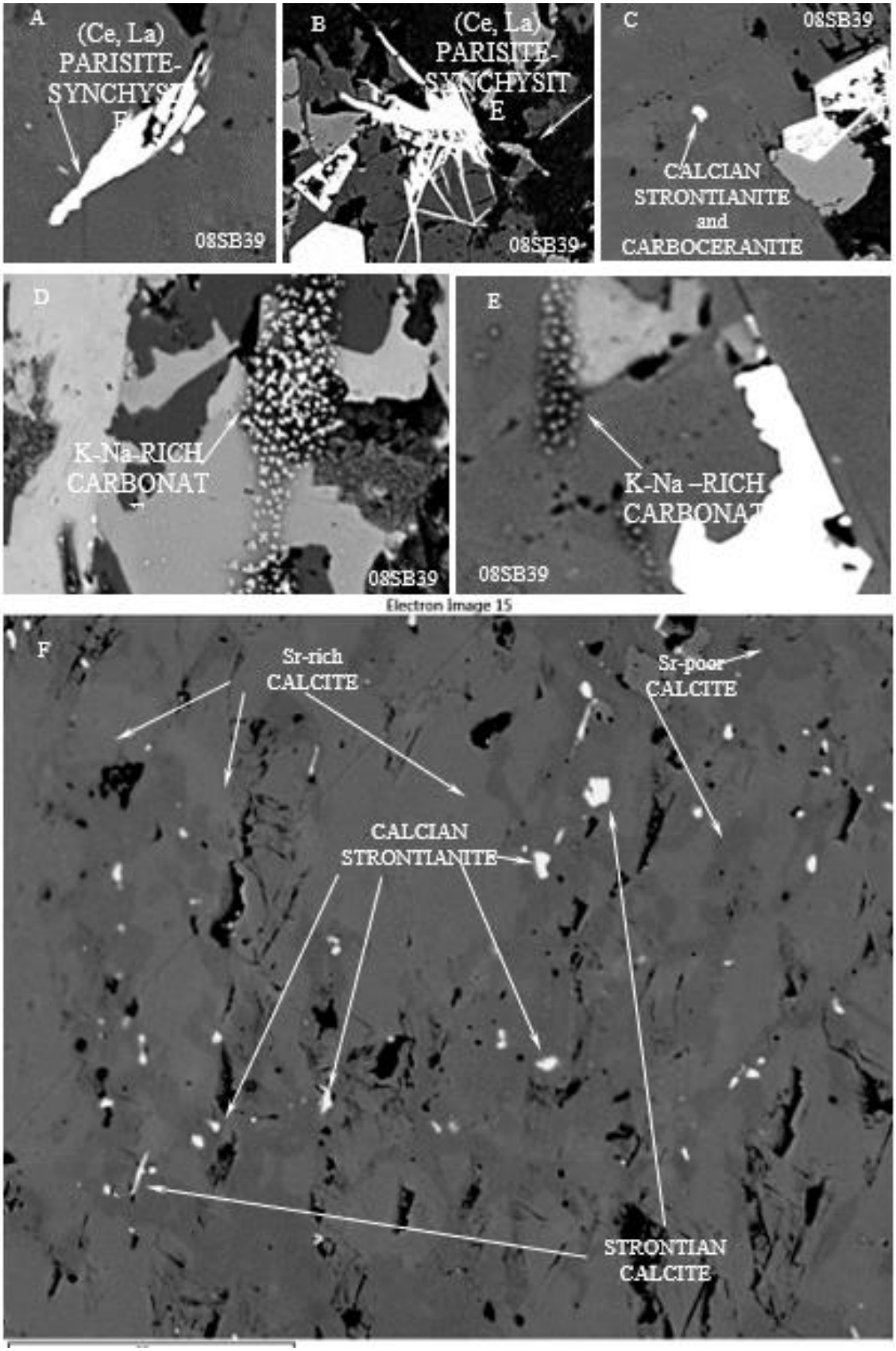

Fig 5.21 Backscatter electron image of Brava sövite 08SB39 containing phases rich in REE.

- minority of carbonatite samples vs majority of alkaline silicate samples reflects the late-stage emplacement of a small carbonatite body into large alkaline suite;
- each sample exhibits different features, implying complex effects of post-magmatic deformation such as shearing during uplift, alteration by hydrothermal fluids, oxidation;
- association of different rock types on a small scale such as glimmerite-syenite-carbonatite reflects close relationship on a bigger scale;
- high concentration of amphibole showing radiating texture with interlocking feldspar implying fast crystallisation with the highest concentration of amphibole found in close approximation to pegmatite feldspar;
- sodic amphiboles or/and sodic pyroxene are most common silicate phases as well as orthoclase and/or albite, indicating high influence of Na and K;
- intense penetration by secondary Sr-poor calcite veining;
- albitisation associated with Na-metasomatism (fenitization);
- fluid-release into silicate rocks leading to enrichment in REE and other rare elements commonly found in primary carbonatites in phases such as apatite etc.;
- trace element enrichment of silicate rocks caused formation of unusual assemblage of REE-phases;
- crystallisation of zeolites from Al-Si-rich fluids, which can also replace calcite;
- apatite forms rare crystals and exhibits different state of alteration or shows intimate association with Nb- or Zr-rich phases, perhaps indicating co-crystallisation of late-stage phases;
- amphibole is mostly affected by post-emplacement processes such as albitisation, calcite invasion (net-veining).

5.4 Electron microprobe analysis

Polished thin-sections (30μm thick) from samples from location L5 were used to obtain major and minor element concentrations.

5.4.1 Calcite

	COMPOSITE		ZEOLITE				ZEOLITE									SYENITE		SYENITE			
EDS	08SB40		08SB43				08SB44									08SB50		08SB46			
CALCITE	ave n=4	st dev n=4	ave n=9	st dev n=9	ave n=10	st dev n=10	ave n=4	st dev n=4	ave n=3	st dev n=3	ave n=1	ave n=1	ave n=4	st dev n=4	ave n=9	st dev n=9	ave n=13	st dev n=13	ave n=7	st dev n=7
SiO_2	0.11	0.08	0.11	0.08	0.12	0.05	0.29	0.13	0.27	0.22	3.49	0.40	9.75	1.95	0.19	0.07	0.16	0.10	0.43	0.15
Al_2O_3	0.00	0.00	0.05	0.05	0.01	0.02	0.10	0.14	0.11	0.12	1.95	3.11	2.99	1.48	0.05	0.07	0.03	0.04	0.26	0.13
FeO	0.42	0.13	0.29	0.09	0.05	0.08	0.06	0.11	0.17	0.23	0.46	0.07	5.89	3.00	0.06	0.06	0.04	0.09	0.52	0.35
MnO	0.21	0.30	1.25	0.31	0.05	0.09	0.14	0.08	0.06	0.06	0.16	0.00	0.25	0.22	0.37	0.10	0.14	0.09	0.05	0.10
MgO	0.24	0.13	0.08	0.06	0.41	0.36	0.01	0.01	0.30	0.18	0.11	0.03	2.16	1.03	0.08	0.06	0.02	0.03	0.99	0.48
CaO	56.31	0.38	54.48	0.84	54.90	0.84	53.10	1.62	54.21	0.24	48.88	49.90	38.86	3.74	55.40	0.59	56.62	0.35	55.22	1.53
BaO	0.08	0.10	0.10	0.12	0.07	0.06	0.04	0.06	0.07	0.12	0.21	0.10	0.33	0.27	0.10	0.14	0.17	0.16	0.05	0.07
Nb_2O_5	0.08	0.09	0.07	0.08	0.14	0.19	0.02	0.05	0.08	0.13	0.09	0.10	0.01	0.01	0.02	0.05	0.02	0.06	0.05	0.09
SrO	0.28	0.35	0.86	0.13	0.19	0.15	1.58	0.14	0.24	0.20	1.09	0.11	0.07	0.13	1.70	0.41	1.89	0.12	0.20	0.09
TOTAL	57.72	0.41	57.23	0.86	55.93	0.86	55.33	1.90	55.51	0.37	56.44	53.82	60.30	2.83	57.96	0.92	59.09	0.42	57.77	0.99
Cations recalculated on the basis of 12 oxygens																				
Si	0.02	0.02	0.02	0.02	0.02	0.01	0.06	0.03	0.05	0.04	0.65	0.08	1.55	0.22	0.04	0.01	0.03	0.02	0.08	0.03
Al	0.00	0.00	0.01	0.01	0.00	0.00	0.02	0.03	0.03	0.03	0.43	0.73	0.56	0.26	0.01	0.02	0.01	0.01	0.06	0.03
Fe^{+2}	0.07	0.02	0.05	0.02	0.01	0.01	0.01	0.02	0.03	0.04	0.07	0.01	0.78	0.39	0.01	0.01	0.01	0.01	0.08	0.05
Mn	0.03	0.05	0.21	0.05	0.01	0.02	0.02	0.01	0.01	0.01	0.03	0.00	0.03	0.03	0.06	0.02	0.02	0.02	0.01	0.02
Mg	0.07	0.04	0.02	0.02	0.12	0.11	0.00	0.00	0.09	0.05	0.03	0.01	0.51	0.22	0.02	0.02	0.01	0.01	0.28	0.14
Ca	11.73	0.05	11.54	0.06	11.75	0.10	11.61	0.10	11.67	0.19	9.77	10.68	6.70	0.90	11.61	0.06	11.67	0.06	11.34	0.27
Ba	0.01	0.01	0.00	0.01	0.00	0.00	0.00	0.01	0.01	0.01	0.02	0.01	0.02	0.02	0.01	0.01	0.01	0.01	0.00	0.01
Nb	0.01	0.01	0.01	0.01	0.01	0.02	0.00	0.00	0.01	0.01	0.01	0.01	0.00	0.00	0.00	0.00	0.00	0.01	0.00	0.01
Sr	0.03	0.04	0.10	0.01	0.02	0.02	0.19	0.01	0.03	0.02	0.12	0.01	0.01	0.01	0.19	0.04	0.21	0.01	0.02	0.01
TOTAL	11.97	0.02	11.96	0.02	11.95	0.03	11.93	0.05	11.92	0.04	11.12	11.54	10.17	0.24	11.95	0.02	11.96	0.02	11.88	0.04

Table 5.3a Electron microprobe data for calcite in the Brava intrusive alkaline complex. Abbreviations: st dev=standard deviation, ave=average. Cations recalculated on the basis of 12 oxygens. Complete tables supplied in Appendix 3a. Some elements are below detection limit.

	SYENITE						SYENITE									FELSIC PEGMATITE					
EDS	08SB45						08SB47									08SB49					
CALCITE	ave n=3	st dev n=3	ave n=2	st dev n=2	ave n=4	st dev n=4	ave n=3	st dev n=3	ave n=5	st dev n=5	ave n=8	st dev n=8	ave n=3	st dev n=3	ave n=11	st dev n=11	ave n=4	st dev n=4			
SiO_2	0.21	0.07	0.30	0.13	0.17	0.04	0.31	0.04	0.35	0.19	0.31	0.12	0.24	0.15	0.19	0.15	0.66	0.31			
Al_2O_3	0.16	0.12	0.08	0.11	0.13	0.12	0.11	0.11	0.12	0.09	0.29	0.22	0.15	0.10	0.07	0.09	0.12	0.09			
FeO	0.39	0.22	0.37	0.04	0.15	0.16	0.69	0.04	0.28	0.27	0.33	0.14	0.32	0.16	0.18	0.16	1.15	0.70			
MnO	1.00	0.16	0.38	0.06	0.29	0.13	0.09	0.07	0.22	0.14	0.28	0.12	0.41	0.50	0.06	0.07	0.17	0.17			
MgO	0.06	0.06	0.15	0.06	0.06	0.12	0.04	0.08	0.16	0.09	0.23	0.25	0.18	0.15	0.51	0.29	1.12	0.65			
CaO	51.13	0.54	51.63	1.16	51.70	0.74	52.31	0.74	52.33	16.33	52.03	0.86	52.32	0.70	56.98	0.74	51.65	1.16			
BaO	0.18	0.16	0.13	0.18	0.21	0.40	0.00	0.00	0.11	0.17	0.07	0.08	0.01	0.01	0.05	0.06	0.09	0.18			
Nb_2O_5	0.10	0.11	0.11	0.15	0.09	0.18	0.10	0.17	0.11	0.11	0.09	0.11	0.18	0.09	0.05	0.10	0.10	0.07			
SrO	0.65	0.20	0.45	0.06	0.90	0.09	3.70	0.44	2.32	1.08	1.78	0.28	0.66	0.34	0.23	0.14	0.20	0.22			
TOTAL	53.87	0.58	53.59	0.96	53.71	0.53	57.35	1.07	55.99	17.60	55.40	0.47	54.47	0.45	58.33	0.56	55.26	1.14			
Cations recalculated on the basis of 12 oxygens																					
Si	0.04	0.01	0.06	0.03	0.04	0.01	0.06	0.01	0.07	0.04	0.06	0.02	0.05	0.03	0.04	0.03	0.13	0.06			
Al	0.04	0.03	0.02	0.03	0.03	0.03	0.03	0.03	0.03	0.02	0.07	0.05	0.04	0.02	0.01	0.02	0.03	0.02			
Fe^{+2}	0.07	0.04	0.06	0.01	0.03	0.03	0.12	0.01	0.05	0.05	0.06	0.02	0.06	0.03	0.03	0.03	0.19	0.11			
Mn	0.18	0.03	0.07	0.01	0.05	0.02	0.01	0.01	0.04	0.02	0.05	0.02	0.07	0.09	0.01	0.01	0.03	0.03			
Mg	0.02	0.02	0.05	0.02	0.02	0.04	0.01	0.02	0.05	0.03	0.07	0.08	0.06	0.04	0.14	0.08	0.34	0.20			
Ca	11.47	0.14	11.58	0.11	11.63	0.14	11.24	0.14	11.38	3.54	11.36	0.16	11.54	0.06	11.70	0.12	11.11	0.19			
Ba	0.01	0.01	0.01	0.01	0.02	0.03	0.00	0.00	0.01	0.01	0.01	0.01	0.00	0.00	0.00	0.00	0.01	0.01			
Nb	0.01	0.01	0.01	0.01	0.01	0.02	0.01	0.02	0.01	0.01	0.01	0.01	0.02	0.01	0.00	0.01	0.01	0.01			
Sr	0.08	0.02	0.05	0.01	0.11	0.01	0.43	0.05	0.27	0.13	0.21	0.03	0.08	0.04	0.00	0.00	0.00	0.00			
TOTAL	11.92	0.04	11.91	0.06	11.94	0.04	11.91	0.04	11.90	3.75	11.89	0.03	11.91	0.05	11.95	0.04	11.84	0.07			

Table 5.3b Electron microprobe data for calcite in the Brava intrusive alkaline complex. Abbreviations: st dev=standard deviation, ave=average. Cations recalculated on the basis of 12 oxygens. Complete tables supplied in Appendix 3a.

08SB48	SYENITE																	
EDS	DARKER AREA								LIGHTER AREA									
CALCITE	SB48 ave n=2	SB48 st dev n=2	SB48 ave n=10	SB48 st dev n=10	SB48 ave n=7	SB48 st dev n=7	SB48 ave n=5	SB48 st dev n=5	SB48 ave n=3	SB48 st dev n=3	SB48 ave n=1	SB48 st dev n=1	SB48 ave n=21	SB48 st dev n=21	SB48 ave n=9	SB48 st dev n=9		
SiO_2	0.25	0.01	0.25	0.10	0.18	0.07	0.21	0.12	0.18	0.06	0.16	0.00	0.21	0.06	0.22	0.03		
Al_2O_3	0.11	0.07	0.05	0.03	0.04	0.04	0.03	0.02	0.07	0.03	0.09	0.00	0.06	0.06	0.02	0.02		
FeO	0.12	0.17	0.36	0.29	0.42	0.28	0.49	0.09	0.12	0.04	0.00	0.00	0.23	0.15	0.40	0.14		
MnO	0.14	0.01	0.71	0.59	1.37	0.33	1.71	1.01	0.14	0.02	0.23	0.00	0.25	0.19	0.29	0.16		
MgO	0.07	0.01	0.05	0.06	0.10	0.07	0.19	0.08	0.09	0.04	0.02	0.00	0.11	0.07	0.13	0.08		
CaO	52.81	0.47	53.89	0.58	52.17	0.87	54.28	1.53	53.28	0.18	54.78	0.00	54.41	1.39	54.26	0.84		
BaO	0.23	0.32	0.04	0.07	0.09	0.13	0.11	0.19	0.64	0.05	0.12	0.00	0.22	0.21	0.20	0.15		
Nb_2O_5	0.18	0.15	0.02	0.04	0.10	0.15	0.08	0.11	0.10	0.06	0.00	0.00	0.08	0.12	0.09	0.14		
SrO	0.83	0.08	0.54	0.25	0.59	0.24	0.52	0.13	1.10	0.06	1.00	0.00	1.42	0.29	1.38	0.18		
TOTAL	54.72	0.48	55.91	0.45	55.07	0.91	57.61	1.95	55.71	0.35	56.40	0.00	56.98	1.49	56.99	1.09		
Cations recalculated on the basis of 12 oxygens																		
Si	0.05	0.00	0.05	0.02	0.04	0.02	0.04	0.02	0.01	0.02	0.03	0.00	0.04	0.01	0.04	0.01		
Al	0.03	0.02	0.01	0.01	0.01	0.01	0.01	0.01	0.02	0.01	0.02	0.00	0.01	0.01	0.00	0.01		
Fe^{+2}	0.02	0.03	0.06	0.05	0.07	0.05	0.08	0.02	0.02	0.01	0.00	0.00	0.04	0.03	0.07	0.02		
Mn	0.02	0.00	0.12	0.10	0.24	0.06	0.28	0.16	0.02	0.00	0.04	0.00	0.04	0.03	0.05	0.03		
Mg	0.02	0.00	0.02	0.02	0.03	0.02	0.06	0.02	0.02	0.01	0.01	0.00	0.03	0.02	0.04	0.02		
Ca	11.64	0.05	11.62	0.15	11.47	0.05	11.40	0.16	11.71	0.06	11.73	0.00	11.59	0.09	11.56	0.04		
Ba	0.02	0.03	0.00	0.01	0.01	0.01	0.01	0.01	0.05	0.00	0.00	0.00	0.02	0.02	0.02	0.01		
Nb	0.00	0.00	0.00	0.00	0.00	0.00	0.00	0.00	0.00	0.00	0.00	0.00	0.00	0.00	0.00	0.00		
Sr	0.10	0.01	0.06	0.03	0.07	0.03	0.06	0.01	0.13	0.01	0.12	0.00	0.16	0.03	0.16	0.02		
TOTAL	11.91	0.03	11.94	0.02	11.94	0.02	11.95	0.03	11.97	0.02	11.96	0.00	11.94	0.02	11.94	0.02		

Table 5.3c Electron microprobe data for calcite in the Brava intrusive alkaline complex. Abbreviations: st dev=standard deviation, ave=average. Cations recalculated on the basis of 12 oxygens. Complete tables supplied in Appendix 3a.

	ALVIKITE		SÖVITE										SÖVITE					
EDS	08SB38						08SB39	HIGH STRONTIUM					08SB39	LOW STRONTIUM				
CALCITE	ave n=4	st dev n=4	ave n=2	st dev n=2	ave n=5	st dev n=5	ave n=19	st dev n=19	ave n=18	st dev n=18	ave n=18	st dev n=18	ave n=19	st dev n=19	ave n=19	st dev n=19	ave n=18	st dev n=18
SiO_2	0.35	0.31	0.17	0.01	0.14	0.08	0.30	0.14	0.21	0.14	0.21	0.14	0.37	0.43	0.33	0.32	0.14	0.09
Al_2O_3	0.32	0.24	0.02	0.02	0.05	0.04	0.05	0.05	0.03	0.04	0.05	0.04	0.10	0.13	0.08	0.11	0.04	0.04
FeO	0.15	0.11	0.05	0.07	0.06	0.11	0.21	0.20	0.18	0.21	0.20	0.30	0.77	0.88	0.92	0.84	0.22	0.24
MnO	0.04	0.05	0.21	0.10	0.05	0.11	0.42	0.24	0.34	0.12	0.42	0.17	0.60	0.36	0.30	0.28	0.34	0.18
MgO	0.49	0.40	1.96	0.35	0.75	0.67	0.04	0.04	0.04	0.05	0.04	0.05	0.11	0.10	0.29	0.33	0.09	0.10
CaO	56.35	1.68	56.32	0.12	56.69	0.87	53.47	0.49	53.82	0.62	53.60	0.41	52.80	1.44	54.10	0.93	54.54	0.84
BaO	0.14	0.15	0.00	0.00	0.05	0.09	0.15	0.15	0.12	0.17	0.18	0.15	0.20	0.19	0.10	0.09	0.12	0.17
Nb_2O_5	0.02	0.03	0.08	0.07	0.14	0.13	0.07	0.10	0.07	0.07	0.05	0.10	0.04	0.09	0.10	0.12	0.05	0.08
SrO	0.18	0.12	0.26	0.17	0.16	0.07	1.78	0.38	1.61	0.50	1.81	0.31	0.60	0.20	0.37	0.25	0.49	0.27
TOTAL	58.04	1.86	59.06	0.19	58.09	0.72	56.48	0.46	56.42	0.56	56.57	0.56	55.58	1.19	56.60	1.09	56.02	0.74
Cations recalculated on the basis of 12 oxygens																		
Si	0.07	0.06	0.03	0.00	0.03	0.02	0.06	0.03	0.04	0.03	0.04	0.03	0.07	0.09	0.06	0.06	0.03	0.02
Al	0.07	0.05	0.00	0.00	0.01	0.01	0.01	0.01	0.01	0.01	0.01	0.01	0.02	0.03	0.02	0.03	0.01	0.01
Fe^{+2}	0.02	0.02	0.01	0.01	0.01	0.02	0.04	0.03	0.03	0.04	0.03	0.05	0.13	0.15	0.15	0.14	0.04	0.04
Mn	0.01	0.01	0.03	0.02	0.01	0.02	0.07	0.04	0.06	0.02	0.07	0.03	0.10	0.06	0.05	0.05	0.06	0.03
Mg	0.14	0.11	0.55	0.10	0.21	0.19	0.01	0.01	0.01	0.02	0.01	0.01	0.03	0.03	0.09	0.10	0.03	0.03
Ca	11.56	0.26	11.30	0.08	11.65	0.15	11.71	0.08	11.78	0.07	11.75	0.10	11.52	0.29	11.52	0.22	11.79	0.08
Ba	0.01	0.01	0.00	0.00	0.00	0.01	0.01	0.01	0.01	0.01	0.01	0.01	0.02	0.02	0.01	0.01	0.01	0.01
Nb	0.00	0.00	0.01	0.01	0.01	0.01	0.01	0.01	0.01	0.01	0.00	0.01	0.00	0.01	0.01	0.01	0.00	0.01
Sr	0.02	0.01	0.03	0.02	0.02	0.01	0.11	0.02	0.10	0.03	0.11	0.02	0.04	0.01	0.02	0.01	0.03	0.02
TOTAL	11.90	0.09	11.96	0.01	11.95	0.03	12.03	0.04	12.04	0.04	12.05	0.04	11.94	0.09	11.93	0.09	11.99	0.03

Table 5.3d Electron microprobe data for calcite in the Brava intrusive alkaline complex. Abbreviations: st dev=standard deviation, ave=average. Cations recalculated on the basis of 12 oxygens. Complete tables supplied in Appendix 3a.

One of the major phases found in all analysed samples is calcite. Tables 7.3a-r (Appendix 3) provide detailed major element compositions. Tables 5.3a-d supply average and standard deviation values of major elements of calcite.

Sövite 08SB39 exhibits consistent CaO contents in calcite (53-54 wt%) with the exception of a few analyses showing lower content (48-52 wt%). SrO enrichment (Table 5.3a) can be grouped into two bands, with higher concentrations of 0.91-2.26 wt% SrO (Table 5.3b-d) and lower ones 0.00-0.91 wt% (Table 5.3e-g). Variation in Sr content confirms petrographic observations that Sr-rich minerals found as inclusions in calcite show an association with Sr-poor regions. Thus Sr-rich phases, such as strontianite, grew on primarily Sr-rich calcite, consequently leaching Sr and depleting the adjacent area. Also the higher CaO values belong to the Sr-depleted sites (most likely an effect of Sr↔Ca substitution). In alvikite CaO varies from 54.5-57.8 wt% and SrO content is low (0.08-0.38 wt%) (Table 5.3a), indicating that calcite is of secondary origin. Calcite in the sövite is depleted in MgO, while calcite in the alvikite contains MgO in the range 0.23-2.21 wt% (Table 5.3a), creating additional Mg-poor and Mg-rich subdivisions. This confirms the petrographic feature of extremely fine-grained dissected Mg-poor calcite ‘islands’ being bordered by fine-grained Mg-rich calcite (slightly coarser and anhedral) displaying triple junctions (Figure 5.5a_C). MnO content in Mg-rich calcite averages 0.21wt% (Table 5.3d). The remnant calcite in the alvikite is depleted in Mn. Sövitic calcite displays variable enrichment in MnO

from 0.00-1.37 wt% (Table 5.3d). In the sövite Sr-rich calcite shows negligible FeO content, whereas in the Sr-poor part FeO can rich 2 wt% (Table 5.3a).

Silicate sample 08SB40, is a glimmerite-syenite-carbonatite. It contains calcite veins cross-cutting all lithologies, being Sr-poor (0.02-0.80 wt% SrO) with variable MgO (0.05-0.35 wt%) and FeO (0.26-0.58 wt%) contents. Thus, calcite is secondary, most likely derived from adjacent rocks. Carbonatite-zeolite sample 08SB43 contains Sr-rich and Sr-poor calcite (average 0.86 wt% and 0.19 wt% SrO respectively, Table 5.3a). SrO-rich calcite has higher MnO (average 1.25 wt%, Table 5.3a), while Sr-poor calcite contains insignificant MnO (average 0.05 wt%, Table 5.3a). MgO content is negligible while FeO shows slight enrichment in higher-Sr calcite (average 0.29 wt%, Table 5.3a). The chemistry and close association of calcite with late-stage zeolite points to crystallisation of calcite from hydrothermal fluids. The other zeolite-carbonatite sample 08SB44 contains primary high-Sr calcite (1.46-1.78 wt% SrO) and secondary Sr-poor calcite (0.00-0.44 wt% SrO). The primary calcite forms the main part of the sample, while the secondary calcite is responsible for net veining and inclusions in other minerals. A rare carbonate phase displays high SiO_2 (average 9.75 wt%), FeO (average 5.89 wt%), MgO (average 2.16 wt%), Al_2O_3 (average 2.99 wt%) and low CaO contents (average 38.86 wt%). This carbonate most likely exsolved from zeolite and/or inherited some elements from the silicate phase.

Syenites 08SB45 and 08SB46 contain calcite intimately associated with amphibole and pyroxene (respectively). 08SB45 has moderate concentrations of SrO in calcite (0.40-0.98 wt%) whereas in 08SB46 calcite is either Sr-rich (1.75-2.13 wt% SrO) or Sr-poor (0.11-0.34 wt% SrO). Sr-rich calcite is also devoid of MgO while Sr-poor calcite contains variable amounts of MgO (0.58-1.54 wt%). Calcite associated with amphibole contains substantial MnO from 0.13 to 1.12 wt%, while calcite in pyroxene lacks MnO.

Syenite 08SB47 is cut by a carbonatite vein, which contains Sr-rich calcite (1.36-2.17 wt%) with MnO (average 0.28 wt%). Calcite in the silicate part is minor though its SrO concentration is high (2.02 to 3.98 wt%), higher than calcite in the vein. The silicate part contains sporadic fine-grained calcite with lower Sr-content (0.32-0.99 wt%, and MnO value ranging 0.03-0.93 wt%. The highest Mn content is in calcite from the vein.

Syenite 08SB48 contains of calcite with lower SrO values (average range 0.52 to 0.83 wt%) which fringes higher-Sr calcite (average range 1.00-1.42 wt%), which is Mn- and Mg-poor. Lower SrO calcite contains substantial MnO (0.14-1.71 wt%) and is

depleted in MgO. Syenite 08SB49 contains calcite with low SrO content (0.07-0.39 wt%), low MnO (0.00-0.48 wt%), and variable enrichment in MgO (0.38-1.58 wt%), FeO (0.00-1.82 wt%), Al2O3 (0.13-3.11 wt%) and SiO2 (1.00-3.96 wt%). Appendix Table 7.3o includes chemistry of hydrothermally deposited carbonate phase (Figure 7.22). This phase has varying amounts of CaO (32.43-49.06 wt%), SiO_2 (4.08-15.43 wt%), Al_2O_3 (1.00-3.43 wt%), FeO (0.00-7.78 wt%), MnO (0.02-0.39 wt%), MgO (0.94-1.48) and is lacking in SrO. Secondary calcite associated with this site shows enrichment in SiO_2 content (1.00-3.96 wt%), Al_2O_3 (0.13-3.11 wt%), FeO (0.00-1.82 wt%), MnO (0.00-0.48 wt%), MgO (0.38-1.53 wt%) and SrO (0.07-0.39 wt%). The calcite-syenite 08SB50 has primary calcite showing enrichment in SrO from 1.13 to 2.16 wt% and MnO between 0.24-0.58 wt%.

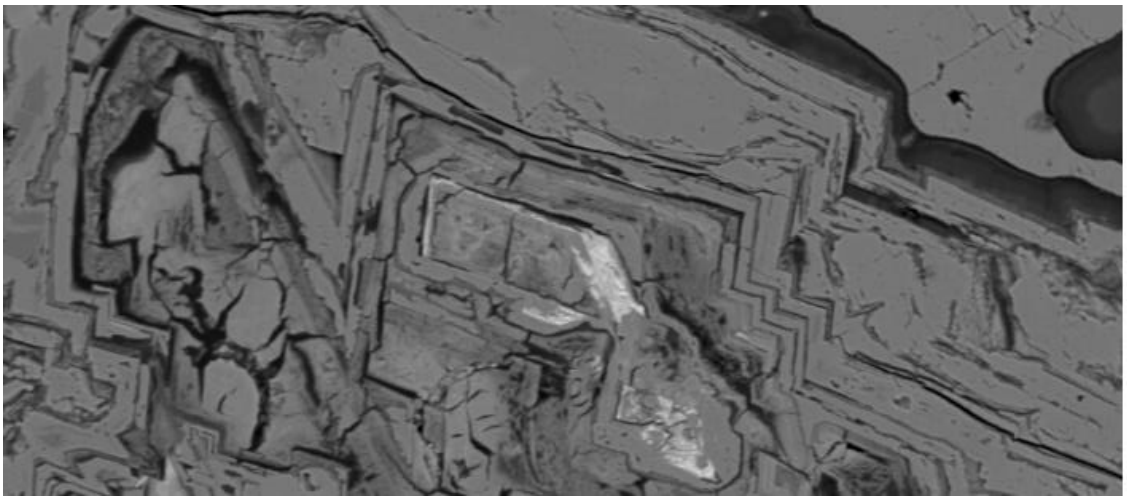

Fig 5.22 BSE image of Brava calcite-feldspar-syenite 08SB49 containing hydrothermally deposited calcite.

In summary calcite in analysed rocks shows high complexity of formation such as primary crystals; secondary recrystallisation; hydrothermal deposition of calcite in vugs leading to complex chemical diversity/zonation (multiple growth events) of calcite-carbonate phase; “patchy” depletion of calcite in some elements, such as Sr leading to formation of inclusions of rare phases such as strontianite; influence of metasomatic processes (albitization/calcification). Thus, the variable chemistry of calcite in all analysed samples records that different processes that have affected the investigated rocks.

5.4.2 Apatite

Apatite is an accessory phase found in only 6 analysed samples in L5 site. Tables 7.4a-c (Appendix 3) provide in detail major element composition of apatite. Table 5.4 supplies average and standard deviation values of major elements.

Apatite is present in both types of carbonatite. Crystals in sövite are elongated, reflecting fast growth. They show a close relationship with orthoclase. Apatite displays fluorine enrichment (1.39-2.13 wt%, Table 5.4a), so it a fluorapatite. Cl was not detected in analysed apatite. Small concentration of SiO_2 (average 0.63 wt%) is also detected, perhaps reflecting the association with silicate phases. Small variation in SrO (1.91-2.35 wt%, Table 5.4a), reflects stable substitution Ca↔Sr during fast crystallisation. Zhang et al. (2011) indicated that interaction with circulating fluids and the state of porosity of apatite can be related to the intensity of Sr enrichment. Total LREE contents are considerable, up to 1.49 wt% (Table 5.4a). Zhang et al. (2011) proposed that enrichment in LREE is also related to substitution Ca↔LREE and the availibity of these elements in fluids.

In alvikite 08SB38 apatite forms fine-grained anhedral crystals associated with calcite and amphibole but it is also found in vugs. All specimens show fluorine enrichment, 1.40-1.85 wt% (Table 5.4), thus can be classify as fluorapatite. Lack of Cl content is evident. SiO_2 (average 0.48 wt%) was also detected. Greater variation in Sr enrichment, compared to sövite, with 1.49-2.31 wt% SrO, reflects substitution Ca↔Sr, likewise the presence of LREE (up to 1.49 wt%) is related to substitution Ca↔LREE. Concentrations of La and Ce in apatite indicate the availability of these elements in circulated fluids.

Syenites contain rare apatite, often in association with rare minerals. In 08SB47, apatite exhibits an association with Nb-rich pyrochlore, suggesting simultaneous crystallisation. Apatite is F-rich (1.70-3.24 wt% F) with consistent SrO enrichment (2.06-2.31 wt%) and Nb_2O_5 (0.49 wt%), at the same time is lacking La and Ce. Broom-Fendley et al. (2016) investigated REE distribution in apatite. They came to the conclusion that changes in REE distribution, from early to late stage in the paragenetic sequence involve the combination of disolution and reprecipitation of apatite aided by transport of LREE by F- (and perhaps Cl-) bearing hydrothermal fluids. This leads to changes in REE distribution in apatite and perhaps transfer to adjacent pyrochlore. Thus, the presence of pyrochlore (enclosed by apatite) having LREE enrichment (while apatite itself lacks LREEs) and apatite inheriting some Nb can indicate two-way system of late-stage re-distribution of elements.

Feldspar-pegmatite 08SB49 contains sporadic apatite showing a close association with Mn-calcite and tazheranite, a rare Zr-rich phase. Apatite contains 70-2.18 wt% F (fluorapatite) and 1.87-2.14 wt% SrO. BaO has on average value of 0.63 wt%, MnO 0.27 wt%, whereas Ce_2O_3 is very low (0.10 wt%), and La_2O_3 also is low (0.43 wt%) but Na_2O is rather high (0.92 wt%). BaO average content in co-existing tazheranite is 0.99 wt% and MnO is 0.21 wt%. The apatite most likely crystallised during the last stages with involvement of hydrothermal fluids, thus causing some enrichment of apatite in elements like Mn and Ba, in which other late-stage minerals are also enriched.

Calcite-rich syenite 08SB46 contains fluorapatite with 1.32 wt% F and 1.79 wt% SrO. The average content of LREE (La and Ce) is low (0.59 wt%). In veined syenite-calcite 08SB50 a few euhedral crystals of apatite cluster together and are associated with primary (Sr-rich) calcite. These specimens are the most pristine of them all. Sample 08SB50 is a calcite-syenite and contains apatite of magmatic origin. It is also fluorapatite with SrO content higher than F (average 2.31 wt% and 1.75 wt% respectively, Table 5.4). Contents of Al_2O_3 and SiO_2 fall into the higher band than in the other investigated apatites (average values 2.68 wt% and 0.94 wt% respectively, Table 5.4). Lack of BaO and MnO is noticeable.

	ALVIKITE		SÖVITE		SYENITE		SYENITE		FELSIC PEGMATITE		SYENITE	
EDS	08SB38		08SB39		08SB46		08SB47		08SB49		08SB50	
APATITE	ave n=10	st dev n=10	ave n=10	st dev n=10	ave n=7	st dev n=7	ave n=3	st dev n=3	ave n=2	st dev n=2	ave n=2	st dev n=2
SiO_2	0.48	0.20	0.63	0.07	0.66	0.09	0.47	0.27	0.48	0.03	0.94	0.37
Al_2O_3	0.27	0.70	0.04	0.04	0.12	0.19	0.18	0.26	0.11	0.07	2.68	2.00
MnO	0.06	0.08	0.05	0.08	0.17	0.15	0.12	0.16	0.27	0.12	0.12	0.09
MgO	0.03	0.05	0.02	0.02	0.03	0.04	0.03	0.03	0.05	0.06	0.01	0.00
CaO	55.69	0.87	54.55	0.89	55.34	0.69	54.68	0.37	55.49	0.68	52.52	1.20
Na_2O	0.09	0.05	0.13	0.07	0.10	0.05	0.07	0.04	0.92	0.03	0.09	0.04
BaO	0.14	0.17	0.03	0.09	0.06	0.09	0.14	0.17	0.63	0.08	0.00	0.00
P_2O_5	37.70	0.68	37.75	0.38	37.80	0.40	37.84	0.27	36.63	0.09	36.54	0.45
La_2O_3	0.19	0.27	0.26	0.23	0.30	0.28	0.11	0.18	0.43	0.30	0.22	0.30
Ce_2O_3	0.35	0.27	0.49	0.33	0.29	0.27	0.09	0.11	0.10	0.13	0.10	0.14
Nd_2O_3	0.11	0.16	n/a	n/a	0.39	0.19	0.07	0.12	0.34	0.37	0.37	0.04
SrO	1.89	0.25	2.11	0.22	1.79	0.17	2.21	0.13	2.01	0.19	2.31	0.10
F	1.67	0.15	1.76	0.24	1.32	0.19	2.47	0.77	1.94	0.34	1.75	0.43
TOTAL	98.80	0.60	97.84	0.81	98.55	0.33	98.60	0.17	99.48	0.03	97.99	0.81
Cations recalculated on the basis of 25 oxygens												
Si	0.08	0.03	0.03	0.05	0.11	0.01	0.08	0.05	0.08	0.01	0.16	0.06
Al	0.05	0.14	0.00	0.01	0.02	0.04	0.04	0.05	0.02	0.01	0.53	0.39
Mn	0.01	0.01	0.00	0.00	0.02	0.02	0.02	0.02	0.04	0.02	0.02	0.01
Mg	0.01	0.01	0.00	0.01	0.01	0.01	0.01	0.01	0.01	0.02	0.00	0.00
Ca	10.08	0.13	5.02	5.30	10.07	0.14	9.78	0.06	10.05	0.18	9.50	0.29
Na	0.03	0.02	0.01	0.02	0.03	0.02	0.02	0.01	0.30	0.01	0.03	0.01
Ba	0.01	0.01	0.00	0.00	0.00	0.01	0.01	0.01	0.04	0.01	0.00	0.00
P	5.39	0.07	0.38	0.50	5.44	0.04	5.35	0.08	5.24	0.01	5.22	0.10
La	0.01	0.02	7.66	2.27	0.02	0.02	0.01	0.01	0.03	0.02	0.01	0.02
Ce	0.02	0.02	0.02	0.03	0.02	0.02	0.01	0.01	0.01	0.01	0.01	0.01
Nd	0.01	0.01	n/a	n/a	0.02	0.01	0.00	0.01	0.02	0.02	0.02	0.00
Sr	0.18	0.02	0.04	0.04	0.18	0.02	0.21	0.01	0.20	0.02	0.23	0.01
F	0.89	0.08	0.19	0.05	0.71	0.10	1.30	0.39	1.04	0.18	0.93	0.24
TOTAL	16.79	0.06	13.36	3.40	16.70	0.04	16.88	0.18	17.17	0.03	16.72	0.11

Table 5.4 Electron microprobe data for apatite in the Brava intrusive alkaline complex. Abbreviations: st dev=standard deviation, ave=average. Cations recalculated on the basis of 12 oxygens. Complete tables supplied in Appendix 3a. Some elements are below detection limit

Although apatite is scarce its existence can deliver important information about the processes affecting the alkaline-carbonatite complex. Apatite can crystallise at different stages, from early to late magmatic and can continue to late hydrothermal stages

(Kapustin 1980; Hogarth 1989). Thus, alongside primary magmatic apatite, other secondary crystals can be found. As Broom-Fendley et al. (2016) determined, sometimes the absence of particular minerals, such as monazite (as a dissolution product after apatite) can provide indirect evidence for dissolution-reprecipitation of apatite and transfer of LREE towards the rim, most likely in presence of Cl-rich fluids (they provide greater stability for fractionation of LREE).

5.4.3 Pyroxene and amphibole

Analysed pyroxenes in L5 sample are plotted in Figure 5.5 (full data in Tables 7.5a-e, Appendix 3a). Pyroxenes are of following compositions: aegirine-augite found in alvikite (08SB38), syenite cut by alkali-feldspar (08SB48) and calcite-syenite (08SB46); diopside found also in alvikite (08SB38), calcite-syenite (08SB46) and zeolite-carbonatite (08SB44); pyroxene in the syenite cut by carbonatite (08SB47) belong to the field bordering enstatite and pigeonite. Orthopyroxene-clinopyroxene assemblage in 08SB47 exists as a minor constituent (perhaps a remnant phase) and is found alongside frequently present ferro-eckermanite to ferro-richterite amphibole Coexistence of orthopyroxene and clinopyroxene in one crystal in syenite implies slow cooling during which pigeonite re-equilibrated to orthopyroxene and consequently exsolution of clinopyroxene occurred. Overall the pyroxene range (Figure 5.23) shows a good linear and continuous trend demonstrating the evolution of pyroxene in the alkaline-carbonatite complex. Ca-Mg-rich clinopyroxene in alvikite (most primitive with regards to the Fe and Na assemblage) fractionated towards more Na-Fe-enriched clinopyroxene reaching the most evolved state of pyroxene which is aegirine.

EDS	SB48 SODIC- ave n=7	st dev	SB48 Na-AEG- ave n=7	st dev	SB38 AEG- ave n=2	st dev	SB46 AEG- ave n=3	st dev	SB38 DIOPSIDE ave n=6	st dev	SB44 DIOPSIDE ave n=14	st dev	SB46 DIOPSIDE ave n=19	st dev	SB47 PIGEONITE ave n=2	st dev	SB47 ENSTATITE ave n=4	st dev
SiO_2	51.35	0.70	51.28	0.46	49.36	0.08	50.71	1.05	50.53	0.56	48.27	0.03	49.58	0.56	53.05	0.68	53.25	0.25
TiO_2	1.58	0.75	0.77	0.41	0.55	0.12	0.37	0.10	0.29	0.17	0.96	0.30	0.62	0.20	0.46	0.15	0.36	0.14
Al_2O_3	1.15	0.20	1.15	0.24	1.91	0.11	1.39	0.51	1.66	0.33	2.81	0.73	1.91	0.26	1.21	0.48	1.23	0.16
FeO	11.14	1.45	11.58	0.90	8.11	0.98	8.00	1.23	5.87	0.71	7.31	0.77	7.81	0.85	1.73	2.44	1.88	1.31
Fe_2O_3	18.21	2.58	15.46	1.50	7.88	0.05	7.66	0.51	6.03	1.99	6.11	1.28	7.87	0.69	14.54	1.68	14.59	1.70
MnO	0.91	0.31	0.82	0.39	0.63	0.01	0.63	0.26	0.39	0.18	0.48	0.13	0.54	0.17	0.20	0.04	0.29	0.20
MgO	0.11	0.11	1.60	1.07	7.88	0.21	8.13	0.13	10.10	1.34	9.29	0.70	8.47	0.27	25.59	0.33	25.75	0.83
CaO	1.14	0.27	3.91	1.89	19.02	0.16	17.89	1.31	20.34	1.64	21.16	0.91	19.91	0.50	2.53	0.08	2.33	0.08
Na_2O	10.57	0.28	8.98	0.92	2.71	0.03	3.29	0.70	2.18	0.51	1.79	0.35	2.31	0.20	0.05	0.07	0.02	0.02
K_2O	0.04	0.04	0.04	0.05	0.01	0.01	0.01	0.02	0.03	0.04	0.01	0.02	0.03	0.03	0.00	0.00	0.04	0.06
La_2O_3	0.55	0.55	0.62	0.42	0.08	0.11	0.36	0.12	0.23	0.08	0.20	0.18	0.07	0.12	0.46	0.15	0.04	0.08
Ce_2O_3	0.25	0.38	0.36	0.36	0.03	0.04	0.24	0.17	0.05	0.09	0.04	0.06	0.02	0.06	0.27	0.23	0.03	0.05
Nd_2O_3	0.53	0.34	0.53	0.35	0.00	0.00	0.18	0.22	0.09	0.11	0.18	0.18	0.11	0.17	0.09	0.12	0.16	0.19
BaO	0.57	0.53	0.48	0.53	0.33	0.08	0.15	0.14	0.30	0.27	0.27	0.27	0.09	0.13	0.32	0.13	0.04	0.06
ZrO_2	0.34	0.27	0.63	0.42	0.22	0.02	0.33	0.08	0.33	0.13	0.29	0.07	0.24	0.13	0.08	0.08	0.04	0.05
Nb_2O_5	0.23	0.23	0.29	0.32	0.08	0.03	0.25	0.05	0.08	0.09	0.18	0.18	0.21	0.17	0.00	0.00	0.00	0.00
PbO	0.36	0.24	0.08	0.08	0.08	0.11	0.07	0.08	0.07	0.09	0.09	0.14	0.11	0.11	0.00	0.00	0.04	0.07
ThO_2	0.23	0.29	0.19	0.33	0.07	0.10	n/a	n/a	0.15	0.13	n/a	n/a	n/a	n/a	0.00	0.00	0.18	0.25
UO_2	0.32	0.37	0.34	0.30	0.16	0.11	n/a	n/a	0.09	0.11	n/a	n/a	n/a	n/a	0.09	0.13	0.19	0.20
TOTAL	99.55	0.37	99.08	0.30	99.08	2.38	99.66	0.71	98.95	0.71	99.43	0.77	99.91	0.73	100.63	0.27	100.44	0.76
Cations recalculated on the basis of 6 oxygens																		
Si	2.06	0.01	2.07	0.01	1.92	0.01	1.96	0.02	1.95	0.02	1.87	0.04	1.91	0.01	1.94	0.04	1.94	0.02
Ti	0.05	0.02	0.02	0.01	0.02	0.00	0.01	0.00	0.01	0.01	0.03	0.01	0.02	0.01	0.01	0.00	0.01	0.00
Al	0.05	0.01	0.05	0.01	0.09	0.01	0.06	0.02	0.08	0.01	0.13	0.03	0.09	0.01	0.05	0.02	0.05	0.01
Fe^{3+}	0.55	0.07	0.47	0.04	0.24	0.03	0.23	0.03	0.17	0.02	0.21	0.02	0.23	0.02	0.05	0.07	0.05	0.04
Fe^{2+}	0.37	0.05	0.39	0.03	0.26	0.00	0.25	0.02	0.20	0.07	0.20	0.04	0.25	0.02	0.45	0.06	0.45	0.06
Mn	0.03	0.01	0.03	0.01	0.02	0.00	0.02	0.01	0.01	0.01	0.02	0.00	0.02	0.01	0.01	0.00	0.01	0.01
Mg	0.01	0.01	0.10	0.06	0.46	0.01	0.47	0.01	0.58	0.07	0.54	0.04	0.49	0.01	1.39	0.01	1.40	0.04
Ca	0.05	0.01	0.17	0.08	0.79	0.01	0.74	0.06	0.84	0.06	0.88	0.03	0.82	0.02	0.10	0.00	0.09	0.00
Na	0.82	0.01	0.70	0.07	0.20	0.00	0.25	0.05	0.16	0.04	0.13	0.03	0.17	0.02	0.00	0.00	0.00	0.00
K	0.00	0.00	0.00	0.00	0.00	0.00	0.00	0.00	0.00	0.00	0.00	0.00	0.00	0.00	0.00	0.00	0.00	0.00
TOTAL	4.00		4.00		4.00		4.00		4.00		4.00		4.00		4.00		4.00	

Table 5.5a Electron microprobe data for pyroxene in the Brava intrusive alkaline complex. Abbreviations: st dev=standard deviation, ave=average. Cations recalculated on the basis of 12 oxygens. Complete tables supplied in Appendix 3a. Some elements are below detection limit.

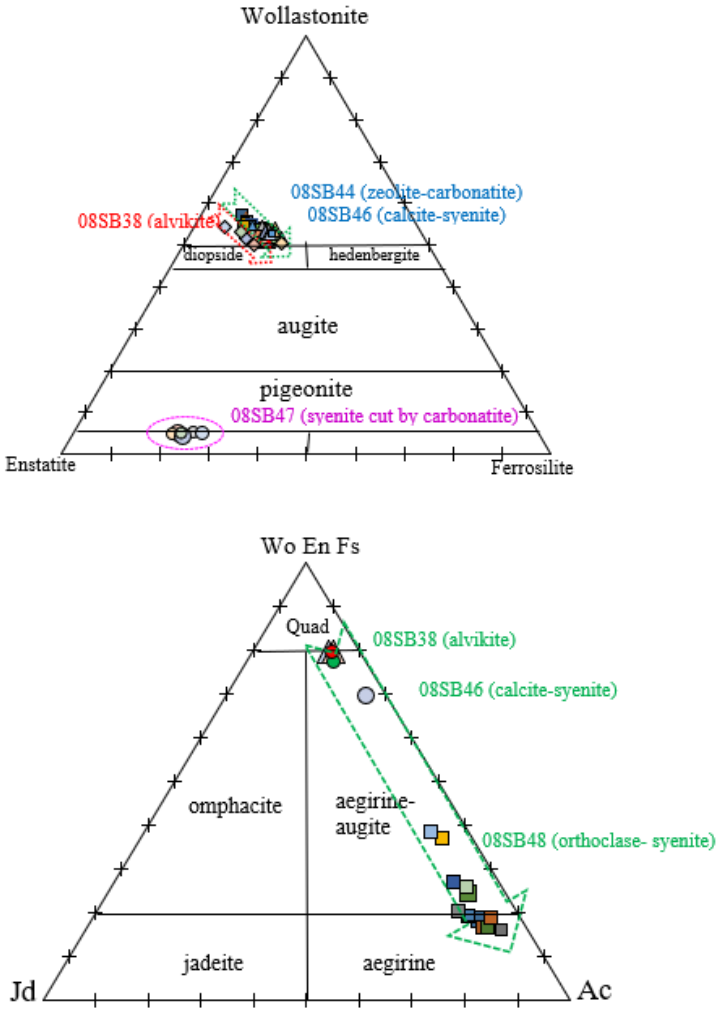

Fig 5.23 Pyroxene composition from Brava intrusive complex plotted on the Jd-Ac-WoEnFs and Enstatite-Ferrosilite-Wollastonite diagrams.

TiO_2 concentration (Table 5.5a-e) in diopside in alvikite ranges from 0.16 to 0.62 wt%; in calcite-syenite 0.16-0.92 wt% and in zeolite-carbonatite 0.60-1.47 wt%. In aegirine-augite in the calcite-syenite sample TiO_2 is 0.26-0.45 wt%, in alvikite 0.48-0.63 wt%, orthoclase-syenite TiO_2 concentration varies between 0.20-1.07 wt% and in aegirine (in the same sample) concentration falls between 0.74-2.47 wt%. TiO_2 concentration in enstatite-pigeonite in carbonatite-syenite shows lowest range (0.18-0.56 wt%). Thus, generally Ti contents in clinopyroxene increase from diopside towards aegirine-augite and aegirine. Enstatite with pigeonite is mostly depleted. Pyroxene is also slightly enriched in ZrO_2. In diopside ZrO_2 content varies: in alvikite between 0.23-0.55 wt%, in calcite-syenite 0.00-0.50 wt% and in zeolite-carbonatite 0.15-0.40 wt%. In aegirine-augite the value varies: in alvikite between 0.20-0.23 wt%, and orthoclase-syenite 0.04-1.17 wt% and calcite-syenite 0.28-0.43 wt%. In aegirine ZrO_2 is present in

orthoclase-syenite 0.00-0.57 wt%. Enstatite-pigeonite is mostly depleted in Zr content (0.00-0.13 wt%). Total average value of LREEs in 08SB46 approaches 0.60 wt%. The highest average concentration of La_2O_3 (0.62 wt%) was found in aegirine-augite in orthoclase-syenite 08SB48 (Table 7.4.3a), which also holds considerable concentration of Ce_2O_3 (0.36 wt%) giving total LREEs value of 1wt%. Combined average sum of ThO_2 and UO_2 in the same sample is around 0.50 wt% in both aegirine and aegirine-augite.

In summary the pyroxene fractionation trend projects from diopside towards aegirine. Clinopyroxene progressively becomes more enriched in trace elements such as Zr, Th, U and LREEs, thus the evolved end-members exhibit and increasing tendency to partition these trace elements into aegirine and aegirine-augite.

Amphibole is the most abundant mafic mineral in samples from the L5 site. The Mg-Ca-Na plot of amphiboles (Figure 5.24) reveals an evolution towards Na (alkali enrichment). The linear trend also reflects a steady Mg/Ca ratio with slight diversion in sövite away from Mg-peak. The most primitive amphibole in the analysed suite is edenite (found in zeolite-carbonatite), which fractionated towards sodic edenite (found in the syenitic part of glimmerite-composite sample). Amphibole in syenite part of glimmeritic rock shows further fractionation towards eckermannite. Alvikite contains ferro-richterite and eckermannite.

Sövite amphibole is mostly of ferro-eckermannite and manganoan-ferro–richterite (Figure 5.25). Amphibole in sövite sometimes exhibits patchy zoning with considerable enrichment in MnO. The Mn-rich regions in amphibole contain 2.5 wt% MnO, leading this phase to alter from calcian to manganoan-rich phase (Figure 5.25). The branching trend away from alkali enrichment reflects localised Mn substitution for Mg (MgO content of this amphibole falls to 0.96 wt% from around 3 wt%, Table 5.5b). Further along the evolution trend, calcian-ferro-eckermannite is common in the calcite-syenite, syenite cut by carbonatite, syenite cut by calcite vein and feldspar-foid-vein samples, though here it is of titanian composition where the analysed crystals reach the end of their fractionation trend.

Overall, the suite of rocks progressively becoming more alkaline, with Na being the main alkaline component as K has a little bearing on the amphibole composition. The linear trend also reflects a steady Mg/Ca ratio with slight diversion in sövite away from Mg-peak. The most primitive amphibole in the analysed suite is edenite (found in zeolite-carbonatite), which fractionated towards sodic edenite (found in the syenitic part of glimmerite-composite sample). Amphibole in syenite part of glimmeritic rock shows further fractionation towards eckermannite. Alvikite contains ferro-richterite and

eckermannite. Sövite amphibole is mostly of ferro-eckermannite and manganoan-ferro–richterite (Figure 5.25).

SÖVITE								
08SB39	CALCIAN-FERRO-ECKERMANNITE		MANGANOAN FERRO-		FERRO-RICHTERITE		FERRO-RICHTERITE	
EDS	ave n=10	st dev n=10	ave n=6	st dev n=6	ave n=25	st dev n=25	ave n=13	st dev n=13
SiO_2	49.74	*1.24*	48.39	*0.54*	49.83	*0.66*	49.51	*0.60*
TiO_2	0.43	*0.20*	0.67	*0.52*	0.41	*0.10*	0.38	*0.10*
Al_2O_3	0.89	*0.13*	0.86	*0.12*	0.92	*0.36*	0.86	*0.13*
FeO	22.62	*0.44*	23.30	*0.91*	22.34	*0.78*	22.38	*0.55*
MnO	0.63	*0.59*	2.52	*0.53*	0.57	*0.34*	0.58	*0.31*
MgO	2.66	*0.43*	0.96	*0.83*	3.04	*0.56*	3.16	*0.34*
CaO	6.91	*0.55*	7.39	*0.70*	7.96	*0.69*	8.21	*0.66*
Na_2O	7.48	*0.20*	6.88	*0.25*	6.94	*0.28*	6.85	*0.28*
K_2O	0.04	*0.04*	0.06	*0.06*	0.04	*0.05*	0.04	*0.04*
La_2O_3	0.11	*0.13*	0.29	*0.35*	0.10	*0.14*	0.07	*0.13*
Ce_2O_3	0.60	*0.74*	0.89	*0.38*	0.37	*0.42*	0.67	*0.38*
BaO	0.13	*0.16*	0.37	*0.26*	0.12	*0.13*	0.11	*0.13*
ZrO_2	0.50	*0.57*	0.10	*0.25*	0.50	*0.47*	0.14	*0.35*
Nb_2O_5	0.26	*0.24*	0.14	*0.11*	0.23	*0.21*	0.21	*0.22*
H_2O*	1.82	*0.03*	1.78	*0.02*	1.83	*0.02*	1.83	*0.02*
TOTAL	94.81	*0.81*	94.58	*0.80*	95.20	*0.82*	95.01	*0.95*
Cations recalculated on the basis of 23 oxygens								
Si	8.18	*0.08*	8.11	*0.06*	8.13	*0.07*	8.10	*0.07*
Al^{iv}	0.00	*0.00*	0.00	*0.00*	0.00	*0.00*	0.00	*0.00*
Al^{vi}	0.17	*0.02*	0.17	*0.02*	0.18	*0.07*	0.17	*0.03*
Ti	0.05	*0.02*	0.08	*0.07*	0.05	*0.01*	0.05	*0.01*
Fe^{3+}	0.00	*0.00*	0.00	*0.00*	0.00	*0.00*	0.00	*0.00*
Fe^{2+}	3.11	*0.07*	3.27	*0.15*	3.05	*0.12*	3.06	*0.07*
Mn	0.09	*0.08*	0.36	*0.08*	0.08	*0.05*	0.08	*0.04*
Mg	0.65	*0.10*	0.24	*0.20*	0.74	*0.13*	0.77	*0.08*
Ca	1.22	*0.10*	1.33	*0.11*	1.39	*0.12*	1.44	*0.11*
Na	2.38	*0.04*	2.24	*0.10*	2.20	*0.08*	2.17	*0.09*
K	0.01	*0.01*	0.01	*0.01*	0.01	*0.01*	0.01	*0.01*
Ba	0.01	*0.01*	0.00	*0.01*	0.00	*0.01*	0.00	*0.00*
TOTAL	17.88	*0.06*	17.84	*0.07*	17.83	*0.06*	17.86	*0.06*
$Mg/(Mg+Fe^{2})$	0.17	*0.03*	0.07	*0.06*	0.19	*0.03*	0.20	*0.02*

Table 5.5b Electron microprobe data for amphibole in the Brava intrusive alkaline complex. Abbreviations: st dev=standard deviation, ave=average. Cations recalculated on the basis of 23 oxygens. Complete tables in Appendix 3a. Some elements are below detection limit.

	EDS						WDS		EDS				
	CALCIAN-FERRO-ECK	FERRO-RICHTERITE		CALCIAN-FERRO-ECKERMANNITE		FERRO RICHTERITE	IN SYENITE CALCIAN-FERRO-ECKERMANNITE		FERRO-ECKERMANNITE		FERRO-RICHTERITE		Ti-FERRO-RICHTERITE
	SB38ave n=1	ave n=11	st dev n=11	SB40ave n=2	st dev n=2	SB40ave n=1	ave n=5	st dev n=5	SB45ave n=10	st dev n=10	ave n=5	st dev n=5	SB45ave n=1
SiO_2	51.26	51.37	*0.24*	48.60	*0.61*	48.83	48.53	*0.75*	49.52	*0.58*	49.80	*0.55*	48.37
TiO_2	0.69	0.43	*0.17*	0.84	*0.18*	1.07	0.93	*0.67*	1.06	*0.79*	0.56	*0.35*	2.17
Al_2O_3	1.05	1.07	*0.18*	1.42	*0.11*	1.43	1.86	*0.62*	1.10	*0.22*	0.93	*0.22*	0.96
FeO	26.47	20.03	*0.95*	24.94	*0.51*	24.65	23.03	*2.33*	22.94	*0.43*	22.55	*0.86*	22.54
MnO	0.00	0.51	*0.17*	0.78	*0.08*	0.79	0.88	*0.10*	1.29	*0.50*	1.18	*0.39*	0.77
MgO	1.80	5.07	*0.49*	1.17	*0.11*	1.30	3.13	*1.32*	2.65	*0.47*	3.22	*0.29*	2.90
CaO	3.56	9.27	*0.93*	7.68	*0.43*	8.59	11.14	*1.64*	6.86	*0.41*	7.78	*0.28*	7.97
Na_2O	9.48	6.87	*0.33*	7.42	*0.66*	7.03	8.72	*1.09*	7.72	*0.19*	7.34	*0.15*	7.26
K_2O	0.00	0.04	*0.05*	0.00	*0.00*	0.00	0.01	*0.02*	0.05	*0.04*	0.02	*0.02*	0.00
BaO	0.10	0.16	*0.15*	0.14	*0.20*	0.30	n/a	*n/a*	0.24	*0.22*	0.16	*0.13*	0.18
ZrO_2	0.55	0.47	*0.21*	0.28	*0.11*	0.54	n/a	*n/a*	0.47	*0.27*	0.67	*0.29*	0.43
H_2O*	1.87	1.91	*0.01*	1.85	*0.03*	1.89	1.91	*0.02*	1.85	*0.02*	1.85	*0.02*	1.84
TOTAL	98.08	97.80	*0.64*	95.74	*1.46*	96.56	100.15	*0.44*	96.29	*0.63*	96.72	*1.39*	96.38
Cations recalculated on the basis of 23 oxygens													
Si	8.23	8.05	*0.05*	8.10	*0.18*	8.15	7.60	*0.12*	8.03	*0.04*	8.05	*0.01*	7.88
Al ^{iv}	0.00	0.00	*0.01*	0.01	*0.02*	0.00	0.33	*0.10*	0.00	*0.01*	0.00	*0.00*	0.12
Al ^{vi}	0.20	0.19	*0.03*	0.23	*0.05*	0.19	0.01	*0.02*	0.21	*0.04*	0.18	*0.04*	0.06
Ti	0.08	0.05	*0.02*	0.09	*0.01*	0.03	0.11	*0.08*	0.13	*0.10*	0.07	*0.04*	0.27
Fe^{3+}	0.00	0.00	*0.00*	0.00	*0.00*	0.00	0.00	*0.00*	0.00	*0.00*	0.00	*0.00*	0.00
Fe^{2+}	3.55	2.63	*0.14*	3.33	*0.31*	2.84	3.02	*0.34*	3.11	*0.06*	3.05	*0.11*	3.07
Mn	0.00	0.07	*0.02*	0.06	*0.09*	0.07	0.12	*0.01*	0.18	*0.07*	0.16	*0.05*	0.11
Mg	0.43	1.18	*0.11*	0.58	*0.21*	1.01	0.73	*0.30*	0.64	*0.11*	0.78	*0.07*	0.70
Ca	0.61	1.56	*0.15*	0.94	*0.47*	1.31	1.87	*0.26*	1.19	*0.07*	1.35	*0.05*	1.39
Na	2.95	2.09	*0.11*	2.63	*0.45*	2.23	2.65	*0.36*	2.43	*0.05*	2.30	*0.03*	2.29
K	0.00	0.01	*0.01*	0.01	*0.02*	0.00	0.00	*0.00*	0.01	*0.01*	0.00	*0.00*	0.00
Ba	0.01	0.01	*0.01*	0.01	*0.00*	0.00	0.00	*0.00*	0.02	*0.01*	0.01	*0.01*	0.01
TOTAL	16.06	15.84	*0.04*	16.01	*0.08*	*15.84*	18.44	*0.16*	*15.95*	*0.08*	15.94	*0.05*	15.90

Table 5.5c Electron microprobe data for amphibole in Brava alkaline complex. Abbreviations: st dev=standard deviation, ave=average. Cations recalculated on the basis of 23 oxygens.

	CALCIAN-FERRO-ECKERMANNITE		FERRO-RICHTERITE		CALCIAN-FERRO-ECKERMANNITE		FERRO-ECKERMANNITE		CALCIAN-FERRO-ECKERMANNITE		FERRO-RICHTERITE		Ba-MnTi-Ca-Fe-ECKERM
EDS	SB47ave n=12	st dev n=12	ave n=2	st dev n=2	SB49ave n=7	st dev n=7	ave n=2	st dev n=2	SB50ave n=8	st dev n=8	ave n=3	st dev n=3	SB50ave n=1
SiO_2	50.99	*0.74*	50.35	*0.39*	49.75	*0.37*	50.64	*0.56*	50.62	*0.42*	50.48	*0.51*	48.54
TiO_2	0.47	*0.15*	0.49	*0.12*	0.68	*0.15*	1.91	*0.13*	0.68	*0.59*	0.41	*0.16*	2.58
Al_2O_3	1.15	*0.94*	0.84	*0.05*	1.11	*0.14*	0.62	*0.06*	1.18	*0.69*	0.78	*0.06*	1.51
FeO	24.28	*1.27*	23.01	*0.47*	25.72	*0.57*	26.57	*0.23*	23.14	*1.56*	22.64	*0.15*	23.91
MnO	0.38	*0.11*	0.48	*0.03*	0.79	*0.09*	1.00	*0.20*	0.73	*0.51*	0.72	*0.05*	3.10
MgO	2.75	*0.32*	3.18	*0.04*	1.33	*0.39*	0.87	*0.39*	2.81	*0.47*	3.15	*0.11*	1.03
CaO	6.61	*0.80*	8.01	*0.14*	5.18	*1.12*	0.66	*0.06*	6.41	*0.55*	7.70	*0.17*	4.91
Na_2O	8.08	*0.41*	7.39	*0.13*	8.36	*0.47*	10.34	*0.06*	8.13	*0.33*	7.42	*0.09*	8.33
K_2O	0.03	*0.05*	0.03	*0.04*	0.04	*0.05*	0.02	*0.01*	0.04	*0.04*	0.04	*0.06*	0.01
Nd_2O_3	0.15	*0.17*	0.30	*0.18*	0.16	*0.21*	0.15	*0.11*	0.13	*0.12*	0.29	*0.44*	0.23
BaO	0.03	*0.06*	0.00	*0.00*	0.17	*0.15*	0.60	*0.00*	0.14	*0.16*	0.21	*0.14*	1.01
ZrO_2	0.59	*0.19*	0.75	*0.32*	0.76	*0.26*	0.48	*0.07*	0.85	*0.53*	0.43	*0.19*	0.33
H_2O*	1.87	*0.03*	1.85	*0.03*	1.83	*0.02*	1.83	*0.03*	1.87	*0.02*	1.86	*0.01*	1.85
TOTAL	97.77	*0.80*	97.01	*0.30*	96.34	*0.85*	96.48	*2.16*	97.33	*0.74*	96.81	*0.25*	97.85
Cations recalculated on the basis of 23 oxygens													
Si	8.12	*0.07*	8.09	*0.01*	8.15	*0.05*	8.29	*0.03*	8.12	*0.06*	8.13	*0.04*	7.89
Al ^{iv}	0.00	*0.01*	0.00	*0.00*	0.00	*0.00*	0.00	*0.00*	0.00	*0.00*	0.00	*0.00*	0.11
Al ^{vi}	0.21	*0.16*	0.16	*0.01*	0.21	*0.03*	0.12	*0.01*	0.22	*0.13*	0.15	*0.01*	0.18
Ti	0.06	*0.02*	0.06	*0.01*	0.08	*0.02*	0.24	*0.02*	0.08	*0.07*	0.05	*0.02*	0.32
Fe^{3+}	0.00	*0.00*	0.00	*0.00*	0.00	*0.00*	0.00	*0.00*	0.00	*0.00*	0.00	*0.00*	0.00
Fe^{2+}	3.23	*0.18*	3.09	*0.03*	3.52	*0.10*	3.64	*0.02*	3.11	*0.24*	3.05	*0.04*	3.25
Mn	0.05	*0.01*	0.07	*0.00*	0.11	*0.01*	0.14	*0.03*	0.10	*0.07*	0.10	*0.01*	0.43
Mg	0.65	*0.08*	0.76	*0.02*	0.32	*0.09*	0.21	*0.09*	0.67	*0.10*	0.76	*0.03*	0.25
Ca	1.13	*0.14*	1.38	*0.04*	0.91	*0.19*	0.11	*0.01*	1.10	*0.08*	1.33	*0.04*	0.85
Na	2.50	*0.12*	2.30	*0.02*	2.66	*0.17*	3.28	*0.03*	2.53	*0.12*	2.32	*0.02*	2.62
K	0.01	*0.01*	0.01	*0.01*	0.01	*0.01*	0.00	*0.00*	0.01	*0.01*	0.01	*0.01*	0.00
Ba	0.00	*0.00*	0.00	*0.00*	0.01	*0.01*	0.04	*0.00*	0.01	*0.01*	0.01	*0.01*	0.06
TOTAL	15.96	*0.06*	15.92	*0.02*	17.99	*0.05*	18.06	*0.03*	17.95	*0.10*	17.90	*0.05*	17.96

Table 5.5d Electron microprobe data for amphibole in the Brava alkaline complex. Abbreviations: st dev=standard deviation, ave=average. Cations recalculated on the basis of 23 oxygens.

Amphibole in sövite sometimes exhibits patchy zoning with considerable enrichment in MnO. The Mn-rich regions in amphibole contain 2.5 wt% MnO, leading this phase to alter from calcian to manganoan-rich phase (Figure 5.25). Thus the branching trend away from alkali enrichment reflects localised Mn substitution for Mg (MgO content of this amphibole falls to 0.96 wt% from around 3 wt%, Table 5.5b). Further along the evolution trend, calcian-ferro-eckermannite is common in the calcite-syenite, syenite cut by carbonatite, syenite cut by calcite vein and feldspar-foid-vein samples, though here it is of titanian composition.

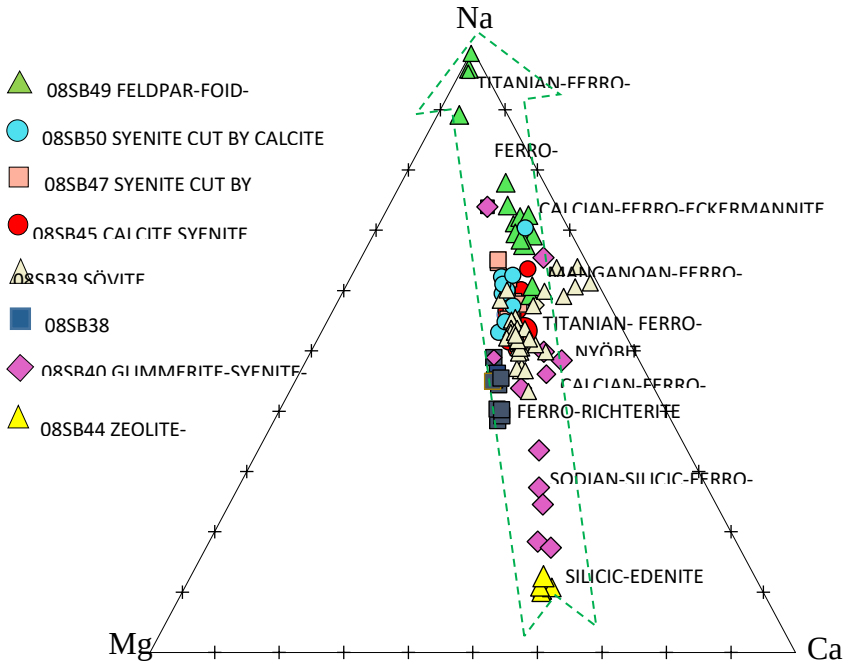

Fig 5.24 Chemical variation diagram of Brava amphibole as a function of Mg-Ca-Na.

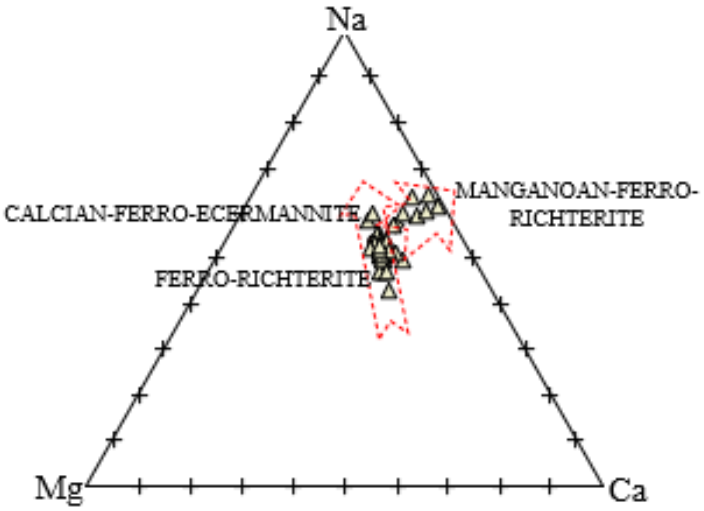

Fig 5.25 Chemical variation diagram of amphibole in Brava sövite as a function of Mg-Ca-Na. The main trend towards alkali enrichment is branching away from Mg

There is a slight enrichment in Zr content in amphibole from the sövite though ZrO_2 fluctuates from 0.50wt% in calcian-ferro-eckermanite to 0.10 wt% in manganoan-ferro-richterite, and in ferro-richterite it varies between 0.14 and 0.50 wt% (Table 5.5b). Then the rest of the analysed samples show a steady average ZrO_2 concentration of 0.5 wt% (Table 5.5c-d). In sövite, amphibole contains some LREEs. The average Ce_2O_3 are 0.37-0.89 wt%, while La_2O_3 average concentration

is 0.07- 0.29 wt% (Table 5.5b). Amphiboles in silicate samples are depleted in Ce_2O_3. Contrary to the low La_2O_3 content in sövite, amphibole in some silicate samples shows higher average concentration of La_2O_3 in ferro-richterite-eckermannite (0.35-0.37 wt%) (Table 5.5 c-d). Thus amphibole shows some enrichment in LREEs and trace elements.

In summary the trace element enrichment such as Zr in amphiboles show higher values than in pyroxenes but both mafic phases contain this element to some degree. The LREEs in pyroxenes show variable content (from being depleted to being enriched up to 1 wt% in total) though the amphiboles show preference for Ce incorporation into sövite rather than silicate samples.

5.4.4 Orthoclase

Alkali feldspar is not as widespread as amphibole or calcite though it was detected in four samples (08SB39, 08SB45, 08SB48 and 08SB50). The high abundance of feldspar in those samples is noticeable as feldspar-rich veins cross-cut several lithologies. Feldspars from L5 site are plotted on Ab-Or-An diagram in Figure 5.26 (full data is in Tables 7.6a-e, Appendix 3a). The plot reveals that alkali feldspars fall into two groups: one being close to pure orthoclase (Or_{95-100}) which is found in sövite 08SB39 and syenites 08SB45, 08SB48 and 08SB50; the second group puts feldspar in the orthoclase field with some Ab-component (Or_{80-85}) and is found in syenites 08SB45 and 08SB48. Figure 5.14A and C reveals that alkali feldspars with lower Or-content belong to the pegmatite facies, where coarse-grained feldspar shows inhomogeneity exsolving rare elongated patches with Or_{80-85} composition (implying slow cooling of alkali feldspar-rich body). The smaller prismatic feldspar crystals in the syenitic body are close to pure orthoclase (Or_{95-100}). No obvious zonation was detected with the exception of exsolution in pegmatitc alkali feldspars.

Table 5.6a reveals that average concentration of BaO in sövite is low (0.25-0.36 wt%). In syenites BaO is somewhat variable. Thus, in 08SB48 the average is 0.16 wt% (WDS) and 0.33-0.52 wt% (EDS)), in 08SB50 is 0.46 wt% and in 08SB45 is 0.48 wt%.

In summary homogeneity and high orthoclase content of the analysed feldspar implies the possibility of interaction with metasomatic fluids, perhaps prior

to or during intrusion of the feldspar vein (pegmatite), leading to alteration of alkali feldspar to orthoclase high in Or-component (late-stage alteration).

	08SB39				08SB48		08SB48		08SB48		08SB45		08SB50	
ORTHOCLASE	EDS				WDS		EDS		PEGMATITIC		EDS		EDS	
	ave n=13	st dev n=13	ave n=14	st dev n=14	ave n=5	st dev n=5	ave n=10	st dev n=10	ave n=15	st dev n=15	ave n=19	st dev n=19	ave n=4	st dev n=4
SiO_2	63.02	0.96	62.01	0.63	64.16	1.30	62.83	0.69	61.72	0.94	62.29	0.59	62.42	0.54
Al_2O_3	16.36	0.37	16.43	0.25	17.51	0.35	17.01	0.31	16.79	0.21	16.96	0.17	16.88	0.11
FeO	0.14	0.11	0.31	0.20	0.15	0.06	0.32	0.31	0.25	0.31	0.26	0.18	0.33	0.23
Na_2O	0.26	0.21	0.36	0.16	1.17	0.81	0.61	0.60	0.86	0.75	0.50	0.31	0.38	0.05
K_2O	15.44	0.44	15.42	0.24	15.44	1.13	15.51	0.85	14.81	1.18	15.72	0.51	15.67	0.05
BaO	0.25	0.34	0.36	0.25	0.16	0.14	0.52	0.33	0.33	0.26	0.48	0.24	0.46	0.46
TiO_2	0.06	0.08	0.02	0.04	0.00	0.00	0.00	0.00	0.37	0.34	0.07	0.08	0.04	0.08
ZrO_2	0.26	0.14	0.27	0.13	n/a	n/a	0.06	0.10	0.00	0.00	0.17	0.14	0.21	0.05
TOTAL	96.13	1.08	95.34	0.46	98.60	0.99	97.36	0.37	95.29	0.88	96.78	0.58	96.63	0.64
Cations recalculated on the basis of 32 oxygens														
Si	12.20	0.08	11.69	1.62	12.05	0.07	12.06	0.03	12.05	0.05	11.97	0.06	12.02	0.02
Al	3.73	0.08	3.70	0.34	3.87	0.08	3.85	0.05	0.00	0.00	3.84	0.04	3.83	0.04
Fe^{2+}	0.02	0.02	0.05	0.03	0.02	0.01	0.05	0.05	3.87	0.05	0.04	0.03	0.05	0.04
Na	0.10	0.08	0.14	0.07	0.42	0.29	0.23	0.22	0.04	0.05	0.19	0.11	0.14	0.02
K	3.81	0.08	4.12	1.01	3.70	0.32	3.80	0.24	0.02	0.02	3.86	0.13	3.85	0.04
Ba	0.02	0.03	0.03	0.02	0.01	0.01	0.04	0.02	0.32	0.28	0.04	0.02	0.04	0.04
Ti	0.00	0.00	0.00	0.00	0.00	0.00	0.00	0.00	3.69	0.32	0.01	0.01	0.01	0.01
TOTAL	19.89	0.07	19.73	0.92	20.08	0.09	20.03	0.04	20.02	0.05	19.98	0.04	19.97	0.04
An	0.00		0.00		0.00		0.00		0.50		0.31		0.00	
Ab	2.48		3.34		10.30		5.61		8.06		4.57		3.58	
Or	97.52		96.66		89.70		94.39		91.44		95.12		96.42	

Table 5.6 Electron microprobe data for alkali feldspar in the Brava intrusive alkaline complex. Abbreviations: st dev=standard deviation, ave=average. Cations recalculated on the basis of 32 oxygens. Complete tables supplied in Appendix 3a.

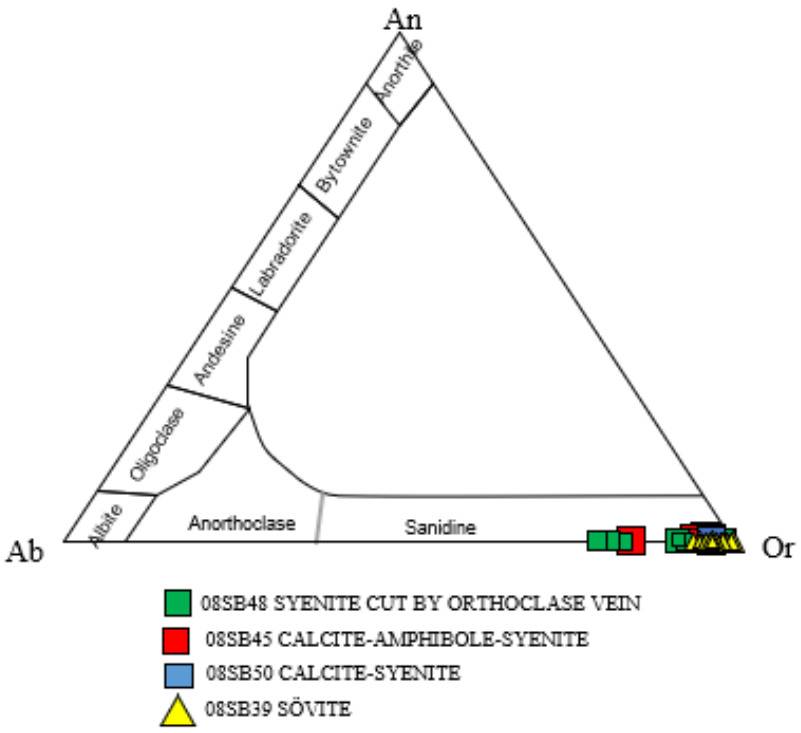

Fig 5.26 Ab-Or-An diagram for feldspars from Brava samples 08SB48, 08SB45, 08SB50 and 08SB38.

5.4.5 Plagioclase

Plagioclase is commonly present in intrusive Brava samples but often shows alteration to sericite or clay mineral or other related phase. Thus collecting good data on pristine crystals is restricted to the glimmerite-composite sample 08SB40 and the syenite cut by orthoclase vein 08SB48 (full data in Table 7.7a-b in Appendix 3b). Both samples yield plagioclase of albite composition (Ab_{94}-Ab_{99}) in glimmerite and Ab_{92}-Ab_{100} in syenite.

			CLEAR GREY		LIGHTER GREY WITH INCLUSIONS	
ALBITE EDS	08SB48 ave n=14	st dev n=14	08SB40 ave n=2	st dev n=2	08SB40 ave n=3	st dev n=3
SiO_2	66.64	0.37	66.56	0.32	66.11	0.28
TiO_2	0.06	0.08	0.20	0.21	0.06	0.07
Al_2O_3	17.61	0.33	21.61	0.05	22.70	0.34
FeO	0.13	0.11	0.12	0.05	0.11	0.02
CaO	0.23	0.46	1.08	0.03	0.18	0.10
Na_2O	11.36	0.40	10.16	0.57	10.84	0.17
K_2O	0.24	0.18	0.02	0.00	0.02	0.01
La_2O_3	0.11	0.15	n/a	n/a	n/a	n/a
Ce_2O_3	0.20	0.25	n/a	n/a	n/a	n/a
Nd_2O_3	0.11	0.15	n/a	n/a	n/a	n/a
BaO	0.08	0.14	0.04	0.05	0.04	0.07
ZrO_2	0.16	0.18	n/a	n/a	n/a	n/a
Nb_2O_5	0.13	0.17	n/a	n/a	n/a	n/a
PbO	0.07	0.13	n/a	n/a	n/a	n/a
TOTAL	97.37	0.61	99.80	0.66	100.07	1.07
	Cations recalculated on the basis of 32 oxygens					
Si	11.68	1.62	11.65	0.00	11.54	0.07
Ti	0.01	0.01	0.03	0.03	0.01	0.01
Al	3.69	0.33	4.46	0.01	4.67	0.06
Fe^{2+}	0.02	0.02	0.02	0.01	0.02	0.00
Ca	0.05	0.09	0.20	0.00	0.03	0.02
Na	4.29	1.05	3.45	0.18	3.67	0.05
K	0.05	0.04	0.01	0.00	0.00	0.00
Ba	0.00	0.00	0.00	0.00	0.00	0.00
TOTAL	19.78	0.91	19.82	0.13	19.95	0.05
An	1.05	2.04	5.54	0.14	0.92	0.50
Ab	97.76	2.29	94.31	0.13	98.95	0.45
Or	1.19	1.15	0.15	0.00	0.13	0.05

Table 5.7 Electron microprobe data for albite in the Brava samples. Abbreviations: st dev=standard deviation, ave=average. Cations recalculated on the basis of 32 oxygens. Complete tables in Appendix 3a.

Plotted data is presented on the Ab-Or-An diagram (Figure 5.27). Albite in both samples shows different petrographic features as in syenite it forms an intimate exsolution from orthoclase found in vein, though the associated syenitic part contains zeolite rather than plagioclase. In the glimmerite-syenite-carbonatite the

plagioclase is abundant forming the main body of syenite and being intensely cross-cut by calcite veinlets. The former albite contains a little K_2O (average 0.24 wt%, Table 7.4.5) while the latter is devoid of potassium. Perhaps albite enriched in K_2O shows its chemical association with the orthoclase host while albite in the glimmerite-composite sample is a product of albitization by Na-rich metasomatic fluids. The question is what host mineral was replaced by metasomatic albite? Perhaps alkali feldspar as primary plagioclase, though abundant, shows widespread alteration to clay minerals and/or other phases.

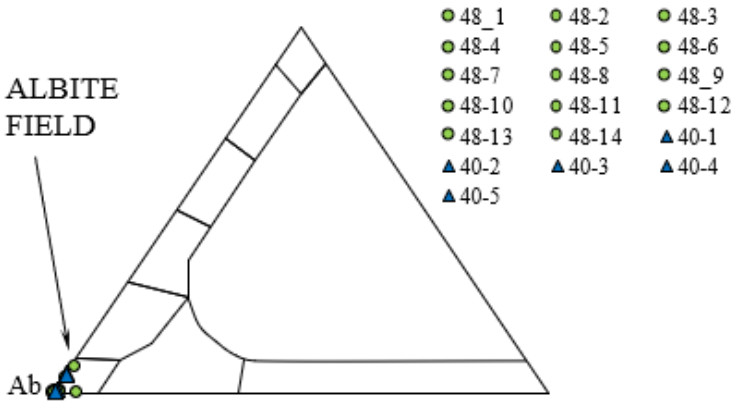

Fig 5.27 Ab-Or-An diagram for feldspar from glimmerite 08SB40 and syenite cut by orthoclase vein 08SB48.

5.4.6 Feldspathoid

08SB46 and 08SB7 samples contain rare, minor and uncommon feldspathoids from the cancrinite subgroup such as pitiglianoite. Cancrinite can form in alkali-rich igneous rocks and in metasomatic ones (Gatta and Lotti, 2016). These alkali-rich rocks are silica-undersaturated principally rich in Na. Cancrinite subgroup can crystallise as primary at late-magmatic stage veins, dykes and pegmatites, or secondary formed during hydrothermal alteration of pre-existing minerals. Its structure contains open cavities, such as channels and cages, occupied by Na^+, K^+, Ca^{2+}cations and CO_3^{2-}, SO_4^{2-}, Cl^- anions (and H_2O). Recognition of the presence of S-, Cl- and Ca/S-pitiglianoite in samples such as 08SB46 and 08SB47 is difficult as the minerals are very small and exist as blotches in inhomogeneous altered feldspar (full data in Table 7.8a-d in Appendix 3a, average figures in Table 5.8).

According to Pekov et al. (2011), cancrinite-subgroup members are indicative of CO_2 activity at postmagmatic stages. Khibiny and Lovozero, two adjacent complexes, were analysed due to geochemical and petrological differences (Kogarko et al. 1995). Pekov et al. (2011) concluded that the carbonate members of the cancrinite subgroup are widespread in Khibiny though at Lovozero they are uncommon. This difference is caused by different redox conditions at the postmagmatic stages: significantly oxidising at Khibiny and reducing at Lovozero (Chukanov et al. 2009a). Pekov et al. (2011) established that "cancrinite-subgroup minerals in derivatives of alkaline intrusive complexes show a strong affinity to CO_3^{2-}: members of the subgroup with other extra-framework anions in the wide channel (SO_4^{2-}, $C_2O_4^{2-}$, PO_4^{3-}, OH^-) can form only under low activity of CO_2". Furthermore, phases like albite, nepheline and zeolites with a wider field of thermodynamic stability are most likely to crystallise and survive than rare pitiglianoite.

	S-PITIGLIANOITE 08SB46		Cl-PITIGLIANOITE		Ca/S-PITIGLIANOITE		S-PITIGLIANOITE 08SB47		CANCRINITE 08SB47	
	ave n=10	st dev n=10	ave n=7	st dev n=7	ave n=4	st dev n=4	ave n=14	st dev n=14	ave n=11	st dev n=11
SiO_2	35.73	0.80	36.56	0.26	37.77	0.69	34.59	1.82	43.15	1.97
Al_2O_3	26.31	0.22	28.83	0.15	26.97	1.21	25.02	0.99	27.12	1.46
FeO	0.13	0.15	0.15	0.14	0.33	0.12	0.14	0.27	0.23	0.38
MgO	0.00	0.00	0.00	0.00	0.00	0.00	0.07	0.10	0.21	0.19
CaO	0.70	0.45	0.08	0.10	4.52	0.40	1.50	1.07	1.59	0.52
Na_2O	10.18	0.99	17.85	0.71	9.60	0.59	10.68	2.06	5.26	1.23
K_2O	5.32	0.47	0.03	0.03	0.19	0.10	5.12	0.93	0.25	0.17
SrO	0.00	0.00	0.00	0.00	0.01	0.03	0.00	0.01	0.00	0.00
BaO	0.02	0.07	0.04	0.09	0.01	0.01	0.17	0.18	0.18	0.17
SO_3	7.05	0.26	0.19	0.35	1.71	0.47	5.56	0.99	0.04	0.06
Cl	0.00	0.00	7.57	0.43	0.00	0.00	0.35	0.49	0.05	0.04
HfO_2	0.75	0.36	0.95	0.25	0.72	0.28	0.63	0.30	0.94	0.26
TOTAL	86.19	0.64	92.25	0.63	81.83	1.53	83.83	9.21	79.02	1.28
CO_2 not calculated										
H_2O not calculated										
Mineral formulae calculated										
on the basis of 12 Si + Al + Fe cations										
Si	6.41	0.06	6.21	0.02	6.49	0.20	6.48	0.23	6.88	0.30
Al	5.57	0.07	5.77	0.03	5.46	0.18	5.52	0.23	5.09	0.28
Fe	0.02	0.02	0.02	0.02	0.05	0.02	0.02	0.04	0.03	0.05
Ca	0.13	0.09	0.02	0.02	0.83	0.08	0.30	0.21	0.27	0.09
Na	3.55	0.38	5.88	0.25	3.20	0.16	3.89	0.80	1.62	0.38
K	1.22	0.11	0.01	0.01	0.04	0.02	1.23	0.24	0.05	0.03
Ba	0.00	0.01	0.00	0.01	0.00	0.00	0.01	0.01	0.01	0.01
TOTAL	16.90	0.36	17.90	0.24	16.07	0.11	17.45	1.76	14.01	0.33

Table 5.8 Electron microprobe data for alkali feldspathoids in the intrusive alkaline complex. Abbreviations: st dev=standard deviation, ave=average. Cations recalculated on the basis of 12 Si + Al + Fe cations. Complete tables supplied in Appendix 3a.

The presence of closely adjacent S-, Cl- and Ca/S-pitiglianoite (Figure 5.13E and F) in sample 08SB46 shows the availability of Cl and S on microscopic scale. Perhaps sample 08SB47 indirectly provides evidence of past existence of Cl-rich fluids. Sample 08SB46 with detectable Cl-content in cancrinite also deliver proof of the existence and activity of chlorine.

Average values of cancrinite and cancrinite-subgroup minerals are presented in Table 5.8. The most variable element is Na_2O as Cl-pitiglianoite contains nearly twice the amount (17.85 wt%) than in S-pitiglianoite (9.6-10.68 wt%) and in cancrinite it is even lower (5.26 wt%). In S-pitigliaonite the average value of the sum of Na_2O and K_2O is around 16 wt%, which equals the average value of Na_2O in Cl-pitigliaonite. Cancrinite and cancrinite-subgroup minerals also have variable contents of SO_3, Cl and Ca which define different names for the phases.

In summary three cancrinite-subgroup phases, although present in minute amounts, can provide information of Cl and S activity in the system.

5.4.9 Zeolite analcime

Zeolite has been found in silicate and carbonatite samples (Table 5.9). In carbonatite-zeolite vein 08SB43, zeolite is coarse-grained with euhedral hexagonal crystals and an interlocking texture (Figure 5.4a_I) which is evolving into a thick vein. In 08SB48 analcime is anhedral and semi-circular, forming cores flanked by pyroxene (Figure 5.15 F). In 08SB47 anhedral zeolite is patchy and associated with other phases such as pyroxene and calcite (Figure 5.15 E).

ZEOLITE	SÖVITE		CARBONATITE-ZEOLITE VEIN		SYENITE	
ANALCIME	08SB39		08SB43		08SB47	
EDS	ave n=8	st dev n=8	ave n=7	st dev n=7	ave n=12	st dev n=12
SiO_2	52.31	*0.69*	50.72	*1.44*	51.41	*0.88*
TiO_2	0.03	*0.04*	0.04	*0.05*	0.05	*0.05*
Al_2O_3	21.08	*0.44*	20.70	*0.66*	21.87	*0.72*
FeO	0.12	*0.09*	0.01	*0.01*	0.48	*0.50*
CaO	0.15	*0.15*	0.04	*0.06*	0.46	*0.30*
Na_2O	9.05	*0.57*	10.32	*0.29*	7.30	*0.63*
K_2O	0.48	*0.10*	0.04	*0.03*	0.10	*0.06*
Nb_2O_5	0.10	*0.15*	0.09	*0.13*	0.12	*0.15*
TOTAL	83.32	*0.25*	81.95	*1.01*	82.00	*1.10*

Table 5.9 Electron microprobe data for zeolite, analcime, in the Brava intrusive alkaline complex. Abbreviations: st dev=standard deviation, ave=average. Complete tables supplied in Appendix

The chemistry of analcime (Table 5.9) shows homogeneity though 08SB43, compared to 08SB39 and 08SB47, displays slight variation in Na and Ca content.

Analcime in the carbonatite-zeolite vein is devoid in CaO, while in the feldspathoid cut by carbonatite vein, CaO varies from 0.05-0.96wt% (average 0.46 wt%) and is much lower in sövite (average 0.15 wt%) (Table 7.9). Na_2O content is higher in the carbonatite-zeolite vein (average 10.32 wt%), while in the sövite it is lower (average 9.05 wt%) and in 08SB47 between 6.59-7.84 wt% (average 7.30 wt%).

Zaitsev et al. (1998) interpreted carbonatites in Kihibina as being polygenetic in origin, ranging from early formed magmatic varieties to late carbonatites formed from volatile-rich carbohydrothermal fluids leading to crystallisation of carbonate-zeolite veins. They also established that residual solutions ("hot brines"), enriched in Na, Ca and CO_2 (aq), were responsible for wall rock fenitization. Perhaps thelack of CaO in zeolites in the carbonate-zeolite sample represents partition of this element from zeolite-rich to calcite-rich sections of the vein. Also the slightly higher Na-content in analcime in this vein implies formation from Na-enriched hydrothermal fluids. Likewise petrographic features, such as the coarse euhedral interlocking analcime crystals, implies crystallisation from a fluid. Conversely zeolite with lower Na-content and higher CaO content in 08SB39 and 08SB7, compared with the carbonatite-zeolite vein, implies metasomatic alteration such as wall rock fenitization where Na had to travel further thus its concentration decreased. Perhaps anhedral grainy zeolites formed during metasomatic alteration of alkali feldspar since the amount of K_2O found in zeolite was low (in sövite and foid-rich specimen showing average values 0.48 and 0.10 wt% respectively, while 08SB43 does not contain potassium).

In summary, samples having zeolite might be the product of crystallisation from the volatite-rich carbohydrothermal fluids and Na-metasomatism (wall rock fenitization) during which alteration of feldspar to zeolite occurred.

5.4.10 Mica

Mica is found in most analysed samples, though it is scarce with the exception of glimmeritic-part of 08SB40, which contains the highest quantity of this phase. Compositional data for micas is given in Table 5.9a-b (average values) and in Table 7.10a-h complete data (Appendix 3a).

Mica can be grouped into two types: Al-poor phlogopite-biotite (average Al_2O_3 values 4.78-11.98 wt%) and Al-rich muscovite (28.47-34.09 wt% Al_2O_3).

SiO_2 content also varies, with the lowest average value (33.09 wt% SiO_2) in 08SB44 and the highest (45.97 w% SiO_2) in 08SB48 (Table 7.4.8a). Muscovite (phengite) is devoid of MgO though phlogopite-biotite hosts MgO varying from 0.22 wt% to 20.48 wt%. The average content of TiO_2 and MnO in all micas, varies up to 3.57 and 2.02 wt% respectively. BaO does not play a major role as the average values oscillate between 0.02 and 0.97 wt%, though fluorine shows higher concentrations between 0.25 and 2.96 wt%.

	EDS ALVIKITE PHLOGOPITE		EDS SÖVITE PHLOGOPITE		EDS SÖVITE PHLOGOPITE		EDS SYENITE	WDS	EDS ZEOLITE-CRBT BIOTITE		WDS SYENITE PHL core		EDS PHL core		inner rim		outer rim		EDS SYENITE Low- Al PHL	
	08SB38		08SB39		08SB39		08SB40	08SB40	08SB44		08SB48		08SB48						08SB50	
	ave n=8	st dev n=8	ave n=11	st dev n=11	ave n=11	st dev n=11	ave n=3	ave n=2	ave n=11	st dev n=11	ave n=2	st dev n=2	ave n=6	st dev n=6	ave n=3	st dev n=3	ave n=4	st dev n=4	ave n=6	st dev n=6
SiO_2	35.97	0.60	40.63	0.77	41.65	0.86	42.25	37.44	33.09	0.62	42.39	0.37	40.98	0.74	45.07	0.93	49.59	0.40	38.24	1.28
TiO_2	1.82	0.27	0.73	0.12	0.63	0.11	0.31	3.57	3.15	0.44	2.11	0.13	1.29	0.14	0.84	0.24	0.49	0.08	1.13	0.31
Al_2O_3	11.40	0.34	9.06	0.48	9.46	1.54	8.12	11.57	11.98	0.54	9.82	0.36	9.59	0.91	9.91	0.85	4.78	0.36	9.61	0.35
FeO	12.59	0.62	8.42	0.83	8.00	0.86	13.46	20.20	20.93	0.37	10.69	0.27	13.24	1.03	3.18	0.31	2.57	0.30	14.54	1.88
MnO	0.32	0.10	1.09	0.16	1.10	0.21	0.27	0.59	0.75	0.16	1.60	0.06	2.02	0.17	0.18	0.06	0.27	0.07	1.92	0.23
MgO	16.59	0.34	18.82	0.76	18.83	1.03	16.31	12.35	10.22	0.43	17.38	0.40	15.49	0.60	18.40	0.64	20.48	0.30	15.22	1.48
CaO	2.19	0.85	0.30	0.25	0.21	0.15	0.21	0.38	0.09	1.02	0.45	0.07	0.05	0.21	0.18	0.17	0.01	0.06	0.06	0.33
Na_2O	0.35	0.11	0.20	0.06	0.17	0.09	0.12	0.26	0.03	0.19	0.07	0.18	0.01	0.16	0.04	0.11	0.05	0.14	0.06	0.20
K_2O	9.35	0.43	9.85	0.29	9.78	0.66	9.48	9.28	0.16	9.36	0.28	10.26	0.27	9.62	0.24	10.46	0.23	10.86	0.13	9.35
BaO	0.43	0.19	0.27	0.22	0.30	0.22	0.02	0.29	0.08	0.79	0.31	0.06	0.09	0.40	0.16	0.25	0.22	0.29	0.22	0.24
F	0.25	0.19	1.61	0.22	1.50	0.27	1.13	0.33	0.07	n/a	n/a	1.69	0.03	0.90	0.16	1.79	0.19	2.96	0.26	0.61
H_2O*	3.68	0.10	3.08	0.09	3.19	0.15	3.32	3.74	0.02	3.63	0.05	3.24	0.01	3.48	0.09	3.19	0.06	2.64	0.14	3.47
O=F,Cl	0.10	0.08	0.68	0.09	0.64	0.11	0.48	0.14	0.03	0.00	0.00	0.71	0.01	0.38	0.07	0.75	0.08	1.25	0.11	0.27
TOTAL	95.05	0.55	94.97	1.75	95.63	0.84	95.48	99.85	0.60	95.11	1.23	100.20	0.69	97.74	0.77	95.21	1.06	96.38	0.60	95.50
Cations recalculated on the basis of 22 oxygens																				
Si	5.69	0.07	6.33	0.06	6.39	0.07	6.57	5.75	0.07	5.47	0.08	6.29	0.01	6.29	0.09	6.83	0.08	7.35	0.07	6.08
Al^{IV}	2.12	0.07	1.65	0.07	1.59	0.05	1.43	2.10	0.06	2.33	0.10	1.69	0.04	1.68	0.09	1.17	0.08	0.65	0.07	1.80
Al^{VI}	0.00	0.00	0.01	0.02	0.12	0.24	0.06	0.00	0.00	0.00	0.00	0.02	0.03	0.05	0.09	0.57	0.09	0.18	0.03	0.00
Ti	0.22	0.03	0.09	0.01	0.07	0.01	0.04	0.41	0.06	0.39	0.05	0.24	0.01	0.15	0.02	0.09	0.03	0.05	0.01	0.14
Fe	1.66	0.08	1.10	0.11	1.03	0.12	1.75	2.60	0.08	2.89	0.06	1.33	0.02	1.70	0.12	0.40	0.04	0.32	0.04	1.94
Mn	0.04	0.01	0.14	0.02	0.14	0.03	0.04	0.08	0.00	0.11	0.02	0.20	0.01	0.26	0.02	0.02	0.01	0.03	0.01	0.26
Mg	3.91	0.08	4.37	0.13	4.31	0.28	3.78	2.83	0.14	2.52	0.10	3.84	0.06	3.54	0.15	4.08	0.12	4.52	0.06	3.61
Ca	0.37	0.15	0.05	0.04	0.03	0.02	0.04	0.06	0.01	0.18	0.08	0.01	0.01	0.03	0.03	0.03	0.00	0.01	0.01	0.06
Na	0.11	0.03	0.06	0.02	0.05	0.03	0.04	0.08	0.01	0.06	0.02	0.05	0.00	0.05	0.01	0.03	0.01	0.04	0.02	0.06
K	1.88	0.09	1.96	0.06	1.92	0.15	1.88	1.82	0.04	1.97	0.06	1.94	0.06	1.88	0.05	1.98	0.02	2.05	0.04	1.90
Ba	0.03	0.01	0.02	0.01	0.02	0.01	0.00	0.02	0.00	0.05	0.02	0.00	0.01	0.02	0.01	0.01	0.01	0.02	0.01	0.02
OH*	3.88	0.10	3.20	0.10	3.26	0.13	3.44	3.84	0.03	4.00	0.00	3.21	0.01	3.57	0.08	3.16	0.08	2.61	0.13	3.68
F	0.12	0.10	0.79	0.10	0.73	0.13	0.56	0.16	0.03	0.00	0.00	0.79	0.01	0.43	0.08	0.84	0.08	1.39	0.13	0.31
Cl	0.00	0.00	0.01	0.01	0.01	0.01	0.00	0.00	0.00	0.00	0.00	0.00	0.00	0.00	0.00	0.00	0.00	0.00	0.00	0.01
TOTAL	20.03	0.10	19.77	0.03	19.67	0.21	19.61	19.73	0.04	20.01	0.04	19.62	0.02	19.66	0.06	19.21	0.03	19.23	0.04	19.86
$Mg/(Fe+Mg)_t$	0.70	0.01	0.80	0.02	0.81	0.02	0.68	0.52	0.02	0.47	0.01	0.74	0.00	0.68	0.02	0.91	0.01	0.93	0.01	0.65

Table 5.9a Electron microprobe data for mica in the Brava intrusive alkaline complex. Abbreviations: st dev=standard deviation, ave=average. Cations recalculated on the basis of 22 oxygens. Complete tables in Appendix 3a

	PHENGITE MICA 08SB48								PENNINTITE, Mn CHLORITE 08SB47				08SB48			
EDS	ave n=2	st dev n=2	ave n=4	st dev n=4	ave n=14	st dev n=14	ave n=11	st dev n=11	ave n=17	st dev n=17	ave n=23	st dev n=23	Cations recalculated on the basis of 14			
SiO_2	41.41	0.13	46.11	3.42	42.43	1.18	42.53	0.98	7.32	2.30	1.75	1.04	Si	1.08	0.28	0.31	0.17
TiO_2	0.37	0.11	n/a	n/a	0.31	0.12	0.16	0.13	0.03	0.07	0.04	0.07	Al^{IV}	2.23	0.37	1.36	0.59
Al_2O_3	31.06	1.60	28.47	3.77	31.75	1.67	34.09	3.22	11.90	2.64	5.98	2.88					
FeO	1.96	0.01	2.12	1.13	2.44	1.27	2.19	2.09	0.04	0.08	0.02	0.04	Al^{VI}	0.00	0.00	0.00	0.00
MnO	0.24	0.30	0.12	0.17	0.09	0.10	0.09	0.09	1.58	0.61	1.01	0.34	Ti	0.00	0.01	0.00	0.00
MgO	1.40	1.19	0.49	0.29	0.10	0.20	0.21	0.35	0.00	0.00	0.00	0.00	Cr	0.00	0.01	0.00	0.00
CaO	0.00	0.00	0.34	0.20	0.12	0.09	0.26	0.18	41.74	3.23	48.35	4.03	Fe^{3+}	0.18	0.07	0.10	0.00
Na_2O	0.36	0.05	0.29	0.11	0.36	0.08	0.52	0.18	4.06	0.32	4.26	1.45	Fe_{2+}	0.00	0.00	0.00	0.00
K_2O	9.57	0.08	8.49	1.54	9.71	0.31	9.35	0.29	2.27	0.33	2.54	0.63	Mn	5.33	0.81	7.56	1.09
BaO	0.45	0.08	0.05	0.10	0.33	0.17	0.31	0.19	3.05	0.56	2.54	0.70	Mg	0.91	0.09	1.15	0.36
La_2O_3	0.29	0.26	0.10	0.12	0.14	0.13	0.11	0.10	0.26	0.09	0.19	0.11	Ca	0.37	0.07	0.50	0.15
Ce_2O_3	0.10	0.13	0.02	0.04	0.03	0.05	0.03	0.06	0.96	0.64	1.9	1.38	Na	1.76	0.28	1.79	0.43
Nd_2O_3	0.39	0.50	0.11	0.10	0.17	0.20	0.20	0.11	0.16	0.17	0.14	0.16	K	0.10	0.03	0.09	0.06
HfO_2	0.89	0.04	0.97	0.18	1.01	0.22	1.21	0.32	0.23	0.21	0.12	0.16	Ba	0.12	0.09	0.28	0.22
F	0.00	0.00	0.00	0.00	0.00	0.00	0.00	0.00	0.10	0.16	0.11	0.16	F	1.71	0.36	1.91	0.51
H_2O*	4.06	0.02	4.12	0.03	4.08	0.04	4.22	0.08	0.36	0.21	0.3	0.19	Cl	0.02	0.02	0.02	0.02
TOTAL	92.52	0.06	91.80	2.23	92.54	1.01	93.91	1.07	0.16	0.13	0.19	0.15	OH*	14.26	0.36	14.07	0.51
Cations recalculated on the basis of 22 oxygens									0.05	0.09	0.05	0.08	TOTAL	28.07	0.40	29.2	0.39
Si	6.12	0.01	6.71	0.52	6.23	0.16	6.05	0.19	0.05	0.07	0.08	0.12					
Al^{IV}	1.88	0.01	1.29	0.52	1.77	0.16	1.95	0.19	1.81	0.37	1.66	0.48					
Al^{VI}	3.53	0.23	3.59	0.14	3.73	0.14	3.76	0.29	0.05	0.04	0.03	0.03					
Ti	0.04	0.01	n/a	n/a	n/a	n/a	0.02	0.01	0.12	0.17	0.37	0.14					
Fe	0.24	0.00	0.26	0.14	0.30	0.16	0.26	0.26	12.89	1.20	10.29	0.74					
Mn	0.03	0.04	0.01	0.02	0.01	0.01	0.01	0.01	89.09	2.77	81.91	1.87					
Mg	0.31	0.26	0.11	0.06	0.00	0.00	0.05	0.08	0.77	0.15	0.71	0.20					
Ca	0.00	0.00	0.05	0.03	0.00	0.00	0.04	0.03	89.86	2.70	82.62	1.83					
Na	0.10	0.01	0.08	0.03	0.10	0.02	0.14	0.05									
K	1.80	0.03	1.57	0.28	1.82	0.06	1.70	0.06									
Ba	0.03	0.00	0.00	0.01	0.02	0.01	0.02	0.01									
OH*	4.00	0.00	4.00	0.00	4.00	0.00	4.00	0.00									
TOTAL	18.09	0.12	17.68	0.33	17.98	0.09	17.99	0.06									
Fe/Fe+Mg	0.50	0.23	0.70	0.22	1.00	0.00	0.90	0.11									
Mn/Mn+Fe	0.10	0.12	0.08	0.15	0.04	0.04	0.06	0.06									

Table 5.9b Electron microprobe data for pennantite chlorite and phengite mica in the Brava intrusive alkaline complex. Abbreviations: st dev=standard deviation, ave=average. Cations recalculated on the basis of 14 oxygens. Complete tables in Appendix 3a.

According to the Al-Mg-Fe diagram, mica belong to the phlogopite-biotite series (Figure 5.28). The plot of mica on Fe+Mg+Ti+Al^{VI} versus Si generated a classification diagram with end-members of phlogopite-Al-rich celadonite-muscovite and disclose the composition of mica in syenites 08SB47 and 08SB48 as phlogopite and phengite.

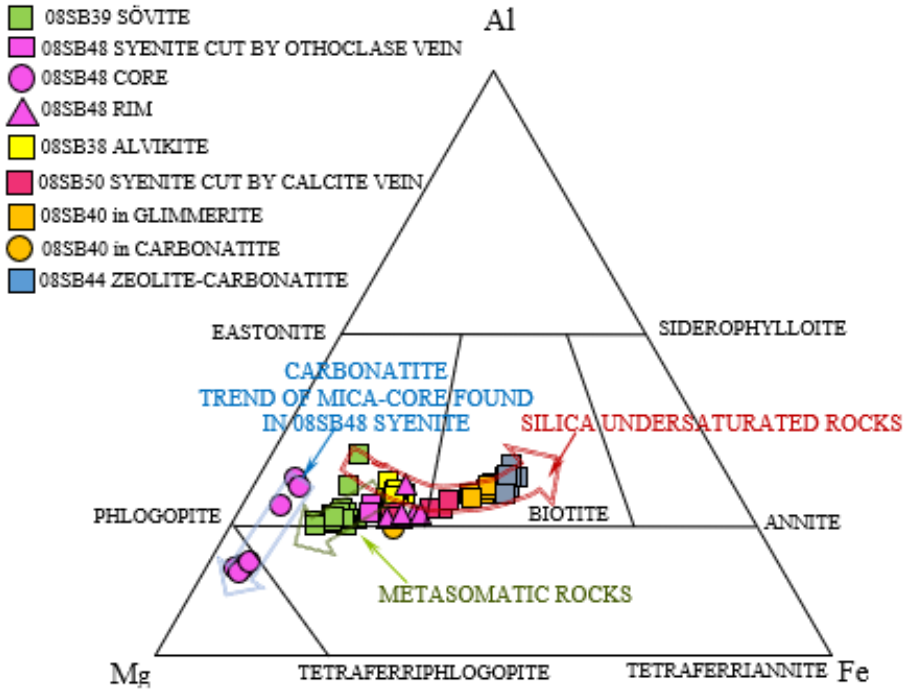

Fig 5.28 Plot of composition of micas on Mg-Fe-Al diagram in samples from Brava, Cape Verde. Trends of mica composition in carbonatite, silica-undersaturated and metasomatic also shown.

The Al-Mg-Fe ternary plot (Figure 5.28) reveals that phlogopite-biotite fractionation occurs along three separate trends. Sövitic phlogopite (sample 08SB39) together with fine-grained mica and rim of the coarse-grained phlogopite in 08SB48, display an evolution along a metasomatic trend towards the Mg-corner. Sövitic phlogopite demonstrates little change as its position is close to carbonatite trend, thus its chemistry shows slight metasomatic alteration. This metasomatic trend bifurcates from the silica undersaturated trend which fractionates towards annite (Al-Fe-enrichment). This field contain phlogopite from the alvikite, which lies in close proximity to sövitic mica thus it exhibits the lowest degree of fractionation. A higher degree of fractionation, towards the Fe-Al site, can be detected in syenitic biotite (cut by calcite vein) and mica from the glimmerite. The greatest fractionation occurs in biotite from zeolite-carbonatite sample. Unusually, the core of large crystal of phlogopite from syenite 08SB48 lies in the carbonatite

field, the rim belongs to the silica-undersaturated trend and the fine-grained mica belongs to metasomatite field. It displays complex chemistry as the mica-core forms two separate clusters (Figure 5.28). Mica from 08SB48 on the Fe+Mg+Ti+Al^{VI} versus Si diagram (Figure 5.29) lies on solid-solution line containing the end-members of phlogopite and Al-celadonite.

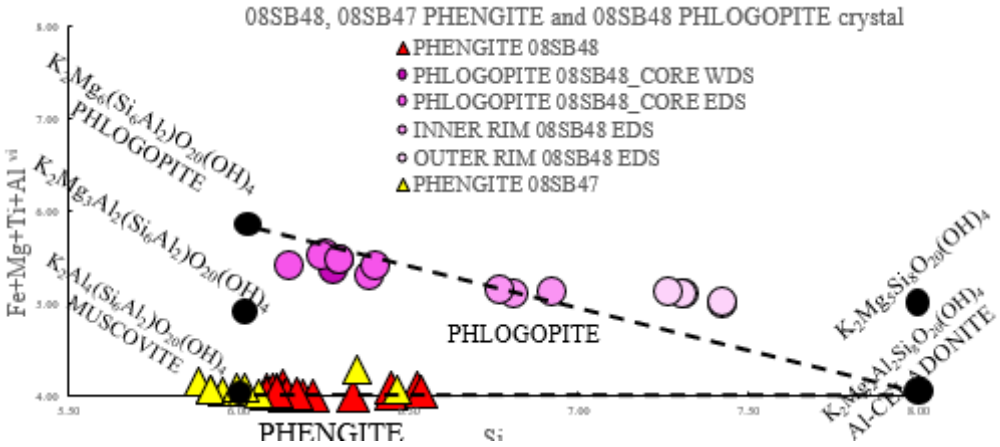

Fig 5.29 Plot of the sum od Fe+Mg+Ti+Al^{VI} versus Si showing composition of 08SB48 phlogopite with variation between core and rim and phengite in 08SB47 and 08SB48 from L5 location, Brava, Cape Verde.

The cores of the large crystal plot close to the phlogopite end-member. Consequently, the circulating fluids altered the outer part of the phlogopite, in effect the rim of the crystal became more silicic at the expense of Fe+Mg+Ti+Al^{VI}, thus attaining an intermediate composition halfway between phlogopite and Al-celadonite. The second influx of hydrothermal or fenitizing fluids further invaded the outer part of the rim, altering it to a more silicic variety thus outer rim lies near the Al-celadonite end-member. The fluids penetrated along crystal boundaries and fractures (Figure 5.30). Figure 5.29 shows the presence of Al-rich phengite, which does not form a close association with phlogopite-biotite crystals. It is also detected in 08SB47 as a clay mineral. Phengite composition displays slight variation within the solid-solution series between muscovite and Al-celadonite. On the Fe+Mg+Ti+Al^{VI} versus Si diagram phengite lies close to the muscovite end-member and spreads slightly towards Al-celadonite (Si-enrichment) (Figure 5.29). Phengite exists in close association with pennantite, which is Mn-chlorite (Figure 5.31). Pennantite belongs to the chlorite family and can incorporate major amounts of MnO with the average values in 08SB48 being 42-48 wt% (Table 7.4.8b). Thus Mn-chlorite must have a structure which allows extensive ionic substitutions, consequently preferentially incorporating Mn. This sample also contain calcite crystals

with patchy enrichment in MnO up to 1.71 wt% (average value, Table 7.3.1c). Also MnO was detected in 08SB43 calcite. Thus the question of availability of this element in the system can be explained through late-stage alteration by Mn- rich fluids.

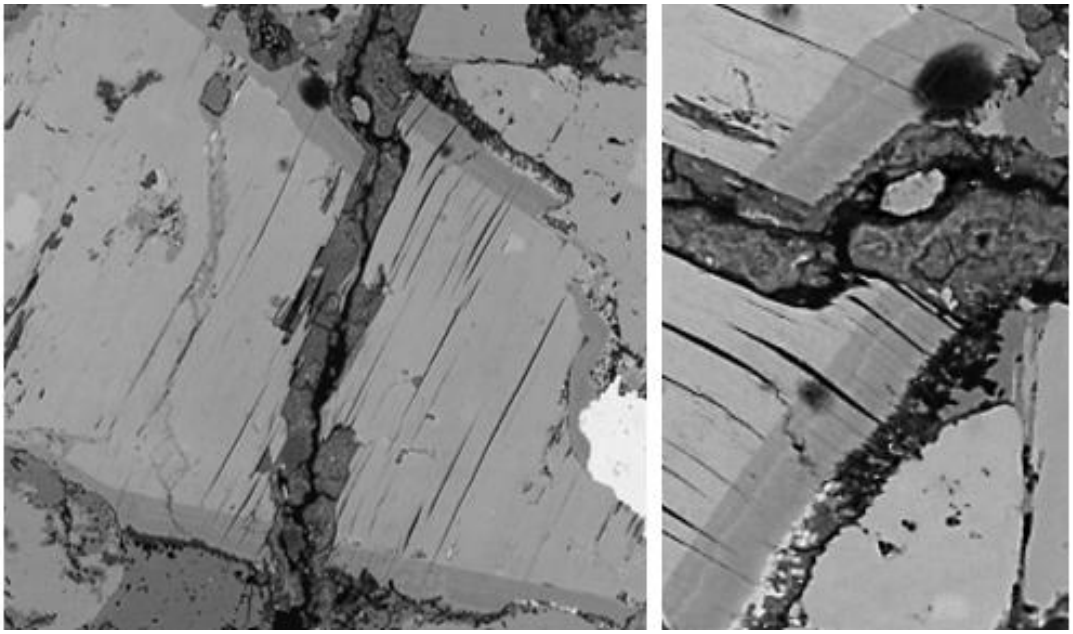

Fig 5.30 BSE image of 08SB48 mica of which core/inner rim/outer rim analyses are plotted on Fe+Mg+Ti+Al^{VI} vs Si diagram showing variation in composition (different shades of grey) from L5 location, Brava, Cape Verde

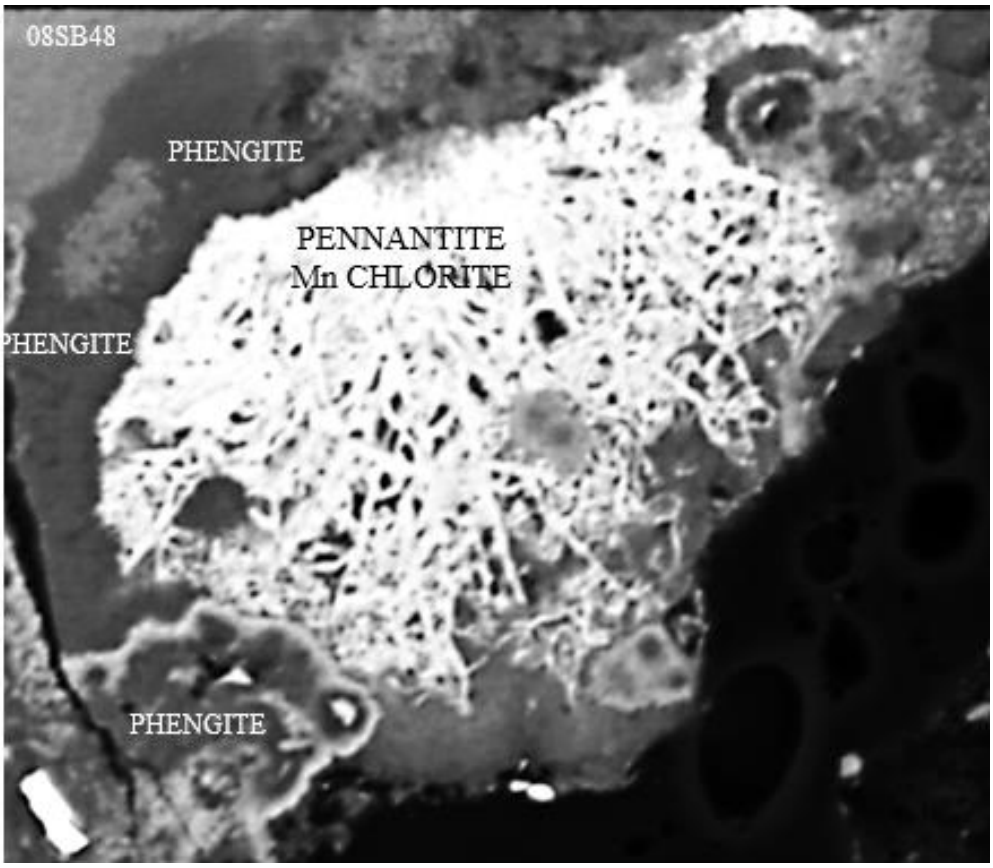

Fig 5.31 BSE image of Al-rich mica phengite in 08SB48 showing close association with chlorite, Mn pennantite.

In summary, micas of various composition occur in carbonatites and silicate rocks from Brava. Phlogopite from the sövite exhibits slight metasomatism and evolution along the Al-Mg trend. The silica-undrsaturated trend shows compositional evolution from phlogopite with low level of fractionation towards highly evolved biotite found in syenite-zeolite samples, where phlogopite-biotite most likely formed as a late-stage phase showing fractionation towards Al-Fe-enrichment. In syenite 08SB48, phlogopite displays complex chemistry. The Fe+Mg+Ti+Al^{VI} vs Si plot reveals that 08SB48 mica belongs to solid-solution series and the core-inner-rim-outer rim of mica crystals ranges in composition between the end-members phlogopite and Al-celadonite. Finally, there is evidence of late-stage fluid circulation altering the mica crystals. Thus, the existence of phengite as a clay mineral is associated with circulation of fluids as is the Mn-chlorite pennantite.

5.4.11 Magnetite, titanomagnetite, ilmenite, titanite, rutile and henrymeyerite

Although Fe-Ti-oxides are common in samples from intrusive Brava complex, difficulties with obtaining reliable data with good totals reduced analyses to just a few thin-sections. Data for magnetite comes from only one sample (08SB44) and ilmenite from 08SB47 and 08SB48 (which also contain Mn-ilmenite). Titanomagnetite is more common and was analysed in 08SB47, 08SB48 and 08SB50. Associated accessory Ti-rich phases such as rutile and titanite are also present. Titanite is present in 08SB44, 08SB46, 08SB47 and 08SB50, whereas a minute amount of rutile was found in 08SB39, 08SB48 and 08SB40, as well as rare Ti-Ba henrymeyerite in 08SB40. Compositional data for Fe-Ti- oxides and titanite and rutile is given in Table 7.4.9a-b (average values) and Table 7.11a-p contains the complete data (Appendix 3a). Overall the highest variety of Ti-Fe phases occurs in syenite cut by orthoclase vein (08SB48) and syenite cut by carbonatite vein (08SB47).

Magnetite from zeolite-carbonatite 08SB44 shows varying TiO_2 content from 1.09 to 3.88 wt%, MnO from 0.72 to 1.62 wt% but low MgO (0.00-0.30 wt%) (Table 7.11o). This mineral shows slight enrichment in La_2O_3 up to 0.32 wt%, Nd_2O_3 up to 0.34 wt% and ZrO_2 up to 0.29 wt%. Average concentration of BaO in magnetite is low (0.30 wt%) (Table 7.4.9a). Titanomagnetites are more widespread than magnetite, reflecting accessibility of titanium in the system. TiO_2 content is highly variable from sample to sample as the average values fall in range of 5-24 wt% (Table 7.4.9b). Overall higher TiO_2 content reflects the lower FeO^T concentration, thus the prevalent Fe↔Ti substitution

is in operation. 08SB47 sample contains the highest average MnO content (1.15 wt%). Unusually 08SB47 contain Ti-magnetite with much lower MnO values; lower values were also detected in 08SB48 and 08SB50 (0.08 to 0.36 wt%).

	Mn ILMENITE		ILMENITE				RUTILE						RUTILE						Nb-RUTILE		HENRYMEYERITE		MAGNETITE	
	08SB48		08SB48				08SB47		08SB39				08SB48		08SB40				08SB48		08SB47		08SB44	
	ave n=18	st dev n=18	ave n=8	st dev n=8	ave n=17	st dev n=17	ave n=13	st dev n=13	ave n=13	st dev n=13	ave n=13	st dev n=13	ave n=4	st dev n=4	ave n=3	st dev n=3	ave n=5	st dev n=3	ave n=2	st dev n=2	ave n=17	st dev n=17
SiO_2	0.21	0.08	0.57	0.53	0.92	1.03	2.67	1.56	0.62	0.28	3.91	5.09	1.42	0.10	1.59	0.31	0.61	0.35	0.48	0.05	0.20	0.10
TiO_2	46.08	0.65	50.34	6.17	57.51	4.74	54.63	2.95	79.44	0.85	73.14	6.14	74.22	0.97	79.73	1.75	72.40	1.98	63.36	0.05	2.53	1.00
Al_2O_3	0.06	0.05	0.38	0.51	0.60	0.83	1.76	1.23	0.15	0.08	0.77	1.27	1.37	0.12	0.17	0.05	0.29	0.37	0.00	0.00	0.23	0.15
Fe_2O_3	2.27	1.03	5.80	6.33	6.22	4.25	0.00	0.00	0.00	0.00	0.00	0.00	0.00	0.00	0.00	0.00	0.00	0.00	0.00	0.00	61.00	2.30
FeO	23.64	1.53	26.21	6.93	15.27	2.65	22.30	4.38	2.37	0.60	2.81	1.15	0.96	0.10	1.69	0.27	6.70	0.99	7.68	0.58	30.93	0.63
MnO	17.72	1.22	0.31	0.10	1.11	1.29	0.27	0.18	0.25	0.13	0.20	0.10	0.25	0.17	0.32	0.15	0.27	0.08	0.00	0.00	1.24	0.31
MgO	0.05	0.06	0.07	0.08	0.08	0.10	0.08	0.07	0.08	0.08	0.17	0.23	0.04	0.02	0.00	0.01	0.08	0.05	0.00	0.00	0.15	0.09
CaO	0.02	0.03	0.07	0.05	0.18	0.17	0.83	0.28	0.76	0.70	1.36	0.66	3.21	0.86	0.45	0.27	0.06	0.04	1.27	0.16	0.13	0.11
K_2O	0.02	0.03	0.04	0.03	0.10	0.13	0.07	0.05	0.07	0.05	0.36	0.80	5.40	0.50	0.03	0.01	0.18	0.03	1.36	0.69	0.04	0.04
BaO	4.23	0.45	4.34	0.99	4.54	0.52	4.82	0.56	7.57	0.52	7.18	0.72	4.60	0.38	4.42	0.73	5.88	0.12	21.00	0.35	0.34	0.24
Nb_2O_5	2.19	0.59	3.79	0.65	3.77	1.26	2.07	1.06	3.62	0.59	3.23	0.69	0.09	0.04	1.82	0.19	6.30	0.85	0.57	0.36	0.08	0.13
La_2O_3	1.75	0.54	1.95	0.45	2.02	0.32	1.95	0.52	3.53	0.51	3.34	0.50	1.95	0.67	1.98	0.40	2.94	0.22	2.41	0.18	0.15	0.13
Nd_2O_3	0.54	0.30	0.58	0.26	0.49	0.23	0.47	0.20	0.00	0.00	0.00	0.00	0.40	0.17	0.48	0.15	0.63	0.13	0.54	0.30	0.17	0.17
ZrO_2	0.04	0.07	0.14	0.21	0.13	0.18	0.07	0.09	0.70	0.78	1.47	1.13	n/a	n/a	1.95	0.17	n/a	n/a	0.00	0.00	0.08	0.11
TOTAL	99.88	0.58	95.32	0.53	93.65	1.03	92.69	1.19	99.25	0.68	98.36	0.92	93.90	1.07	95.22	0.93	98.32	0.76	98.67	0.13	97.67	0.88
	Cations recalculated on the basis of 3 oxygens																2 oxygens		16 oxygens		4 oxygens	
Si	0.01	0.00	0.02	0.01	0.02	0.03	0.07	0.04	0.01	0.00	0.06	0.08	0.02	0.00	0.02	0.01	0.01	0.01	0.07	0.01	0.01	0.00
Ti	0.94	0.01	1.02	0.10	1.12	0.07	1.07	0.06	0.93	0.01	0.87	0.09	0.86	0.01	0.94	0.01	0.88	0.01	6.54	0.02	0.08	0.03
Al	0.00	0.00	0.01	0.02	0.02	0.02	0.05	0.04	0.00	0.00	0.01	0.02	0.02	0.00	0.00	0.00	0.01	0.01	0.00	0.00	0.01	0.01
Fe^{+3}	0.05	0.02	0.12	0.13	0.12	0.08	0.00	0.00	0.00	0.00	0.00	0.00	0.00	0.00	0.00	0.00	0.00	0.00	0.00	0.00	1.82	0.07
Fe^{+2}	0.53	0.03	0.60	0.18	0.33	0.06	0.52	0.17	0.03	0.01	0.04	0.01	0.06	0.00	0.02	0.00	0.09	0.01	0.88	0.07	1.02	0.02
Mn	0.41	0.03	0.01	0.00	0.03	0.03	0.01	0.00	0.00	0.00	0.00	0.00	0.00	0.00	0.00	0.00	0.00	0.00	0.00	0.00	0.04	0.01
Mg	0.00	0.00	0.00	0.00	0.00	0.00	0.00	0.00	0.00	0.00	0.00	0.01	0.00	0.00	0.00	0.00	0.00	0.00	0.00	0.00	0.01	0.01
Ca	0.00	0.00	0.00	0.00	0.00	0.00	0.02	0.01	0.01	0.01	0.02	0.01	0.05	0.01	0.01	0.00	0.00	0.00	0.19	0.02	0.01	0.00
K	0.00	0.00	0.00	0.00	0.00	0.00	0.00	0.00	0.00	0.00	0.00	0.00	0.00	0.00	0.00	0.00	0.00	0.00	0.24	0.12	0.00	0.00
Ba	0.04	0.00	0.05	0.01	0.05	0.01	0.05	0.01											1.13	0.02	0.01	0.00
Nb	0.03	0.01	0.05	0.01	0.05	0.02	0.03	0.01	0.03	0.00	0.02	0.01	0.03	0.00	0.01	0.00	0.05	0.01	0.04	0.02	0.00	0.00
TOTAL	2.03	0.00	1.88	0.08	1.76	0.05	1.83	0.07	1.02	0.00	1.03	0.01	1.06	0.01	1.01	0.00	1.04	0.00	9.07	0.28	3.01	0.00

Table 5.10a Electron microprobe data for ilmenite, rutile, henrymeyerite and magnetite in the Brava intrusive alkaline complex. Abbreviations: st dev=standard deviation, ave=average. Cations recalculated on the basis of 3, 2, 16 and 4 oxygens. Complete tables supplied in Appendix 3a. Some elements are below detection limit.

	TITANOMAGNETITE 08SB47		08SB47		08SB48		08SB48		08SB48		08SB50		TITANITE 08SB44		08SB46		08SB47		08SB50	
	ave n=17	st dev n=17	ave n=17	st dev n=17	ave n=9	st dev n=9	ave n=13	st dev n=13	ave n=5	st dev n=5	ave n=17	st dev n=17	ave n=16	st dev n=16	ave n=9	st dev n=9	ave n=8	st dev n=8	ave n=10	st dev n=10
SiO_2	4.59	0.74	0.33	0.09	0.37	0.22	1.58	1.33	2.79	1.64	0.31	0.15	28.93	0.98	29.67	0.26	29.46	0.18	29.06	0.15
TiO_2	21.14	1.65	4.78	2.09	13.97	1.37	16.68	1.21	18.13	2.52	24.33	3.71	32.53	0.59	32.90	0.91	32.55	0.63	31.72	0.69
Al_2O_3	1.41	0.06	0.47	0.24	0.17	0.10	0.55	0.47	1.13	1.16	0.14	0.17	1.06	0.17	0.83	0.64	0.39	0.23	0.38	0.36
Fe_2O_3	13.57	4.80	52.11	3.62	33.83	2.43	24.64	3.16	18.16	1.99	14.58	7.66	0.00	0.00	0.00	0.00	0.00	0.00	0.00	0.00
FeO	52.28	1.82	32.89	1.95	40.99	1.16	44.78	1.78	47.71	1.31	50.72	3.08	1.75	2.21	1.16	0.51	1.50	0.28	1.19	0.31
MnO	1.15	0.05	0.08	0.09	0.09	0.12	0.36	0.19	0.24	0.18	0.33	0.13	0.19	0.13	0.14	0.13	0.09	0.13	0.21	0.12
MgO	1.11	0.19	0.02	0.03	0.07	0.07	0.03	0.05	0.12	0.15	0.03	0.05	0.02	0.04	0.06	0.05	0.03	0.05	0.06	0.07
CaO	0.55	0.11	0.13	0.06	0.11	0.05	0.05	0.05	0.08	0.07	0.06	0.06	28.21	1.10	28.24	0.34	28.30	0.58	27.23	0.44
K_2O	0.02	0.05	0.02	0.02	0.06	0.07	0.38	0.35	0.44	0.47	0.04	0.05	0.00	0.00	0.00	0.00	0.00	0.00	0.00	0.00
BaO	1.93	0.36	0.30	0.32	1.66	0.40	2.13	0.48	2.19	0.70	2.66	0.47	3.14	0.49	3.20	0.47	3.00	0.51	2.95	0.32
Nb_2O_5	0.11	0.10	0.11	0.20	0.90	0.27	0.95	0.22	0.81	0.31	1.45	0.38	0.53	0.22	0.64	0.26	1.71	0.94	1.74	0.65
La_2O_3	0.86	0.25	0.05	0.08	0.71	0.34	0.77	0.48	0.64	0.44	0.95	0.37	1.54	0.29	1.20	0.41	1.33	0.24	1.11	0.39
Nd_2O_3	0.47	0.18	0.65	0.42	0.35	0.15	0.37	0.25	0.56	0.24	0.40	0.29	0.51	0.24	0.46	0.19	0.34	0.27	0.40	0.25
ZrO_2	0.11	0.10	0.40	0.30	0.55	0.26	0.25	0.14	0.14	0.15	0.22	0.26	0.47	0.25	0.60	0.31	0.56	0.17	1.90	1.08
TOTAL	99.74	0.79	92.96	1.22	94.51	0.73	94.07	0.73	94.03	1.19	96.76	1.15	98.98	0.42	99.28	0.44	99.62	0.40	98.42	0.76
	Cations recalculated on the basis of 4 oxygens												5 oxygen							
Si	0.17	0.03	0.01	0.00	0.02	0.01	0.06	0.05	0.11	0.07	0.01	0.01	1.00	0.02	1.02	0.01	1.01	0.00	1.01	0.00
Ti	0.60	0.05	0.15	0.06	0.44	0.04	0.52	0.04	0.56	0.09	0.74	0.11	0.85	0.01	0.85	0.02	0.84	0.01	0.83	0.02
Al	0.06	0.00	0.02	0.01	0.01	0.01	0.03	0.02	0.05	0.05	0.01	0.01	0.04	0.01	0.03	0.03	0.02	0.01	0.02	0.01
Fe^{+3}	0.38	0.14	1.64	0.12	1.06	0.08	0.77	0.11	0.56	0.06	0.44	0.23	0.00	0.00	0.00	0.00	0.00	0.00	0.00	0.00
Fe^{+2}	1.64	0.06	1.15	0.06	1.42	0.04	1.55	0.04	1.63	0.04	1.71	0.11	0.05	0.07	0.03	0.01	0.04	0.01	0.03	0.01
Mn	0.04	0.00	0.00	0.00	0.00	0.00	0.01	0.01	0.01	0.01	0.01	0.00	0.01	0.00	0.00	0.00	0.00	0.00	0.01	0.00
Mg	0.06	0.01	0.00	0.00	0.00	0.00	0.00	0.00	0.01	0.01	0.00	0.00	0.00	0.00	0.00	0.00	0.00	0.00	0.00	0.00
Ca	0.02	0.00	0.01	0.00	0.00	0.00	0.00	0.00	0.00	0.00	0.00	0.00	1.05	0.03	1.04	0.01	1.04	0.02	1.02	0.02
K	0.00	0.00	0.00	0.00	0.00	0.00	0.02	0.02	0.02	0.02	0.00	0.00	0.00	0.00	0.00	0.00	0.00	0.00	0.00	0.00
Ba	0.00	0.00	0.00	0.00	0.03	0.01	0.03	0.01	0.04	0.01	0.04	0.01	0.00	0.00	0.00	0.00	0.00	0.00	0.00	0.00
Nb	0.03	0.01	0.00	0.01	0.02	0.01	0.02	0.00	0.02	0.01	0.03	0.01	0.00	0.00	0.00	0.00	0.00	0.00	0.00	0.00
TOTAL	3.02	0.00	3.01	0.00	3.02	0.00	3.03	0.01	3.04	0.01	3.02	0.00	3.09	0.02	3.08	0.01	3.09	0.01	3.08	0.01

Table 5.10b Electron microprobe data for titanomagnetite and titanite in the Brava intrusive carbonatite. Abbreviations: st dev=standard deviation, ave=average. Cations recalculated on the basis of 4 and 5 oxygens. Complete tables supplied in Appendix 3a. Some elements are below detection limit.

An average BaO content of 2 wt% is found in Ti-magnetite from 08SB48, though concentration in 08SB50 is higher (2.66 wt%). Sample 08SB47 (with the lowest TiO_2 content) has also lowest average BaO content (0.30 wt%). Rare elements, such as La_2O_3

and Nb_2O_5, was also detected in titanomagnetite but again some titanomagnetites in 08SB47 have low values. Ti-magnetite average enrichments in ZrO_2 and Nd_2O_3 show greater constancy as they fall in range 0.11-0.55 wt% and 0.35-0.55 wt%, respectively.

Ilmenite is detected in two samples (08SB47 and 08SB48) though the second sample also contains Mn-rich ilmenite. BaO content in ilmenite is stable in all samples (4.23-4.82 wt%) (Table 7.4.9a). Enrichment in Nb_2O_5 is higher than in titanomagnetite (2.07-3.79 wt%). Also La_2O_3 content is higher (average value varies from 1.75 to 2.02 wt%). Ilmenite is closely associated with titanite which has the highest BaO (~3 wt%). The average sum of La_2O_3+ Nd_2O_3 is close to 2 wt%. Nb_2O_5 concentrations vary between 0.53 and 0.64 wt% in 08SB44 and 08SB46, respectively, and in 08SB47 and 08SB50 Nb_2O_5 is 1.71-1.74 wt%, respectively.

Rutile, the most Ti-rich phase, occurs in 08SB39, 08SB40 and 08SB48. In the latter sample there is variation in Nb-content as rutile either is lacking in Nb or shows an average of 6.30 wt% (Table 7.4.9a), most likely as a result of Nb-rutile holding a cluster of pyrochlore crystals thus enriching the host-phase in Nb_2O_5. Rutile in 08SB40 and 08SB39 contains average concentration of Nb_2O_5 from 1.82 to 3.62 wt%. The average La_2O_3 content is high (2 to 3.5 wt%) but Nd_2O_3 is mostly depleted. The high average of BaO content varies from 4.42 to 7.57 wt%. A very small amount of henrymeyerite is found in close association with ilmenite and titanite. Henrymeyerite is enriched in BaO up to 21 wt% and La_2O_3 up to 2.41 wt% and contains small amounts of Nb_2O_5 and Nd_2O_3 up to 0.5 wt%. All Fe-Ti phases also show progressive enrichment in ZrO_2. The least enrichment is detected in magnetite, titanomagnetite and ilmenite and progressively increasing in titanite and rutile. The evolution:

magnetite → titanomagnetite → ilmenite → titanite → rutile →henrymeryeite

is progressive as all analysed phases are related to each other according to their petrography and chemistry. Titanite replaces ilmenite (Figure 5.32) as does rutile. Progressive increase in REEs, Nb, Zr and Ba demonstrates progressive incorporation of elements, leading to alteration of earlier formed minerals by interaction with late-stage fluids rich in rare elements and those fluids were able to invade the rocks through the vugs, cracks or grain-boundaries.

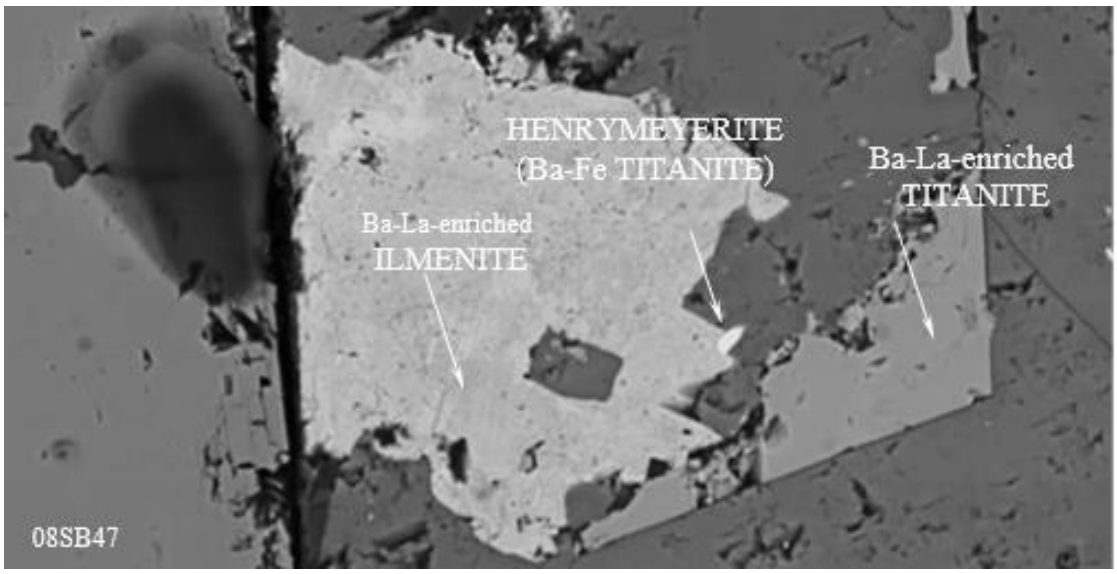

Fig 5.32 BSE image of 08SB47 showing close association between Ti-Fe-rich phases such as ilmenite-titanite-henrymeryeite.

5.4.12 Pyrochlore

Pyrochlore is present in four samples, in carbonatites (08SB38 and 08SB39) and syenites (08SB47 and 08SB48). Compositional data for pyrochlore is given in Table 5.11 (average values) and in Table 7.12a-f complete data (Appendix 3). Pyrochlore mostly forms subhedral to euhedral fine-grained crystals often clustering together, sometimes displaying zonation either around the rim or forming oscillatory zones from core to rim (Figure 5.33). As the chief carrier of niobium in the Brava alkaline complex pyrochlore is characterised by variable Nb_2O_5 ranging from 37.44 wt% (sövite 08SB39) to 60.32 wt% (syenite cut by orthoclase vein 08SB48) (Table 7.12a-f, Appendix 3a). CaO concentration also fluctuates from 14.36 wt% in sövite to 18.66 wt% in alvikite 08SB38, as does TiO_2 (5.14 wt% in 08SB48 to 11.45 wt% in 08SB39). Na_2O and BaO contents are steady (average 4-5 wt% and 1-2 wt% respectively, Table 5.11). Fluorine average content varies in sövite between 0.59-0.88 wt% (UO_2 average content in the same sample is 25.75-22.96 wt%), in syenite 08SB47 is 1.61 wt% (UO_2 11.51 wt%) and in syenite 08SB48 is 2.22 wt% (uranium 4.24 wt%) and finally reaching the highest average value of 2.60 wt% in alvikite 08SB38, though UO_2 concentration drops to 0.63 wt%. Thus fluorine versus uranium exhibits negative correlation in associated samples. As the microprobe analyses revealed a very high concentration of UO_2 in sövite 08SB39, it is uranium pyrochlore. The average concentration of ThO_2 is low (0.11-0.25 wt%) (Table 5.10c). In contrast, the carbonatite from Monte Almada on Fogo contains pyrochlore which is highly enriched in ThO_2.

EDS	ALVIKITE 08SB38 ave	st dev	SÖVITE 08SB39 ave	st dev	ave	st dev	SYENITE 08SB47 ave	st dev	SYENITE 08SB48 ave	st dev
Na_2O	5.15	0.15	4.07	0.19	3.78	0.17	4.48	0.26	4.07	0.26
CaO	18.31	0.36	12.84	0.36	12.19	0.48	16.27	1.13	16.78	1.07
MnO	0.13	0.17	0.07	0.10	0.10	0.13	0.11	0.12	0.12	0.10
SrO	1.08	0.23	0.63	0.15	0.52	0.11	0.85	0.21	1.23	0.22
BaO	0.98	0.36	2.15	0.43	2.28	0.36	1.14	0.36	0.98	0.44
PbO	0.85	0.31	n/a	n/a	n/a	n/a	0.76	0.35	0.86	0.22
La_2O_3	0.62	0.34	0.97	0.29	1.16	0.49	0.45	0.30	0.50	0.38
Ce_2O_3	0.24	0.33	0.07	0.23	0.09	0.16	0.17	0.23	0.21	0.23
Nd_2O_3	0.32	0.22	n/a	n/a	n/a	n/a	0.17	0.19	0.29	0.23
ThO_2	0.10	0.15	0.13	0.22	0.13	0.17	0.25	0.22	0.22	0.21
UO_2	0.63	0.49	22.96	2.48	25.75	1.01	11.51	5.23	4.24	4.25
HfO_2	0.13	0.16	n/a	n/a	n/a	n/a	0.08	0.11	0.16	0.17
SiO_2	1.25	0.40	0.26	0.13	0.36	0.33	0.24	0.09	0.41	0.17
TiO_2	6.19	0.20	10.29	1.03	11.02	0.31	7.73	1.13	6.13	1.26
ZrO_2	0.80	0.49	0.45	0.35	0.56	0.34	0.48	0.33	0.48	0.29
FeO	0.13	0.13	0.16	0.15	0.26	0.17	0.12	0.12	0.15	0.15
Nb_2O_5	57.45	1.34	41.94	2.17	38.52	0.76	52.20	4.09	57.58	3.85
F	2.60	0.14	0.88	0.23	0.59	0.20	1.61	0.41	2.22	0.40
P_2O_5	0.98	0.22	0.43	0.19	0.33	0.20	0.86	0.21	1.02	0.19
TOTAL	97.94	1.71	98.30	0.89	97.63	0.89	99.46	0.54	98.55	0.73
Formulae based on 2 B-site cations, a.p.f.u.										
Na^{1+}	0.62	0.02	0.58	0.03	0.55	0.03	0.58	0.02	0.00	0.00
Ca^{2+}	1.21	0.02	1.02	0.03	0.98	0.04	1.16	0.05	1.14	0.05
Mn^{2+}	0.01	0.01	0.00	0.01	0.01	0.01	0.01	0.01	0.01	0.01
Sr^{2+}	0.03	0.01	0.02	0.00	0.01	0.00	0.02	0.01	0.03	0.01
Ba	0.02	0.01	0.06	0.01	0.07	0.01	0.03	0.01	0.02	0.01
Pb^{2+}	0.01	0.01	n/a	n/a	n/a	n/a	0.01	0.01	0.01	0.00
La^{3+}	0.01	0.01	0.03	0.01	0.03	0.01	0.01	0.01	0.01	0.01
Ce^{3+}	0.01	0.01	0.00	0.01	0.00	0.00	0.00	0.01	0.00	0.01
Nd^{3+}	0.01	0.00	n/a	n/a	n/a	n/a	0.00	0.00	0.01	0.01
Th^{4+}	0.00	0.00	0.00	0.00	0.00	0.00	0.00	0.00	0.00	0.00
U^{4+}	0.01	0.01	0.36	0.05	0.43	0.02	0.17	0.08	0.06	0.07
Hf^{4+}	0.00	0.00	n/a	n/a	n/a	n/a	0.00	0.00	0.00	0.00
$\sum A$	1.94	0.03	2.07	0.05	2.09	0.05	2.01	0.05	1.31	0.05
Si^{4+}	0.08	0.02	0.02	0.01	0.03	0.02	0.02	0.01	0.03	0.01
Ti^{4+}	0.29	0.01	0.55	0.07	0.62	0.01	0.39	0.07	0.30	0.07
Zr^{4+}	0.02	0.01	0.02	0.01	0.02	0.01	0.02	0.01	0.01	0.01
Fe^{3+}	0.01	0.01	0.01	0.01	0.02	0.01	0.01	0.01	0.01	0.01
Nb^{5+}	1.60	0.04	1.40	0.06	1.31	0.03	1.57	0.07	1.66	0.07
$\sum B$	2.00	0.00	2.00	0.00	2.00	0.00	2.00	0.00	2.00	0.00
F	0.51	0.02	0.22	0.05	0.14	0.04	0.34	0.08	0.45	0.07
O	7.10	0.09	7.17	0.10	7.17	0.08	7.16	0.08	6.68	0.05

Table 5.11 Electron microprobe data for pyrochlore in the Brava. Abbreviations: st dev=standard deviation, ave=average. Formulae based on 2 B-site cations, a.p.f.u. Complete tables in Appendix 3a.

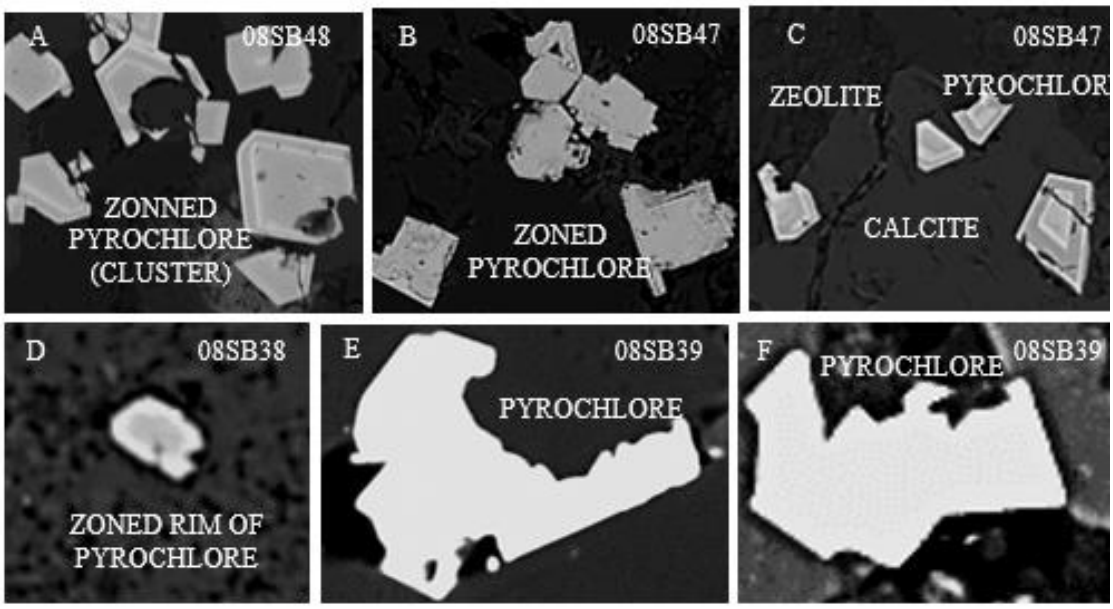

Fig 7.33 Backscatter electron image of Brava syenites (08SB47 and 08SB48) and carbonatites (08SB38 and 08SB39) containing pyrochlore

The plot of Nb+Ti versus Si of pyrochlore from Brava and Fogo reveals linear and negative relationship (Figure 5.34). Thus, with decreasing Si content, the Fogo thoriopyrochlore just overlaps with calciopyrochlore from the Brava alvikite. With the further increase of Nb and Ti, alvikite merges with the sövitic uranium pyrochlore, which finally overlaps pyrochlore crystallised in syenite.

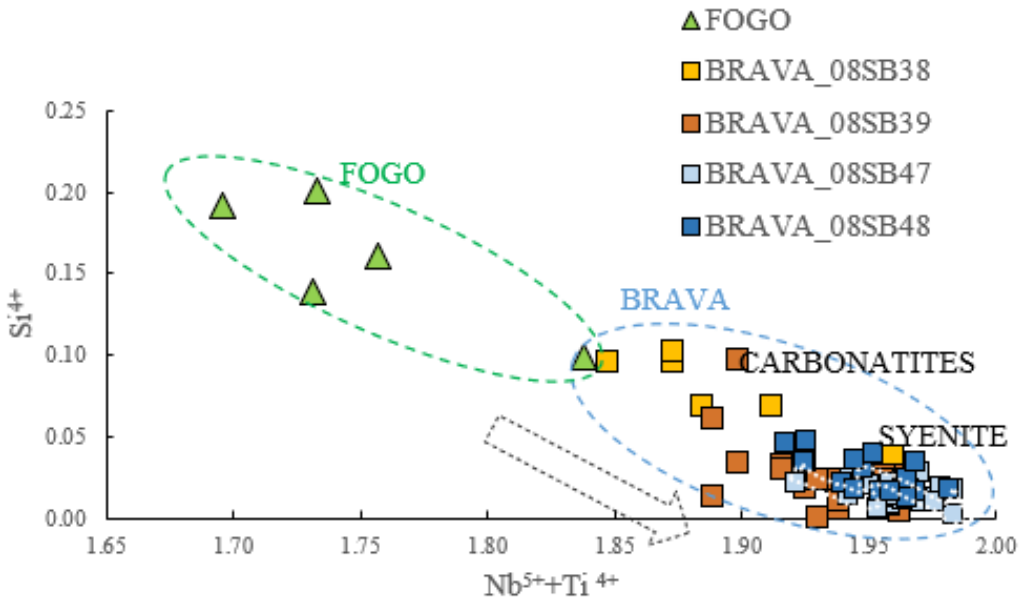

Fig 5.34 Variation diagram of Si vs Nb+Ti in pyrochlore from Brava carbonatites and syenites. Complex oscillatory zoning detected in pyrochlore crystal in syenite 08SB47 (light blue squares) might indicate the overall evolution trend for Brava pyrochlore. Crystals are very fine-grained thus difficult to analyse for core-rim variation. Fogo Nb-pyrochlore (08SF03) is included, being also Th-U-rich, most likely hydrothermal in origin.

The evolution of Brava (and perhaps Fogo) pyrochlore towards Nb-enrichment is highlighted by a zoned crystal in syenite 08SB47 (Figure 5.35) which shows oscillatory evolution towards increasing Nb. Zoning reflects changes in the system, which is rather complex though the overall final core-rim chemistry reflects increase in Ca-Na-Nb as well as Mn-Sr-Zr and decrease in U-Ti. Hodgson and Le Bas (1992) analysed zonation in pyrochlore from Cape Verde (San Vicente). They recognised different types of zonation such as concentric, oscillatory, rhythmic and sector out of which concentric zonation was also recognised in Brava pyrochlore showing similar trend: increase in U, Ti and Si concentration towards the core and increase in Nb, Ca and Na towards the margins. Perhaps the first stage of magmatic crystallisation on Brava formed U-Ti-rich pyrochlore followed by the next stage during which alkalinity of the system increased as well as availability of Ca and Nb. The latter stage is most likely indicative of activity of hydrothermal fluids during which the rim became more enriched in Mn, Sr and Zr. The

circulating fluids would also cause characteristic partial resorbed texture on the boundary between zeolite and calcite areas (fluids would have easy access along the boundary) as seen in Figure 5.33c. Zoned pyrochlore, although an accessory phase, contains valuable information about processes affecting the system such as magmatic ones, progressively becoming alkaline, followed by increase in activity of hydrothermal fluids rich in Mn, Sr and Zr.

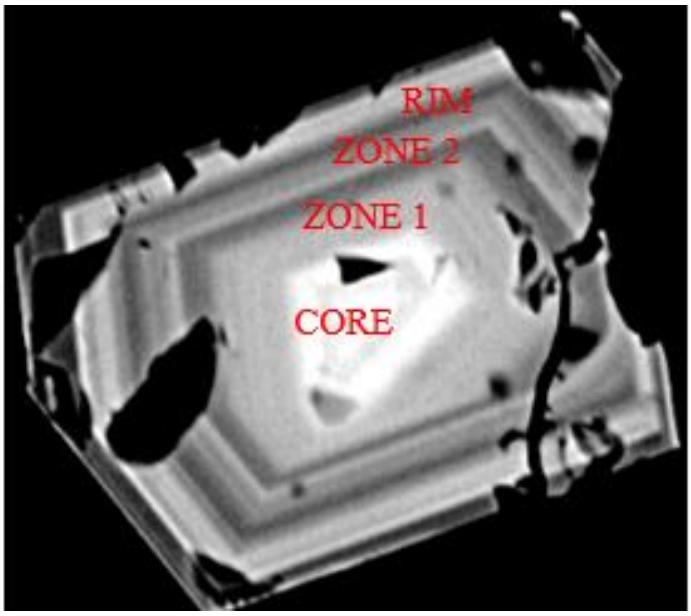

Fig 5.35 Backscatter electron image of zoned pyrochlore from Brava syenite 08SB47.

5.4.13 Zr-rich minerals

Rare Zr-rich minerals are restricted to three samples, i.e. glimmerite-carbonatite-syenite 08SB40 containing hilairite, feldspar-foid pegmatite 08SB49 which also contains hilairite and tazheranite, and carbonatite-zeolite 08SB43 containing undefined and minor Zr-silicates. Compositional data for Zr-phases is given in Table 5.12 (average values) and in Table 7.13a-c complete data (Appendix 3a).

Composition of hilairite from 08SB40 and 08SB49 is consistent, showing only some variations in Na_2O content (in 08SB40 the average value 8.37 wt% and in 08SB49 the average is 6.73 wt). The average ZrO_2 content is 27.75-28.97 wt% and SiO_2 is 42.26-44.29 wt%. Average content of REE such as Nd, Ce and La is << 1 wt% with the exception of Nb_2O_5 which shows average values of 0.87 wt% (08SB40) and 1.05 wt% (08SB49).

The second rare Zr-rich phase found in the feldspar-foid pegmatite 08SB49 has been classified as tazheranite, bearing similarity to tazheranite from Kaapvaal Craton

(Konzett at al. 2013), although the content of Zr and Ti is higher, and Ca lower, than that of the metasomatic Zr-phases found in a Kaapvaal spinel-harzburgite xenolith. Thus, in the Brava tazheranite, ZrO_2 content varies from 69.72-76.25 wt% (in the xenolith the average value is 61.50 wt%), CaO content is 1.32-3.03 wt% (in xenolith sample average content is 7.50 wt%) and TiO_2 shows variation from 2.84 to 6.32 wt%, while the xenolith shows the average value 20.50 wt% (Table 7.13c, Appendix 3a). The concentration of other elements (from Brava and Kaapvaal Craton) are alike, thus on Brava the average values of Nb_2O_5 is 2.75 wt%, BaO around 0.99 wt% and HfO_2 is 1.54 wt%.

			HILAIRITE									
	08SB40		08SB49		08SB49		08SB40		08SB40		08SB40	
EDS	ave	st dev	ave	st dev	ave	st dev	ave	st dev	ave	st dev	ave	st dev
Na_2O	8.37	1.02	6.73	0.93	0.17	0.09	0.31	0.13	0.35	0.04	0.23	0.09
K_2O	0.05	0.04	0.03	0.04	0.06	0.07	0.56	0.76	0.27	0.20	1.22	1.00
CaO	0.27	0.29	0.13	0.14	1.95	0.62	0.32	0.15	0.87	0.75	1.38	0.64
BaO	0.18	0.19	0.12	0.15	0.99	0.46	1.41	0.40	1.04	0.35	0.92	0.74
FeO	0.05	0.06	0.11	0.12	2.60	0.63	64.83	6.65	48.21	7.64	35.71	10.42
Al_2O_3	0.07	0.06	0.06	0.07	0.71	0.34	1.40	1.02	2.01	1.54	8.82	7.27
SiO_2	42.26	0.55	44.29	0.49	3.17	0.63	3.86	3.61	5.26	4.44	15.97	9.23
TiO_2	0.16	0.15	0.08	0.10	3.56	0.99	10.31	5.71	5.74	2.15	5.80	5.02
MnO	0.01	0.01	0.07	0.10	0.21	0.15	0.11	0.10	0.39	0.50	0.10	0.11
MgO	0.01	0.02	0.02	0.03	0.12	0.09	0.70	1.62	0.21	0.21	1.21	1.11
ZrO_2	27.57	0.49	28.97	0.45	73.63	2.29	2.78	1.61	18.67	4.62	8.04	1.67
HfO_2	0.04	0.09	0.10	0.20	1.54	0.26	0.11	0.17	0.25	0.15	0.44	0.34
La_2O_3	0.16	0.19	0.22	0.30	0.24	0.26	0.36	0.35	0.06	0.12	0.09	0.11
Ce_2O_3	0.02	0.05	0.21	0.22	0.00	0.00	0.00	0.00	0.00	0.00	0.01	0.02
Nd_2O_3	0.14	0.12	0.18	0.15	0.44	0.22	0.24	0.27	0.15	0.11	0.16	0.20
Nb_2O_5	0.87	0.30	1.05	0.46	2.75	0.63	0.27	0.35	0.94	0.17	0.46	0.42
P_2O_5	0.23	0.23	0.37	0.26	2.30	0.51	0.21	0.15	0.88	0.25	0.33	0.25
SrO	0.00	0.00	0.00	0.00	0.93	0.22	0.14	0.22	0.14	0.24	0.08	0.17
H_2O	not											
TOTAL	80.43	0.53	82.71	0.47	95.29	1.23	87.91	1.99	85.41	3.25	80.95	5.25

	Cations recalculated				on the basis			Zr-Ti 08SB40		Zirconо- 08SB43	
								ave	st dev	ave	st dev
Na	1.20	0.14	0.45	0.47	0.00	0.00	Na_2O	3.69	0.95	2.03	1.50
K	0.00	0.00	0.00	0.00	0.00	0.00	K_2O	0.12	0.11	0.19	0.27
Ca	0.02	0.02	0.01	0.01	0.02	0.02	CaO	2.50	2.32	1.01	0.60
Ba	0.01	0.01	0.00	0.00	0.00	0.00	BaO	3.55	0.33	2.01	1.67
Fe	0.00	0.00	0.01	0.01	0.02	0.02	FeO	16.27	5.93	3.59	3.61
Al	0.01	0.00	0.00	0.01	0.01	0.01	Al_2O_3	0.97	0.31	5.25	2.51
Si	3.12	0.04	1.58	1.66	0.02	0.03	SiO_2	22.56	4.70	12.76	4.70
Ti	0.01	0.01	0.00	0.01	0.03	0.04	TiO_2	34.61	3.75	1.73	1.02
Mn	0.00	0.00	0.01	0.02	0.00	0.00	MnO	0.42	0.45	5.91	6.62
Mg	0.00	0.00	0.00	0.00	0.00	0.00	MgO	1.26	1.35	0.28	0.31
Zr	0.99	0.02	2.56	1.63	0.91	0.07	ZrO_2	3.09	2.12	45.57	3.97
Hf	0.00	0.00	0.00	0.01	0.01	0.00	HfO_2	0.00	0.00	0.68	0.25
La	0.01	0.01	0.02	0.03	0.00	0.00	La_2O_3	1.48	0.02	0.61	0.04
Ce	0.00	0.00	0.02	0.03	0.00	0.00	Ce_2O_3	0.00	0.00	0.05	0.09
Nd	0.00	0.00	0.01	0.01	0.03	0.01	Nd_2O_3	0.33	0.07	0.24	0.23
Nb	0.03	0.01	0.09	0.06	0.00	0.00	Nb_2O_5	0.97	0.37	0.78	0.27
P	0.01	0.01	0.05	0.06	0.04	0.01	P_2O_5	0.23	0.25	1.33	0.44
Sr	0.00	0.00	0.00	0.00	0.01	0.00	SrO	0.00	0.00	0.27	0.17
TOTAL	5.41	0.11	4.81	0.35	1.01	0.03	H_2O	not			
							TOTAL	92.03	4.30	84.28	1.26

Table 5.12 Electron microprobe data for Zr-rich phases in the alkaline Brava complex. Abbreviations: st dev=standard deviation, ave=average. Cations for hilairite and tazheranite recalculated on the basis of 9 and 2 oxygens. Complete tables in Appendix 2

According to Pekov et al. (2003), hilairite is the most widespread member of the hilarite group of minerals. Hilairite occurs in association with hydrothermally altered alkaline rocks (Pekov et al. 2003) thus it has a late pegmatitic paragenesis. Hilairite has a zeolite-like structure and therefore hilairite-group minerals are sensitive indicators of crystallisation from hydrothermal solution and conditions can be narrowed down to the temperature < 150°C (Pekov et al. 2003).

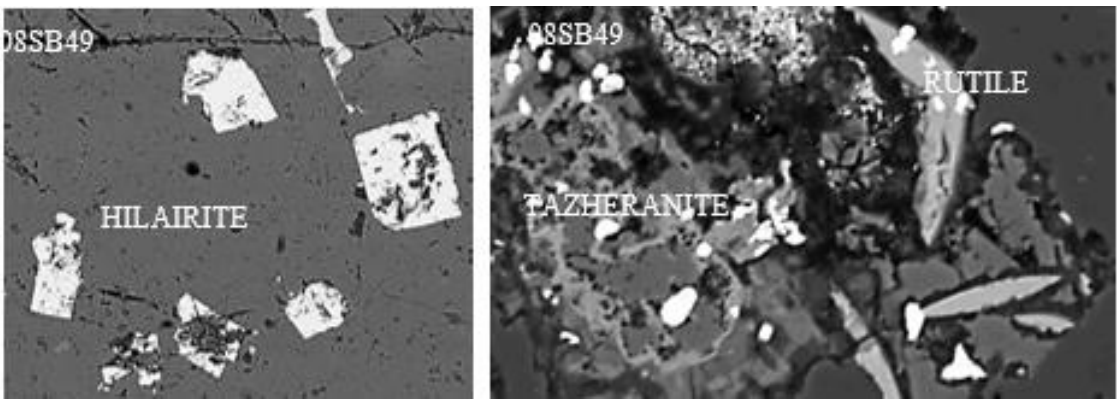

Fig 5.36 Backscatter electron image of hilairite and tazheranite from Brava feldspar-foid syenite 08SB49.

According to Mitchell (1995) and Konzett et al. (2013) spinel-harzburgite xenolith from Kaapvaal craton kimberlites show two metasomatic events. Those two periods of fluid interaction with the host rock gave rise to specific assemblages of LILE-HFSE-rich minerals. The second event produced tazheranite (rare natural cubic zirconium oxide with Ti-Ca stabilizing cubic zirconia). Tazheranite most likely formed from a predecessor zircon in the presence of a high-density fluid (Konzett et al., 2013).

Figure 5.36 shows BSE images of hilairite and tazheranite in 08SB49. Hilairite displays a strong association with fractures which were most likely conduits for metasomatic fluids influencing the paragenesis of hilairite. Thazeranite is set in highly metasomatised environment with an assemblage of altered minerals formed by circulating fluid.

In summary, multiple stages of fluid interaction with the host rock led to progressive modification of the original composition and texture. Metasomatic fluids finally generated specific assemblages for given conditions. Thus, the last stage of hydrothermal activity in 08SB49 can be narrowed down to <150℃, during which hilairite was able to form. Lower concentration of TiO_2 in tazheranite most likely reflects the very close association of this phase with rutile and transfer of Ti to rutile by fluid activity.

5.4.14 Minerals having REE, Sr and Ba as major elements

A small quantity of rare phases was found in the analysed samples. There are three types of minerals of which one holds considerable quantity of REEs, another is Sr-rich and the third is Ba-rich. Tables 5.13, 5.14 and 5.15 contain average values of analysed REEs-Sr-Ba minerals in sövite 08SB39, syenite cut by feldspar-pegmatite vein 08SB48 and carbonate-zeolite vein 08SB43. REE rhabdophane (phosphate phase) is present in

08SB48 as well as La-Ce-rich törnebohmite-silicate. The carbonatite-zeolite vein 08SB43 is enriched in La-Ce-Nd lanthanite.

	RHABDOPHANE (La, Ce)				PARISITE-(Ce) - SYNCHYSITE-(Ce) analysed as PARISITE-(Ce)				TORNEBOHMITE				TORNEBOHMITE akin towards PARISITE		BURBANKITE		LANTHANITE-(Na,Ce) La>Nb Nb≥La			
	08SB48				08SB48				08SB48				08SB48		08SB48		08SB43			
EDS	ave n=12	st dev n=12	ave n=3	st dev n=3	ave n=1	st dev n=1	ave n=15	st dev n=15	ave n=8	st dev n=8	ave n=2	st dev n=2	ave n=3	st dev n=3	ave n=2	st dev n=2	ave n=12	st dev n=12	ave n=11	st dev n=11	ave n=13	st dev n=13
Na_2O	n/a	n/a	n/a	n/a	n/a	n/a	n/a	n/a	n/a	n/a	0.31	0.10	0.25	0.11	0.14	0.03	2.79	0.17	2.75	0.17	0.01	0.03	0.05	0.09
SiO_2	3.32	1.65	11.79	2.67	8.49	3.50	0.44	0.15	5.74	2.59	20.84	1.77	8.81	0.71	4.62	0.25	n/a	n/a	n/a	n/a	1.22	1.41	0.32	0.13
Al_2O_3	1.18	1.26	6.15	1.05	4.30	3.14	0.25	0.17	4.01	1.84	20.88	1.52	9.20	0.66	5.23	0.37	n/a	n/a	n/a	n/a	0.92	0.54	0.29	0.21
MgO	n/a	n/a	n/a	n/a	n/a	n/a	n/a	n/a	n/a	n/a	0.23	0.05	0.14	0.20	0.04	0.07	n/a	n/a	n/a	n/a	0.09	0.10	0.05	0.07
FeO	0.59	0.26	0.65	0.29	1.05	0.35	0.09	0.13	1.14	0.78	1.19	1.04	0.69	0.51	0.18	0.25	n/a	n/a	n/a	n/a	0.30	0.52	0.02	0.05
MnO	0.62	0.26	0.85	0.23	1.17	0.04	n/a	n/a	n/a	n/a	0.25	0.05	0.41	0.11	0.28	0.12	n/a	n/a	n/a	n/a	0.54	1.29	0.34	0.25
CaO	5.67	0.36	4.68	0.57	4.11	0.23	3.76	1.30	4.06	0.74	4.57	0.11	5.56	0.65	5.53	0.16	11.26	0.51	11.91	1.91	6.35	3.45	6.57	2.63
K_2O	0.02	0.03	0.02	0.03	n/a	n/a	n/a	n/a	n/a	n/a	n/a	n/a	n/a	n/a	n/a	n/a	n/a	n/a	n/a	n/a	0.02	0.03	0.02	0.03
ThO_2	0.26	0.19	0.27	0.10	0.51	0.59	0.51	0.15	0.41	0.25	0.00	0.00	0.30	0.25	0.37	0.06	n/a	n/a	n/a	n/a	n/a	n/a	n/a	n/a
PbO	0.13	0.09	0.15	0.05	0.43	0.05	n/a	n/a	n/a	n/a	n/a	n/a	n/a	n/a	n/a	n/a	n/a	n/a	n/a	n/a	n/a	n/a	n/a	n/a
HfO_2	0.27	0.15	0.27	0.45	0.59	0.11	n/a	n/a	n/a	n/a	1.01	0.30	0.33	0.15	0.13	0.03	0.57	0.15	0.56	0.15	n/a	n/a	n/a	n/a
P_2O_5	16.64	1.37	12.09	2.01	7.88	1.51	0.18	0.12	0.16	0.15	0.08	0.01	0.06	0.05	0.05	0.07	n/a	n/a	n/a	n/a	0.12	0.13	0.18	0.15
La_2O_3	25.27	2.09	18.91	4.04	10.92	0.91	19.10	1.19	16.42	1.70	15.98	0.51	22.59	0.77	25.30	0.65	1.21	0.45	1.16	0.45	19.33	2.55	12.36	2.03
Ce_2O_3	12.43	4.35	12.09	3.64	29.22	1.76	27.83	1.19	25.40	2.42	16.81	0.59	23.23	1.19	24.61	0.65	3.45	0.51	3.28	0.51	24.56	1.51	23.73	1.59
Nd_2O_3	8.60	0.65	7.15	1.25	5.45	0.69	8.37	0.51	6.67	0.70	2.79	0.10	3.81	0.35	3.58	1.09	0.99	0.35	1.00	0.40	4.95	0.59	10.37	2.62
SrO	2.31	0.25	1.30	0.25	1.34	0.20	1.81	0.29	1.57	0.64	0.80	0.37	1.07	0.09	0.96	0.29	28.43	1.46	27.99	1.52	0.69	0.15	1.38	0.70
SO_3	n/a	n/a	n/a	n/a	n/a	n/a	0.10	0.09	0.07	0.09	n/a	n/a	n/a	n/a	n/a	n/a	n/a	n/a	n/a	n/a	n/a	n/a	n/a	n/a
F	n/a	n/a	n/a	n/a	n/a	n/a	3.15	0.42	2.75	0.34	2.69	0.19	3.31	0.12	2.87	0.04	n/a	n/a	n/a	n/a	n/a	n/a	n/a	n/a
BaO	n/a	n/a	n/a	n/a	n/a	n/a	n/a	n/a	n/a	n/a	n/a	n/a	n/a	n/a	n/a	n/a	12.91	2.17	12.95	2.60	n/a	n/a	n/a	n/a
CO_2	n/c	n/c	n/c	n/c	n/c	n/c	n/c	n/c	n/c	n/c	n/p	n/p	n/p	n/p	n/p	n/p	35.00	1.51	34.25	1.27	n/c	n/c	n/c	n/c
H_2O	n/c	n/c	n/c	n/c	n/c	n/c	n/p	n/c	n/c	n/c	n/c	n/c	n/c	n/c	n/c	n/c	n/p	n/c	n/c	n/c	n/c	n/c	n/c	n/c
TOTAL	77.30	2.41	76.35	3.45	75.42	0.70	65.57	2.13	68.41	2.69	88.57	0.30	79.80	2.69	73.89	1.90	96.63	2.10	95.85	2.67	59.13	3.64	55.75	0.13
Cations recalculated on the basis of 16 oxygens							Formula proportions calculated on basis of 3 cations					formula proportions calculated on base of 5					formula based on 5 $(CO_3)_2$- groups							
Si	0.67	0.25	2.13	0.37	1.81	0.61	0.04	0.01	0.39	0.15	1.39	0.07	0.77	0.03	0.49	0.02	n/a	n/a	n/a	n/a				
Na	n/a	n/a	n/a	n/a	n/a	n/a	n/a	n/a	n/a	n/a	0.04	0.01	0.04	0.02	0.03	0.01	0.80	0.04	0.80	0.05				
Al	0.28	0.27	1.32	0.29	1.06	0.70	0.02	0.02	0.32	0.12	1.64	0.05	0.95	0.03	0.66	0.04	n/a	n/a	n/a	n/a				
Mg	n/a	n/a	n/a	n/a	n/a	n/a	n/a	n/a	n/a	n/a	0.02	0.01	0.02	0.03	0.01	0.01	n/a	n/a	n/a	n/a				
Fe	0.10	0.04	0.10	0.05	0.19	0.09	0.01	0.01	0.06	0.04	0.07	0.05	0.05	0.05	0.02	0.02	n/a	n/a	n/a	n/a				
Mn	0.11	0.04	0.13	0.04	0.21	0.01	n/a	n/a	n/a	n/a	0.01	0.00	0.03	0.01	0.03	0.01	n/a	n/a	n/a	n/a				
Ca	1.25	0.07	0.91	0.10	0.96	0.14	0.33	0.10	0.30	0.05	0.33	0.02	0.52	0.03	0.63	0.02	1.77	0.09	1.91	0.27				
Th	0.01	0.01	0.01	0.00	0.03	0.04	n/a	n/a	n/a	n/a	0.00	0.00	0.01	0.01	0.01	0.00	n/a	n/a	n/a	n/a				
Pb	0.01	0.01	0.01	0.00	0.02	0.00	n/a	n/a	n/a	n/a	n/a	n/a	n/a	n/a	n/a	n/a	n/a	n/a	n/a	n/a				
Hf	0.02	0.01	0.02	0.03	0.04	0.00	n/a	n/a	n/a	n/a	0.02	0.01	0.01	0.01	0.00	0.00	0.03	0.01	0.03	0.01				
P	2.89	0.25	1.85	0.27	1.46	0.41	0.01	0.01	0.01	0.01	0.00	0.00	0.00	0.01	0.00	0.01	n/a	n/a	n/a	n/a				
La	1.91	0.15	1.26	0.24	0.88	0.15	0.59	0.04	0.42	0.07	0.39	0.03	0.73	0.00	1.00	0.02	0.09	0.03	0.06	0.03				
Ce	0.94	0.35	0.81	0.25	2.33	0.35	0.85	0.05	0.65	0.10	0.41	0.03	0.75	0.01	0.96	0.04	0.24	0.07	0.18	0.04				
Nd	0.63	0.05	0.46	0.05	0.42	0.05	0.25	0.02	0.17	0.02	0.07	0.00	0.12	0.01	0.14	0.04	0.05	0.01	0.05	0.02				
Th	n/a	n/a	n/a	n/a	n/a	n/a	0.01	0.00	0.01	0.00	n/a	n/a	n/a	n/a	n/a	n/a	n/a	n/a	n/a	n/a				
Sr	0.18	0.02	0.09	0.02	0.11	0.03	0.09	0.01	0.07	0.03	0.03	0.02	0.05	0.01	0.06	0.02	2.47	0.05	2.43	0.15				
F	n/a	n/a	n/a	n/a	n/a	n/a	0.82	0.05	0.61	0.09	0.57	0.02	0.92	0.00	0.97	0.03	n/a	n/a	n/a	n/a				
Ba	n/a	n/a	n/a	n/a	n/a	n/a	n/a	n/a	n/a	n/a	n/a	n/a	n/a	n/a	n/a	n/a	0.75	0.14	0.76	0.15				
TOTAL	8.99	0.10	9.10	0.14	9.53	0.00	3.02	0.02	3.01	0.03	5.00	0.01	4.98	0.01	5.01	0.02	6.18	0.06	6.22	0.04				

Table 5.13 Electron microprobe data for REE-carbonate and silicate phses in syenite and zeolite-carbonatite vein in the Brava intrusive alkaline complex. Abbreviations: st dev=standard deviation, ave=average, n/c=not calculated. Cations recalculated on the basis of 16, 3, 5 oxygens in radophane, parisite törnebohmite respectively and on $5(CO_3)_2$- groups in burbankite. Complete tables in Appendix 3A. Some elements are below detection limit.

Strontium-rich phases also occur in three samples (08SB39, 08SB47 and 08SB48). Sr-carbonates such as burbankite and carbocernaite crystallised in 08SB48 and 08SB39 (respectively). Strontianite is also found (Table 5.154.

Three analysed Brava samples contain REE-phases (08SB39, 08SB43 and 08SB48). Parisite (a carbonate mineral) can be found in syenite cut by carbonatite vein 08SB47. Sövite 08SB39 contains strontian-calcite forming a close relationship with calcian-strontianite. An unusual K-Cl-Na carbonate (?) also occurs in sövite forming minute star-like radiating clusters of minerals. Thus two samples, sövite 08SB39 and feldspar-pegmatite vein 08SB48, are enriched in a variety of REE- and Sr-rich minerals.

	SYENITE STRONTIANITE		SÖVITE CALCIAN STRONTIANITE		SÖVITE STRONTIAN CALCITE		ALVIKITE BARITE		SYENITE BARITE	
	08SB47		08SB39		08SB39		08SB38		08SB48	
EDS	ave n=3	st dev n=3	ave n=16	st dev n=16	ave n=7	st dev n=7	ave n=2	st dev n=2	ave n=11	st dev n=11
SiO_2	1.21	0.17	1.05	0.47	0.47	0.36	6.79	2.45	0.78	0.31
TiO_2	0.00	0.00	0.00	0.00	0.02	0.04	0.00	0.00	0.00	0.00
Al_2O_3	0.06	0.07	0.00	0.00	0.09	0.05	4.87	1.05	0.17	0.13
CaO	16.95	8.59	21.77	5.00	40.51	6.24	2.75	0.68	0.04	0.04
Na_2O	0.03	0.03	0.23	0.14	0.92	0.48	0.19	0.04	0.16	0.07
K_2O	0.01	0.01	0.00	0.00	0.07	0.04	0.33	0.18	0.44	0.06
SrO	44.22	9.50	37.86	8.55	11.44	5.33	2.19	1.07	1.98	0.51
BaO	1.11	1.05	1.80	2.10	0.66	0.42	52.88	0.29	63.53	0.23
MgO	0.00	0.00	0.00	0.00	0.05	0.07	0.83	0.23	0.04	0.04
FeO	0.06	0.04	0.00	0.04	0.06	0.07	0.92	0.40	0.06	0.08
Nb_2O_5	0.07	0.12	0.00	0.00	0.01	0.05	0.28	0.38	0.29	0.23
SO_3	0.00	0.00	0.00	0.00	0.01	0.06	24.26	3.14	30.56	0.29
P_2O_5	1.22	0.20	1.17	0.34	0.37	0.20	0.22	0.08	0.02	0.06
La_2O_3	0.68	0.33	0.42	0.42	0.79	0.70	0.21	0.21	0.00	0.00
Ce_2O_3	0.45	0.36	0.84	0.60	1.48	1.42	0.00	0.00	0.00	0.00
Nd_2O_3	0.12	0.09	0.04	0.01	0.02	0.00	0.00	0.00	0.06	0.14
HfO_2	0.82	0.17	0.28	0.00	0.16	0.18	0.66	0.11	0.25	0.20
F	0.04	0.05	0.00	0.00	0.02	0.05	0.26	0.06	0.32	0.16
Cl	0.01	0.01	n/p	n/p	0.02	0.02	0.41	0.43	0.07	0.05
ZrO_2	0.00	0.00	0.00	0.00	0.00	0.00	0.15	0.08	0.15	0.19
ThO_2	0.00	0.00	0.00	0.00	0.05	0.10	0.06	0.08	0.37	0.23
CO_2	not calculated						n/p	n/p	n/p	n/p
TOTAL	67.06	2.24	65.42	4.61	56.81	4.49	98.24	1.51	99.28	0.52

Table 5.14 Electron microprobe data for strontianite (in sövite and syenite) and barite (in alvikite and syenite) in Brava.Abbreviations: st dev=standard deviation, ave=average. Complete tables in Appendix 3A.

Parisite (Ce) belongs to parisite (Ce)-synchysite (Ce) series and is characterised by high concentrations of REEs such as Ce, La and Nd. This phase forms often intergrowths with synchystite, thus it exhibits some degree of chemical inhomogeneity (Table 5.15). Parisite average values of LREEs in 08SB39 range from 34.58- to 44.66 wt% and in 08SB48 48.49-55.30 wt%. Accordingly, CaO average content is 5.49-9.26 wt% in carbonatite and 3.76-4.06 wt% in silicate sample.

The higher average CaO concentration is related to lower average LEE concentrations in sövite and *vice versa* lower average CaO concentration reflects higher average concentration of LREEs in silicate sample. This reflects substitution of LREE↔Ca but also/and the higher availability of Ca in carbonatite. SrO content in parisite oscillates between 1.57-1.81 wt% in 08SB48 and 0.15-1.32 wt% in 08SB39, F content is 2.75-3.15 wt% in 08SB48 and 1.63-2.85 wt% in 08SB39 (i.e. higher Sr and F values in silicate sample) (Table 5.15).

	PARISITE-(Ce) - SYNCHYSITE-(Ce) series						CARBOCERNAITE			(Akin towards GREGORYITE-NYERERETTE?))		
	PARISITE-(Ce)									K-Na Cl CARBONATE (?)		
	08SB39						08SB39			08SB39		
EDS	ave n=5	st dev n=5	ave n=9	st dev n=9	ave n=4	st dev n=4	EDS	ave n=4	st dev n=4	EDS	ave n=11	st dev n=11
CaO	9.09	2.40	5.49	0.99	9.26	3.16	Na_2O	0.85	0.92	Na_2O	3.11	0.66
P_2O_5	0.15	0.10	0.16	0.13	0.31	0.25	CaO	17.00	3.02	CaO	39.08	3.51
SrO	1.03	0.29	1.32	0.62	0.15	0.29	SrO	26.49	5.52	K_2O	7.97	1.66
SiO_2	1.87	1.83	0.76	0.34	4.44	3.11	BaO	2.69	1.98	MgO	0.27	0.10
Al_2O_3	0.92	1.06	0.27	0.11	2.06	2.36	La_2O_3	5.30	2.81	La_2O_3	0.09	0.10
FeO	0.03	0.06	0.35	0.30	2.76	2.66	Ce_2O_3	7.30	3.27	Ce_2O_3	0.06	0.08
ThO_2	0.31	0.24	1.39	0.32	0.87	0.29	SiO_2	1.07	0.45	SiO_2	1.70	1.59
La_2O_3	12.73	0.81	15.13	2.57	8.62	2.92	P_2O_5	0.73	0.05	Al_2O_3	0.90	0.81
Ce_2O_3	31.93	1.64	27.58	0.82	25.96	3.02	HfO_2	0.52	0.31	SO_3	0.19	0.08
Nd_2O_3	n/a	n/a	n/a	n/a	n/a	n/a	TOTAL	61.93	5.70	Cl	4.75	1.41
F	2.11	0.36	2.85	0.60	1.63	0.92				TOTAL	57.96	1.64
TOTAL	60.18	0.92	55.31	3.28	56.04	4.57						
CO_2	n/c		n/c		n/c		formula based on 2 $(CO_3)_2$- groups					
Formula proportions calculated on bases of 3 cations												
Ca	0.77	0.17	0.54	0.13	0.82	0.38						
P	0.01	0.01	0.01	0.01	0.02	0.02	Na	0.08	0.10			
Sr	0.05	0.01	0.07	0.03	0.01	0.01	Ca	0.92	0.10			
Si	0.15	0.14	0.07	0.03	0.33	0.20	TOTAL	1.00	0.00			
Al	0.09	0.10	0.03	0.01	0.18	0.19	Sr	0.05	0.02			
Fe	0.00	0.00	0.03	0.02	0.17	0.15	Ba	0.04	0.03			
Th	0.01	0.00	0.03	0.01	0.02	0.00	La	0.09	0.05			
Hf	0.06	0.01	0.00	0.00	0.00	0.00	Ce	0.12	0.06			
La	0.38	0.04	0.50	0.06	0.25	0.06	Si	0.67	0.08			
Ce	0.94	0.10	0.92	0.05	0.77	0.20	P	0.03	0.00			
F	0.54	0.10	0.81	0.13	0.40	0.20	Hf	0.01	0.00			
TOTAL	3.00	0.02	3.01	0.02	3.01	0.03	TOTAL	1.00	0.00			

Table 5.15 Electron microprobe data for REE-carbonate phases in sövite in the Brava intrusive alkaline complex. Abbreviations: st dev=standard deviation, ave=average, n/c=not calculated. Cations recalculated on the basis of 3 cations and $2(CO_3)_2$-. Complete tables in Appendix 3A.

The second REE phase found in 08SB48 is törnebohmite forming tabular tiny crystal (Figure 5.37). Törnebohmite has high though variable La_2O_3+Ce_2O_3 concentration (Table 5.16) which decrease with increasing SiO_2+Al_2O_3. Interestingly the concentration of La corresponds to almost equal concentration of Ce in every analysed sites. The same correlation applies to Si versus Al. Thus the ratios Ce/La and Si/Al are stable having 1:1 value. Analyses of törnebohmite can be grouped accordingly to the sum of LREE versus ∑Si,Al (average values, Table 7.4.12a) as follows: lower value La+Ce =32 wt% versus higher value Si+Al = 42 wt%; higher La+Ce =46 wt% versus lower Si+Al=18 wt%; and

slightly higher value La+Ce=50 wt% versus slightly lower Si+Al=10 wt%. The pattern shows that with increasing enrichment in LREEs the aluminium with silica content is proportionally decreasing. This phase has also a noticeably high amount of F ranging from 2.69 to 3.31 wt%, thus it is fluorotörnebohmite. The lower LREE concentrations in a single crystal (Figure 5.37) were found in contact with the host phengite, while core, sheltered from the mica, exhibits highest La and Ce values.

According to Hirtopanu et al. (2013), formation of törnebohmite could be a consequence of variation in concentrations of SiO_2, REE activities in the fluid and a decrease temperature. Thus the activity of the SiO_2 increases with decreasing activity of LREEs, which is the Brava case. The close association with Al-rich mica According to Hirtopanu et al. (2013), formation of törnebohmite could be a consequence of variation in concentrations of SiO_2, REE (phengite) in 08SB48 advocates for a Al-rich fluid not only influencing crystallisation of the mica but also assisting in accommodation of Al in higher concentration in törnebohmite than the one found in Ditrau alkaline massif, Romania (6-7.5 wt%) (Hirtopanu et al., 2013). Here its composition also differs in LREE content (ca 60 wt%). Hence the Brava conditions with double the Al_2O_3 concentration indicate higher Al activity in the fluid, thus preventing törnebohmite from having greater concentration of LREEs.

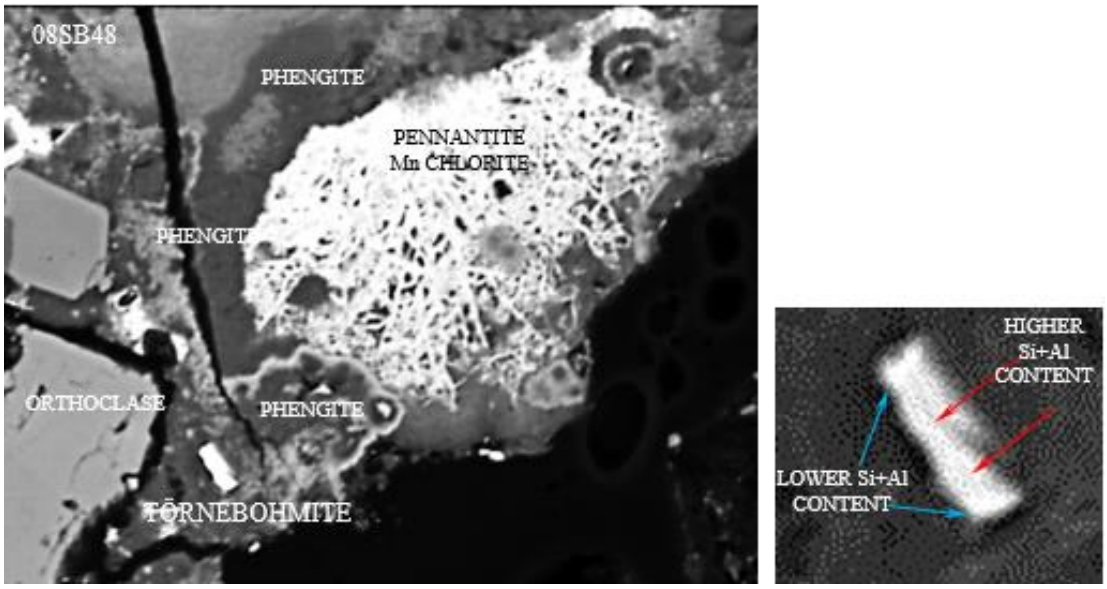

Fig 5.37a BSE image of törnebohmite and associated minerals from syenite cut by orthoclase vein 08SB48.

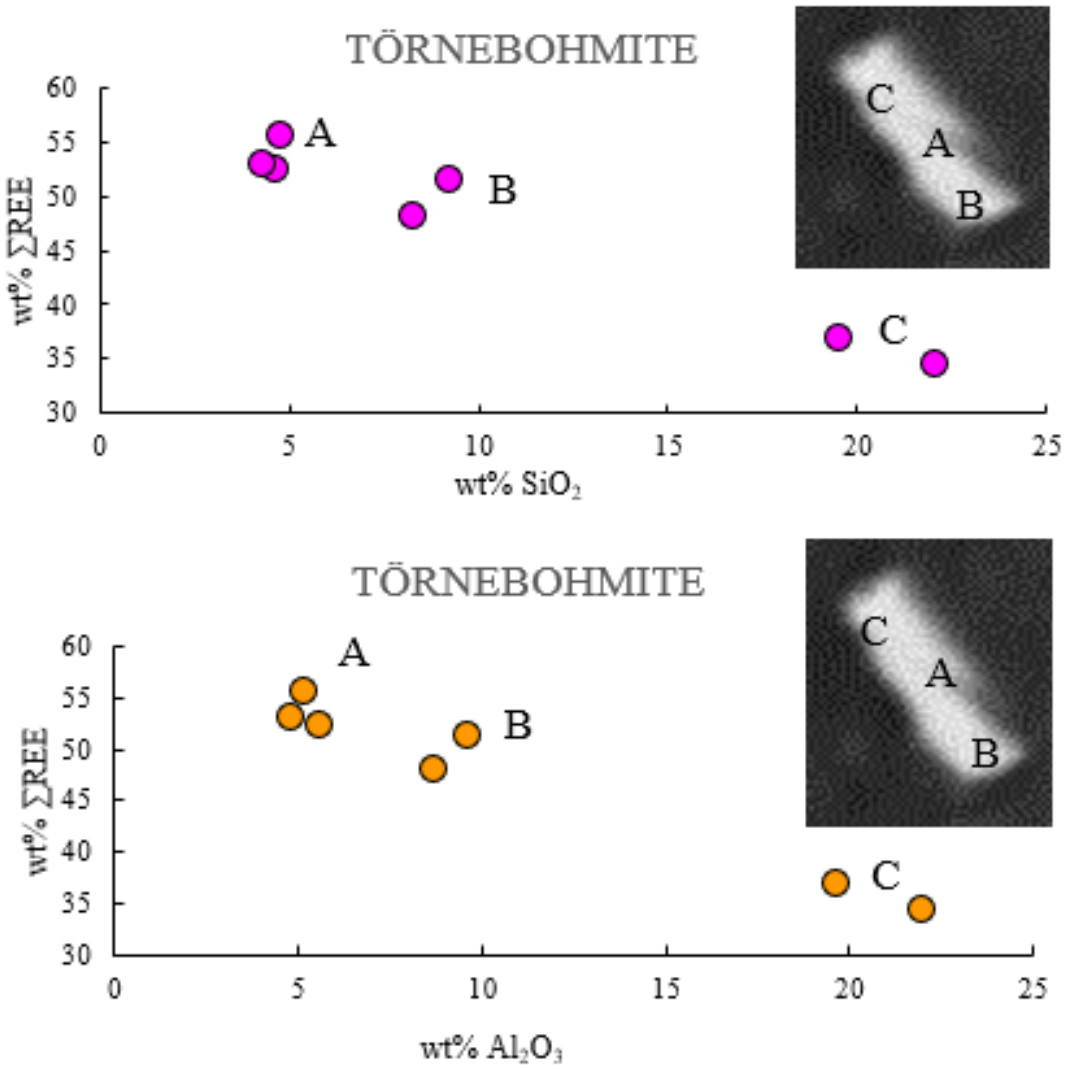

Fig 5.37b Diagram of törnebohmite crystal in 08SB48 dividing the chemistry of the single crystal into A, B and C parts according to wt% ∑REE vs wt% SiO_2 and wt% Al_2O_3.

Hirtopanu et al. (2013) also suggest that törnebohmite originated by hydrothermal fluids in a F-poor environment and most likely under relatively reducing conditions (F content in törnebohmite in Bastnäs is 0-0.13 wt%, Holtstam and Andersson (2007)). In contrast the Brava 08SB48 törnebohmite contains considerable amount of F meaning that hydrothermal fluids were most likely enriched in F which played an important part in mineralization of REE-silicates.

Sample 08SB48 contains another REE-phase which is the hydrated phosphate rhabdophane, associated with host zeolite. It shows a granular texture assembled in elongated acicular and bent crystals adjacent to pyroxene or between pyroxene and ilmenite (possibly exploiting a cavity). BSE images revealed inhomogeneity of crystals (Figure 7.38a and b) and rhabdophane chemical variation can be clustered into three

groups (Table 7.4.12a). The highest P_2O_5 content (16.64 wt%) is related to high LREEs (37.7 wt%) and low SiO_2+Al_2O_5 (4.5 wt%). Crystals with slightly lower content of P_2O_5 (12.09 wt%) show also lower LREEs value (31 wt%) though higher SiO_2+Al_2O_5 concentration of 17. 94 wt%. The lowest P_2O_5 content (7.88 wt%) is associated with the highest LREEs value of 40.14 wt% and considerable sum of Si and Al (12.79 wt%). CaO content is rather stable around 5 wt%, though Nd_2O_3 varies slightly from 8.60-5.45 wt% (increasing LREEs correspond to decreasing Nd). Rhabdophane low totals are accounted for by H_2O content (not calculated). Benaouda et al. (2017) referred to the crystal structure of rhabdophane being hexagonal (Mooney, 1950) and postulated nH_2O content (n is number of water molecules) between 0.5 and 1.5. Petrographic features and association of rhabdophane with zeolite indicated formation of this mineral from hydrothermal fluid not alteration after apatite.

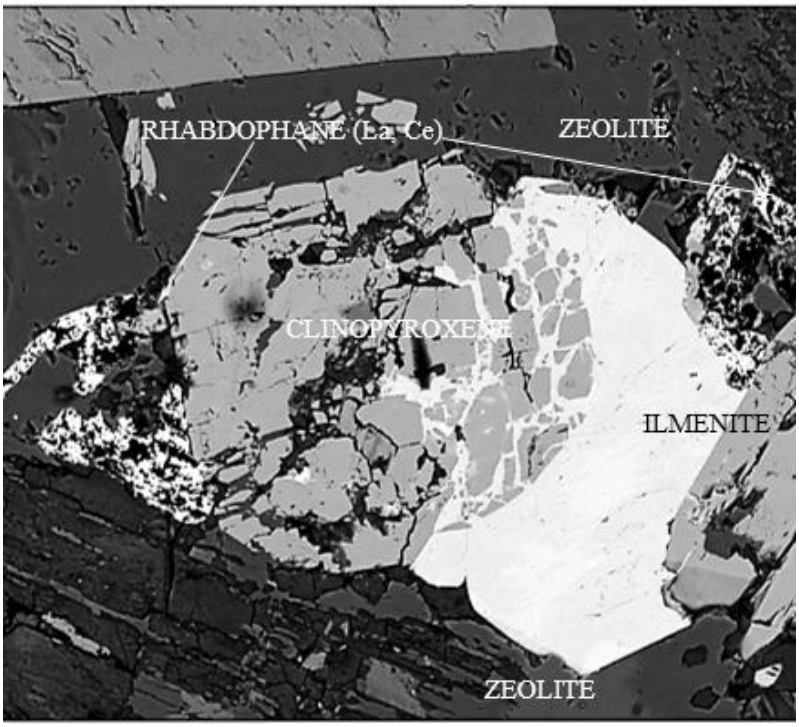

Fig 5.38a Backscatter electron image of rhabdophane and associated minerals from syenite cut by orthoclase vein 08SB48 from L5 location, Brava, Cape Verde

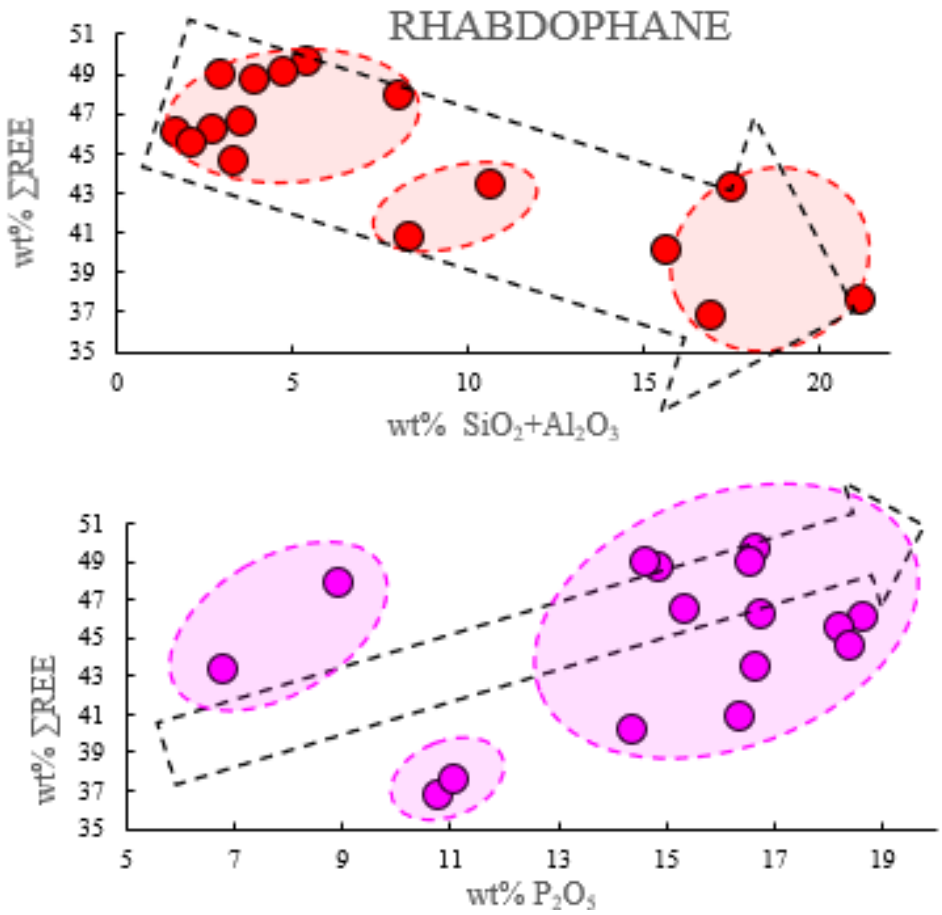

Fig 5.38b Diagram of rhabdophane crystal in 08SB48 dividing the chemistry into three areas according to concentration of wt% ∑REE vs SiO_2+Al_2O_3 and vs wt% P_2O_5.

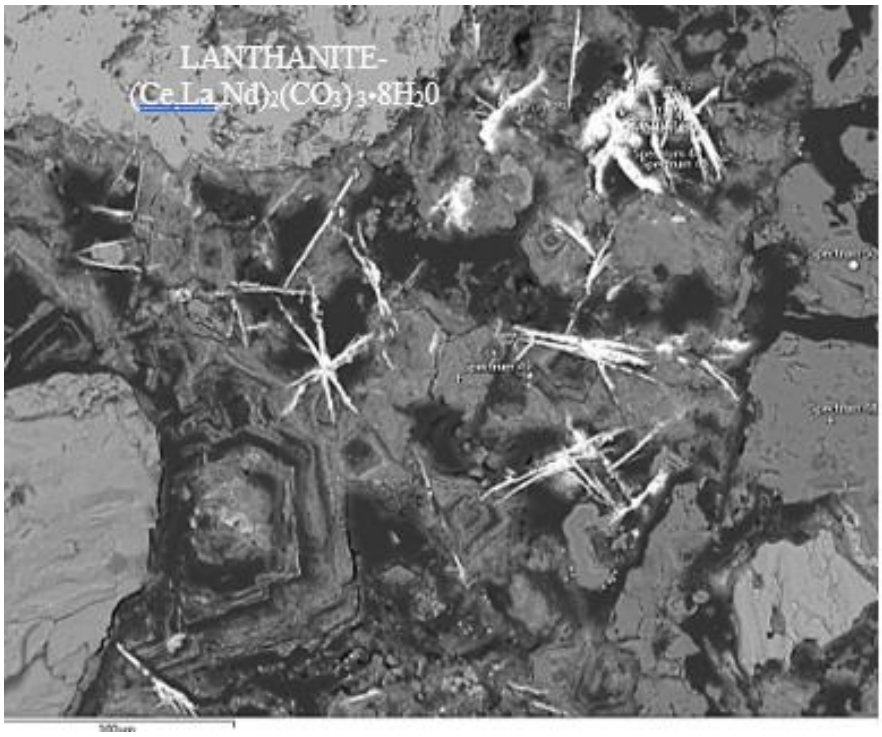

Fig 5.39 Backscatter electron image of lanthanite (La,Ce) and associated hexagonal zeolite-calcite from Brava carbonatite cut by zeolite vein 08SB43.

In carbonatite-zeolite sample 08SB43 sporadic REE lanthanite-(Ce,La) forms tiny concretions in vugs from which radiating and acicular crystals grew (spherulites). Sometimes lanthanites are attached to the side of the adjacent zeolite (Figure 5.39). Lanthanite is a hydrous REE-carbonate enriched in La, Ce and Nd, with average sum of REE oxides close to 50 wt% (Table 7.4.12a). There are two variations of lanthanites, La>Nb and Nd≥La, reflecting internal distribution in La and Nb. CaO is present in moderate amounts ranging from 6.35 to 6.57 wt% with traces of SiO_2 (0.32-1.22 wt%) and Al_2O_3 (0.29-0.92 wt%) (Table 7.4.12a and Table 7.4.12d). Lanthanite in the zeolite-vein results from fast crystallisation in highly changeable conditions as the carbonate also has a spherulitic texture and the zeolite shows concentric zonation.

LANTHANITE

La>Nd

	SB43 lnth1	SB43 lnth2	SB43 lnth3	SB43 lnth4	SB43 lnth5	SB43 lnth6	SB43 lnth7	SB43 lnth8	SB43 lnth9	SB43 lnth10	SB43 lnth11	SB43 lnth12	SB43 lnth13
SiO_2	1.32	0.60	0.52	0.68	0.48	0.18	0.75	4.45	4.01	1.73	0.30	0.52	0.29
Al_2O_3	1.12	1.79	0.10	0.93	0.75	0.07	0.60	2.40	2.58	0.66	0.14	0.30	0.54
MnO	0.39	0.18	0.13	0.00	0.18	0.08	0.17	0.07	0.47	4.79	0.00	0.03	0.50
CaO	3.67	5.36	3.99	5.34	5.09	4.48	4.09	4.75	3.97	5.03	12.88	10.43	13.50
La_2O_3	19.50	20.81	20.43	22.73	21.18	21.44	20.68	19.54	21.15	11.67	17.33	16.97	17.85
Ce_2O_3	24.35	24.07	24.90	27.31	24.90	26.31	25.45	25.02	26.18	21.90	22.87	23.99	22.08
Nd_2O_3	4.62	4.63	4.17	4.76	5.05	3.81	5.64	5.27	6.02	3.06	5.53	5.82	5.96
SrO	0.53	0.79	0.79	0.51	0.83	0.82	0.58	0.83	0.53	0.36	0.93	0.55	0.87
TOTAL	55.50	58.23	55.03	62.26	58.46	57.19	57.96	62.33	64.91	49.20	59.98	58.61	61.59

Nd≥La

	SB43 lnth14	SB43 lnth15	SB43 lnth16	SB43 lnth17	SB43 lnth18	SB43 lnth19	SB43 lnth20	SB43 lnth21	SB43 lnth22	SB43 lnth23	SB43 lnth24	SB43 lnth25	SB43 lnth26
SiO_2	0.17	0.28	0.46	0.29	0.62	0.38	0.32	0.40	0.21	0.09	0.31	0.28	0.32
Al_2O_3	0.19	0.69	0.16	0.18	0.20	0.51	0.26	0.18	0.30	0.06	0.21	0.17	0.71
MnO	0.27	0.34	0.06	0.55	0.22	0.22	1.03	0.27	0.42	0.03	0.60	0.00	0.41
CaO	5.09	5.26	4.64	8.26	4.51	4.76	7.84	4.10	6.92	12.96	4.71	8.96	7.44
La_2O_3	11.18	12.69	10.50	16.62	11.94	11.39	14.07	9.90	10.47	15.53	11.19	11.91	13.28
Ce_2O_3	24.83	26.03	22.60	23.50	26.55	24.89	21.74	23.09	22.73	20.97	23.79	23.61	24.11
Nd_2O_3	12.41	13.49	11.57	6.07	13.52	10.44	7.31	12.21	12.08	7.04	12.13	8.28	8.31
SrO	1.68	1.86	2.08	0.42	1.91	1.94	0.89	1.93	1.58	0.00	2.00	0.71	0.90
TOTAL	55.82	60.64	52.07	55.89	59.47	54.53	53.46	52.08	54.71	56.68	54.94	53.92	55.48

Table 5.16 Electron microprobe data for lanthanite (Ce) (in carbonatite-zeolite sample) from Brava.

According to Vallina et al. (2015) "The crystallisation of La or Nd bearing-carbonates is always initiated by the nucleation and growth of amorphous La or Nd carbonate precursors. Both of the precursors are highly hydrated nanoparticulate compounds with similar spherical morphologies and sizes. However, the most striking difference between the amorphous La and Nd precursors is related to their stabilities. These depend directly on the ionic potential of the REEs: the higher ionic potential the longer the lifetime of the amorphous phase because the energy needed to dehydrate the

Nd^{3+} ion is higher compared to the La^{3+}. After the breakdown of the precursors under different dry heated, ambient or hydrothermal conditions and over a range of temperatures, they transform to a variety of crystalline REE carbonates with different structures, compositions and stabilities. Hydrated carbonates like lanthanite-(REE) were obtained at lower temperatures (< 95 °C), whereas at higher temperatures (165 and 220 °C) anhydrous carbonates were dominant. Above 60 °C (La system) and 95 °C (Nd system) the minerals develop spherulitic morphologies when they crystallise directly from amorphous precursors. This development of the spherulitic growth requires high supersaturation levels that can only be obtained by the rapid dissolution of the amorphous precursors or the hydrated crystalline carbonates in some specific cases". Therefore, natural hydrothermal solutions must have been very complex in composition and crystallisation of LREE-carbonates was also complex, nonetheless the temperature of the fluid must have been relatively low to trigger crystallisation of spherulitic lanthanites.

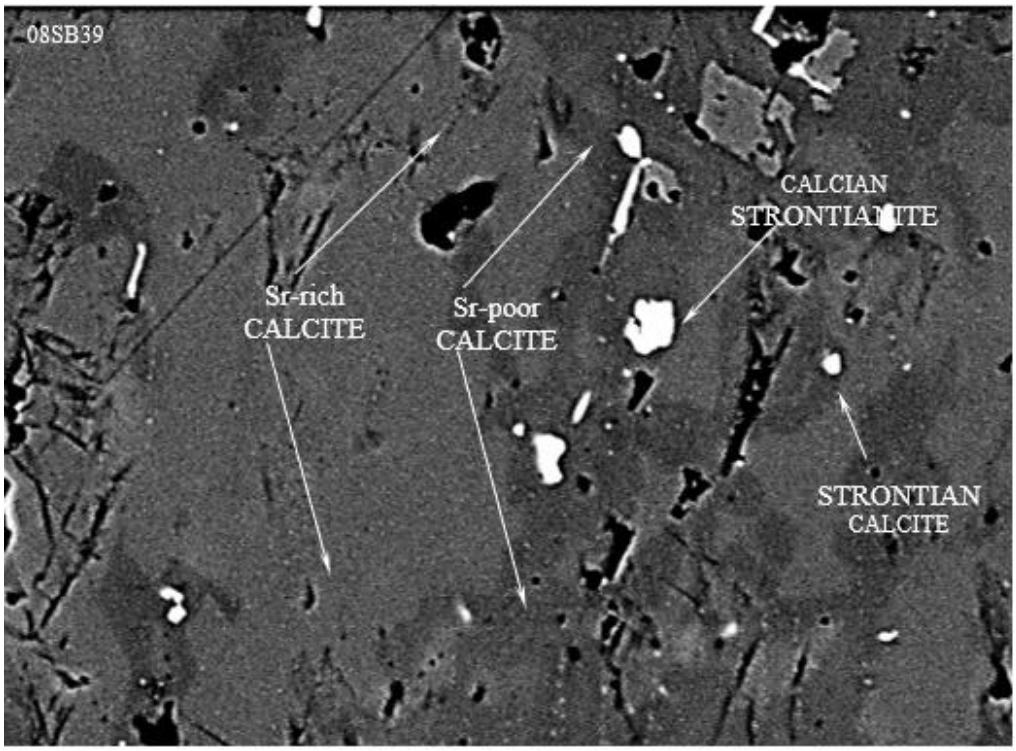

Fig 5.40 Backscatter electron image of calcian strontianite-strontianite calcite-Sr-poor calcite-Sr-rich calcite in Brava sövite 08SB39.

Sr-rich carbonate minerals are found in three samples (carbocernaite in 08SB39, burbankite in 08SB48 and strontianite in 08SB39 and 08SB47). Strontianite is mostly enriched in SrO from 37.86 to 44.22 wt% and CaO 17-22 wt% (in 08SB39 and 08SB47, respectively) (Table 7.4.12a-c), burbankite and carbocernaite have similar enrichment in SrO (28-27 wt%) though CaO exhibits a higher concentration in carbocernaite (17 wt%)

than in burbankite (12 wt%). Burbankite contain 13 wt% BaO but in carbocernaite and strontianite BaO concentration declines to 3 and 2 wt%, respectively. Additionally REEs are present having total value in carbocernaite up to 13 wt%, in burbankite 6 wt% and in strontianite 1 wt%. Only strontianite contains P_2O_5 (2 wt%) while Na_2O was detected in burbankite and carboceranite (3 and 1 wt%, respectively). Minor concentration of HfO_2 (0.6 wt%) was detected in burbankite and strontianite. Futhermore in sövite 08SB39, calcian-strontianite and strontian-calcite coexist forming irregular rounded blebs of Sr-Ca-carbonates. Sr-rich calcite contains 41wt % CaO and 12 wt% SrO, while calcian strontianite contains 22 wt% CaO. The host calcite was originally homogenous and rich in Sr but progressively during the patchy exsolution of Sr-Ca-rich carbonates it turned (in close proximity to the exsolved phases) into Sr-poor regions. Sr-Ca-carbonates form fine-grained blebs composed of calcian-strontianite to strontian-calcite solid-solution series. The remaining host calcite, away from the regions depleted in Sr, continue to be Sr-rich (Figure 7.40). Carbocernaite also exsolved from host being Sr-rich calcite and can be found in depleted in strontium calcic region (Figure 7.41). The major difference between carbocernaite and other Sr-Ca-rich carbonates is enrichment in LREEs showing an average concentration of 12.6 wt% (Ce>La).

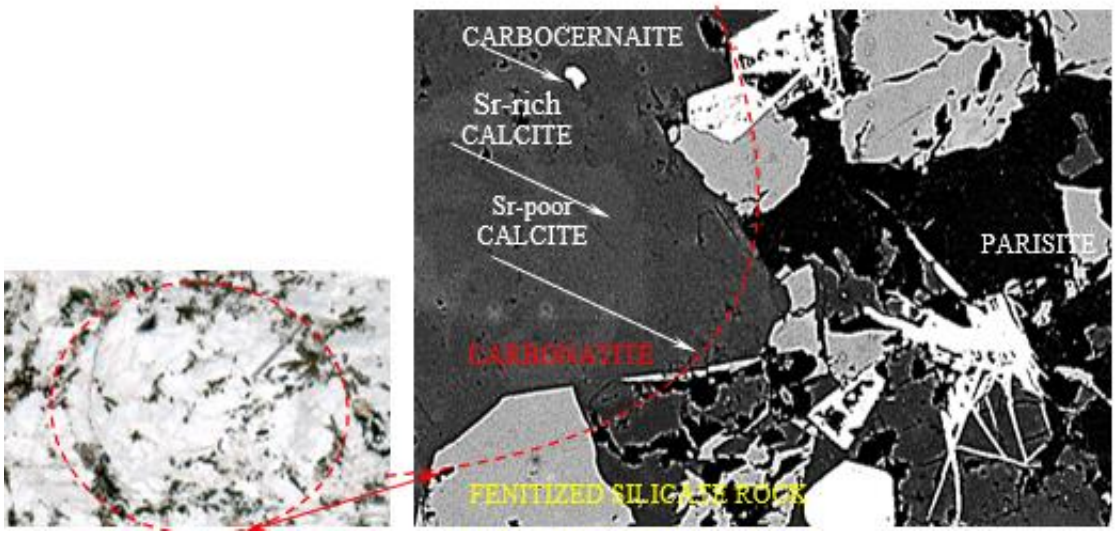

Fig 5.41 Scanned thin section of Brava sövite 08SB39 showing calcic regions influenced by metamorphic event (shearing during emplacement/uplift) and backscatter electron image of calcite-silicate association showing exsolution of carbocernaite from primary calcite in sövite 08SB39. Also crystallisation of parisite demonstrate association with silicate part of the section crystallised within metasomatic margin rimming the calcic regions.

According to Wall et al. (1993), carbonatites enriched in REE mostly form during the last stages of emplacement as dykes into alkaline suites. Secondary texture is influenced by hydrothermal alteration which contrast with primary magmatic texture. The authors listed the unusual chemistry of the Sarnu dyke containing carbocernaite, Sr-rich

calcite and Ca-rich strontianite in contrast with the secondary assemblage in Kangankunde and Nkombwa carbonatites of Ca-poor strontianite and calcite and the presence of oxides and RE-minerals. Wall et al. (1993) emphasised the influence of high level of SrO in magmatic system at Sarnu on crystallisation of carbocernaite and stabilisation of REE-rich carbonate phases leading to complex crystallisation of strontian calcite, carbocernaite and calcian strontianite. Thus, cotectic carbocernaite and strontian calcite was joined later by calcian strontianite (Figure 5.42).

Wall et al. (1993) stressed the importance of limits of solid solution not accounted for previously in nature as Sarnu calcite is enriched up to 13 wt% SrO and the strontianite up to 20 wt% CaO. The strong similarity in chemistry and assemblage of Brava sövite in strontian calcite (enriched up to 12 wt% SrO), the calcian strontianite (up to 22 wt% CaO) and presence of exsolved carbocernaite suggest a primary origin of 08SB39. The associated silicate phases rimming the calcic regions are of metasomatic origin.

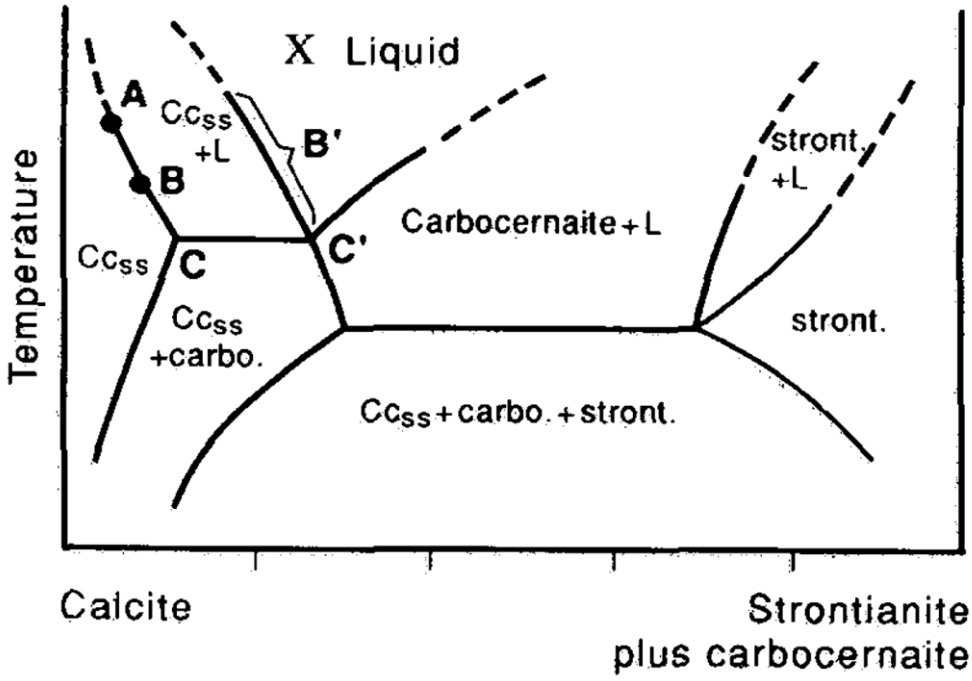

Fig 7.42 Possible pseudobinary system (sketch) for Sarnu carbonatite where Cc_{ss} = calcite, stront = strontianite, carbo = carbocernaite. X = bulk composition of Sarnu dyke; L = liquid (after Wall et al., 1993).

Burbankite is found only in syenite-orthoclase 08SB48 together with barite forming minute rare inclusions in Mn-calcite. Burbankite is an anhydrous carbonate phase enriched in REEs with the average total content of 4.5 wt%. The SrO concentration is high (28 wt%) as well as BaO (13 wt%), though with lower Na_2O (2.8 wt%). This carbonate phase is set in calcite (in syenite) extensively cross-cut by orthoclase veins. Barite is composed of BaO (average content 64 wt%) and SO_3 (average value 31wt%).

All average values are in Table 7.4.12a. As both phases reside in Mn-calcite, closely associated with fenite orthoclase net-veining, they are considered to be hydrothermal in origin.

5.4.15 Summary from mineral chemistry

Calcite formed both primary and secondary crystals with chemical diversity and zonation implying multiple events of growth. Calcite hosts unusual rare primary phases such as strontianite and secondary such as burbankite, barite and other.

Primary apatite although scarce, yields important information about processes affecting the Brava alkaline complex. The absence of monazite (as a dissolution product after apatite) provides indirect evidence for transfer of LREE in associated phases with apatite towards the rim, most likely in presence of Cl-rich fluids even though chlorine is no longer detected.

Clinopyroxene is a primary mineral and fractionation trend demonstrates evolution from diopside towards aegirine being progressively more enriched in trace elements such as Zr, Th, U and LREEs. Amphibole occurs as a primary or secondary, when alteration after clinopyroxene takes place. The trace element enrichment such as Zr in an amphiboles show higher values than in pyroxenes. The LREEs in Brava pyroxenes show variable content (up to 1wt% in total) though the Brava amphiboles show preference for Ce incorporation into sövite rather than silicates.

Homogeneity of orthoclase throughout analysed samples place its origin as metasomatic (fenitic). Albite is a product of albitization by Na-rich metasomatic fluids. It is not clear what host mineral was replaced by metasomatic albite, but probably orthoclase (?).

Metasomatic feldspathoids of cancrinite-subgroup phases such as S-, Cl- and Ca/S-pitiglianoite, although present in minute amount, provide information of Cl (and S) activity in the system providing the evidence of circulation Cl-rich fluids such as chlorine. Zeolite is the product of volatile-rich carbohydrothermal fluids and Na-metasomatism (wall rock fenitization) during which alteration of feldspar to zeolite occurred.

Primary mica forms rather fine and numerous crystals with exception of glimmerite. In sövite phlogopite is metasomatised. The silica undersaturated trend shows a wide compositional evolution from least fractionated phlogopite towards highly evolved

biotite. There is evidence of late-stage fluid circulation altering mica to phengite and further circulated fluid transformed mica to Mn-chlorite pennantite.

Evolution of magnetite to titanomagnetite → ilmenite → titanite → rutile → henrymeryeite was progressive. Increase in REEs, Nb, Zr and Ba demonstrates progressive incorporation of these elements leading to alteration earlier formed minerals by interaction with late-stage fluids.

Originally primary zoned pyrochlore (core and inner rims) as an accessory phase presents valuable information about fluctuating magmatic processes affecting the system such as becoming more alkaline, followed by increase in activity of hydrothermal fluids rich in Mn, Sr and Zr (outer rim).

Zr-rich minerals provide information about condition during which they crystallised. Thus one of the last stage of hydrothermal activity can be narrowed down to temperature < 150°C, during which hilairite was able to form. Lower concentration of Ti in tazheranite most likely reflects the very close association of this phase with rutile and activity of fluids (interaction and transfer of elements).

REE-phases such as parisite provide some insight into fluoride and chloride activity aiding their crystallisation. Törnebohmite contains considerable amounts of fluorine, meaning that hydrothermal fluids were F-rich and played important part in mineralization of REE-silicates. Petrographic features and association of rhabdophane with zeolite also argues for formation of this mineral from a hydrothermal fluid. Development of spherulitic texture in lanthinite crystals requires high supersaturation and rapid dissolution of the amorphous precursors of the hydrated crystalline form, with fluid temperature being low (60-90°C). The chemistry and assemblage (in sövites) of strontian calcite and calcian strontianite with presence of carbocernaite, all exsolved in calcite, is primary in origin. The associated silicate phases rimming calcic-areas and holding parisite are of metasomatic origin. Burbankite and barite, both residing in Mn-calcite, are considered to be hydrothermal in origin.

Crystallisation history of primary and secondary minerals can be captured as:

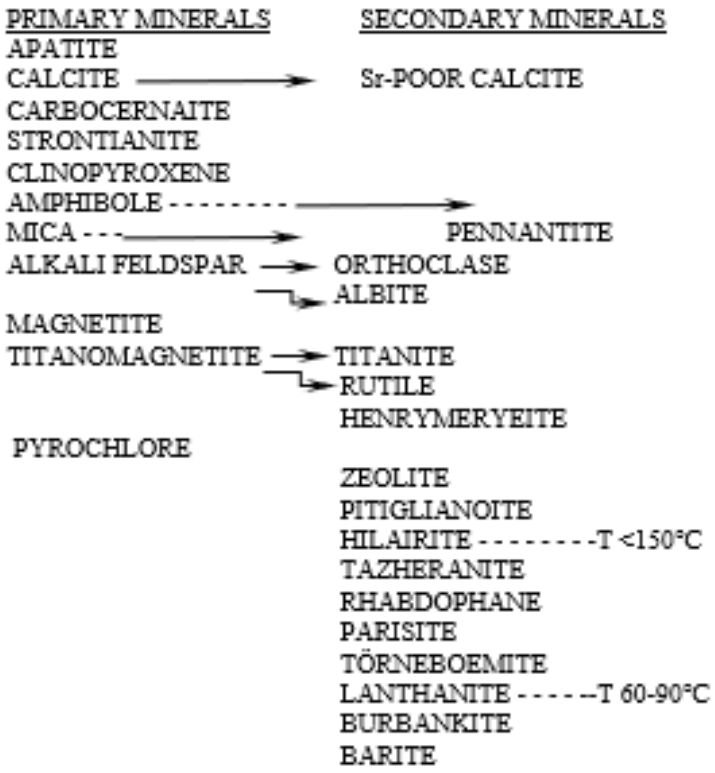

5.6 Trace element distribution in minerals from Brava samples

The Brava samples analysed for trace elements consist of sövite, veined composite rock (glimmerite/carbonatite/syenite), syenite cut by orthoclase vein, feldspar/foid pegmatite and veined syenite-calcite rock. REE and trace element analyses were performed on major and minor phases. Regrettably many minor phases were too fine-grained for LA-ICP-MS method.

Calcite trace element data is presented in Table 7.5.1a (Appendix 3b). The average values and standard deviation are given in Table 5.16. The average values are shown in Figure 5.43. All analysed Brava samples contain calcite; average Sr content in calcite is highest in sövite (100000 to 300000 ppm), followed by veined syenite-calcite sample (10000 ppm). Pegmatite and syenite calcite have lower Sr contents (5000 and 8000 ppm respectively). The Ba average contents are also highest in calcite in sövite (5000-16000 ppm), intermediate in syenite calcite (1200 ppm) and relatively low in calcite from veined syenite and feldspar/foid pegmatite (500-800 ppm). Trace elements such as Rb, Th, Nb, Ta, Zr and Hf show negative anomalies in calcite.

CALCITE

Trace Element

	ave n=6	st dev n=6	ave n=4	st dev n=4	ave n=11	st dev n=11	ave n=2	st dev n=2	ave n=3	st dev n=3
Ti	bdl	*bdl*	2.460	*bdl*	321.6	*bdl*	0.003	*bdl*	0.001	*bdl*
Cr	3.500	*bdl*	2.57	*bdl*	2.960	*bdl*	141.52	*39.59*	35.98	*18.64*
Mn	1155	*173*	3569	*726*	bdl	*542.9*	6.572	*0.419*	2.152	*0.978*
Co	0.179	*0.048*	0.608	*0.233*	0.201	*0.056*	0.300	*0.284*	0.082	*0.020*
Ni	bdl	*bdl*	bdl	*bdl*	bdl	*bdl*	bdl	*bdl*	0.942	*0.054*
Cu	bdl	*bdl*	bdl	*bdl*	0.600	*bdl*	bdl	*bdl*	0.376	*0.132*
Ga	3.433	*0.426*	1.483	*0.90*	2.592	*0.364*	57.55	*27.83*	17.64	*5.757*
Ge	2.543	*0.494*	1.625	*0.007*	1.505	*0.208*	65.96	*47.32*	12.20	*6.753*
Rb	bdl	*bdl*	bdl	*bdl*	bdl	*bdl*	4.900	*5.469*	1.136	*0.029*
Sr	8205	*967.1*	5161	*1837*	17960	*1852*	349701	*97486*	101175	*27203*
Y	278.9	*54.62*	226.7	*104.6*	66.55	*11.40*	1235	*418.1*	327.1	*63.38*
Zr	bdl	*bdl*	0.280	*0.156*	0.154	*0.008*	2.218	*2.139*	0.21	*bdl*
Nb	0.024	*0.024*	0.009	*0.000*	0.023	*0.012*	0.066	*0.054*	0.05	*0.04*
Ba	1241	*502.3*	488.4	*484.7*	789.3	*97.3*	15978	*2047*	4886	*2036*
La	85.49	*16.02*	45.88	*28.00*	167.8	*24.61*	3449	*1967*	821.6	*196.5*
Ce	247.6	*30.72*	101.8	*66.51*	255.4	*37.74*	6035	*3434*	1386	*322.9*
Pr	37.07	*3.417*	14.98	*9.516*	23.77	*3.726*	523.4	*271.2*	125.3	*28.87*
Nd	200.5	*21.96*	81.86	*52.74*	73.93	*11.62*	1848	*984.6*	451.0	*123.9*
Sm	62.96	*11.89*	34.65	*20.62*	11.33	*2.044*	252.9	*124.5*	64.33	*7.460*
Eu	22.27	*4.580*	13.93	*7.800*	3.583	*0.545*	84.01	*33.57*	18.38	*3.265*
Gd	68.24	*14.91*	45.27	*23.99*	10.92	*2.131*	258.4	*134.0*	58.60	*17.14*
Tb	10.14	*2.466*	7.468	*3.741*	1.632	*0.334*	33.05	*14.19*	7.751	*1.782*
Dy	55.32	*11.68*	43.82	*21.44*	10.50	*2.141*	207.6	*79.38*	49.33	*6.892*
Ho	10.42	*2.161*	8.363	*3.939*	2.185	*0.335*	40.80	*14.05*	11.35	*2.018*
Er	24.56	*4.545*	20.56	*9.780*	7.055	*1.272*	113.3	*28.54*	33.02	*6.084*
Tm	2.470	*0.406*	2.080	*0.824*	1.089	*0.195*	18.84	*7.398*	4.298	*0.431*
Yb	11.15	*1.667*	9.298	*3.543*	6.756	*1.102*	120.3	*44.57*	30.91	*2.451*
Lu	0.947	*0.149*	0.863	*0.305*	0.825	*0.126*	14.46	*5.36*	4.348	*0.820*
Hf	0.049	*0.066*	0.012	*0.004*	0.024	*0.008*	bdl	*bdl*	0.024	*bdl*
Ta	0.004	*0.002*	0.003	*0.002*	0.007	*0.003*	bdl	*bdl*	0.010	*0.010*
Pb	0.995	*0.174*	0.322	*0.283*	5.370	*0.688*	94.33	*37.02*	22.72	*11.60*
Th	0.921	*0.523*	0.600	*0.939*	0.010	*0.003*	0.074	*0.064*	0.020	*0.005*
U	0.006	*0.001*	bdl	*bdl*	0.008	*0.004*	bdl	*bdl*	0.003	*0.000*

Table 5.17 Average and standard deviation values of trace element contents (ppm) of calcite in the Brava syenite cut by orthoclase vein (08SB48), feldspar/foid pegmatite (08SB49), veined syenite-calcite rock (08SB50) and sövite (08SB39).

The REE pattern in Brava calcite shows variations (Figure 5.43). The most REE-enriched concave upwards patterns established in sövite 08SB39_1 and 2; also concave upwards pattern found in syenite-calcite (08SB50) though less enriched up to two orders than in sövite; in orthoclase vein (08SB48) and feldspar/foid pegmatite (08SB49) the patterns are concave downwards showing elevated LREE and MREE enrichment (this points to variable but largely stronger LREE and MREE fractionation into calcite in orthoclase vein and feldspar/foid pegmatite). The trace elements in calcite can be group in three different patterns: 08SB39, 08SB48 with 08SB49 and 08SB50. Calcite ranges for La from 50 to 3500 ppm and Ce 100-6000 ppm (average values in 08SB48, 08SB49, 08SB50, 08SB39_cc1 and 08SB39_cc2) with sövite being most enriched. The degree of enrichment of calcite expressed as La/Yb (LREE to

HREE chondrite-normalised values) and in calcite these values are overall low of 5-9 in pegmatite and orthoclase vein and nearby 20 in syenite and sövite.

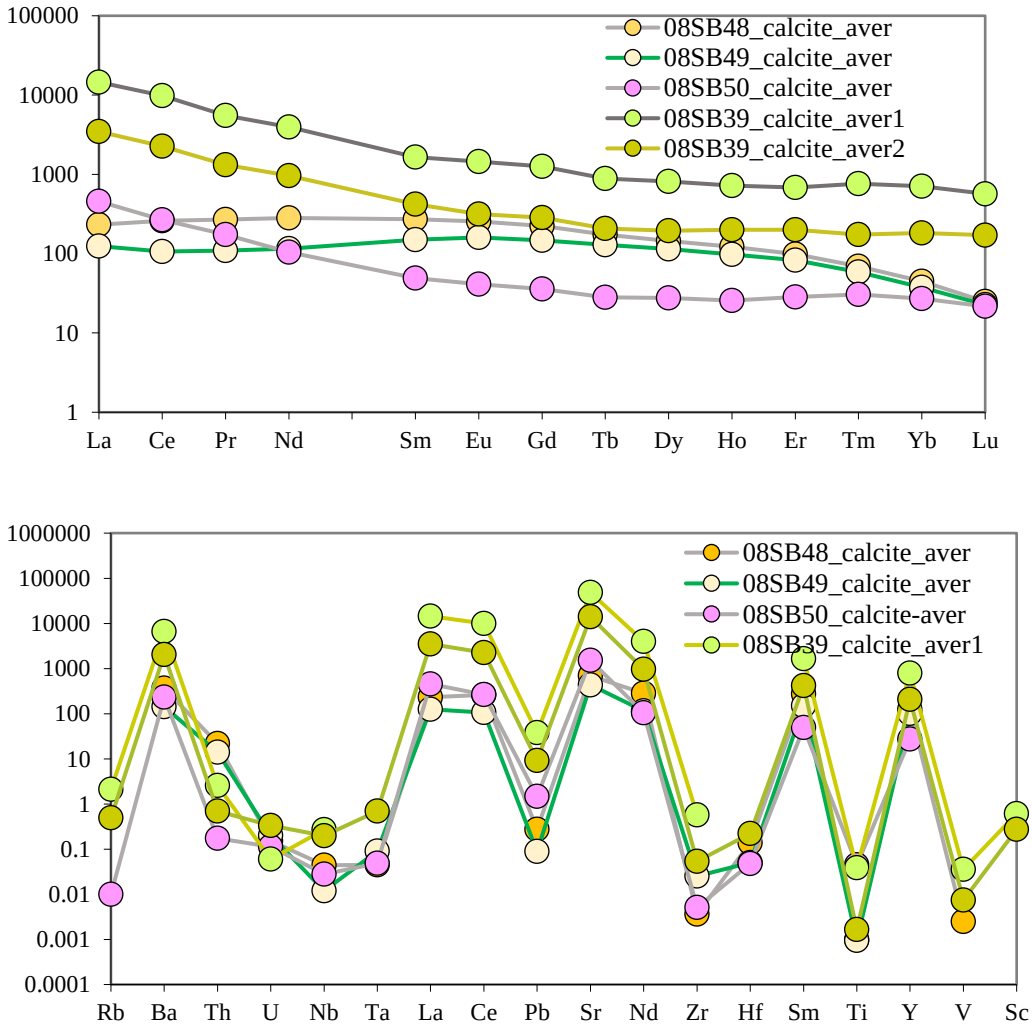

Fig 5.43 Chondrite-normalised REE and trace element distribution patterns of calcite in the Brava syenite cut by orthoclase vein (08SB48), feldspar/foid pegmatite (08SB49), veined syenite-calcite rock (08SB50) and sövite (08SB39).

Apatite trace elements data is presented in Table 7.5.2a respectively (Appendix 3b). The average values and standard deviation are given in Table 5.18. The data is shown in Figure 7.44.1 (Appendix 3b) with the average values shown in Figure 5.44.

Apatite was analysed in veined syenite (08SB50) and sövite (08SB39). Its Sr content is variable, being higher in sövite (100000 ppm) and one order lower in veined syenite (13000 ppm). Ba shows the same trend with an enrichment of 300 ppm in sövite and syenite 35 ppm. Apatite contains significant amounts of Y in sövites (2000 ppm) and lower in syenite (400 ppm). Zr is also substantial in sövite apatite being 100 times higher than in syenite.

	Trace Element Concentrations ppm					normalised to chondrite			
	08SB50		08SB39			08SB50		08SB39	
	ave n=4	st dev n=4	ave n=2	st dev n=2		ave n=4	st dev n=4	ave n=2	st dev n=2
Sc	0.560	bdl	5.275	3.433	La	4259	2419	34652	23705
Ti	33.04	11.54	0.049	0.057	Ce	2936	1350	27274	17951
V	10.44	1.916	358.31	98.54	Pr	2099	928.5	18764	12324
Cr	bdl	bdl	33.27	22.41	Nd	1310	511.2	14255	9069
Mn	260.3	84.13	0.295	0.103	Sm	592.0	232.0	6516	3986
Co	0.236	0.054	0.779	0.043	Eu	475.6	164.1	4434	2476
Ni	2.290	bdl	2.650	1.660	Gd	395.7	138.6	3610	2009
Cu	bdl	bdl	15.55	17.55	Tb	266.5	85.55	2453	1240
Ga	33.20	15.40	210.5	127.1	Dy	209.2	68.35	1925	834.5
Ge	12.60	5.038	137.0	85.86	Ho	171.6	61.70	1516	618.5
Rb	4.330	4.285	3.580	1.768	Er	146.2	48.09	1211	468.0
Sr	13017	1437	106041	71456	Tm	108.5	37.60	950.5	328.6
Y	368.2	132.2	2113	857.1	Yb	72.67	25.64	683.4	240.8
Zr	3.577	3.885	330.5	446.1	Lu	42.56	12.63	430.5	151.7
Nb	0.764	0.564	3.272	2.280					
Cs	0.280	bdl	0.231	0.028					
Ba	35.47	20.17	290.2	238.9					
						ave n=4	st dev n=4	ave n=2	st dev n=2
La	1563	887.8	8213	5618	Rb	0.627	1.018	1.543	0.762
Ce	2810	1292	16692	10986	Ba	10.40	5.92	120.4	99.13
Pr	287.5	127.2	1783	1171	Th	4608	4166	7453	105.7
Nd	931.1	363.5	6657	4235	U	859.1	631.2	1949	107.6
Sm	136.7	53.59	996.9	609.8	Nb	2.041	1.510	13.30	9.269
Eu	41.38	14.28	257.2	143.6	Ta	0.223	0.352	0.550	0.184
Gd	121.1	42.42	741.9	412.8	La	4259	2419	34652	23705
Tb	15.46	4.961	91.73	46.37	Ce	2936	1350	27274	17951
Dy	79.70	26.04	488.8	212.0	Pb	0.697	0.409	4.339	2.902
Ho	14.61	5.249	85.80	35.01	Sr	1094	121.0	14606	9842
Er	36.41	11.97	200.4	77.45	Nd	1310	511.1	14255	9069
Tm	3.863	1.341	23.48	8.117	Zr	0.483	0.655	85.41	115.3
Yb	18.02	6.354	116.2	40.94	Hf	0.270	0.457	57.82	77.69
Lu	1.623	0.481	10.94	3.853	Sm	592.1	232.2	6516	3986
Hf	0.097	0.104	6.164	8.282	Ti	0.051	0.018	0.651	0.759
Ta	0.012	0.011	0.008	0.003	Y	72.70	25.6	1346	545.9
Pb	2.548	1.497	10.72	7.169	V	0.123	0.023	6.398	1.760
Th	195.8	177.1	216.1	3.066	Sc	0.016	0.033	0.891	0.580
U	10.49	7.696	15.59	0.861					

Table 5.18 Average and standard deviation values of trace element contents (ppm) and chondrite-normalised contents of apatite in the Brava veined syenite-calcite rock (08SB50) and sövite (08SB39).

The REEs patterns in apatite are sub-parallel to each other. Apatite in sövites displays higher concentrations of La and Ce with the average values of 8000 ppm La and 17000 ppm Ce. In veined syenite-calcite rock (08SB50) these values are rather high though lower than in carbonatite (1600 and 3000 ppm). The degree of enrichment of apatite expressed as La/Yb (LREE to HREE chondrite-normalised values) is 80 for the carbonatite and 99 for the syenite. Thus the apatite enrichment is higher than in calcite expressing stronger LREE fractionation into apatite. The REEs concentrations in apatite are considerably higher than in calcite. Also trace elements in apatite in sövite display enrichment on an average one order then then that of veined syenite-calcite. Apatite is highly enriched in Th and U (10000 and 1000 times of chondritic values respectively).

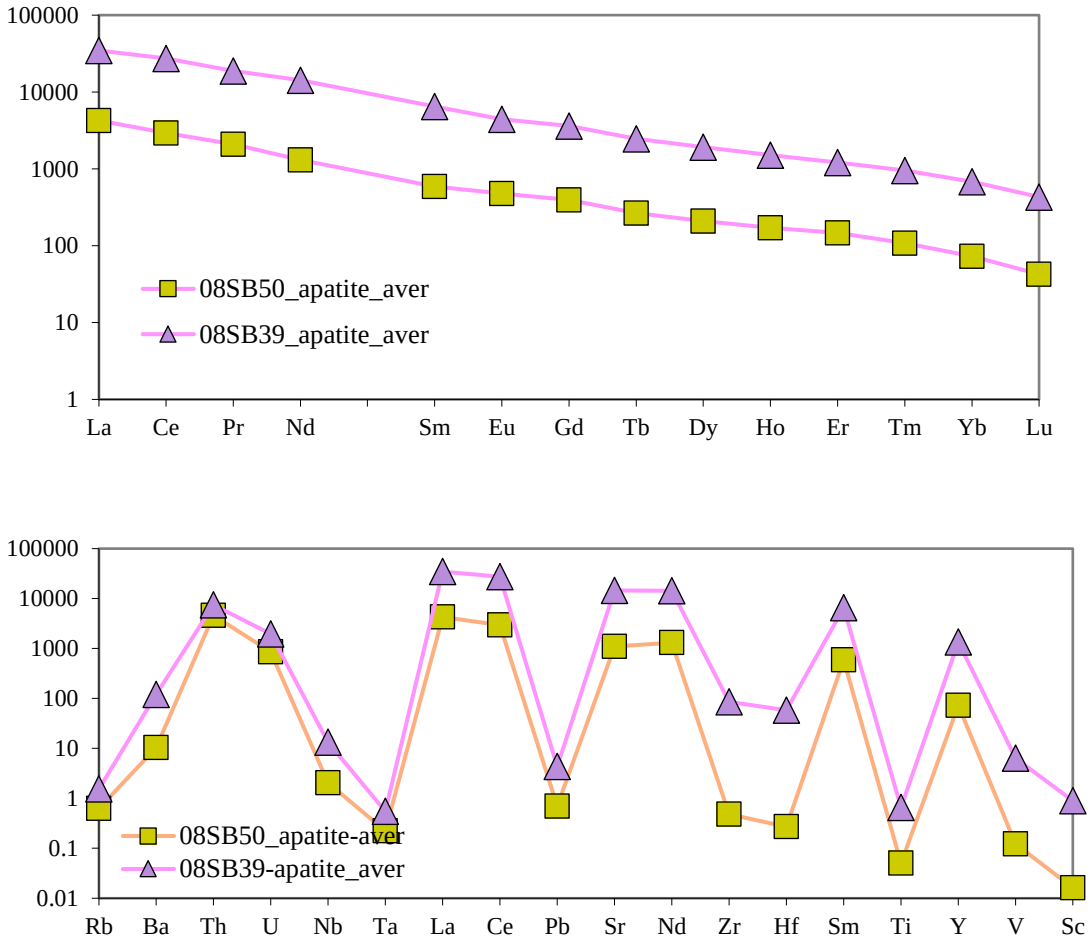

Fig 5.44. Chondrite-normalised REE and trace element distribution patterns of apatite in the Brava veined syenite-calcite rock (08SB50) and sövite (08SB39).

Amphibole was found in composite glimmerite/carbonatite/syenite sample (08SB40), feldspar/foid pegmatite (08SB49), and veined syenite-calcite rock

(08SB50) and sövite (08SB39). Compositional data for amphibole is given in Table 7.5.3a and Figure 7.45.1 (Appendix 3b). The average values and standard deviation are shown in Table 5.19 and Figure 5.45.

AMPHIBOLE
Trace Element Concentrations
ppm

	08SB40		08SB49		08SB50		08SB39	
Sc	11.50	2.760	76.86	43.36	10.27	0.775	0.264	0.027
Ti	5175	2202	142826	134205	5086	3255	1.389	0.156
V	669.1	153.5	7703	4173	1247	311.4	6.978	0.448
Cr	25.43	6.101	bdl	bdl	5.970	bdl	1.226	0.282
Mn	7483	1299	64302	64992	6380	1042	0.052	0.006
Co	12.66	2.722	95.86	119.2	5.113	0.401	0.002	0.000
Ni	4.500	1.967	58.61	bdl	bdl	bdl	0.007	0.001
Cu	bdl	bdl	bdl	bdl	0.770	bdl	0.002	0.001
Ga	22.43	4.393	300.8	234.1	57.27	25.39	0.663	0.033
Ge	4.562	1.5075	30.62	21.19	5.477	1.070	0.030	0.003
Rb	1.853	0.9500	10.33	9.277	8.255	8.832	0.119	0.277
Sr	257.9	94.40	93.96	21.74	123.9	23.17	2.439	0.410
Y	18.06	5.672	23.55	9.596	2.937	1.231	0.269	0.161
Zr	2265	1360	8954	3392	6569	1220	200.2	30.36
Nb	43.25	46.33	5430	6718	98.52	166.0	0.835	0.342
Cs	0.483	bdl	bdl	bdl	0.245	bdl	0.017	0.017
Ba	44.99	31.97	73.04	55.07	99.83	49.02	0.226	0.280
La	10.36	6.447	3.036	1.815	3.277	1.467	2.918	6.137
Ce	26.19	15.11	10.00	5.792	13.21	12.33	1.741	3.060
Pr	3.315	1.900	1.804	1.201	0.652	0.202	1.172	1.562
Nd	11.48	6.08	6.416	3.723	2.130	0.791	0.966	1.090
Sm	2.287	0.928	2.647	0.387	0.377	0.095	0.548	0.438
Eu	0.722	0.296	0.603	0.401	0.175	0.016	0.385	0.228
Gd	2.067	0.777	2.300	1.388	0.396	0.250	0.329	0.240
Tb	0.341	0.096	0.510	0.247	0.062	0.026	0.297	0.139
Dy	2.488	0.595	4.364	2.136	0.430	0.036	0.261	0.099
Ho	0.624	0.185	1.100	0.596	0.097	0.024	0.276	0.099
Er	3.195	1.478	5.976	4.299	0.593	0.111	0.43	0.13
Tm	1.114	0.587	2.218	1.589	0.236	0.078	0.907	0.240
Yb	14.69	9.838	50.65	44.909	3.330	1.444	2.148	0.462
Lu	3.328	2.049	24.40	24.77	0.985	0.333	4.075	0.986
Hf	38.27	39.86	140.2	80.32	86.90	20.53	122.9	19.01
Ta	0.246	0.284	68.59	67.60	0.251	0.412	0.120	0.114
Pb	0.347	0.222	1.675	2.072	3.752	4.622	0.007	0.006
Th	1.051	0.339	5.141	7.199	0.798	0.443	8.364	21.16
U	0.260	0.189	0.868	1.108	0.048	0.010	1.463	3.459

Table 5.19 Average and standard deviation values of trace element contents (ppm) of amphibole in the Brava veined composite rock (glimmerite/carbonatite/syenite) (08SB40), feldspar/foid pegmatite (08SB49), veined syenite-calcite rock (08SB50) and sövite (08SB39).

The highest enrichment in trace elements in amphibole occurs in sample 08SB40 and 08SB49, while the veined syenite-calcite rock followed by the sövite are less enriched. Overall the total REEs in amphibole in the associated silicate samples

is much higher than in the sövite. The chondrite-normalised REE pattern of amphibole (Fig 7.45.2) has a somewhat sinusoidal pattern with lower LREEs and MREEs and elevated HREEs. Amphibole in Brava carbonatite shows much lower Ba, U, Nb, Ta and Y values than in associated silicate rocks. Ba in the sövite develops trough rather than peak. Amphibole undergone alteration by circulated fluid and associated apatite is enriched in those elements (excluding Ta). Perhaps it is why this amphibole shows such as low values. Pegmatite contains highest Nb and Ta content while carbonatite lowest.

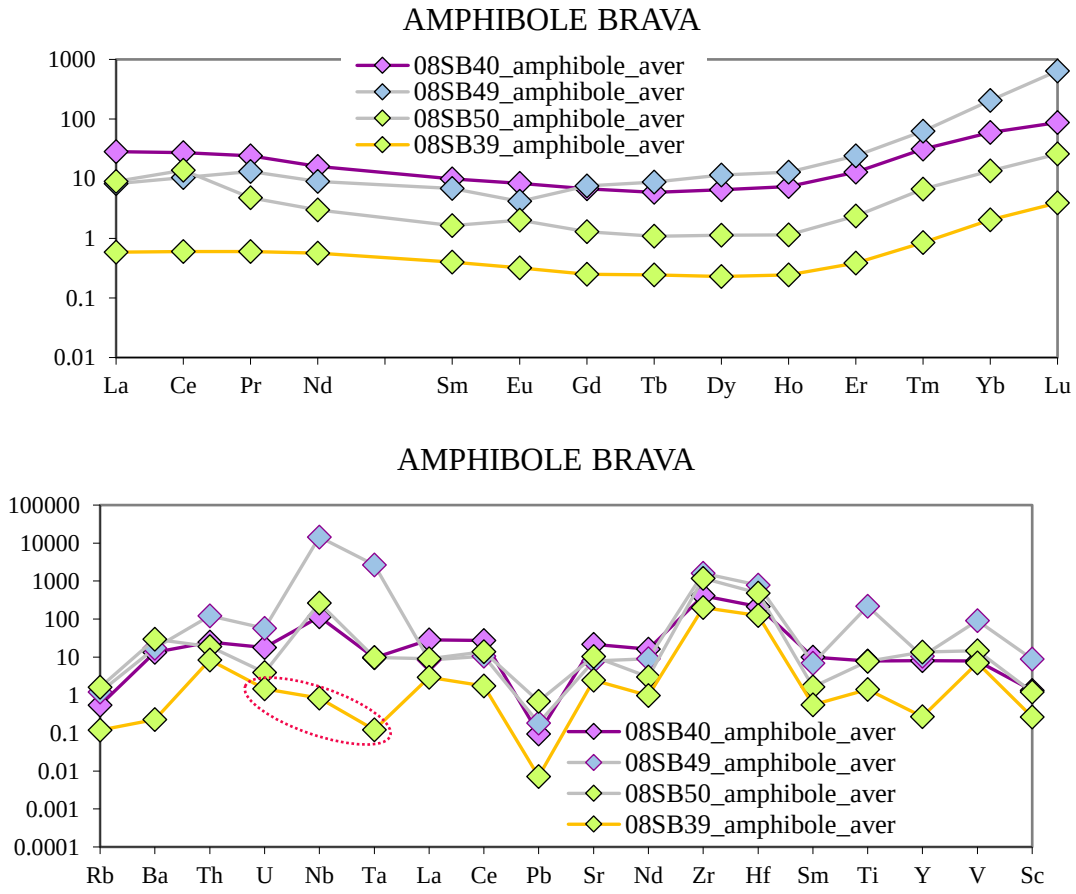

Fig 5.45a Chondrite-normalised REE and trace element distribution patterns of amphibole in the Brava in veined composite rock (glimmerite/carbonatite/syenite) (08SB40), feldspar/foid pegmatite (08SB49), veined syenite-calcite rock (08SB50) and sövite (08SB39).

Amphibole in the feldspar/foid pegmatite (08SB49) stands out in showing the highest concentration in Hf (140 ppm), Ta (70 ppm), Mn (64000 ppm), Zr (9000 ppm) and Nb (5400 ppm). To a lesser degree the glimmerite/carbonatite/syenite sample (08SF40) shows enrichment mainly in Mn (7400 ppm), Sr (260 ppm) and Zr (2300 ppm). The Ba enrichment in veind syenite-calcite rock and feldspar/foid pegmatite varies 70 -100 ppm. The sövite (08SB39) shows the lowest concentration in analysed

trace elements. The REE and trace element amphibole diagrams show consistently higher concentration of these elements in silicate samples than in sövite. Out of all silicate samples the most enriched in trace elements is composite glimmerite/carbonatite/syenite rock (08SB40).

Similarity in REE patterns (Figure 5.45b) of amphibole on Fogo and Brava confirms that the same processes operated in both localities. The Vuoriyarvi pattern is different having higher enrichment with convex upward trend (opposite to Cape Verde samples) indicating different processes occurring in the magma.

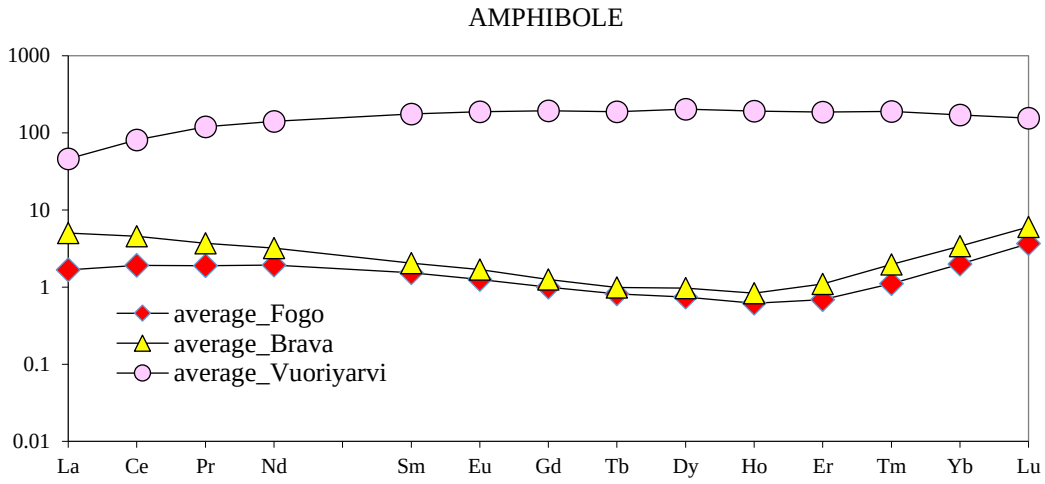

Fig 5.45b. Chondrite-normalised REE patterns of average amphibole on Brava, Fogo and Vuoriyarvi.

Trace elements in phlogopite was analysed in syenite cut by orthoclase vein (08SB48). The data are presented in Table 7.5.4a (Appendix 3b) and Figure 7.46.1 and average values are shown in Table 5.20 and Figure 5.46. Phlogopite shows low contents of LREEs (close to chondrite values) declining towards HREEs (convex upward patterns). Overall phlogopite is depleted in trace elements. Only Ba and Sr concentration are slightly above chondritic values and values of U, Nb, Ta, Zr, Hf and Ti are extremely low (below detection limit).

Figure 5.46 captures REE in phlogopite-biotite found on Brava, Fogo and Vuoriyarvi. Fogo pattern is largely subparallel to Vuorijarvi. The Vuoriyarvi samples are mostly enriched in LREEs and MREEs forming a peak at Eu. The Brava phlogopite-biotite is close to chondritic values except for HREEs, which are below these values. Mica from Fogo are mostly depleted in REEs with the exception of La (close to chondrite values) declining futher towards HREEs.

PHLOGOPITE				PHLOGOPITE	
Trace Element Concentrations ppm				normalised to chondrite	
08SB48					
	ave n=6	st dev n=6		ave n=6	st dev n=6
Sc	0.008	0.004	La	2.423	0.529
Ti	0.029	0.003	Ce	2.470	0.815
V	0.006	0.003	Pr	2.290	0.539
Mn	31.08	20.36	Nd	2.179	0.528
Co	0.001	0.001	Sm	1.743	0.470
Ga	0.099	0.085	Eu	1.512	0.424
Ge	0.018	0.007	Gd	1.240	0.327
Rb	0.454	0.358	Tb	1.017	0.289
Sr	65.13	8.24	Dy	0.911	0.248
Y	1.656	0.565	Ho	0.830	0.250
Zr	2.444	4.878	Er	0.753	0.226
Nb	0.003	0.002	Tm	0.628	0.184
Cs	845.4	786.5	Yb	0.508	0.159
Ba	13.92	4.96	Lu	0.348	0.118
La	0.888	0.191		[illegible]	[illegible]
Ce	2.365	0.779	Rb	0.110	0.107
Pr	0.314	0.074	Ba	4.083	1.452
Nd	1.547	0.374	Th	0.324	0.136
Sm	0.403	0.108	U	0.002	0.004
Eu	0.132	0.037	Nb	0.005	0.006
Gd	0.379	0.100	Ta	0.001	0.001
Tb	0.059	0.017	La	2.423	0.529
Dy	0.347	0.095	Ce	2.470	0.815
Ho	0.071	0.021	Pb	0.004	0.002
Er	0.188	0.057	Sr	5.472	0.693
Tm	0.022	0.007	Nd	2.179	0.528
Yb	0.126	0.040	Zr	0.294	0.718
Lu	0.013	0.005	Hf	0.000	0.000
Pb	0.016	0.006	Sm	1.743	0.470
Th	0.014	0.006	Ti	0.000	0.000
			Y	0.736	0.251

Table 5.20 Average and standard deviation values of trace element contents (ppm) and chondrite-normalised contents of phlogopite in the Brava syenite cut by orthoclase vein (08SB48).

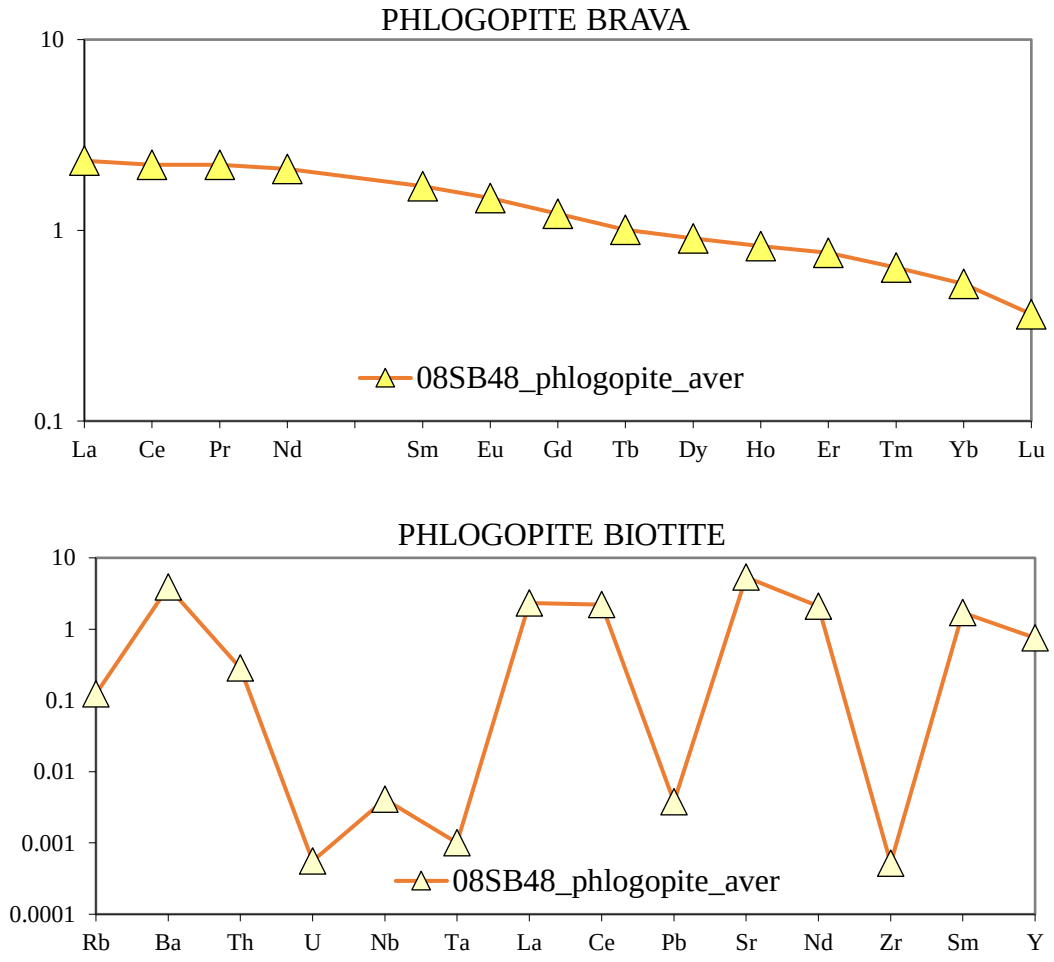

Fig 5.46a Chondrite-normalised REE and trace element distribution patterns of phlogopite in the Brava syenite cut by orthoclase vein (08SB48).

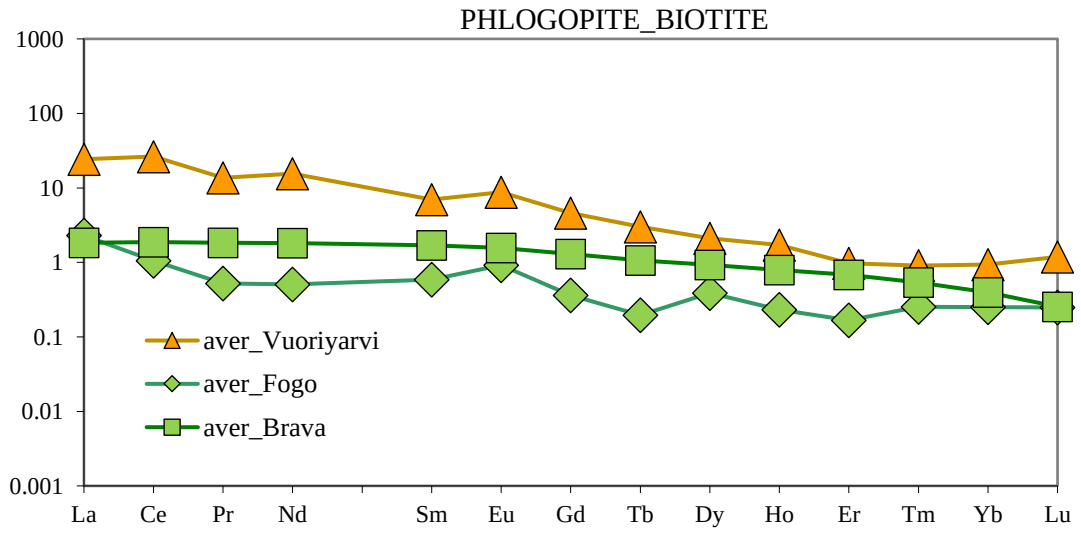

Fig 5.46b Chondrite-normalised REE patterns of average phlogopite-biotite series on Brava, Fogo and Vuoriyarvi.

Feldspar occurs in orthoclase vein (08SB48), feldspar/foid pegmatite (08SB49), glimmerite/carbonatite/syenite sample (08SF40) and sövite (08SB39). The trace element data presented in Table 7.5.5a (Appendix 3b) are for orthoclase. The average values are presented in Table 5.21. The REEs and trace elements diagram for feldspar is given in Figure 7.47.1 (Appendix 3b). The REEs and trace elements diagram for listed phases with their average values is presented in Figure 5.47.

	ORTHOCLASE						FELD_1		FELD_2	
	Trace Element Concentrations_ppm									
	08SB40		08SB48		08SB49		08SB39		08SB39	
Sc	1.067	*0.691*	2.353	*0.313*	2.837	*4.774*	0.891	*0.128*	1.014	*0.158*
Ti	47.61	*70.342*	6.613	*1.081*	bdl	*bdl*	0.153	*0.035*	0.010	*0.011*
V	1.464	*2.318*	1.075	*0.634*	bdl	*bdl*	232.33	*28.36*	13.67	*12.95*
Cr	bdl	*bdl*	2.930	*bdl*	bdl	*bdl*	7.143	*3.331*	1.292	*bdl*
Mn	7.715	*12.106*	2.740	*0.736*	9.639	*13.436*	0.008	*0.001*	0.015	*0.011*
Co	0.055	*dbl*	0.154	*bdl*	bdl	*bdl*	1.495	*0.640*	0.459	*0.158*
Ni	bdl	*dbl*	bdl	*bdl*	bdl	*bdl*	1.246	*0.202*	3.921	*2.742*
Cu	0.407	*0.435*	1.658	*1.419*	4.640	*bdl*	5.253	*2.854*	11.602	*5.027*
Ga	5.750	*2.628*	44.69	*10.06*	27.79	*46.811*	148.5	*18.20*	87.56	*27.71*
Ge	bdl	*dbl*	bdl	*bdl*	bdl	*bdl*	1.379	*0.350*	1.097	*0.421*
Rb	7.280	*5.777*	12.11	*4.335*	11.61	*19.57*	465.9	*57.14*	291.2	*93.66*
Sr	89.38	*15.69*	456.06	*39.36*	77.97	*66.39*	1984	*1182*	1375	*159.5*
Y	0.286	*0.120*	4.663	*0.790*	1.031	*0.494*	0.967	*0.342*	2.693	*1.362*
Zr	2.823	*3.032*	9.802	*2.215*	2.825	*3.925*	110.96	*23.92*	31.68	*10.21*
Nb	0.030	*0.032*	0.236	*0.144*	bdl	*bdl*	4.573	*0.310*	0.873	*0.972*
Cs	0.595	*0.503*	8.982	*1.379*	14.21	*23.90*	9.379	*3.347*	21.01	*10.38*
Ba	68.33	*23.23*	320.0	*65.72*	62.21	*96.42*	350.0	*105.6*	585.2	*246.5*
La	0.656	*0.023*	9.607	*2.695*	5.165	*0.658*	0.491	*0.033*	2.378	*1.332*
Ce	0.151	*0.150*	0.254	*0.087*	0.095	*0.071*	0.883	*0.276*	2.086	*1.620*
Pr	0.107	*0.040*	1.755	*0.472*	0.932	*0.995*	0.101	*0.023*	0.352	*0.196*
Nd	0.345	*0.130*	6.493	*1.673*	4.705	*3.627*	0.296	*0.031*	1.252	*0.653*
Sm	0.082	*0.024*	1.098	*0.248*	0.633	*0.534*	0.078	*0.028*	0.240	*0.079*
Eu	0.016	*0.009*	0.358	*0.087*	0.159	*0.129*	0.029	*0.005*	0.103	*0.044*
Gd	0.073	*0.035*	0.905	*0.188*	0.355	*0.268*	0.069	*0.004*	0.326	*0.123*
Tb	0.008	*0.005*	0.133	*0.015*	0.041	*0.031*	0.015	*0.001*	0.058	*0.038*
Dy	0.052	*0.031*	0.788	*0.194*	0.237	*0.178*	0.158	*0.048*	0.423	*0.196*
Ho	0.010	*0.004*	0.130	*0.040*	0.035	*0.024*	0.021	*0.009*	0.084	*0.040*
Er	0.031	*0.007*	0.397	*0.096*	0.085	*0.034*	0.079	*0.052*	0.313	*0.164*
Tm	0.004	*0.002*	0.052	*0.017*	0.012	*0.007*	0.020	*0.005*	0.053	*0.030*
Yb	0.043	*0.031*	0.376	*0.063*	0.051	*0.033*	0.153	*0.078*	0.416	*0.257*
Lu	0.005	*0.003*	0.055	*0.011*	0.008	*0.000*	0.013	*0.009*	0.061	*0.037*
Hf	0.259	*0.223*	0.260	*0.106*	0.690	*bdl*	7.865	*2.462*	0.929	*0.147*
Ta	0.009	*0.006*	0.006	*0.002*	0.067	*bdl*	0.258	*0.032*	0.029	*0.029*
Pb	0.125	*0.043*	1.012	*0.231*	bdl	*bdl*	1.489	*0.541*	1.553	*0.636*
Th	0.007	*0.004*	0.233	*0.039*	0.010	*0.012*	0.116	*0.037*	1.271	*1.319*
U	0.002	*bdl*	0.041	*0.012*	0.003	*0.001*	0.047	*0.018*	0.091	*0.039*

Table 5.21 Average and standard deviation values of trace element contents (ppm) of orthoclase in the Brava veined composite rock (glimmerite/carbonatite/syenite) (08SB40), syenite cut by orthoclase vein (08SB48), feldspar/foid pegmatite (08SB49) and sövite (08SB39).

Orthoclase from both silicate and sövite rocks show similar REE patterns but feldspar from sövite either has a Ce negative anomaly or none while that from silicate samples developed a pronounced Ce negative anomaly. Feldspar from samples are slightly enriched in LREE with the MREES and HREEs falling below chondritic values.

Feldspar from sövite has highest content of Sr (1400-2000 ppm), whereas that from orthoclase vein is lower (450 ppm Sr) and the remaining silicate samples have much lower concentrations (80-90 ppm Sr). Feldspar in the sövite 08SB39 is also enriched in Rb (300-500 ppm) with silicate samples having only 10 ppm Rb. Ba content is also elevated in the sövite (350-600 ppm).

Figure 7.43.6c compares REE in orthoclase found on Brava and Fogo (absent in Vuoriyarvi). Both patterns are largely subparallel though the Fogo shows higher enrichment than the Brava orthoclase. Also the Brava feldspar developed trough in Ce (absent in Fogo). Most likely alteration (formation of low-T secondary minerals such as hilairite) has affected trace element distribution.

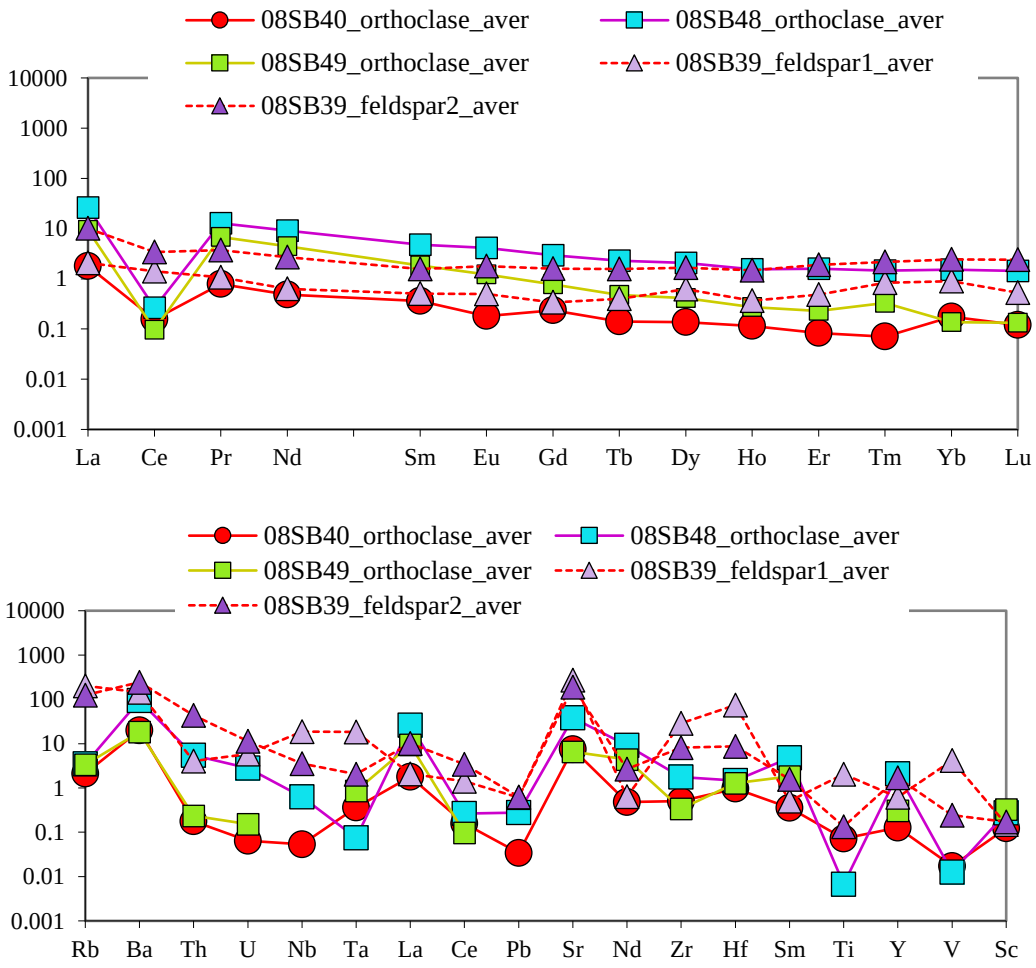

Fig 5.47a Chondrite-normalised REE and trace element patterns of orthoclase in the Brava veined composite rock (glimmerite/carbonatite/syenite) (08SB40), syenite cut by orthoclase vein (08SB48), feldspar/foid pegmatite (08SB49) and sövite (08SB39).

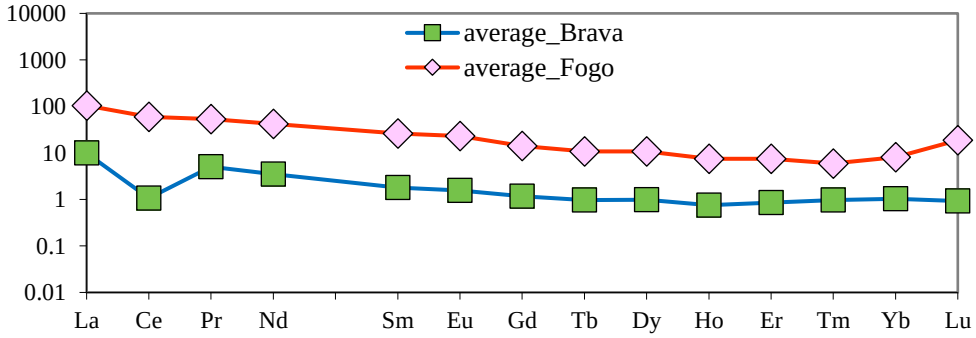

Fig 5.47b Chondrite-normalised average REE patterns of orthoclase in the Brava and Fogo rocks.

The chemical compositions of Brava hilairite and ilmenite are presented in Table 7.5.7a (Appendix 3b) with average values given in Table 5.21 and Figure 5.48.

	HILAIRITE 08SB40		ILMENITE 08SB48	
	Laser-ICPMS analyses ppm			
	ave n°4	st.dev n°4	ave n°5	st.dev n°5
Sc	11163	18684	1.807	0.357
Ti	116953	203379	219830	154752
V	132.4	166.7	236.7	159.5
Cr	bdl	bdl	bdl	bdl
Mn	467.9	729.2	12961	15617
Co	bdl	bdl	1.674	1.002
Ni	bdl	bdl	bdl	bdl
Cu	97.23	bdl	1.842	0.933
Ga	600.9	723.7	77.5	42.72
Ge	bdl	bdl	1.360	bdl
Rb	1255	2227	33.41	37.39
Sr	10739	16032	538.6	126.1
Y	11769	21845	27.49	8.334
Zr	3693742	2028165	503.8	587.7
Nb	76259	136494	13320	8331
Ba	2544	3340	902.9	567.3
La	20.87	34.39	83.28	34.19
Ce	99.99	169.5	116.3	63.55
Pr	17.51	29.70	16.75	6.228
Nd	46.61	77.27	61.1	21.05
Sm	40.39	54.57	10.57	3.169
Eu	11.00	18.14	3.086	1.011
Gd	86.42	140.2	7.466	2.194
Tb	39.51	74.31	1.087	0.379
Dy	725.6	1368.8	5.998	2.105
Ho	273.9	511.4	1.215	0.414
Er	1507	2767	3.248	1.196
Tm	401.9	719.1	0.400	0.084
Yb	4474	7908	2.66	0.518
Lu	624.4	1080	0.296	0.079
Hf	366171	635368	13.48	16.02
Ta	1025	1810	135.3	83.98
Pb	109.9	132.2	155.5	92.72
Th	2186	3977	1.721	1.077
U	1909	3307	0.581	0.332

	HILAIRITE 08SB40		ILMENITE 08SB48	
	Trace element concentrations normalised to chondrite.			
	ave n°4	st.dev n°4	ave n°5	st.dev n°5
La	42.66	81.63	226.9	93.15
Ce	78.36	153.8	121.5	66.4
Pr	95.87	188.2	122.3	45.48
Nd	49.17	94.59	85.94	29.61
Sm	87.42	169.7	45.77	13.72
Eu	94.82	181.6	35.47	11.62
Gd	211.8	400.0	24.4	7.163
Tb	681.1	1281.2	18.72	6.55
Dy	1905	3593	15.74	5.531
Ho	3218	6010	14.29	4.859
Er	6051	11114	13.05	4.801
Tm	11290	20200	11.23	2.36
Yb	18041	31886	10.74	2.092
Lu	16390	28353	7.762	2.076
	ave n°4	st.dev n°4	ave n°5	st.dev n°5
Rb	363.8	645.4	9.686	10.84
Ba	746.1	979.5	264.8	166.4
Th	51433	93565	40.53	25.35
U	156478	271064	47.67	27.28
Nb	203358	363983	35519	22215
Ta	39440	69631	5205	3230
La	42.66	81.63	226.9	93.15
Ce	78.36	153.8	121.5	66.40
Pb	15.06	27.19	61.78	28.39
Sr	902.4	1347	45.26	10.60
Nd	49.17	94.59	85.94	29.61
Zr	666695	366061	90.94	106.1
Hf	2045649	3549540	75.29	89.48
Sm	87.42	169.7	45.77	13.72
Ti	178.8	311.0	336.1	236.6
Y	5231	9709	12.22	3.704
V	0.778	1.444	2.787	1.878
Sc	1292	2162	0.125	0.118

Table 5.21 Average and standard deviation values of trace element contents (ppm) and chondrite-normalised contents of hilairite and ilmenite in the Brava veined composite rock (glimmerite/carbonatite/syenite) (08SB40) and syenite cut by orthoclase vein (08SB48) respectively.

Both minerals show enrichment in the REEs (Figure 5.48) and particularly high concentration in LREEs. Ilmenite shows greater enrichment in La (83 ppm) than hilairite (21 ppm La). The chondrite-normalised diagram displays steady trend in enrichment in LREEs, but there is a pronounced difference between hilairite and ilmenite in MREEs and HREEs. Hilairite exhibits convex upward patterns with the high preference for MREEs and HREEs while ilmenite exhibit steadily decline pattern towards HREEs. Some other trace element concentrations also differ between ilmenite and hilairite. HFSE enrichment in Zr in ilmenite is 500 ppm, Nb 80000 ppm and 10000 ppm, Hf 400000 ppm and 10 ppm, and Ta 1000 ppm and 130 ppm. Hilairite is also rich in Th (2000 ppm) and U (2000 ppm) while in ilmenite concentration is low (2 ppm Th; 0.6 ppm U). Hilairite and ilmenite also contain Sr (10000 ppm and 500 ppm, respectively) and other LILE such as Ba (2500 ppm and 900 ppm) and Rb (1200 ppm and 30 ppm). Mn concentration is

significant in ilmenite (13000 ppm) and to lesser degree in hilairite (500 ppm). The V enrichment is slightly lower in hilairite than ilmenite (130 ppm and 240 ppm). Even though both phases are rare, hilairite and to a lesser degree ilmenite, play important role in incorporating trace elements. Hilairite reveals a significant enrichment in HFSE together with Th and U. Also hilairite contain considerably high concentration of MREEs and HREEs as well as LILE. Ilmenite plays important role in incorporation of Nb and Ta.

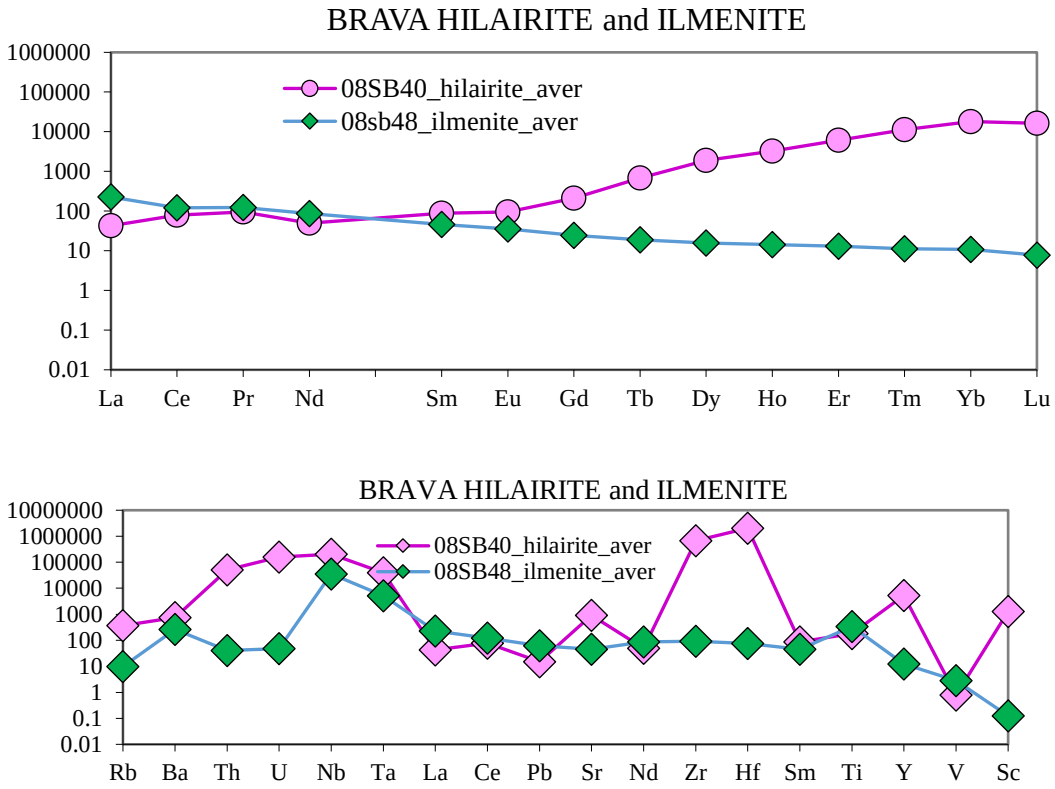

Fig 5.48 Chondrite-normalised REE and trace element patterns of hilairite and ilmenite in veined composite rock (glimmerite/carbonatite/syenite) (08SB40) and syenite cut by orthoclase vein (08SB48) respectively.

5.7 Summary of trace element distribution

The REEs diagrams of Brava apatite and calcite show sub-parallel LREE-enriched profiles, spread over three to four degrees of enrichment. Syenite cut by orthoclase vein and feldspar/foid pegmatite is slightly different with similar calcite LREEs and MREEs concentration, evidence of comparable fractionation of elements. Rb, Ta, Zr and Hf show negative anomalies in calcite though apatite in sövite displays enrichment up to 100 times of chondritic value. Apatite is also highly enriched in Th and Nb though calcite is depleted in those elements as well as U. Both apatite and calcite from Brava show highest enrichment in trace elements in carbonatite and to lesser degree in associated silicate rocks. Similar pattern is found in carbonatites from Fogo, also sub-parallel.

The concentration of trace elements in amphibole is rather low though Hf, Ta, Mn, Zr and Nb found in the feldspar/foid pegmatite and in the glimmerite-carbonatite-syenite samples is considerable. Ba enrichment is highest in veined syenite-calcite rock and in feldspar/foid pegmatite. Overall, the sövite displays the lowest enrichment, however some significant amounts of Hf and Zr was found here. The REEs enrichment in amphibole from silicate samples is higher in than in sövite. Generally, amphibole from the silicate samples is the most enriched, with the highest values in the composite glimmerite/carbonatite/syenite rock. Comparison of amphibole in REE from Fogo, Brava and Vuoriyarvi reveals that similar processes operated in Cape Verde rocks though the Vuoriyarvi samples were affected by different processes occurring in the magma.

Phlogopite is present only in two Brava samples. It is overall depleted in trace elements. However, concentration of Ba and Sr is above the chondritic values. Also, elements such as Mn and Cs occur in considerable amounts. Trace elements in phlogopite-biotite from Brava, Fogo and Vuoriyarvi reveals that Fogo pattern is sub-parallel to Vuorijarvi while Brava samples display depletion in REEs most likely affected by alteration and formation of low-T phases and REE-phases.

Orthoclase shows slight enrichment in LREE. Overall, all feldspars REEs pattern is similar though they differ in Ce content and development of trough is due to formation of hilairite which affected trace element distribution. The feldspar in sövite also shows highest enrichment in Sr however in the silicate samples contain low concentration. Sövite feldspar is also enriched in Rb and Ba with silicate samples holding much lesser content of trace elements. Brava and Fogo orthoclase, being chiefly subparallel, shows higher enrichment in Fogo samples with Brava feldspar also developing depletion in Ce content, which again is due to formation of low-T secondary minerals (hilairite).

Along the major phases some accessory minerals such as hilairite and ilmenite were found, both from silicate samples. They demonstrate high concentration in LREEs with greater enrichment in La in ilmenite and slighter lower in hilairite. There is a pronounced difference between hilairite and ilmenite in MREEs and HREEs with hilairite having higher preference for MREEs and HREEs, while ilmenite show steady down drift towards HREEs. The HFSE concentration in Zr, Nb, Hf and Ta in hilairite is higher than in ilmenite. Also, hilairite is more abundant in Th and U than in ilmenite. The same applies to Sr and LILE such as Ba and Rb. The opposite relates to Mn concentration which is significant in ilmenite as well as the V content. Both accessory minerals from the Brava samples are important in incorporating most of the trace elements.

CHAPTER 6
CONCLUSIONS AND FURTHER WORK

Of the investigated sites, Vuorijarvi is least affected by fenitization and covers the best-preserved evidence of magmatic processes. The Vuorijarvi carbonatite formed in an early stage, most likely just after immiscibility from its silicate counterpart. During emplacement of the carbonatite into pyroxenite (and associated phoscorite), the primary tabular calcite texture was obliterated by a secondary mosaic one. Investigation of globular calcite and apatite in silicate phases ruled out the possibility of immiscibility. They were formed by solid state precipitation from a silicate melt as a high temperature polymorph. The rare calcite-monticellite intergrown texture formed by simultaneous crystallisation of both phases. Subsolidus recrystallisation of olivine to monticellite reflects the early stages of carbonatite formation.

The influence of early fenitization is shown by the existence of adjacent zones containing anhydrous monticellite and hydrous amphibole (Na-rich edenite). Presence of perovskite and lack of pyrochlore can result from a deficiency of F in the system. Formation of Zr-garnet might result from complex substitution in perovskite leading to formation of Zr-rich garnet. Resorption of xenocrystic phlogopite modified the carbonatite liquid in its Si- and Mg-components. The complex core-rim zonation in the Vuoriyarvi magnetite reflects changeable conditions influenced by crystallisation, assimilation and post-solidus alteration. Two rock-forming phases, calcite and apatite, contain the majority of LREE, though enrichment in calcite is two orders lower than in apatite. Exotic phases such as Zr-garnet alongside perovskite exhibit partition coefficients with strong compatibility for many trace elements such as Zr and Nb and HREE (perovskite) and LREE (Zr-garnet). The remaining phases do not play important role in hosting trace elements.

The second investigated site of Fogo shows more deformation than Vuorijarvi and also is affected to higher degree by hydrothermal processes. Fogo carbonatites contain a large amount of primary calcite with a lesser amount of secondary calcite found in veins, voids and as inclusions in other phases. Two populations of apatite can be distinguished by texture, grain size and chemistry. Crystallisation of apatite was continuous. Hopper crystals show enrichment in LREEs due to rapid crystallisation though a preference for Ce over other LREEs is apparent. Samples from the Rib. de Almada have more primitive pyroxene than those from Monte Almada which also is the case for the evolution of mica.

Rib. de Almada is associated with emplacement of potassic (glimmeritic) sheets into intrusive carbonatite during which stress produced fractures in the form of net-veining. This created pathways for hydrothermal fluids (fenitization) and crystallisation of accessory minerals. Robeira Domingo Santo site represents a highly oxidised carbonatite, which lacks mafic silicates due to reduced activity of silica. Monazite formed as a replacement of apatite. Metamorphism, induced by localised shear zones accounts for formation of preferred orientation and passage of REE-rich hydrothermal fluids, hence alteration of early-formed phases. Highly oxidised state reflects low-temperature hydrothermal alteration. Monte Almada contains amphiboles not found in other sites. This reflects K-fenitization formed in the shallow levels of sövite. Na-fenitization is found at deeper levels and formed earlier (above 600ºC). Higher mobility of K allows it to be transferred to shallow levels while Na would stay close to the carbonatite intrusion (deeper levels).

Existence of phlogopite, intimately associated with rare phases, provides insight into crystallisation of titanite, zirconolite, zircon and pyrochlore in Fogo sites. Hf enriched phlogopite is associated with zircon, which is lacking in this element. This reflects the lower mobility of HREEs over LREEs which can travel further away from the system. Zircon, zirconolite and titanite are depleted in Hf as the system was already exhausted in Hf content. Geochemistry of zeolites and feldspathoids argue for their derivation from the hydration and alteration of pre-existing feldspathoids. Turbid texture of feldspar, together with assemblage of alkali amphibole/pyroxene, apatite, garnet and calcite, indicates that fenitization controlled modification of texture and chemistry in a form of pervasive fenitization, which was responsible for alkali fluid circulating around phases, while veined fenitization runs through fractures in present phases. As zircon is an uncommon phase in carbonatites due to low silica activity, its presence reflects high localised silica-saturation in overall undersaturated carbonatite. Nb-pyrochlore (Th-U-rich) has a hydrothermal origin causing localised dissolution of Zr-rich precursors by hydrothermal fluids (rich in Nb/Th/U) and recrystallisation into current assemblage. This process operated in later stages and was also highly dependent on precursor minerals. Postmagmatic changes, also involving metasomatic fluids, led to continuous alteration of magnetite → titanomagnetite → ilmenite → garnet and finally to titanite.

The main phases showing enrichment in trace elements are calcite and apatite. Different levels of enrichment in calcite reflect inhomogeneity of this phase. The concentration of trace elements in pyroxene and amphibole is rather low. The same applies to mica (close to the chondritic values) though LILE (Rb and Ba) and HFSE (Nb

and Ta) together with Sr and Zr showing substantial enrichment. Other major phases do not play an important role in hosting trace elements though accessory minerals such as garnet and titanite (similar trace element patterns) have been largely enriched in REEs and HFSE (Th, U and Nb), reflecting post-magmatic metasomatism by fluids enriched in these elements.

The third site, Brava, shows greatest degree of low temperature alteration. Brava seamount samples consist of scarce sövite and an abundant variety of silicate rocks reflecting a small body of carbonatite present in L5 site. The field association and analyses of alkaline rocks provided the conclusion that the carbonatites formed during the later stages of formation of the Brava alkaline complex. The silicate counterpart inherited the rare elements and REE-signature in the form of unusual mineralogical assemblages during fenitization (loss of alkalis) and hydrothermal alteration (which also altered/replaced some carbonatites). The upward movement of the seamount produced fractures that were exploited by the fluids and crystallisation of zeolites filling the voids. Also Al-Si-rich fluids formed zeolites by replacement of calcite. Primary and secondary calcite show chemical diversity/zonation implying complex events of growth. Rare apatite displays alteration and shows an intimate association with Nb- or Zr-rich phases (co-crystallisation of late-stage phases). Albitisation was associated with Na-metasomatism (fenitization). Homogeneous orthoclase originated from metasomatic (fenitic) fluids.

Clinopyroxene shows a magmatic fractionation trend from diopside towards aegirine with progressive enrichment in Zr, Th, U and LREEs. Amphibole occurs as a primary or secondary phase (alteration after clinopyroxene). Mica in sövite is phlogopitic formed during metasomatism. The silica-undersaturated samples show an evolution of phlogopite towards highly evolved biotite and involvement of late-stage fluid circulation altering mica to phengite and to the Mn-chlorite pennantite. Evolution of magnetite to titanomagnetite, ilmenite, titanite, rutile and finally to henrymeyerite was progressive. Increase in REEs, Nb, Zr and Ba demonstrates progressive incorporation of these elements leading to alteration of earlier formed minerals by interaction with late-stage fluids.

Increase in activity of hydrothermal fluids rich in Mn, Sr and Zr is displayed in zoned pyrochlore. Zr-rich minerals crystallised in the last stages of hydrothermal activity at temperature < 150°C, during which hilairite was able to form. Lower concentration of Ti in tazheranite reflects the very close association with rutile and interaction with fluids. REE-phases provide some insight into fluoride and chloride activity aiding their

crystallisation (törnebohmite holds considerable amounts of fluorine). Petrographic features of rhabdophane argues for formation of this mineral from a hydrothermal fluid. Spherulitic texture in lanthainite requires high supersaturation and rapid dissolution of the amorphous precursors of the hydrated crystalline form, with very low fluid temperatures (60-90°C). The chemistry and assemblage in sövites of strontian calcite and calcian strontianite with the presence of carbocernaite, all exsolved in calcite, is primary in origin. The associated silicate phases rimming calcic-areas and containing parisite are metasomatic. Burbankite and barite, both residing in Mn-calcite, are considered to be hydrothermal in origin. The REE patterns of apatite and calcite show sub-parallel profiles, spread over three to four degrees of enrichment. The concentration of trace elements in amphibole is low though Hf, Ta, Mn, Zr and Nb found in the feldspar/foid pegmatite and in the glimmerite-carbonatite-syenite samples is considerable. Phlogopite is depleted in trace elements. Accessory hilairite and ilmenite demonstrate high concentration in LREEs with greater enrichment in La in ilmenite. There is a pronounced difference between hilairite and ilmenite in MREEs and HREEs, with hilairite having higher preference for MREEs and HREEs, while ilmenite show steady decrease towards HREEs. The HFSE concentration in Zr, Nb, Hf and Ta in hilairite is higher than in ilmenite. Also hilairite has higher Th and U concentrations than ilmenite.

Further work would involve making thin-sections of the Cape Verde samples with oil-based polishing instead of water-based, hopefully to preserve phases during section preparation. Also to calculate the partition coefficient for REE, HFSE and LILE to determine more precise the role of the trace elements in the Cape Verde samples. The sövite and associated silicate melt in proposed study would be represented by the whole rock composition, which would involve obtaining the data for the bulk-rock composition of the appropriate samples as the Cape Verde samples are unique and diverse. To carry out a bulk-rock analysis would be important but also time consuming as all hand specimens are higly varied. Thus obtaining these data would be completed in near future.